

FINAL REPORT

Physics-based Prediction of Unexploded Ordnance Penetration in Granular Materials

SERDP Project MR-2630

MAY 2017

Jae H. Chung
Theodor Krauthammer

Postdoctoral Researchers
Amirata Taghavi
Michael Davidson
Michael Faraone

Graduate Research Assistants:
Nikhil Mishra, Yu Zhang,
Michael Stone, Adam Taylor,
Kapyia Ilay
University of Florida

Distribution Statement A

This document has been cleared for public release



Page Intentionally Left Blank

This report was prepared under contract to the Department of Defense Strategic Environmental Research and Development Program (SERDP). The publication of this report does not indicate endorsement by the Department of Defense, nor should the contents be construed as reflecting the official policy or position of the Department of Defense. Reference herein to any specific commercial product, process, or service by trade name, trademark, manufacturer, or otherwise, does not necessarily constitute or imply its endorsement, recommendation, or favoring by the Department of Defense.

Page Intentionally Left Blank

(Revised March 2003)

1. Report No.	2. Government Accession No.	3. Recipient's Catalog No.	
4. Title and Subtitle Physics-based Prediction of Unexploded Ordnance Penetration in Granular Materials, Final Report		5. Report Date May 2017	
		6. Performing Organization Code	
7. Author(s) Chung, J. H., Krauthammer, T., Zhang, Y., Mishra, N., Taghavi, A., Stone, M., Davidson, M. T., Taylor, A., Faraone, M., Patil, A., Ilay, K.		8. Performing Organization Report No.	
9. Performing Organization Name and Address Computer Laboratory for Granular Physics Studies University of Florida 1949 Stadium Rd. Suite 365 P.O. Box 116580 Gainesville, FL 32611		10. Work Unit No. (TRAIS)	
		11. Contract or Grant No. MR2630 SEED	
12. Sponsoring Agency Name and Address Strategic Environmental Research and Development Program (SERDP) 4800 Mark Center Drive, Suite 17D08, Alexandria, VA 22350-3605		13. Type of Report and Period Covered Final Report 3/7/2016 - 2/28/2017	
		14. Sponsoring Agency Code	
15. Summary The present research report contains a combined analytical, numerical, and experimental methodology for the quantification of the maximum penetration depth of unexploded ordnance (UXO) into dry granular media at thermodynamic equilibrium under gravitational lithostatic stress states. Penetration into in-situ granular media is considered to be an unsteady-state boundary-value problem that may refer to transient phenomena at a number of interrelated scales. These scales span across apparent contact areas of sub-microscopic and microscopic surface roughness, corresponding intragrain heterogeneous deformation and interparticle friction at grain scales, grain-scale damping and inertia in formation of force chains and corresponding particle rearrangement at continuum scales, and collective intergranular motion through semi-infinite domains. The research findings are presented for the proof-of-concept of proposed physics-based predictive methodology on high-velocity impact and penetration of granular media at prototype scales, in relation to variational thermodynamic states at underlying scales, where mass densities (i.e., packing densities) under lithostatic stress states may vary with respect to controlled, gravitational packing processes. The results obtained from physical laboratory testing at various scales, including nano-indentation, measurement of surface energy, scanning electron and probe microscopies, grain-to-grain force-deformation in loading and unloading cycles, tri-axial compression, and prototype projectiles' penetration into a granular material in a geotechnical centrifuge, are presented alongside a series of corresponding analytical and numerical models that have been implemented in a new soft-particle contact algorithm for the combined Finite-Discrete Element Method. The test data measured at the interrelated scales are used to benchmark corresponding grain-, continuum-, and system-scale discrete and finite element analysis models. As for prototype system-scale validation, centrifuge tests of penetration depths and changes in body-force fields are conducted in mono- and poly-disperse systems for impact scenarios of a scaled-down semi-armor piercing (SAP) 2,000 lbs. projectile into assemblies of aluminosilicate spheres with two various mean diameters of 0.93 ± 0.08 mm and 0.55 ± 0.05 mm. The prediction of penetration depths per low-velocity impact scenarios is found to be strongly dependent on initial lithostatic states as per packing density distributions at system scales (e.g., relative density distributions in an in-situ condition), where momentum transfer through intergranular kinematics controls energy dissipation mechanisms through collapse (buckling) of granular assembly (structure), volumetric changes in a control volume, particulate sliding and rolling friction, and corresponding intragrain deformation and intergranular motion during projectile penetration events in the time domain. In addition, a numerical parametric study is conducted to highlight the proof-of-concept with respect to a selected number of scale-interrelated model parameters.			
16. Key Words Granular Materials; Soft-particle Contact Mechanics; Scale-dependent Shear Behaviors, Discrete Element Method		17. Distribution Statement No restrictions.	
18. Security Classif. (of this report) Unclassified	19. Security Classif. (of this page) Unclassified	20. No. of Pages 342	21. Price

Page Intentionally Left Blank

DISCLAIMER

The opinions, findings, and conclusions expressed in this publication are those of the authors and not necessarily those of the Strategic Environmental Research and Development Program (SERDP).

SI (MODERN METRIC) CONVERSION FACTORS (FROM FHWA)

APPROXIMATE CONVERSIONS TO SI UNITS

SYMBOL	WHEN YOU KNOW	MULTIPLY BY	TO FIND	SYMBOL
LENGTH				
in	Inches	25.4	millimeters	Mm
ft	Feet	0.305	meters	M
yd	Yards	0.914	meters	M
mi	Miles	1.61	kilometers	Km

SYMBOL	WHEN YOU KNOW	MULTIPLY BY	TO FIND	SYMBOL
AREA				
in²	square inches	645.2	square millimeters	mm ²
ft²	square feet	0.093	square meters	m ²
yd²	square yard	0.836	square meters	m ²
mi²	square miles	2.59	square kilometers	km ²

SYMBOL	WHEN YOU KNOW	MULTIPLY BY	TO FIND	SYMBOL
VOLUME				
fl oz	fluid ounces	29.57	milliliters	mL
ft³	cubic feet	0.028	cubic meters	m ³
yd³	cubic yards	0.765	cubic meters	m ³

NOTE: volumes greater than 1,000 L shall be shown in m³

SYMBOL	WHEN YOU KNOW	MULTIPLY BY	TO FIND	SYMBOL
MASS				
oz	Ounces	28.35	grams	G
lb	Pounds	0.454	kilograms	Kg
T	short tons (2,000 lb)	0.907	megagrams (or "metric ton")	Mg (or "t")

SYMBOL	WHEN YOU KNOW	MULTIPLY BY	TO FIND	SYMBOL
TEMPERATURE (exact degrees)				
°F	Fahrenheit	5 or (F-32)/1.8	(F-32)/9 Celsius	°C

SYMBOL	WHEN YOU KNOW	MULTIPLY BY	TO FIND	SYMBOL
ILLUMINATION				
fc	foot-candles	10.76	lux	lx
fl	foot-Lamberts	3.426	candela/m ²	cd/m ²

SYMBOL	WHEN YOU KNOW	MULTIPLY BY	TO FIND	SYMBOL
FORCE and PRESSURE or STRESS				
lbf	pound force	4.45	newtons	N
kips	Kips	4,448.22	newtons	N
lbf/in²	pound force per square inch	6.89	kilopascals	kPa
ksi	kips per square inch	6,894.76	kilopascals	kPa
tsf	tons (short) per square foot	95.67	kilopascals	kPa
pcf	pound force per cubic foot	156.967	newtons per cubic meter	N/m ³

APPROXIMATE CONVERSIONS TO SI UNITS

SYMBOL	WHEN YOU KNOW	MULTIPLY BY	TO FIND	SYMBOL
LENGTH				
mm	Millimeters	0.039	inches	in
m	Meters	3.28	feet	ft
m	Meters	1.09	yards	yd
km	Kilometers	0.621	miles	mi

SYMBOL	WHEN YOU KNOW	MULTIPLY BY	TO FIND	SYMBOL
AREA				
mm ²	square millimeters	0.0016	square inches	in ²
m ²	square meters	10.764	square feet	ft ²
m ²	square meters	1.195	square yards	yd ²
ha	Hectares	2.47	acres	ac
km ²	square kilometers	0.386	square miles	mi ²

SYMBOL	WHEN YOU KNOW	MULTIPLY BY	TO FIND	SYMBOL
VOLUME				
mL	Milliliters	0.034	fluid ounces	fl oz
L	Liters	0.264	gallons	gal
m ³	cubic meters	35.314	cubic feet	ft ³
m ³	cubic meters	1.307	cubic yards	yd ³

SYMBOL	WHEN YOU KNOW	MULTIPLY BY	TO FIND	SYMBOL
MASS				
g	Grams	0.035	ounces	oz
kg	Kilograms	2.202	pounds	lb
Mg (or "t")	megagrams (or "metric ton")	1.103	short tons (2,000 lb)	T

SYMBOL	WHEN YOU KNOW	MULTIPLY BY	TO FIND	SYMBOL
TEMPERATURE (exact degrees)				
°C	Celsius	1.8C+32	Fahrenheit	°F

SYMBOL	WHEN YOU KNOW	MULTIPLY BY	TO FIND	SYMBOL
ILLUMINATION				
lx	Lux	0.0929	foot-candles	fc
cd/m ²	candela/m ²	0.2919	foot-Lamberts	fl

SYMBOL	WHEN YOU KNOW	MULTIPLY BY	TO FIND	SYMBOL
FORCE and PRESSURE or STRESS				
N	Newtons	0.225	pound force	lbf
N	Newtons	0.000224809	kips	kips
kPa	Kilopascals	0.145	pound force per square inch	lbf/in ²
kPa	Kilopascals	0.000145	kips per square inch	ksi
kPa	Kilopascals	0.000145038	kips per square inch	ksi
N/m ³	newtons per cubic meter	0.0104526	pound force per cubic foot	pcf

*SI is the symbol for International System of Units. Appropriate rounding should be made to comply with Sec. 4 of ASTM E380.

ACKNOWLEDGEMENTS

The authors would like to thank the Strategic Environmental Research and Development Program (SERDP) for providing the funding that made this study possible.

ABSTRACT

Objectives: In accordance with the Munitions Response Program of the Exploratory Development of the Strategic Environmental Research and Development Program (SERDP) (i.e., MRSEED-16-01), the objectives of the present study are to:

- Quantify statistical penetration depths through explicit numerical simulations of projectile penetration for a variety of soil types, moisture contents, and impact conditions;
- Evaluate the influence that pertinent microscopic parameters have on projectile-penetration resistance, including: projectile size and trajectory, mesoscopic changes in thermodynamic states of soil media, and soil macroscopic characteristics;
- Quantify the effect of Coulombic damping at interparticle contacts in energy-dissipative capacities;
- Quantify the influence that size ratios of UXO to grain can have on penetration depths, and with respect to soil relative densities.

Technical Approach: The present research contains a combined analytical, numerical, and experimental methodology for the quantification of the maximum penetration depth of unexploded ordnance (UXO) into dry granular media at thermodynamic equilibrium under gravitational lithostatic stress states. Penetration into in-situ granular media is explicitly simulated using a combined Discrete Element and Finite Element Methods. Solutions to the governing equations are sought specific to a set of unsteady-state boundary values that may refer to transient phenomena at a number of interrelated scales. These scales span across apparent contact areas of sub-microscopic and microscopic surface roughness, corresponding intragrain heterogeneous deformation and interparticle friction at grain scales, grain-scale damping and inertia in formation of force chains and corresponding particle rearrangement at continuum scales, and collective intergranular motion through semi-infinite domains. The research findings are presented for the proof-of-concept of proposed physics-based predictive methodology on high-velocity impact and penetration of granular media at prototype scales, in relation to variational thermodynamic states at underlying scales, where mass densities (i.e., packing densities) under lithostatic stress states may vary with respect to controlled, gravitational packing processes. The results obtained from physical laboratory testing at various scales, including nano-indentation, measurement of surface energy, scanning electron and probe microscopies, grain-to-grain force-deformation in loading and unloading cycles, tri-axial compression, and prototype projectiles' penetration into a granular material in a geotechnical centrifuge, are presented alongside a series of corresponding analytical and numerical models that have been implemented in a new soft-particle contact algorithm for the combined Finite-Discrete Element Method. The test data measured at the interrelated scales are used to benchmark corresponding grain-, continuum-, and system-scale discrete and finite element analysis models. As for prototype system-scale validation, centrifuge tests of penetration depths and changes in body-force fields are conducted in mono-disperse systems for impact scenarios of a scaled-down semi-armor piercing (SAP) 2,000 lbs. projectile into assemblies of aluminosilicate spheres with two various mean diameters of 0.93 ± 0.08 mm and 0.55 ± 0.05 mm.

Results: The prediction of penetration depths per subsonic-velocity impact scenarios is found to be strongly dependent on initial lithostatic states as per packing density distributions at system scales (e.g., relative density distributions in an in-situ condition), where momentum transfer through intergranular kinematics controls energy dissipation mechanisms through collapse (buckling) of granular assembly (structure), volumetric changes in a control volume, particulate sliding and rolling friction, and corresponding intragrain deformation and intergranular motion during projectile penetration events in the time domain. In addition, a numerical parametric study is conducted to highlight the proof-of-concept with respect to a selected number of scale-interrelated model parameters.

Benefits: Both synthesis and critical analysis of the numerically generated and physically measured data from this project are to be carried out in establishing practical conclusions and recommendations for field applications. More specifically, those parameters which hold greatest significance can be identified by: 1) Tabulating numerical predictions of the UXO-soil system response alongside model input values and then, 2) Identifying trends in the tabulations of input values with respect to the penetration-depth quantities. Those parameters that retain significance (i.e., give indications of meaningful input-response trends) when processed in this way can be directly packaged (via graphs and tables) into graphical guidelines for use by the munitions response community. Further, this physics-based multi-scale quantification can further be elaborated as to complement previous research findings. For instance, given datasets for interrelated values of rate-dependent shearing resistance, damping forces, effective inertia, particle breakage and drag forces, corresponding terminal penetration depths can be evaluated as per granular properties, including, but not limited to, scale-dependent intergranular friction coefficient, grain size and shape, moisture contents and in-situ relative density states in comparison to cataloged and empirical parameter values of the existing design guidelines (e.g., “Demonstration of UXO-PenDepth for the Estimation of Projectile Penetration Depth,” ESTCP Project MR-0806, 2010). The successful outcome of the proposed research and development in phases includes:

- Cultivating design-oriented input parameters to account for development of dynamic link libraries (DLLs), which can be functionally integrated (as modules) into the existing UXO PenDepth software program; and,
- Cultivating design-oriented practical recommendations to incorporate the research findings into the Response Surface Map (RSM) module of the software PENCVR3D (Adley et al., 1999).

EXECUTIVE SUMMARY

The following report presents a combined numerical and empirical methodology for the physics-based quantification of the scale-dependent mechanical behavior of dry granular material subjected to the impact of unexploded ordnance (UXO), with particular attention paid to observable quantities such as the maximum penetration depth of the UXO. Herein, physical specimens and combined finite-discrete element models are documented, and primarily consist of high-uniformity, spherical granules. The specimens and models considered are utilized in conjunction with specialized preparation procedures to achieve pre-determined, mechanically-stable granular assemblies. Namely, for the granular assemblies considered, pluviation processes are controlled for loading history to achieve optimally-uniform relative density states, i.e., initial, gravitational lithostatic stress conditions. For physical and corresponding numerical experimentation setups, statistically-homogeneous granular assemblies are determined to be an initial condition for dry granular media subjected to low-velocity penetration tests, in association with rigid UXO. To facilitate the fundamental understanding of scale-dependent granular behaviors, a centrifuge apparatus is used to produce in-situ penetration at prototype-scales. Complimentarily, the analytical models based on extended Hertzian and Mindlin's contact theory are developed, and subsequently implemented into an existing commercial software code, which is verified against physical test results from laboratory experimentation at grain and macro (continuum) scales. The volume-averaged continuum and prototype scale strain-rate dependent shear behaviors of the granular mass, including the final penetration depth of the UXO, is shown to have strong dependence on the boundary-value parameters at a number of underlying scales. This includes intergranular contact phenomena at what is called the grain scale are originated from sub-microscopic thermodynamic states called surface energy, which in turn produces the variation of surface forces at the grain scale, i.e., the surface topography of the grains. The importance of the microscopic variation is unique because the mechanical stability of granular assemblies can be influenced by load-dependent contact stiffnesses, which determines contact deformations during and after the formations of force chains. Further, in modeling mechanically stable states of granular assemblies, the evolution of intergranular surface-contact forces may vary with respect to the kinematics of discrete particles in contact. Thus, for soft-particle dynamic analyses aimed at characterizing observational behaviors of granular materials (e.g., simulation of tri-axial compression test), considerations are warranted in accounting for the viscoelastic contact of rough surfaces, which nonlinear normal contact stiffness depends as much on the characteristics of the surface topography as on the material properties of the granule itself. As aforementioned, importance is also placed on the effects that the load history and method of sample (granular assembly) preparation have on the steady-state initial conditions of the granular mass that represent relative density states, i.e., mass density averaged over a control volume and corresponding density distribution in a semi-infinite half space, prior to the penetrative introduction of a structural element. By using a standardized pluviation method to achieve gravitational lithostatic stress states under markedly consistent, repeatable conditions, the initial thermodynamic-equilibrium state and packing configuration of the assemblies considered, therefore, promote reduced uncertainty and increased repeatability in homogeneous weight-density distributions, e.g., potential energy-density distribution. Of important is to warrant the physical model that simulates geostatic in-situ stress profiles, and thus, the numerical procedures in controlling the packing density and resulting constituent particle-to-particle morphological texture (e.g., known as soil fabrics in soil mechanics) are based on gravitational development of grain-to-grain contact-force chains during the pluviation.

This way, phase transitions from an unsteady state to a steady state can be simulated in a manner consistent with sedimentary processes of natural granular soil. Correspondingly, macroscopic volume-averaged stress distributions, densities, and ultimately the relevant contractive and dilative behaviors during a high strain-rate shearing event, i.e., the penetrating UXO, all benefit from variance identification and reduction across the reported dataset at the four various scales, i.e., micro-, grain-, continuum-, and prototype system-scale.

The well-known scaling laws of geotechnical centrifuge testing also allow for the representation and study of in-situ impact phenomena in a controlled laboratory setting. Experiments are conducted in which scaled projectiles are propelled from a prototype gas-powered projectile emission device into a granular body consisting of size and shape controlled aluminosilicate proppants at high gravitational accelerations of the centrifugal rotation. The granular media are prepared in a calibrated pluviation procedure to attain target initial densities using a pluviation device of new design, and is instrumented to record real-time area-averaged stress distributions on customized pressure cells, and ground-surface displacements during the sequential loading stages. The report contains an overview of the experimental components and sample-preparation procedures, as well as descriptions of representative measurements from three various testing scenarios for the validation of scaling law and the quantification of scale-effects.

The corresponding numerical analysis is performed and presented as it is within a statistical margin of errors so as to model the laboratory experimentation as closely as possible without introduction of empiricism. Libraries of numerical granular matrix have been compiled which correspond to the physical proppants utilized in the laboratory experiments. Because the presented discrete element contact models are based on the application of soft-particle dynamic theory (extended Hertzian and Mindlinian contact mechanics) to analyses of physical data of surface topography and grain-to-grain contact force-deformation, they are expansible to a wide range of granular mechanics which can be numerically parametrized based on direct measurements using existing experimental technology at the two interrelated scales. In this way, microscopic laboratory tests assessing surface roughness (and surface energy) and asperity distributions across the surface of individual grains have been integrated into the calculation of individual discrete element (grain scale) parameters such as normal and tangential contact stiffness, and scale-dependent frictional resistance, which ultimately determine the degree of penetration resistance as per levels of energy dissipation mechanisms available at the system scale. The pluviation procedure of the laboratory sample preparation is simulated numerically in order to verify the soft-particle dynamics, and obtain target (maximum) relative density states of choice. The rapid penetration of a finite-element UXO is then simulated to system initial and boundary conditions, i.e., mixtures of discrete-element particle assemblies that are confined within nonreflecting boundaries for the representation of a semi-infinite half space. A parametric-sensitivity study at the prototype scale is performed in consideration of the variation of grain-scale parameters. The numerical results are catalogued and compared within the measurements of the scale effects per the three centrifuge test scenarios.

TABLE OF CONTENTS

DISCLAIMER	I
SI (MODERN METRIC) CONVERSION FACTORS (FROM FHWA)	II
ACKNOWLEDGEMENTS	V
ABSTRACT.....	VI
EXECUTIVE SUMMARY	VIII
TABLE OF CONTENTS.....	X
LIST OF FIGURES	XIII
LIST OF TABLES	XX
 1 INTRODUCTION	 1
1.1 Introduction.....	1
1.2 Background and Motivation	3
1.3 Scope of Report.....	4
 2 PROJECTILES CONSIDERED FOR CENTRIFUGE EXPERIMENTS.....	 6
2.1 Overview.....	6
2.2 SAP- 2000 Projectile.....	6
2.3 General Remarks on Centrifuge Testing.....	6
2.4 Pertinent Scaling Relationships	7
2.5 Centrifuge Testing Scenarios	7
2.6 Projectiles in Centrifuge Experiments	8
 3 GRANULAR MATERIALS USED IN CENTRIFUGE TESTING	 10
3.1 Overview.....	10
3.2 Motivation for Use of Manufactured Granules.....	10
3.2.1 Advantages for Physical Testing.....	10
3.2.2 Advantages for Numerical Modeling.....	10
3.2.3 Types of Assemblies Considered	11
3.3 Preparation and Characterization of Granular Materials	11

3.3.1	Procurement	11
3.3.2	Washing and Drying.....	11
3.3.3	Sieving.....	11
3.3.4	Microscopic Laboratory Tests Conducted	12
3.3.5	Grain-scale Laboratory Tests Conducted.....	16
3.3.6	System-scale Laboratory Tests Conducted	17
3.4	Proppants (0.93±0.08 mm)	18
3.4.1	General Description.....	19
3.4.2	Microscopic Variability of Surface Roughness	19
3.4.3	Grain- scale Parameters.....	21
3.4.4	Continuum-scale empirical observation.....	28
3.5	Proppants (mean diameter of 0.55 ± 0.05 mm)	30
3.5.1	General Description.....	30
3.5.2	Microscopic Properties of 0.55 ± 0.05 mm Proppants	30
3.5.3	Grain-scale Parameters.....	30
3.5.4	Continuum-scale Empirical Observation	31
4	CENTRIFUGE MODELING OF PROJECTILE PENTERATION INTO GRANULAR ASSEMBLIES	32
4.1	Overview.....	32
4.2	Centrifuge Test Set-up	33
4.2.1	Dry Pluviation of Granular Materials.....	36
4.2.2	Instrumentation and Data Acquisition.....	38
4.3	Centrifuge Tests Observations.....	38
4.4	Fictitious Forces on a Projectile in the Centrifuge.....	54
4.4.1	The Trajectory and Acceleration in the Rotational Coordinate Frame	56
4.4.2	Coriolis Effects in Tests 1 and 2	58
4.4.3	Sources of Error: Ejection Angle and other Variables.....	61
5	NUMERICAL MODELING OF PROJECTILE PENETRATION TESTS	64
5.1	Overview.....	64
5.2	Numerical Model of 0.93±0.08 mm Granules	64
5.2.1	Geometry and Density.....	64
5.2.2	Normal Contact Stiffness	65
5.2.3	Tangential Contact Stiffness	68
5.2.4	Sliding Friction.....	70
5.2.5	Damping coefficient.....	70
5.3	Numerical Model of 0.55±0.05 mm Granules	71
5.3.1	Geometry and Density.....	71
5.3.2	Normal Contact Stiffness	71
5.3.3	Tangential Contact Stiffness	71
5.3.4	Sliding Friction.....	72
5.3.5	Coefficient of Restitution	72

5.4	Simulation of Pluviation Process	72
5.4.1	Simulation Stages	72
5.4.2	Comparisons between Computed and Measured Density States	74
5.4.3	Computed Geostatic Stresses	76
5.5	Numerical Model of Centrifuge Test	79
5.5.1	Considerations for Boundary Conditions	79
5.5.2	Numerical Model of Projectile	82
5.5.3	Considerations for Interactions between Projectiles and Granules	83
5.5.4	Simulation Stages	84
5.6	Test Scheme 1: Projectile Penetration into Monodisperse Assembly	88
5.6.1	Computed versus Measured Projectile Penetration Depth	89
5.6.2	Computed Stresses in Granular Assemblies	90
5.7	Test Scheme 2: Projectile Penetration into Monodisperse Assembly	93
5.7.1	Computed versus Measured Projectile Penetration Depth	94
5.7.2	Computed Stresses in Granular Assemblies	95
5.8	Test Scheme 3: Projectile Penetration into Monodisperse Assembly	98
5.8.1	Computed versus Measured Projectile Penetration Depth	99
5.8.2	Computed Stresses in Granular Assemblies	100
5.9	Parametric Simulations of Projectile Penetration	103
5.9.1	Parametric Simulation Results	104
5.9.2	Observations	106
6	SUMMARY AND CONCLUSIONS	128
6.1	Summary of Physical Testing	128
6.2	Summary of Numerical Modeling	129
6.3	Proof-of-Concept and Conclusions	130
7	PROPOSED RESEARCH FOR A CONTINUAL DEVELOPMENT	133
7.1	Topological Consideration	133
7.2	Averaging Methods	136
7.3	Morphological Characteristics of Granular Structure	141
7.4	Continuity Equation, Partitioning, and Averaging Methods	147
7.5	Heat and Particle Breakage	150
APPENDIX A: INVESTIGATION INTO THE FUNDAMENTAL NATURE OF INTERACTIONS BETWEEN CONSTITUENTS OF GRANULAR MEDIA		A-1
APPENDIX B: REPOSITORY OF LABORATORY TEST DATA		B-1
APPENDIX C: PROPOSED MANUSCRIPT		C-1

LIST OF FIGURES

<u>Figure</u>	<u>Page</u>
Figure 2.1 Schematic of the SAP 2000 pound projectile (Livingston and Smith 1951)	6
Figure 2.2 Associated parameters with ogive nose projectiles	8
Figure 2.3 Model scale dimensions of the projectiles used in centrifuge experiments with different centrifugal acceleration levels: a) 26.5-g; and (b) 46.0-g (Dimensions in mm)	9
Figure 2.4 Photos of the projectiles used in centrifuge tests.....	9
Figure 3.1 Pictorial display of surface texture (Bhushan 2001)	13
Figure 3.2 General typology of solid surfaces (Bhushan 2001)	14
Figure 3.3 Physical test set up for micro-indentation test.....	17
Figure 3.4 Schematic sketch for scratch test.....	17
Figure 3.5 Packing apparatus for granules.....	18
Figure 3.6 SPM and SEM images for proppants with diameter 0.93 ± 0.08 mm; a) $1 \times 1 \mu\text{m}$ scan size; b) $10 \times 10 \mu\text{m}$ scan size; c) $100 \times 100 \mu\text{m}$ scan size	19
Figure 3.7 (a) SPM image of scan size $1 \mu\text{m} \times 1 \mu\text{m}$; (b) Histogram of surface height distribution; (c) Power spectral density function; and (d) Radius of asperity peak and asperity density	20
Figure 3.8 Contac forces acting normal to contact planes with surface roughness illustrated by a fractal structure of Archard's stacked hemispheres	21
Figure 4.1 Geotechnical centrifuge at the University of Florida	32
Figure 4.2 Bull barrels used in centrifuge tests.....	34
Figure 4.3 Firing assembly used in centrifuge models (Dimensions in millimeters)	35
Figure 4.4 Schematic sketch of the pluviator.....	36
Figure 4.5 Pluviating proppant inside the rigid centrifuge container	37
Figure 4.6 Surface of the granular profile after pluviation	37
Figure 4.7 Projectile velocity - air tank pressure relationship obtained during 1-g tests.....	39
Figure 4.8 Centrifugal acceleration – time history during centrifuge testing ($a_{\text{max}} = 26.5\text{-g}$)	39
Figure 4.9 Surface displacement – time history during Test 3a	40
Figure 4.10 Surface displacement – time history during Test 3b	40
Figure 4.11 Schematic sketches of the penetrated projectile in test 1 and the formed crater: plan view (dimensions in mm).....	41

Figure 4.12 Schematic sketches of the penetrated projectile in test 1 and the formed crater: a) elevation view at A-A cross section, and b) elevation view at B-B cross section (dimensions in mm)	42
Figure 4.13 Schematic sketches of the penetrated projectile in test 2 and the formed crater: plan view (dimensions in mm).....	43
Figure 4.14 Schematic sketches of the penetrated projectile in test 2 and the formed crater: a) elevation view at A-A cross section, and b) elevation view at B-B cross section (dimensions in mm)	44
Figure 4.15 Schematic sketches of the penetrated projectile in test 3a and the formed crater: plan view, b) elevation view at A-A cross section, and c) elevation view at B-B cross section (dimensions in mm)	45
Figure 4.16 Schematic sketches of the penetrated projectile in test 3a and the formed crater: a) plan view, b) elevation view at A-A cross section, and c) elevation view at B-B cross section (dimensions in mm)	46
Figure 4.17 Schematic sketches of the penetrated projectile in test 3b and the formed crater: plan view (dimensions in mm).....	47
Figure 4.18 Schematic sketches of the penetrated projectile in test 3b and the formed crater: a) elevation view at A-A cross section, and b) elevation view at B-B cross section (dimensions in mm)	48
Figure 4.19 Crater elevation relative to the ground surface after the test 3a (dimensions in millimeters)	49
Figure 4.20 Crater elevation relative to the ground surface after the test 3b (dimensions in millimeters)	50
Figure 4.21 Profile after excavation at the end of test 3a	51
Figure 4.22 Relative position of the penetrated projectile with respect to the pressure cells (shown after test 3b).....	51
Figure 4.23 Predicted and measured vertical stresses at top and bottom of PC4 and bottom of PC2 during test 3a.....	52
Figure 4.24 Predicted and measured vertical stresses at top and bottom of PC4 and bottom of PC2 during test 3b.....	52
Figure 4.25 Measured horizontal stresses at two sides of PC3 during test 3a	53

Figure 4.26 Measured horizontal stresses at two sides of PC3 during test 3b.....	53
Figure 4.27 The ratio of horizontal to vertical stress (K_0) during test 3a.....	54
Figure 4.28 The ratio of horizontal to vertical stress (K_0) during test 3b	54
Figure 4.29 Coordinate System and Forces acting on projectile in Flight.....	57
Figure 4.30 Coriolis Effect on projectile in Test 1	58
Figure 4.31 Coriolis Effect on Projectile in Test 2	60
Figure 5.1 Curve fits for the micro-indentation data on ceramic proppants (aluminosilicate with MOH scale of 6.5).....	67
Figure 5.2 Pluviation simulation staging: a) Initial configuration; b) Stage 1; c) Stage 2	73
Figure 5.3 Mechanically stable DSE assembly obtained from simulation of the pluviation process	74
Figure 5.4 Physical versus numerical bulk densities achieved for 0.5 mm and 0.85 mm proppants (normalized to 1g).....	76
Figure 5.5 Plan view location of column of REV's within DSE assemblies	77
Figure 5.6 Physical versus numerical vertical stresses achieved for 0.5 mm and 0.85 mm proppants (normalized to 1g)	77
Figure 5.7 Physical versus numerical K_0 values achieved for 0.5 mm and 0.85 mm proppants (normalized to 1g).....	78
Figure 5.8 Conceptual schematic of local non-reflecting boundary condition (LNRBC).....	80
Figure 5.9 Numerical model of pluviated DSE assembly (normalized to 1g): a) Interior spheres; b) Boundary spheres	81
Figure 5.10 Applied pressure distributions to circumferential and bottom boundaries of DSE assemblies (normalized to 1g)	82
Figure 5.11 Finite element model of unscaled projectile: a) Elevation view; b) Ogive nose augmentation (normalized to 1g).....	83
Figure 5.12 State of FE projectile and DSE assembly just prior to onset of projectile penetration (Numerical representation of centrifuge models at 1g)	85
Figure 5.13 State of FE projectile and DSE assembly during projectile penetration (normalized to 1g)	86
Figure 5.14 State of FE projectile and DSE assembly upon termination of simulation (at 1g scale)	87

Figure 5.15 State of Test 1 FE projectile and DSE assembly just prior to onset of projectile penetration (prototype scale: 26.5g)	89
Figure 5.16 Projectile penetration simulation result for interparticle friction coefficient of 0.47, particle-to-projectile friction coefficient of 0.65, and 70 m/s projectile velocity (at prototype scale of 26.5g).....	90
Figure 5.17 Projectile penetration simulation vertical stress plots for interparticle friction coefficient of 0.47, particle-to-projectile friction coefficient of 0.65, and 70 m/s projectile velocity (prototype scale: 26.5g): a) 25% of maximum penetration; b) 50% of maximum penetration; c) 75% of maximum penetration; d) 100% of maximum penetration	91
Figure 5.18 Projectile penetration simulation horizontal stress plots for interparticle friction coefficient of 0.47, particle-to-projectile friction coefficient of 0.65, and 70 m/s projectile velocity (prototype scale: 26.5g): a) 25% of maximum penetration; b) 50% of maximum penetration; c) 75% of maximum penetration; d) 100% of maximum penetration	92
Figure 5.19 State of Test 2 FE projectile and DSE assembly just prior to onset of projectile penetration (prototype scale: 46g)	94
Figure 5.20 Projectile penetration simulation result for interparticle friction coefficient of 0.47, particle-to-projectile friction coefficient of 0.65, and 110 m/s projectile velocity (prototype scale: 46g)	95
Figure 5.21 Projectile penetration simulation vertical stress plots for interparticle friction coefficient of 0.47, particle-to-projectile friction coefficient of 0.65, and 110 m/s projectile velocity (prototype scale: 46g): a) 25% of maximum penetration; b) 50% of maximum penetration; c) 75% of maximum penetration; d) 100% of maximum penetration	96
Figure 5.22 Projectile penetration simulation horizontal stress plots for interparticle friction coefficient of 0.47, particle-to-projectile friction coefficient of 0.65, and 70 m/s projectile velocity (prototype scale: 26.5g): a) 25% of maximum penetration; b) 50% of maximum penetration; c) 75% of maximum penetration; d) 100% of maximum penetration	97
Figure 5.23 State of Test 3 FE projectile and DSE assembly just prior to onset of projectile penetration (prototype scale: 26.5g)	99
Figure 5.24 Projectile penetration simulation results for interparticle friction coefficient of 0.47, particle-to-projectile friction coefficient of 0.65, and 70 m/s projectile velocity (prototype scale: 26.5g)	100

Figure 5.25 Projectile penetration simulation vertical stress plots for interparticle friction coefficient of 0.47, particle-to-projectile friction coefficient of 0.65, and 70 m/s projectile velocity (prototype scale: 26.5g): a) 25% of maximum penetration; b) 50% of maximum penetration; c) 75% of maximum penetration; d) 100% of maximum penetration	101
Figure 5.26 Projectile penetration simulation horizontal stress plots for interparticle friction coefficient of 0.47, particle-to-projectile friction coefficient of 0.65, and 70 m/s projectile velocity (prototype scale: 26.5g): a) 25% of maximum penetration; b) 50% of maximum penetration; c) 75% of maximum penetration; d) 100% of maximum penetration	102
Figure 5.27 Parametric simulation results for Test Scheme 1 (projectile-to-granule ratio: 10.58)	104
Figure 5.28 Parametric simulation results for Test Scheme (projectile-to-granule ratio: 10.36)	105
Figure 5.29 Parametric simulation results for Test Scheme 3 (projectile-to-granule ratio: 17.62)	105
Figure 5.30 Effects of contact friction on terminal penetration depth.....	107
Figure 5.31 Variation of terminal penetration depths with respect to impact velocity as per standard deviations of intergranular friction coefficients and the two packing assemblies	108
Figure 5.32 Average coordination number versus contact detection tolerance	110
Figure 5.33 Elevation view of columnated volume for Assembly A: a) Steady-state geometry at equilibrium (per prior pluviation); b) Steady-state distribution of grain body forces through contact force chain under gravity; c) Elevation view of grain mass distribution in cylindrical volume (disk) extracted from 1250 mm depth within columnated volume.....	112
Figure 5.34 Elevation view of columnated volume for Assembly B: a) Steady-state geometry at equilibrium (per prior pluviation); b) Steady-state distribution of grain body forces through contact force chain under gravity; c) Elevation view of grain mass distribution in cylindrical volume (disk) extracted from 1250 mm depth within columnated volume.....	113
Figure 5.35 Penetration phenomena in Assembly A (top row) and Assembly B (bottom row): Diameter of cavity formation is given at the impact point by the projectile with velocity of 70 m/s: The projectile dimensions are 238.3 mm in diameter, 854.6 mm in length, and 354.8 mm of orgive radius: for dimensional comparison purposes, only the center part of the radial dimension of Test 1 simulation is shown approximately same as the radial dimension of Test 3 simulation in visual illustration.....	114

Figure 5.36 Resultant velocity plots for Assembly A: a) 0.002 sec; b) 0.008 sec	115
Figure 5.37 Resultant velocity plots for Assembly B: a) 0.002 sec; b) 0.008 sec	115
Figure 5.38 Energy variation in granular systems during penetration.....	116
Figure 5.39 Radial velocity fields in the system domains of Assembly A (top row) and Assembly B (bottom row).....	118
Figure 5.40 Force generation in granular masses during momentum transfer from the projectile: Radial (top row) and vertical (bottom row) force components of in the XZ-plane of Assembly B	119
Figure 5.41 Balance of system energy components in the UXO-Granular systems.....	121
Figure 5.42 Control volumes sampled for HSR tri-axial compression test simulations.....	122
Figure 5.43 High-strain rate triaxial compression test simulation: a) Deviatoric stress versus axial strain; b) Volumetric strain versus axial strain	123
Figure 5.44 Streamlines in Assembly A (top row) and Assembly B (bottom row): The projectile dimensions are 238.3 mm in diameter, 854.6 mm in length, and 354.8 mm of ogive radius: for dimensional comparison purposes, only the center part of the radial dimension of Test 1 simulation is shown approximately same as the radial dimension of Test 3 simulation	125
Figure 5.45 Mean resultant-velocity field (top row) and corresponding boundary (bottom row) of rapid-flow regime in Assembly A.....	126
Figure 5.46 Mean resultant-velocity field (top row) and corresponding boundary (bottom row) of rapid-flow regime in Assembly B.....	127
Figure 7.1 Two-dimensional projection schematics of random assembly of eight angular sand particles (left), transformation to platonic solids composites (middle), and DSEs with SA:V roughly equivalent to angularity (right): Mass densities decrease as volumes increase from left to right. Representation of point mass at the centers of the circles requires force mapping to account for the moments of inertia and rolling resistances accordingly to shape factors (Refer to A.1.7)	134
Figure 7.2 Surface-area-to-volume ratio and Scanning Electron Microscope (SEM) images of sand particles.....	135
Figure 7.3 Particles with various shape factors for use in sand-pile tests.....	136
Figure 7.4 Triangulation of two-dimensional closest packed arrays	137

Figure 7.5 Meso DSE (constituent DSEs' diameter = 5 mm; Meso DSE's diameter = 25.4 mm)	138
Figure 7.6 A definition of mesoscopic discrete-element sphere.....	139
Figure 7.7 Numerical model of upscaling (top) and resulting meso-scale DSE normal contact stiffness (bottom)	140
Figure 7.8 Morphological changing between packed hexagons and closest packed circles	141
Figure 7.9 Random packings of DSE assemblies: a) Binary system (with a cut plane across the center of the section, Plane A); b) Monodisperse system created via removal of smaller spheres (with a cut plane across the center of the section, Plane B).....	142
Figure 7.10 Triaxial compression test simulations of monodisperse and binary systems: a) Deviatoric stress versus axial strain; b) Volumetric strain versus axial strain. Note that the deviatoric stresses highlighted in red are based on a conjecture. For final reporting, we present part of the simulation (which has not been completed at this point of time).....	143
Figure 7.11 Evolution of particle rearrangement and in-plane displacement using the cut planes from Fig. 7.9: a) Sequence of shear deformation patterns in the binary system; b) Formation of homogeneous deformation fields in the monodisperse system.....	144
Figure 7.12 Development of force chains in the cut planes of Fig. 7.9: networks in color of blue are strong contact forces; green and red particles are spectators: a) Vertical force chains in the binary system; b) Weaker force chains in the monodisperse system.....	145
Figure 7.13 Comparison to laboratory test data at strain rate of 1750% per second: (a) Deviatoric stress vs axial strain; (b) Volumetric strain vs axial strain	149
Figure 7.14 Comparison to laboratory test data at strain rate of 900% per second: (a) Deviatoric stress vs axial strain; (b) Volumetric strain vs axial strain	150

LIST OF TABLES

<u>Tables</u>	<u>Page</u>
Table 2.1 Centrifuge Scaling Factors.....	7
Table 2.2 Projectile and granular material pairings selected for centrifuge testing.....	8
Table 3.1 Roughness parameters for ceramic proppants with 0.93 ± 0.08 mm diameter.....	20
Table 4.1 Characteristics of granular profiles in centrifuge tests	38
Table 4.2 Coriolis Effects in Test 1	59
Table 4.3 Coriolis Effects in Test 2	61
Table 5.1 Geometric parameters of 0.85 mm diameter DSEs	64
Table 5.2 Power law parameters	65
Table 5.3 Input parameters for numerical model.....	66
Table 5.4 Input parameters for nonlinear contact stiffness.....	68
Table 5.5 Friction coefficients used in numerical models	70
Table 5.6 Viscous damping coefficients in numerical model.....	71
Table 5.7 Calculated bulk densities of mechanically stable DSE assemblies composed of 0.5 mm diameter spheres (normalized to 1g).....	74
Table 5.8 Calculated bulk densities of mechanically stable DSE assemblies composed of 0.85 mm diameter spheres	75
Table 5.9 Physical measurements of sliding friction between 4 mm spherical bauxite proppants and stainless steel (SS3042B) plates (Grima et al. 2010)	84
Table 5.10 Test Scheme 1 parameters for projectile penetration simulations	88
Table 5.11 Test Scheme 2 parameters for projectile penetration simulations	93
Table 5.12 Test Scheme 3 parameters for projectile penetration simulations	98
Table 5.13 Catalog of parametric variations for projectile penetration simulations.....	103
Table 5.14 Relative density of ceramic proppants.....	109
Table 7.1 Model parameters for DSEs that are used in the demonstration of partitioning.....	148

CHAPTER 1

INTRODUCTION

1.1 Introduction

Leftover unexploded ordnance (UXO) from past armed conflicts or munitions testing operations pose an ongoing environmental and personal threat and may detonate years after their initial use. Furthermore, the location and removal of UXO is complicated by the fact that they are often embedded into the earth, due to a failure to detonate after high-velocity contact with the ground. A reliable means to estimate UXO penetration depths (with consideration of heterogeneous in-situ soil conditions) has been in demand for the munitions response community. Additionally, such estimates are of use by regulators concerned with the recovery of UXO at ranges on military installations; sites designated for base realignment and closure; and, Formerly Used Defense Sites (FUDS). Therefore, the high-fidelity analysis of the multi-dimensional problem of a high-velocity projectile impacting and penetrating granular materials offers a valuable guide to the possible locations of UXO.

Much of the modern macroscopic continuum-based theory of low velocity impact originated with works of Robins, Euler, and Poncelet. The analysis of this phenomenon is naturally divided into the empirical measurement of experimental penetrations into real granular materials, and the physics-based mathematical modelling of the impact and penetration problem. The objective of the study is to develop physics-based prediction models for use in the determination of maximum penetration depths of common military munitions in various in-situ soil conditions for support of planning for munitions response actions and subsequent risk management decisions. A three-dimensional extended discrete and finite element analysis model has been developed per the work energy principle to numerically quantify, and statistically evaluate, maximum penetration depths that are attained in granular masses (with various density states) due to high velocity impacts by prototype UXO. This document provides comprehensive methodologies and results along both branches of investigation, namely, from geotechnical centrifuge models, and from various numerical models employing an extended finite-discrete element method.

The geotechnical centrifuge provides a technique for controlled laboratory measurements of penetrations into varied granular media which theoretically correspond to site-scaled impact phenomena. The theoretical laws associated with this experimental method provide scaling factors for distances, masses, and time with respect to the increase in gravitational (centrifugal) acceleration, allowing for the penetration depths and body-force distributions measured at the laboratory scale to correspond to prototype-scale UXO phenomena in an in-situ condition. The experimental procedure developed during the SEED phase is described briefly as follows; the granular medium, consisting of manufactured aluminosilicate proppants with controlled size and shape, is prepared to a target relative-density state at an initial equilibrium state by way of a controlled pluviation process as per a constant particle-mass flow rate using a customized pluviation device. The granular medium is instrumented with pressure cells and other devices to track development of stress fields and surface displacement behavior, respectively, in real time during centrifuge flight. Miniaturized projectiles with scale ratios proportional to centrifugal g-levels are then propelled from a prototype gas-powered projectile emission device into a granular body at static equilibrium under the artificial gravitational acceleration due to the angular rotation of the centrifuge. The scaled model of the UXO-granular soil system is then removed from the

centrifuge, and the final penetration depth of the projectile is measured. It is also noted that the centrifuge testing provides physical data measured at the scale, and thus, the macroscopic volume-averaged stress fields and corresponding force-distributions (reactions) inside the granular body are directly simulated at the same scale as per observed maximum penetration depths of the projectile both physical and numerical. In Chapter 4, the more detailed description is given for the centrifugal system components and model preparation procedures. Quantitative measurements obtained from a number of tests per various testing scenarios are provided in variation of projectile sizes and mean diameters of granules, which are numerically simulated at the 1g prototype scale.

In the subsequent chapter, the numerical simulations are described in a consistent manner of the centrifuge modeling so as to maintain the scaling effects in the prediction of penetration phenomena measured in the centrifuge experimentation within a margin of statistical errors. A combined finite-discrete element method (FEM-DEM) is one of the most effective means of capturing the kinetics and kinematics of discrete granules through interparticle motion and intragrain deformation, respectively, during rapid penetration by a relatively rigid projectile that is discretized with finite elements based on continuum-based mechanics. Libraries of discrete element models have been developed corresponding to the ceramic proppants of the prototype centrifuge (physical) model. These discrete particle assemblies have been parametrized according to empirical testing results on the grains (individual proppants) on numerous scales, including nano-indentation tests for the material properties (hardness, strain-hardening coefficient, and reduced modulus), scanning electron and probe microscopies that measure the surface topography and the distribution of asperity density and radius of curvature, macro contact force-displacement measurements of a pair of granules in contact, and tri-axial compression tests at macroscopic scales (continuum scales). The data obtained from these interrelated-scale empirical considerations is used to develop a theoretical contact model as per extended Hertzian and Mindlinian contact theories. Analytical closed-form solutions of normal and tangential contact stiffnesses specific to microscopic boundary conditions (described by surface topography) establishes the basis for which nonlinear viscoelastic particle-to-particle interaction can be accounted for in the calibration of interparticle friction (Coulombic damping), and restitution (viscous damping) on the numerical discrete element assemblies, where the authors ultimately attempt to conceptually understand the scale-dependent distributions of surface forces (and intragrain deformation) and corresponding energy-dissipation mechanisms at the macroscopic continuum scale; a minimal empiricism is desired as any phenomenological description of UXO penetration processes is in contrast to the proposed proof-of-concept otherwise. In turn, the shear resistance of the granular mass is quantified as per the variations of control parameters at the grain scale against external loading, in this case the penetration of the greater size of the penetrator, i.e., UXO. The standardized pluviation procedure employed in the laboratory testing of relative density states is numerically simulated in order to obtain a packing density in the model which mimics the prototype granular body with consistent point-mass distributions. In Chapter 5, the results of varied simulations are presented in which the finite-element UXO structure penetrates a number of various discrete element models that represent the prototype granular mixtures. The numerical results in each case are compared to the physical test results obtained from a corresponding centrifuge test scheme. A parametric study is also performed in which the parameters which have been discussed are varied, with a critical analysis of representative results based on energy principles.

1.2 Background and Motivation

The problem of the response of a granular material due to the rapid penetration of a projectile has historically been studied towards a number of different applications. These include the obvious military application to the design of weapons effect in underground targets, as well as for the design of bunkers and other protective structures against the use of such weapons. Civilian applications include the penetration of instrumentation for the subsurface investigation of soil and rock bodies, the installation of deep foundations and deep sea anchors, subterranean waste disposal, and the interaction of landing terrestrial and extraterrestrial aircraft with an underlying soil surface. There is a history of empirical, analytical, and numerical efforts to model the problem with these applications in mind (Omidvar et al. 2014).

Traditionally, soil bodies and other granular materials have been modeled as continua at the macroscopic scale, often defined by Representative Elementary Volumes (REV). Along this line of averaged representation, the discrete, discontinuous particulate nature of the material is averaged over representative length, area, and volume scales. Continuum models of granular material often carry with them the major difficulty of the complexity of defining a suitable constitutive model which captures the phenomenology of the assemblage of particles that is being represented. These empirical or semi-empirical relations of macroscopic responses of the material are used to approximate a continuum-based behavior which is rather a system response subjected to a specific boundary condition at that scale. Following phenomenological observations can be erroneous to expand to a generalized solution to the complex boundary-value problem that span over underlying scales. In essence, knowledge of the behavior of a collective group of granules is assumed to be known *a priori*, which is then translated into parameters of material constants such as weight density and elastic moduli within the confines of predetermined constitutive relationships, for the boundary conditions of an already established model. In general, the more the continuum is able to approximate the behavior of a granular assembly, the more complex its constitutive model, and the more material parameters predetermined for solving the governing equations as per a specific set of boundary values. This continuum-based approach leads to the problem of increasing uncertainty in mathematical prescription of boundary conditions and/or exacerbating numerical complexity, and the inability for concise analytical or closed-form solutions due to lack of generality. Furthermore, the phenomenological nature of the model necessitates to rely upon the macroscopically-averaged material parameters sometimes having no clear physical meaning, i.e. they cannot be understood outside of the predetermined context of the continuum-mechanical model. These issues clearly all relate to the fact that the material being modeled is inherently discrete, discontinuous and heterogeneous; our past attempts at volume-averaged continuity or homogenization have been proven to detract from the physical reality of the scale-dependent boundary-value problem hidden in seemingly disdain scales.

The Discrete Element Method (DEM) and soft-particle dynamics provide an alternative medium for the distinctive modeling of granular matters, which can be utilized to disconcert with the above-mentioned complications. It is quite evident that variations unpredicted in the macroscopic observations in is an emergent property of the assemblage of the individual dynamics and contacts of its constituent grains. When choosing to model the distinct granular components of the macroscopic body, the continuous nonlinearity, volume dilations, apparent transitions in constitutive behaviors, and sensitivity to loading history (e.g. “memory” of sand; Vanel et al. 1999), which are ever-present in a granular material and so complicate continuum models, appear almost

automatically (Cundall, 2001). This is not to say that the DEM does not present its own host of problems. For instance, the computational cost of modeling the motions and contacts of each individual particle increases exponentially with the number of elements. Also, material parameters representing the contact phenomena between grains must still be closely characterized in a statistical manner to which a limited amount of empirical (measured) data forces to face the same challenges of uncertainty at a smaller scale of several orders of magnitude. However, recent and ever increasing advances in computational technology has made the calculation of large-scale DEM models tractable, and finally caught up with the advances in experimental mechanics in the 20th century. Towards the second point, the parameters representing contact stiffnesses, frictional coefficients, etc., have a direct physical interpretation, contrary to those in a continuum model. In this respect, the values of these coefficients can be deduced for a particular material through multi-scale empirical measurements on individual grains. Thus, the grain itself represents a macroscopic body with its own boundaries.

There are, however, a great many materials for which DEM is not the most efficient numerical method. Most structural components are not granular in nature and therefore admit to far more concise interpretation as a mathematical continuum. For systems involving a granular material interacting with such structural components, and in particular, the problem of a relatively rigid projectile penetrating a granular mass, it is desirable to include both discrete and finite elements in the numerical simulation. This extension to a combined Finite-Discrete Element Method (FEM-DEM) provides its own numerical difficulties, but has been developed into its own robust system of analysis. The following report contains the modeling techniques adopted in FEM-DEM, in which the penetrating UXO is represented by finite elements, while the granular medium is modeled by discrete elements as described above.

There is also a standing history of employing the geotechnical centrifuge in the analysis of penetration phenomena in granular material. As discussed above, this approach allows for the empirical measurements of in-situ penetrations on a laboratory scale, which by well-established scaling laws, can then be used to describe behaviors at much larger scales. Particular laboratory studies of interest to the study of geomechanics include the penetration into dry sand (Fragaszy and Taylor, 1989) and wet clays (Zelikson et.al, 1986). The use of manufactured proppants instead of naturally occurring soils in the laboratory tests allows for increased ease of direct comparison with numerical FEM-DEM models at that scale, in which the granules are not idealized as spherical and exhibit more predictable heterogeneity than occurs in a natural granular soil.

It is therefore desirable to present a comprehensive approach to the analysis of the rapid penetration problem incorporating all of the aspects here discussed. The following report is an attempt to incrementally achieve this goal.

1.3 Scope of Report

The purpose of this report is to document the findings made in satisfaction of the proposed SEED deliverable, i.e., proof-of-concept. More specifically, the purpose is to: 1) Document (physical) microscopic, laboratory-scale, and centrifuge tests involving characterization of proppants granules, controlled preparation of granular assemblies, and penetration of custom-manufactured projectiles into said assemblies; 2) Document the combined FEM-DEM numerical models simulating the laboratory-scale phenomena of projectile-soil interaction under different

initial conditions (e.g., various particle-to-projectile scales; projectile impact velocity and angle; and, interparticle friction coefficients).

This report is organized as follows:

- In Ch. 2, attention is given to the parameters of unexploded ordnance being used in the centrifuge experiments. A brief introduction of centrifuge testing scenarios is also provided.
- In Ch. 3, focus is placed upon detailing the granular materials and their properties for use in the centrifuge testing. In addition, multiscale laboratory tests and properties of the selected granules are documented.
- In Ch. 4, emphasis is given to cataloging the centrifuge testing procedures, including discussions of calibration efforts and experimental devices. Examples include schematics and technical descriptions of pluviation equipment, the centrifuge apparatus, and the projectile emission device. The detailed setups for three test schemes are described, while the projectile terminal behavior and stress are measured for each of the tests.
- In Ch. 5, those efforts specific to numerical modeling of the centrifuge test (using the combined FEM-DEM modeling technique) are documented. Considerations include the establishment of constitutive parameter values for the granules, formulation of mechanically stable granular assemblies via simulation of the pluviation process, numerical descriptions of projectile geometry and contact/friction interactions with proppant granules, and simulations with regard to the three aforementioned centrifuge test schemes.
- In Ch. 6, a summary of work completed during the SEED phase of the larger research program is reported. Also, a brief introduction to preliminary plans for the next phase of research is provided in the end. Further, contributions (and advances) made in this research area are summarized.
- In Ch. 7, based on the advances made during the SEED phase of the research, the platform for the in-progress Phase II proposal is given. The subjects discussed will provide support for the thermodynamics-based analytical description of projectiles penetrating into granular assemblies.

CHAPTER 2

PROJECTILES CONSIDERED FOR CENTRIFUGE EXPERIMENTS

2.1 Overview

Terminal ballistic behavior of penetrators depend on different factors including penetration velocity, angle of attack (AoA), the mechanical and geometrical properties of the projectile, and various characteristics of the granular media. Details of the projectiles being used in the centrifuge experiments are provided in this chapter.

2.2 SAP- 2000 Projectile

Shown in Fig. 2.1 is a schematic of the 2,000 pound semi-armor piercing (SAP) ordnance (Livingston and Smith 1951); this projectile constitutes the penetrating object of interest in the current study. Whereas full-scale (physical) penetration experiments are not practical within the study scope, centrifuge testing permits scale models to be investigated while maintaining direct, quantitative mappings to behaviors that would be expected at the full scale. Further, air gun blast experiments, as associated with penetrations into granular media, can be conducted on-board while the centrifuge is being operated.

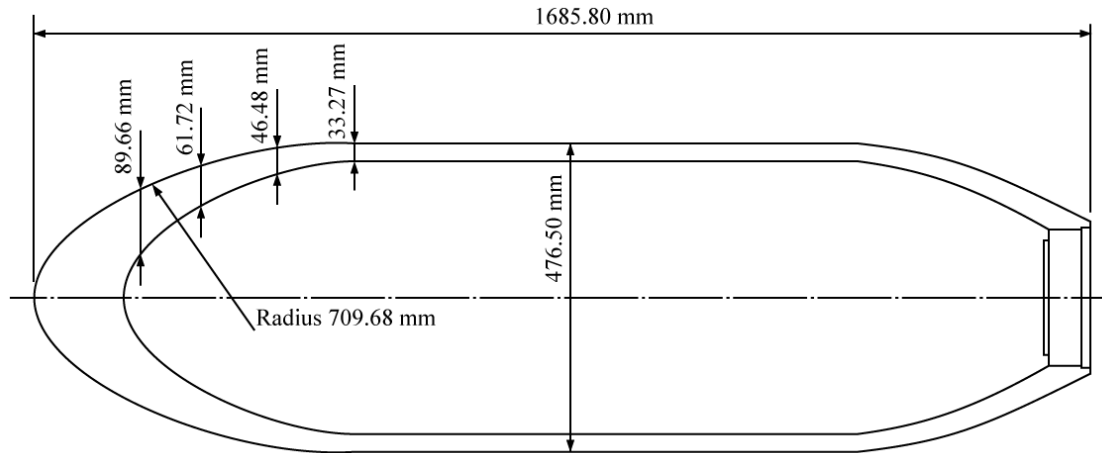


Figure 2.1 Schematic of the SAP 2000 pound projectile (Livingston and Smith 1951)

2.3 General Remarks on Centrifuge Testing

Analyzing projectile penetration into a granular media is a highly complex undertaking; however, with advances in computer hardware, mechanics, and computational techniques, huge leaps in our ability to digitally simulate these systems have been made. In fact, our ability to computationally model geo-structural systems has outstripped our ability to physically model these complex systems. Physical models are, however, necessary to validate computational simulations as well as to understand the failure mechanisms of complex structures. Creating full-scale physical models (e.g. instrumenting a real projectile as it is built) is very costly and time consuming.

Furthermore, field conditions such as subsurface soil profiles are often unknown, it is difficult to take a real structure to the failure state, and only limited loading conditions can be studied. Small-scale centrifuge models can solve all of these problems and make it possible to study geotechnical systems under a variety of conditions. A geotechnical centrifuge makes it possible to accurately model deep deposits with realistic stress conditions, control the repeatability of test results, directly observe failure mechanisms, apply a wide range of dynamic or quasi-static loads, validate numerical and empirical models, and is often used in consulting (Mitchell 1991). The centrifuge tests are also time and cost effective compared to full-scale tests.

2.4 Pertinent Scaling Relationships

In centrifuge modeling, the scale factor for length may be expressed as $L^* = 1/N$. L^* is the ratio of length in the model to length in the prototype. The scaling laws for centrifuge model tests can be found in Schofield (1981), Kutter (1995), and Garnier et al. (2007). A list of the main scaling factors used to convert the measured data to prototype-scale units is provided in Table 3.1.

Table 2.1 Centrifuge Scaling Factors

Quantity	Symbol	Scale Factor
Gravity	g	N
Length	l	N^{-1}
Volume	v	N^{-3}
Mass	m	N^{-3}
Force	F	N^{-2}
Stress	σ	1
Strength	s	1
Moduli	E	1
Time (dynamic)	t_{dyn}	N^{-1}
Time (diffusion)	t_{dif}	N^{-2}

2.5 Centrifuge Testing Scenarios

Three centrifuge tests are planned for the current study, involving the scaled projectiles and granular materials listed in Table 2.2. For each planned test, the diameter and mass of the projectile being fired, relative to the diameter and mass of the SAP 2,000 pound ordnance (Fig. 2.1), dictates the desired level of centrifugal acceleration. Namely, for Tests 1 and 3, a projectile 9 mm in diameter is utilized, and the corresponding level of centrifugal acceleration is 26.5-g. For Test 2, the projectile diameter is 5.185 mm and the desired level of centrifugal acceleration is 46-g. Note that Test 3 is included among the experimental program specifically to facilitate characterization of the effect that different projectile-to-granule diameter ratios have, within the context of the overall test procedure. In all tests the prototype scale mass of the projectiles are identical. Also, a muzzle velocity equivalent (at full scale) to approximately 70 m/sec is tentatively

planned for Tests 1 through 3. In projectile penetration studies, this velocity is categorized as subsonic. Having the same mass and velocity, it is expected that the applied kinetic energy by the projectile to the granular media is identical in all tests.

Table 2.2 Projectile and granular material pairings selected for centrifuge testing

Test number	Centrifugal Acceleration (g)	Projectile diameter (mm)	Projectile mass (gr)	Proppant diameter (mm)
1	26.5	8.99	13.61	0.93 ± 0.08
2	46.0	5.18	2.58	0.55 ± 0.05
3	26.5	8.99	13.61	0.55 ± 0.05

2.6 Projectiles in Centrifuge Experiments

The terminology used in defining the shape of an ogive projectile is illustrated in Fig. 2.2. As it is presented in Table 2.2 and shown in Figs. 2.3, and 2.4 two stainless steel projectiles with different sizes are used in the centrifuge experiments. Both projectiles have an ogive nose with a Caliber Radius Head (CRH) of 1.49. The prototype scale properties of the projectiles are provided in Table 2.3.

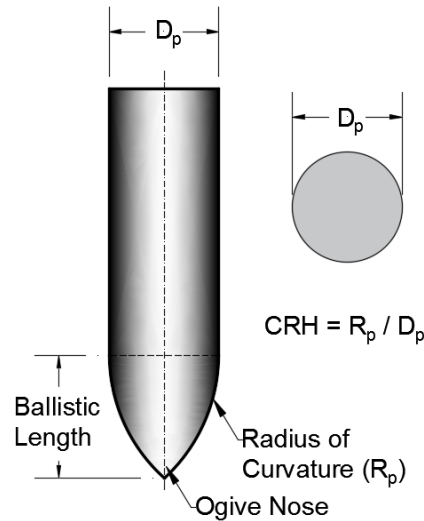


Figure 2.2 Associated parameters with ogive nose projectiles

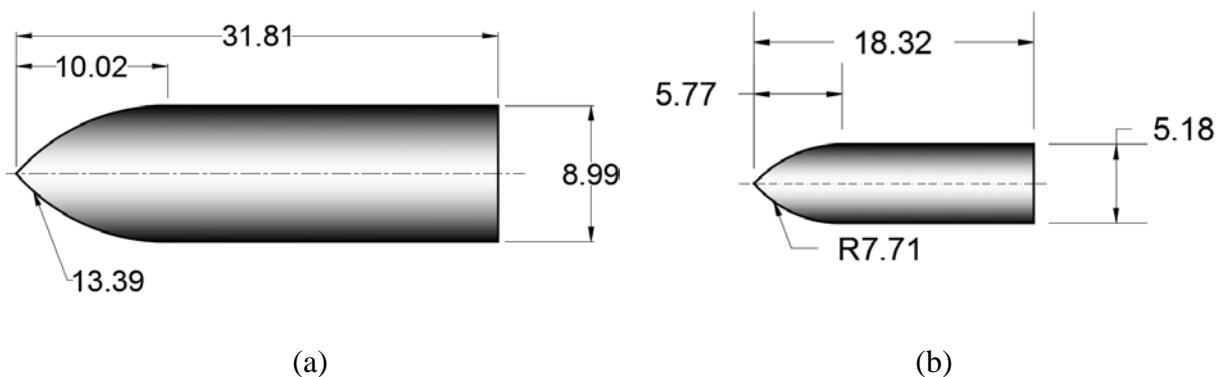


Figure 2.3 Model scale dimensions of the projectiles used in centrifuge experiments with different centrifugal acceleration levels: a) 26.5-g; and (b) 46.0-g (Dimensions in mm)



Figure 2.4 Photos of the projectiles used in centrifuge tests

Table 2.3 Projectile properties in prototype scale

Projectile	Centrifugal Acceleration (g)	Projectile diameter (mm)	Ballistic length (mm)	Projectile mass (kg)
a	26.5	238.24	265.27	253.28
b	46.0	238.28	265.42	251.13

CHAPTER 3

GRANULAR MATERIALS USED IN CENTRIFUGE TESTING

3.1 Overview

The mechanical and engineering properties of granular samples used in the centrifuge and triaxial compression tests are characterized in Ch. 3. Instead of using naturally occurring sand samples, we have made use of artificially manufactured ceramic and sintered bauxite (high-strength proppants) granules with different sizes conforming to a spherical volume. Ceramic and sintered bauxite granules were manufactured by Catalyst Trading Company, Ltd (CTC) and Saint-Gobain, respectively. Ceramic granules manufactured by CTC are often used as support beds, and play a key role in combatting splitting, cracking, and spalling causing major catalyst change-outs. Sintered bauxite (high-strength proppants) was sought out due to the high levels of crush resistance (50 MPa to 100 MPa), sphericity (approximately 0.9), and uniformity. These proppants are mostly used in hydraulic fracturing in petroleum engineering. Different sized granules are employed in the centrifuge experiments, specifically grains with 0.85 mm and 0.5 mm diameters. Using these granules with different sizes allows for the study of scale and size effects in system and element scale tests.

3.2 Motivation for Use of Manufactured Granules

The discrete element method (DEM) idealizes granular materials as spherical volumes of nominal sizes. The shapes and sizes of naturally occurring granular material are highly variant and randomly distributed. This makes it very impractical to model naturally occurring sand using DEM. Even though granules of very small dimensions can be modeled, the corresponding computational costs to model system scale or site-wide problems often becomes too high for this direct approach to be practical. To overcome this obstacle, spherical shaped granules were used in conducting physical tests. Controlling the size and shape of manufactured granules is not very difficult. All the granules conforming to a specific size are found to be very similar in shape with only microscopic deviations.

3.2.1 Advantages for Physical Testing

Naturally occurring sand exhibits high levels of heterogeneity and randomness of the distributions of the shapes and sizes of individual grains. It therefore becomes very difficult to study the individual contributions of these characteristics of granules to the overall system response. By employing spherical granules, all the randomness based on particle size and shape can be eliminated. The homogeneity of an assembly is maximized when using uniform, identical constituent particles. Also, as the physical test results are to be compared to numerical results using DEM, using identical granules eliminates the need to represent a sand granule of random shape and size with a spherical volume.

3.2.2 Advantages for Numerical Modeling

As mentioned earlier, one of the shortcomings of DEM is that we are only capable of modelling granular material as spherical elements. Attempting to replicate the effects of the

geometries of natural grains with spherical discrete elements introduces a source of complication and error in numerical models. One of the other shortcomings of DEM is that the number of input parameters used to define discrete elements is too high. To determine these input parameters using properties of sand grains introduces many statistical variations in the calculations. The characteristics of sand may vary from individual particle to particle. All these statistical variations can be eliminated by using the relatively homogenous and spherical ceramic granules. In the following, the characteristics and attributes of ceramic granules at different scales are measured and are used in calculating the input parameters for the numerical granular material.

3.2.3 Types of Assemblies Considered

A variety of initial relative density states were manufactured through the controlled pluviation of the ceramic granules. By dropping granules from variable heights, different bulk densities were achieved. Most of the assemblies generated for physical tests consist granules with the same size (monodisperse). Also, assemblies with mixed granules were manufactured using two sizes of proppants.

3.3 Preparation and Characterization of Granular Materials

Different batches of proppants were obtained that required careful preparation and characterization. Using the procedure outlined in the American Society for Testing and Materials (ASTM) C 136, each batch was sieved to obtain separate collections of proppants with desired sizes. For the purpose of this investigation, two sizes of ceramic proppants are used. The preparation and characterization of these proppants are explained in the following sections.

3.3.1 Procurement

Ceramic granules were purchased from Catalyst Trading Company, Ltd (CTC), while the sintered bauxite were procured from Saint-Gobain. Prior to running the physical tests using ceramic proppants, the material was sieved using standard ASTM sieves and then washed to get rid of any dust particles. The details of washing and sieving the material are given below.

3.3.2 Washing and Drying

To clean proppant surfaces from the potential dusts produced during sieving, they were rinsed with deionized water and then oven dried at 230 °F for at least 24 hours. After rinsing and oven drying, proppants were stored in air/water-tight barrels.

3.3.3 Sieving

Using the procedure outlined in the American Society for Testing and Materials (ASTM) C 136, each batch of proppants were sieved to obtain desired sizes. 0.85 mm proppants were passed through the ASTM No. 18 sieve and were retained on the ASTM No. 20 sieve. 0.5 mm proppants were passed through the ASTM No. 30 sieve and were retained on the ASTM No. 35 sieve.

3.3.4 Microscopic Laboratory Tests Conducted

Previous research has established that the macroscopic and system scale response of an assembly of granular material is heavily influenced by the microscopic characteristics of the individual grains of the assembly. These microscopic properties are a direct manifestation of surface texture. Surface texture is the repetitive or random deviation from the nominal surface that forms the three-dimensional topography of the surface. Surface texture is a function of (1) roughness (nano- and micro-roughness); (2) waviness (macro-roughness); (3) lay; and (4) flaws. Nano- and micro-roughness represent the features of a granule resulting from the manufacturing process. Waviness is the surface irregularity of longer wavelengths and is referred to as macro-roughness. Lay is the principal direction of the predominant surface pattern, ordinarily dictated by the production method. Flaws are unintentional, unexpected and unwanted interruptions in the texture (Bhushan 2001). A typical display of the surface texture is given below (Fig. 3.1).

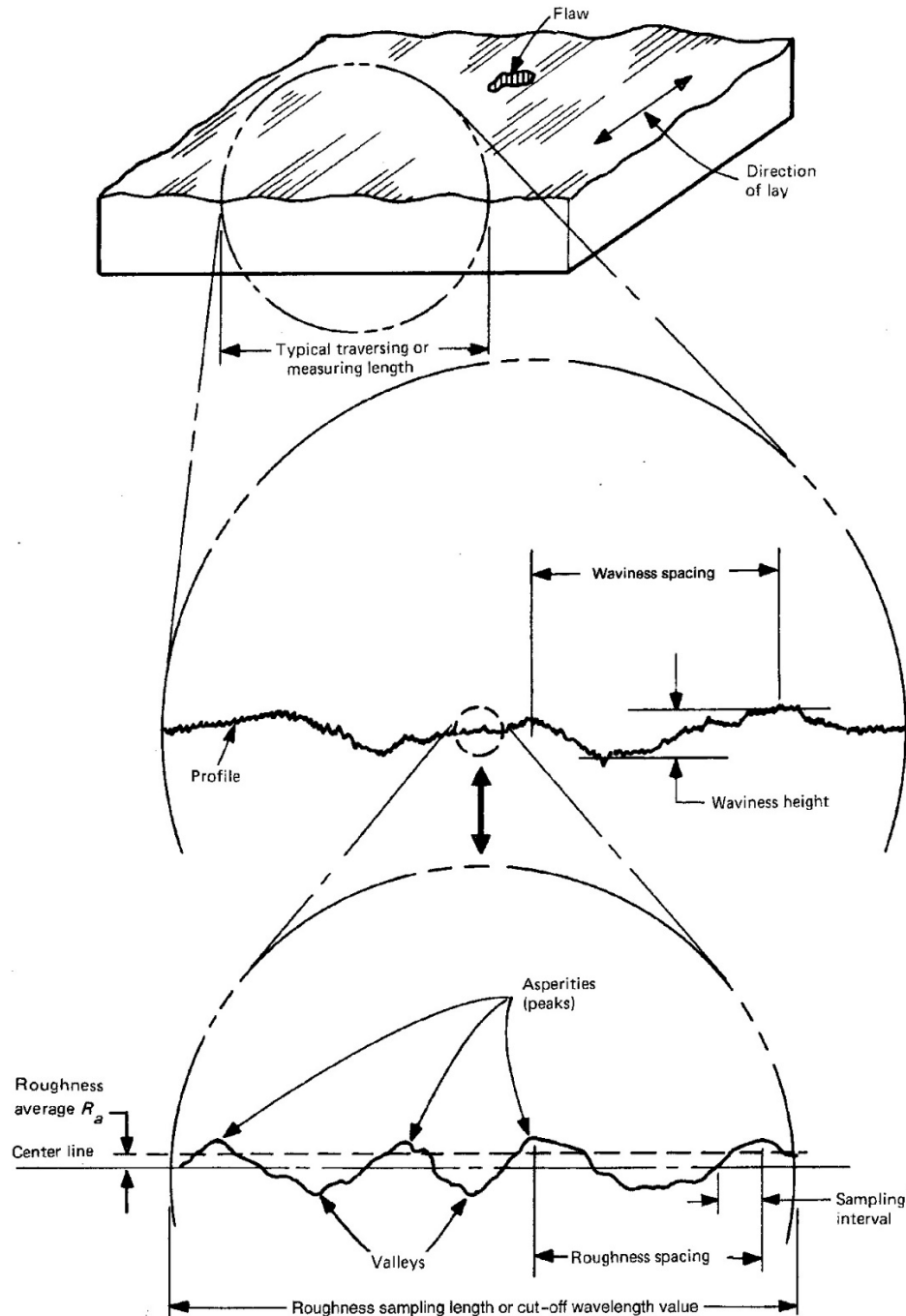


Figure 3.1 Pictorial display of surface texture (Bhushan 2001)

The general typology of solid surfaces is summarized in Fig. 3.2., which is first described by the homogeneity of the material. Next, the roughness of the surface profile can be quantified as being random or deterministic (i.e. triangular or sinusoidal). Analysis for a deterministic surface is relatively straightforward; however most surfaces occurring in nature exhibit certain degree of randomness. This randomness in surface texture can be further classified as being isotropic or anisotropic by analyzing the spatial correlation structure of the surface. If the spatial correlation

function exhibits isotropic randomness, the distribution of surface perturbations or surface heights can be established as being Gaussian or non-Gaussian.

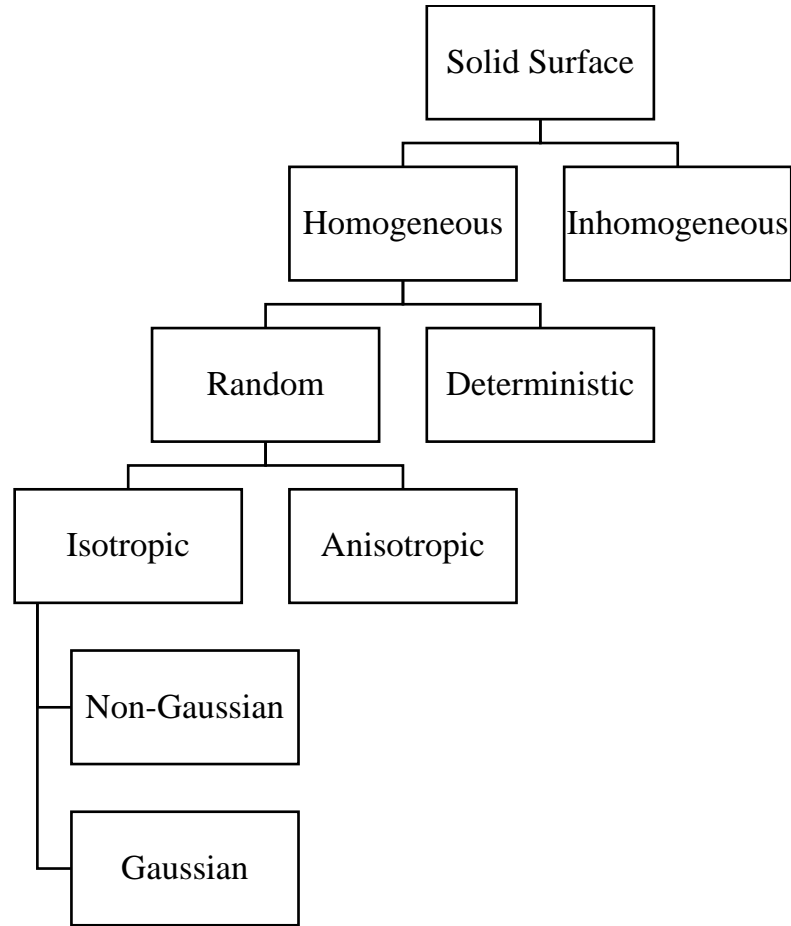


Figure 3.2 General typology of solid surfaces (Bhushan 2001)

The surface height distribution is represented using many different average roughness parameters. These parameters are calculated on the basis of a reference plane over which the surface height distribution is measured. The statistical descriptors advocated by the American National Standards Institute (ANSI) and the International Standardization Organization (ISO) are (1) R_a , CLA (center-line average), or AA (arithmetic average); and (2) the standard deviation or variance (σ) or R_q , RMS root mean square. The mathematical form of the parameters is given below (Bhushan 2001):

$$m = \frac{1}{N} \sum_{i=1}^N z_i \quad (3.1)$$

$$\sigma^2 = \frac{1}{N} \sum_{i=1}^N (z_i - m)^2 \quad (3.2)$$

$$R_a = \frac{1}{N} \sum_{i=1}^N |z_i - m| \quad (3.3)$$

$$R_q = \sqrt{\sigma^2 + m^2} \quad (3.4)$$

The average roughness parameters are a measure of variability of surface height distribution in the vertical direction only and do not give any information regarding the slopes, shapes and sizes of the surface peaks or about the frequency or regularity of occurrence of the peaks. These parameters are not sufficient to completely characterize the surface profile because it is possible for surfaces of widely differing profiles with different frequencies and different shapes to have the same average roughness parameters. To completely characterize the surface height distribution, additional parameters need to be quantified. These parameters are known as the spatial parameters. One of the most common mathematical descriptions for the surface profile is the covariance $C(\tau)$ and corresponding power spectral density $P(\omega)$ functions. In a functional form, these mutually-dependent surface descriptions can be written as (Bhushan 2001):

$$C(\tau) = \frac{1}{N(\tau)} \sum_{i=1}^N (z(x_i) - m)(z(x_i + \tau) - m) \quad (3.5)$$

$$P(\omega) = P(-\omega) = \int C(\tau) \exp(-i\omega\tau) d\tau \quad (3.6)$$

The above mentioned statistical parameters are enough to extract all the information for a measured surface height distribution. The two most important quantities that are extracted from the power spectral density functions are asperity density η (number of peaks per unit area) and the radius of curvature of asperity peak β . Given by Nayak (1971), m_n denotes the n^{th} moment of the power spectral density function:

$$m_n = \int \omega^n G(\omega) d\omega \quad (3.7)$$

$$\beta = \frac{3\sqrt{\pi}}{8\sqrt{m_4}} \quad (3.8)$$

$$\eta = \frac{1}{6\pi\sqrt{3}} \left(\frac{m_4}{m_2} \right) \quad (3.9)$$

Based on the mathematical method, physical measurement on the surface profile is discussed next. Physical testing methods are, in general, categorized: (1) contact type; and (2) non-contact type. In contact type measurement of surface height distribution, a component of the measuring instrument, like a stylus, is actually in contact with the surface. Most importantly the probe must have a very sharp apex. The detailed shape of the scanning tip is sometimes difficult to determine. Its effect on the resulting data is particularly noticeable if the specimen varies greatly in height over lateral distances of 10 nm or less. Consequently, these scanning techniques are generally

slower in acquiring images, due to the scanning process. The resolution of the microscopes is not limited by diffraction, only by the size of the probe-sample interaction volume (i.e., point spread function), which can be as small as a few picometres. The capability to measure small local differences in object height (like that of nano-scale) is unparalleled. Though, its effect on the resulting data is very sensitive if the specimen varies greatly in height over lateral distances of 10 nm or greater. Consequently, the maximum image size is generally much smaller by orders of magnitude than nominal contact areas of granules with rough surface. Thus, this type of measurement technique may not be appropriate for surface profiling on the lower end of spectrum in asperities. In addition, a (relatively) large normal-contact force would be required on the stylus to move along a larger slope of low-frequency wavy surfaces, and thus, even if possible without causing tip buckling, its sliding motion may cause damages during “scratching”.

Other non-contact techniques include optical methods, electrical methods, and scanning electron microscopy (SEM) methods. Of application interest is a type of electron microscope that produces images of a sample by scanning it with a focused beam of electrons, namely scanning electron microscopy (SEM). SEM is not a camera and the detector is not continuously image-forming like a film. Unlike an optical system, the resolution of SEM is not limited by hardware fineness (lenses or mirrors) and/or detector resolution. The spot size and the interaction volume are both large compared to the distances between atoms, so the resolution of the SEM is not high enough to image individual atoms, as has compensating advantages, though, including the ability to image a comparatively large area of the sample's surface. In the present study, this type of noncontact-based scanning electron microscopy is mainly employed in surface profiling for lower-frequency asperity distribution over a nominal contact area (e.g., 100 microns by 100 microns), whereas a contact-based scanning probe microscopy (SPM) is used in “spot checking” for high-frequency asperities with tip radii, ranging from one micro to a few microns. Data analysis on both spectra is used to construct the surface topography of ceramic proppants.

3.3.5 Grain-scale Laboratory Tests Conducted

To measure mechanical contact behaviors of granules, a variety of grain-scale laboratory tests were conducted, i.e., micro-indentation and surface sliding tests. Micro-indentation tests were performed between pairs of granules to obtain the load-displacement relationship for the granular material. The loading scheme of 0-30-0 N at a N/min loading rate was used. A schematic sketch of the micro-indentation test set up is given below (Fig. 3.3). To determine the static and kinematic friction coefficients for the specimen, sliding tests were performed under varying normal loads. For each stage of normal loading, 5 measurements were taken at a sliding speed of 0.2 mm/s. Static friction and kinetic friction measurements were taken separately due to the spherical shapes of sliding counterparts. To measure static friction, the test was initiated with the spheres in an apex to apex position, and a sliding distance of 1mm. Kinetic friction measurements were also taken across a sliding distance of 1 mm, but the tests were initialized with the top ball offset from the apex of bottom ball such that it would slide across the apex of the bottom ball once sliding motion was in progress. A schematic sketch of set up for the sliding test of static and kinetic friction coefficients is shown in Fig. 3.4.

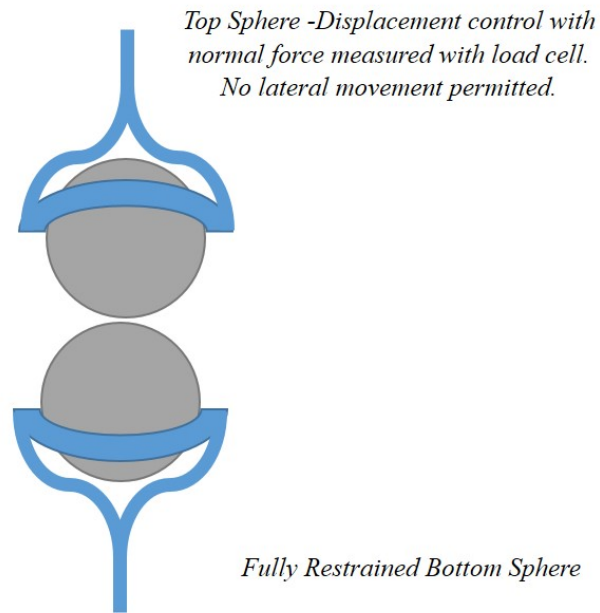


Figure 3.3 Physical test set up for micro-indentation test.

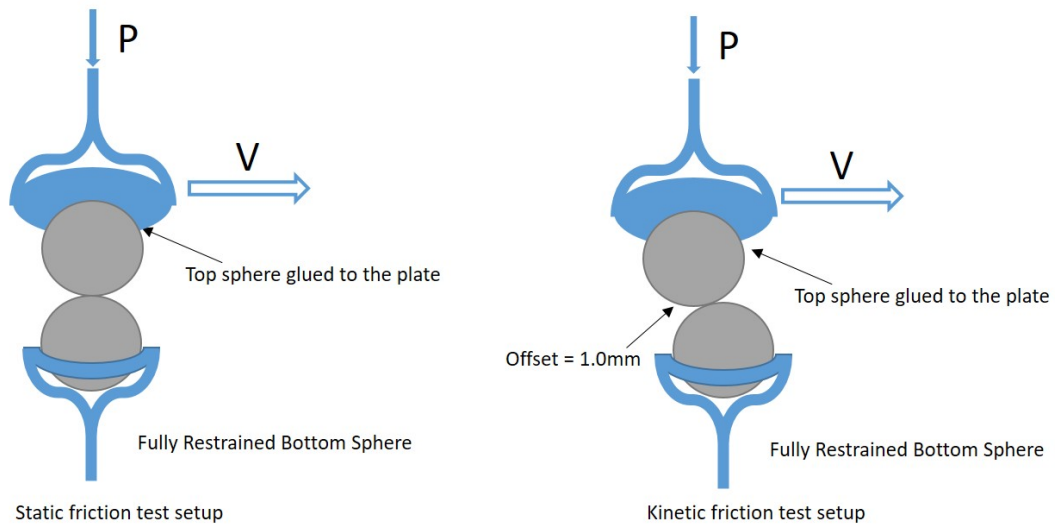


Figure 3.4 Schematic sketch for scratch test.

3.3.6 System-scale Laboratory Tests Conducted

To observe the system scale response of granular material, consolidated drained tri-axial compression tests were performed at three different confining pressures – 40 kPa, 70 kPa and 100 kPa. A cylindrical assembly of granular material with dimensions 4 in x 8 in was used to determine the shear strengths of granular material. The assembly was created by dropping the granules inside

the chamber from a drop height of 223.12 mm from the bottom of the chamber. The granules were dropped through a funnel with an opening of 37.55 mm diameter. The test setup for packing of the granules inside a tri-axial chamber is given in Fig. 3.5.

Once the packing is created, the tri-axial chamber is hermetically sealed. A specified confining pressure is then applied to the chamber using water. It is important for the applied pressure to be equal in the horizontal and vertical directions prior to shearing the sample. Therefore, the pressure that develops within the chamber and the pressure that arises at the top and bottom plate interfaces are constantly measured. The final stage of tri-axial compression test consists of shearing the sample by imposing a controlled vertical translation to the top plate relative to the bottom plate. During this controlled shearing process, the tri-axial chamber pressure is maintained constant. The force required to maintain the controlled vertical translation of the top plate is recorded. The volume change of the specimen is measured by the amount of water moving in and out of the tri-axial chamber to maintain the prescribed confining pressure on the specimen. Data recorded during the testing permits quantification of: 1) Deviatoric stress versus axial strain; and, 2) Volumetric strain versus axial strain. Ultimately, such quantities facilitate the generation of Mohr-Coulomb failure envelopes, as well as the characterization of macroscopic properties. The results from tri-axial compression tests performed using ceramic proppants are given below.

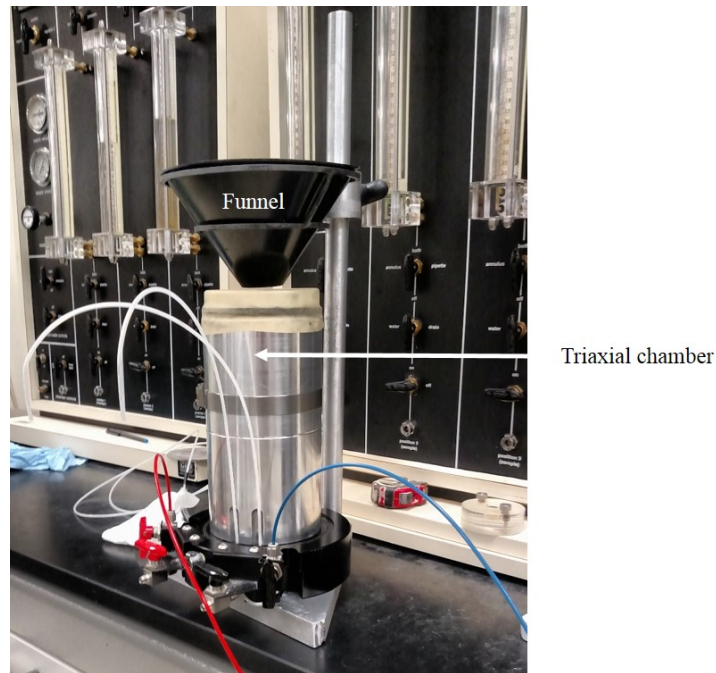


Figure 3.5 Packing apparatus for granules

3.4 Proppants (0.93 ± 0.08 mm)

In this section, we shall focus on the characterization of physical properties demonstrated by ceramic proppants with diameter 0.93 ± 0.08 mm across micro, macro (grain) and system scales.

3.4.1 General Description

The parameterization of microscopic as well grain-scale properties exhibited by granular material is of key importance to predict the system scale behavior of any assembly comprised of these granules. Following the procedure described in the above sections, microscopic properties such as surface roughness are measured using SEM and SPM imaging; grain-scale properties like contact stiffness, nano-hardness and the coefficients of friction are measured and the system scale response under tri-axial compression is then observed.

3.4.2 Microscopic Variability of Surface Roughness

To determine the surface roughness of proppants using SPM imaging, two scan areas of $1 \times 1 \mu\text{m}$ and $10 \times 10 \mu\text{m}$ were imaged at the apex of six spheres. Similarly, to determine the surface roughness of proppants using SEM imaging, a scan area of $100 \times 100 \mu\text{m}$ was imaged at the apex of six spheres. The surface roughness parameters measured are average roughness, RMS roughness, etc. The SPM and SEM images for proppants are shown in Fig. 3.6. The roughness parameters calculated based on the SPM and SEM images are tabulated below (Table 3.1).

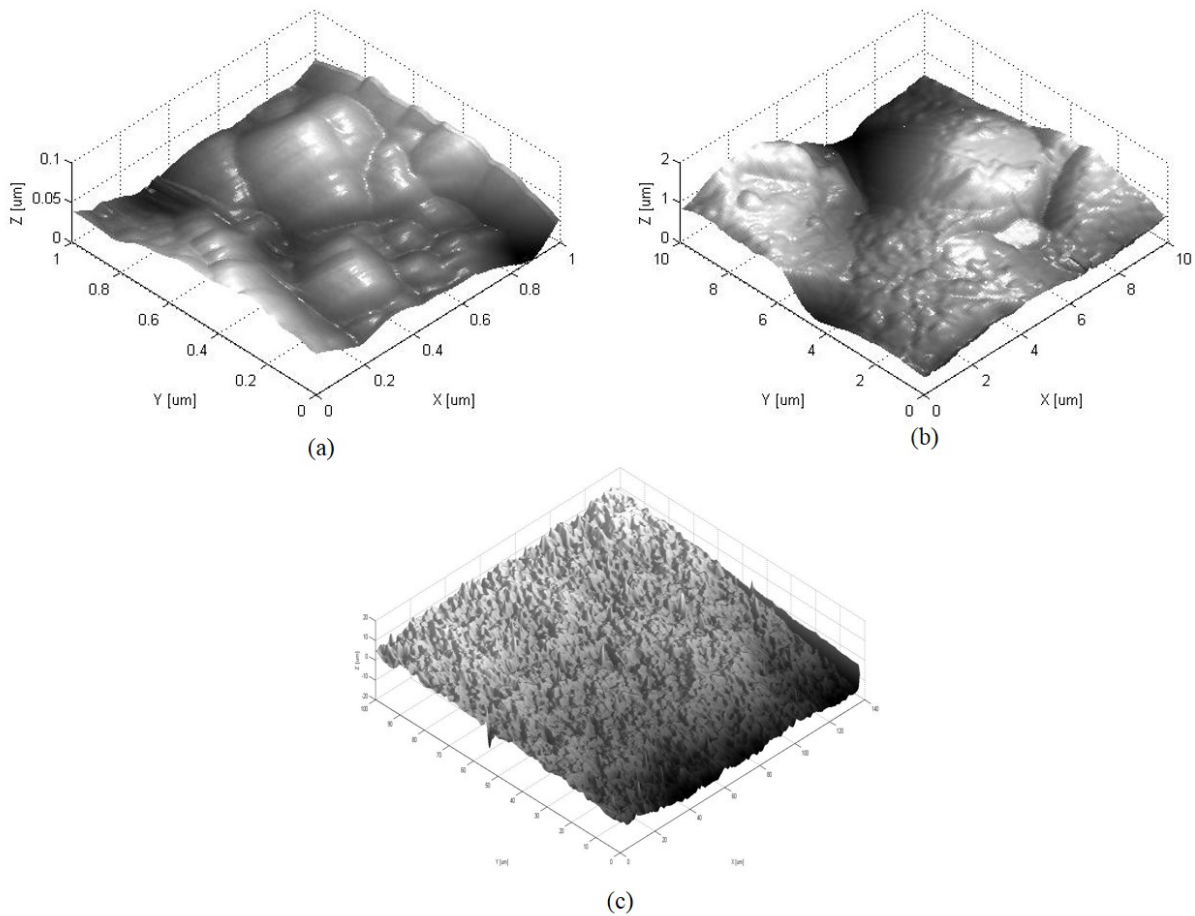


Figure 3.6 SPM and SEM images for proppants with diameter $0.93 \pm 0.08 \text{ mm}$; a) $1 \times 1 \mu\text{m}$ scan size; b) $10 \times 10 \mu\text{m}$ scan size; c) $100 \times 100 \mu\text{m}$ scan size

Table 3.1 Roughness parameters for ceramic proppants with 0.93 ± 0.08 mm diameter

Scan size	Average roughness	RMS roughness	Peak to valley heights
1 μm x 1 μm	22.75 nm	28.63 nm	171.63 nm
10 μm x 10 μm	0.26 μm	0.33 μm	2.00 μm
100 μm x 100 μm	2.34 μm	2.89 μm	17.55 μm

Following the procedure outlined in section 3.3.4, spatial functions and surface roughness parameters were calculated. One instance of these results are given below (Fig. 3.7). More detailed results are reported in Appendix B.

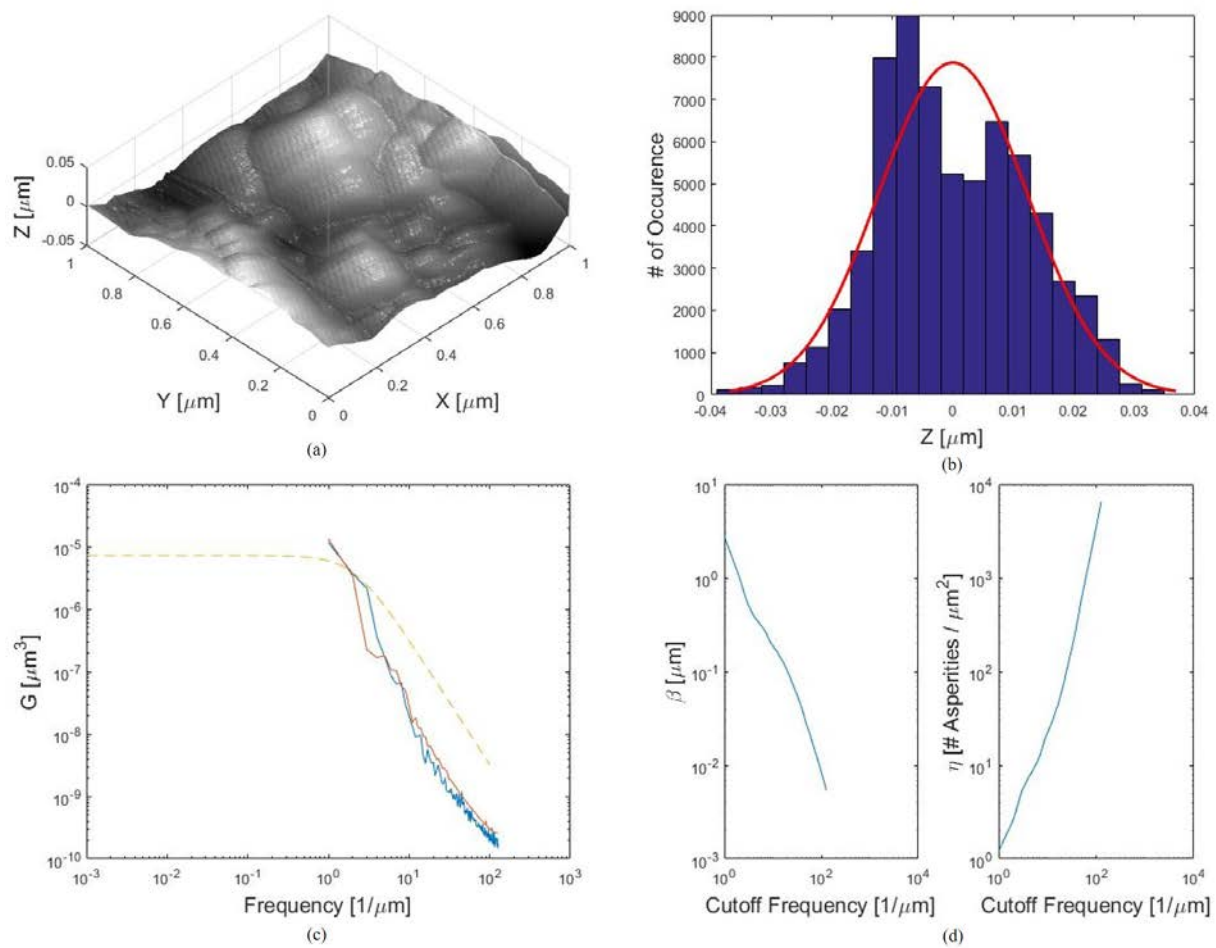
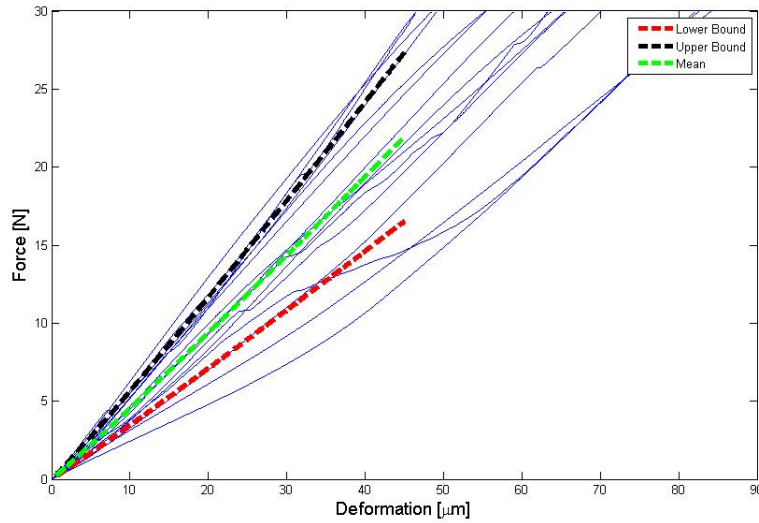


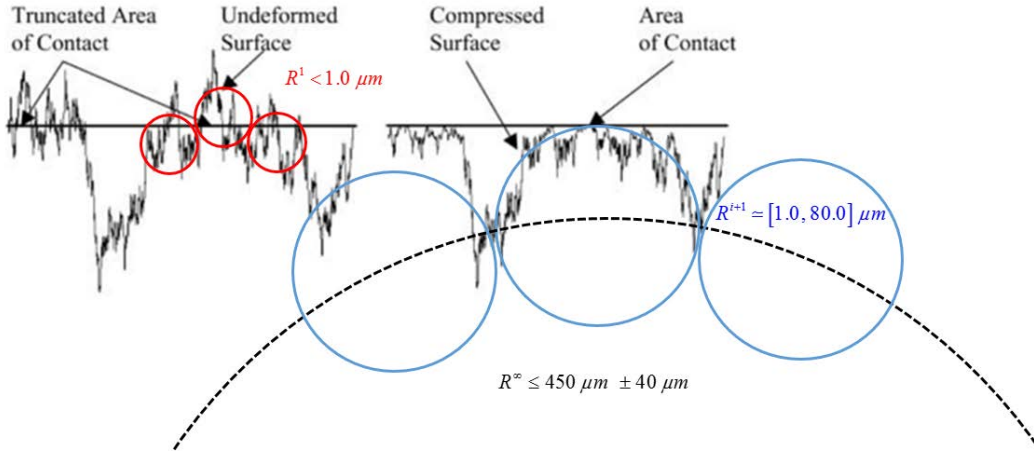
Figure 3.7 (a) SPM image of scan size $1\mu\text{m}$ x $1\mu\text{m}$; (b) Histogram of surface height distribution; (c) Power spectral density function; and (d) Radius of asperity peak and asperity density

3.4.3 Grain- scale Parameters

Physical measurements on grain-to-grain contact force-displacement were performed in total 15 micro-indentation tests with ceramic proppants with a mean diameter of 0.9 mm. Shown in Fig. 3.3.8a, micro-indentation displacement exhibits variation with respect to applied normal loads. The changes in the tangent slopes, i.e., normal contact stiffness, are deviated from the classical Hertz solution by a few orders of magnitude.



(a) Micro-indentation test results for ceramic proppants with 0.93 ± 0.08 mm diameter



(b) Schematic sketches of asperities at underlying scales in relation to nominal contact planes: the contact radius of curvature is limited to a maximum value of the ceramic proppants' mean radius: Truncated areas of contact indicate the onset of plastic deformation on asperities at a high frequency level (Not scaled).

Figure 3.8 Contac forces acting normal to contact planes with surface roughness illustrated by a fractal structure of Archard's stacked hemispheres

It is because apparent contact area of rough surfaces is much greater than a point contact between the pairing smooth surfaces. Local contacts on the summits of microscopic asperities at a scale in contact may still be regarded as smooth contact at that scale, and thus, sum of the local elastic contact areas increase monotonically with respect to the Hertz contact theory. However, at grain-scale contact with rough surfaces, the square root of a product of radius of curvature (i.e., a radius of the curved contact plane) and normal displacement (i.e., a gap closure between the two contacting planes) does not obey to the assumption of point-contact by Hertz; it must be incrementally evaluated at closing distances between the rough surfaces: $A_{app}^i - A_{app}^{i-1} = \Delta A_{app} \propto \Phi(\langle \lambda^i \rangle, \langle R^i \rangle, \langle \Delta \delta_n^i \rangle)$ where ΔA_{app} represents incremental apparent contact area that can be written in a closed-form function Φ of statistical means of frequency level λ , representative radius of curvature (R) at that frequency level, and an increment of gap closure distance $\Delta \delta_n$ at i th loading step. Spatial frequency of asperity distributions is the reciprocal of wave length (ω): $\lambda = 1/\omega$. That is, the changes in the tangent slope of the micro-indentation curves (i.e., normal contact stiffness) vary with the rate growth of apparent contact areas where fractal surfaces possess various radii of microscopic curvatures and distributions of asperity heights consisting of deviations from a nominal contact plane in Fig. 3.8b. In relation to a grain-scale point contact problem as illustrated in Fig. 3.4, it is quite challenging (and perhaps impractical) to solve the equations of motion at the microscopic scale as per the actual geometry (often referred to as a deterministic contact model). Instead, we establish a conceptual basis for the development of a closed-form solution to the equations of motion specific to *representative* microscale boundary values, but the resultant forces are subjected to surface averaging over the apparent contact surface per growth rates in the grain-scale boundary conditions.

Present efforts are aimed to estimate average contact pressures over an apparent contact area per increment of gap closure (i.e., separation distance between two non-conforming contact surfaces), which, in turn, can define the contact force-displacement relationships of the grains with rough surfaces. A closed-form solution to surface averaged forces and corresponding incremental separation distances of the non-conforming planes of contact has been being derived with respect to statistical mean boundary values. In accordance with given surface topography, an iterative procedure is adopted based on Archard's stacked asperity concept. For instance, asperity-tip contact pressures at each scale of conceptualized fractal topology (Fig. 3.8b) increases until the asperities undergo full plastic stages. Local contact pressures (p) that account for in the onset of plastic deformation result in "flattening" of high-frequency asperities. Once the contact size surpasses a critical value of mean radius of curvature at each scale (when the asperities in higher frequencies have been flatten out), the lower frequency asperities take up the load increment and deform elastically. Transitions from elastic to full plastic states of local asperities at each scale (i) are to be calculated in the analytical contact stiffness model, which has two parts, i.e., elastic (f_i^e) and plastic (f_{i-1}^p):

$$\begin{aligned}
F_i &= F_i^e + F_i^p \\
&= \frac{4}{3} \cdot \langle N_i \rangle \cdot \langle E^* \rangle \cdot \left(\frac{\langle \gamma_i \rangle}{2} \right)^{\frac{1}{2}} \cdot \langle \lambda_i \rangle^{\frac{3}{2}} \cdot H(\xi_i - \xi_{i-1}) + \langle N_{i-1} \rangle \cdot \Gamma(\xi_{i-1}) \cdot \langle \sigma_y \rangle \\
&= A(\Delta\xi, N, E^*, \lambda, \sigma_y)
\end{aligned} \tag{3.10}$$

where, per a given total number of local maxima per unit area $\langle N_i \rangle$ of the i th scale, elastic contact force is a function H of normalized separation distance, i.e., normal displacement (of the micro-indentation) divided by surface roughness, a radius of curvature $\langle \gamma \rangle$ of asperity tips, a reduced elastic modulus E^* , and surface roughness $\langle \lambda \rangle$ (Greenwood and Williamson, 1966);, and plastic force is a function of total plastic area of asperities at the $(i-1)$ th scale and yield stress $\langle \sigma_y \rangle$. A closed-form solution for the elastic force and corresponding apparent area has been completed. Model prediction solely based on the elastic solution, though, was found to be deviated from micro-indentation test results. That necessitated the inclusion of elastic-plastic analysis in the contact model, i.e., the plastic force term on the right hand side of Eqn. (3.10).

Another factor that contributes to the variation of the micro-indentation as shown in Fig. 3.8a is possible stick-slip phenomena of contacting asperities, which may have influence in the global (grain-scale) normal force equilibrium, subjected to relative displacement along local contact boundaries. Local asperities engaged in oblique angles of elastic contact in lower frequency domains can substantiate asperity-interlocking against tangential relative motions of the grains. That is, at each incremental normal “displacement” measured in the micro-indentation tests, mobilization of local tangential resistance could substantially vary with respect to anisotropic distribution of asperity density and height on the non-conforming contact planes. Even if the micro-indentation test is performed perfectly normal to an assumed conforming plane of contact, the occurrence of slippage in low-frequency contact asperities may lead to the lower bound of “normal” contact stiffness measured in the micro-indentation tests. Thus, Eqn. 3.10 becomes

$$A(\Delta\xi, N, E^*, \lambda, \sigma_y, \psi) \tag{3.11}$$

where ψ is mean value of tangential stress correction factor (Brown and Scholz 1985). Thus, given surface topographical and material parameters, the normal contact force can be written in a function A of gap closure increment $\Delta\xi$. For the micro-indentation by an equal-sized sphere, the appropriate scaling is derivable from a single (mean) relation which may be given in the power-law form:

$$\frac{F}{A(\Delta\xi, N, E^*, \lambda, \sigma_y)} \propto (d_n)^{m(\lambda, \gamma_{\max})} \tag{3.11}$$

where the function m is assumed to depend upon the growth of apparent contact area ΔA_{app} at an increment of macro normal displacement Δd_n per maximum radius of asperity summit γ_{\max} (e.g.,

the lowest frequency). With increasing gap closure, the micro-indentation response becomes dominated by plastic flow. It is to be reasonably expected that the elastic parameters become irrelevant; then, the non-dimensional contact size $\Delta A/R$ and contact pressure F/A_{app} will depend only upon non-dimensional gap-closure $\Delta d_n/\gamma_{max}$. In iterative solution procedures, $\Delta d_n/\gamma_{max}$ is being solved for incremental forces in the micro-indentation tests. In the meantime, numerical contact models are developed in the power-law form, which is empirically determined based on curve fits of the micro-indentation test data, in order to facilitate the SEED timeline.

Note that in the Hertz solution, Poisson's ratio ν appears combined with the Young's modulus E in the form of a single elastic constant $E^* \equiv E/2(1-\nu^2)$. Experiments and early numerical results summarized by Johnson (1985, p. 176) suggest that the elastic constant E^* adequately describes the elastic contribution to deformation in the elastic-plastic indentation regime. To determine the elastic constant E^* (and yield stress σ_y for the elastic-plastic analysis), nano-indentation tests were performed on two different types of ceramic proppants (aluminosilicate) by Dr. Dehua Yang and his colleagues (Ebatco, LLC). To obtain nano-hardness and indentation surface area, 10 indents, sufficiently spaced, were made on the apex of each of the proppants by the Vickers indenter. These indents were incrementally made up to a maximum load of 400 μN . In order to validate the values of elastic constants and hardness provided to us, the relation between elastic constant and load-displacement curves of the nano-indentation is calculated for one set of data (randomly selected out of ten data tests) using classical Hertzian contact theory and the self-similarity solution (Mesarovic and Fleck, 1998), independently of their calculations. Due to a lengthy calculation, detailed data analysis on the nano-indentation test is omitted in the report. A summary of results from nano-indentation tests is given in Table 3.2. All the data obtained from nano-indentation tests are given in Appendix B.

Table 3.2 Nano-indentation test results for ceramic proppants with 0.93 ± 0.08 mm diameter

Test	Hardness (GPa)	Reduced modulus (GPa)
Sphere 1	9.76	69.37
Sphere 2	8.30	140.12
Sphere 3	10.50	168.90
Average	9.52	126.13

To assess friction coefficients, five measurements were made at constant normal loads mentioned in section 3.3.5. The results from scratch tests are given in Table 3.3. All the results from scratch tests are elaborated in Appendix B. Limiting tangential force results are plotted in Fig. 3.9 through 3.14. Additional data of tangential force vs. applied normal loads, and measurement of surface energy (Parks 1984) are necessary for analysis to draw a correlation with normal displacement based on tribological theories; a theoretical derivation based on the JKR theory is given in A34 of Appendix A.

Table 3.3 Tangential contact stiffness from static friction tests

Applied normal force (N)	constant	Average static friction coefficient	Sliding distance (mm)
0.245		0.694	0.1124
0.49		0.682	0.1393
0.98		0.407	0.191
1.96		0.367	0.2868
4.90		0.437	0.4623

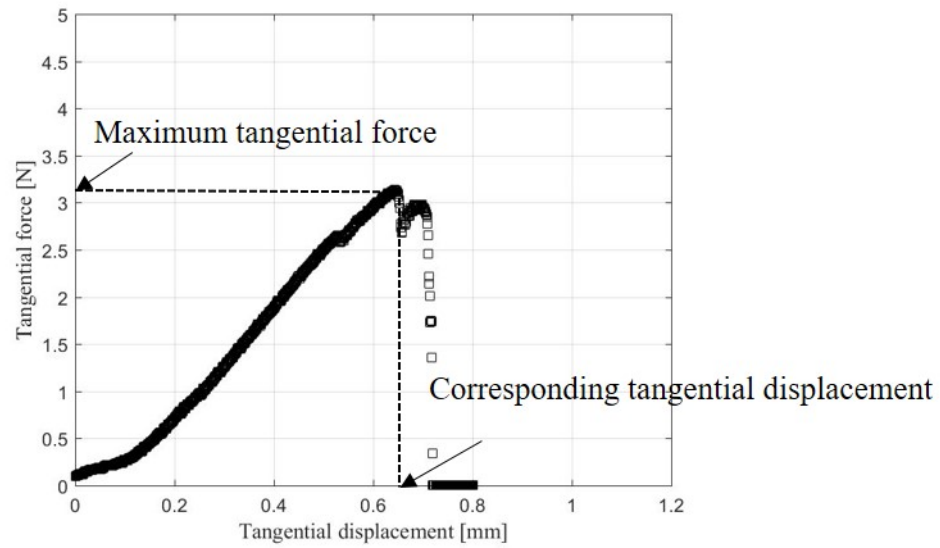


Figure 3.9 Maximum tangential force and corresponding tangential displacement from static friction test

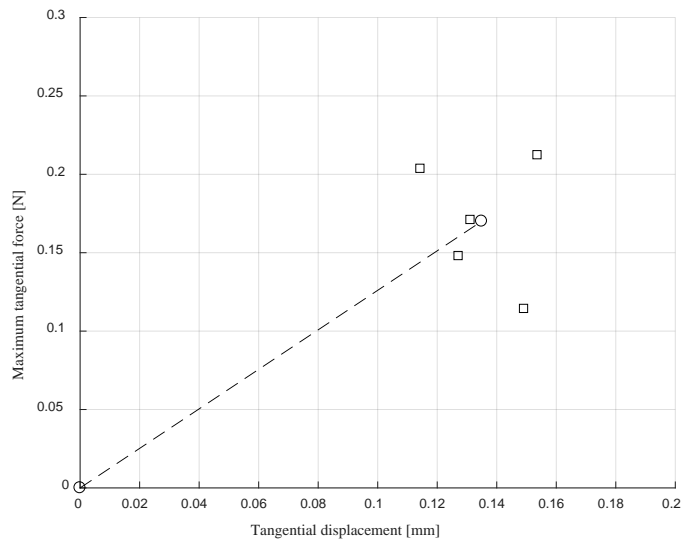


Figure 3.10 Tangential force-displacement results from static friction test at 25 gf normal force

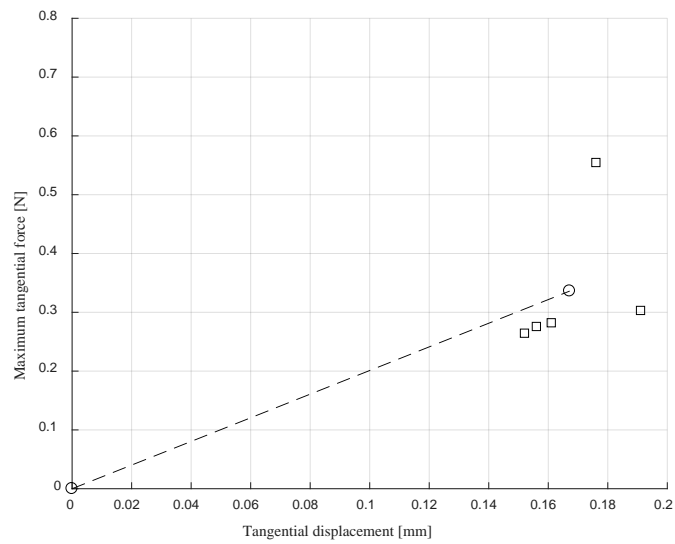


Figure 3.11 Tangential force-displacement results from static friction test at 50 gf normal force

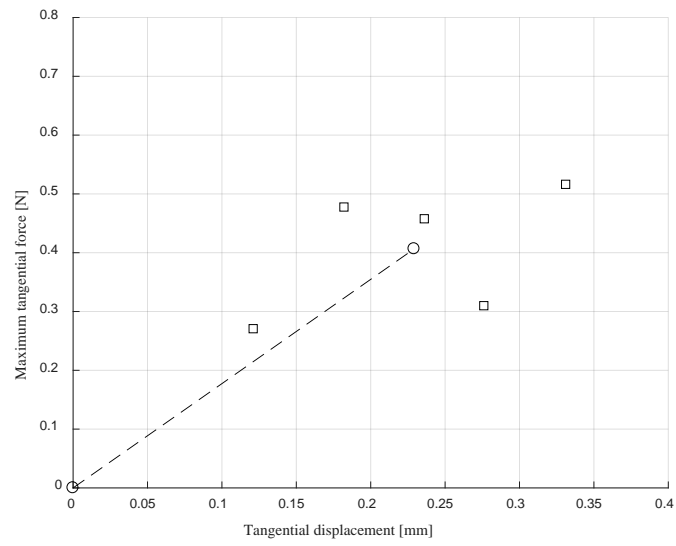


Figure 3.12 Tangential force-displacement results from static friction test at 100 gf normal force

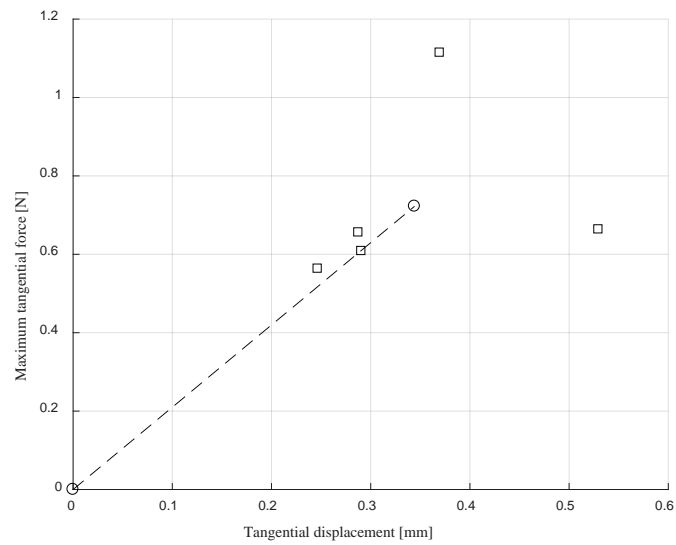


Figure 3.13 Tangential force-displacement results from static friction test at 200 gf normal force

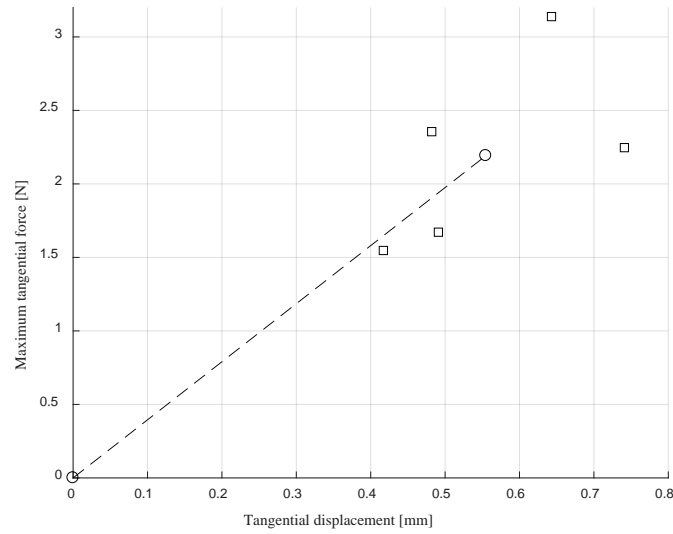


Figure 3.14 Tangential force-displacement results from static friction test at 500 gf normal force

3.4.4 Continuum-scale empirical observation

The continuum-scale quasi-static response of ceramic proppants with 0.93 ± 0.08 mm mean diameter is estimated in laboratory-scale tri-axial compression tests at three different confinements. Deviatoric stress axial strain relationship is given in Fig. 3.15; volumetric strain vs axial strain relationship is given in Fig. 3.16; and a failure envelope is given in Fig. 3.17. The purpose of the tests is to make phenomenological comparison to volume-averaged shear strength of natural sands. The slope of failure envelope is 0.52.

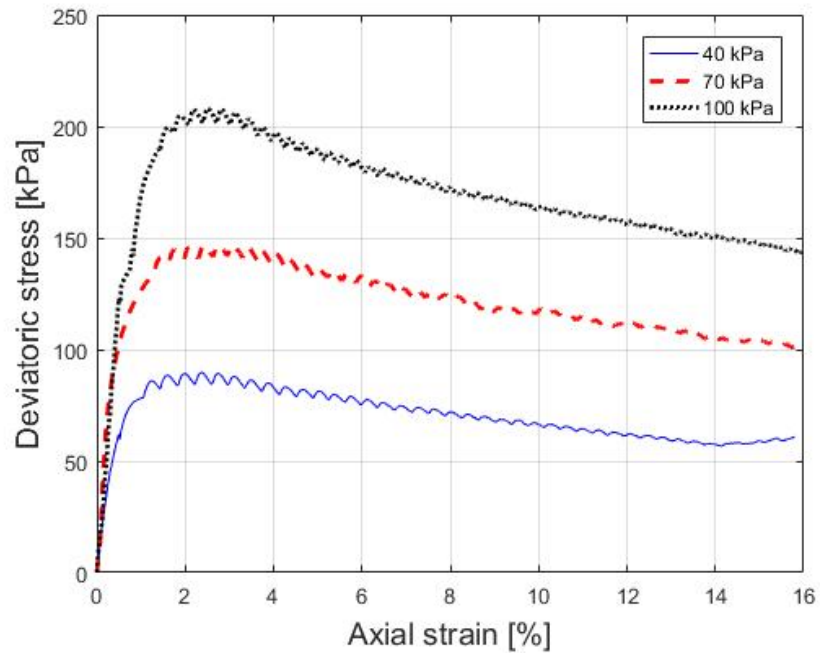


Figure 3.15 Deviatoric stress vs axial strain relationship

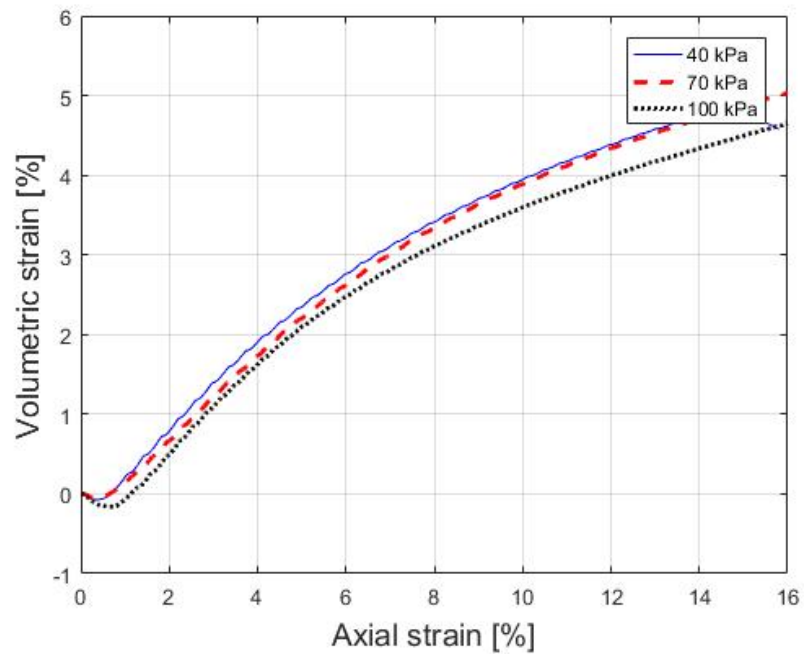


Figure 3.16 Axial strain vs volumetric strain relationship

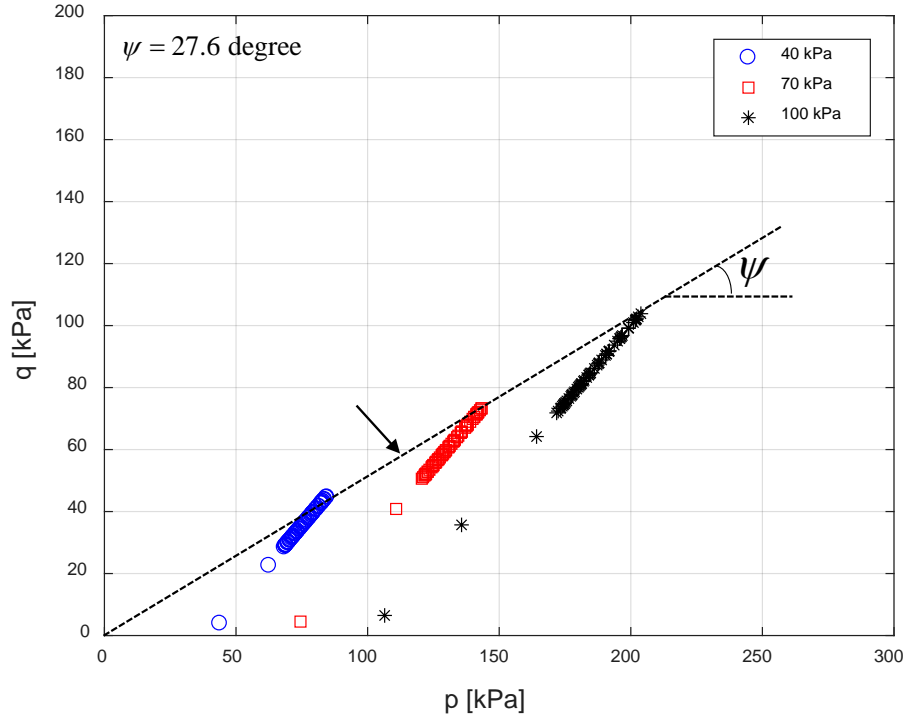


Figure 3.17 Stress paths and the failure envelope

3.5 Proppants (mean diameter of 0.55 ± 0.05 mm)

In this section, we are going to focus on the characteristics exhibited by ceramic proppants with 0.5 mm mean diameter.

3.5.1 General Description

Similar to the case for ceramic proppants with mean diameter 0.93 ± 0.08 mm, it is important to parametrize the physical characteristics exhibited by ceramic proppants with mean diameter 0.55 ± 0.05 mm. These are given in subsequent sections.

3.5.2 Microscopic Properties of 0.55 ± 0.05 mm Proppants

Both sizes of ceramic proppants are composed of the same material with similar material properties, and are manufactured using the same technique. As, surface texture (roughness) is a manifestation of manufacturing process, we expect both the proppants to possess similar average roughness parameters and spatial function.

3.5.3 Grain-scale Parameters

The nano-hardness and reduced modulus are a function of material properties and surface texture. Thus, the nano-hardness and reduced modulus for proppants of both the sizes are similar.

These are given in Table 3.2. The measured static and kinetic friction coefficients are given in Table 3.3.

3.5.4 Continuum-scale Empirical Observation

The continuum-scale test results for the 0.55 ± 0.05 mm proppants are not available.

CHAPTER 4

CENTRIFUGE MODELING OF PROJECTILE PENTRATION INTO GRANULAR ASSEMBLIES

4.1 Overview

Centrifuge testing allows the investigation of system-level, complex problems that would otherwise only be possible by full-scale testing. An important aspect to be considered in testing reduced-scale centrifuge models is their similitude with field-scale prototypes. Because the strength, stiffness, deformation, and volume change in soils is stress-dependent, the key objective of a centrifuge model is to keep the stresses identical to that of a prototype. The geotechnical centrifuge used in the preliminary phase of this study at the University of Florida is shown in Fig. 4.1. These centrifuge tests are aimed to benchmark numerical analysis of prototype scale projectile penetration in granular media. Complimentary precision tests are also planned at the US Army Centrifuge Research Center of the Engineer Research and Development Center (ERDC) in Vicksburg, Mississippi.

Centrifuge testing includes several key steps. After constructing the reduced-scale centrifuge model, it sits inside a basket located at one end of the centrifuge arm with its long dimension parallel to the direction of arm. Adjustable counterweights on the other end balance the weight on the model side (Fig. 4.1). The container gradually rotates 90° from a horizontal stationary position as the centrifuge is spun-up. This step takes about 15-20 minutes and allows for a gradual transition of stresses. After reaching the target centrifugal acceleration, the model is tested.



Figure 4.1 Geotechnical centrifuge at the University of Florida

According to Table 2.2, the centrifuge model tests in this study were carried out at centrifugal accelerations of 26.5-g or 46-g (at the ground surface of the model) in a rigid container. The maximum payload for the University of Florida centrifuge is 12.5 g-ton and the available basket area is approximately 3.7 ft². The beam radius is 59 in (1.5 m) and the maximum centrifugal acceleration is 80 g.

The rigid container had internal dimensions of 533.4 mm (length) × 431.8 mm (width) × 406.4 mm (height). The rigid container consisted of aluminum solid plates connected to a rigid Plexiglas transparent plate in front. Placement of the instruments is based on a preliminary analysis of numerical simulations, which give the prediction of shock wave velocities. Given the incident of the terminal penetration per an initial impact velocity, focus is made on an overall design of the centrifuge model that warrants the reflected stress waves (from the rigid boundaries of the container) to neither interfere the penetration nor contaminate the data acquisition. Equally important is target impact velocity. The impact velocity of projectile is selected, which produces meaningful penetration depths, but causes no macro fracture, as per analysis of maximum strain rates and contact forces, in consideration of fracture toughness of granules. Energy dissipation mechanisms associated with friction-induced heat and fracture are important subjects to be investigated in a subsequent phase of the SEED.

4.2 Centrifuge Test Set-up

The firing assembly was consisted of a Nitrogen tank, a solenoid, a barrel, and a muzzle brake. A 1-Liter Nitrogen tank was supplying air pressure required to fire the projectile. The solenoid, mounted on the barrel, was used to trigger the air gun. The solenoid was connected to the Data Acquisition System (DAQ) and triggering was taking place through the control room. Based on the caliber of two projectiles used in this study (see chapter 2), two stainless steel bull barrels were manufactured (see Fig. 4.2). The length of the barrels was calculated to provide the desired range of projectile velocities for given supplied air pressures. The muzzle brake at the end of the barrel was mainly designed to house the photoelectric sensors and also release the air trapped in behind of the projectile. The firing assembly was fixed on a rigid aluminum plate providing 1.5 inch clearance between end of the muzzle brake and the granular media surface in all tests. The firing assembly is depicted in Fig. 4.3.

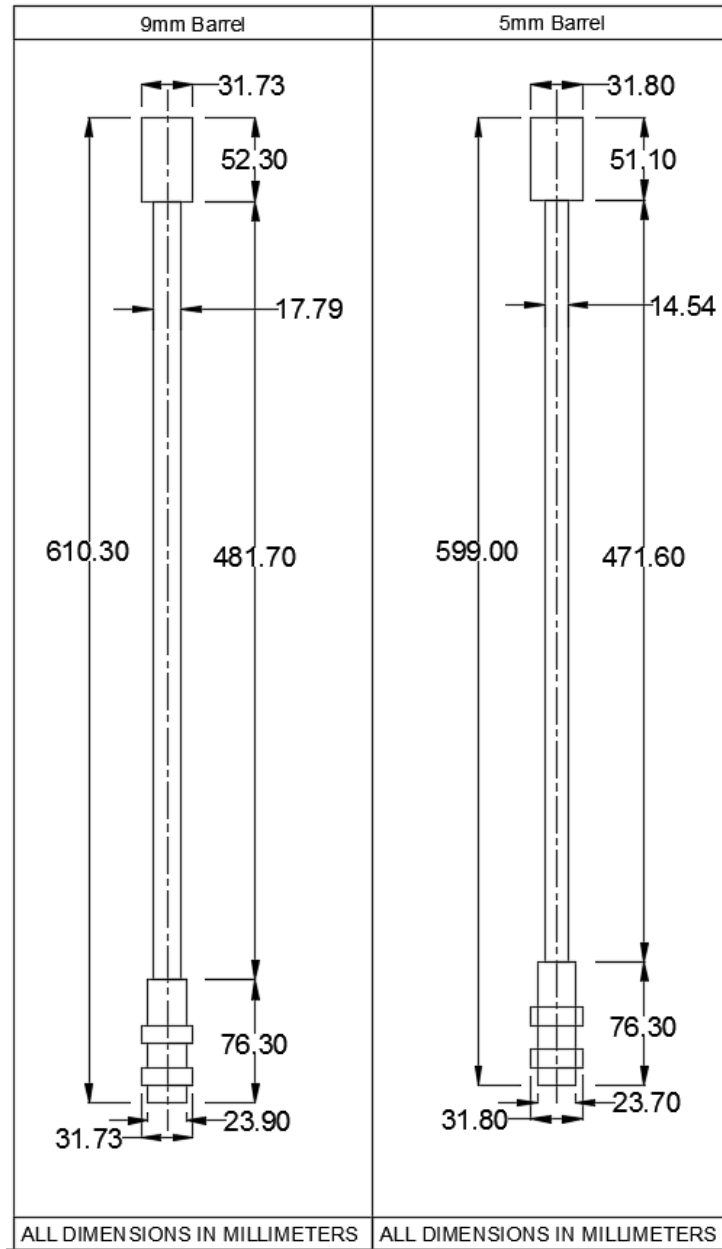


Figure 4.2 Bull barrels used in centrifuge tests

Technical drawing of the M249 machine gun showing dimensions and centerlines. The drawing includes the following dimensions and labels:

- Overall height: 647.70
- Distance from top to muzzle centerline: 127.00
- Distance from muzzle centerline to backplate centerline: 304.80
- Distance from backplate centerline to bottom: 44.45
- Distance from bottom to muzzle centerline: 25.40
- Distance from bottom to backplate centerline: 76.20
- Distance from backplate centerline to muzzle centerline: 126.96
- Distance from muzzle centerline to bottom: 177.80
- Muzzle centerline
- Backplate centerline
- 31.75mm outer diameter

PL 304.8x647.7x12.7

L 50.8x101.6x50.8

L 50.8x50.8x50.8

L 571.5x50.8x50.8

L 50.8x50.8x333.375

B

B

Technical drawing of a rectangular plate. The overall dimensions are 571.50 (height) and 333.375 (width). The plate features four holes, two on each of the long vertical legs. The holes are specified as 4- $\phi(6.35\text{mm})$ @ 38.1mm o/c each leg. The drawing shows a cross-section of the plate with a central vertical slot and two side legs.

35

4.2.1 Dry Pluviation of Granular Materials

To prepare a homogenous granular layer, the proppants were air pluviated to achieve the desired relative density and a void ratio. For this purpose, a novel pluviator was designed and fabricated by Bridge Software Institute (BSI). The pluviator consisted of a hopper, a shutter, and a single diffuser-sieve. The holes in the shutter were 7 mm in diameter and were spaced at 40 mm with a triangular pattern. The aperture size of 3.35 mm was used in the diffuser-sieve. Okamoto and Fityus (2006) and Vaid and Negussey (1984) showed that this shutter and diffuser-sieve configuration would result in a uniform distribution of grains. As this pluviator covered the entire area of the centrifuge container, a homogenous distribution of grains in the entire model area was achieved. The proppant layer density was controlled by maintaining a nearly constant drop height and rate. Proppant was pluviated into the model container in successive layers, with each layer followed by leveling of the surface using a vacuum. Each lift corresponded to the elevation of a horizontal instrument array. A schematic sketch of the pluviator is shown in Fig. 4.4. Pictures of the model during pluviation and the model surface after the pluviation are shown in Figs. 4.5 and 4.6, respectively.

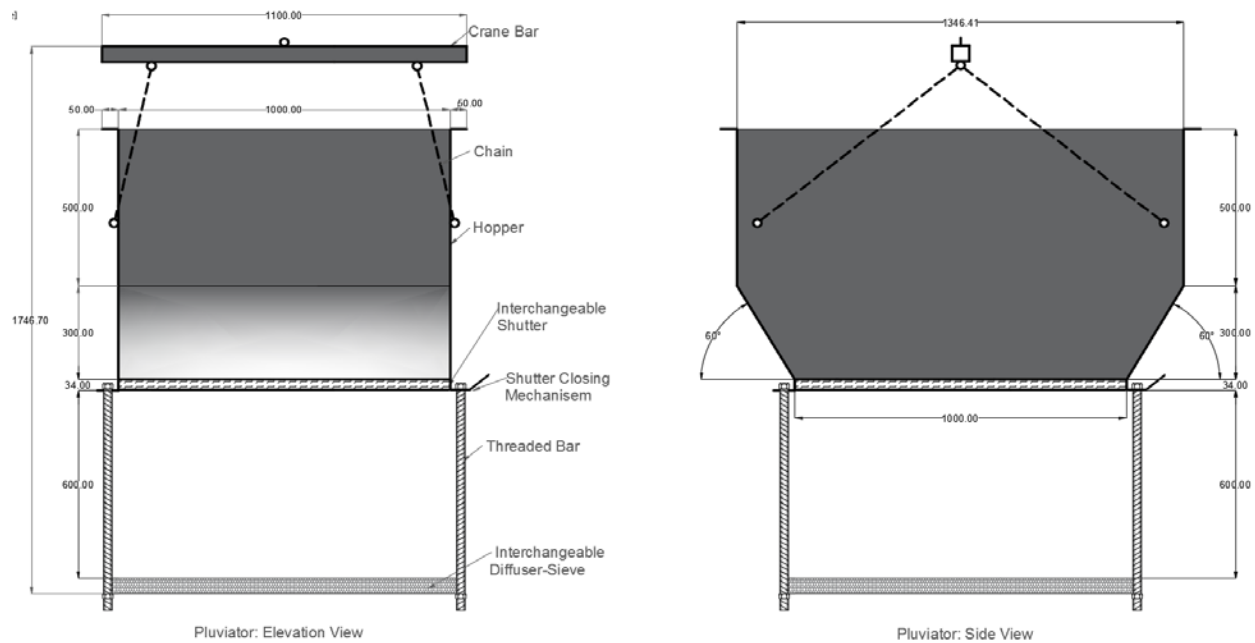


Figure 4.4 Schematic sketch of the pluviator



Figure 4.5 Pluviating proppant inside the rigid centrifuge container

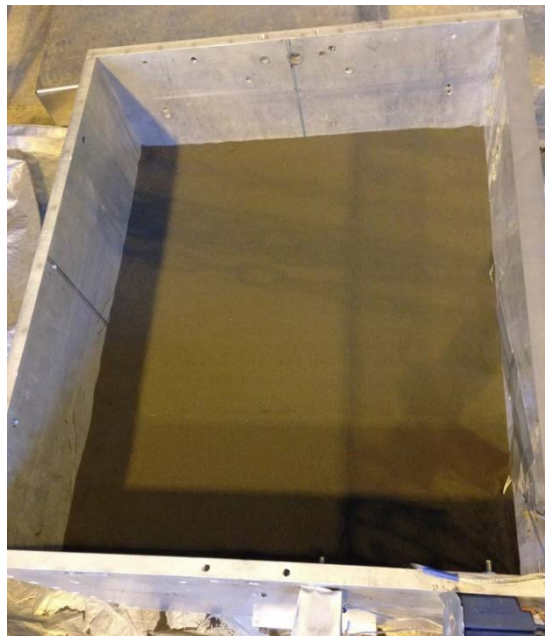


Figure 4.6 Surface of the granular profile after pluviation

4.2.2 Instrumentation and Data Acquisition

The model was instrumented with pressure cells (PCs), linear variable displacement transducers (LVDTs), photoelectric sensors, and cameras. Two Micro-Electro-Mechanical Systems (MEMS) accelerometers were also utilized to monitor centrifugal acceleration. LVDTs were used to measure the vertical displacement of the ground surface during centrifuge tests. PCs were placed in the influence zone of the projectiles and in free field to monitor vertical and horizontal stresses during the tests. The air tank pressure was monitored using a digital pressure gage. Two pairs (transmitter and receiver) of photoelectric sensors housed in the muzzle brake (in a 1 inch distance from each other) were recording the projectile travel time and, therefore, velocity. Analog cameras were also used to monitor centrifuge tests. The instruments were attached to National Instruments RIO (NI RIO) channels which in turn communicate with a RIO control unit (housed in a wall mounted enclosure in the control room). This unit controlled the centrifuge system and communicates with the LabVIEW based GUI program (CICADA).

4.3 Centrifuge Tests Observations

Four centrifuge tests were conducted. Details of tests including unit weight of granular profiles and measured tank pressure before each test is provided in Table 4.1. Test 3b was the repeat of the test 3a but was conducted at a higher tank pressure.

Table 4.1 Characteristics of granular profiles in centrifuge tests

Test number	Centrifugal Acceleration (g)	Projectile diameter (mm)	Tank Pressure (MPa)	Projectile velocity in 1-g (m/s)	Proppant diameter (mm)	Unit Weight (kN/m ³)
1	26.5	8.99	13.42	70	0.93 ± 0.08	21.43
2	46.0	5.18	13.33	110	0.55 ± 0.05	21.38
3a	26.5	8.99	11.58	70*	0.55 ± 0.05	21.78
3b	26.5	8.99	12.41	70	0.55 ± 0.05	21.40

* - Value estimated based on extrapolation of available pressure-velocity data.

Due to the sampling rate limitations in DAQ, direct projectile velocity measurements using photoelectric sensors were not successful. However, based on the air tank pressure – projectile velocity relationships obtained in 1-g (Fig. 4.7), the projectile velocity was estimated and provided in Table 4.1.

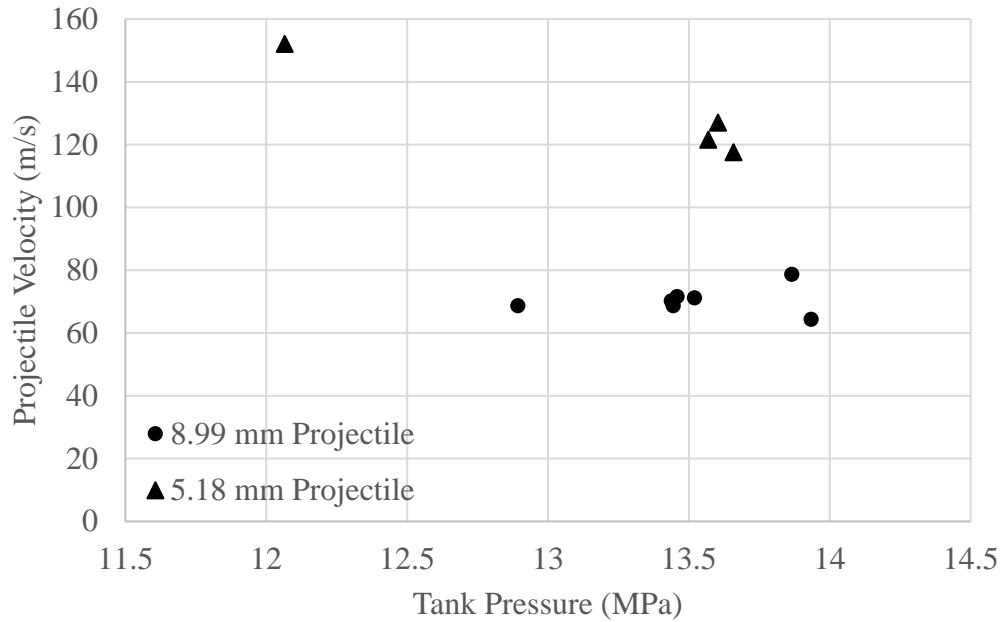


Figure 4.7 Projectile velocity - air tank pressure relationship obtained during 1-g tests

From this point onwards, all the results are presented in prototype scale unless otherwise stated. Fig. 4.8 shows the centrifugal acceleration-time history during test 3a. Once the centrifugal acceleration was stabilized and maintained in the desired value (i.e. 26.5-g), the projectile was fired.

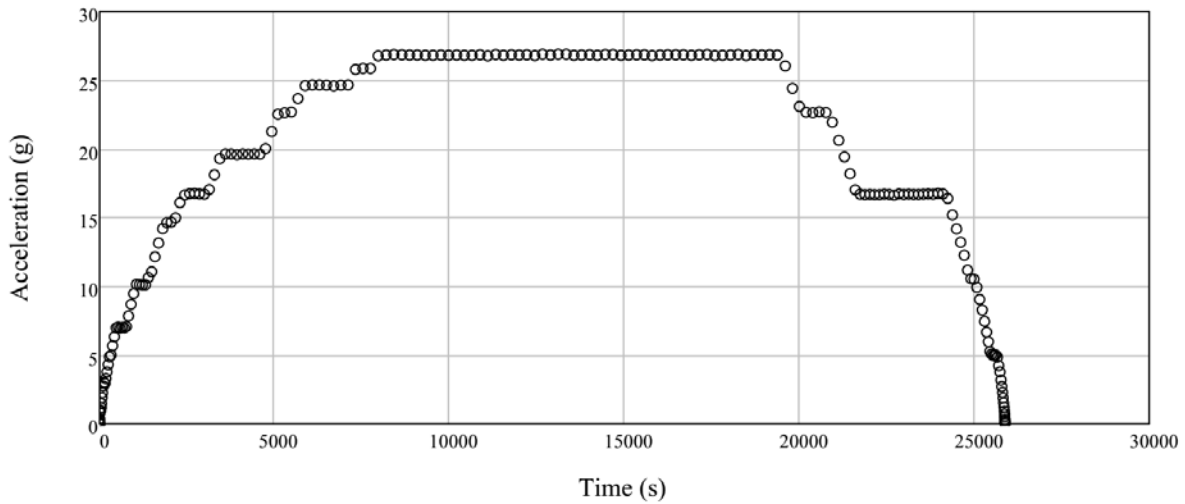


Figure 4.8 Centrifugal acceleration – time history during centrifuge testing ($a_{max} = 26.5\text{-g}$)

Figs. 4.9 and 4.10 show vertical displacement-time history in the ground surface during tests 3a and 3b, respectively. Considering these settlements during spinning up from 1-g to 26.5-g, the unit weight was increased in average by 1.2% and 2.8% in Tests 3a and 3b, respectively.

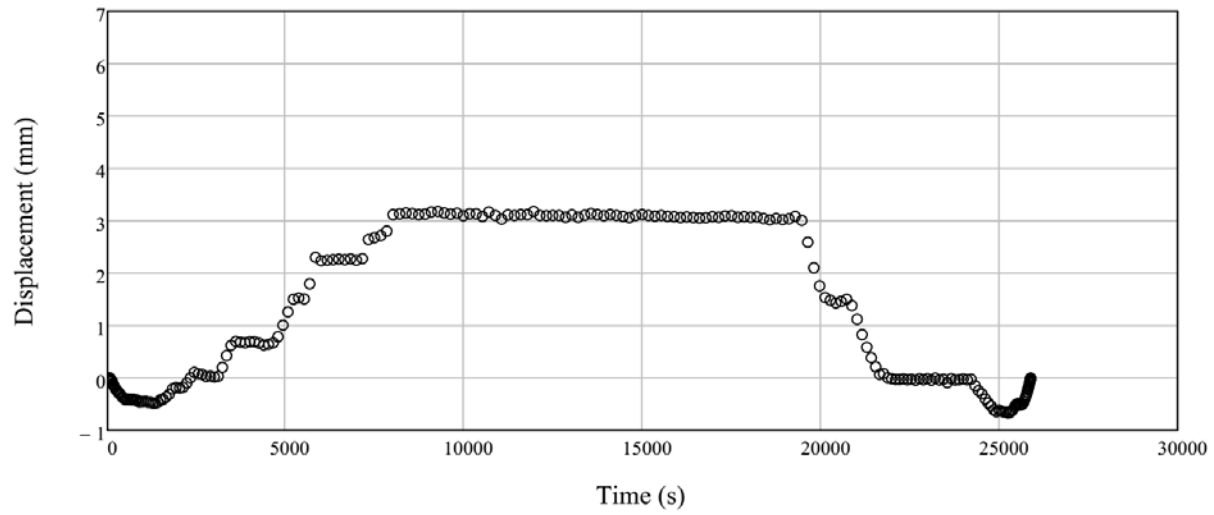


Figure 4.9 Surface displacement – time history during Test 3a

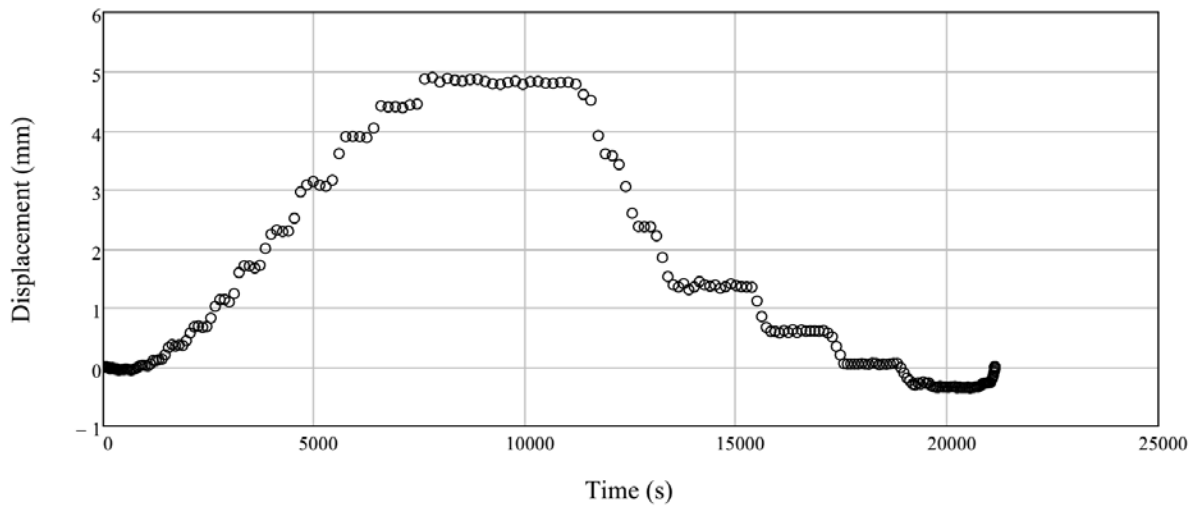


Figure 4.10 Surface displacement – time history during Test 3b

Figs. 4.11 – 4.18 present the terminal location of the penetrated projectile in the conducted 4 centrifuge tests. The plan views and elevation views at two cross sections are depicted. Due to the higher internal friction angle, the lowest penetration depth has been obtained in test 1. Because the incidence velocity of the projectile was greater in test 3b than test 3a, the projectile penetrated a greater depth in test 3b. All projectiles were found inclined in the granular profile. The inclination of the projectiles were in “-x” direction in the local coordinate system (i.e., the centrifuge container) for the bigger projectile and opposite for the smaller one. A precedent for findings of inclinations

in the final projectile position exists in the literature: Zelikson et al. (1986) carried out numerous centrifuge tests where projectiles were fired into a clay medium. As reported therein, a wide range of inclinations (both inclined and declined) were observed despite their best efforts to control the centrifuge test conditions. This phenomenon is recognized as warranting further investigation as part of subsequent research efforts.

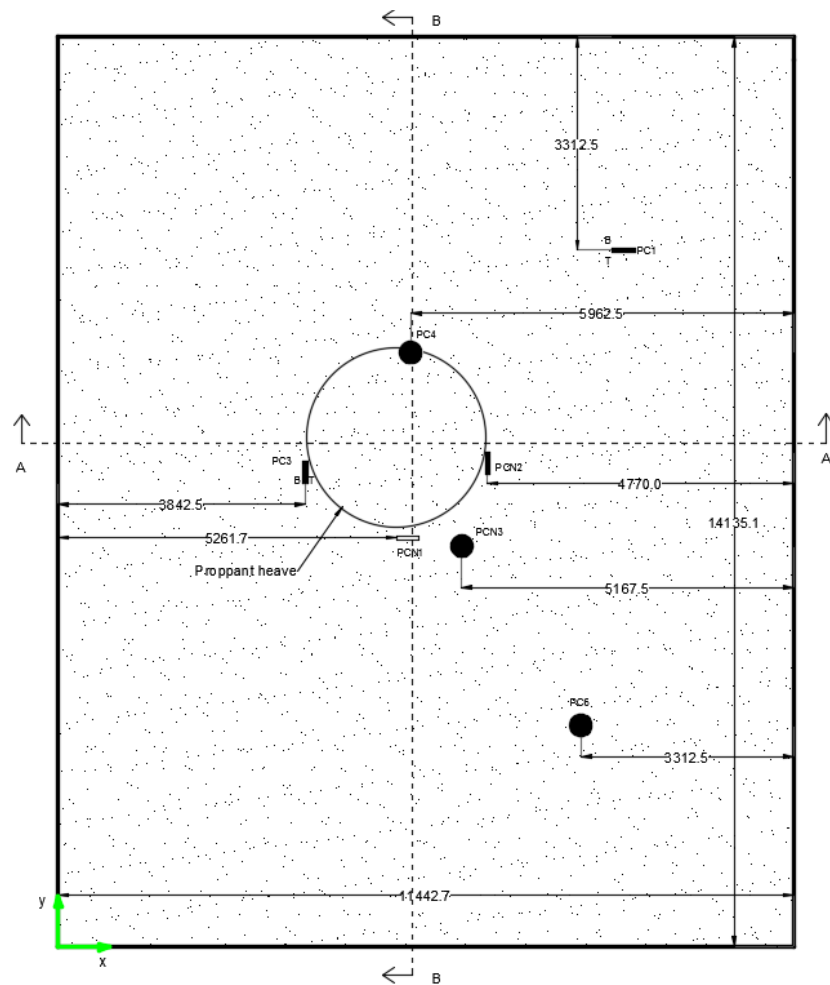
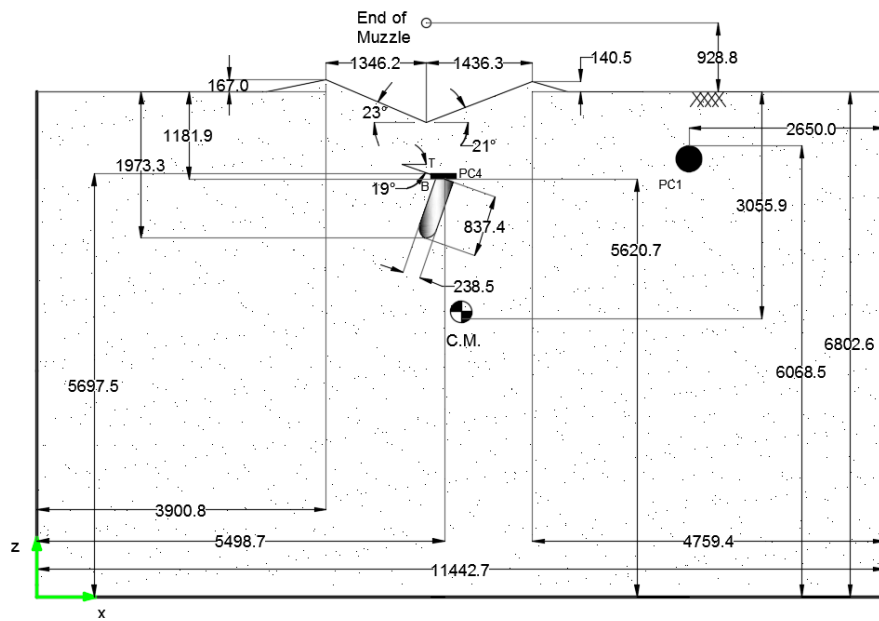
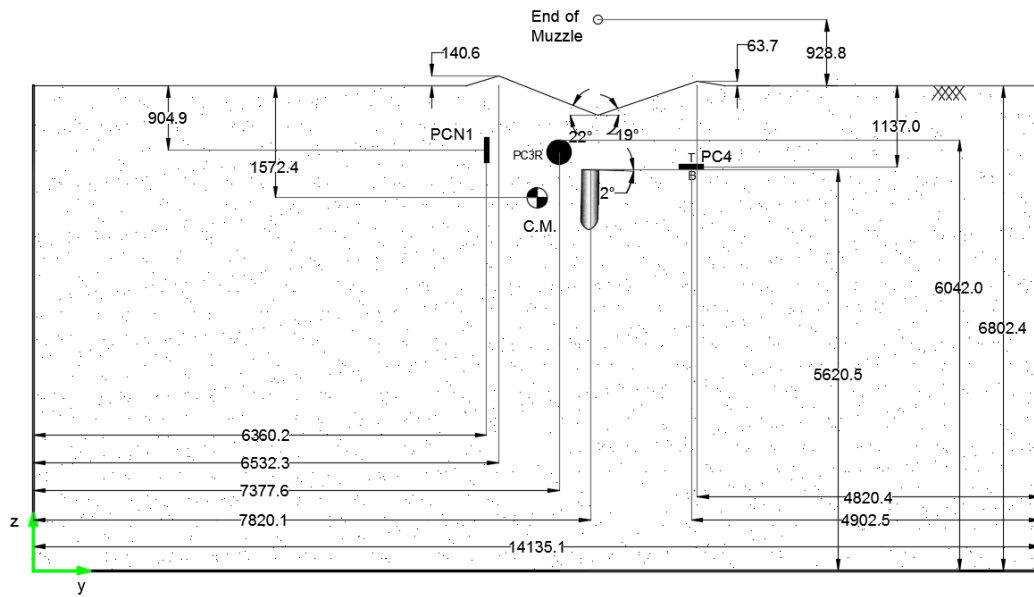


Figure 4.11 Schematic sketches of the penetrated projectile in test 1 and the formed crater: plan view (dimensions in mm)



(a)



(b)

Figure 4.12 Schematic sketches of the penetrated projectile in test 1 and the formed crater: a) elevation view at A-A cross section, and b) elevation view at B-B cross section (dimensions in mm)

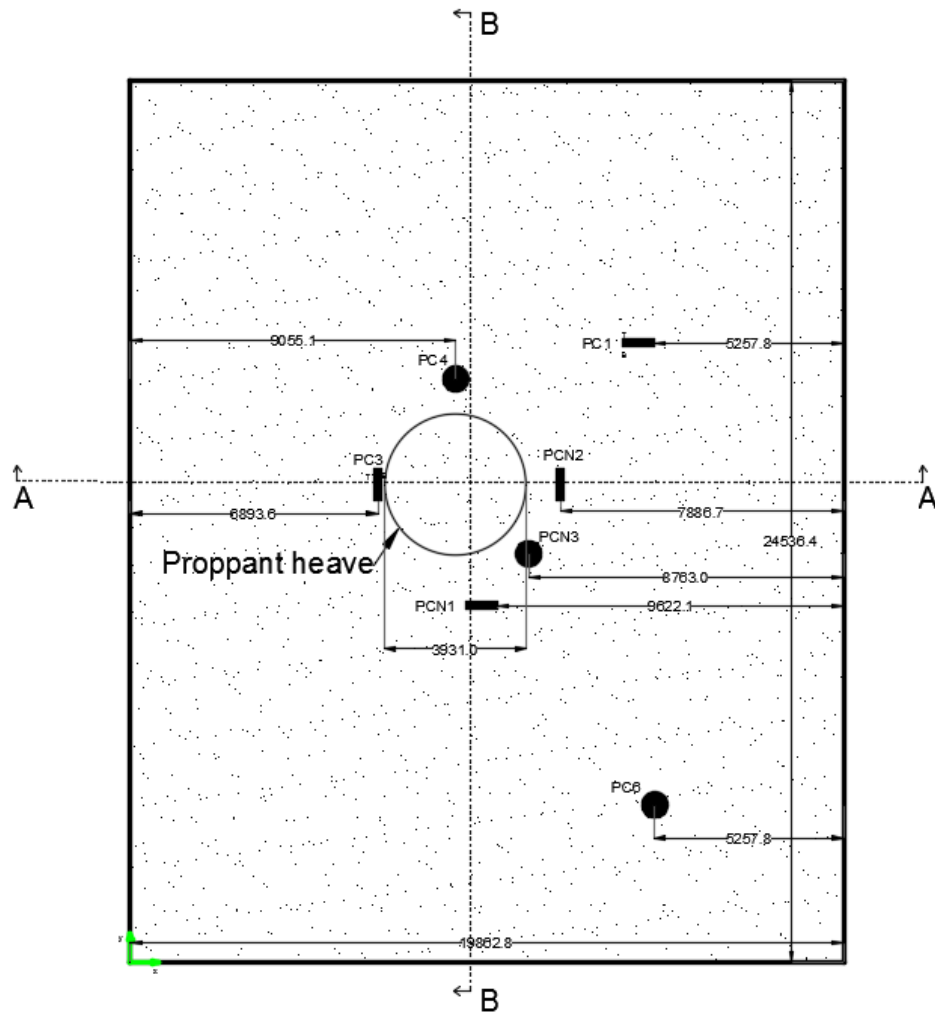
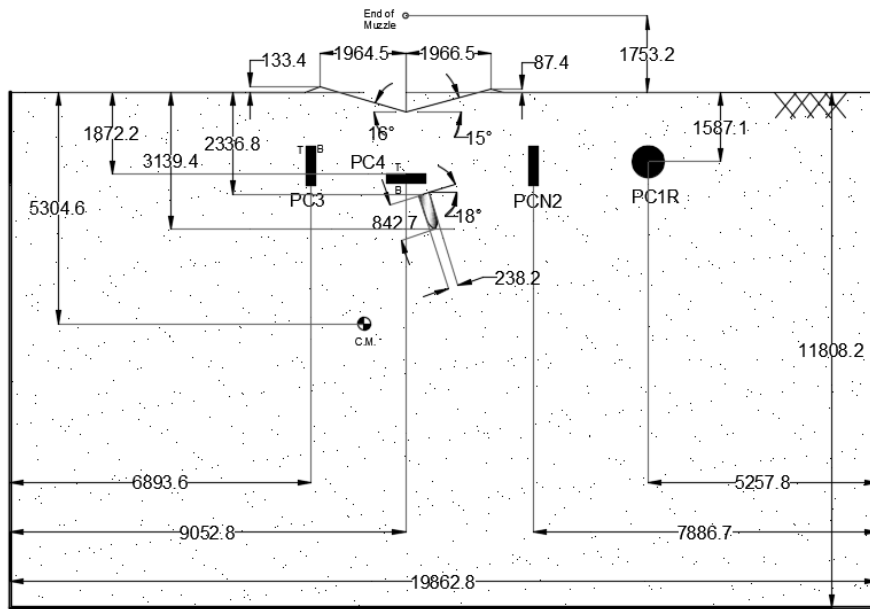
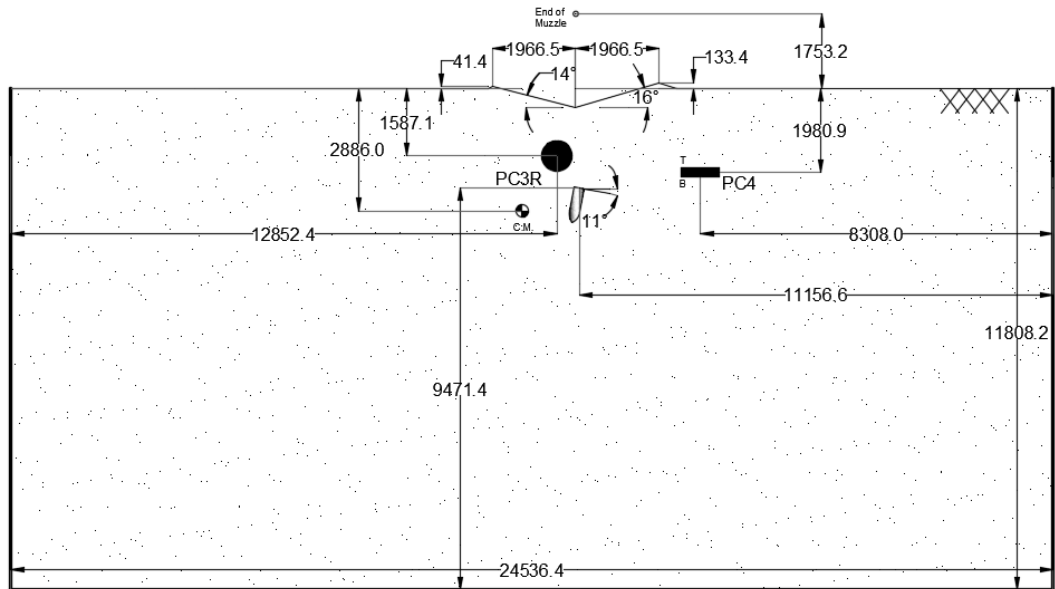


Figure 4.13 Schematic sketches of the penetrated projectile in test 2 and the formed crater: plan view (dimensions in mm)



(a)



(b)

Figure 4.14 Schematic sketches of the penetrated projectile in test 2 and the formed crater: a) elevation view at A-A cross section, and b) elevation view at B-B cross section (dimensions in mm)

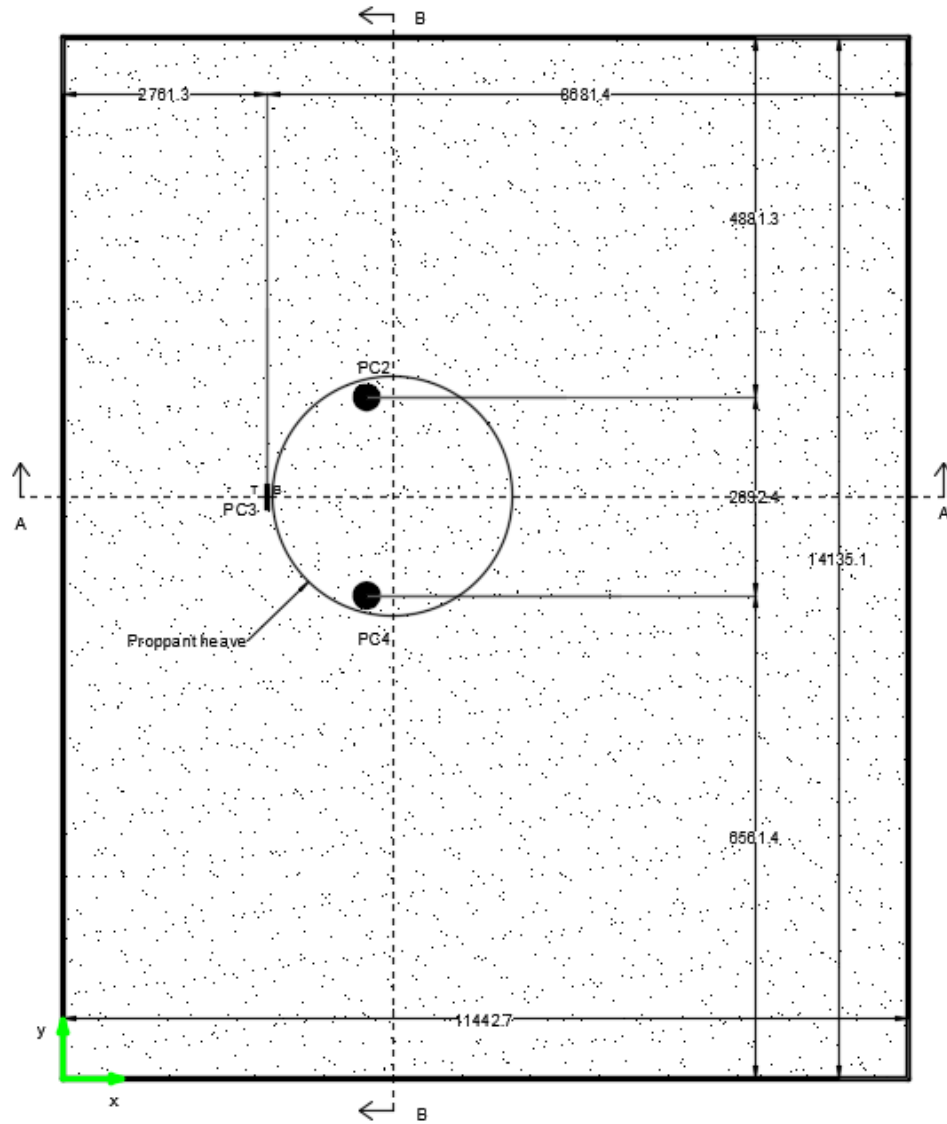
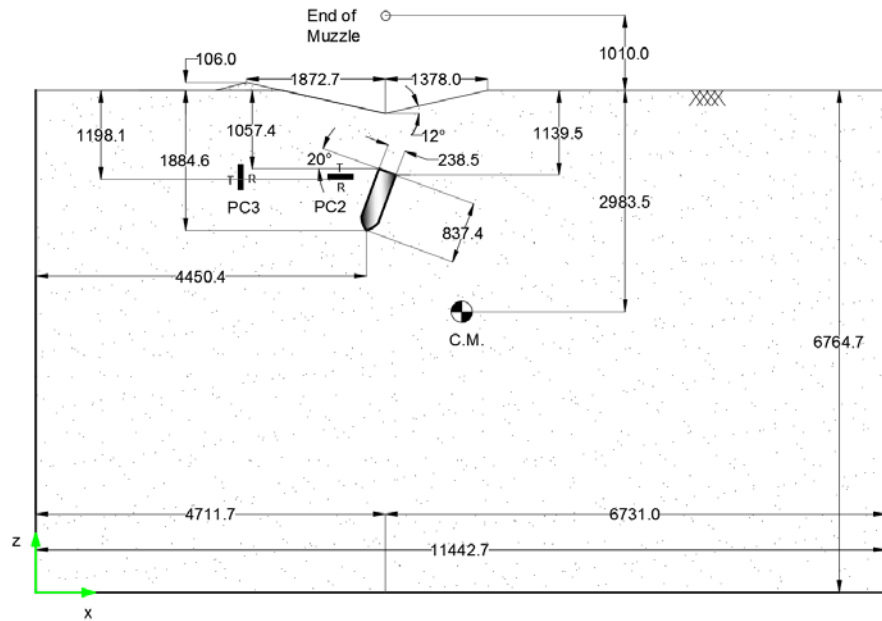
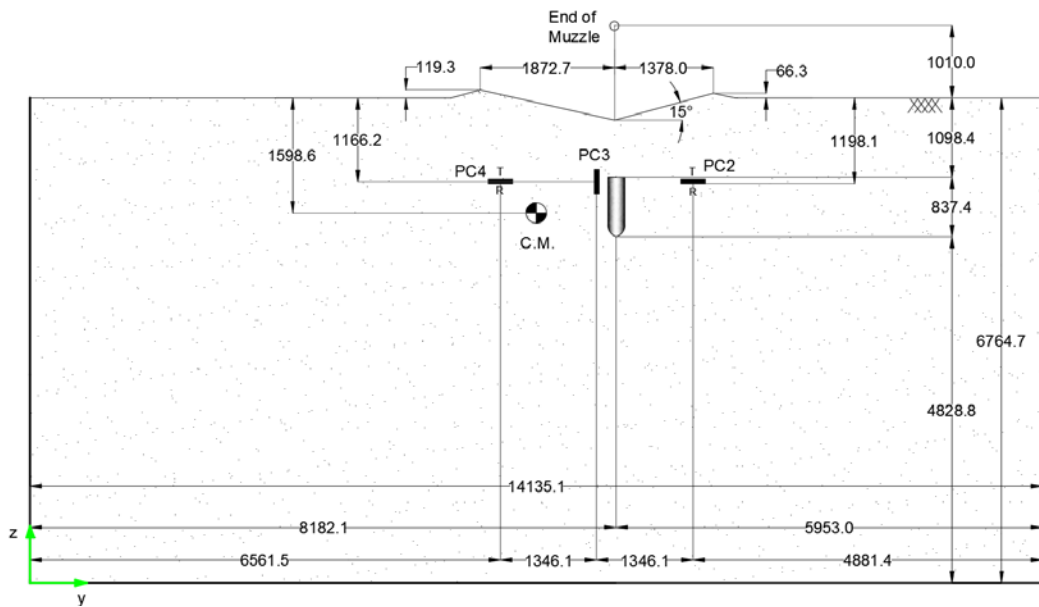


Figure 4.15 Schematic sketches of the penetrated projectile in test 3a and the formed craterplan view, b) elevation view at A-A cross section, and c) elevation view at B-B cross section (dimensions in mm)



(a)



(b)

Figure 4.16 Schematic sketches of the penetrated projectile in test 3a and the formed crater: a) plan view, b) elevation view at A-A cross section, and c) elevation view at B-B cross section (dimensions in mm)

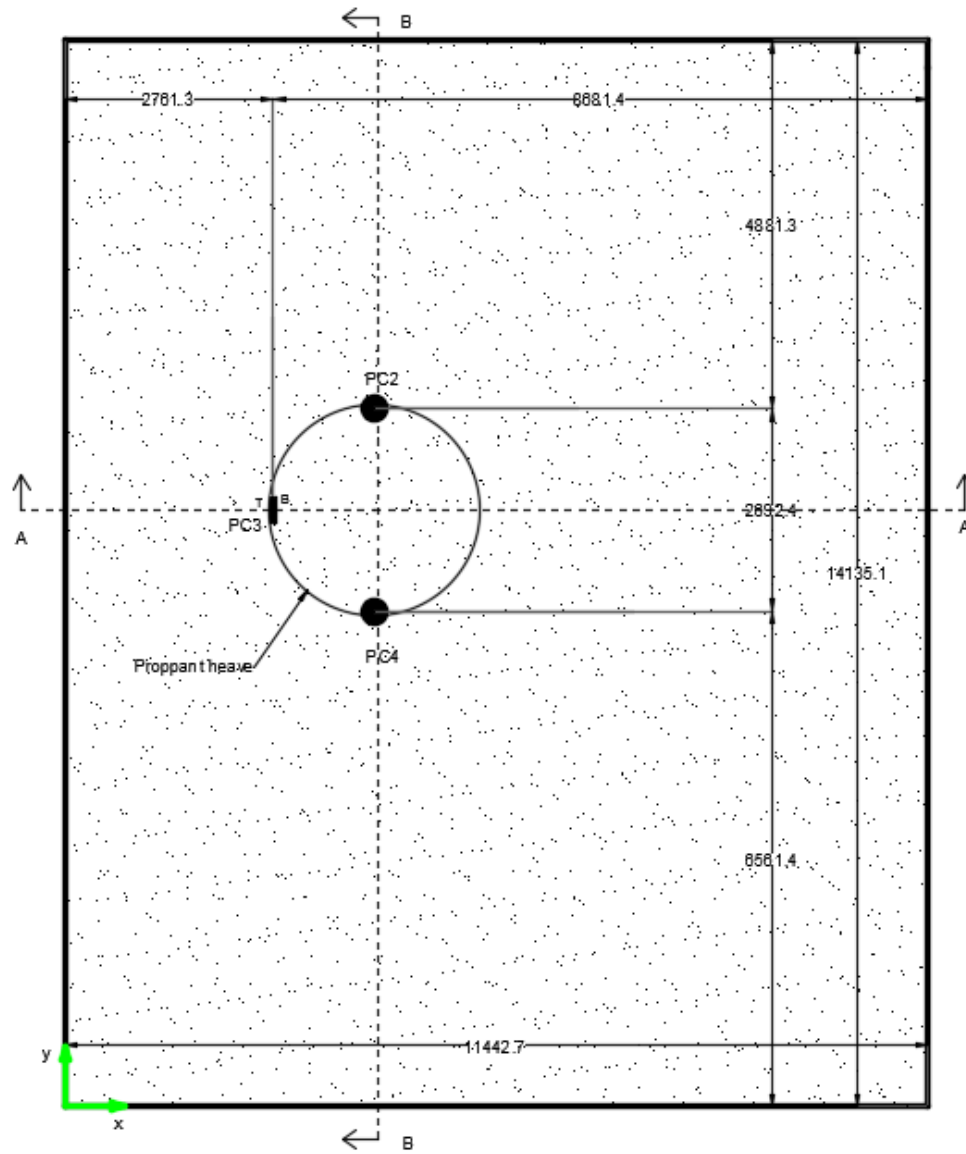
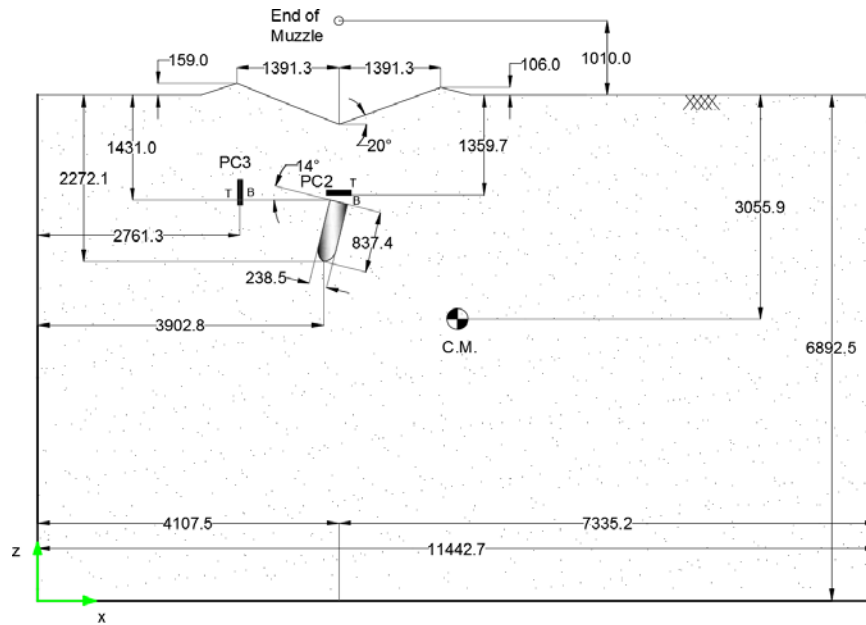
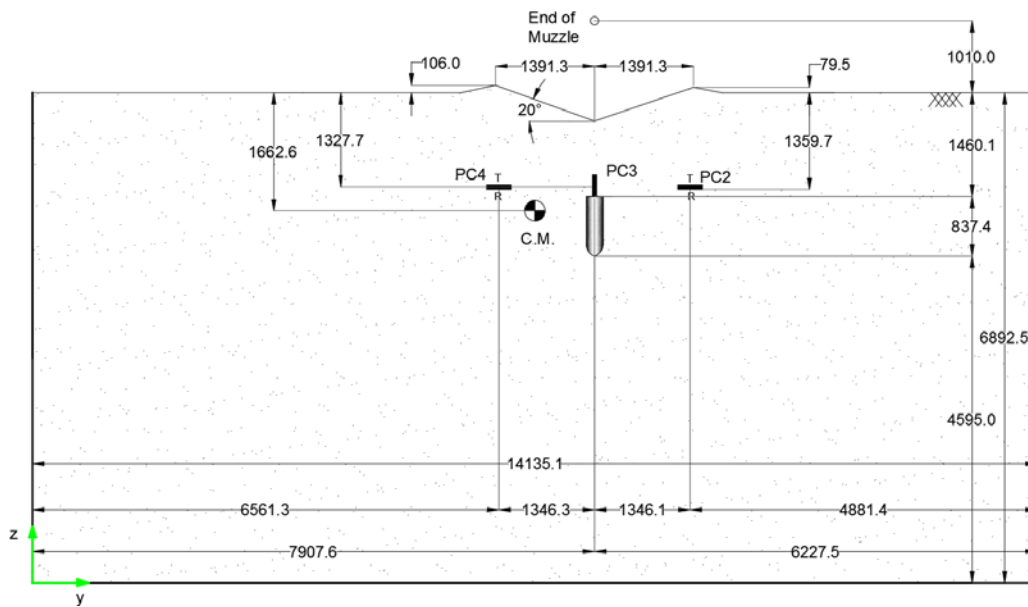


Figure 4.17 Schematic sketches of the penetrated projectile in test 3b and the formed crater: plan view (dimensions in mm)



(a)



(b)

Figure 4.18 Schematic sketches of the penetrated projectile in test 3b and the formed crater: a) elevation view at A-A cross section, and b) elevation view at B-B cross section (dimensions in mm)

Figs. 4.19 and 4.20 show the formed craters after tests 3a and 3b, respectively. The relative elevation of different points of proppant craters with respect to the ground surface are also shown.

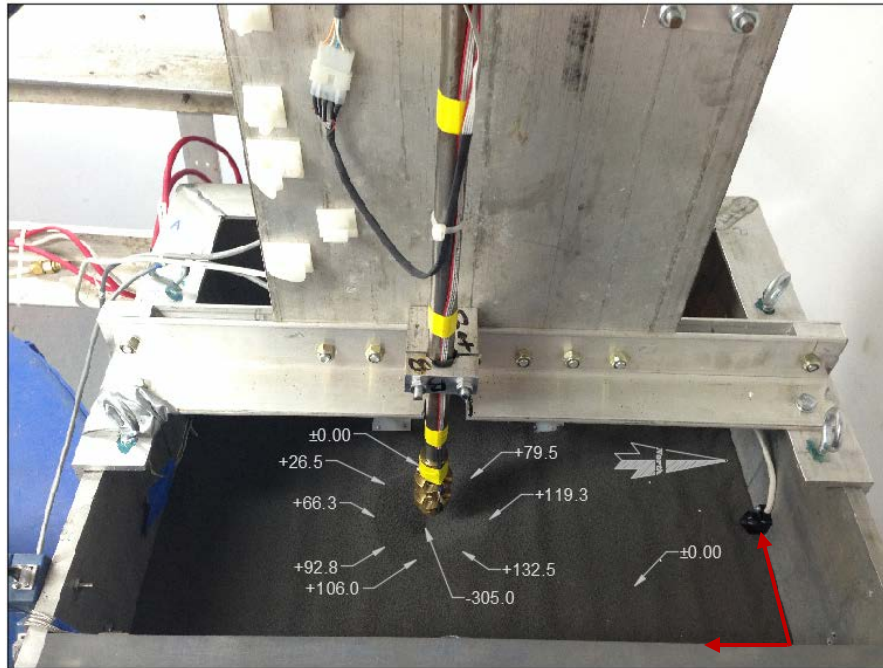


Figure 4.19 Crater elevation relative to the ground surface after the test 3a (dimensions in millimeters)

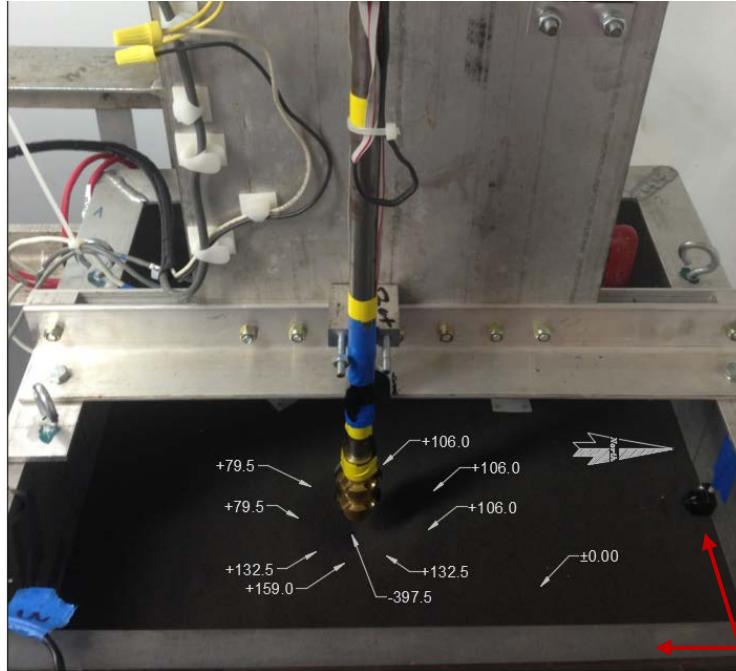


Figure 4.20 Crater elevation relative to the ground surface after the test 3b (dimensions in millimeters)

Figs. 4.21 and 4.22 show the centrifuge models after excavation in tests 3a and 3b, respectively. The relative location of the projectile with respect to the pressure cells are also shown.



Figure 4.21 Profile after excavation at the end of test 3a



Figure 4.22 Relative position of the penetrated projectile with respect to the pressure cells (shown after test 3b)

Figs. 4.23 and 4.24 show the PC measured and calculated vertical stresses during tests 3a and 3b, respectively. After the projectile penetration, vertical stresses at the bottom of both PC2 and PC4 (denoted by “R”) have been decreased. On the other hand, vertical stresses at top of PC4 has been increased and remained constant. It appears, as the pressure cells are located in the influence zone of the projectile, the projectile has pushed the grains against the top surface of the

PCs, while removing them from the bottom of PCs, causing a reduction in internal friction of granular media in these bottom regions.

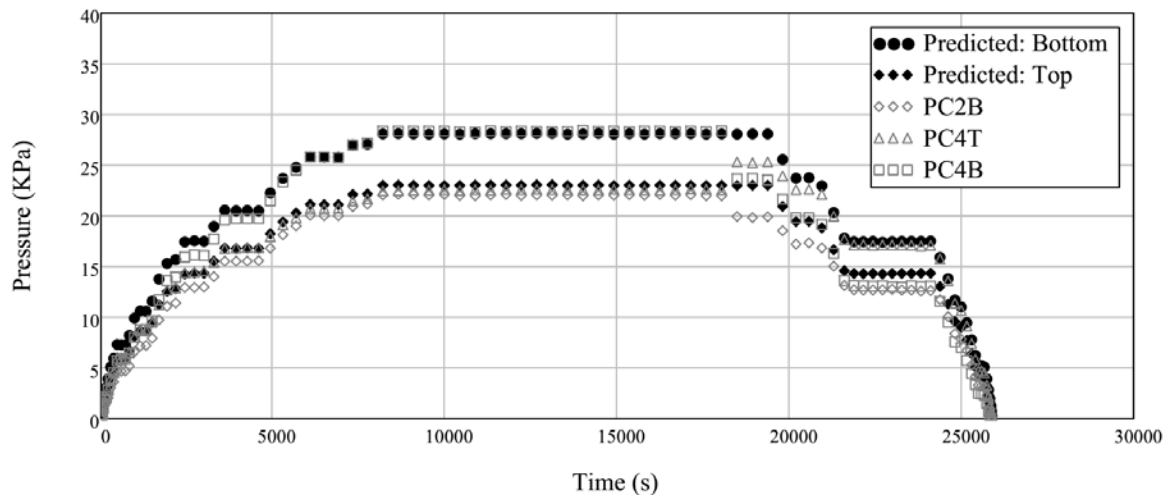


Figure 4.23 Predicted and measured vertical stresses at top and bottom of PC4 and bottom of PC2 during test 3a

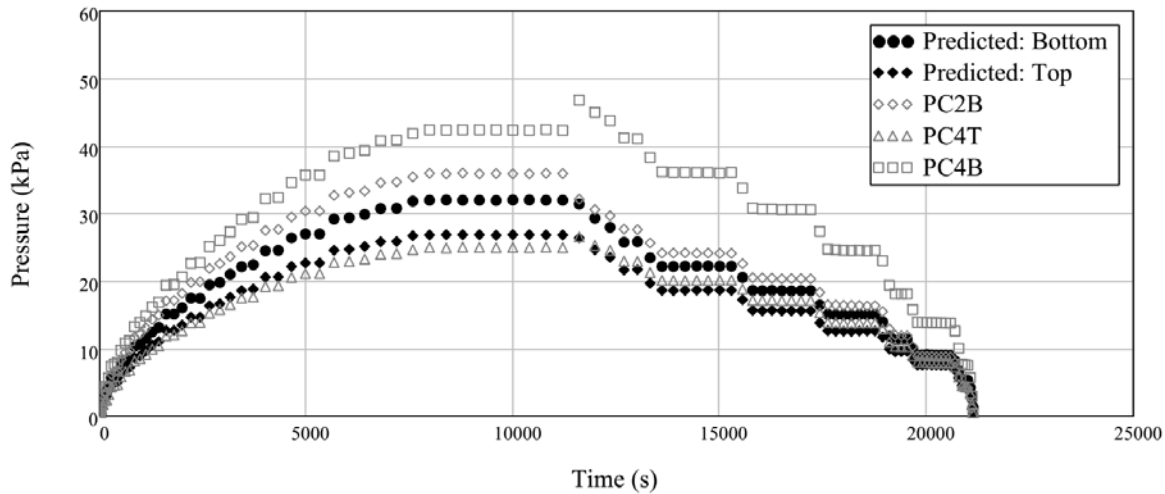


Figure 4.24 Predicted and measured vertical stresses at top and bottom of PC4 and bottom of PC2 during test 3b

Figs. 4.25 and 4.26 show the PC measured horizontal stresses during tests 3a and 3b, respectively. After the projectile penetration, horizontal stresses at both sides of PC3 have been increased and remained constant. It appears, as this pressure cell is located in the influence zone

of the projectile and the projectile has penetrated toward this pressure cell (with penetration angle of 20° in local “-x” direction), the projectile has pushed the grains against both sides of the PC, causing an increase in internal friction of granular media in these regions.

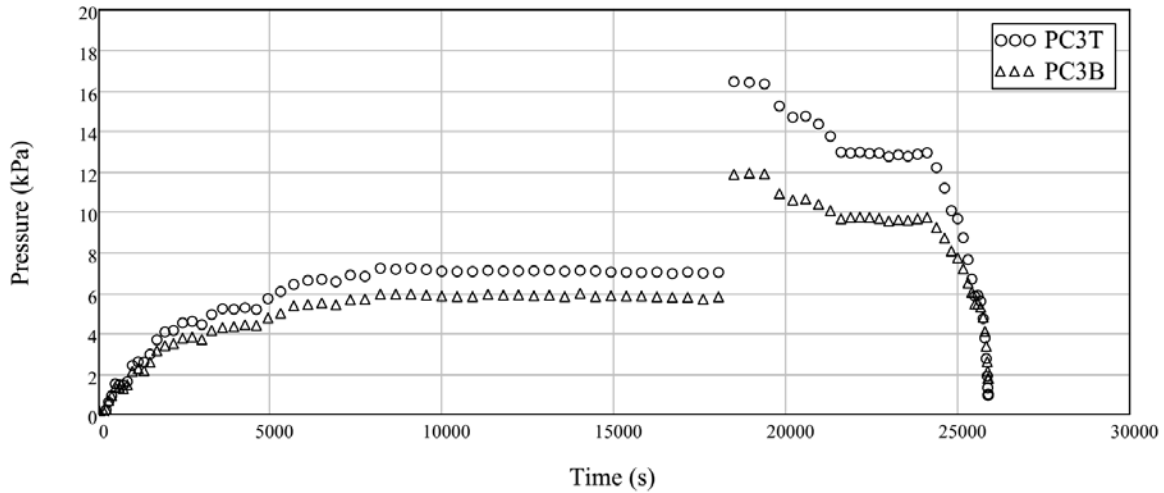


Figure 4.25 Measured horizontal stresses at two sides of PC3 during test 3a

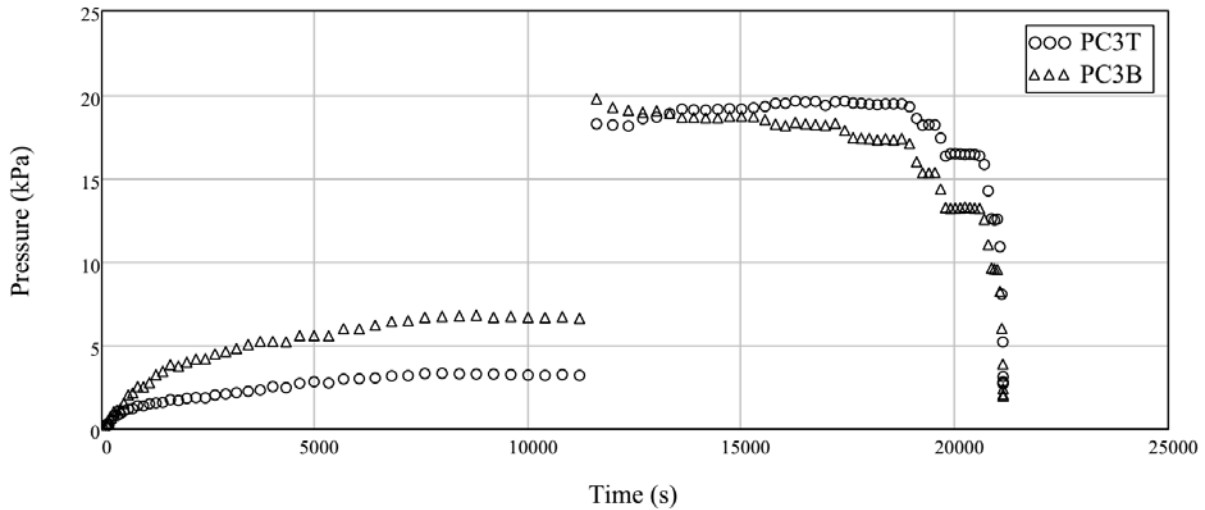


Figure 4.26 Measured horizontal stresses at two sides of PC3 during test 3b

Figs. 4.27 and 4.28 show the ratio of horizontal to vertical stresses. These ratios are shown from 20-g to 26.5-g and 26.5-g to 20-g centrifugal acceleration, where it can be ensured that centrifugal forces are perpendicular to the ground surface in the centrifuge container and the container is in its final horizontal position.

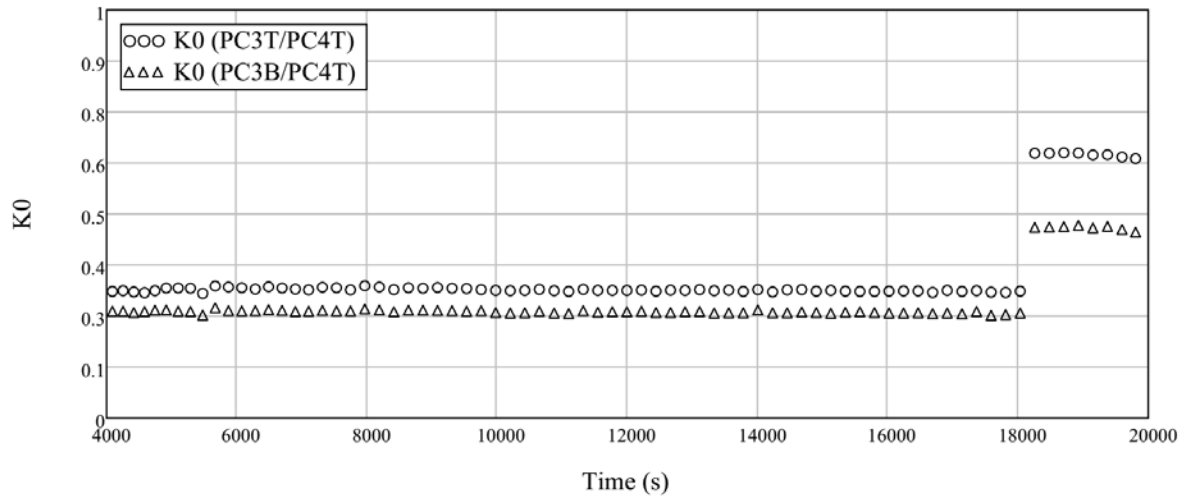


Figure 4.27 The ratio of horizontal to vertical stress (K_0) during test 3a

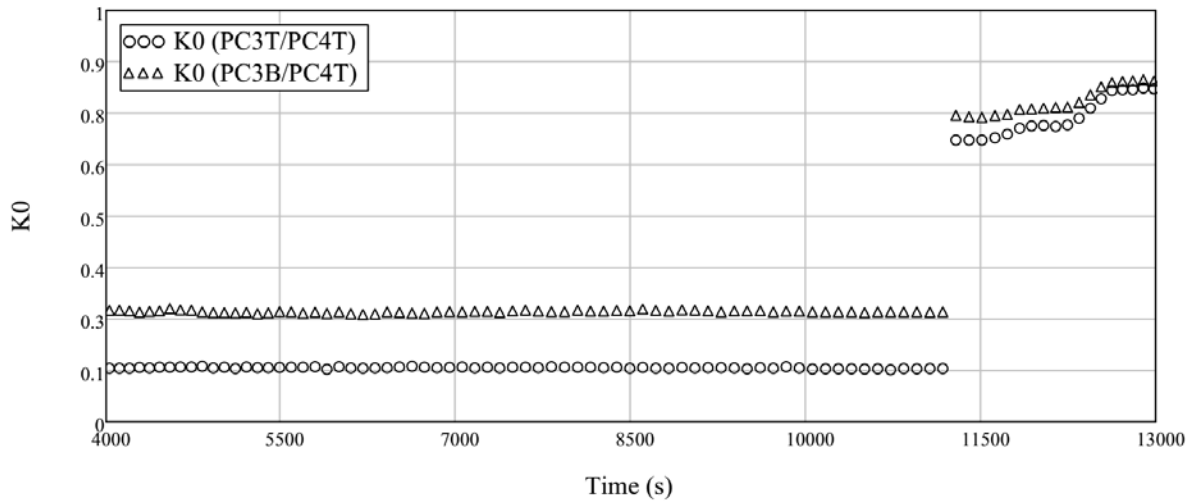


Figure 4.28 The ratio of horizontal to vertical stress (K_0) during test 3b

4.4 Fictitious Forces on a Projectile in the Centrifuge

The following considerations are made under the assumption that the centrifuge is spinning counterclockwise with a constant angular velocity $\vec{\omega}$. There are two pertinent set of coordinates. The objective, Newtonian, or “space” coordinate system is designated s , while a system of

coordinates rotating with the system is designated r . The former coordinate system can be thought to be fixed with the entire centrifuge system rotating inside it; in the later, the centrifuge system can be considered at rest. The forces acting upon the projectile while it travels from the muzzle of the rifle to the surface of the granular material are then understood, and ultimately its path can be derived.

The basic kinematical law upon which the dynamical equations of motion for a rigid body in a rotational frame are founded is given in terms of the following operator:

$$\left(\frac{d}{dt}\right)_s = \left(\frac{d}{dt}\right)_r + \vec{\omega} \times \quad (4.1)$$

That is, the total time derivative of a vector with respect to the spatial reference frame is equal to that in the rotating frame plus the cross-product of the angular velocity with that vector. Let \vec{v}_s be the linear velocity of the projectile in the spatial frame. Then from the above law,

$$\vec{v}_s = \vec{v}_r + \vec{\omega} \times \vec{r} \quad (4.2)$$

where \vec{r} is the position vector relative to the rotating system of axes. The projectile's acceleration in the reference frame is thus

$$\begin{aligned} \vec{a}_s &= \left(\frac{d\vec{v}_s}{dt}\right)_s = \left[\left(\frac{d}{dt}\right)_r + \vec{\omega} \times\right] [\vec{v}_r + \vec{\omega} \times \vec{r}] \\ &= \vec{a}_r + 2(\vec{\omega} \times \vec{v}_r) + \vec{\omega} \times (\vec{\omega} \times \vec{r}) \end{aligned} \quad (4.3)$$

The equation of motion in the spatial system then becomes

$$\vec{F} = m\vec{a}_s = m\vec{a}_r + 2m(\vec{\omega} \times \vec{v}_r) + m\vec{\omega} \times (\vec{\omega} \times \vec{r}) \quad (4.4)$$

Then, within the rotating reference frame, the projectile will appear to move under the effective force

$$\vec{F}_{eff} = \vec{F} - 2m(\vec{\omega} \times \vec{v}_r) - m\vec{\omega} \times (\vec{\omega} \times \vec{r}) \quad (4.5)$$

The third term on the right-hand side of this equation is the centrifugal force felt by the particle due to the angular acceleration of the centrifuge. Assuming that the centrifuge is rotating counter-clockwise, the angular velocity vector points upwards, and we find that the centrifugal force points radially outwards along the centrifuge arm with a magnitude of $m\omega^2 r$, where ω, r are the scalar magnitudes of the angular velocity and position vectors, respectively. It is noted then that if it is desired to simulate a gravitational acceleration of magnitude cg to an object a distance r along the centrifuge arm, the required angular velocity has a magnitude

$$\omega_c = \sqrt{\frac{cg}{r}} \quad (4.6)$$

The second term on the right-hand side of the effective force equation is the Coriolis force. To an observer on the centrifuge arm looking outward this force acts to the right (opposed to the tangential direction of rotation) with a magnitude of $2m\omega v_r$.

4.4.1 The Trajectory and Acceleration in the Rotational Coordinate Frame

The dynamical problem of the path of the projectile between the muzzle of the gun and the soil surface can then be formulated within the rotational coordinate system as a particle in free-fall under the centrifugal force and being acted upon perpendicularly by the Coriolis force. Note that the entire centrifuge system is being acted upon by the standard constant acceleration of gravity downwards, but this is often relatively small in comparison to the centrifugal force at high angular velocities and will here be neglected. We analyze the problem two-dimensionally in the xy Cartesian plane which is assumed to be rotating with the centrifuge arm and whose origin is the axis of rotation; let y be in the direction of the arm, with x perpendicular and positive in the direction of the Coriolis force.

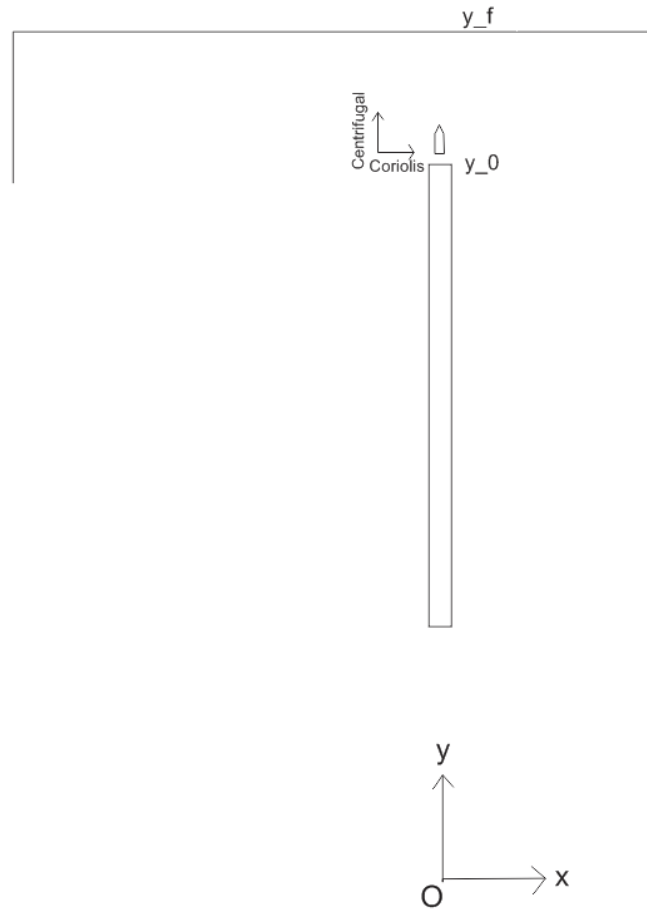


Figure 4.29 Coordinate System and Forces acting on projectile in Flight

The initial conditions are $x_0 = 0$ and $y_0 \neq 0$ (being the distance of the projectile down the arm when it leaves the barrel). Similarly, $\dot{x}_0 = 0$, while $\dot{y}_0 \neq 0$ is the initial velocity of the projectile measured when it leaves the barrel. The dynamical equations of motion are then

$$\ddot{x} = 2\omega\dot{y} \quad (4.7)$$

$$\ddot{y} = -\omega^2 y \quad (4.8)$$

Note that the equation of motion for the y variable is independent of the x coordinate and is of the same form of a simple harmonic oscillator. The solutions for the paths in time for the given initial conditions are

$$y(t) = \frac{1}{2} \left(y_0 + \frac{\dot{y}_0}{\omega} \right) e^{\omega t} + \frac{1}{2} \left(y_0 - \frac{\dot{y}_0}{\omega} \right) e^{-\omega t} \quad (4.9)$$

$$x(t) = \left(y_0 + \frac{\dot{y}_0}{\omega} \right) e^{\omega t} - \left(y_0 - \frac{\dot{y}_0}{\omega} \right) e^{-\omega t} - 2\omega y_0 t - 2 \frac{\dot{y}_0}{\omega} \quad (4.10)$$

4.4.2 Coriolis Effects in Tests 1 and 2

The following provides a discussion of all relevant values for projectiles and centrifuge testing configurations for two empirical tests and the expected drift in the x-direction of the projectile by the Coriolis effect, as well as the final momenta in the x and y directions and the resulting angle of the velocity or momentum vector upon impact with the granular body.

Test 1: Applying the parameters from Test 1 to our equations, we find that the projectile travels the distance between the end of the muzzle and the soil surface (not including the breaker), $\Delta y = 114.4$ mm, in time $t_f = 0.00162$ s, or around 1.62 milliseconds. The final drift in the x direction due to the Coriolis effect is $x_{f1} = x(t_f) = 0.00263$ m, or about 2.638 mm. The final components of linear momentum of the particle upon contact with the grains are of interest: these are $m\dot{x}(t_f) = 0.046 \text{ kg} \frac{\text{m}}{\text{s}}$ and $m\dot{y}(t_f) = 0.958 \text{ kg} \frac{\text{m}}{\text{s}}$. Then the final angle of the velocity vector from the vertical (y) axis is $\theta_f = 2.635$ degrees in the direction of the Coriolis force. Table 4.2 lists and categorizes these results. Figure 4.30 shows the Coriolis Effect on the trajectory of the projectile in time from eqn. (4.10).

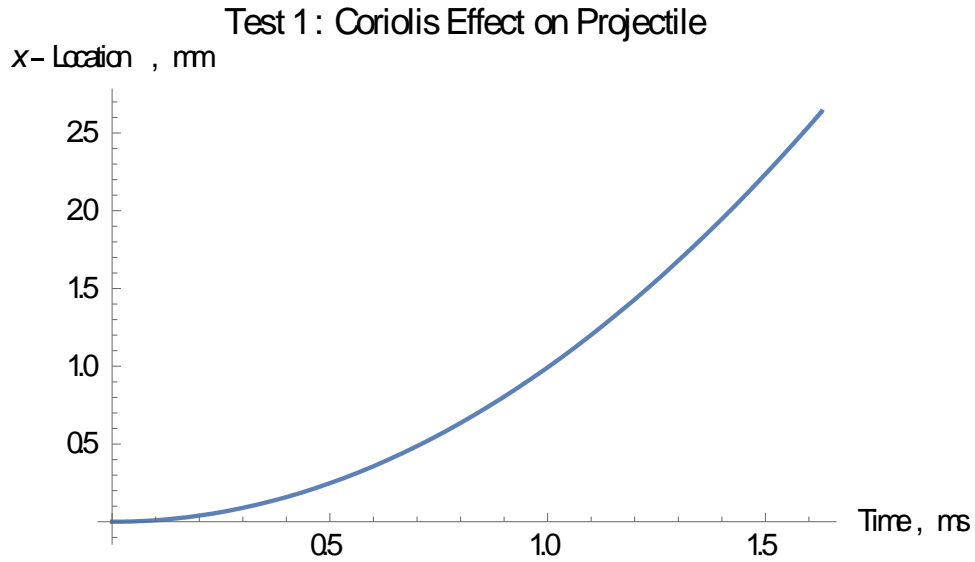


Figure 4.30 Coriolis Effect on projectile in Test 1

Table 4.2 Coriolis Effects in Test 1

Parameter	Value	Description
a (g)	26.5	Centrifugal acceleration
y_0 (mm)	1179.40	Distance of muzzle end to axis of rotation
y_f (mm)	1293.80	Location of soil surface
ω (1/sec)	14.18	Angular velocity
m (kg)	0.01361	Projectile mass in 1-g
\dot{y}_0 (m/sec)	70	Ejection velocity of projectile
x_f (mm)	2.638	Coriolis effect (drift)
t_f (ms)	1.629	Flight time (time to impact)
$m\dot{x}_f$ (kg m/s)	0.046	x-Direction momentum at impact
$m\dot{y}_f$ (kg m/s)	0.958	y-Direction momentum at impact
θ_f (Degrees)	2.635	Angle of momentum vector at impact

Test 2: Applying the parameters from Test 2 to our equations, we find that the projectile travels the distance between the end of the muzzle and the soil surface, $\Delta y = 38.1$ mm, in time $t_f = 0.00103$ s, or around 1.03 milliseconds. The final drift in the x direction due to the Coriolis Effect is $x_f = x(t_f) = 0.0022$ m, or about 2.21 mm; this is actually slightly smaller than the result for the larger but slower projectile. The final components of linear momentum of the particle upon

contact with the grains are $m\dot{x}(t_f) = 0.011 \text{ kg} \frac{\text{m}}{\text{s}}$ and $m\dot{y}(t_f) = 0.285 \text{ kg} \frac{\text{m}}{\text{s}}$. Then the final angle of the velocity vector from the vertical (y) axis is $\theta_f = 2.214$ degrees in the direction of the Coriolis force. Table 4.3 lists and categorizes these results. Figure 4.31 shows the Coriolis Effect on the trajectory of the projectile in time from eqn. (4.10).

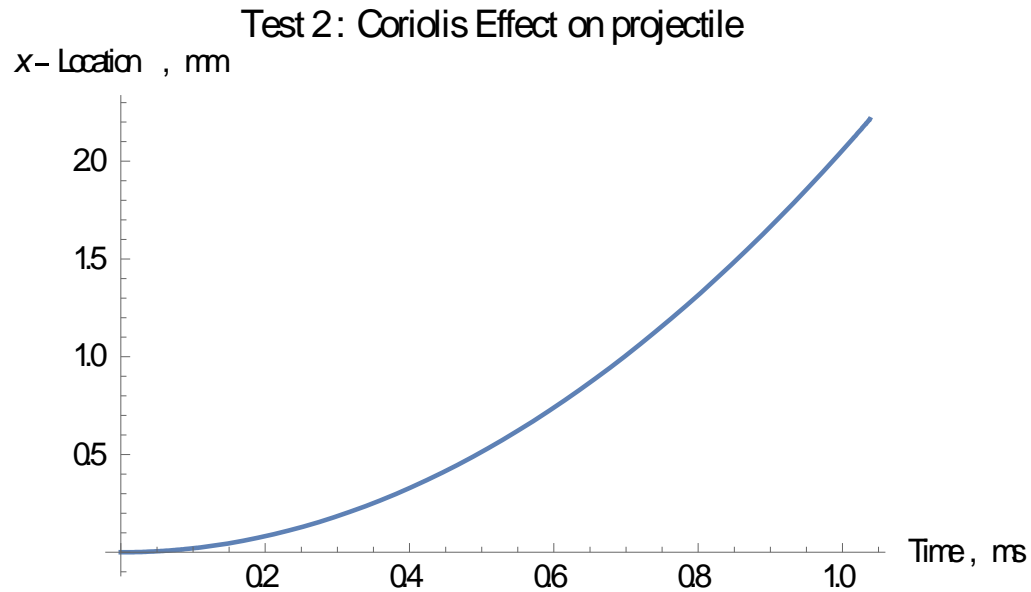


Figure 4.31 Coriolis Effect on Projectile in Test 2

Table 4.3 Coriolis Effects in Test 2

Parameter	Value	Description
a (g)	46	Centrifugal acceleration
y_0 (mm)	1179.40	Distance of muzzle end to axis of rotation
y_f (mm)	1293.80	Effective radius
ω (1/sec)	18.66	Angular velocity
m (kg)	0.00258	Projectile mass in 1-g
\dot{y}_0 (m/sec)	110	Ejection velocity of projectile
x_f (mm)	2.21	Coriolis effect (drift)
t_f (ms)	1.03	Flight time (time to impact)
$m\dot{x}_f$ (kg m/s)	0.011	x-Direction momentum at impact
$m\dot{y}_f$ (kg m/s)	0.285	y-Direction momentum at impact
θ_f (Degrees)	2.214	Angle of momentum vector at impact

4.4.3 Sources of Error: Ejection Angle and other Variables

Results of penetration tests for the projectile used in Test 1 repeatedly show the final location of the projectile horizontally opposed to the Coriolis force. Intuition clearly suggests that the projectile ought to favor motion in the direction of the force acting on it, although the results of the previous section show that this force is largely negligible. Here, a possible source of error in the test is analyzed which could explain this phenomenon. It is hypothesized that the projectile is launched initially at a small angle θ_0 in the direction opposite to the Coriolis force. If the

projectile is launched with initial velocity v_0 , the new initial conditions for the path equations become

$$\dot{x}_0 = -v_0 \sin \theta_0 \quad (4.11)$$

$$\dot{y}_0 = v_0 \cos \theta_0 \quad (4.12)$$

The new solutions of eqns. (4.7) and (4.8) become

$$x(t) = (y_0 + \frac{v_0 \cos \theta_0}{\omega})e^{\omega t} - (y_0 - \frac{v_0 \cos \theta_0}{\omega})e^{-\omega t} - (v_0 \sin \theta_0 + 2\omega y_0)t - 2\frac{v_0 \cos \theta_0}{\omega} \quad (4.13)$$

$$y(t) = \frac{1}{2}(y_0 + \frac{v_0 \cos \theta_0}{\omega})e^{\omega t} + \frac{1}{2}(y_0 - \frac{v_0 \cos \theta_0}{\omega})e^{-\omega t} \quad (4.14)$$

Using the conditions for Test 1, these equations show that an angle $\theta = 1.33$ degrees completely overcomes the Coriolis Effect on the position and momentum of the particle at impact. Under these conditions, the location of the projectile at impact is $x_f = -0.009$ mm, showing that the impact occurs opposite of the direction of the Coriolis force from the initial launch position. Such a small initial angle is a reasonable source of experimental error which could lead to the phenomena observed in Test 1.

The actual contact angles of projectiles and their final orientations at rest within the granular mass are ultimately a function of a number of indeterminate variables. The analysis presented here models the projectile as a single mass point with a known initial velocity; in reality, the effects of the pressurized gas leaving the barrel, as well as aerodynamic considerations dependent on the projectile's shape will have an unknown effect on the true projectile path within the centrifuge. Furthermore, the local orientation of the projectile at the point of surface contact with the first individual surface grains will have an indeterminate effect upon the initial path of the projectile within the granular body. It is noted that all components of the prototype model, namely, the particles in the centrifuge box as well as the projectile, experience a Coriolis Effect proportional to this velocity. It is clear from the numerical results of the DEA models that a region of particles around the projectile within the body experience flow with non-negligible velocities. A particle in front of the projectile and moving along with it within the mass will also experience a larger centrifugal acceleration than the projectile itself; it is feasible to suggest that the particles immediately in front of the projectile could, therefore, experience a larger Coriolis effect than the projectile itself. In such circumstances, the projectile would experience local motion opposed to the Coriolis Effect relative to the surrounding granules. Theoretically, drastic alterations to its penetration path result in a final resting angle, such as are seen in the results of Test 1. In order to provide definitive answers, a scaled model can be modeled as it is spun at the same angular velocity as the centrifuge. Numerical simulation is, then, compared to precision testing using high-speed

cameras to measure AoA, and laser sensors to measure the surface elevation of a granule at an initial contact relative to the mean surface elevation. In essence, Angles of Attack (AoAs) of projectile impact are indeterministic since initial contact angles can vary in two different scales; (1) local contact orientation between the nose tip and a spherical granule in initial contact, and (2) global impact orientation between the centerline of the projectile and macroscopic surface waviness (formed by discrete granules) at the surface elevation.

CHAPTER 5

NUMERICAL MODELING OF PROJECTILE PENETRATION TESTS

5.1 Overview

Introduced in Ch. 5 are the numerical modelling techniques that are utilized to characterize the effects of penetration of an unexploded projectile in a granular medium. To understand the mechanical features describing granule-projectile interaction, several numerical tests are established. In numerical models built to predict the penetration depths of unexploded ordnance, the granular medium is simulated using discrete spherical elements (DSEs), while the projectile is modeled using shell finite elements. Both the discrete and finite element components are modeled such that they bear close resemblance to physical characteristics of the respective physical entities.

Granular assembly formulation (packing) is one of the most important prerequisite techniques preceding introduction of any structural object into DSE assemblies. The multi-physics simulation software LS-DYNA (LSTC 2016) is used in current study. The procedure followed in quantification of phenomenological parameters based on physical attributes of granular matter are described in subsequent sections. Also, exhaustive descriptions of the numerical techniques used to create numerical models are presented.

5.2 Numerical Model of 0.93 ± 0.08 mm Granules

In Sec. 5.2, we shall focus on quantifying the input parameters for DSEs used in numerical simulations based on measured physical quantities. Note that, within the scope of the Phase I research, monodisperse DSE assemblies are considered for all projectile penetration simulations. Therefore, for the purpose of numerical simulations of centrifuge tests, granular media are represented by DSE sized at diameters most near to the size of the bottommost retained sieve (recall Sec. 2.5). Accordingly, monodisperse assemblies discussed in Ch. 5 consist of DSE sized at 0.85 mm (corresponding to 0.93 ± 0.08 mm) or 0.5 mm (corresponding to 0.5 ± 0.05 mm) diameters. Sieve on which the sample is retained. In Sec. 3.4, we have discussed the microscopic and grain-scale characteristics exhibited by the “0.85 mm” diameter proppants. Based on the available (physical) measurements, we can derive the input parameters to be used in the numerical models. In this way, the DSE assemblies are ensured to consist of monodisperse discrete elements with material and geometric properties that are representative of the physical proppants.

5.2.1 Geometry and Density

The mass density of DSEs was calculated based on weight measured 0.93 ± 0.08 mm diameter ceramic proppants. A total of 30 weight measurements were done for ceramic spheres. Based on the measured data, mass density was calculated using average weight of granules. The mass density used in numerical models is given below (Table 5.1). For 0.55 ± 0.05 mm diameter proppants, similar density has been used.

Table 5.1 Geometric parameters of 0.85 mm diameter DSEs

Parameters	Value	Units
------------	-------	-------

Radius	0.425	mm
Volume	0.3215	mm ³
Mass density	3430	kg/m ³

5.2.2 Normal Contact Stiffness

LS-DYNA binaries with build 103703 and greater allow us to define a nonlinear elastic contact stiffness as function of normal displacement for discrete elements. The normal contact stiffness defined for discrete spherical elements (DSE) is derived from measured load-displacement curves for ceramic proppants (Fig. 3.8). Recall the load-displacement measurements were made on 15 pairs of ceramic proppants. An incremental displacement method was used to stochastically determine average slope of the measured force-displacement plots. Based on the stochastic analysis, a mean, lower bound and upper bound force-displacement curves were plotted. These representative curves were fitted into a Power law function (Oliver et al. 2003). The Power law to define force-displacement relationship is given below. The Power law parameters for representative contact stiffness are given for force in unit of Newton and normal displacement in unit of millimeter in Table 5.2.

$$F = \chi d^m \quad (5.1)$$

Table 5.2 Power law parameters

Parameters	χ	m
Mean	572.6515	1.0528
Upper bound	721.1105	1.0560
Lower bound	424.338	1.0476

In a current beta version of LS-DYNA algorithms (binaries) direct input routines of test measurement on granular contact analysis are not implemented to model the unloading behavior represented by the physically measured load-displacement profiles. Per discussion with the developer of LS-DYNA, the micro-indentation contact is implemented as a piece-wise nonlinear force function of displacement.

An official version of LS-DYNA does not facilitate the definition of nonlinear contact stiffness for DSEs. Instead, the linear contact stiffness has been modeled as a function of bulk modulus and macro radius of granule.

$$K_{n_{linear}} = K_b^* R_{min} \quad (5.2)$$

where, $K_b^* = \frac{K_{b_1} K_{b_2}}{K_{b_1} + K_{b_2}}$ is effective bulk modulus for contact stiffness between two elastic bodies.

For normal contact forces by the Hertz solution, the tangent stiffness is written:

$$K_n = \frac{\partial F_n}{\partial d_n} = 2E^* (R^*)^{1/2} \delta_n^{1/2} \quad (5.3)$$

The Hertz contact stiffness is nonlinear. To account for this nonlinearity, we introduce a factor α which is the rate of change of normal contact stiffness. Eqn. (5.2) becomes:

$$K_{n_{non-linear}} = \alpha^H K_b^* R_{min} \quad (5.4)$$

where the rate of change in Hertzian tangential slopes is denoted by α^H : $\alpha^H = \frac{2E^* (R^*)^{1/2} \delta_n^{1/2}}{K_b^* R_{min}}$.

Subsequently, we can calculate an input bulk modulus based on Eqn. (5.3) based on the load-displacement curves obtained from the micro-indentation test data of Fig. 5.1. As per nano-indentation test data on aluminosilicate composite films obtained from the literature (Ponitzsch et al. 2016), a value for modulus of elasticity is evaluated for given empirical data of Poisson's ratio. The calculated values of modulus of elasticity and Poisson's ratio are given in Table 5.3.

Table 5.3 Input parameters for numerical model

Parameters	Mean value	Units
Young's modulus	550	MPa
Poisson's ratio	0.27	--

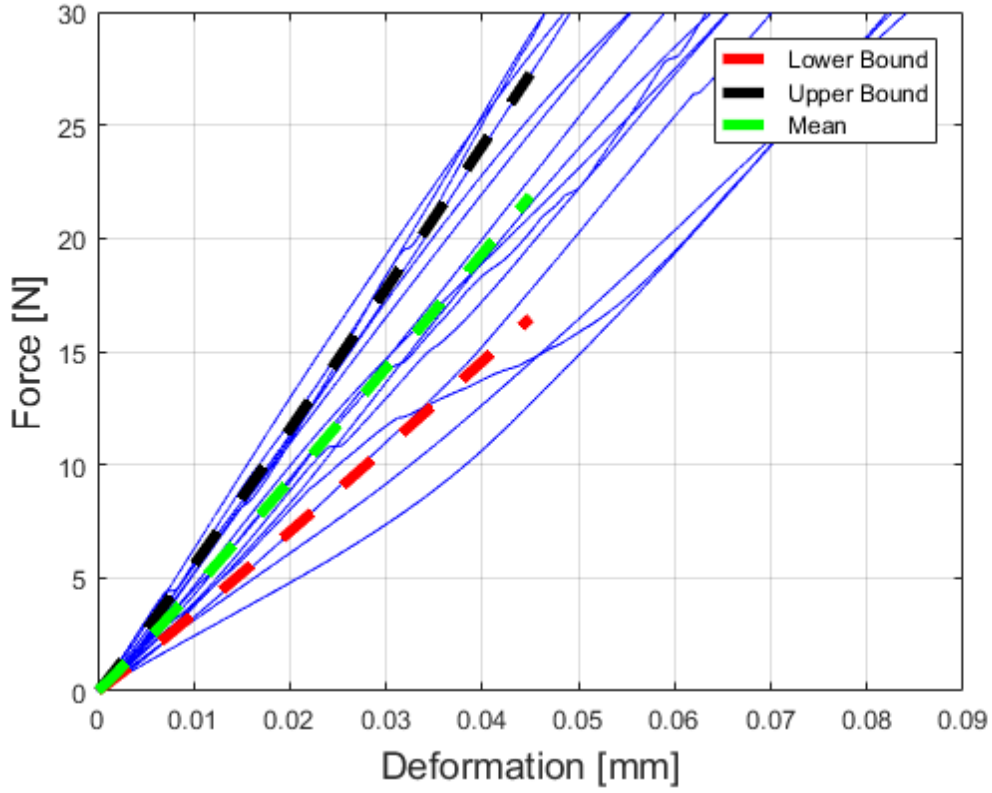


Figure 5.1 Curve fits for the micro-indentation data on ceramic proppants (aluminosilicate with MOH scale of 6.5)

With the parameter of bulk modulus, we can write:

$$F_n = \frac{K_{b_1} \cdot K_{b_2}}{K_{b_1} + K_{b_2}} \alpha R_{\min}^2 \quad (5.4)$$

where, $R_{\min} = \min(R_1, R_2)$ and α is the rate of change of the stiffness for rough surface contact., which can be defined as a function of normalized normal displacement δ_n with the macro radius of DSEs:

$$\alpha = f(\delta_n) \quad (5.5)$$

$$\delta_n = \frac{\text{Normal displacement}}{\text{Radius of DSE}} \quad (5.6)$$

α is then approximated at increments in displacement from the micro-indentation test data. A resulting piecewise curve for the mean is given in Table 5.4. As discussed in Chap. 3, α is a functional of the rate of change of apparent contact area in the frequency domain, and yielding/hardening of the material. It is expected to complete a closed-form solution to

microscopic boundary values in the subsequent year, and corresponding functionals are derived for the code implementation of microscopic input parameters in LS-DYNA.

Table 5.4 Input parameters for nonlinear contact stiffness

δ_n (mm)	α
0.0	0.0
0.05	0.253
0.1	0.526
0.15	0.805
0.2	1.090
0.25	1.379

5.2.3 Tangential Contact Stiffness

Tangential contact stiffness for interacting DSEs are calculated based on the Mindlinian theory of compliance of elastic bodies in contact (Mindlin 1949). In his publication, Mindlin categorizes the tangential interaction between two elastic bodies into two categories: no-slip condition and partial slip condition. In a newly-developed numerical implementation, tangential contact stiffness is defined as a function of normal contact displacement as per an extended Hertzian-Mindlinian contact theory. Alternatively stated, normal contact forces and resulting contact areas have direct control in the development of tangential relative motion (i.e., slip) at planes of contact with rough surface. Thus, the tangential limit load under no partial-slip (stick) conditions is dependent on normal displacement per applied normal force. Mathematical methods of tribological tangential-contact stiffness are given in details in Appendix A. The concept of Mindlinian tangential compliance is briefly explained in relevance to adhesive bond formed by micro asperities in contact.

The tangential compliance of two elastic bodies is given by Mindlin (1949):

$$C_t = \frac{1}{8a} \left(\frac{2-\nu_1}{G_1} + \frac{2-\nu_2}{G_2} \right) \quad (5.7)$$

where, G and ν are shear modulus and Poisson's ratio of the material of elastic bodies, and a is the radius of normal contact area. For the case of identical DSEs, the above equation reduces to:

$$C_t = \frac{1}{8a} \left(\frac{2-\nu_1}{G_1} + \frac{2-\nu_2}{G_2} \right) = \frac{1}{4a} \left(\frac{2-\nu}{G} \right) \quad (5.8)$$

The tangential contact stiffness is taken as the inverse of tangential compliance. Thus, the tangential contact stiffness is given by:

$$K_t = \frac{4aG}{(2-\nu)} = \frac{4a}{(2-\nu)} \frac{E}{2(1+\nu)} \quad (5.9)$$

In LS-DYNA terminology, tangential contact stiffness is defined using an input parameter known as “SHEARK”. This input parameter is defined as:

$$\text{SHEARK} = \frac{K_t}{K_n} \quad (5.10)$$

For example, taking the derivative of force with respect to Hertzian displacement, normal contact stiffness (K_n) and contact area radius (a) are defined in terms of macro radius of curvature (R) and normal displacement (d_n):

$$\begin{aligned} K_n &= 2 \frac{E}{1-\nu^2} \left(R^{1/2} d_n^{1/2} \right) \\ a &= R^{1/2} d_n^{1/2} \end{aligned} \quad (5.11)$$

If there is no partial slip prior to a full slip on contact surfaces, Eqn. (5.10) becomes $\frac{K_t}{K_n} = \frac{2(1-\nu)}{(2-\nu)}$,

where “SHEARK” is a function of Poisson’s ratio only; a value of SHEARK can vary between 0.4 and 0.9 depending on Poisson’s ratio of elastic granular materials (Johnson 1985).

As discussed in Chap. 3, the apparent contact area of rough surfaces can be a few to several times larger than Hertzian contact area of smooth surfaces described by Eqn. (5.11). The variable “SHEARK” is a functional with respect to a growth rate of apparent contact area per normal-load increments; it becomes no longer a constant value. In the ongoing efforts, an average value of “SHEARK” over a range of expected normal displacement is estimated with a limited number of data points obtained from the static friction tests. As for an input parameter, a value of 0.9 is averaged in a range of normal forces up to 5 N and corresponding averaged apparent contact area. No yielding of micro asperities was considered in the calculation of apparent contact area. But, a function of “SHEARK” is being derived as progress is being made in a closed-form solution of the normal contact stiffness. It is recommended that adhesive bond (p. 125 of Johnson, 1985) in contact between rough surfaces be investigated, which, in turn, couples contact behaviors in the orthogonal directions. Having derived an adhesive-elastic frictional model (refer to Appendix A; Barthel, 1998) of the JKR theory (Johnson, Kendall and Roberts, 1971; Johnson, 1985), we propose to conduct physical measurement on a number of manufactured granules and natural grains for micro scratch resistance and nano-scale surface energy as part of the continuation phase in Chap. 7. Choice of either the JKR theory or the DMT theory (Derjaguin, Muller, Toporov, 1975) is based on the Tabor coefficient ζ of the granules with effective radius of curvature R^* :

$$\zeta \equiv \left(\frac{R^* \Delta \gamma^2}{(E^*)^2 \varepsilon^3} \right)^{1/3} \quad (5.12)$$

where surface energy is denoted by $\Delta \gamma$, and equilibrium separation between the two surfaces in contact is represented by ε . The tabor coefficient can be regarded as the ratio of the effective ranges of the internal force of elastic deformation and the surface force caused by adhesion. When $\zeta < 0.1$, particles (and asperities in a high frequency domain) exist with a small radius of curvature, a high adhesion, and a high elastic modulus, which is suitable for the DMT theory. When $\zeta > 5$, particles (and asperities in a low frequency domain) exist with a large radius of curvature, a low adhesion, and a low elastic modulus, which is suitable for the JKR theory. Thus, depending on gap closure and asperity yielding, the JKR regime may be meaningful in interpretation of the micro-indentation and scratch test data, i.e., macroscopic contact stiffnesses. It is noted that the particles with adhesive bonds described by the DMT theory are considered to be an important factor in modeling jammed states. The partitioning of granular soil in a semi-infinite half space by DSEs could be accounted for in larger particles' motions with respect to these seemingly insignificant particles, i.e., jamming transition in granular force network (Majmudar et al. 2007).

5.2.4 Sliding Friction

Numerical input parameters for sliding friction was based on physically-measured coefficient of friction. Physical measurement on sliding friction coefficient indicates the variation of tangential limit load per applied normal contact force, i.e. scale-dependent friction (A. A statistical mean as per upper bound and lower bound values (standard deviation) is used as a representative input parameter of intergranular friction coefficient. The coefficient of rolling friction is averaged to be one-tenth (as discussed in detail in App A.1.7) of the coefficient of sliding friction.

Table 5.5 Friction coefficients used in numerical models

Coefficient of	Mean	Upper bound	Lower bound
Static friction	0.47	0.817	0.209
Rolling friction	0.047	0.0817	0.021

5.2.5 Damping coefficient

For the modelling of granular media in industrial applications, the normal coefficient of damping $NDAMP$ is set to relatively high values (approximately 0.5 to 0.9; Karajan et al. 2014). The tangential coefficient of damping is defined using input parameter $TDAMP$ in LS-DYNA. $NDAMP$ and $TDAMP$ are ratios to the critical damping of the contact in normal and tangential directions, respectively. Numerical experimentation was performed in the variation of normal and tangential *restitution* coefficients based on mathematical methods (a full derivation given in App A.4.4).

Later, a set of restitution coefficients was evaluated for the damping coefficients used in the numerical simulation of weight density and stress distribution per pluviation in the centrifuge box. Numerically-measured viscos damping coefficients are given in Table 5.6. The ratio of normal to tangential damping coefficients is based on the ratio of the tangential to normal frequencies of contact resonance for solid spheres, which is roughly equal to 1.7 (p. 357 of Johnson, 1985; refer to mathematical methods explained in A.4.3 and A.4.4). For generic use in vibroimpact analysis, the mathematical models of viscoelastic rough-surface contact are currently being written in the context of the UXO-Granular interaction for publication.

Table 5.6 Viscous damping coefficients in numerical model

Coefficient of viscous damping	Value
NDAMP	0.7
TDAMP	0.4

5.3 Numerical Model of 0.55 ± 0.05 mm Granules

The numerical input parameters used for modelling DSEs to represent 0.55 ± 0.05 mm diameter ceramic proppants are discussed in this section. As mentioned earlier (Sec. 3.5), the micro-scale and grain-scale characteristics of 0.55 ± 0.05 mm diameter ceramic proppants are consistent with 0.93 ± 0.08 mm diameter ceramic proppants, the input parameters for 0.55 ± 0.05 mm ceramic proppants are adopted from those of 0.93 ± 0.08 mm ceramic proppants.

5.3.1 Geometry and Density

The density of DSEs are determined from the measured mass density of 0.93 ± 0.08 mm ceramic proppants. These are given in Table 5.1.

5.3.2 Normal Contact Stiffness

The input parameters for contact stiffness for 0.5 mm ceramic proppants was characterized using the same procedure as described in Sec. 5.2.2. The input parameters for contact stiffness are given in Table 5.4.

5.3.3 Tangential Contact Stiffness

The tangential contact stiffness is solely a function of Poisson's ratio. Poisson's ratio for ceramic proppants was found to be 0.27. Based on this value of Poisson's ratio, the input parameter S_{HEARK} that defines the ratio of tangential contact stiffness to normal contact stiffness was 0.84.

5.3.4 Sliding Friction

Numerical input for sliding and rolling friction for 0.55 ± 0.05 mm diameter ceramic proppants were the same as that for 0.93 ± 0.08 mm proppants. These are given in Table 5.5.

5.3.5 Coefficient of Restitution

The normal and tangential coefficient of restitution are given in Table 5.6.

5.4 Simulation of Pluviation Process

As discussed previously in Sec. 4.2, physical pluviation processes are made use of in the current study to construct mechanically stable granular assemblies. Consequently, the granular assemblies studied possess bulk properties that may be categorized as homogenous with respect to bulk properties. For example, pluviation permits construction of granular assemblies that (approximately) possess direction-independent bulk density throughout the assembly volumes. In Sec. 5.4, numerical modeling efforts that are complimentary to the physical testing program—with respect to bulk preparation of granular assemblies—are documented. As reported below, the simulation of pluviation processes (albeit computationally expensive) are demonstrated to produce numerical packings of 0.85 mm diameter and 0.5 mm diameter assemblies of DSE that give good agreement with physical measurements of bulk properties involving assemblies composed of proppants granules.

5.4.1 Simulation Stages

Numerical models dedicated to simulation of pluviation processes are divided into three stages, as depicted in Fig. 5.2 and Fig. 5.3. As formulated, the numerical simulations employ a generative procedure, where progressively more DSE are introduced into the model as the simulation progresses. Initially, the model consists of only two components (Fig. 5.2a): a rigid cylindrical container and circular plane, where the plane is positioned flush with the top of the container. Note that a drop height of 381 mm is maintained throughout all stages of the pluviation simulations. The diameter of the cylinder nominally exceeds that of the circular plane, and the planar (circular) region is defined exclusively to introduce DSE into the model. Accordingly, the circular entity serves as an entry plane from which DSE emanate in a manner that satisfies an input mass flow rate (*DEFINE_DE_INJECTION, LSTC 2016). The unscaled mass flow rate values for 0.5 mm and 0.85 mm diameter sphere generation are taken as averaged values from physical measurements (reported in Sec. 4.2): $5.78\text{E}+4$ mm³/s and $4.26\text{E}+4$ mm³/s, respectively.

The unscaled diameter of the circular plane is influenced by three factors: 1) Timescale of the Phase I research; 2) Current hardware capabilities; and, 3) Unscaled depth of the granular assemblies constructed for physical testing (approximately 260 mm). Collectively, these constraints limit element counts in models to approximately $9\text{E}+06$ or fewer DSE. To accommodate this limiting number of DSE, two unscaled rigid cylinder diameters are defined (66 mm for the 0.5 mm spheres and 116 mm for the 0.85 mm spheres). As a result, when the unscaled depth of settled spheres within the containers reach depths as near as feasible to 260 mm (Fig. 5.3),

the total number of settled DSEs remain below the $9\text{E}+06$ limit (7,765,143 spheres at 0.5 mm diameter and 4,936,504 spheres at 0.85 mm diameter), regardless of other parameter variations.

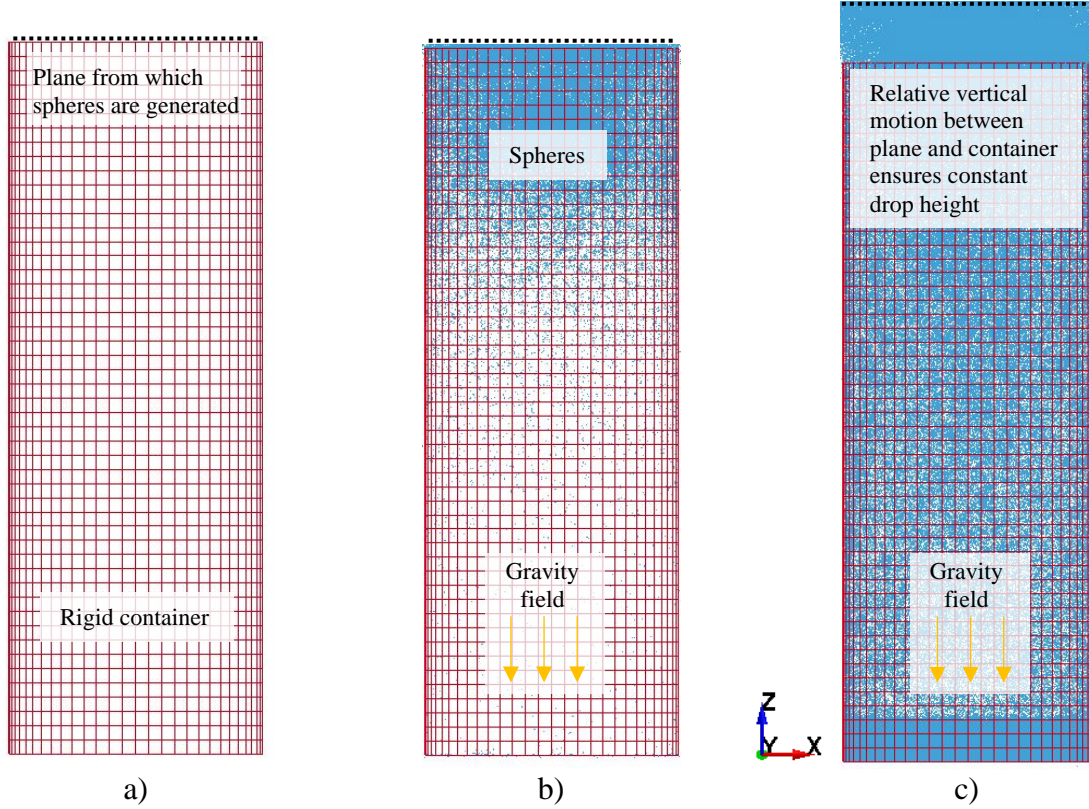


Figure 5.2 Pluviation simulation staging: a) Initial configuration; b) Stage 1; c) Stage 2

The first stage of the pluviation simulation (Fig. 5.2b) consists of restraining the elevation of the circular plane during DSE generation until the instant at which initial contact is made between the DSE and the rigid cylinder bottom. Subsequently, during the second stage of the simulation (Fig. 5.2c), the circular plane undergoes prescribed upward translation such that the vertical distance between the circular plane and the top surface of the accumulated DSE (i.e., the “drop height”) remains constant. As detailed in Sec. 4.2, maintaining a constant drop height (381 mm) throughout the pluviation process is critical in fostering consistent, homogenous packing conditions. The third and final stage of the pluviation simulation consists of halting the emanation of DSE from the circular plane, and permitting a mechanically stable state to form (Fig. 5.3).

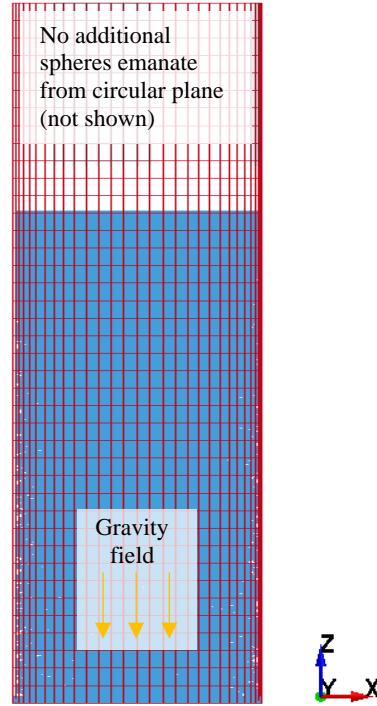


Figure 5.3 Mechanically stable DSE assembly obtained from simulation of the pluviation process

5.4.2 Comparisons between Computed and Measured Density States

As a benefit of the physical testing activities dedicated to use of pluviation techniques to construct assemblies of proppants granules (recall Sec. 4.2), measurements are made available for bulk mass density (among other quantities, as discussed in Sec. 5.4.3). Subsets of these physical measurements, taken immediately following completion of the pluviation process, are identified as datum values for judging the fidelity of the simulated pluviation process (*viz.*, bulk density). To satisfy these datum measurements, a parametric set of pluviation simulations is carried out, wherein for each simulation, one of a range of interparticle friction values is selected (0.2 to 0.7 per microscopic measurements, as detailed in Sec. 3.4.3 and Sec. 3.5.3). Shown in Table 5.7 and Table 5.2 are the bulk densities calculated upon reaching mechanically stable states for assemblies comprised of 0.5 mm diameter spheres, and for assemblies comprised of 0.85 mm diameter spheres.

Table 5.7 Calculated bulk densities of mechanically stable DSE assemblies composed of 0.5 mm diameter spheres (normalized to 1g)

Interparticle friction coefficient	Bulk density (tonnes/mm ³)
0.2	2.74E-09
0.3	2.46E-09
0.4	2.34E-09
0.5	2.17E-09
0.6	2.10E-09
0.7	1.84E-09

Table 5.8 Calculated bulk densities of mechanically stable DSE assemblies composed of 0.85 mm diameter spheres

Interparticle friction coefficient	Bulk density (tonnes/mm ³)
0.2	2.70E-09
0.3	2.46E-09
0.4	2.31E-09
0.5	2.14E-09
0.6	2.11E-09
0.7	1.78E-09

Recall from the measurements listed in Sec. 4.2 that (average-valued) bulk mass densities of 2.27E-09 tonnes/mm³ and 2.18E-09 are associated with pluviated packings of 0.5 mm and 0.85 mm diameter granules, respectively. Comparing these datum values to the (computed) bulk mass density values listed in Table 5.7 and Table 5.8, respectively, indicate that interparticle friction values ranging between 0.4 and 0.5 are capable of producing numerical density states that align well with physical measurements.

As an extension of the pluviation simulations, the coordinates of all DSE associated with mechanically stable packings and an interparticle friction coefficient of 0.4 are exported into two new models—one model to represent the 0.5 mm diameter spheres, and one model to represent the 0.85 mm diameter spheres. Subsequently, these models are initialized and permitted to achieve a new mechanically stable state, but with specification of an interparticle friction coefficient of 0.47. Note that the interparticle friction of 0.47 is the average value obtained from physical testing of proppants (recall Sec. 3.4.3 and Sec. 3.5.3). The through-depth profiles of computed bulk density are plotted in Fig. 5.4, and indicate good to excellent agreement with the (physical) point-valued bulk density measurements. Further, these bulk density profiles reveal only small variations in bulk density regardless of elevation, where the bulk densities computed for the uppermost portions of the profiles fall within 10% of those values computed for the bottommost portions of the profiles. The narrow bands of computed bulk densities support the assertion that the pluviation simulation process promotes the formation of homogenous conditions.

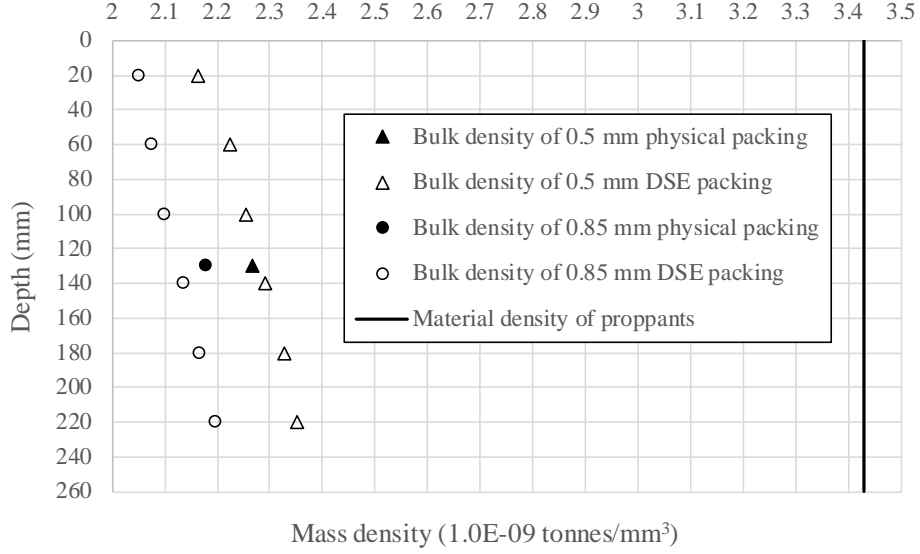


Figure 5.4 Physical versus numerical bulk densities achieved for 0.5 mm and 0.85 mm proppants (normalized to 1g)

5.4.3 Computed Geostatic Stresses

Comparisons between physically measured and computed stresses of granular assemblies are also made, after said assemblies have reached a mechanically stable state under gravitational acceleration. In this context, stresses that manifest throughout the granular bodies are referred to as geostatic stresses, containing both vertical and horizontal components. As discussed in Sec. 4.4.2, pressure cells are positioned within the physically constructed assemblies to provide measurements of vertical and horizontal stresses at selected depths. In contrast, a volume-averaged stress approach is elected to quantify those stresses that develop throughout the bodies of corresponding DSE assemblies. Accordingly, the following formula is utilized:

$$\bar{\sigma}_{ij} = \left(\frac{1-n}{\sum_{N_P} V_P} \right) \sum_{N_P} \bar{\sigma} V_P \quad (5.13)$$

where $\bar{\sigma}_{ij}$ is the volume-averaged stress tensor over a given volumetric subdomain within the granular assembly; n is the porosity of the subdomain; N_P is the number of spheres within the subvolume; V_P is the volume of sphere P , and $\bar{\sigma}$ is the stress tensor of sphere P .

As shown in Fig. 5.5, a column of separate but consistent representative elementary volumes (REVs) are defined within the DSE assemblies to facilitate calculation of volume-averaged stresses. Note that the REV dimensions are proportional to those of the triaxial compression test chambers utilized in the physical testing program (recall Sec. 3.3.5): each cylindrical REV possess a 20 mm diameter and 40 mm length. So as to preclude any boundary effects (due to the presence of the rigid cylinder container throughout the pluviation simulations),

the REVs are positioned end-to-end along the vertical central axis of the DSE assembly. Volume-averaged vertical and horizontal stresses are computed based on the stresses attributed to constituent spheres located within each REV. Profiles of (vertical) volume-averaged stresses, with comparisons to available physical measurements, are plotted in Fig. 5.6, and show excellent agreement.

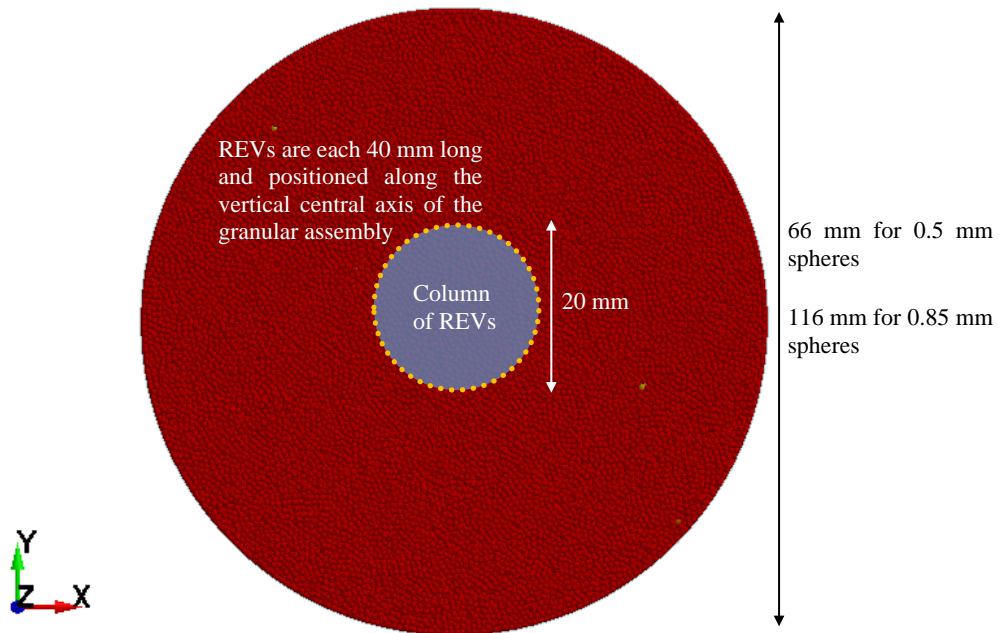


Figure 5.5 Plan view location of column of REV within DSE assemblies

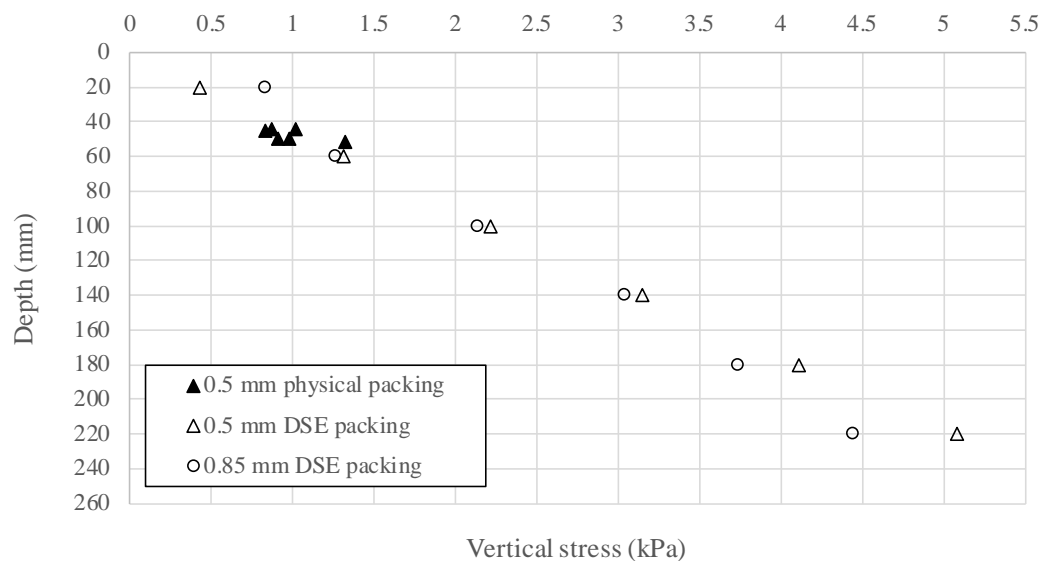


Figure 5.6 Physical versus numerical vertical stresses achieved for 0.5 mm and 0.85 mm proppants (normalized to 1g)

Relatively fewer physical measurements are available for assessing numerical model fidelity of (geostatic) horizontal stress distributions. Therefore, supplemental physical data are introduced, based on measurements from triaxial compression testing of 0.5 mm assemblies and 0.85 mm assemblies (recall Sec. 3.3). Shown in Fig. 5.7 are comparisons of K_0 values (i.e., ratios of horizontal to vertical stresses) associated with the collective physical measurements (including available pressure cell readings for pluviated assemblies, as discussed in Sec. 4.3.3) and numerical results. The following expression is used to enable comparisons between computed results and the triaxial compression test data:

$$K_0 = 1 - \sin(\phi) \quad (5.14)$$

where ϕ is the internal friction angle reported among the triaxial compression test results.

A significant range of K_0 values are observed among the various physical measurements (0.12 to 0.53), and the REV-based profile of computed K_0 values fall among the upper bounds of said range. This phenomenon is consistent with findings from several previous studies. For example, both Wiqcek et al. (2017) and Chung and Ooi (2006) found—in comparing physical tests to DEM models of highly spherical granules—that the numerical results over-predict K_0 values by up to 200%. Given this previously established phenomenon, the level of agreement observed for this aspect of the current study is considered to be acceptable. Additionally, as discussed later, the stress magnitudes achieved in the numerical models during penetration simulations dwarf the vertical and horizontal geostatic stresses. Consequently, maximum penetration depths are not significantly affected by the relatively large (computed) K_0 values.

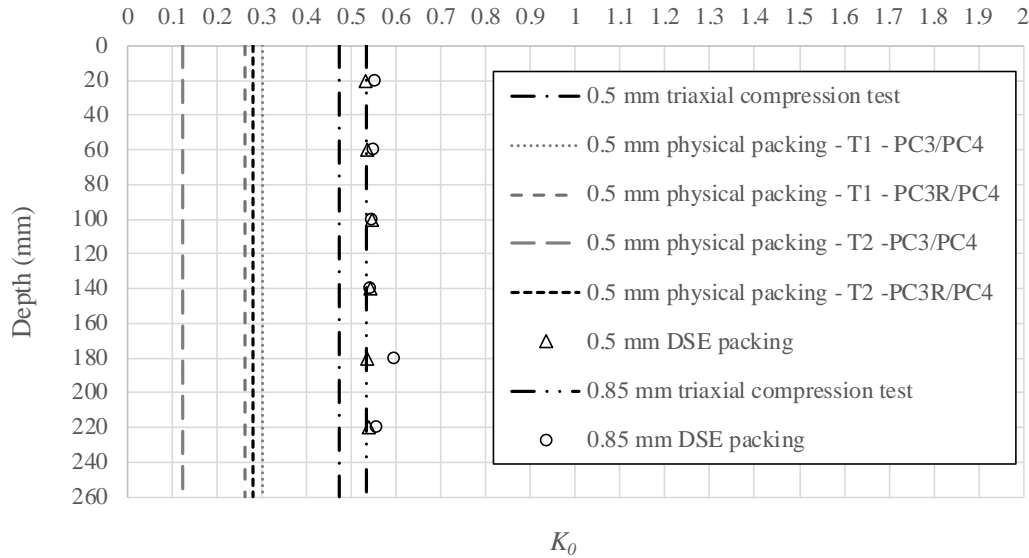


Figure 5.7 Physical versus numerical K_0 values achieved for 0.5 mm and 0.85 mm proppants (normalized to 1g)

5.5 Numerical Model of Centrifuge Test

Assemblies of DSEs that are packed via pluviation simulations, and are verified to satisfy the previously described bulk density and geostatic stress metrics, are combined with FE models of projectiles to carry out myriad projectile penetration simulations. In Sec. 5.5, critical aspects of numerical models used in the projectile penetration simulations are discussed. In particular, the means by which modeling of DSE assembly boundary conditions are presented, where a novel approach to modeling non-reflection of stress waves is presented. Additionally, considerations for modeling of the projectiles are reported, as are the stages of the projectile penetration simulations conducted as part of the Phase I research efforts.

5.5.1 Considerations for Boundary Conditions

The computational cost of DEM simulations increases prodigiously with increasing numbers of DSE. As noted previously, the scope of the Phase I research and current hardware limits restrict the total number of spheres to $9\text{E}+06$ or fewer, where this restriction comes into play primarily during the assembly preparations (i.e., pluviation simulations). Compounding the computational cost of simulating the forces and motions of several million DSE is that, due to the rapid nature of projectile penetrations, time step sizes may not exceed approximately $1\text{E}-06$ sec. Given the limitation on the maximum number of spheres and the exceedingly small time step sizes required for simulating projectile penetration, the full domain of the granular assembly within the centrifuge box (recall Ch. 4) cannot be modeled.

To offset the inability to model the entire domain of proppants within the centrifuge box, a half-space modeling approach is elected, and demonstrated to be successful, in the current study. Alternatively stated, a subvolume of the physical granular assembly is modeled, and special considerations are made for modeling of boundary conditions so as to mimic the presence of the proppants that are exterior to the subvolume. In Sec. 5.5.1, the DSE assembly associated with 0.85 mm spheres is discussed to clarify those considerations made toward modeling of boundary conditions, where those same considerations are applied for the assembly of 0.5 mm spheres.

Integral to the elected approach is that boundary conditions must not reflect stress waves that emanate from within the subvolume during penetration. This class of boundary conditions is referred to as “non-reflecting” boundary conditions, and specific to DSE assemblies, such entities are referred to as local non-reflecting boundary conditions (LNRBC). The main advantage of utilizing this approach is that it efficiently permits simulation of a semi-infinite domain, where only a subvolume of DSE are included in the model, relative to the physical assembly.

Yet another description of the LNRBC concept is that LNRBCs act as energy absorbing mechanisms with limited constraints on the boundary elements. From one point of view, LNRBCs permit motions that lie somewhere between a fixed (restrained) boundary and free (unrestrained) boundary on the selected elements. Even so, stress wave propagation should be such that the LNRBC absorbs the energy associated with the stress wave, while transmitting none or only nominal amounts of said energy back into the interior of the DSE assembly. This characteristic of LNRBC is precisely what constitutes an approximation of a boundary at infinity.

Viscous dampers are well suited for modeling LNRBCs, as dampers tend to mitigate abrupt changes in nodal velocities. Further, towards preventing creeping motions of DSE under sustained stress waves, springs are additionally utilized to build up LNRBCs in the current study. Consequently, the LNRBCs are actually critically damped springs applied to boundary spheres of DSE assemblies. This concept is illustrated schematically in Fig. 5.8, where the motion (velocity, v) of the leftmost sphere is transmitted via contact to the progressively more exterior spheres. When some portion of the leftmost particle motion reaches the boundary sphere, both the spring and damper are engaged. Because the spring is critically damped, the motion of the boundary sphere is undertaken with minimal acceleration, and minimal oscillatory amplitude. Further, due to the presence of the spring, the position of the boundary sphere will undergo (at least) partial restoration to its original state. From an energy-based perspective, kinetic energy transferred to the boundary sphere by stress wave propagation is dissipated by the viscous damper, while restorative (strain) energy is stored in the spring. So, while the boundary sphere may undergo some rebound, the associated (leftward) motion is also distinctly non-abrupt due to the presence of the (critical) damper. In this way, minimal reflection of the incident stress wave occurs.

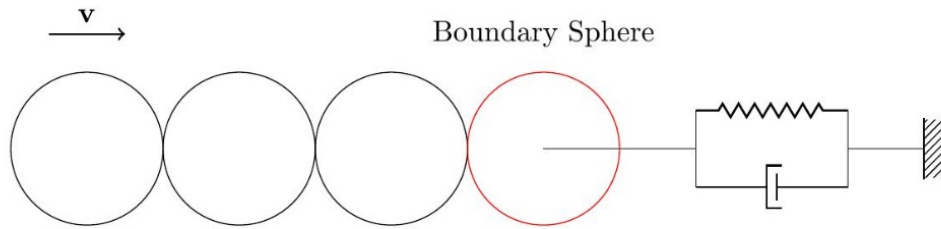


Figure 5.8 Conceptual schematic of local non-reflecting boundary condition (LNRBC)

Shown in Fig. 5.9 is an isometric view of a DSE assembly that is representative of those assemblies used in the penetration simulations. The monodisperse assemblies possess rheological properties reported for the 0.5 mm or 0.85 mm proppants (discussed in Sec. 5.3 and 5.2, respectively), as appropriate. As annotated in Fig. 5.9b, the unscaled DSE cylindrical assembly is 116 mm in diameter and encompasses a 260 mm depth. The DSE assembly is categorized into two sets of DSE. Nearest to the vertical-centroid axis of the assembly are interior spheres, which are intended to interact with the shell elements of the projectile. A network of boundary spheres circumferentially surround the sides of the assembled interior spheres, as well as the bottom of region of the model. This latter category of spheres is intended to hold the assembly intact while absorbing (but not reflecting) stress waves that emanate as a result of interactions between the projectile and interior spheres. For the projectile simulations conducted as part of the Phase I research, the annular region of boundary spheres has been found to robustly uphold mechanical stability of the assembly when the “wall” thicknesses of the annuli are three or more sphere diameters thick.

Note that each boundary sphere is fitted with three orthogonal spring-dashpot elements so as to promote critically damped motion. The intended utility of imposing local, critical damping to each boundary sphere is to prevent non-physical reflection of stress waves that are generated during interactions between the interior spheres and the projectile. Stated alternatively, these

spring-dashpot pairs operate in conjunction with pressure-derived force boundaries to bring about local non-reflecting boundary conditions to the overall DSE assembly.

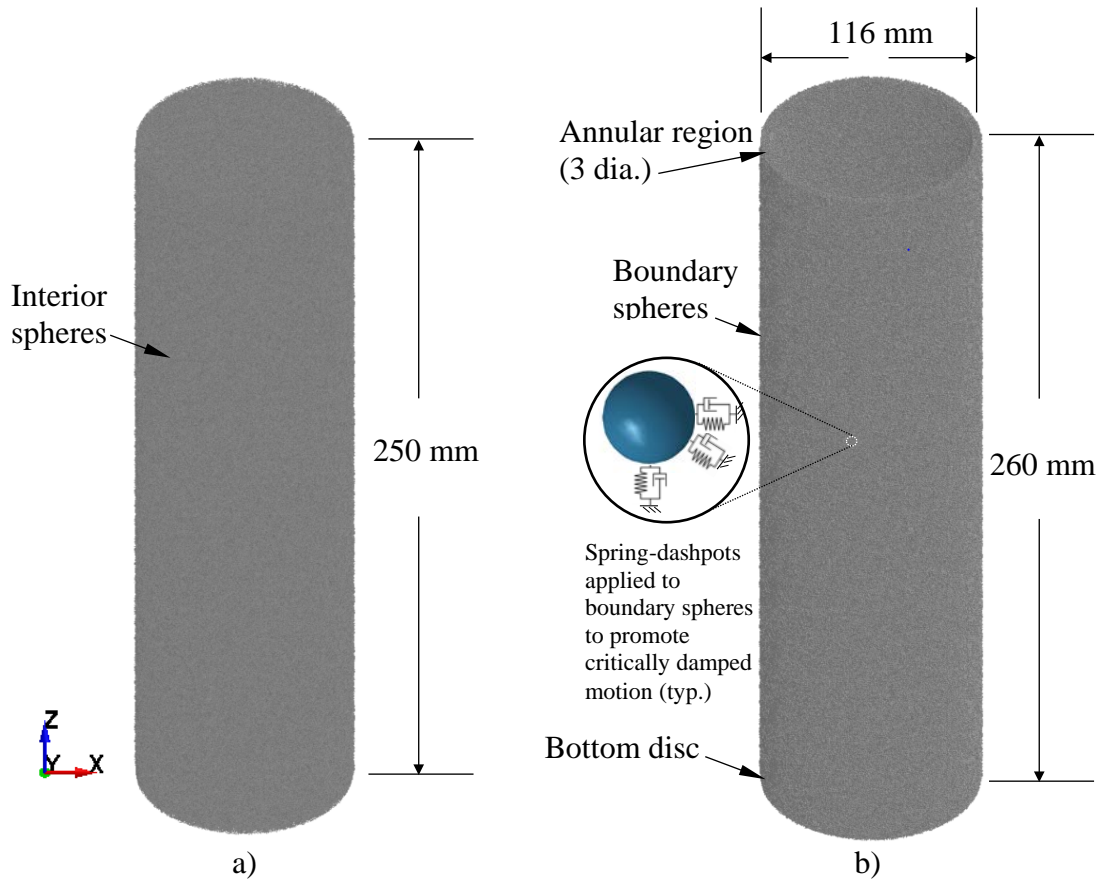


Figure 5.9 Numerical model of pluviated DSE assembly (normalized to 1g): a) Interior spheres; b) Boundary spheres

Recalling Figs. 5.4 and 5.7, the through-depth profiles of vertical and horizontal stresses that arise within the pluviated DSE assembly are used to form the force components of the boundary conditions that hold the subvolume assembly intact under gravitational acceleration. More specifically, the cataloged stress profiles are integrated over the tributary areas of boundary spheres of the subvolume assembly, and applied as forces to each boundary sphere. The distribution of pressures is illustrated in Fig. 5.10. Horizontal stresses are resolved into forces acting on boundary spheres within the annular region, and are oriented toward the central vertical axis of the assembly. Vertical stresses are resolved into tributary-area forces acting on all boundary spheres, and all vertical forces are oriented upwards. In this way, the catalog of stresses is used to impose boundary conditions that, in turn, maintain a mechanically stable state of the subvolume, when said subvolume is subjected to gravitational acceleration.

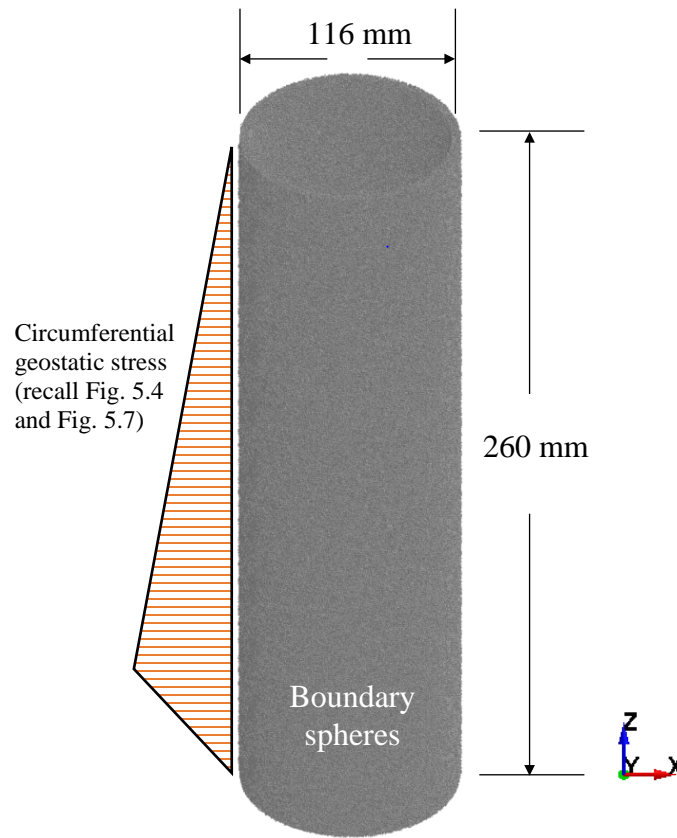


Figure 5.10 Applied pressure distributions to circumferential and bottom boundaries of DSE assemblies (normalized to 1g)

5.5.2 Numerical Model of Projectile

The FE model of the unscaled projectile (Fig. 5.11) is comprised of shell elements, with exterior dimensions (length, diameter, ogive nose) that are proportional to the physical projectiles (Sec. 2.4). Importantly, the thickness of the shell elements and the density of the material assigned to the shell elements are such that the mass and center of mass (C.M.) of the projectile models used in the projectile penetration simulations are identical (with respect to prototype scale) to those used in the physical centrifuge tests. For the Phase I research, the projectile is assumed to be relatively rigid compared to the DSE granules, and therefore the `MAT_RIGID` material model (LSTC 2016) is made use of in the projectile penetration simulations. Even so, to compute fidelity in particle-projectile contact interactions (discussed in Sec. 5.5.3), a modulus of elasticity is specified at 200 GPa for the stainless steel material.

The most pronounced difference between the numerical model of the projectile and the physical projectile specimens is found at the tip of the projectile nose (Fig. 5.11). While, physically this region of the projectile converges to a sharp point, an exact replication of this geometry is prone to numerical instability, particularly when contact possibilities arise. To eliminate this

potential source of numerical instability (via undetected contact with DSE granules), the nose of the projectile is augmented with a small hemisphere. Note that the hemisphere diameter is comparable to that of a single DSE, and further, the hemisphere is subdivided into a relatively dense mesh of shell elements. As a result, undetected contact between the nose of the projectile and the DSE proppants is not found to occur across the set of simulations discussed in Secs. 5.6-5.9.

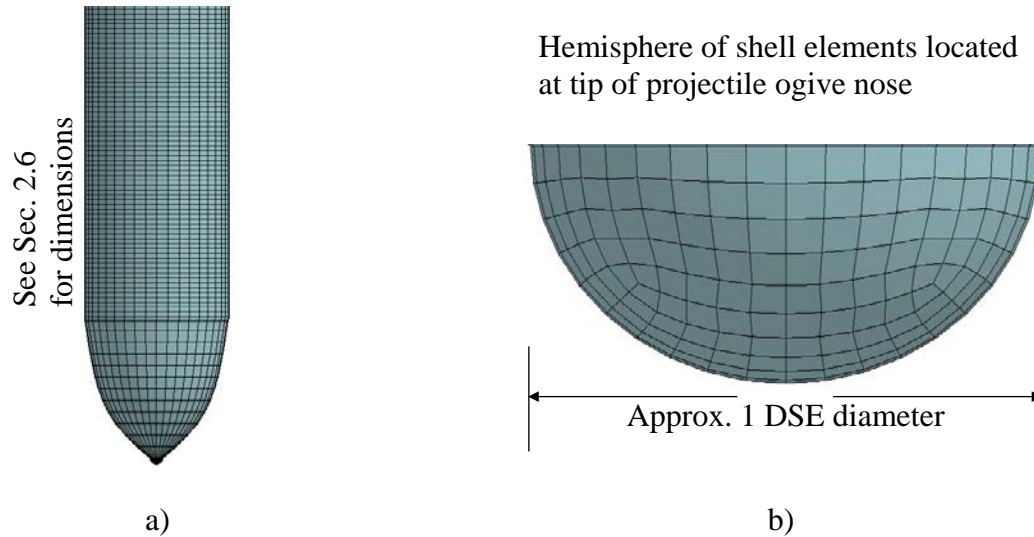


Figure 5.11 Finite element model of unscaled projectile: a) Elevation view; b) Ogive nose augmentation (normalized to 1g)

5.5.3 Considerations for Interactions between Projectiles and Granules

Considerations for interactions between the DSE proppants and FE projectile shell elements are critical to the accuracy of the simulation results. Such interactions are primarily driven by normal and tangential contact, where normal contact interactions are dictated by the elastic modulus assigned to the shell elements (200 GPa) and the normal contact stiffness of any interacting DSE (recall Sec. 5.2.2). However, the tangential contact interactions are significantly affected by the specification of a friction coefficient for particle-projectile tangential motions.

Within LS-DYNA (LSTC 2016), the contact definition (and appropriate friction coefficients) for particle-projectile interactions is established by making use of the `DEFINE_DE_TO_SURFACE_COUPLING` card. In this context, two friction coefficients are supplied: a static friction coefficient, which limits the tangential resistance between two parts before kinematic motion occurs; and, the dynamic friction coefficient, which quantifies the least external tangential force required to maintain motion of the interacting DSE. While the appropriate value for both coefficients could be found by laboratory testing, scarce data are available specific to tangential contact force interactions between sintered bauxite proppants and stainless steel objects. However, Grima et al. (2010) documented the results of several laboratory tests to measure the static friction coefficient for interactions between bauxite proppants and stainless steel (SS3042B) plates. As shown in Table 5.9, a somewhat narrow range of static friction coefficients were measured, over two distinct levels of normal stress. While in Sec. 5.9, the effects of variations in this friction

coefficient are investigated, a value of 0.65 is selected for general use, and as discussed in Secs. 5.6-5.8, consistently contributes to optimal agreement between the projectile penetration simulations and the physical centrifuge test measurements of maximum penetration.

Table 5.9 Physical measurements of sliding friction between 4 mm spherical bauxite proppants and stainless steel (SS3042B) plates (Grima et al. 2010)

Normal stress (kPa)	Interparticle friction coefficient
1	0.60
1	0.65
10	0.57
10	0.6

5.5.4 Simulation Stages

Shown in Fig. 5.12 is the combined DEM-FEM model configuration used for the projectile penetration simulations involving the 0.85 mm granules, where the same simulation staging is applicable to the model configuration associated with the 0.5 mm granules. Note that the DSE assembly is initialized in the pluviated state, under the full application of confining pressures, and the gravitational field. In contrast, the projectile is subjected to the gravitational field, but additionally subjected to a prescribed initial velocity. In accordance with the Coriolis-effect calculations discussed in Sec. 4.5.3, the components of the initial velocity are decomposed into horizontal and vertical components, where the decomposition is a function of the total velocity. Correspondingly, the projectile is initialized a nominal distance above the top surface of the DSE assembly in an inclined position (with rotation about the Y axis), consistent with the horizontal and vertical velocity components. Specific velocities and inclinations considered are discussed later in Secs. 5.6-5.9.

The projectile penetration simulations are divided into two stages, where the first stage consists of those times over which the projectile retains non-zero velocity components (Fig. 5.13). As discussed later (in Sec. 5.9), the simulated duration over which the projectile continues to plunge into the DSE medium is a function of several parameters. At the instant in which the projectile reaches maximum penetration, the second stage of the simulation begins (Fig. 5.14, 5.12). All times beyond which the maximum penetration depth is reached are categorized as belonging to the second stage of the simulation. During this second and final stage, the projectile motion is monitored, and continued, until no further changes to the projectile position are observed.

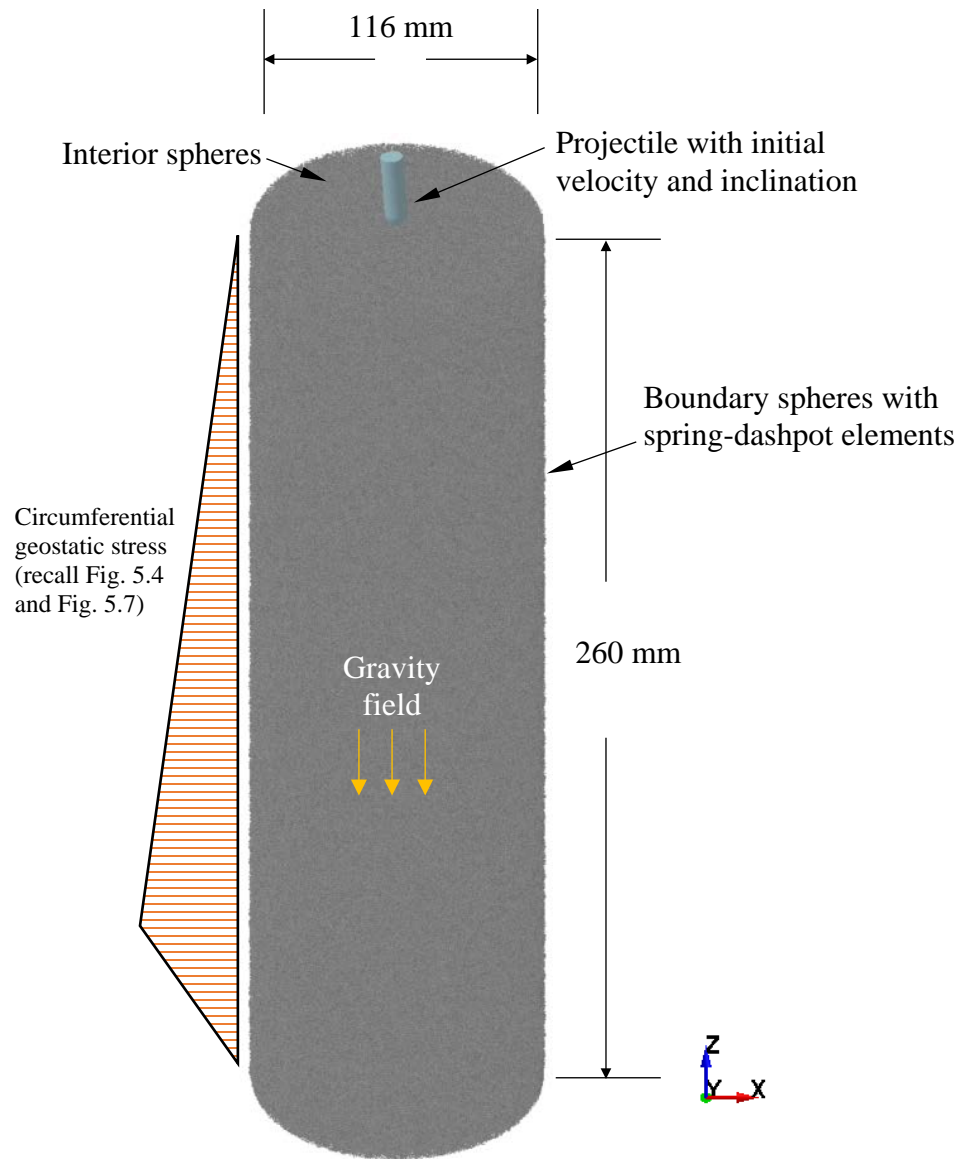


Figure 5.12 State of FE projectile and DSE assembly just prior to onset of projectile penetration (Numerical representation of centrifuge models at 1g)

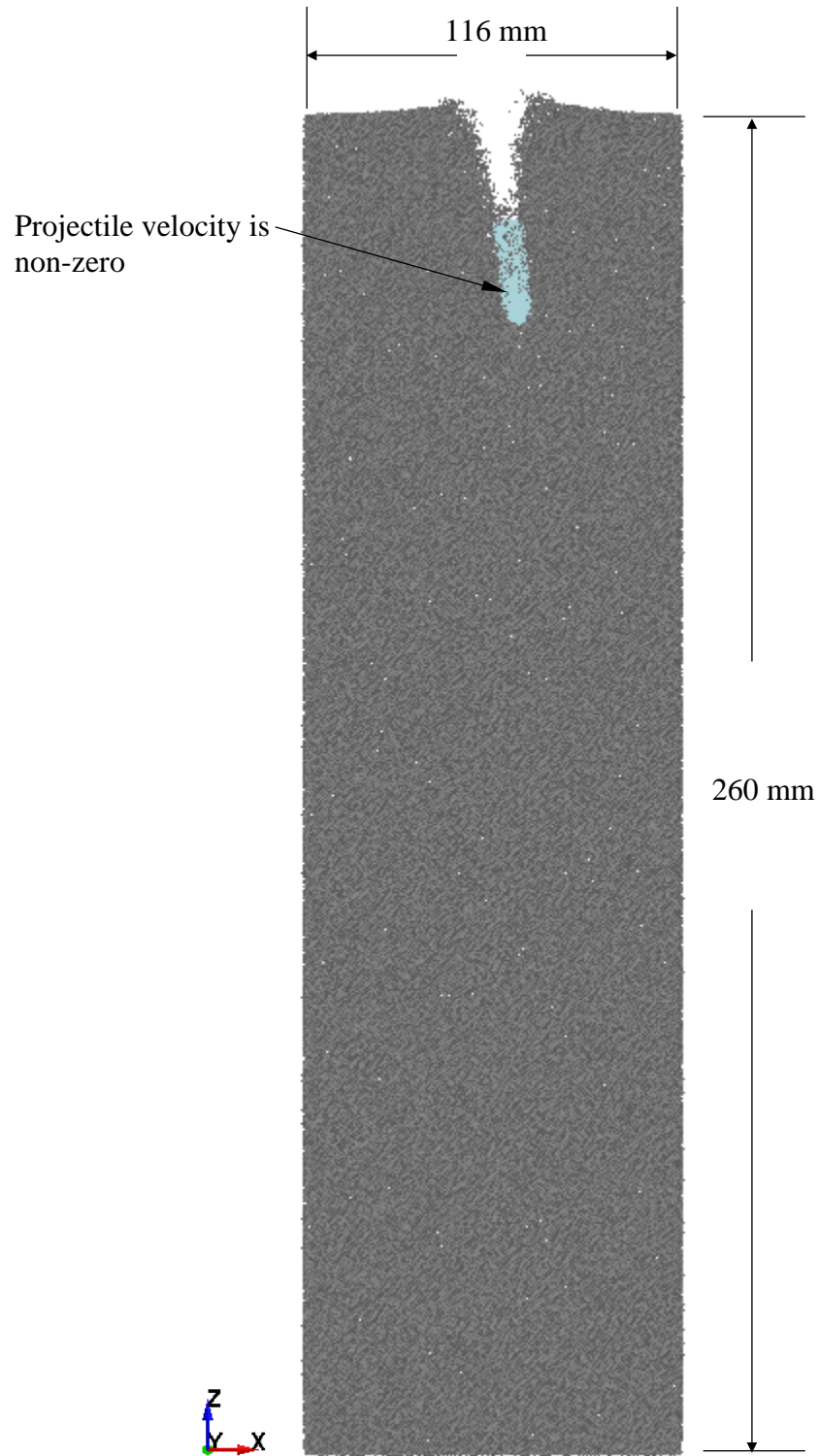


Figure 5.13 State of FE projectile and DSE assembly during projectile penetration (normalized to 1g)

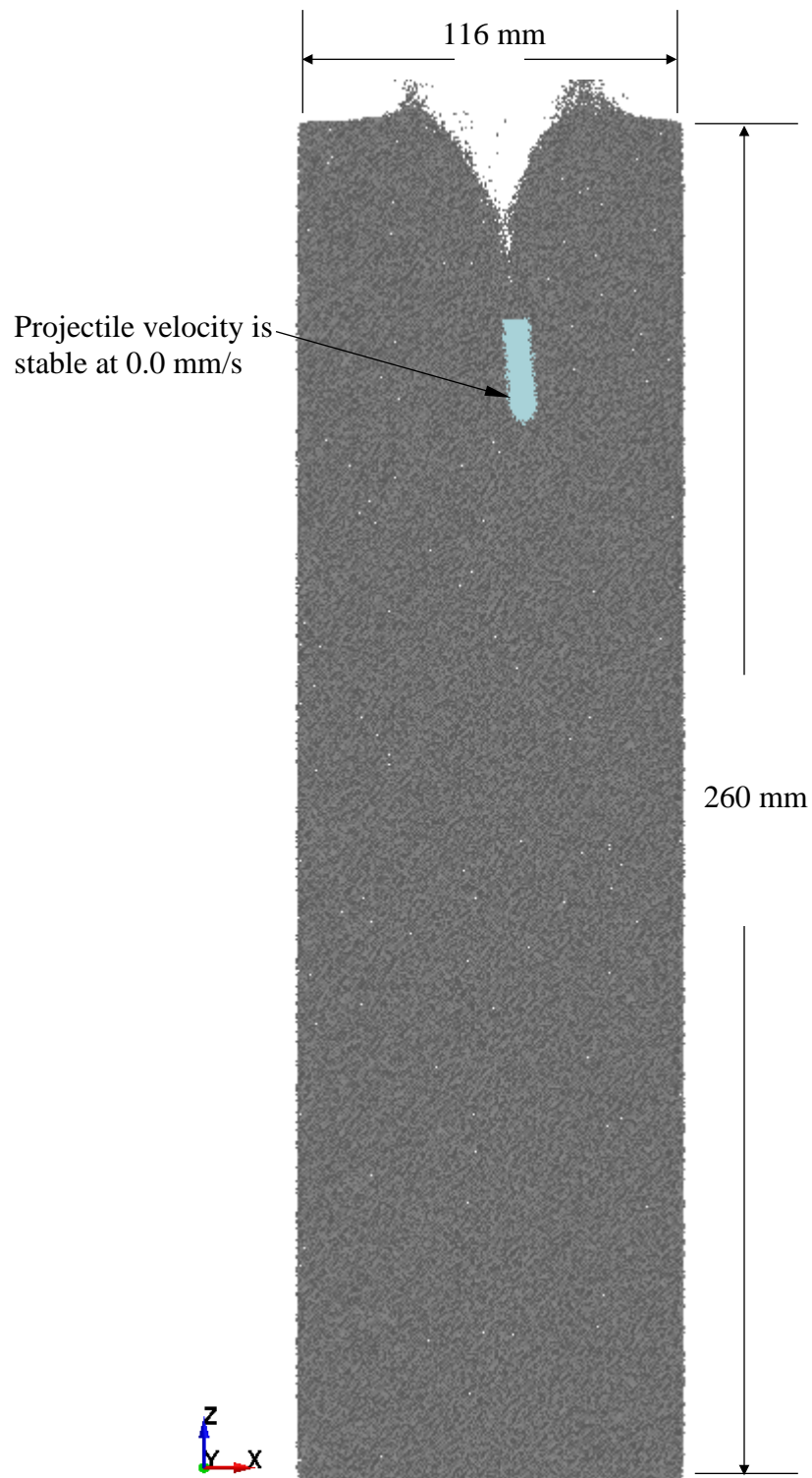


Figure 5.14 State of FE projectile and DSE assembly upon termination of simulation (at 1g scale)

5.6 Test Scheme 1: Projectile Penetration into Monodisperse Assembly

Three projectile penetration test schemes are established as part of the Phase I research, and care is taken to leverage the test conditions to facilitate validation of the centrifuge testing across multiple centrifugal acceleration levels. In addition, the test schemes are crafted to enable assessments of relative scale effects (e.g., the effect of varying the ratio of projectile diameter to proppants granule diameter). Complimentary to the physical test setups and measurements reported in Ch. 4, are projectile penetration simulation, which are presented in the remainder of Ch. 5. These simulations provide the only feasible means of gleaning additional insights into phenomena such as assembly-wide stress wave propagations, and therefore, constitute a critical thrust of the Phase I research. Unless otherwise noted, all discussion for the remainder of Ch. 5 is made with respect to test-specific prototype scale (or centrifugal acceleration level).

Sec. 5.6 is paired with Sec. 4.5, and gives documentation of the projectile penetration simulation corresponding to Test Scheme 1. For convenience, salient parameters of the configuration are listed in Table 5.10, and displayed in Fig. 5.15. For this first of three test setups, the centrifugal acceleration level of 26.5g is employed, along with 22.525 mm diameter proppants and a 238.235 mm diameter projectile. A mean-valued friction coefficient (0.47) is supplied for particle-particle tangential contact interactions, while an upper-bound value (0.65) is supplied for particle-to-projectile tangential contact interactions (recall Sec. 5.5.3).

As previously noted in Sec. 5.5.4, the projectile is assigned prescribed initial velocity components in both the horizontal (X) and vertical (Z) and directions (V_{X0} and V_{Z0} , respectively) in compliance with the Coriolis Effect. Given that a muzzle velocity of approximately 70 m/s is associated with the (physical) Test 1 conditions, the predominant component of velocity is parallel to the Z direction, as listed in Table 5.10. The projectile is inclined (ψ_{Y0}) at 7.55° about the horizontal (Y) axis so as to align with the prescribed initial velocity components (Fig. 5.15).

Table 5.10 Test Scheme 1 parameters for projectile penetration simulations		
Parameter description	Value	Units
Prototype base scale factor	26.5	g level
DSE diameter	22.525	mm
DSE assembly diameter	3074	Mm
DSE assembly depth	6890	Mm
Particle-to-particle friction coefficient	0.47	--
Projectile diameter	238.235	mm
Particle-to-projectile friction coefficient	0.65	--
Projectile velocity, V_{X0}	9088.0	mm/s
Projectile velocity, V_{Z0}	-69407.5	mm/s
Projectile inclination, ψ_{Y0}	7.55	°

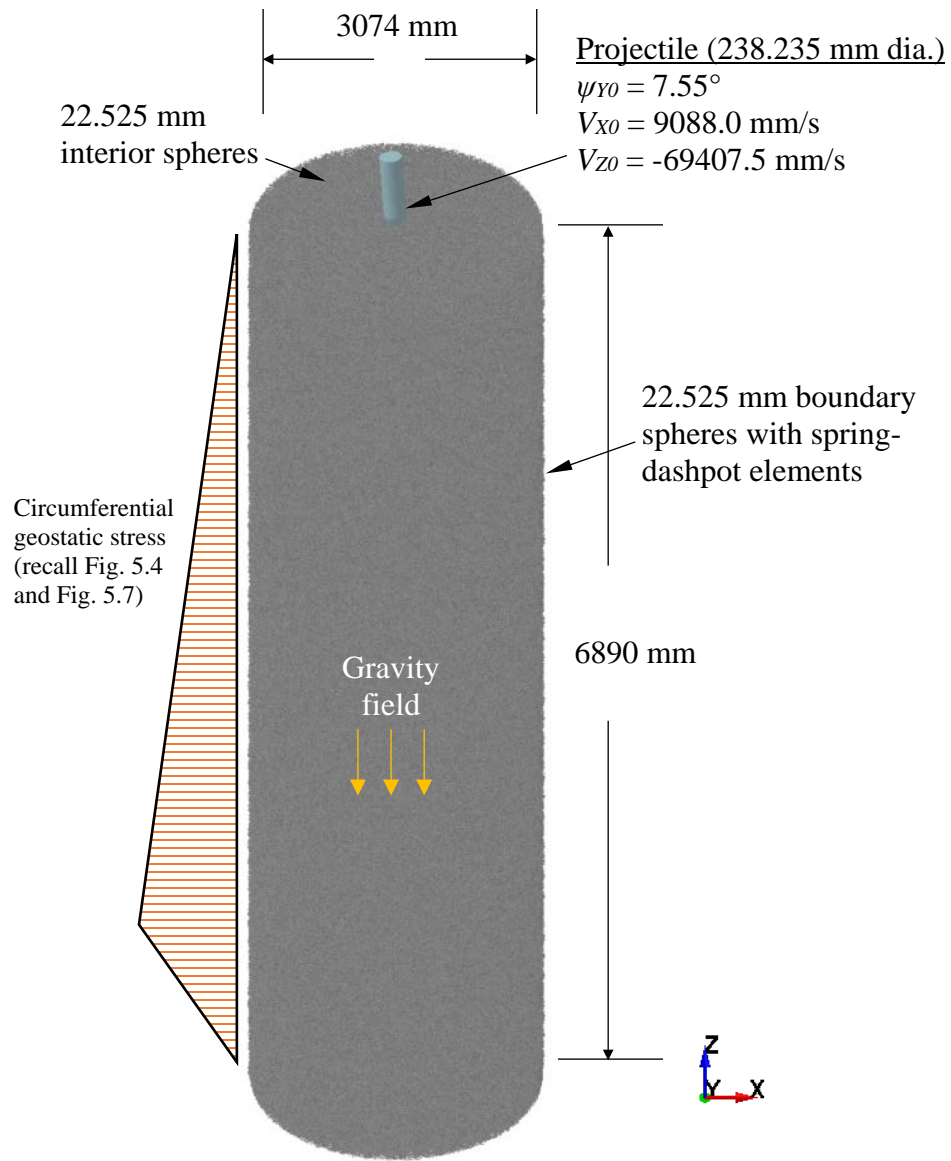


Figure 5.15 State of Test 1 FE projectile and DSE assembly just prior to onset of projectile penetration (prototype scale: 26.5g)

5.6.1 Computed versus Measured Projectile Penetration Depth

As one of the critical outcomes of the Phase I research, the ability to predict maximum projectile penetration depths is assessed, relative to the available (physical) centrifuge test data. Shown in Fig. 5.16 is a time-history plot of the projectile vertical displacement (i.e., the projectile penetration). Additionally plotted in this (physical) penetration depth measured for test 1 (1973.3 mm). For Test 1, the penetration simulation produces moderately conservative (17% greater) penetration depth of 2324 mm. However, as demonstrated in Secs. 5.8-5.9, this result comparison

is the least agreeable among the three test series. Therefore, elucidation of the source of the observed over-prediction is reserved for subsequent research efforts, where said discrepancy may stem from: 1) Repeatability of physical centrifuge testing; and, 2) Unaccounted for phenomena in the numerical model.

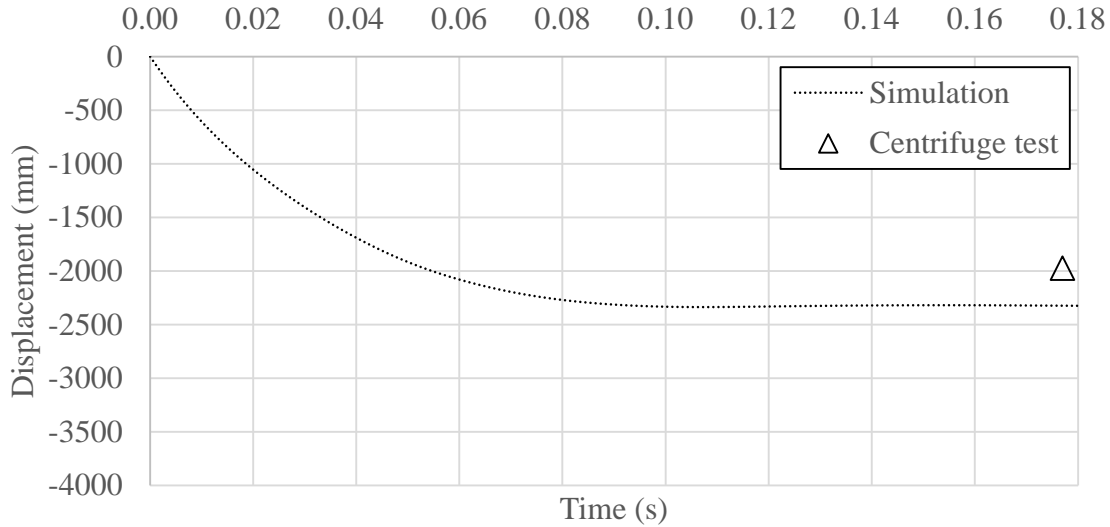


Figure 5.16 Projectile penetration simulation result for interparticle friction coefficient of 0.47, particle-to-projectile friction coefficient of 0.65, and 70 m/s projectile velocity (at prototype scale of 26.5g)

5.6.2 Computed Stresses in Granular Assemblies

Shown in Fig. 5.17 and Fig. 5.18, respectively, are vertical and horizontal stress plots of the Test 1 DSE assembly. Recall that the projectile is considered to be rigid as part of the Phase I research, and so, only those stresses that develop throughout the DSE assembly are of interest. A fringe plot ranging from -2 MPa to 0 MPa is qualitatively found to accentuate the most intensive portions of the penetration-induced stress waves, while still permitting some semblance of the overall stress state of the DSE assembly. Note that the four stress plots in each of Fig. 5.17 and Fig. 5.18 depict a snapshot of the instantaneous stress state at penetration depths equal to: 25% (Fig. 5.17a and Fig. 5.18a); 50% (Fig. 5.17b and Fig. 5.18b); 75% (Fig. 5.17c and Fig. 5.18c); and, 100% (Fig. 5.17d and Fig. 5.18d) of the maximum penetration depth. In this context, the plots corresponding to “100%” of the maximum penetration depth are taken at the end of the simulation, when the projectile has been verified to have relinquished practically all of its initial kinetic energy.

A visual scan of Fig. 5.17a and Fig. 5.18a indicates the formation of ellipsoidal stress waves, where the vertical stress components (Fig. 5.17a) may be more aptly described as semi-spherical. In contrast, the penetration-induced horizontal components of the stress wave (Fig. 5.18a) are flatter and approximately 20% wider. Upon reaching 50% of the maximum penetration depth (Fig. 5.17b and Fig. 5.18b), the stress wave components have reached the horizontal extents of the

cylindrical DSE assembly, and the shape of the stress wave, all though still loosely ellipsoidal, has become obscured.

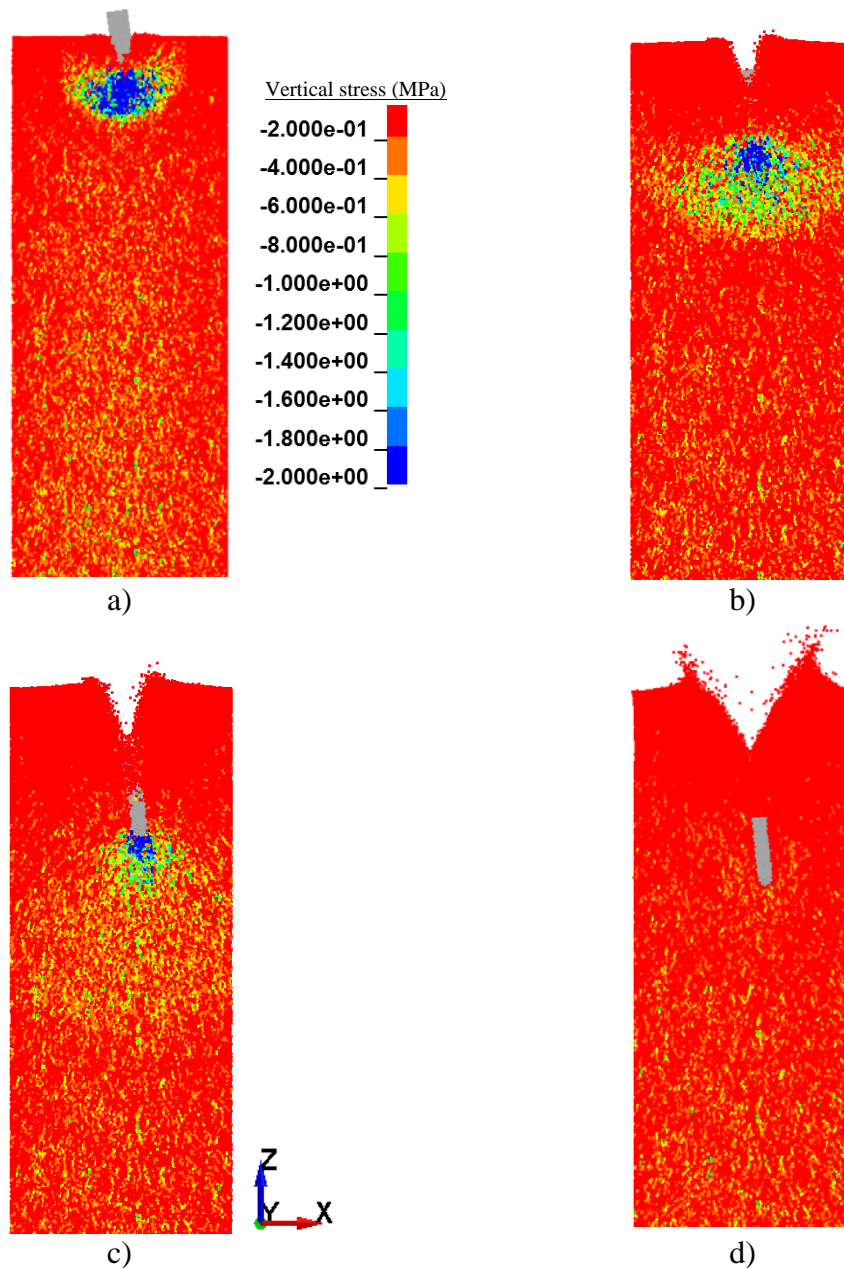


Figure 5.17 Projectile penetration simulation vertical stress plots for interparticle friction coefficient of 0.47, particle-to-projectile friction coefficient of 0.65, and 70 m/s projectile velocity (prototype scale: 26.5g): a) 25% of maximum penetration; b) 50% of maximum penetration; c) 75% of maximum penetration; d) 100% of maximum penetration

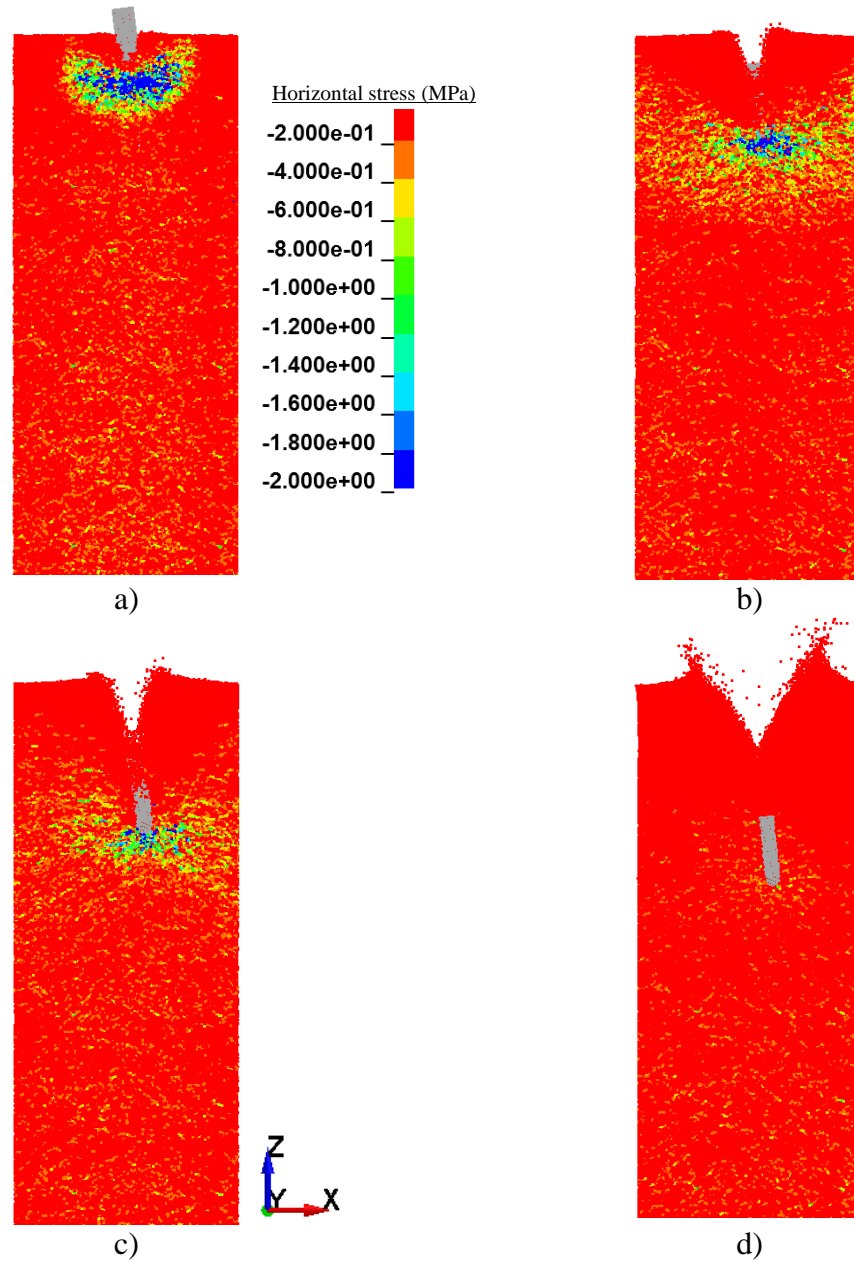


Figure 5.18 Projectile penetration simulation horizontal stress plots for interparticle friction coefficient of 0.47, particle-to-projectile friction coefficient of 0.65, and 70 m/s projectile velocity (prototype scale: 26.5g): a) 25% of maximum penetration; b) 50% of maximum penetration; c) 75% of maximum penetration; d) 100% of maximum penetration

As the projectile penetration transitions from 50% to 75% (Fig. 5.17c and Fig. 5.18c) of the maximum penetration depth, the necessity of incorporating LNRBCs (recall Sec. 5.5.1) becomes apparent. More specifically, due to the presence of LNRBCs, elevated stresses (i.e., those near or exceeding 2 MPa) do not persist for regions of the DSE assembly that are positioned above the projectile. If, instead, the boundaries of the cylindrical DSE assembly were to be fully restrained, then those portions of the penetration-induced stress generated during earlier stages of the penetration (e.g., at 25% of maximum penetration, Fig. 5.17a) would be reflected until

dissipated via contact-based damping long after the projectile had reached a greater penetration depth. Upon termination of the simulation, a localized region of elevated stress (ranging from -0.4 MPa to -0.8 MPa) remains near the projectile nose. These localized, residual stresses can be ascribed to unresolved densification of the immediately surrounding DSEs. Further, consistent with the physical centrifuge tests (recall Sec. 4.3), the final position of the projectile entails an appreciable amount of inclination (6°). The development of analytical and numerical modeling techniques are warranted as part of future studies to promote better predictions of projectile terminal inclination.

5.7 Test Scheme 2: Projectile Penetration into Monodisperse Assembly

Sec. 5.7 is paired with Sec. 4.6, and gives documentation of the projectile penetration simulation corresponding to Test Scheme 2. For convenience, salient parameters of the configuration are listed in Table 5.11, and displayed in Fig. 5.19. A centrifugal acceleration level of 46g is utilized in this second of three test setups.

Although (physically) a binary mixture assembly is investigated for Test 2, the binary mixture consists of proppants with diameters that vary over a relatively narrow range (see Sec. 4.6 for details). As a measure of numerical modeling simplification, a monodisperse DSE assembly is utilized in the Test 2 projectile penetration simulations, where the mean value of constituent granule diameters (23.0 mm) is assigned to all DSEs. As is shown later in Sec. 5.7.1, this modeling simplification does not adversely affect comparative results between the physical measurements and simulated values of maximum projectile penetration depth.

As listed in Table 5.11, a mean-valued friction coefficient (0.47) is supplied for particle-particle tangential contact interactions, while an upper-bound value (0.65) is supplied for particle-to-projectile tangential contact interactions (recall Sec. 5.5.3). The projectile, with 238.28 mm diameter, is necessarily assigned prescribed initial velocity components in both the horizontal (X) and vertical (Z) and directions (V_{x0} and V_{z0} , respectively) to satisfy the Coriolis Effect. For the Test 2 muzzle velocity of approximately 110 m/s, the velocity remains predominantly parallel to the Z direction. Even so, the projectile is inclined 4.78° about the horizontal (Y) axis (Fig. 5.19).

Table 5.11 Test Scheme 2 parameters for projectile penetration simulations		
Parameter description	Value	Units
Prototype base scale factor	46	g level
DSE diameter	23.0	mm
DSE assembly diameter	5336	mm
DSE assembly depth	11960	mm
Particle-to-particle friction coefficient	0.47	--
Projectile diameter	238.28	mm
Particle-to-projectile friction coefficient	0.65	--
Projectile velocity, V_{x0}	9128.0	mm/s
Projectile velocity, V_{z0}	-109261.0	mm/s
Projectile inclination, ψ_{Y0}	4.78	$^\circ$

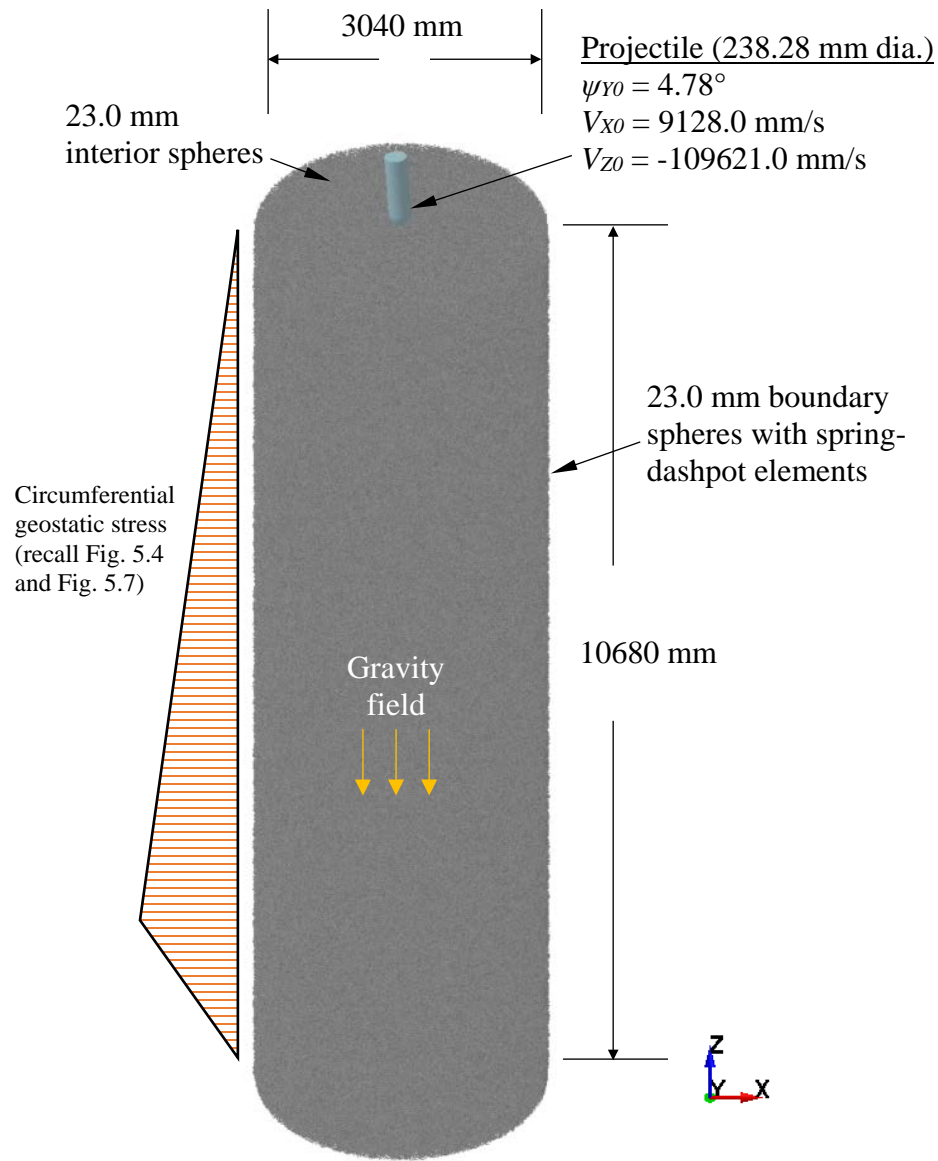


Figure 5.19 State of Test 2 FE projectile and DSE assembly just prior to onset of projectile penetration (prototype scale: 46g)

5.7.1 Computed versus Measured Projectile Penetration Depth

Plotted in Fig. 5.20 is the time-history of Test 2 projectile vertical displacements, obtained from the corresponding projectile penetration simulation. Also plotted is the physically measured penetration depth for Test 2 (3139 mm), where excellent agreement (2% difference) is observed between the physical measurement and numerical prediction (3089 mm). Regardless, repeatability of physical centrifuge testing, and possibly unaccounted for phenomena in the numerical model remain to be investigated as part of future research efforts.

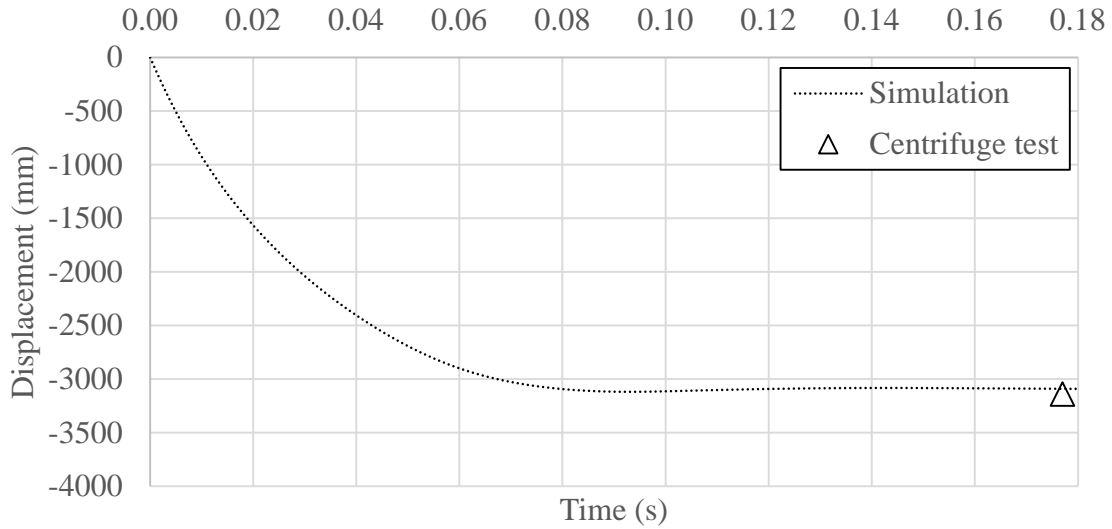


Figure 5.20 Projectile penetration simulation result for interparticle friction coefficient of 0.47, particle-to-projectile friction coefficient of 0.65, and 110 m/s projectile velocity (prototype scale: 46g)

5.7.2 Computed Stresses in Granular Assemblies

Presented in Fig. 5.21 and Fig. 5.22 are vertical and horizontal stress plots (respectively) of the Test 2 DSE assembly for: 25% (Fig. 5.21a and Fig. 5.22a); 50% (Fig. 5.21b and Fig. 5.22b); 75% (Fig. 5.21c and Fig. 5.18c); and, 100% (Fig. 5.21d and Fig. 5.22d) of the maximum penetration depth. Note that the plots corresponding to “100%” of the maximum penetration depth are taken at the end of the simulation, when the rigid projectile is no longer in motion. A fringe plot ranging from -2 MPa to 0 MPa is (as with Test 1) qualitatively found to accentuate the most intensive portions of the penetration-induced stress waves, while not excessively obfuscating the stress state for DSE assembly regions not in the immediate vicinity of the projectile.

At 25% of maximum penetration (Fig. 5.21a and Fig. 5.22a), semi-spherical stress waves are evident around the bottom half of the projectile. Given that the muzzle velocity for Test 2 (110 m/s) is significantly greater than that of Test 1, the regions of elevated stress are relatively more symmetrical for Test 2. Even at 50% of the maximum penetration depth (Fig. 5.21b and Fig. 5.22b), the stress wave components still indicate a distinct wave front, despite having reached the horizontal extents of the cylindrical DSE assembly. Importantly, if LNRBCs were not imposed, then the upper portions of the stress wave would collapse back toward the centroidal vertical axis of the cylindrical DSE assembly, and as a result, the projectile would be subjected to artificially inflated horizontal confinement.

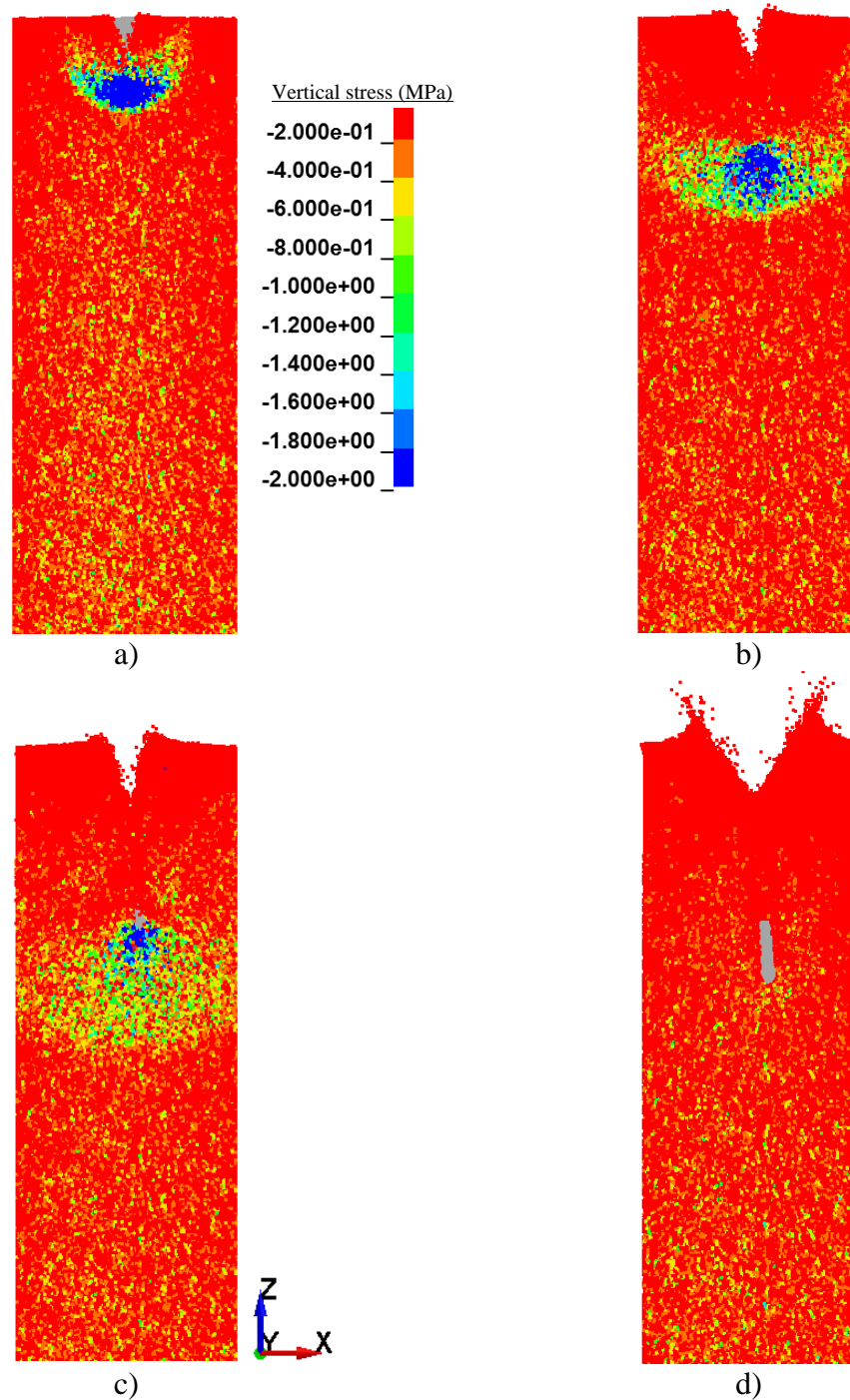


Figure 5.21 Projectile penetration simulation vertical stress plots for interparticle friction coefficient of 0.47, particle-to-projectile friction coefficient of 0.65, and 110 m/s projectile velocity (prototype scale: 46g): a) 25% of maximum penetration; b) 50% of maximum penetration; c) 75% of maximum penetration; d) 100% of maximum penetration

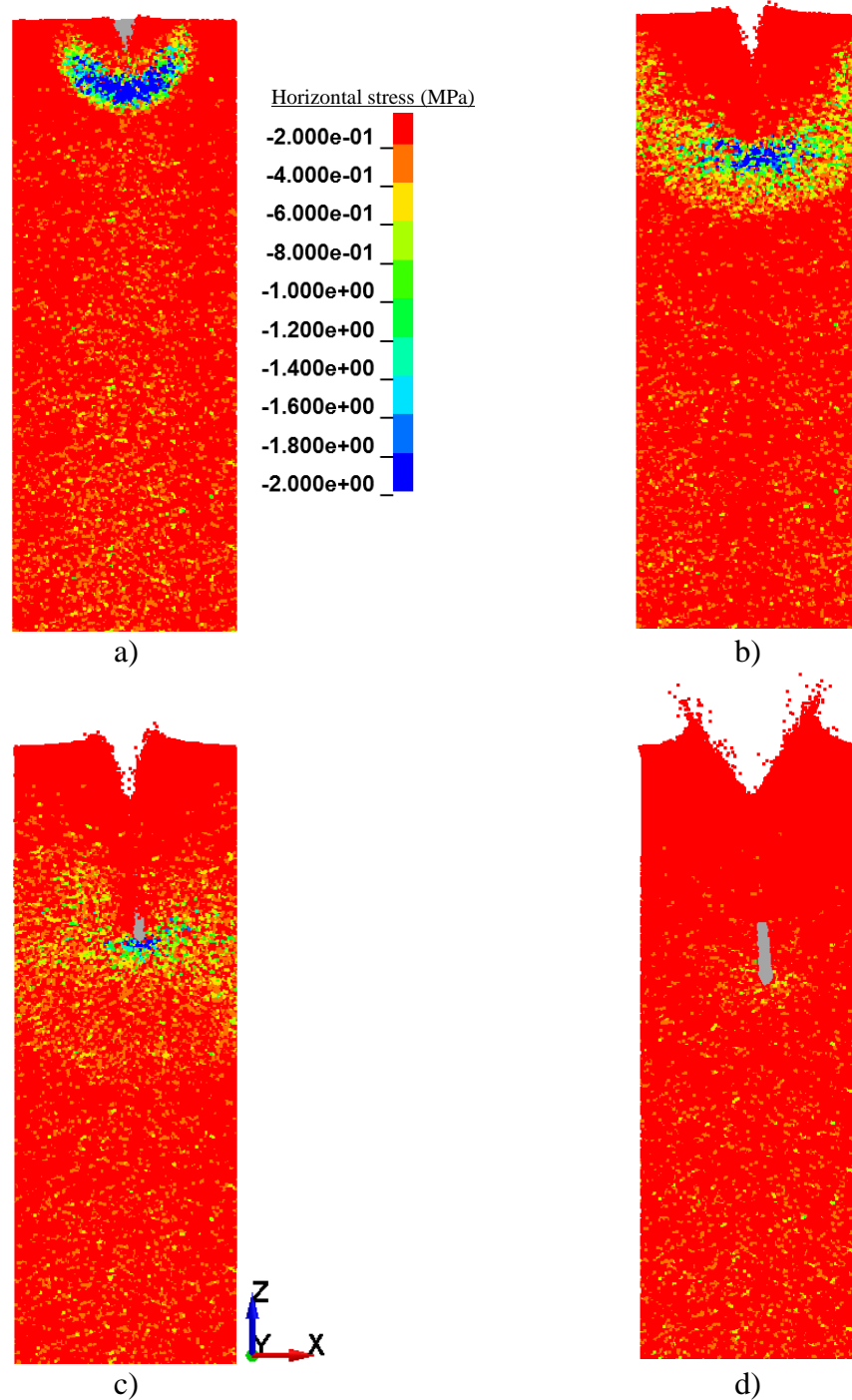


Figure 5.22 Projectile penetration simulation horizontal stress plots for interparticle friction coefficient of 0.47, particle-to-projectile friction coefficient of 0.65, and 70 m/s projectile velocity (prototype scale: 26.5g): a) 25% of maximum penetration; b) 50% of maximum penetration; c) 75% of maximum penetration; d) 100% of maximum penetration

Upon reaching 75% of the maximum penetration depth, the stress wave has become less distinct, particularly with respect to horizontal stress components (Fig. 5.22c). When the Test 2 projectile has reached its final position (100% of maximum penetration depth; Fig. 5.21d and Fig.

5.22d), elevated stresses persist (ranging from -0.4 MPa to -0.8 MPa) near the projectile nose. Consistent with the physical centrifuge tests (recall Sec. 4.3), the terminal position of the projectile is inclined (4.2°) from the vertical axis.

5.8 Test Scheme 3: Projectile Penetration into Monodisperse Assembly

Sec. 5.8 is paired with Sec. 4.7, and documents the projectile penetration simulation for Test Scheme 3. Salient parameters of the configuration are listed in Table 5.12, and depicted in Fig. 5.23. For the third and final test setup, the centrifugal acceleration level of 26.5g is again employed.

As was the case for the Test 2 penetration simulation (recall Sec. 5.7), the (physical) binary mixture assembly is again approximated as a monodisperse assembly, based on the mean value of constituent granule diameters (13.25 mm) is assigned to all DSEs. As before, this modeling simplification does not adversely affect comparative results between the physical measurements and simulated values of maximum projectile penetration depth, given the level of agreement observed (see Sec. 5.8.1). A mean-valued friction coefficient (0.47) is supplied for particle-particle tangential contact interactions, while an upper-bound value (0.65) is supplied for particle-to-projectile tangential contact interactions (recall Sec. 5.5.3).

Taking the Coriolis Effect into consideration, the 238.235 mm diameter projectile is assigned prescribed initial velocity components in both the horizontal (X) and vertical (Z) and directions (V_{X0} and V_{Z0} , respectively). A muzzle velocity of approximately 70 m/s is associated with the (physical) Test 3 conditions, and accordingly, the component of velocity parallel to the Z axis is dominant. The projectile is inclined 7.55° about the horizontal (Y) axis so as to align with the prescribed initial velocity components (Fig. 5.23).

Table 5.12 Test Scheme 3 parameters for projectile penetration simulations		
Parameter description	Value	Units
Prototype base scale factor	26.5	g level
DSE diameter	13.25	mm
DSE assembly diameter	3074	mm
DSE assembly depth	6890	mm
Particle-to-particle friction coefficient	0.47	--
Projectile diameter	238.235	Mm
Particle-to-projectile friction coefficient	0.65	--
Projectile velocity, V_{X0}	9088.0	mm/s
Projectile velocity, V_{Z0}	-69407.5	mm/s
Projectile inclination, ψ_{Y0}	7.55	$^\circ$

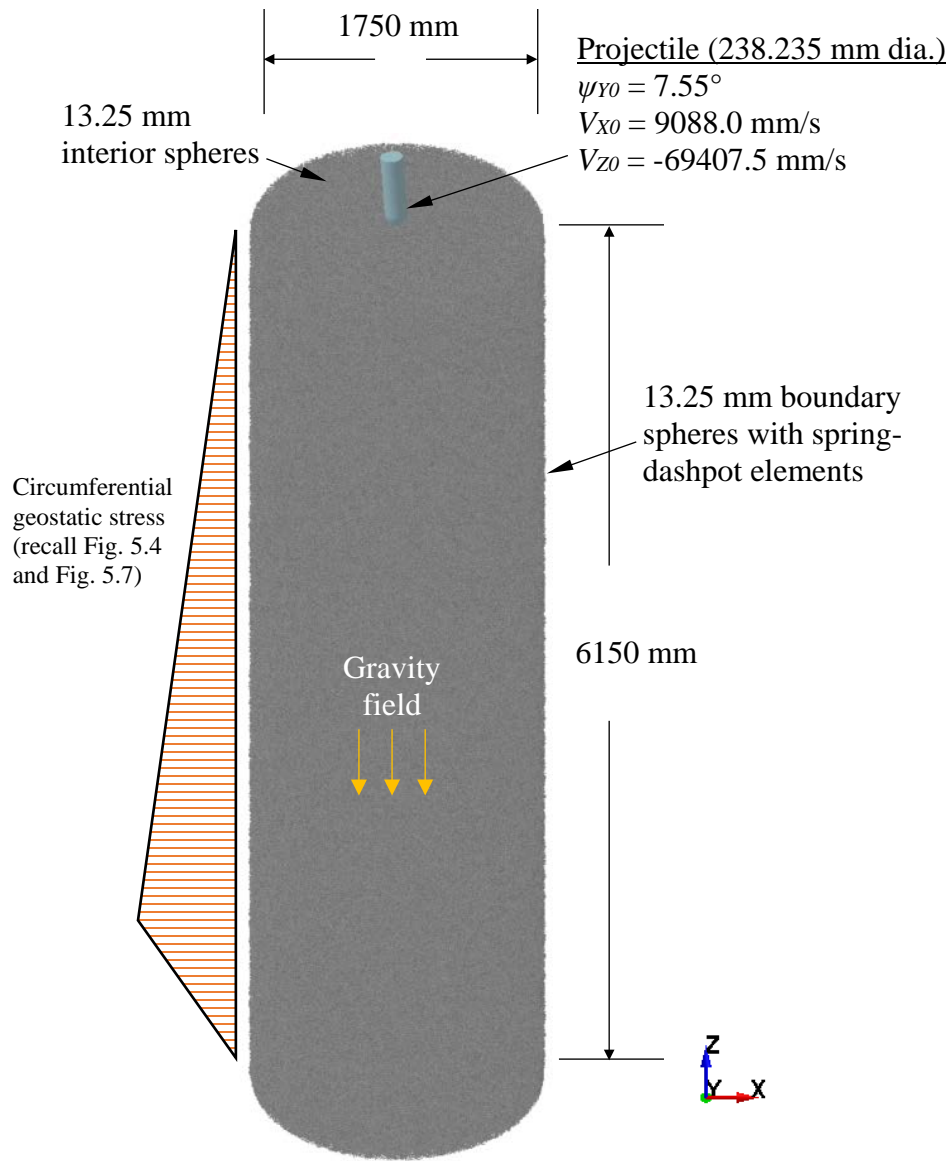


Figure 5.23 State of Test 3 FE projectile and DSE assembly just prior to onset of projectile penetration (prototype scale: 26.5g)

5.8.1 Computed versus Measured Projectile Penetration Depth

The time-history of Test 3 projectile vertical displacements (obtained from the respective projectile penetration simulation) are plotted in Fig. 5.24. With a terminal penetration depth of 1783 mm, the simulation results fall within 14% of the average of the two available physical measurements of projectile penetration (1884 mm and 2272 mm) for Test 3. It is worth again emphasizing that both repeatability of physical centrifuge testing and possibly unaccounted for

phenomena in the numerical model warrant further investigation during subsequent research phases.

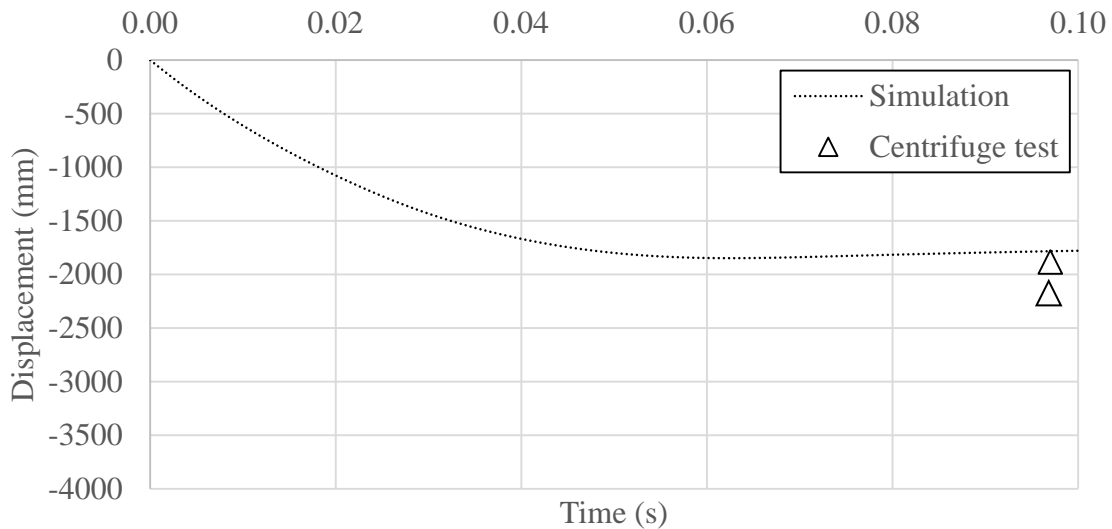


Figure 5.24 Projectile penetration simulation results for interparticle friction coefficient of 0.47, particle-to-projectile friction coefficient of 0.65, and 70 m/s projectile velocity (prototype scale: 26.5g)

5.8.2 Computed Stresses in Granular Assemblies

Fig. 5.25 and Fig. 5.26, respectively, consist of vertical and horizontal stress plots of the Test 3 DSE assembly. As done in Sec. 5.6.2 and 5.7.2, fringe plots ranging from -2 MPa to 0 MPa are qualitatively found to give a desirable balance between indicating the penetration-induced stress waves while not obscuring the overall stress state of the DSE assembly. The four stress plots in each of Fig. 5.25 and Fig. 5.26 give a visual representation of the instantaneous stress state at penetration depths equal to: 25% (Fig. 5.25a and Fig. 5.26a); 50% (Fig. 5.25b and Fig. 5.26b); 75% (Fig. 5.25c and Fig. 5.26c); and, 100% (Fig. 5.25d and Fig. 5.26d) of the maximum penetration depth. The lattermost plots (corresponding to 100% of maximum penetration) draw from the final plot state of the simulation, when the projectile is at rest.

Ellipsoidal stress waves are observed during the early stages of penetration (Fig. 5.25a and Fig. 5.26a). Given that, for Test 3, the projectile-granule diameter ratio is greatest among all three test sets, the stress wave encompasses nearly the entire width of the cylindrical DSE assembly even at only 25% of maximum penetration. Elevated stresses remain widespread as the projectile progresses to 50% (Fig. 5.25b and Fig. 5.26b), and even as the stress wave begins to lose its distinct shape at 75% of maximum penetration (Fig. 5.25c and Fig. 5.26c).

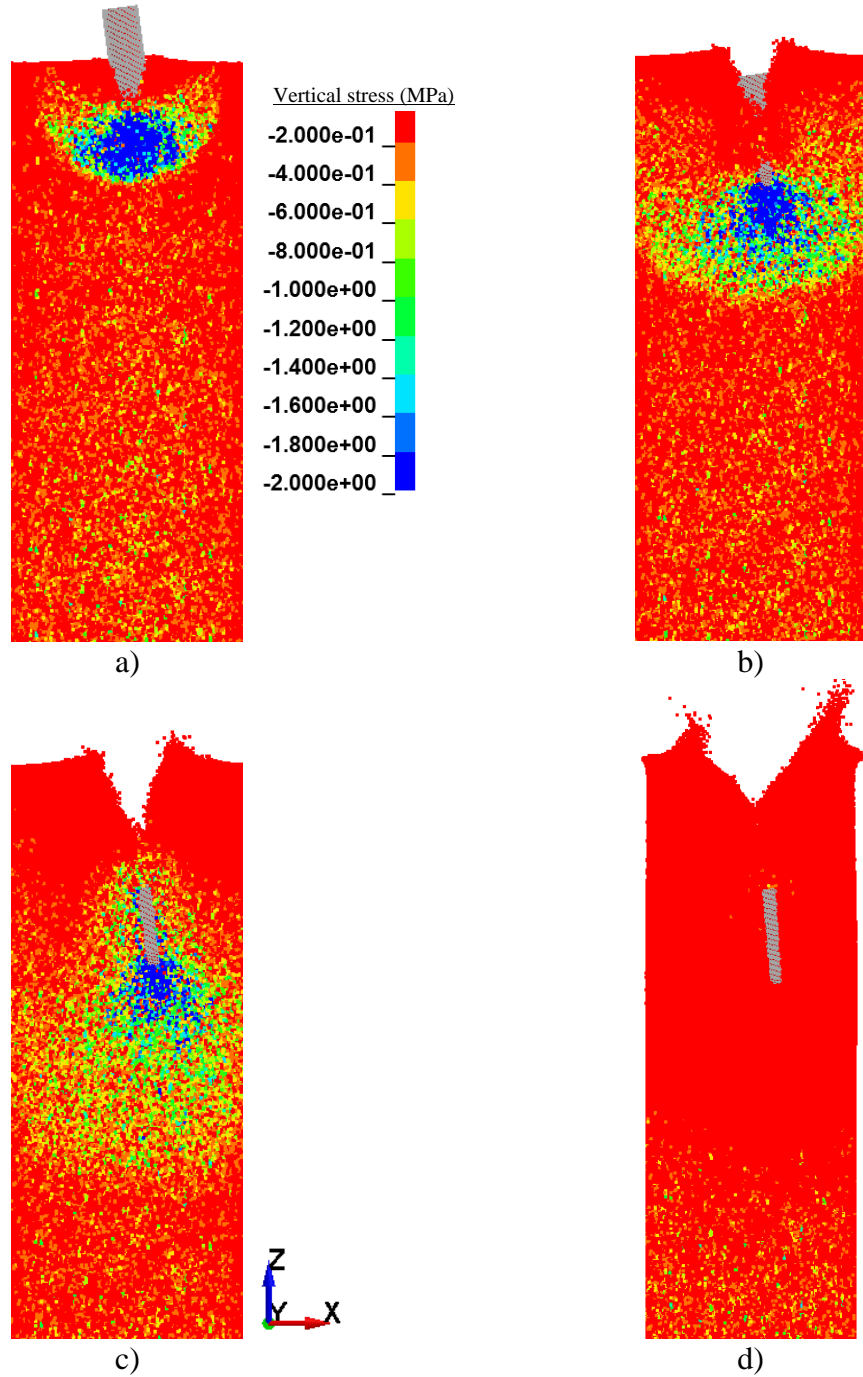


Figure 5.25 Projectile penetration simulation vertical stress plots for interparticle friction coefficient of 0.47, particle-to-projectile friction coefficient of 0.65, and 70 m/s projectile velocity (prototype scale: 26.5g): a) 25% of maximum penetration; b) 50% of maximum penetration; c) 75% of maximum penetration; d) 100% of maximum penetration

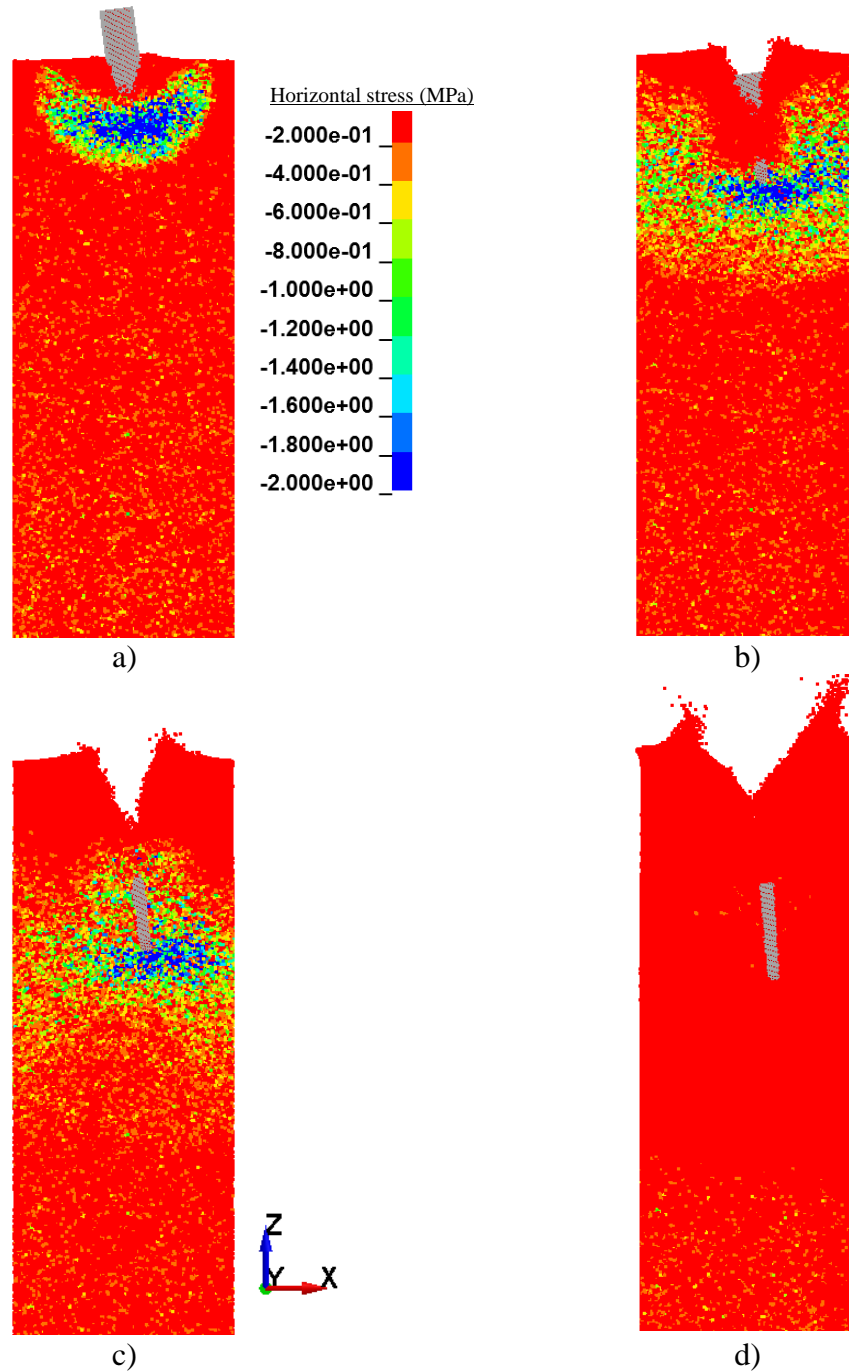


Figure 5.26 Projectile penetration simulation horizontal stress plots for interparticle friction coefficient of 0.47, particle-to-projectile friction coefficient of 0.65, and 70 m/s projectile velocity (prototype scale: 26.5g): a) 25% of maximum penetration; b) 50% of maximum penetration; c) 75% of maximum penetration; d) 100% of maximum penetration

From among all three test sets, the projectile penetration simulation for Test 3 produces a minimum of elevated stresses at 100% of maximum penetration (Fig. 5.25d and Fig. 5.26d). More specifically, DSEs within the vicinity of the projectile appear to have retained stresses at less -0.2 MPa. This phenomenon may be a consequence of halting the simulation at 0.10 sec (as opposed

to 0.18 sec for Test 1 and Test 2); while the Test 3 projectile is no longer undergoing appreciable motion, the DSE positioned above the projectile (inclined at 4.4°) have not yet re-succumbed to gravitational forces after being disturbed by rapid introduction of the projectile.

5.9 Parametric Simulations of Projectile Penetration

A parametric study of projectile penetration simulations are conducted to further investigate relationships between model parameters and projectile penetration depth. Interparticle friction, particle-projectile friction, and projectile velocity are varied as listed in (Table 5.13).

Table 5.13 Catalog of parametric variations for projectile penetration simulations

Model No.	Interparticle friction	Projectile to particle friction	Projectile vel. (mm/s)	ψ_{Y0} (°)	V_{Z0} (mm/s)	V_{X0} (mm/s)
1	0.4	0.57	70000	7.46	-69408	9088
2	0.4	0.57	80000	6.54	-79479	9112
3	0.4	0.57	90000	5.81	-89538	9111
4	0.4	0.57	100000	5.23	-99584	9115
5	0.4	0.57	110000	4.76	-109621	9128
6	0.4	0.61	70000	7.46	-69408	9088
7	0.4	0.61	80000	6.54	-79479	9112
8	0.4	0.61	90000	5.81	-89538	9111
9	0.4	0.61	100000	5.23	-99584	9115
10	0.4	0.61	110000	4.76	-109621	9128
11	0.4	0.65	70000	7.46	-69408	9088
12	0.4	0.65	80000	6.54	-79479	9112
13	0.4	0.65	90000	5.81	-89538	9111
14	0.4	0.65	100000	5.23	-99584	9115
15	0.4	0.65	110000	4.76	-109621	9128
16	0.47	0.57	70000	7.46	-69408	9088
17	0.47	0.57	80000	6.54	-79479	9112
18	0.47	0.57	90000	5.81	-89538	9111
19	0.47	0.57	100000	5.23	-99584	9115
20	0.47	0.57	110000	4.76	-109621	9128
21	0.47	0.61	70000	7.46	-69408	9088
22	0.47	0.61	80000	6.54	-79479	9112
23	0.47	0.61	90000	5.81	-89538	9111
24	0.47	0.61	100000	5.23	-99584	9115
25	0.47	0.61	110000	4.76	-109621	9128
26	0.47	0.65	70000	7.46	-69408	9088
27	0.47	0.65	80000	6.54	-79479	9112
28	0.47	0.65	90000	5.81	-89538	9111
29	0.47	0.65	100000	5.23	-99584	9115
30	0.47	0.65	110000	4.76	-109621	9128
31	0.54	0.57	70000	7.46	-69408	9088
32	0.54	0.57	80000	6.54	-79479	9112
33	0.54	0.57	90000	5.81	-89538	9111
34	0.54	0.57	100000	5.23	-99584	9115
35	0.54	0.57	110000	4.76	-109621	9128
36	0.54	0.61	70000	7.46	-69408	9088
37	0.54	0.61	80000	6.54	-79479	9112
38	0.54	0.61	90000	5.81	-89538	9111
39	0.54	0.61	100000	5.23	-99584	9115
40	0.54	0.61	110000	4.76	-109621	9128
41	0.54	0.65	70000	7.46	-69408	9088
42	0.54	0.65	80000	6.54	-79479	9112
43	0.54	0.65	90000	5.81	-89538	9111
44	0.54	0.65	100000	5.23	-99584	9115
45	0.54	0.65	110000	4.76	-109621	9128

In total, the parametric study consists of 135 simulations. For each of interparticle friction, particle-to-projectile friction, and projectile velocity, three values are selected and pivoted upon. As a result, 45 projectile penetration simulations (Table 5.13) are carried out relative to each of Test 1, Test 2, and Test 3. Regarding interparticle friction, the mean value from physical testing of proppants granules (0.47, as discussed in Sec. 5.2.4) is used as a pivot-basis. Given the favorable levels of agreement observed between the Test 1 through Test 3 projectile penetration simulations (recall Sec. 5.6 through Sec. 5.8), a relatively narrow range of friction values are utilized, relative to the mean value. In particular, interparticle friction values of 0.4 and 0.54 are selected (respectively) as lower and upper bounds.

With respect to particle-to-projectile friction, the full range of values discussed in Sec. 5.5.3 (0.57 to 0.65, with mean-value of 0.61) are explored. As the third and final pivot within the parametric simulation set, velocities ranging from 70 m/s to 110 m/s (in increments of 10 m/s) are considered. Note that each selected velocity is decomposed into horizontal and vertical components per the Coriolis Effect (recall Sec. 4.4). In this way, the parametric study encompasses the velocities measured as part of the physical centrifuge tests (recall Sec. 4.3).

5.9.1 Parametric Simulation Results

Plotted in Figs. 5.27-5.29 are the full parametric families of projectile vertical displacement time-histories (i.e., projectile penetration). The curves plotted in Fig. 5.27 correspond to parametric variations relative to the Test 1 configuration, while those of Fig. 5.28 and Fig. 5.29 correspond to parametric variations relative to the Test 2 and Test 3 configurations, respectively.

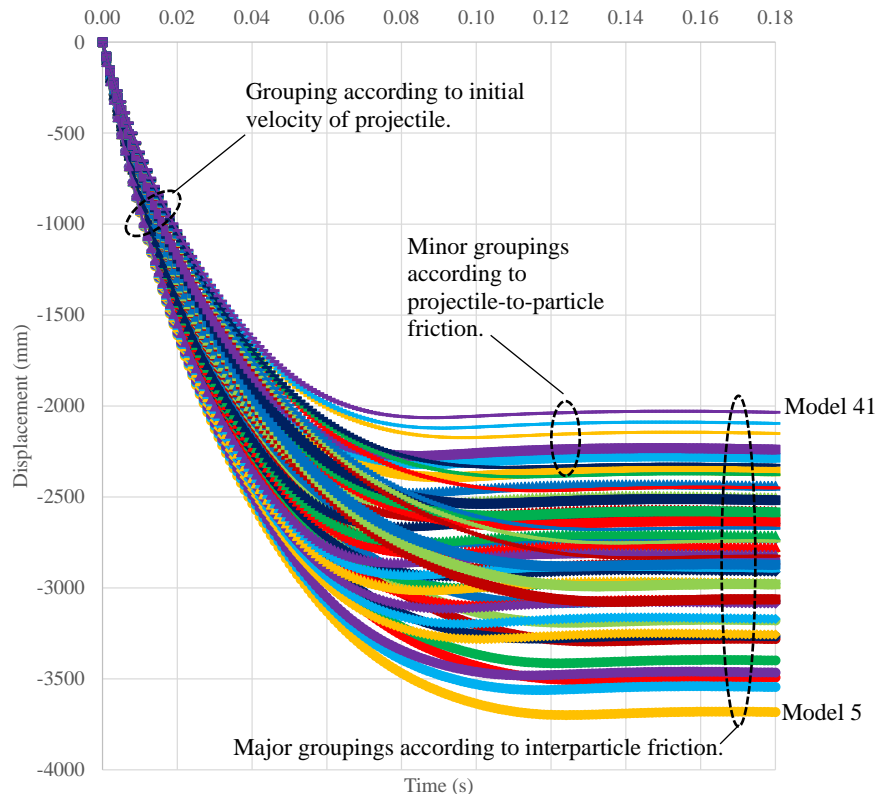


Figure 5.27 Parametric simulation results for Test Scheme 1 (projectile-to-granule ratio: 10.58)

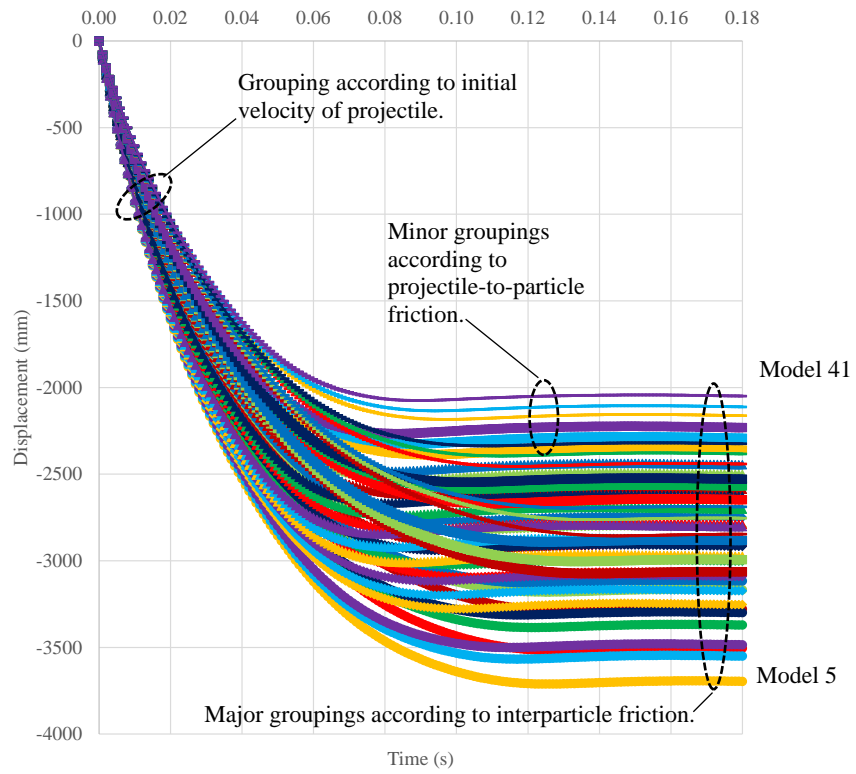


Figure 5.28 Parametric simulation results for Test Scheme (projectile-to-granule ratio: 10.36)

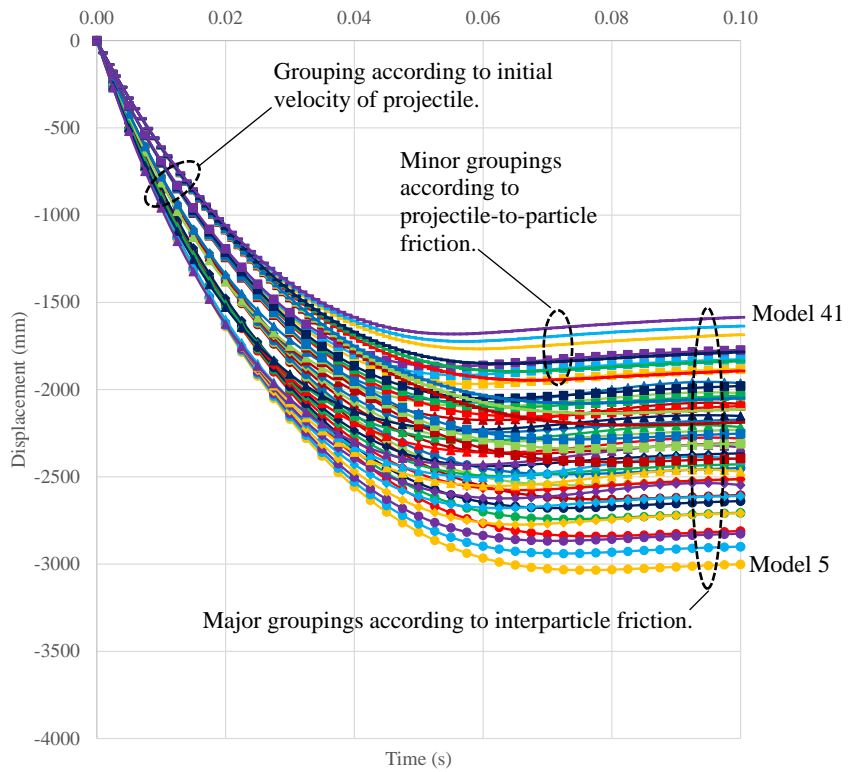


Figure 5.29 Parametric simulation results for Test Scheme 3 (projectile-to-granule ratio: 17.62)

5.9.2 Observations

For each of three subsets of parametric results (Figs. 5.27-5.29), the families of curves behave in line with expectations. For instance, model 3 (recall Table 5.13) is assigned the minimum values of interparticle friction (0.4) and particle-to-projectile friction (0.57), while also being subjected to penetration at the greatest magnitude of velocity (110 m/s), and the respective simulation produces the maximum penetration. Similarly, model 41 possesses maximum values of interparticle and particle-to-projectile friction (0.54 and 0.65, respectively), paired within minimum projectile velocity (70 m/s), and produces the minimum penetration. Also for instance, the family of curves associated with Test 2 (Fig. 5.28) consistently correspond to greater-valued penetration depths relative to the Test 1 and Test 3 counterparts (Fig. 5.27 and Fig. 5.29, respectively).

The parametric results also indicate the presence of pronounced, consistent phenomena across all three batches of time-history plots. For example, a careful examination of the steepest portions of the curves (leftmost portions) reveals five groupings, which correspond to the five values of initial projectile velocity. As expected, the topmost of these five groupings correspond to the projectiles initialized at 70 m/s, and the bottommost groupings correspond to projectiles prescribed initial velocities of 110 m/s. Further, subsequent to reaching terminal penetration depths, both minor and major groupings emerge. As annotated in the right-central portions of Figs. 5.27-5.29, the interparticle friction constitutes the most substantial predictor of terminal penetration depth, where this friction value and terminal penetration depth appear to be correlated. The aforementioned minor groupings are dictated by particle-to-projectile friction, which this latter type of friction appears to be also correlated with terminal penetration depth.

To facilitate characterization of stopping forces, predictions of terminal penetration depth are plotted per intergranular friction coefficients in Figure 5.30. An inverse proportionality between frictional forces and terminal penetration depth is observed in all three physical test scenarios, which indicates a potential correlation between energy dissipation by multitudes of frictional and inertial forces (acting on grains) and corresponding kinetic energy of the projectile. The trend in terminal penetration depths is practically identical in Test Scenarios 1 and 2. The scale ratio of the projectile diameter to granule mean diameters is equal within a margin of error equal to the standard deviation of the physical diameter of the granules (at prototype scales). This numerical prediction verifies the scaling relation values; the similitude parameters specific to the two system scales used in the numerical representation of the centrifuge tests represent not only models of the two prototype sizes, but also relational models of each other. The results obtained from the physical scale-modeling under centrifugal accelerations are comparable to one another as discussed in Chap. 4, which validate the scaling relation values. Equally importantly, consistency in sample preparation of both the physical and numerical models has been verified, given the fact that the scaling relation values are found to be valid in the extrapolations across scales for both the scale testing and numerical prototype. Thus, it is proven to model repeatable initial and boundary conditions at the system scales, through explicit simulation of colloidal discrete particles in pluviation, *both* numerically and physically.

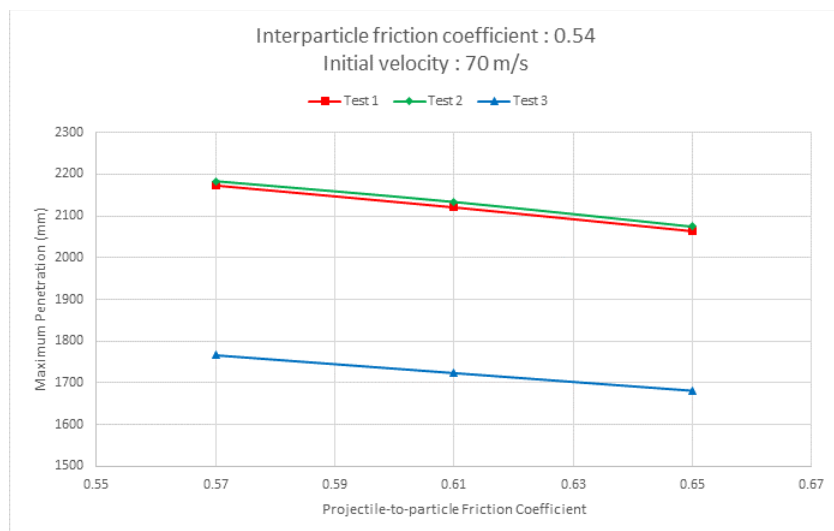
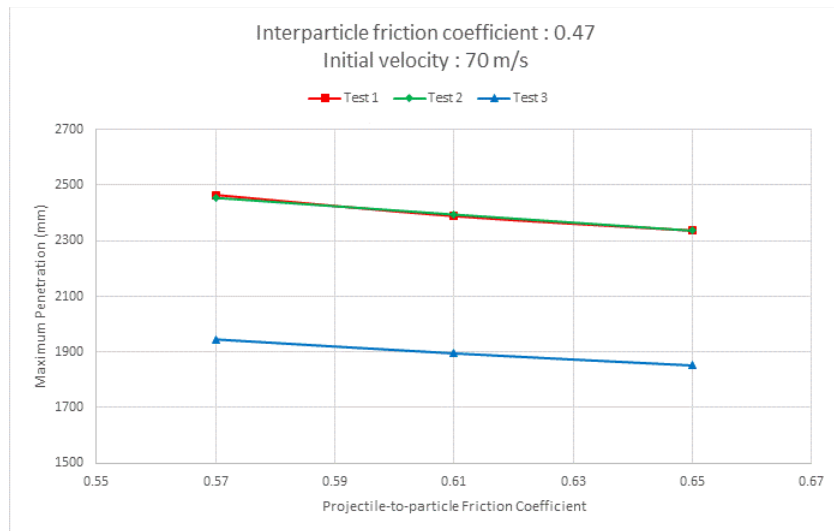
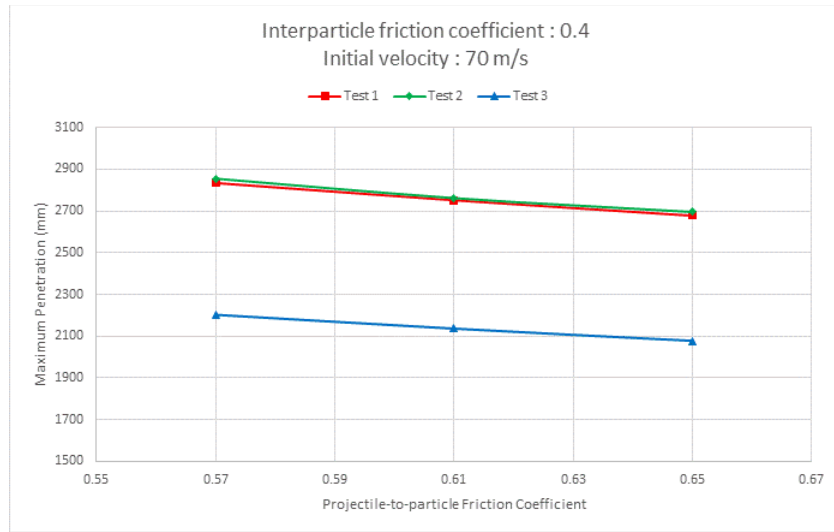


Figure 5.30 Effects of contact friction on terminal penetration depth

Given a (controlled) relative density state, particle size relative to the projectile dimension may have direct influence on terminal penetration depth. Within the range of impact velocities considered, the granular system of Test 3 appears to be notably more effective in generating stopping forces against the penetration. As shown in Fig. 5.31, two distinct mechanisms exist for the DSE assemblies considered. In particular, the larger-diameter granules associated with Test 1 constitute a (relatively) lower *packing* density (with 137,702 spheres), and the smaller-diameter granules associated with Test 3 constitute a denser packing density (with 712,237 spheres) over a columnated volume of 530 mm diameter by 6150 mm height. The packing density of Assembly B is 5.17 times greater than that of Assembly A. In the context of the following discussion regarding the effects of packing density and particle size (relative to the projectile dimension) in the penetration, the assembly associated with Test 1 is referred to as Assembly A, and the assembly associated with Tests 2 and 3 is referred to as Assembly B.

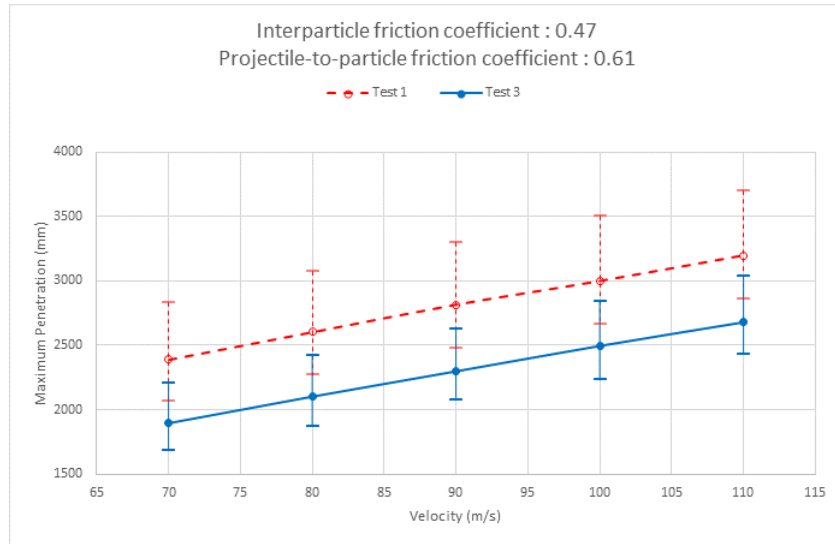


Figure 5.31 Variation of terminal penetration depths with respect to impact velocity as per standard deviations of intergranular friction coefficients and the two packing assemblies

Note that the particle-diameter ratio of DSEs from Assembly A relative to those of Assembly B is equal to 1.77. Even so, bulk masses of the DSE assemblies fall within a margin of error of one another (recall Sec. 5.4.2), and the assemblies mutually evince upper-bound relative density states. In validation of the packing densities of mechanically stable DSE assemblies at initial equilibrium states (refer to Tables 5.7 and 5.8), macroscopic volume-averaged unit weight is measured per the mean diameters of the granules in laboratory tests in accordance with ASTM standards. Both the monodisperse packings exhibit an averaged, repeatable 110% relative density (Table 5.14). This is evidenced by considering the average coordination numbers of Assembly A and Assembly B (Fig. 5.32) under mechanically stable conditions (i.e., steady-state conditions under gravity). Consistent with the use of a rough-surface contact model (recall Sec. 5.2.2) and (Kristiansen et al. 2005), average coordination numbers are calculated based on the coordinates of all spheres within the columnated volumes defined in Sec. 5.4.3, and the following equation:

$$|k| < (r_1 + r_2) + \varepsilon \quad (5.15)$$

where k is the center-to-center distance between any two candidate DSEs whose spherical boundaries may overlap at any point on surfaces projected from their centroids; r_1 is the radius of sphere 1; r_2 is the radius of sphere 2; and, ε is a tolerance. Note that the computed average coordination numbers range from approximately 4.2 (with a zero-valued tolerance) up to approximately 6.0 (with a tolerance of 1% of sphere diameter, or 0.23 mm). Clearly, the computed values are sensitive to the selected tolerance, where Kristiansen et al. (2005) utilized a tolerance of 0.0005 (relative to sphere radius). Nonetheless, a numerical tolerance of 0.23 mm produces more or less a physical phenomenon in initial density states, which are measured in relative density tests. Recall that the relative densities of both assemblies exceed 100%. That is, the weight density averaged over macroscopic volumes (per ASTM standards) has reached a maximum value as per the pluviation process, which indicates that the packing assemblies are near a theoretical maximum coordination. Alternatively stated, Assemblies A and B would contain theoretically the same number of particles within scale-proportional volumes.

Table 5.14 Relative density of ceramic proppants

Granule Mean Diameter	^{1a} 0.85 mm	^{1b} 0.5 mm
² Specific gravity	3.38	3.38
³ Maximum dry unit weight (γ_{\max})	$21.05 \pm 0.05 \text{ kN/m}^3$	$21.24 \pm 0.05 \text{ kN/m}^3$
⁴ Minimum dry unit weight (γ_{\min})	$19.35 \pm 0.05 \text{ kN/m}^3$	$19.37 \pm 0.05 \text{ kN/m}^3$
Void ratio (γ_{\min})	0.55 ± 0.005	0.54 ± 0.005
Unit weight of centrifuge model (γ)	$21.3 \pm 0.05 \text{ kN/m}^3$	$21.6 \pm 0.05 \text{ kN/m}^3$
Relative density $\frac{\gamma - \gamma_{\min}}{\gamma_{\max} - \gamma_{\min}} \cdot \frac{\gamma_{\max}}{\gamma} \cdot 100(\%)$	$110.9 \pm 2.9 \%$	$115.9 \pm 1.4 \%$

^{1a} Passed ASTM sieve #18 and retained on #20, and ^{1b} passed #30 and retained on #35

² per ASTM D854 conducted by GeoComp Testing, LLC

³ per ASTM D4253

⁴ per ASTM D4254

⁵ per dry pluviation in centrifuge tests

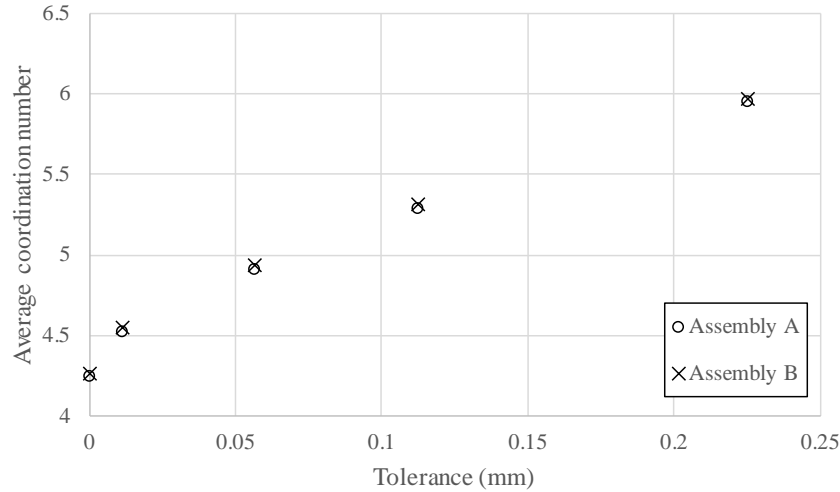


Figure 5.32 Average coordination number versus contact detection tolerance

A physical interpretation of numerical tolerance is given as follows. The tolerance of 0.23 mm can represent scaled-up surface roughness at prototype scales. Should averaged surface roughness be 8 micron on 0.85 mm proppants at 26.5g, then it is equivalent to 0.212 mm on 22.525 mm DSEs at 1g. That is, at static equilibrium of the packing assemblies considered under gravity, an averaged separation distance between two adjacent DSEs is 0.106 mm. Because surface roughness is independent of grain size, a separation distance of a pair of contacting prototype-scale spheres increases proportionally with scaled-up asperity height distributions and corresponding nominal contact areas. Thus, sphere-to-sphere contact stiffnesses remain unchanged between gravity levels. Given separation distances, grain body forces are largely supported across frictional bonds between the grains, and, as such, the geometry of the body-force distribution forms structure-like geometry (i.e., contact-force chains) where those bonds can support the gravity. Such a structure of force chains at equilibrium under gravity is shown in Figs. 5.33b and 5.34b, respectively, for Assemblies A and B. Recall that the volume-averaged weight of Assembly A is nearly equal to that of Assembly B in a constant columnated volume. However, the DSE-diameter of Assembly A is 1.77 times larger, and corresponding DSE mass (point mass) is 5.6 times greater. The difference is visually apparent; the larger granule, the looser distribution, the larger contact forces.

Despite the fact that both the assemblies possess comparable (scalar) relative densities, the variation in penetration-depth phenomena of Fig. 5.31 can be elucidated by examining differences in the distribution of *point* mass (i.e., Figs. 5.33c and 5.34c) simulated by the DSE assemblies of two different particle sizes. In Fig. 5.35, the projectile penetration is evidently influenced by the DSEs that move along with the projectile and transfer momentum to surrounding DSEs through contact. From the perspective of the Eulerian domain, the phenomenon of cavity expansion at the entry level is influenced by the point mass density per particle size along the projectile path. Macroscopic expansions in the radial direction substantially differ from one another; the rates of change in radial expansion are approximately 16.8 m/s for Assembly A and 25.7 m/s for Assembly B during the initial penetration. Subsequently, the motions of the point masses become rapid enough to break their bodies free of the frictional bonds to neighboring DSEs. The local slip lines

grow into regions where every DSE moves rather collectively together to make up a moving mass relative to surrounding, stationary point masses. Namely, the rapid-flow regime develops. In this rapid-flow regime, the velocity of each DSE can be described by a sum of the mean velocity of the mass flow and a component of random motion of each DSE relative to the mean velocity. According to the instantaneous deviation from the mean, interparticle collisions are observed in both the assemblies. However, as the projectile transfers its momentum and kinetic energy to DSEs that come into contact, the patterns in momentum retardation and corresponding energy dissipation emerge to be distinctively different from one assembly to the other.

In-plane particle resultant velocity fields are presented in Figs. 5.36 and 5.37 during the development of the rapid-flow regime in Assembly A and Assembly B, respectively. Fig. 5.36 shows that these larger (point) masses engaged in the early stages of the penetration move (relatively) freely and independently collide with nearest neighbors. Particle colloidal impact velocities develop relatively at a higher rate and spread over a larger region. Accordingly, damping and internal forces develop as plotted in Fig. 5.38 for the ratios of damping and internal energies to the initial kinetic energy of the projectile. The projectile penetration retarding mechanism associated with Assembly A is influenced by the inertia of the larger DSEs (point mass) during the initial impact and entry event.

In contrast, the primary mechanism associated with Assembly B is mobilization of tangential contact forces (i.e., frictional bonds) through particle interlocking in the smaller, but more numerous, DSEs over a smaller region (Fig. 5.37). Local bondings of the smaller, but numerous, DSEs (as opposed to inertia of the larger, but fewer, DSEs) produce ultimately a jammed state of the matter, where the random motion of each DSE is constrained relative to the mean velocity of the mass flow. This jamming phenomenon retards the random velocity field by attenuating outward forming gradients in the transverse direction to the mass flow. Figure 5.38a of particle damping energy shows that interparticle colloidal velocities are much lower in Assembly B during the incident of 25% terminal penetration depth. Moving in condensed particle-blocks, the smaller DSEs form a denser-mass flow regime as per a lower mean velocity. Accordingly, the pattern of accumulation in particle kinetic energy is nearly identical in both the assemblies during the incident of 25% terminal penetration (Fig. 5.38b).

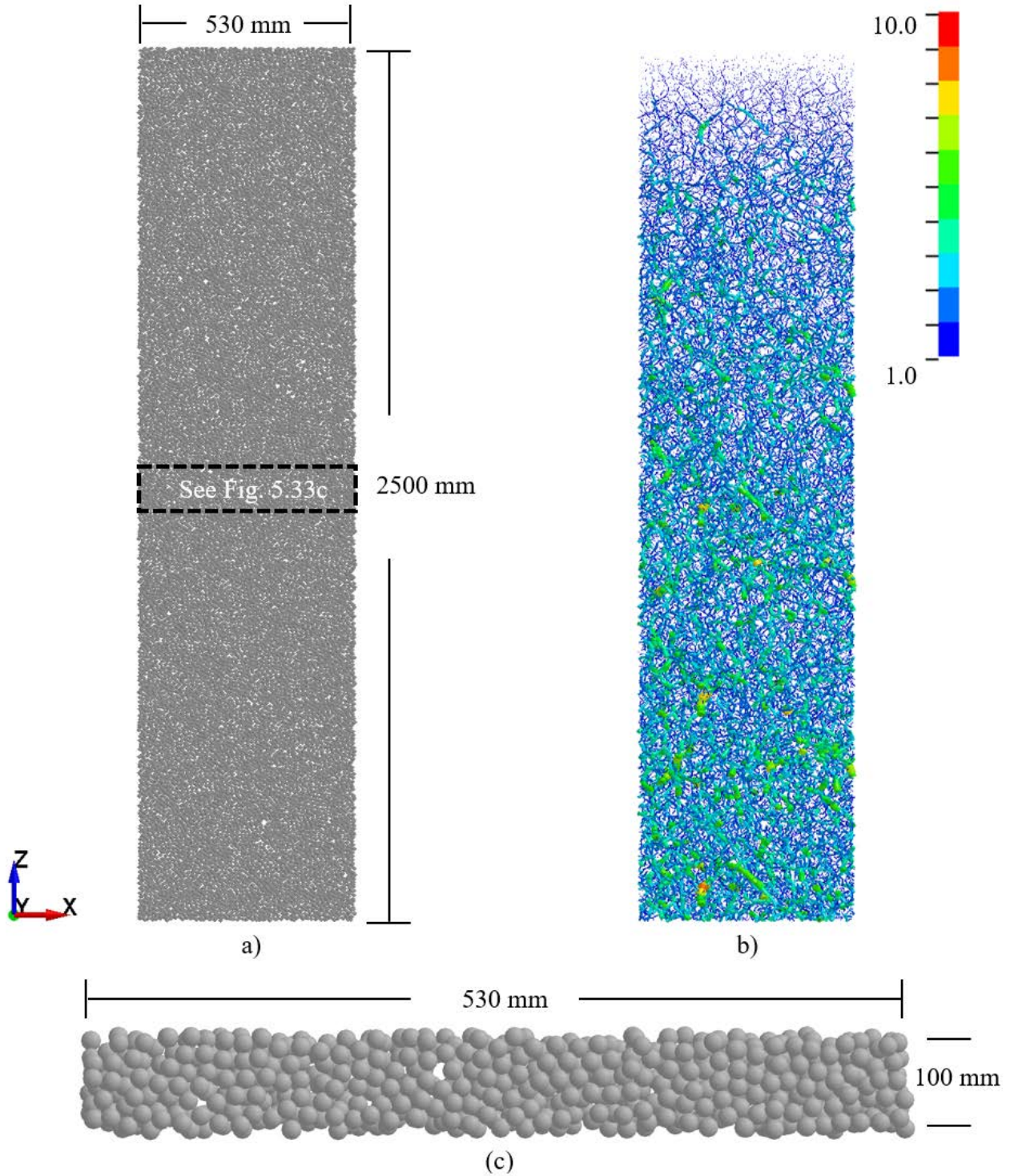


Figure 5.33 Elevation view of columnated volume for Assembly A: a) Steady-state geometry at equilibrium (per prior pluviation); b) Steady-state distribution of grain body forces through contact force chain under gravity; c) Elevation view of grain mass distribution in cylindrical volume (disk) extracted from 1250 mm depth within columnated volume

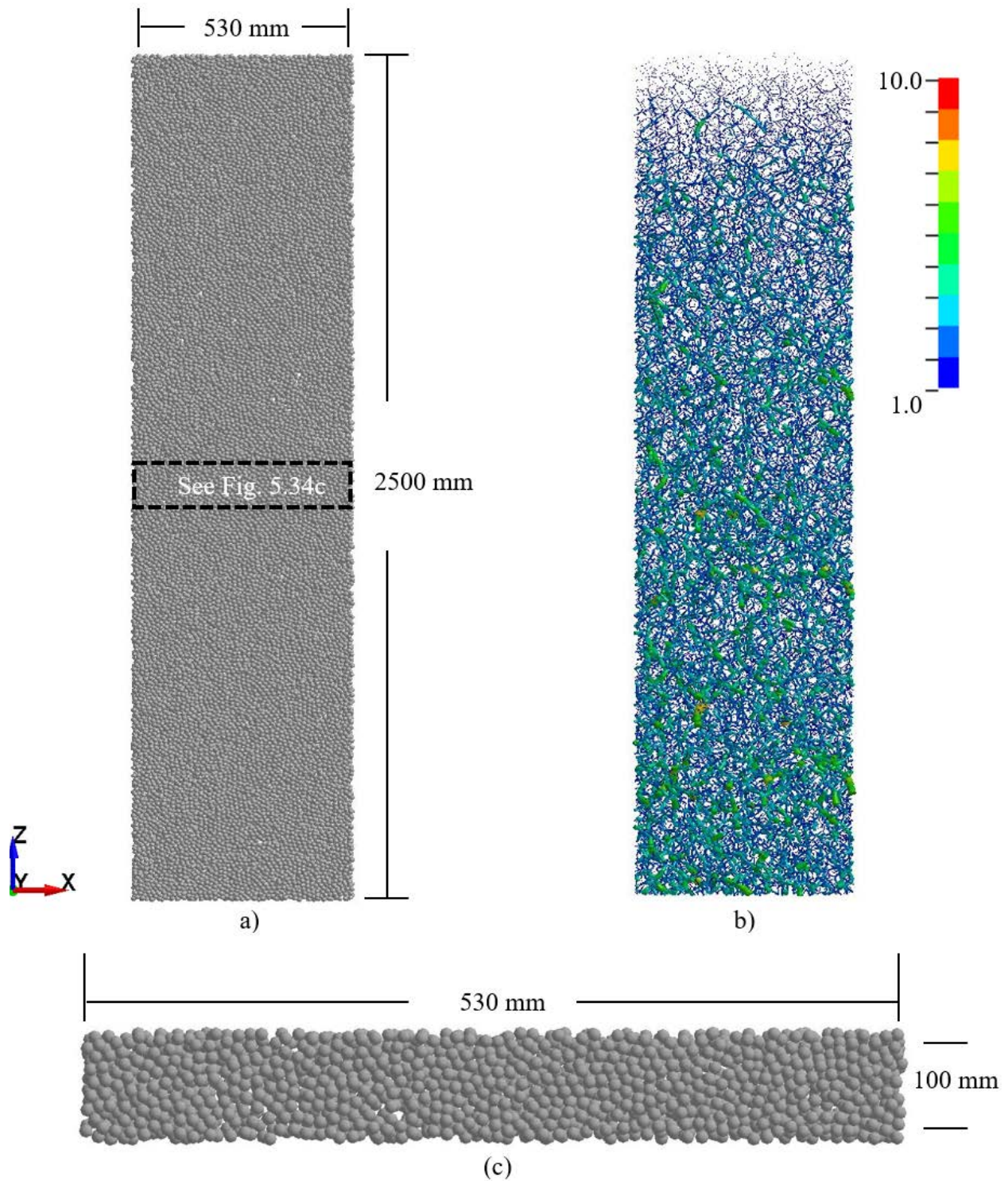


Figure 5.34 Elevation view of columnated volume for Assembly B: a) Steady-state geometry at equilibrium (per prior pluviation); b) Steady-state distribution of grain body forces through contact force chain under gravity; c) Elevation view of grain mass distribution in cylindrical volume (disk) extracted from 1250 mm depth within columnated volume

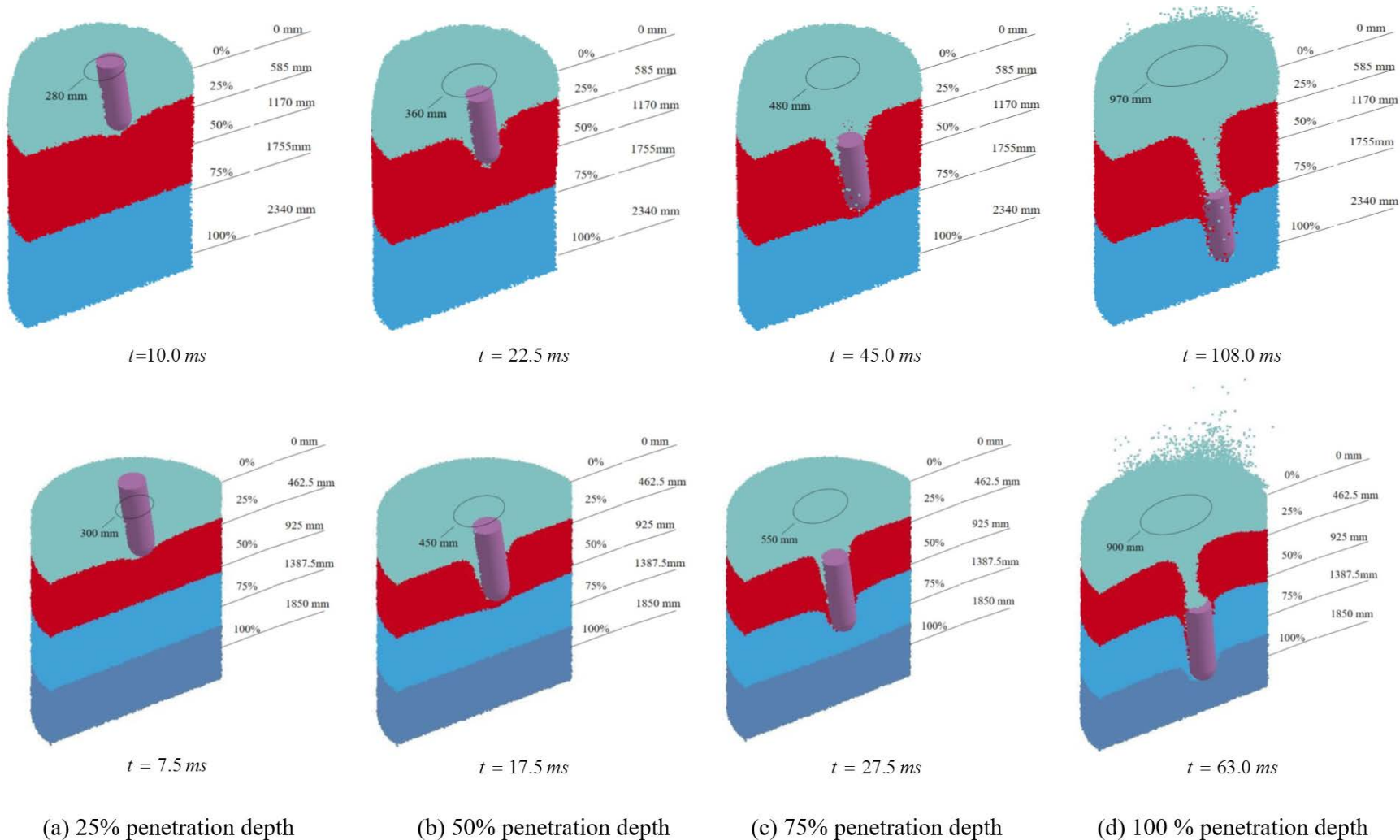


Figure 5.35 Penetration phenomena in Assembly A (top row) and Assembly B (bottom row): Diameter of cavity formation is given at the impact point by the projectile with velocity of 70 m/s: The projectile dimensions are 238.3 mm in diameter, 854.6 mm in length, and 354.8 mm of orgive radius: for dimensional comparison purposes, only the center part of the radial dimension of Test 1 simulation is shown approximately same as the radial dimension of Test 3 simulation in visual illustration

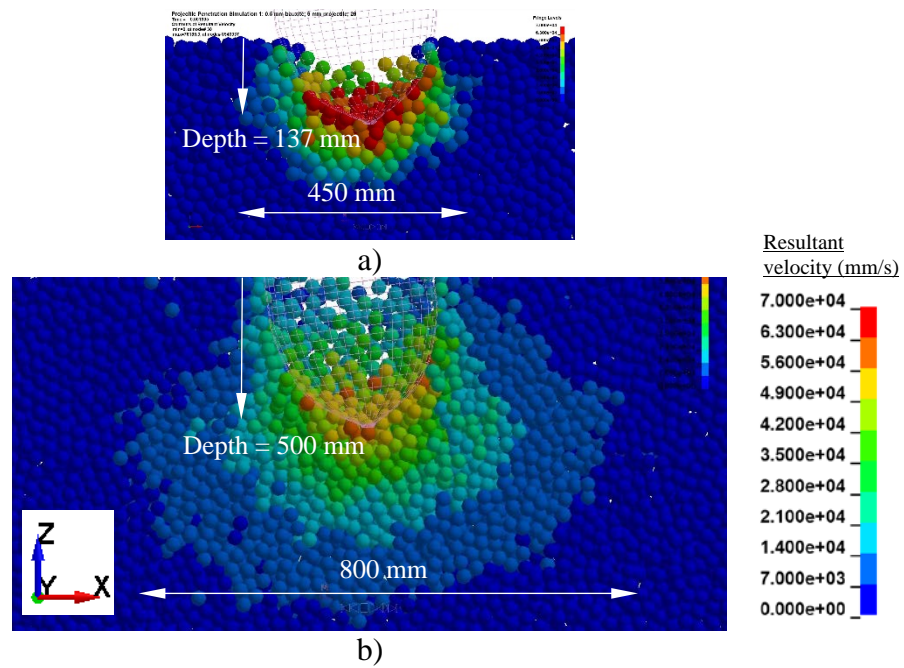


Figure 5.36 Resultant velocity plots for Assembly A: a) 0.002 sec; b) 0.008 sec

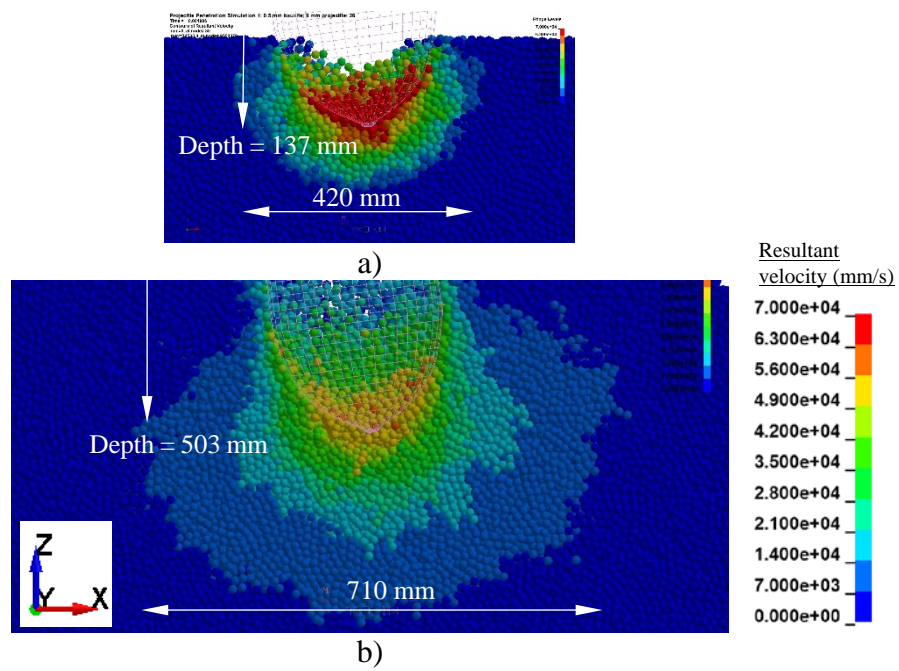
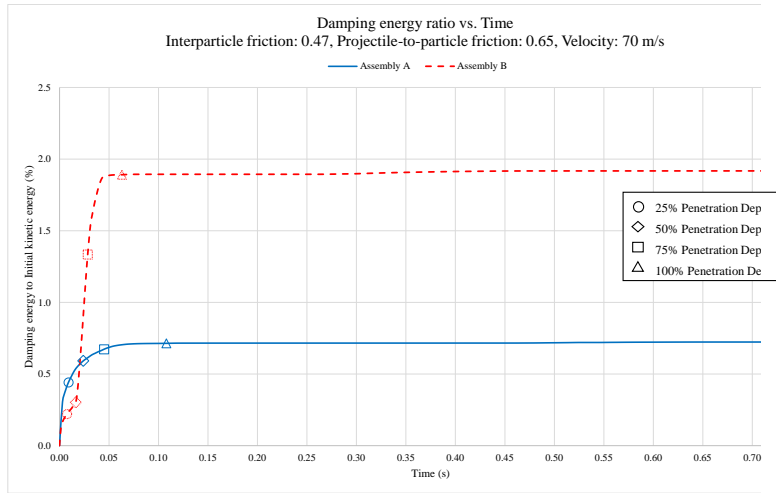
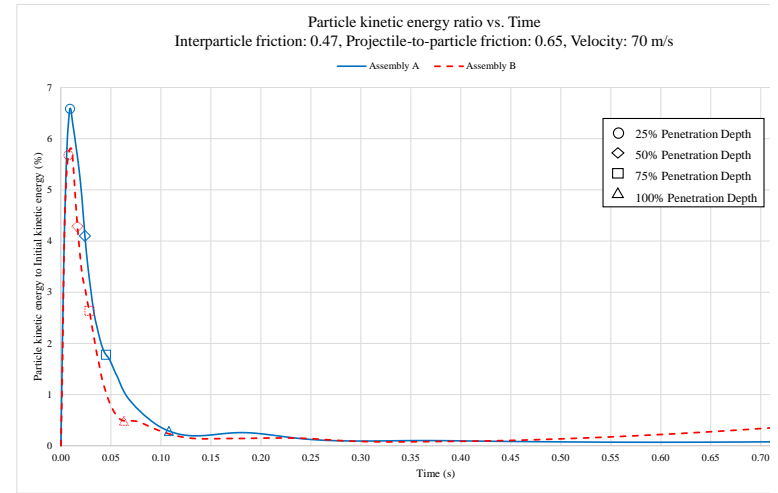


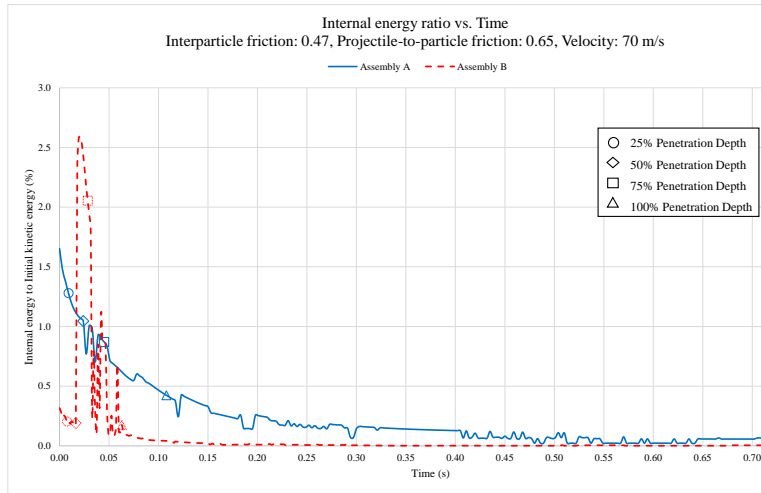
Figure 5.37 Resultant velocity plots for Assembly B: a) 0.002 sec; b) 0.008 sec



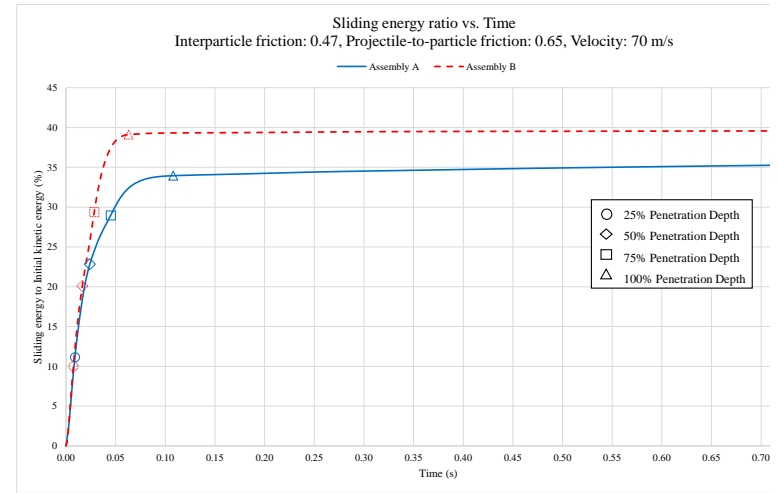
(a) Interparticle damping energy



(b) Particle kinetic energy



(c) Intragrain strain energy



(d) Interparticle frictional-sliding energy

Figure 5.38 Energy variation in granular systems during penetration

An abrupt change is observed around the expanding cavity in the hemispherical mean velocity field (Fig. 5.38c). Established radial velocities of particles shows the initial (macro) failure slip surface: this incident “quasi-static” regime of granular flow describes modified continuum-based plasticity models based on Coulombic friction criterion. The large slip near the wall of the projectile is a direct result of the frictional coupling between the particle surface and the wall. Upon departure, after collisions with the wall boundary, minimal (almost zero) local slip between the surfaces of the smaller DSEs and the incipient boundary is observed. Each DSE (i) with radius of R appear to adopt a rotational velocity (ω_i) such that its surface velocity ($R\omega_i$) matches to counter its slip velocity at the wall boundary. That is, the smaller DSEs undergo a much larger rotational rate (Campbell and Brennen, 1985). This large rotation is not random. All the DSEs that collide with the wall boundary rotate at nearly the same rate. On subsequent collisions, all the DSEs, however, transfer their angular momenta (rotational potentials) to adjacent DSEs through surface frictional interactions. In jammed states, some of the the transferred rotational momenta rapidly generate local translational velocities, which are randomly distributed. These incoherent rotational motions of the DSEs induce asymmetrical stress fields (volume-averaged contact forces) to balance the internal moment exerted across a surface internal to the material, i.e., failure slip surface. Antisymmetries in the shear stress field cause an antisymmetry in the velocity field which disrupts the steady flow. The DSEs smaller in size are, thus, more prone to the phenomenon, which is illustrated for Assembly B in Fig. 5.39.

Disruptive effects of particle rotation at a higher rotational rate promote random particle motions deviated from the mass flow (at $t = 10\text{ ms}$ in Fig. 5.38a and corresponding radial velocity field shown in 5.39a). Subsequent chaotic interparticle collisions, in turn, retard the mean velocity of the flow itself. At this time, two different flow forms appear in the rapid-flow regime, that is, the formation resembles an ordered boundary-layer flow in the front subregions and equivalently disordered (seemingly turbulent) boundary-layer flows in the rear subregions affected by particle-velocity distortion as shown in Fig. 5.39b. Interparticle collisions rapidly increase relatively to the ever decreasing mass flow. Intragrain deformation sharply increases. These sudden particle colloidal motions can be seen in the spikes in the internal and damping energy plots of Fig. 5.38b-c. Since collisions between DSEs are inelastic, momentum associated with excited particle random motions transforms through interparticle collisions into particle frictional sliding, damping, and internal energies. The distorted velocity field ultimately lowers the particle kinetic energy (Fig. 5.38d). Further, the rapid-flow regime is influenced by pronounced antisymmetric shear-stress fields when two distinct subregimes appear to form. The vertical momenta of the subregimes are opposite to each other in the direction (Fig. 5.40). In turn, the upward mass-flow exerts a force on the projectile, which contributes to momentum loss. Ultimately, the distortion in the mean velocity fields causes this opposing force (resistance), i.e., namely “dragging” force.

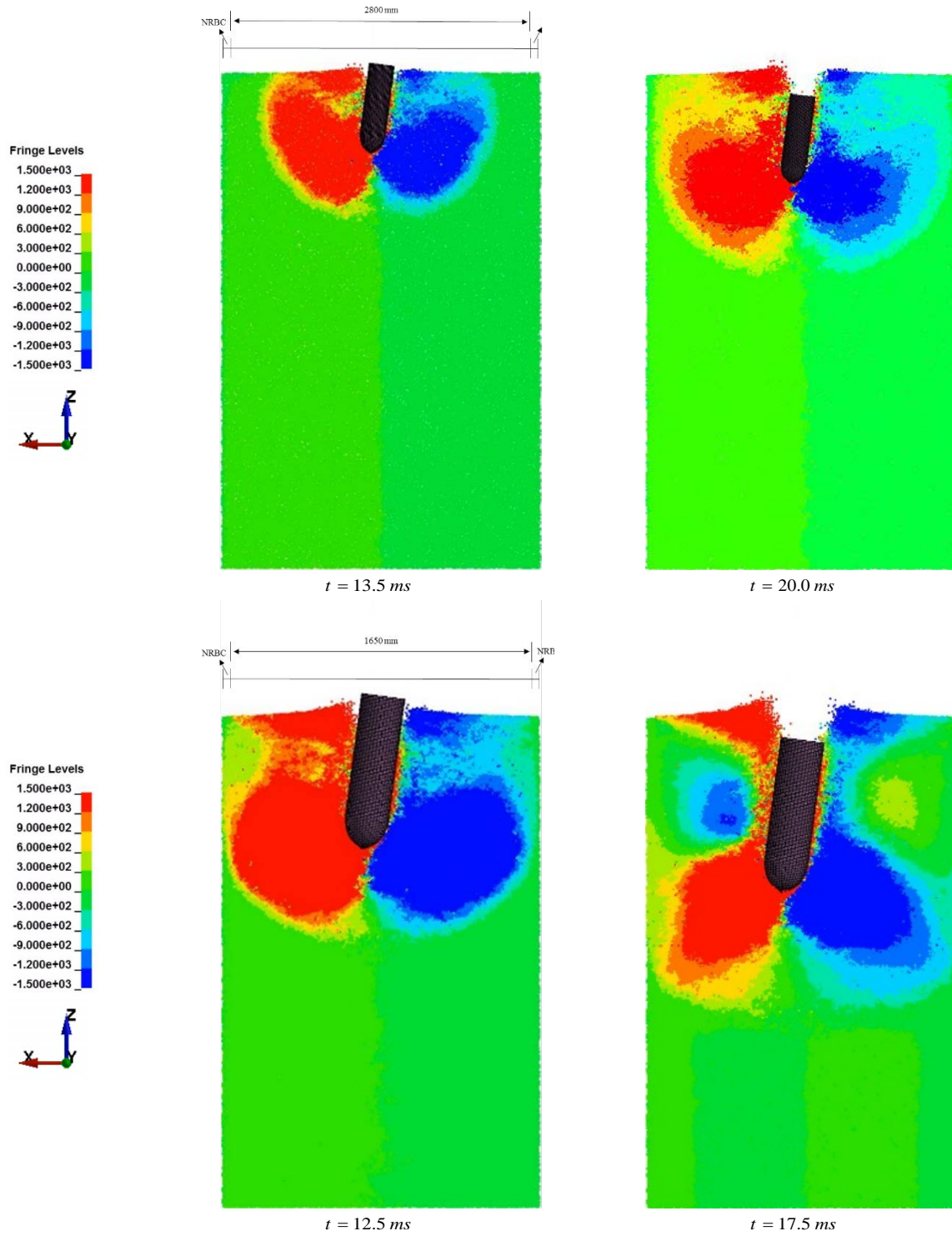


Figure 5.39 Radial velocity fields in the system domains of Assembly A (top row) and Assembly B (bottom row)

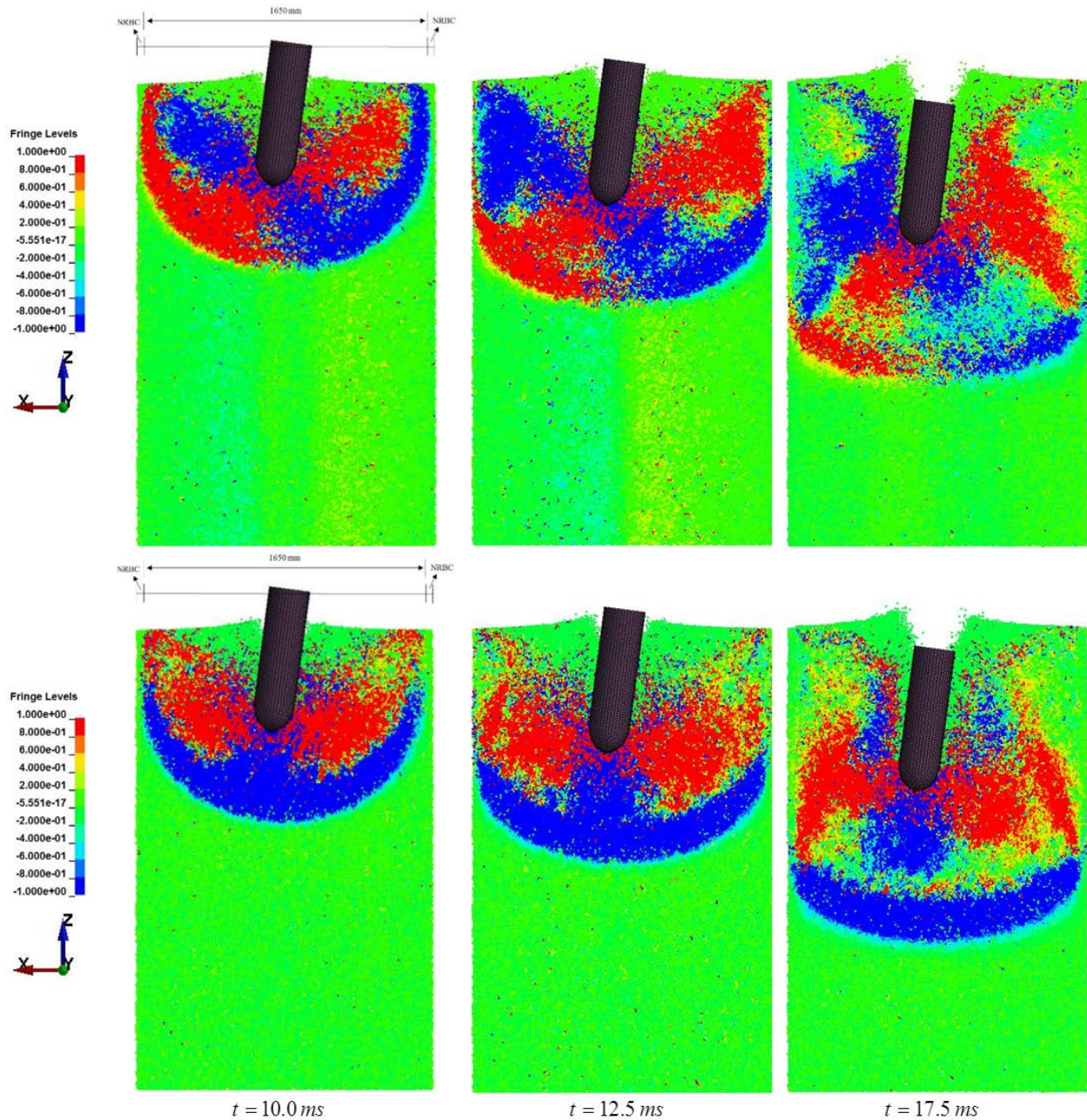


Figure 5.40 Force generation in granular masses during momentum transfer from the projectile: Radial (top row) and vertical (bottom row) force components of in the XZ-plane of Assembly B

Equally important is examining the balance of system energy components as shown in Fig. 5.41. Monitoring energy components also serves as a key step in identifying the presence and causes of numerical instabilities that may arise in explicit transient-dynamic simulation. Interpreting energy balance information is most easily accomplished by first considering the principle of the conservation of energy for the UXO-Granular system.

At any given instant in time, t , the total mechanical energy (E) of a system can be expressed as: $E = T + W$ where T is the kinetic energy and W is the potential energy. Furthermore, W can be

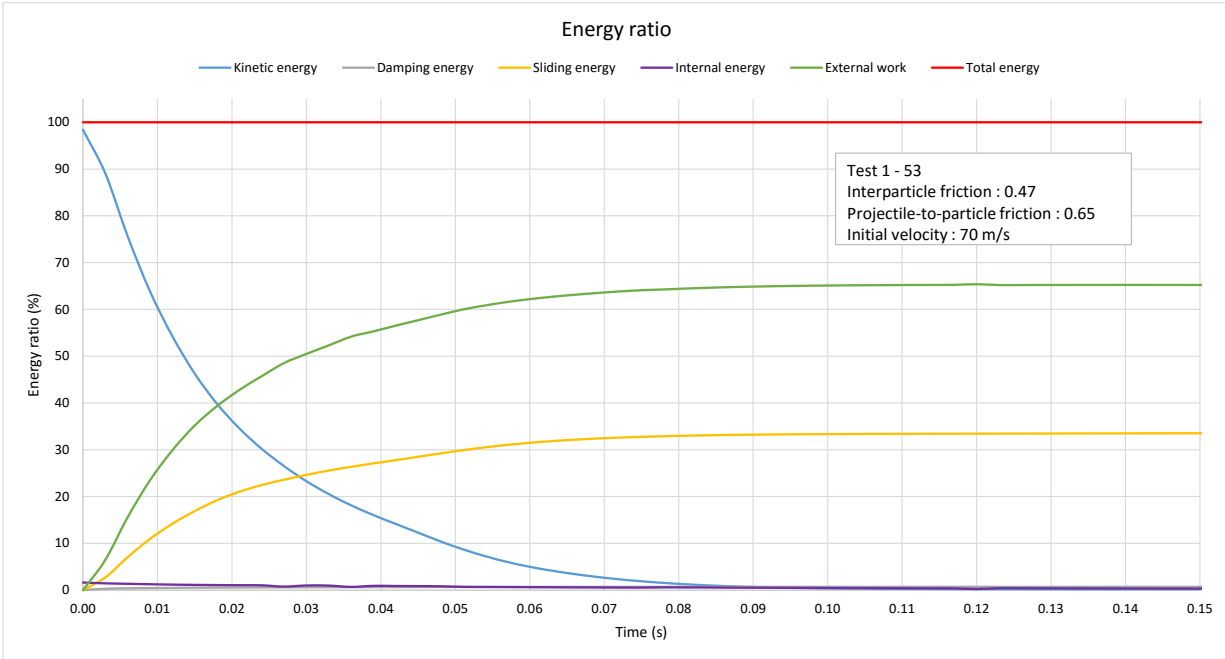
split into internal (strain) energy and external work done denoted by $W^{internal}$ and $W^{external}$ respectively: $E = T + W^{internal} - W^{external}$. If all of the forces acting on a system are purely conservative, then the balance of kinetic energy, internal strain energy, and external work done are conserved at all points in time. The law of conservation of mechanical energy then states that the total mechanical energy of the system (E) is constant with respect to time, and changes in kinetic energy (T) are balanced by changes in potential energy (W) as:

$$\Delta T + \Delta W = \Delta T + \Delta W^{internal} + \Delta W^{external} = 0 \quad (5.15)$$

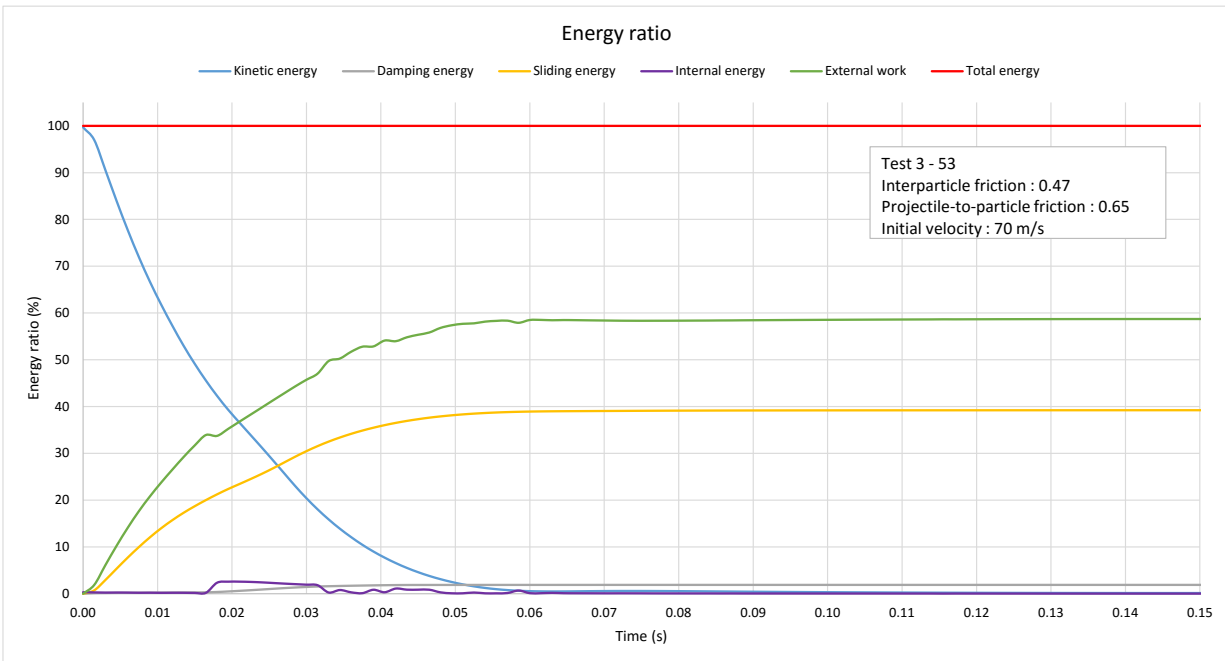
To account for the reduction in mechanical system energy associated with the effects of non-conservative forces, a dissipation term must be added to the conservation of energy equation:

$$\Delta T + \Delta W^{internal} + \Delta W^{external} + \Delta U^{dissipation} = 0 \quad (5.16)$$

where ΔT represents the change of kinetic energy occurring over some increment of time, $\Delta W^{internal}$ represents the change of internal (strain) energy, $\Delta W^{external}$ is the external work done, and $\Delta U^{dissipation}$ represents energy dissipated by frictional and damping forces. Given the energy balances, Assembly B shows more dissipation in the kinetic energy by frictional sliding. However, the larger DSEs produce more external work done to the granular system of Assembly A. The difference between the work done and the frictional sliding energies may be associated with volumetric changes in the system and/or potential energies of DSEs that are still moving upward near the impact surface and due to elastic rebounds at the end of the simulation when the projectile reaches a steady state at terminal penetration depths.



(a) Assembly A

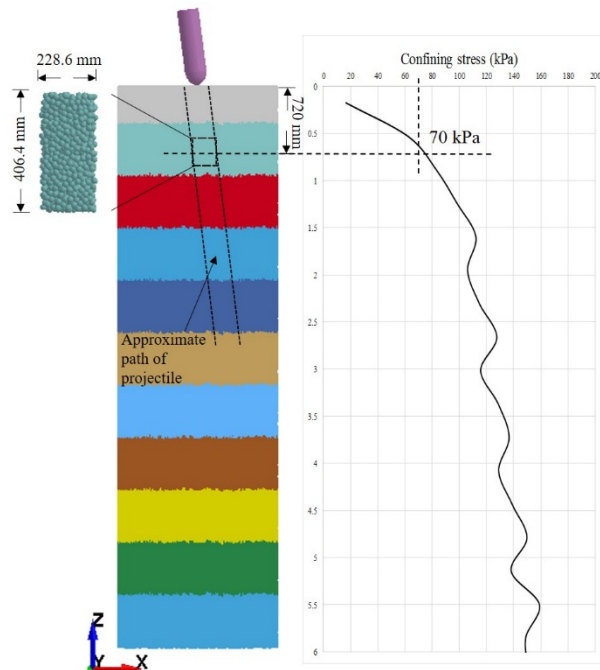


(b) Assembly B

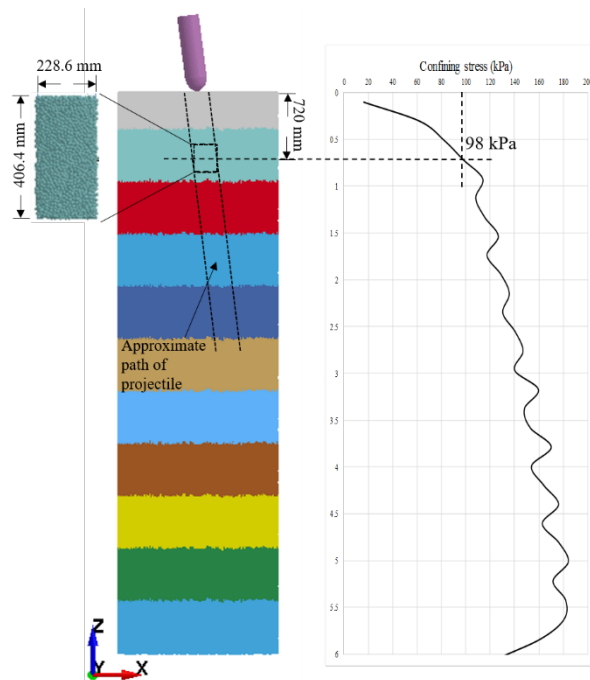
Figure 5.41 Balance of system energy components in the UXO-Granular systems

As part of the ongoing investigation to quantify high-strain rate (HSR) effects associated with dilation of granular volume, tri-axial compression testing is numerically simulated for the assemblies. The particle arrangement for HSR tests used in a cylindrical control volume of diameter 228.6 mm and length 406.4 mm is sampled directly from a location, i.e., at the same

depth along the penetration path. At a strain rate of 1750%/sec, the particle assembly from Assembly B exhibits a greater dilation-induced increase in the shear resistance (Fig. 5.43).



(a) Assembly A and variation of confining stresses (radial) through depth



(b)

Figure 5.42 Control volumes sampled for HSR tri-axial compression test simulations

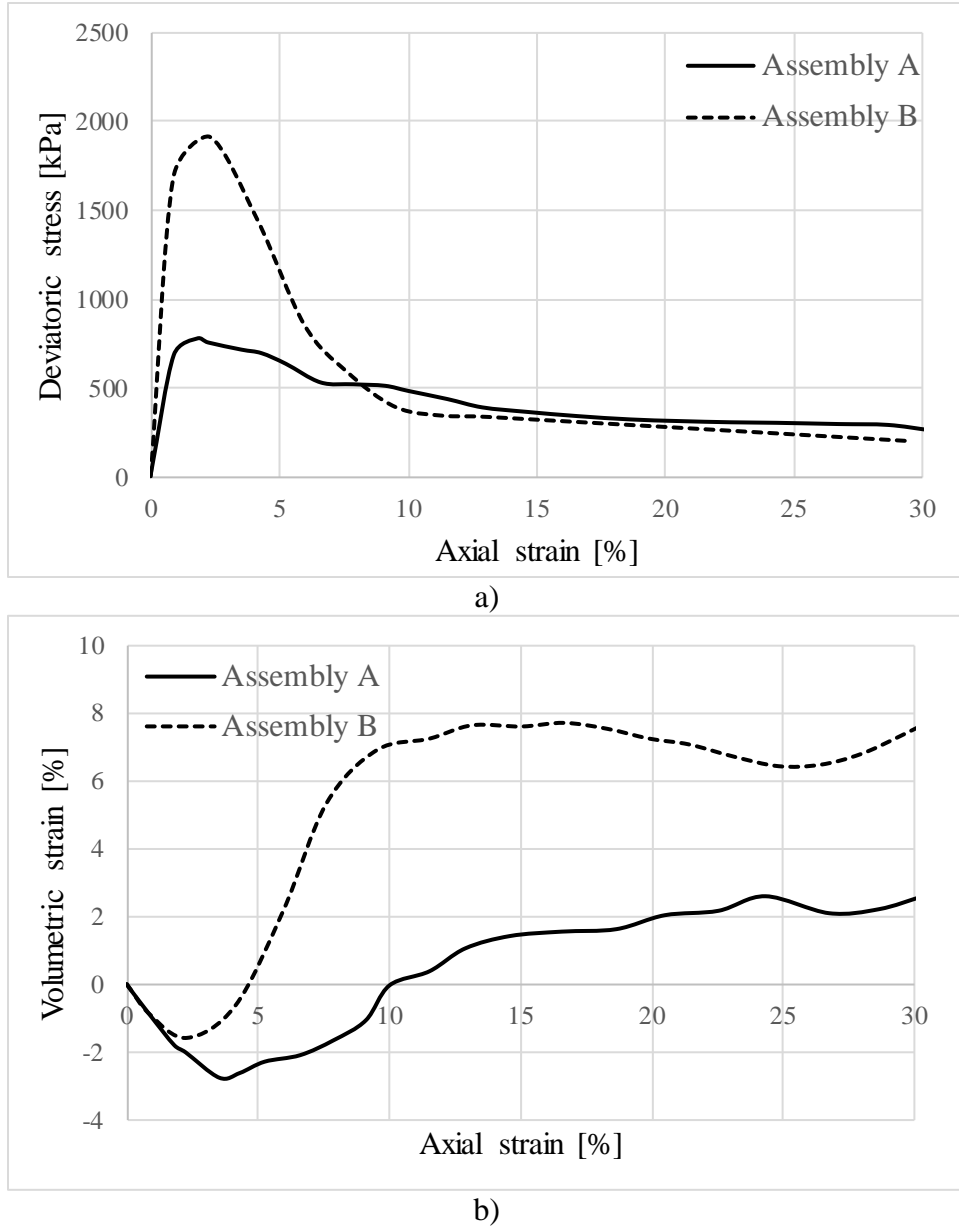


Figure 5.43 High-strain rate triaxial compression test simulation: a) Deviatoric stress versus axial strain; b) Volumetric strain versus axial strain

Lastly, similitude in flows of fluids is explored to hypothesize a moving boundary of UXO that has been consistently observed in the numerical simulations. To this end, the remainder of this discussion is focused on explaining the main concepts of moving granular mass and its boundary at the system scale more physically based on the simulation data, without using extensive mathematical methods. The rapid fluidization by the particles appears to vary in particle velocity in the direction normal to the sheared surface-near layer (e.g., the boundary layer). Being dragged through DSEs along the penetration path, the projectile momentum transfer creates the “streamlines” of the particle flow, which are made visible by tracking the thin layers of tracer particle layers (with different colors as shown in Fig. 5.44). At the leading edge just behind a hemispherical shock front, there is a constant velocity field perpendicular to the ogive of the nose. It

can be also seen that directly in vicinity of the wall of the projectile is a thin layer where the particle velocity is considerably higher than it is at some distance from the wall. In further distances from the leading edge, the layer of particles slowed down by the intergranular friction becomes ever larger as more and more DSEs are caught up by the retardation. The thickness of the flow regime seems to increase monotonically toward the top surface of the domain. Energy absorption by moving boundary layers may play the central role of stopping force generation in the UXO-granule systems (Fig. 5.44). In turn, Assembly B utilizes a greater total surface area in jamming formed by smaller yet more numerous DSEs in the entropy production over a shorter period of time, in compliance with the second law of Thermodynamics. The rate of work done by frictional forces in Assembly B is, therefore, higher.

Assuming that the no-slip condition is satisfied at the interfaces between penetrating UXO and granules in direct contact, the velocity transition from the limiting solution ($Re = \infty$) close to the surface of the projectile to the value of zero at the surface must take place, forming *the boundary layer* named by Prandtl (1904). As per the concept of the boundary layer, within the boundary layer of granular mass, two different flow forms may simultaneously occur, which we have seen in Fig. 5.39 and 5.40. The flow is, then, described as laminar or turbulent per (granular) Reynolds numbers. We will refer to laminar and turbulent boundary flows equivalently to the terms defined in the boundary layer theory. That is, advantages of considerable simplifications can be taken in the division of the flow field into inviscid outer flow and the boundary layer per relative velocities to the projectile movement. Close to the surface of projectile is a thin layer of granules whose particle relative velocities are considerably lower than it is at some distance from the surface, e.g., boundary-layer thickness. The thickness of this layer varies in space and time (Fig. 5.45 and Fig. 5.46 for Assembly A and Assembly B, respectively); it tends to increase along the projectile in the length direction from nose to end through time. Additionally, the layer undergoes thinning as the projectile slows down in space, respectively. Interestingly, the boundary layer tends to be thinner for increases in the pseudo Reynolds number; i.e., the smaller intergranular friction coefficient. This similitude between granular and viscous fluid flows can be further seen in particle velocity profiles along the length. The gradients of the velocity field must be continuous regardless of packing densities, which necessitates a smooth transition from namely boundary-layer flow to outer flow (in our case outer flow means the outer stationary region of no flow). Conversely speaking, for granular boundary layers, the boundary-layer thickness (for steady flow) in an incident of time can be correlated to total dragging forces: in the boundary layer the internal, frictional-sliding, and damping forces are in equilibrium with the inertial force per unit volume of the mass flow. Quantitative investigation of the rate of changes in thickness of the boundary layers is of great importance in future research efforts.

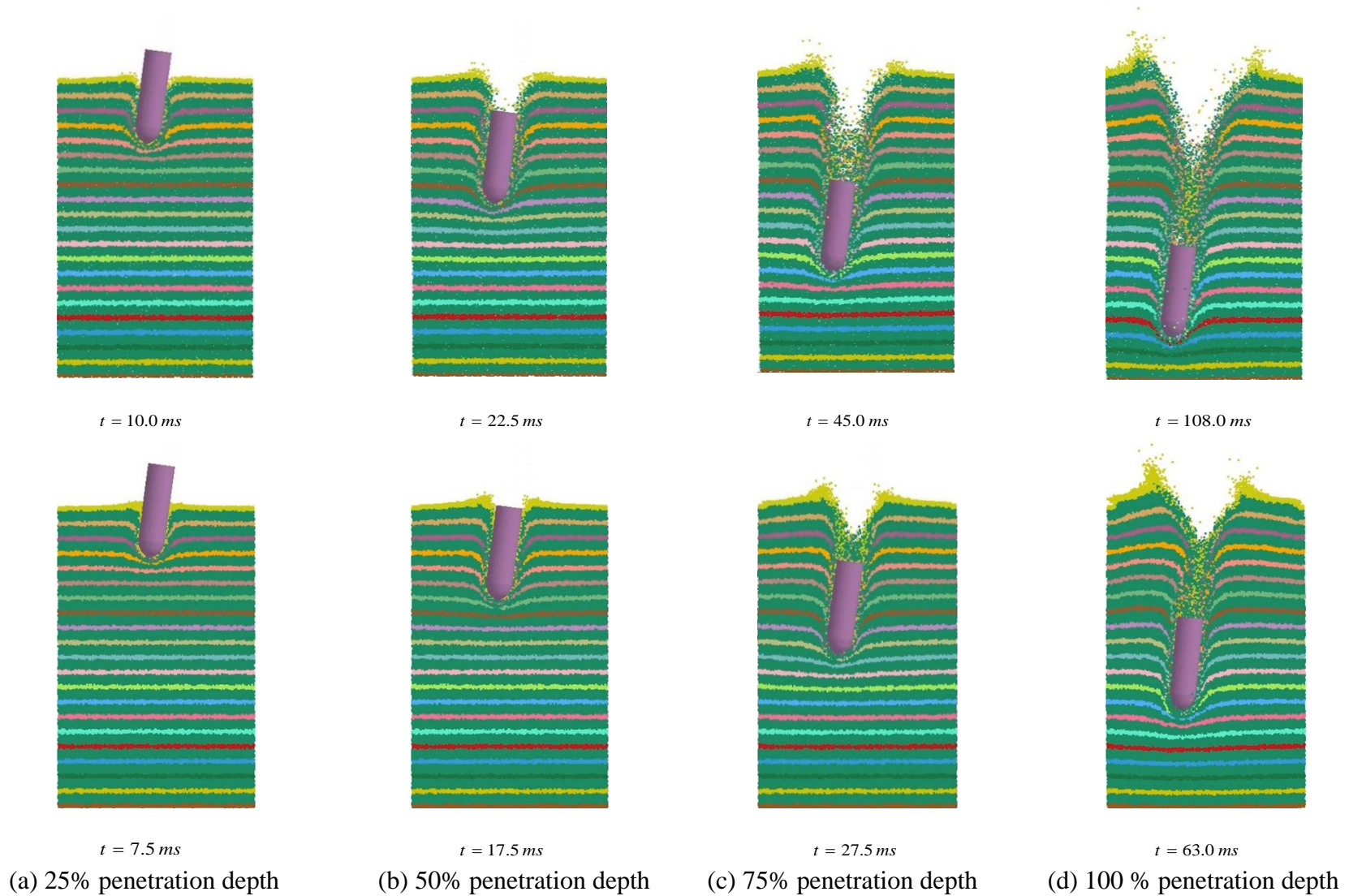


Figure 5.44 Streamlines in Assembly A (top row) and Assembly B (bottom row): The projectile dimensions are 238.3 mm in diameter, 854.6 mm in length, and 354.8 mm of ogive radius: for dimensional comparison purposes, only the center part of the radial dimension of Test 1 simulation is shown approximately same as the radial dimension of Test 3 simulation

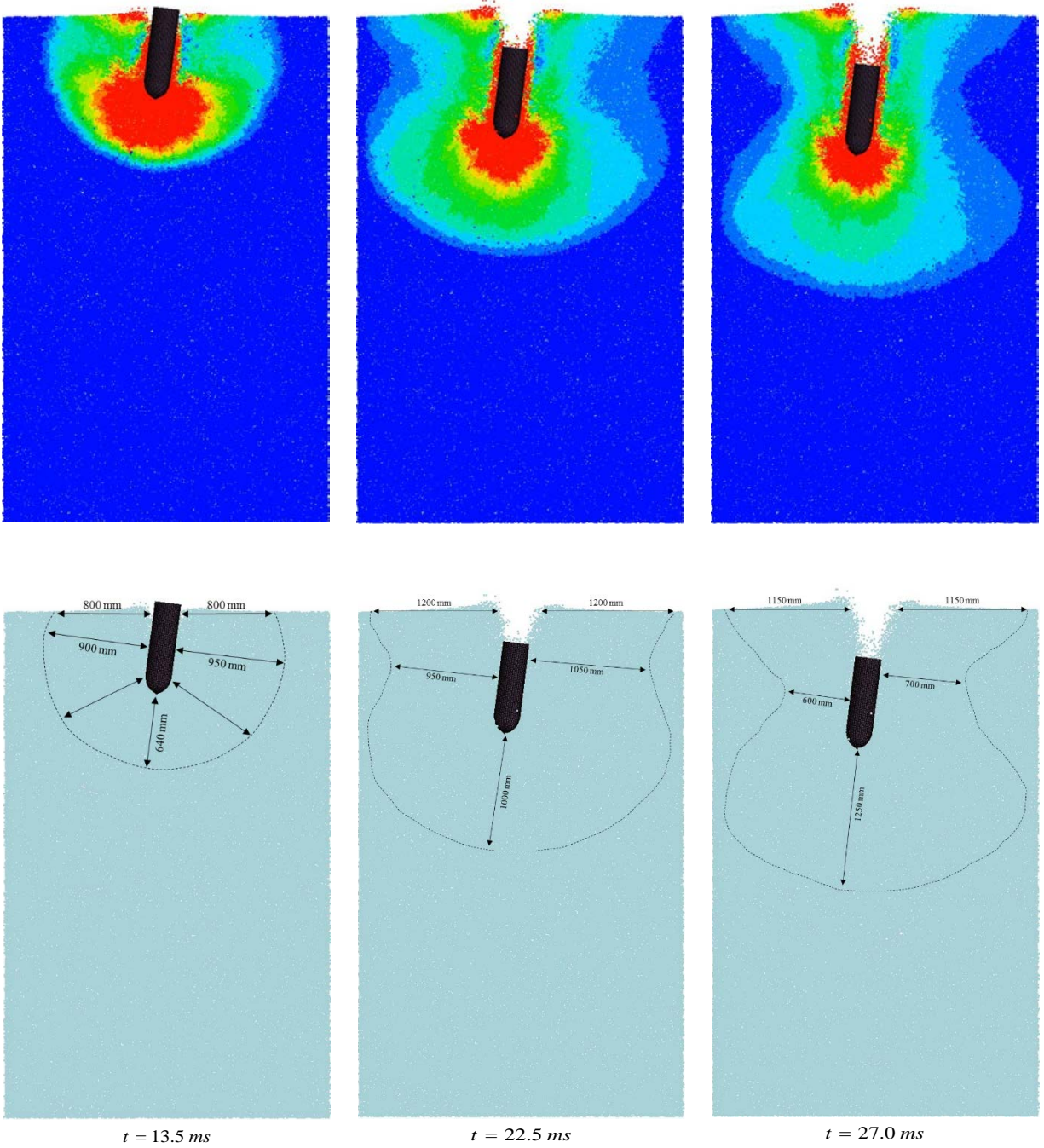


Figure 5.45 Mean resultant-velocity field (top row) and corresponding boundary (bottom row) of rapid-flow regime in Assembly A

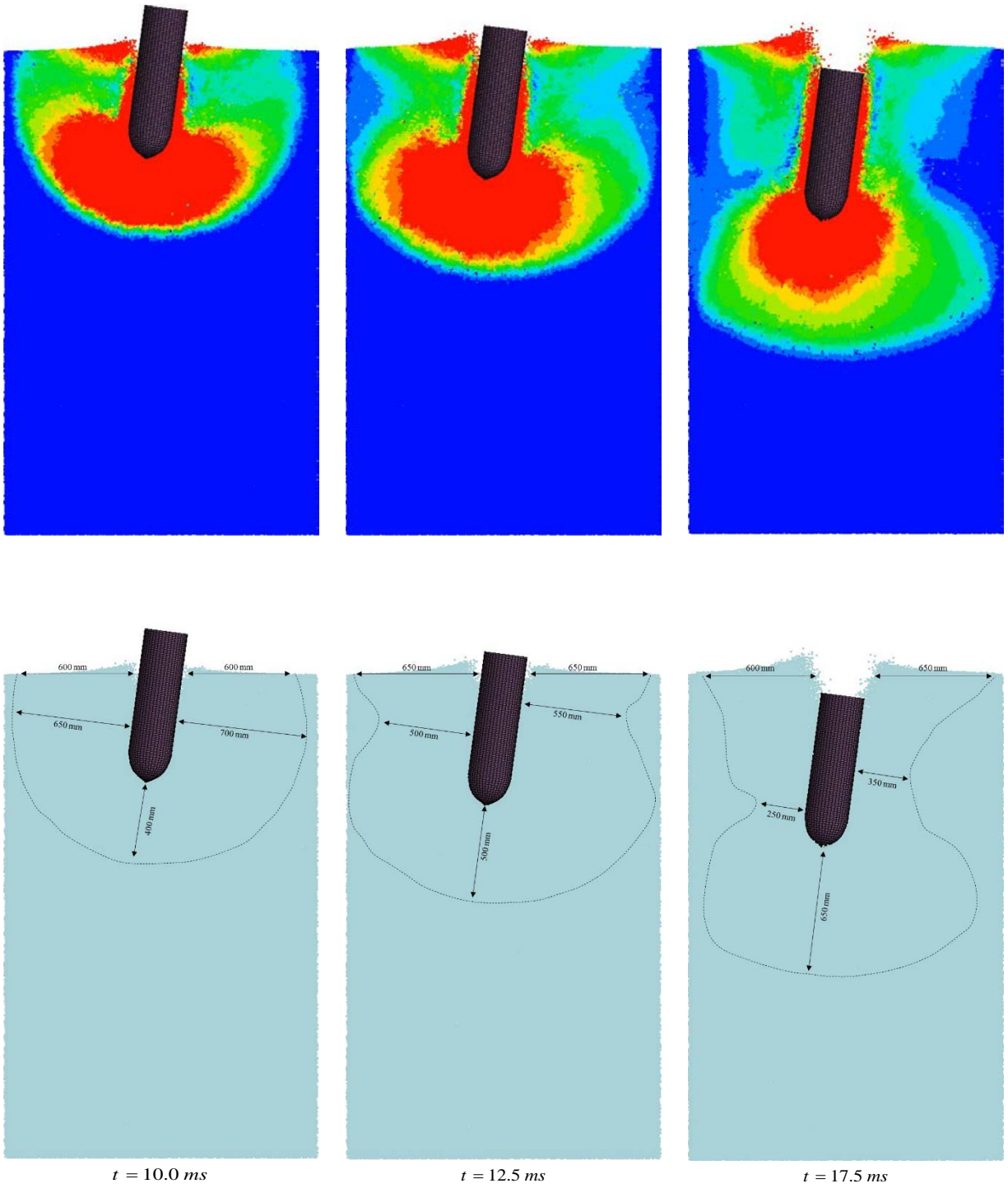


Figure 5.46 Mean resultant-velocity field (top row) and corresponding boundary (bottom row) of rapid-flow regime in Assembly B

CHAPTER 6

SUMMARY AND CONCLUSIONS

The overall objective for the SEED phase of this research is to study interactions between unexploded ordnance and granular assemblies, with emphases on characterizing: 1) Terminal penetration depths; and, 2) Mechanical responses of granular assemblies across multiple scales. In turn, the research outcomes will prove integral to the success of a subsequent research phase(s) in revealing fundamental system variables that span over underlying scales for phenomenological variation in penetration phenomena. The focus of the current report is to document those technical tasks completed in satisfaction of the Phase I research, including physical testing and numerical modeling. In Ch. 6, both the physical testing and numerical modeling thrusts are summarized. In addition, critical advances that have been made thus far are delineated, and in turn, preliminary considerations for subsequent research phases are documented.

6.1 Summary of Physical Testing

This project has been divided into two mutually supporting and validating research approaches, being empirical laboratory testing and numerical modeling of the same penetration problem. Based on the size, measurement, and repeatability requirement of physical testing, the geotechnical centrifuge technique is deemed to be appropriate for the fulfillments of the requirement of laboratory testing.

Being an essential initial procedure for the centrifuge test, the preparation of granular assembly is performed by means of a specialized pluviation procedure. This is done primarily in order to simulate body-force distributions at grain scales and corresponding geostatic stress states; the granular assembly should have reasonable homogeneity, and be subjected to a loading history that is similar to the specimen obtained in natural deposits formed by sedimentation. The pluviation process is time efficient and provides the added benefit of populating the granular domain with a desired relative density, which is controlled by selecting various dropping heights. Different granular assemblies are produced in this way which are either monodisperse assemblies or binary mixture assemblies, according to the criterion of each testing scheme.

When using sand particles to conduct physical tests, the variation in particle shape, surface roughness and material property will lead to discrepancies in the macroscopic behavior of the granular assembly even with an identical pluviation procedure. Therefore, to achieve repeatability of physical tests, the granules chosen for the centrifuge tests artificially manufactures ceramic spheres with average sphericity of 0.9, relatively uniform surface roughness, and contact friction coefficient. Two groups of proppants with different mean diameter are used to generate monodisperse and binary mixture assemblies for the purpose of different test schemes.

Test projectiles scaled according to the centrifugal acceleration level are designed based on the geometry of an ordnance. The desired impact velocity and angle of projectile is produced by controlling the air pressure of a prototype gas-powered projectile emission device. These two parameters along with three test schemes described in Chapter 4 formulate the parametric study of system configuration, which are replicated in the numerical modeling. The projectile velocity, terminal penetration depth, and stress distribution in the granular assemblies are of primary interest for direct measurements for the SEED phase.

6.2 Summary of Numerical Modeling

The projectile-soil interaction simulation requires the employment of both finite element and discrete element assemblies in the same model, a method which has been coined the combined FEM-DEM. Applications in the numerical analysis software LS-DYNA show the particular advantages of this method to the study of the problem of high-velocity penetration into a granular material.

As has already been discussed, the physical testing and numerical modeling serve as individual but mutually supporting research tools in studying the behavior of unexploded ordnance penetrating into granular assembly, as each method is used in turn to validate the outcomes of the other. Towards this end, the numerical simulations presented here have been designed so as to follow the procedures and materials present in the physical tests as closely as possible; each of the components in a centrifuge test, including the granules, pluviation procedure, testing dimensions and projectile initial impact information should be simulated numerically as realistically as possible.

A library of numerical granules has been compiled containing materials which correspond to each assemblage employed in the physical laboratory tests. The numerical model of granules is supposed to correspond directly to the real ceramic proppants in geometry, density and mechanic behavior. The geometry and density is easily matched by the spherical discrete elements with manually inputted mass densities, keeping in consideration the acceleration scaling factors employed in the centrifuge. The surface roughness and coefficients of contact friction of the ceramic spheres is simulated by means of the contact stiffness and sliding friction parameters in the numerical model. The energy dissipation within the real granular body are approximated numerically by means of damping coefficients and the coefficient of restitution. Standard empirical procedures like the direct shear tests and triaxial tests have been simulated for the numerical materials, which are calibrated further by direct comparison to the real tests performed on the proppants.

An LS-DYNA functionality to randomly generate discrete elements from a designated plane, allows for a good approximation of the laboratory pluviation procedure. Similar to the calibration progress for the relation between initial dropping height and assembly relative density in pluviation procedure, the initial height of this designated plane to the container of discrete elements requires several simulations to calibrate for appropriate values. As an index for the quality of the numerical granular assembly, the density state and stress distribution is calculated and compared with target values under geostatic stress conditions.

The projectiles employed in experiment are modeled with finite elements using geometry as close to reality as possible. It is a particular numerical difficulty to model the interaction between finite and discrete elements; in this case, the frictional interaction between projectile and granules is of particular importance and influences the ultimate penetration depth significantly. Since in-depth laboratory results related to this matter are currently unavailable, a parametric study on the influence of the friction coefficient on penetration depth is added to the list of varied parameters already including impact velocity, and angle in the various test schemes.

It is important to draw attention to and keep track of the many scaling factors based on acceleration level employed in the centrifuge analysis when designing the numerical models.

Instead of actually applying a higher acceleration field, the size of granules and projectile along with other related parameters is increased by amounts determined by these scaling factors to match with the theoretical conditions in the centrifuge test. This has the added benefit of allowing for the increase in time step size in the numerical simulation, resulting in a lower computational cost of the numerical calculation.

This report has presented the results of three different successful numerical simulations and their corresponding empirical centrifuge testing schemes. These have been directly compared and there is good agreement in final penetration depths. This serves to validate both the empirical and numerical methods here employed in the measurement of UXO penetration.

6.3 Proof-of-Concept and Conclusions

Penetration into in-situ granular media is an unsteady-state boundary-value problem that may refer to transient phenomena at a number of interrelated scales. In turn, these scales span across apparent contact areas of sub-microscopic and microscopic surface roughness, corresponding intragrain heterogeneous deformation and interparticle friction at grain (macro) scales, grain-scale damping and inertia in formation of force chains and corresponding particle rearrangement at continuum scales, and collective intergranular motion through semi-infinite domains. The Proof-of-Concept of the SEED MR2630 is given for practical applications to the determination of the UXO terminal penetration depths, and validated as per low-velocity impact and penetration of granular media at prototype scales, in relation to physical processes at underlying scales, where relative densities (i.e., packing densities) under lithostatic stress states may vary. As per particle size distributions in mono- and poly-disperse systems, centrifuge tests of penetration depths and changes in spatial internal-stress fields are conducted for vertical impact scenarios of a semi-armor piercing (SAP) 2,000 lbs. projectile into assemblies of aluminosilicate spheres. The test data are used to benchmark corresponding system-scale discrete and finite element analysis models. The prediction of penetration depths is strongly dependent on initial (thermodynamic) equilibrium states, i.e., initial conditions of mass density distributions at system scales where momentum transfer through intergranular motion controls energy dissipation mechanisms of projectile penetration in the time domain. Accomplishment of objectives is given in bullet points leading to the proof of concept in the end.

- **Development of Novel Pluviation Technique**

Based on a series of planned centrifuge test scenarios conducted at the University of Florida's Centrifuge Facility, the control parameter was substantiated in the design and manufacturing of a novel pluviator device, which was successfully utilized to achieve uniform, homogenous, and repeatable granular profiles to a relative-density state of interest. Specific to the physical centrifuge testing using said granular profiles, use of scaling laws made it possible to reduce artificial soil-arching effects, and maintain K_0 conditions throughout the granular assemblies.

- **Design and Use of Projectile Firing Assembly under Centrifuge Conditions**

The precisely designed firing assembly and projectiles produced controlled range of penetration velocities and Angles of Attack (AoAs). Comprehensive instrumentation of the model and data acquisition made it possible to record the behavior and observe the mechanisms involved in the centrifuge testing of projectile penetration into granular media. Obtaining consistent results further validated the centrifuge tests.

- **Combined Finite-Discrete Element Modeling of Projectile Penetration**

Complimentary to the physical test program, a three-dimensional extended discrete and finite element analysis model has been developed to numerically quantify, and parametrically evaluate, maximum penetration depths that are attained in dry granular masses (with various initial states) due to high velocity impacts by unexploded ordnance (UXO). Penetration depths have been explicitly assessed by solving the equations of motion at the grain scales subjected to surface boundary conditions at microscales, which the scale-specific descriptions of the system constituents are used in the explicit simulations of UXO penetration in granular media in a time domain. Local force equilibria at the grain scale are identified, through use of energy principles, to be the main drivers to system-scale phenomena.

The numerical modeling methodology developed for the SEED research has combined explicit time-integration finite element (FEM) and extended discrete element (DEM) methods in a novel manner, which has led to numerous advances in computational mechanics. For example, new methodologies for preparing DSE assemblies (i.e., pluviation simulation) and incorporating non-reflecting boundary conditions have proven successful, within the auspices of the SEED research. Furthermore, the modeling techniques have facilitated comprehensive, quantitative response assessments of interparticle contact-force propagation and resulting residual stress distributions that can arise in association with in-situ geostatic stress equilibrium states, UXO impact, and subsequent penetration. The numerical tools reliably capture transient boundaries at the grain scale, and explicitly simulate particulate behavior based on a series of numerical experiments that have methodically transitioned from theoretical contact mechanics to thermodynamic treatment of overall UXO-granular soil systems. The methodology has been motivated by the importance of using particle-scale contact mechanics to drive predictions of overall system responses.

- **Prediction of Maximum Projectile Penetration Depths into Granular Media**

Therefore, in accordance with the Munitions Response Program of the Exploratory Development of the Strategic Environmental Research and Development Program (SERDP), the concept of this SEED research has been the systematic scale-specific analyses, which lead to quantify terminal penetration depths through explicit numerical simulations of projectile penetration, inertial and damping forces at the scale ratios of projectile dimensions to mean diameters of granules, initial conditions of steady-state mass density (grain) distributions, and corresponding transient mobilization of shear resistance (unsteady-state granular flows around a penetrating UXO).

- **Significance of Achieving Proof of Concept**

The significance of the proof-of-concept is the scale-dependent variance reduction and isolation, which is of paramount importance in the study of penetration into granular media. The methodology is aimed to quantify discrete-grain boundary forces that evidently manifest in the interrelationship of the energy dissipation and stopping force generation in the penetration. With controlled topological variation in grain geometry, microscopic origin of inelastic collisional forces can be numerically represented as grain-scale boundary values such that the role of interparticle contact forces can be rheologically simulated in projectile dynamics for associated particle kinematics. Effects of energy dissipation mechanisms at the grain scale could be further enhanced by the introduction of grain-scale topological variation, which makes it possible to formulize virtual power (namely, work done capacity), with respect to thermodynamic variables of natural grains, e.g., granular velocity (and temperature) field. This way, particle breakage and friction-induced fracture can be accounted for in relation to surface energy of grains under supersonic impact scenarios. Further, as per virtual work theory, the balance of local energy components becomes a utility means to quantitatively upscale multi-body microscopic interactions to an idealized (mesoscopic) control volume for use in design application of DEA. Equivalent to hydrodynamic drags, rates of momentum transfer and non-conservative forces would be formulized in characteristics of (macroscopic) rapid-flow regime per mesoscopic control volumes around the geometry of projectile. Ultimately, each milestone of these four objectives in parallel efforts is one step closer to the development of a simplified design solution for pertinent scale-dependent model parameters that have direct influence on the generation of stopping forces (e.g., in formation of the boundary layer) in the UXO penetration. In the following chapter, topological variances at grain-scales are introduced for which the characteristics of morphological texture granular structure are conceptualized at mesoscopic scales. Subsequently, rate of entropy production in intergranular motion and intragrain deformation is discussed in relation to virtual power capacity of control-volume DSEs, leading to achieving the design solution.

CHAPTER 7

PROPOSED RESEARCH FOR A CONTINUAL DEVELOPEMNT

The impact of an UXO on a soil target generates shock waves that propagate through the soil and the projectile. These stress waves are ultimately attenuated through geometric dispersion of grain-to-grain contact. The resistance of a granular structure to the penetrating rigid UXO with the lower end of the subsonic regime is its capacity of work done and efficiency of energy dissipation originating largely from point-mass frictional sliding and colloidal damping. The physical phenomena that we have observed in the present study are a result of energy transfer to granules in motion causing development of rapid mass-flow regimes, structural collapse, and significant compression and shear of the granular volume. The motions of individual granules and resulting particle interactions are, in essence, found to be the source of stopping forces. Alternatively stated, focus was made on obtaining solutions to the equations of motion of the constituents specifically for initial and boundary conditions mathematically prescribed at the homogeneous grain boundaries.

Upon an established solution methodology, subsequent efforts in Task 4 (of the MR2630 proposal) are in a twofold approach focused on topological variances of natural grains. First, topology of natural grains is considered in four morphological features which are independent of one another for describing the geometry of grains, i.e., size, shape, roundness, and roughness, by quantitatively pragmatic descriptors for polydispersity, shape factor (angularity and sphericity), and surface roughness. Concept of *surface mapping* is presented for rheological treatment for use in DEM. Second, mesoscopic texture of granular structure is methodologically simulated through geometric partitioning by compositional space-filling arrays.

Subsequently presented would be discussion in expanding the solution to supersonic impact on the granular medium, based on the energy equation. Narratives about the expected outcome of the proposed research are given in the end.

7.1 Topological Consideration

The silica sand possesses external surface (Fig. 7.1), the area of which increases with decreasing particle size in a predictable relationship that has direct influence on particle motions relative to penetrating UXO. Namely the surface-area-to-volume ratio (SA:V) is an important factor of total potential for use in frictional sliding and associated entropy production; similitude is found in chemical reactivity, i.e., the rate of which chemical reaction (involving a solid material) will proceed, is dependent on SA:V.

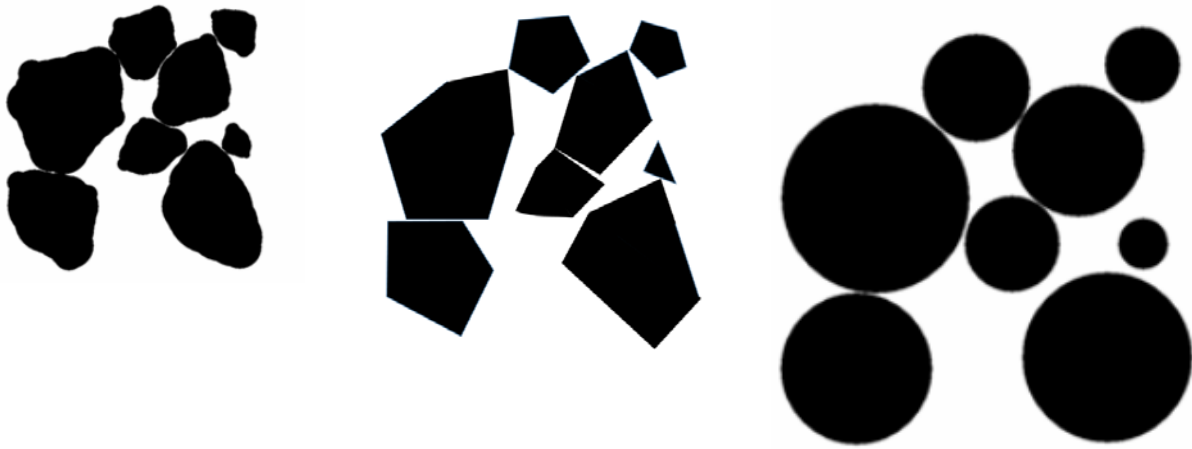
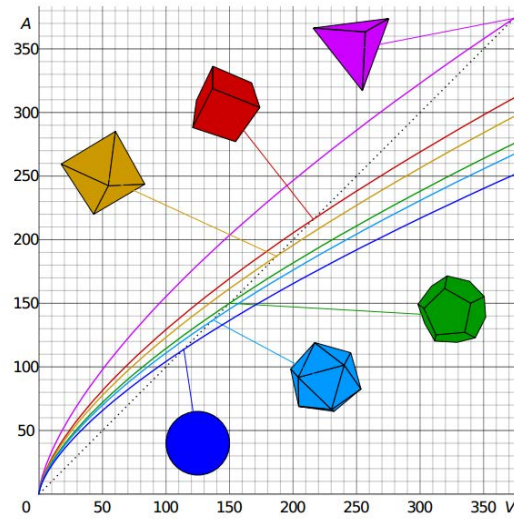
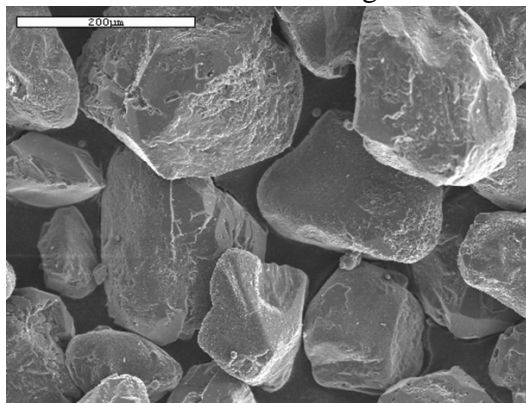


Figure 7.1 Two-dimensional projection schematics of random assembly of eight angular sand particles (left), transformation to platonic solids composites (middle), and DSEs with SA:V roughly equivalent to angularity (right): Mass densities decrease as volumes increase from left to right. Representation of point mass at the centers of the circles requires force mapping to account for the moments of inertia and rolling resistances accordingly to shape factors (Refer to A.1.7).

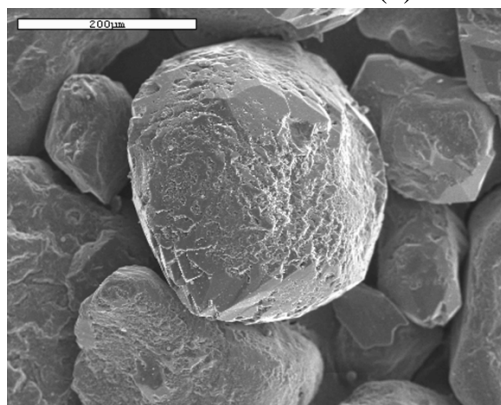
For a given volume, the object with the smallest surface area (and thus with the smallest SA:V) is the sphere, known as a consequence of the isoperimetric inequality in three dimensions, as illustrated in Fig. 7.2a. With a given effective diameter (refer to Appendix A), DSEs possess much smaller surface areas than non-spherical sand particles. Natural sand grains possess sphericity dependent on the particle's elongation, and roundness dependent of sharpness or angularity. The enhancement of the DEA model incorporates this SA:V based on experimentally determined shape factors. With shape factors obtained by the digital image processing techniques, the amount of surface area per unit volume of a particle (or, a scaled control volume of collection of particles) is statistically quantified in the Fourier analysis method. Equivalent to rough, nonporous, and non-spherical granules with controlled shape parameters as shown in Fig. 7.3, the tribological parameters of the DSE contact models can be modified to account for SA:V. In particular, micro friction values are calculated using (1) micro scratch testing and (2) tribological theories. A sufficient number of static friction tests should be conducted on various silica granules and analyzed based on a theoretical derivation (A.34) of the JKR theory given in Appendix A, where microscopic friction coefficient in relation to surface topography is calculated from surface energy per unit surface area. Thus, the lower sphericity the larger surface area, the higher surface roughness the larger surface area.



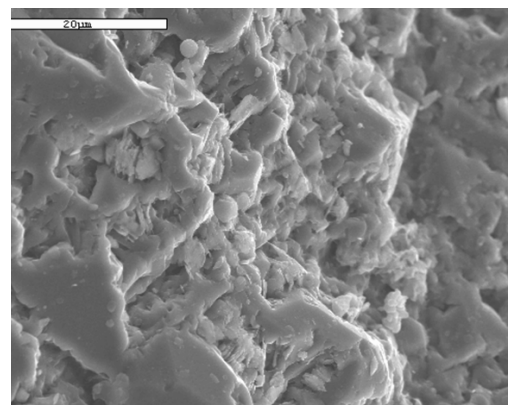
(a) Surface areas of Platonic solids and a sphere, showing that the surface area decreases for rounder shapes, and the surface-area-to-volume ratio (SA:V) decreases with increasing volume.



(b) Nevada sand



(c) Low-magnification SEM of Nevada sand



(d) Surface roughness at high magnification

Figure 7.2 Surface-area-to-volume ratio and Scanning Electron Microscope (SEM) images of sand particles

The frictional-sliding energy of non-spherical particles with an effective diameter can, then, be evaluated for the potentials for work done by spherical particles in contact. With high coordination numbers at jammed states, tangential (shearing) resistance of non-spherical particles in contact can be mapped on spherical particles occupying the same volume in space. Conversely speaking, the frictional bonds of DSEs can be increased accordingly to the product of SA:V and surface energy of non-spherical particles on an equivalent contact area.

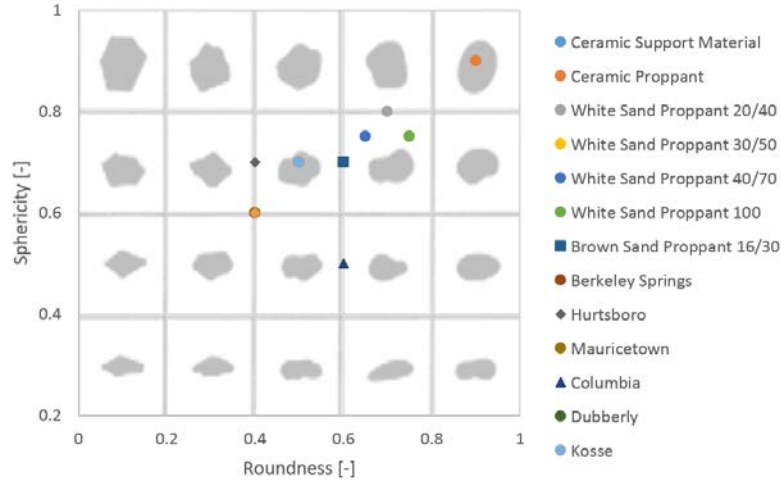


Figure 7.3 Particles with various shape factors for use in sand-pile tests

7.2 Averaging Methods

Let us further hypothesize that frictional debonding (slip) can occur only on a given contact plane of larger (meso-scale) spheres, which enclose multiple non-spherical particles within their spherical volumes. Translational momentum associated with slip is resulted from sum of translational and angular momenta of the smaller, non-spherical particles. The frictional resistance of these constituents along the direction of motion is then superimposed on the geometry of surface waviness at the lower frequency levels (where “macro” surface roughness is formed by rearrangement of constituent particles). The limiting tangential load becomes the combining of friction resistance at two different scales. Physical interpretation of the rheological and tribological treatment on DSEs is such that, for a given geometry of spherical volume, the potential energy required for non-equilibrium frictional sliding may be in relation to total surface energy available on all the contact areas of constituent non-spherical particles per SA:V, with centers of point masses occupying the same locations in space. For example, local tangential limit load on the circles (spheres) in Figure 7.4 increases to generate the same amount of work done by hexagons (polygons) in frictional sliding based on the second law of Thermodynamics.

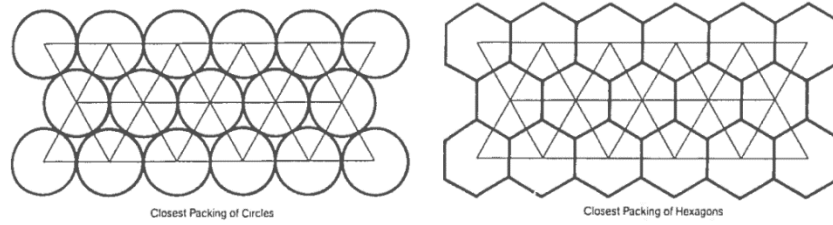


Figure 7.4 Triangulation of two-dimensional closest packed arrays

Scalar quantities of relative density (commonly found in the literature) may not adequately define initial conditions, i.e., steady-state thermodynamic equilibrium conditions, of the granular system. We have demonstrated the effect of the particle size in the development of rapid-flow regimes around penetrating UXO. It must be understood that the grains as distinct individuals interact through laws governing states of matter and account for friction in ensuring stability with neighbors, which together create finite dimensional structure (assemblies) giving the positions and the shapes of prior loading history (the importance of the controlled drop height and mass flow rate in pluviation processes). Thus, each pluviation process composes a unique, kinematically-admissible form for periodic structure per thematic design of particle size and loading history. Thematic design refers to the repetition of similar (or even identical) assemblies in a mesoscale volume in space. Periodic structure refers to patterns in emerging contact force chains at steady states under gravity. The interaction of thematic design and periodic structure creates a variety of, namely, relative densities. It is conjectured that these two are independent, since it is quite possible to compose different themes in the same periodic structure or the same theme in different periodic structures. In relation to aforementioned topographical and topological variations in granular constituents, the particle size distribution should be presented for the interaction of thematic design and periodic structure in the morphological texture of granular structure.

From the granulometry of particle sieve analysis, particle size distributions are considered for the simulation of morphological texture of granular structure. Two representative diameters are selected based on the mixture theory, i.e., volume- and mass-averaging methods. The first method is to average the solutions of the equations of motion of constituent particles derived from the conservation of linear and angular momenta over a control volume subjected to scale-dependent boundary conditions, e.g., apparent cohesion due to capillarity and confinement by lithostatic stresses. The latter method is to satisfy the conservation of mass in spatial discretization of a semi-infinite half space. This binary-disperse representation of the particle size distribution is composed of primary and secondary DSEs. The primary DSEs is responsible for the development of contact force chains, which warrant the existence of local (constituent-level) thermodynamic equilibrium states. Inclusion of secondary DSEs develops a morphological texture in partitioning and corresponding point-mass distribution, and increases structural stability of texture by imposing local constraint conditions on the primary DSEs.

More specifically, the primary DSE represents a spherical volume (V) of monodispersed grains with effective diameters (Fig. 7.5) that vary with respect to grain size distributions of coarse-grained sands with mean particle diameters ranging from a few hundred microns to several millimeters. Hereby we refer to the terms “local and global” in order to indicate scale-specific boundary conditions. Equilibrium states of local boundary forces on the individual viscoelastic

subspheres constitutes an initial state (condition) of the mesoscopic bodies prior to contact. Assuming that local thermodynamic equilibrium states exist as per degrees of interparticle constraints, local mass redistributions take place in particle rearrangement. These constituents' motions are source of equilibrating local forces in the momentum transfer between the two contacting agglomerates subjected to prescribed transient boundary conditions on ∂V (e.g., relative motions in normal and/or tangential directions).

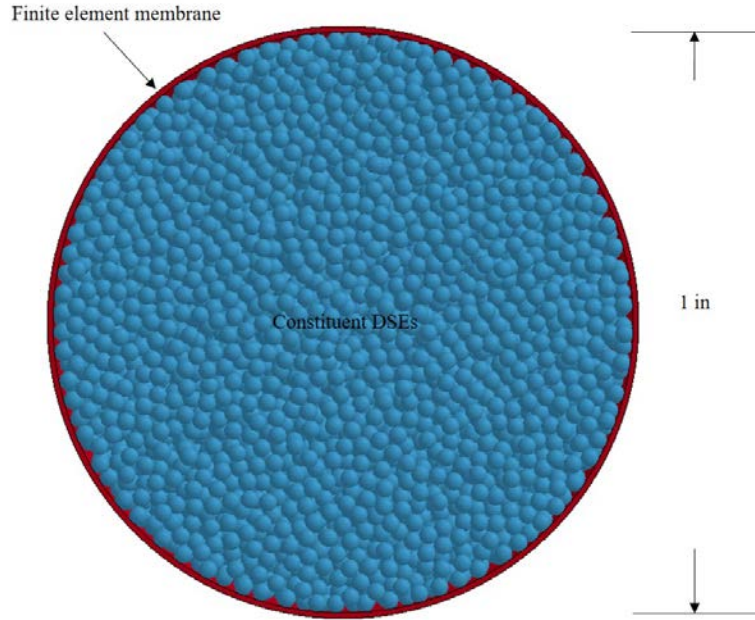
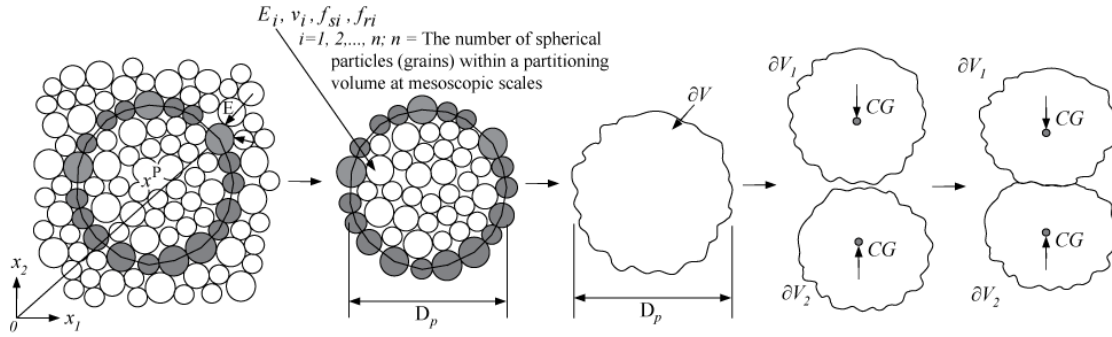


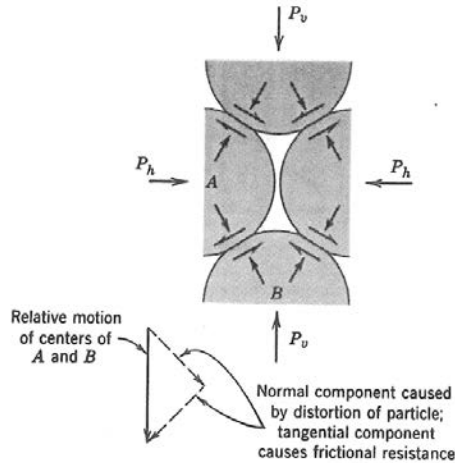
Figure 7.5 Meso DSE (constituent DSEs' diameter = 0.5 mm; Meso DSE's diameter = 25.4 mm)

To numerically predict the mesoscopic contact forces, a spherical volume is first defined with an effective diameter D_p equal to variational partitioning in a semi-infinite half space. The particle arrays within each of the partitions are generated using random packing of bi-dispersed spherical subparticles. These partitions (mesoscopic control volumes) may be determined in a possible correlation with a representative mean diameter of subspheres d_i (given a particle size distribution), but with various centers of the mass of the partition (CM). As mentioned earlier, contact forces of subspheres are defined in a closed-form solution specific to surface topology and kinematics of microscopic asperities. Interlocking, yielding and hardening, and shearing of the asperities are accounted for in the mobilization of resistances against relative motions at the local boundaries. In terms of these local boundary values, local momenta transfer among grains in contact influence the kinematics of the contacting mesovolumes, V_i . Corrugated surface ∂V in accordance with grain size distributions are subjected to surface traction (e.g., hydrostatic pressures acting on the boundaries of a mesoscopic volume (∂V) and/or degrees of constraints as nonessential boundary conditions imposed on nominal contact points with adjacent mesoscopic volumes. Repeated simulations are performed in numerical experimentation for relative motions subjected to vertical compression (normal contact), and subsequent tangential sliding (and rolling due to angular momentum with respect to global CMs) to quantify the mean of mesoscopic sliding and rolling friction coefficients f_{cs} and f_{cs} (Fig. 7.6a) per global nonessential boundary

conditions. In addition, volumetric compression is simulated to quantify volume-averaged bulk modulus and Poisson's ratio as per local variables. Corresponding mean values (and standard deviations) represent input parameters for use in the contact definitions of mesoscopic discrete elements (V) with state variables of ∂V , e.g., tangential slip velocities or functionals of multiple variables. It is noted that the surface roughness of V is varied with respect to the local distributions of particle size and interparticle friction coefficient, which is defined by mesoscopic surface topology with contact radii of curvature distributed on ∂V . The concept of self-similarity of great utility as a means to apply the Williamson-Greenwood contact theory (Williamson and Greenwood 1966) to the scale which establishes the DEM representation of the granular volumes at the mesoscopic scale. Thus, specific to the mesoscopic surface topology of ∂V , physically-admissible contact force-displacement relationships would be numerically derived for solutions to the equations of motion of the mesoscopic system subjected to the boundary conditions. The scale-dependent inertial, Coulombic and viscos damping, and internal forces are functionals of the interrelated scales. These mesoscopic discrete elements specific to the boundary values on ∂V are used to partition a large-scale system volume subjected to a set of system-scale boundary conditions.



(a) A partitioning volume bounded by an imaginary boundary ∂V with surface roughness



(b) Constituent particle interaction inside a mesoscopic volume (V) subjected to surface tractions, e.g., gravitational lithostatic compression

Figure 7.6 A definition of mesoscopic discrete-element sphere

Illustrated in Fig. 7.7, a mesoscopic volume, which encloses several thousand constituent DSEs with particle diameters ranging from 0.15 mm to 2.0 mm, is in static equilibrium under hydrostatic pressures acting on imaginary membrane boundaries. The particle size distribution is based on experimental data on a medium dense sand (Muzenko 1965). Constituent DSEs can be modeled to represent dry or partially-saturated states. Capillary suction forces on constituent DSEs can be introduced as another set of grain-scale boundary values: pretension forces are calculated for liquid bridges (refer to A.4.7) in pendular regimes with respect to a volume fraction of water, i.e., degrees of saturation. Subsequently, the mesoscopic volume is gradually compressed at a constant velocity downward against a rigid plane, simulating a quasi-static condition. However, particle interactions are transient and nonconservative as damping and frictional sliding dissipate the translation momentum. From a perspective of the conservation of energy, some of exerted mechanical energy of the mesoscopic volume is dissipated in order to balance with the work done by interparticle contact forces and moving local boundaries.

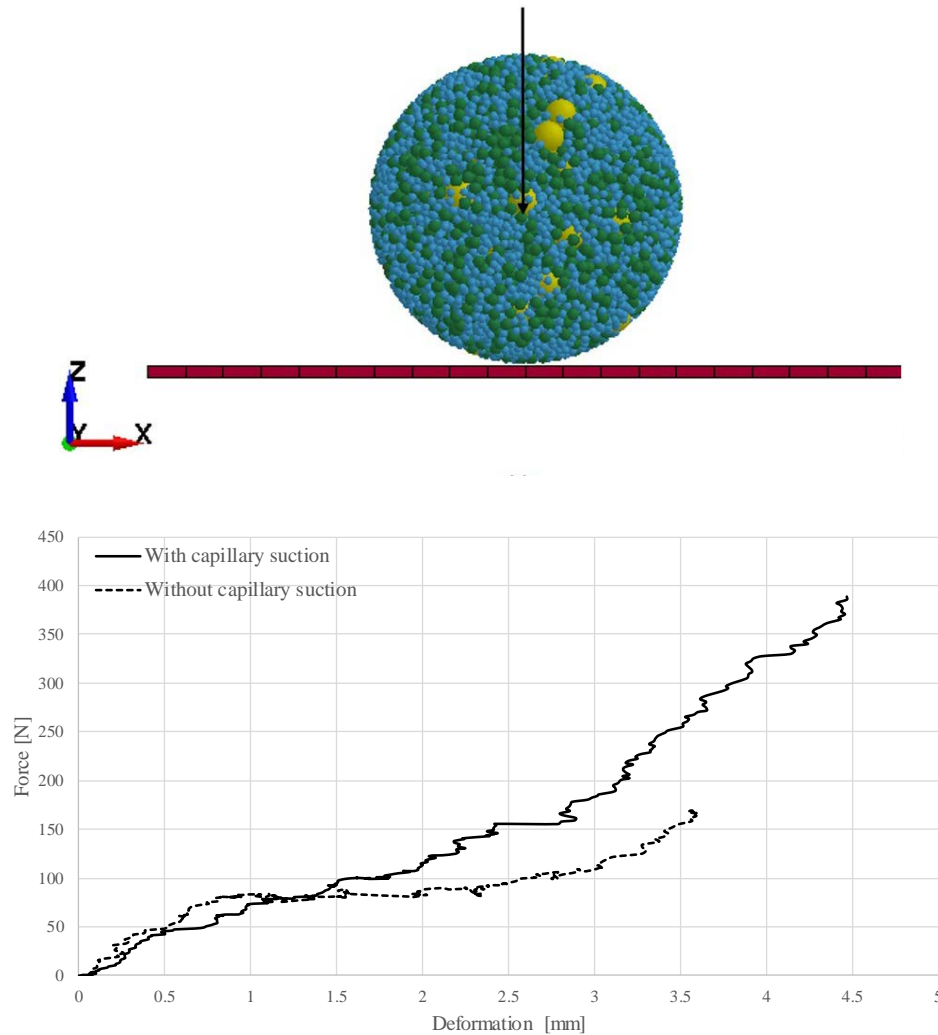


Figure 7.7 Numerical model of upscaling (top) and resulting meso-scale DSE normal contact stiffness (bottom)

A numerical solution to the equations of motion of the meso DSE depends not only on prescribed macroscopic boundary conditions but also local boundary-value solutions. The computed macro “normal” contact force and displacement relationship is, thus, a volume-averaged parameter of control (spherical) volumes. Given in Fig. 7.7, the contact stiffnesses are specific to (1) macroscopic nonessential boundary conditions imposed on a control volume with diameter of 25.4 mm, (2) packing density per a given constituent size distribution, (3) constitutional parameters of contact models, and (4) scale-dependent boundary values (surface roughness).

7.3 Morphological Characteristics of Granular Structure

Next, morphological texture is simulated at the mesoscopic scale. Consider partitioning formed by closest packed circles in a plane where small concave triangles of void space exist between circles in Fig. 7.8. Consequently, circle packing is not the most effective system to partition the entire plane. Now, let the shape of circles change to fill up the concave triangles. That would form hexagons, which give the most effective method for partitioning a plane surface into equal constituents of area. Hexagon partitioning is also economical which discretizes a space into units of maximum size for a given perimeter (or a minimum amount of the wall material seen in honeycombs). Further, the packing of hexagons reveals the fundamental relationship of the triangular order of close packed circles with minimal partitioning. Since the closest random packing of DSEs is associated with finite-size spheres, and not comprised of line-segments jointed at vertices, the triangular order of sphere packing gives the closest packed assembly, i.e., a three-dimensional network of equilateral triangles forming the faces of tetrahedra and octahedra in a *space filling* array. Consequently, a maximum theoretical coordination number of sphere packing is twelve. This concept “space filling” is taken advantage by the combining of either similar or complementary bodies in a three-dimensional packing being repeated, in such a way that there is less unoccupied space, i.e., “dead” space. The smaller dead space the larger mass over a given volume. Or, the denser point-mass distribution the less deviated from the most effective partitioning of a semi-infinite half space. Given a constant SA:V in DEM, space filling is thus evidently limited to usage of smaller DSEs. These DSEs smaller in size (than primary DSEs) are named “secondary” DSEs.

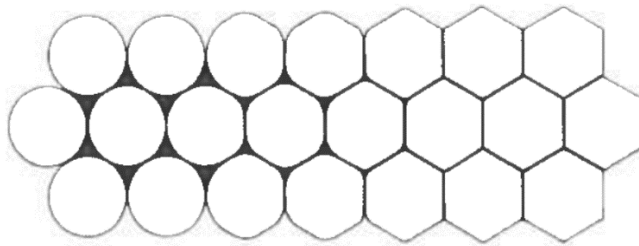


Figure 7.8 Morphological changing between packed hexagons and closest packed circles

Reiterating “economical partitioning”, an economical mixture of primary and secondary spheres is investigated in the literature (Guyon et al. 1987; Kristiansen et al. 2005; Shi and Zhang 2006). That mixture is economical which give rise to packing density. That is, the coordination number of packing assembly clearly depends on the binary-mixture composition per size and compositional ratios. Characterization of a binary system is conceptualized by preliminary DEA where focus is placed on demonstrating the utility of binary systems for the concept of space-

filling. Accordingly, two random packings of DSE assemblies are shown in Fig. 6.9: a binary system (Fig. 7.9a); and, a monodisperse system (Fig. 7.9b), where the latter packing is achieved by removing the smaller sized spheres from the former. To an extent, frictional bonds between primary DSEs is parametrized so that the removal would cause minimal (even no) changes in the morphological texture of prior loading history. The volume composition of the binary mixture is 50:50. The ratio of sphere radii is assigned as 1.6, and is selected such that the secondary DSEs are similar bodies in space filling, which is also classified as “similar-sized” (by O’Toole and Hudson, 2011). Alternatively stated, if the primary DSEs (of radius 5 mm) were to be assembled in a simple cubic packing, then the secondary DSEs (of radius 3 mm) would not fit within the octahedral interstices between the larger spheres.

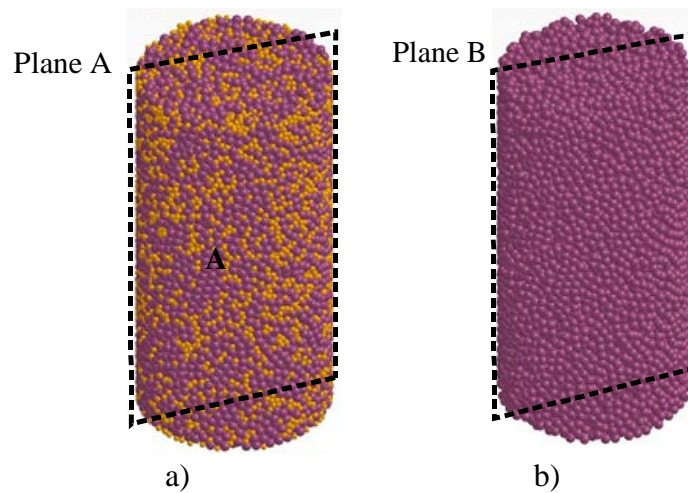
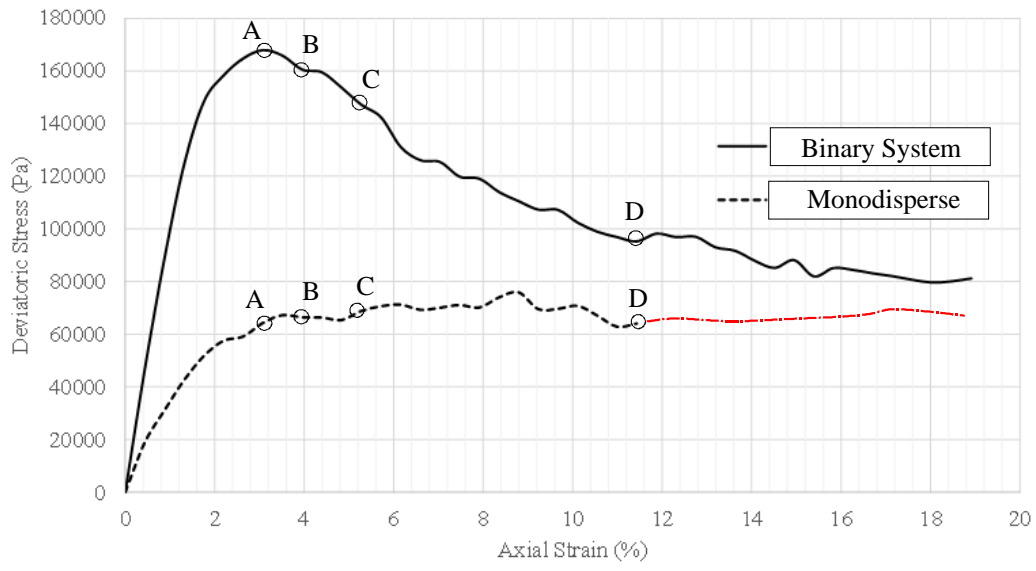
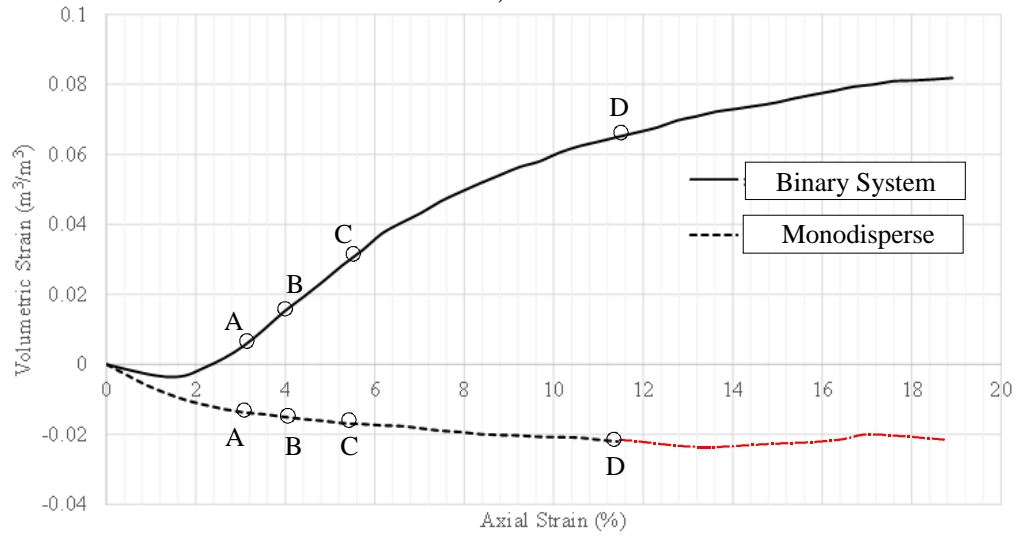


Figure 7.9 Random packings of DSE assemblies: a) Binary system (with a cut plane across the center of the section, Plane A); b) Monodisperse system created via removal of smaller spheres (with a cut plane across the center of the section, Plane B)

The packed binary system and corresponding monodisperse system, with input parameter values given in Chap.3, are put to the test in triaxial compression test simulations. A confining pressure of 70 kPa is prescribed on a cylindrical volume of continuum-mechanics scale, where this level of confinement is selected solely to maintain comparability between the numerical results. Comparative plots of deviatoric stress versus axial strain and volumetric strain versus axial strain are shown in Fig. 7.10. As expected, the binary system exhibits behavior that more closely resembles that of a physical, granular soil under a jammed state. Also, the monodisperse system exhibits behaviors that align with those of (physical) granular soil in a looser state. Such pronounced differences in phenomenological behavior are observed in development of displacement fields and contact force chains (Figs. 7.11 and 7.12) even though the two as-configured DSE assemblies each occupy spaces of approximately equal volume. As a final observation for these demonstration simulations, the binary system response (with respect to macroscopic volumetric behavior) is consistent with that previously discussed in Chap. 5 for Assembly B of the UXO-Granular system, i.e., at a relatively higher packing-density state. Summarily, the two sets of triaxial compression test results indicate that economical partitioning of dry sand can be simulated by making *judicious* use of binary systems.



a)



b)

Figure 7.10 Triaxial compression test simulations of monodisperse and binary systems: a) Deviatoric stress versus axial strain; b) Volumetric strain versus axial strain. Note that the deviatoric stresses highlighted in red are based on a conjecture. For final reporting, we present part of the simulation (which has not been completed at this point of time).

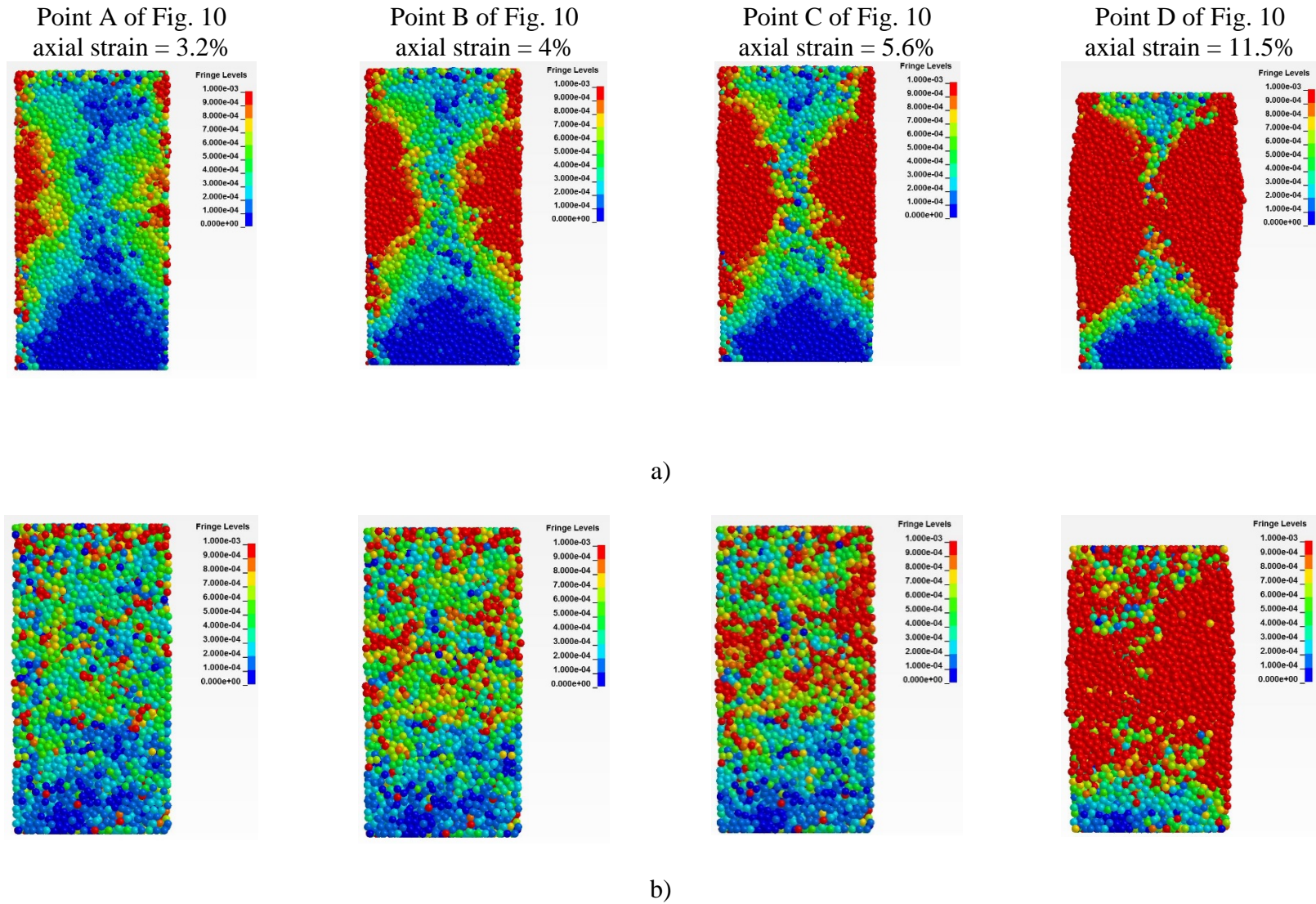
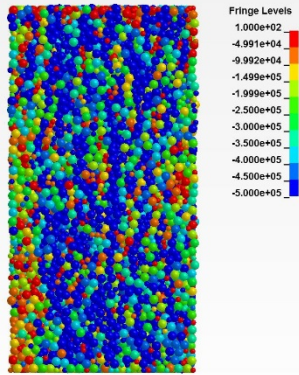
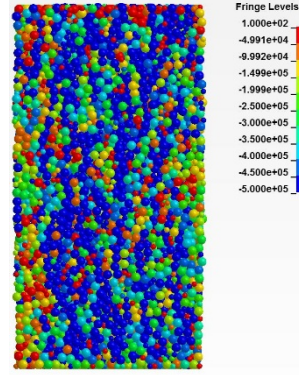


Figure 7.11 Evolution of particle rearrangement and in-plane displacement using the cut planes from Fig. 7.10: a) Sequence of shear deformation patterns in the binary system; b) Formation of homogeneous deformation fields in the monodisperse system

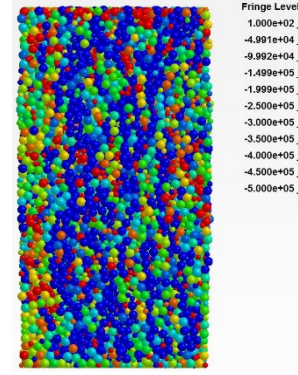
Point A of Fig. 10
axial strain = 3.2%



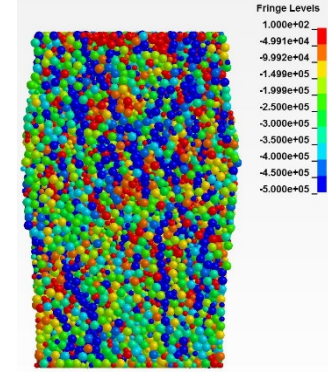
Point B of Fig. 10
axial strain = 4%



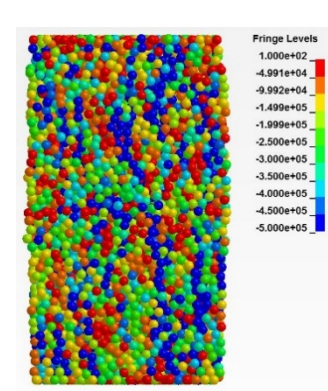
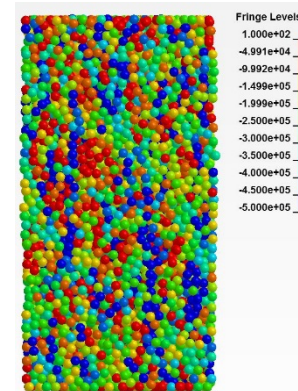
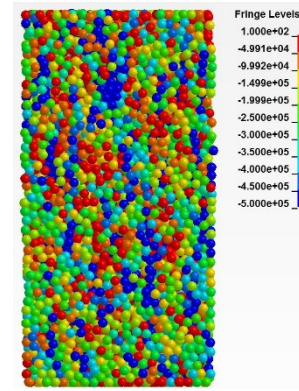
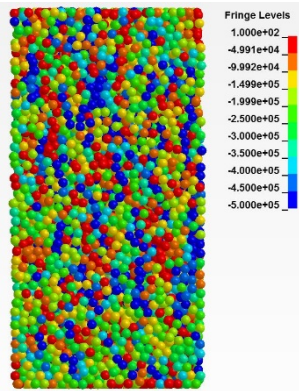
Point C of Fig. 10
axial strain = 5.6%



Point D of Fig. 10
axial strain = 11.5%



a)



b)

Figure 7.12 Development of force chains in the cut planes of Fig. 7.9: networks in color of blue are strong contact forces; green and red particles are spectators: a) Vertical force chains in the binary system; b) Weaker force chains in the monodisperse system

7.4 Continuity Equation, Partitioning, and Averaging Methods

The continuity equation is a statement about the conservation of mass. It expresses the fact that, per unit volume, the sum of all mass flowing in and out per unit time must be equal to the change in mass due to change in density per unit time. The velocity of particles (molecules) of constituent A (relative to the laboratory frame of reference, e.g., the based plate of sand-pile testing) can be denoted v_A . In the frame of reference, the particle mass flow (flux) N_A of constituent A is $N_A = c_A v_A$ where c_A is the particle concentration of A (a number of particle of A/volume). For example, we calculate how many particles of A flow through an area A_c per unit time: Amount of A carried through A_c per unit time $= N_A A_c = c_A v_A A_c$ (particles/time). More generally, for any arbitrary direction of N_A and a differential area dB , the rate of A transport through dB would be: flux of A though $dB = -c_A v_A \cdot n dB$ (particles/time) where n is the outward normal vector to dB . $-v_A \cdot n dB$ is the volumetric flowrate of A (volume/time) passing across dB from “outside” to “inside”, where “outside” is pointed at by the unit normal vector. Multiplying the volumetric flowrate by c_A (the number of particles of A per volume) equals the particles of A passing through dB per unit time. To this end, the volumetric flowrate is related to the total particle number C (irrespective of particle shape and size per volume). That is, $c_A = x_A C$ where x_A is the mass fraction of A. Summing over the mass fractions of all particle types must equal the unity. If we have the total number of different particles present in flow regime n , then $\sum_{i=1}^n x_i = 1$. Similarly, a mass flux of A can be defined as $q_A = \rho_A v_A$ where v_A is the velocity of A. ρ_A is the mass density (point mass) of A (mass of A per volume of flow): $\rho_A = \psi_A \rho$ where ρ is the total mass (the summed mass of all particles, irrespective of particle type, per volume). ψ_A is called the mass fraction of A. Summing the mass fractions of all particle types must equal unity: $\sum_{i=1}^n \psi_i = 1$. In each particle types “ i ” in a multicomponent mixture has a different velocity v_i . As described in Chap. 5, the velocity of each particle (DSE) can be described by a sum of the mean velocity of the mass flow and a component of random motion of each DSE relative to the mean velocity, e.g., an average over the v_i 's in flow regimes: $V = \sum_{i=1}^n x_i v_i$ and $v = \sum_{i=1}^n \psi_i v_i$. V is a volume fraction based average, while v is a mass fraction based average of the individual particles' velocities. Note that if all particles have the same mass m (either per uniform size or per various sizes), then $x_i = \psi_i$, and thus, $V = v$.

From its definition, the mass average velocity is needed to solve the governing equations of momentum, i.e., a property that depends on how much mass is in motion: the amount of momentum per unit volume of a flowing multicomponent mixture (e.g., binary mixture) is $\rho v = m v / \text{volume}$. On the other hand, if in a system there is no bulk flow of particles from one location to another so that, during the mass transfer process the number of particles at each point in space stays the same, i.e., quasi-static testing on a continuum-scale specimen, then $V = 0$.

Based on the volume-fraction based averaging of mass, we test the concept of partitioning in relation to rapid-flow simulations of natural soil using DEM-FEM. We first consider a partitioning by uniform-sized DSEs (i.e., monodisperse system). For example, DSEs with diameter of 3.2 mm are used to partition the continuum-scale volume of sand which particles are much smaller, i.e., $D_{50} = 0.32$ mm. Subsequently, the monodisperse system is subjected to tri-axial compression at a high shearing rate, i.e., high-strain rate (HSR). The detailed description of physical test procedures are given in Yamamuro et al. (2011). Given a weight density and void ratio of the sand, the mass density of the monodisperse system (total mass/total volume per packing density) is set equal to a volume-averaged mass density of the sand over the continuum-scale volume. It is worthy to note that the surface analysis, micro-indentation, nano-indentation, and scratch tests were conducted on the ceramic composite spheres with mean diameter of 3.2 mm, separately from the ceramic proppants used in the centrifuge tests. That is, all numerical model parameters listed in Table 7.1 have physical meaning except the mathematical mass density as per volume fraction averaging. The results presented in Figs. 7.13 and 7.14 indicate an increase in dilation tendency of the granular system with increase in applied strain rate. This phenomenon can be attributed to the inertia by granules in packing density. The rate of changes in dilation, and corresponding shear strength increase of natural soil can, therefore, be simulated using the proposed partitioning and averaging method.

Table 7.1 Model parameters for DSEs that are used in the demonstration of partitioning

Parameter	Value	Units
Mass density	1680	Kg/m ³
Young's Modulus	550	MPa
Poisson's ratio	0.27	--
Sliding friction	1.53	--
Rolling friction	0.153	--
Normal damping coefficient	0.7	--
Tangential damping coefficient	0.4	--
Ratio of tangential to normal contact stiffness	0.84	--
Applied high strain rate	900, 1750	% per second
Confining stress	98	kPa

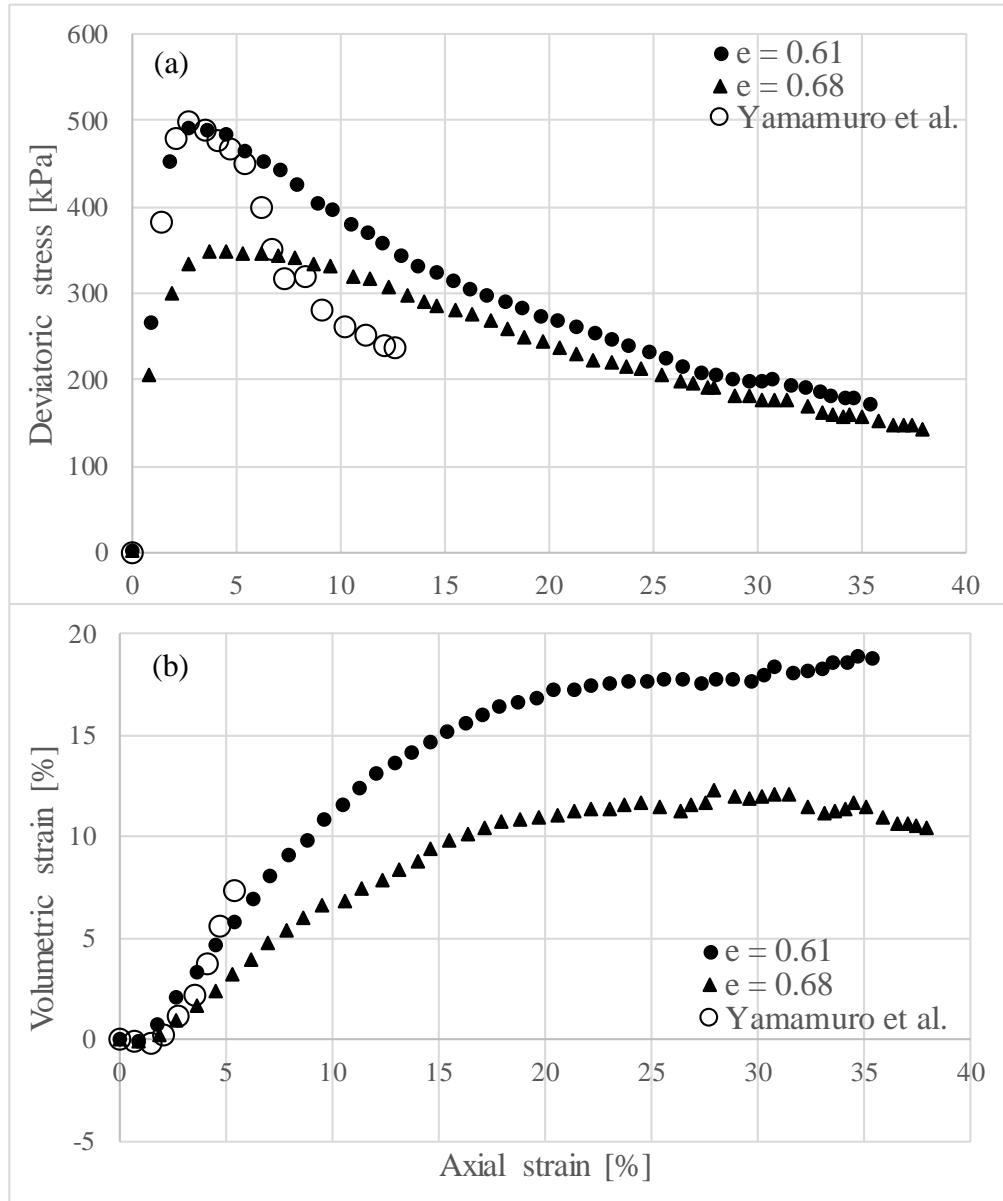


Figure 7.13 Comparison to laboratory test data at strain rate of 1750% per second: (a) Deviatoric stress vs axial strain; (b) Volumetric strain vs axial strain

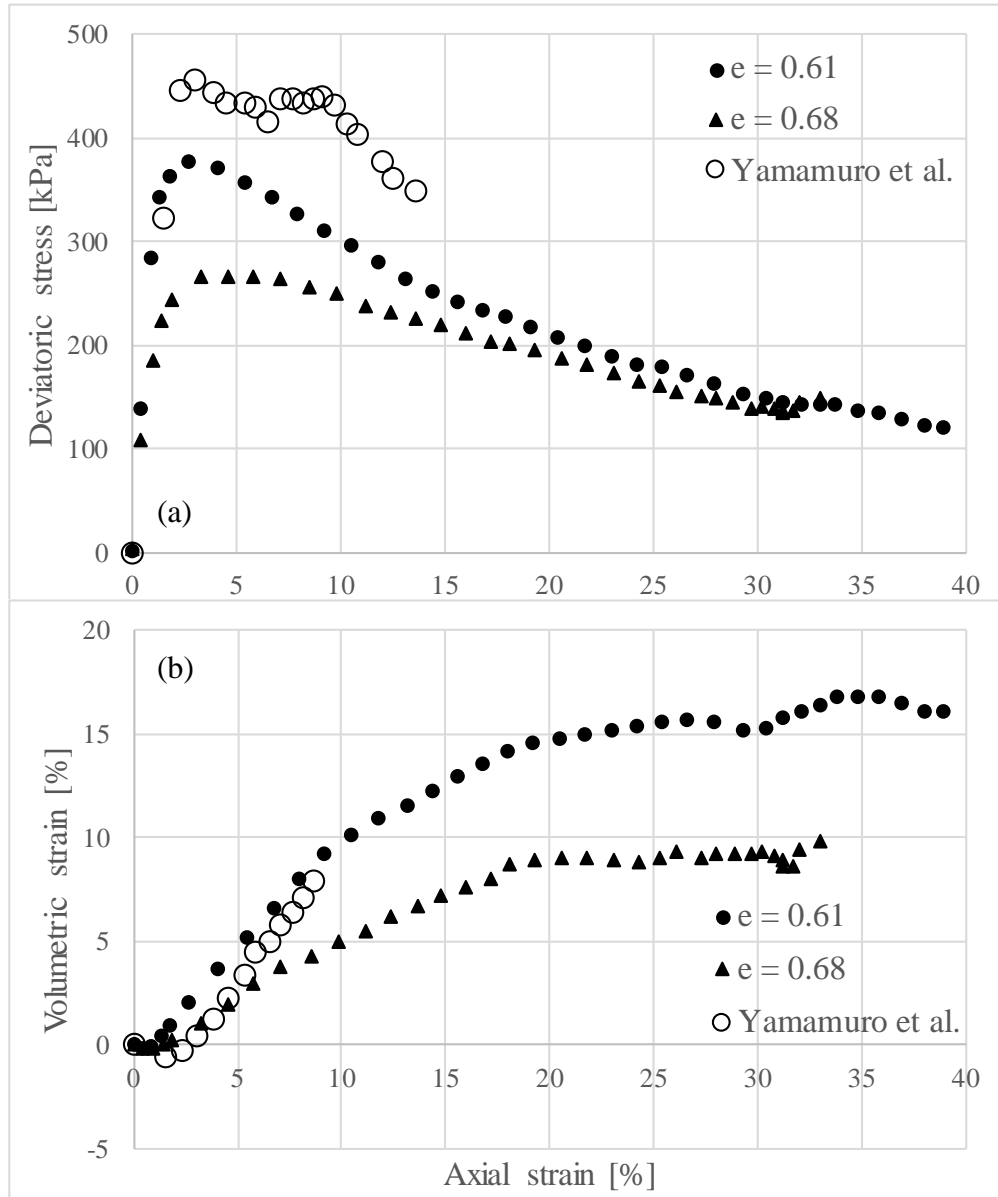


Figure 7.14 Comparison to laboratory test data at strain rate of 900% per second: (a) Deviatoric stress vs axial strain; (b) Volumetric strain vs axial strain

7.5 Heat and Particle Breakage

So far, our task of finding solutions of the continuity equation and the equations of motion has been in virtue of the conservation laws in which conservation of mass, momentum and energy (i.e., first law of Thermodynamics). Ultimately, thermodynamic states of the mesoscopic volume are to be simulated in accordance with local thermodynamic equilibria at the constituent scale.

In particular, friction occurs whenever two solid bodies slide against each other. It takes place by a variety of mechanisms in and around the real area of contact between the sliding or rolling/sliding bodies. It is through frictional processes that velocity differences between the bodies

are accommodated. It is also through these processes that mechanical energy is transformed into internal energy or heat, which causes the temperature of the sliding bodies to increase. The exact mechanism by which this energy transformation occurs may vary from one sliding situation to another, and the exact location of that transformation is usually not known for certain. It is known that solid friction and related frictional processes, including frictional heating, are concentrated within the real area of contact between two bodies in relative motion. It is conjectured that most energy dissipation occurs in the bulk solid beneath the contact region by plastic deformation processes. Some experimental work has shown that at least 95% of the energy dissipation occurs within the top 5 μm of the contacting bodies (Kennedy, 1982). Although there may be disagreement about the exact mechanism of the energy transformation, most tribologists agree that nearly all of the energy dissipated in frictional contacts is transformed into heat. This energy dissipation, called frictional heating, is responsible for increases in the temperatures of the sliding bodies, especially within the contact region on their sliding surfaces where the temperatures are highest. For the purposes of proposal, it will be assumed that all frictional energy is dissipated as heat which is conducted into the contacting bodies at the actual contact interface.

Upon establishment of scale-interrelated boundary-valued solutions to the equations of motion of the binary system, i.e., the prerequisite of the conservation of energy, all the work done in the meso volume should further include *heat* Q generated between all the local contact surfaces with a relative velocity (v). A total amount of heat produced by all the frictional work may be written in a form (p. 34 of Part I of Bowden and Tabor, 1950):

$$Q \propto \frac{\mu F_n g v}{J} \square \sum_i^n \left(\frac{\mu_i f_n g v_i}{J_i} \right) \quad (\text{in unit of calories per second}) \quad (7.1)$$

where μ is coefficient of kinetic friction, F_n is normal force acting on control-volume DSE, g is constant of gravity, J is mechanical equivalent of heat, f_n is local normal force acting on constituent DSEs, and the subscript “ i ” denotes index to particle local contact. Accordingly, in explicit time-integration DEM, the heat generated during a time step Δt is computed as

$$q \square \chi \mu f_n v_t \Delta t \quad (\text{in unit of calories}) \quad (7.2)$$

where $\chi \leq 1$ for portion of frictional work converted to heat, and v_t is local slip velocity. The evolution of the temperature of particle i is computed as

$$\Delta T_i = \frac{\sum_j \left(H_c (T_j - T_i) + \frac{1}{2} \chi \mu F_n V_t \right) \Delta t}{m_i C_i} \quad (7.3)$$

where H_c is contact conductance between particles, T is temperature, m is point mass, and C is heat capacity.

The impact heat transfer to granular masses is a complex, challenging modeling task because the thermal contact resistance between the penetrator and the collector (granular particles) are unknown. The available theoretical treatment of the heat transfer between two colliding media

is based on the Hertzian theory of elastic contact in semi-infinite half-spaces. We explore a hypothesis for which heat transferred by conduction during the impact of a projectile, and subsequent frictional contacts with the surrounding DSEs, can be equated to a factored product of shear stresses and plastic strain rate per a volumetric heat capacity at the macroscopic scale; “Factor” is a constant that gives the fraction of plastic deformation to be converted to heat energy and vice versa. Alternatively stated, thermodynamic states can be explicitly accounted for in solutions of the equations of motion of the UXO-soil systems include probabilistic kinetic energy conversion to heat by introducing numerical energy dispersion through meso-scale damping to drive predictions of overall control-volume energy balances. Thus, the likelihood of bond failures and the degree of (numerical) heat energy conversion can be investigated in a parametric study of the “Factor.” Note that this approach permits investigation of decreases in bond failure rates with reduction in particle size (per simulation of greater numerical bond strengths). Additionally, increases in bond failure rates can be investigated since strain rates (both normal and tangential) are considered among the simulation set, over ranges of impact velocities and obliqueness. In summary, it is feasible to explicitly simulate heat energy loss in the development of rapid-flow regimes (shown in Chap. 5). Data per measurement on the surface temperatures of actual contacting granules becomes important if the inclusion of tribological components is to satisfy the conservation of energy. In addition, frictional heating has such an important influence on the rheological contact behavior of the frictional-sliding systems that ultimately contribute to the generation of stopping forces against the UXO penetration. Frictional heating must be considered in interpreting the results of the energy balances both at local and global scales.

Irrecoverable energy dissipation due to breakages of brittle grains is also to be incorporated in the control-volume DSEs. First, the mesoscopic DSE is further discretized into two separate discrete spheres, but these sub-spheres are numerically linked together, i.e., numerical bonds are defined (Fig. 7.15). This numerical approach simulates a mathematical link between two discrete spheres together at a common interface. Parts linked together in this manner may still deform and respond to tensile force, as the interface between them, but the edges of the two parts remain linked to each other on a point-by-point (or node-by-node) basis.

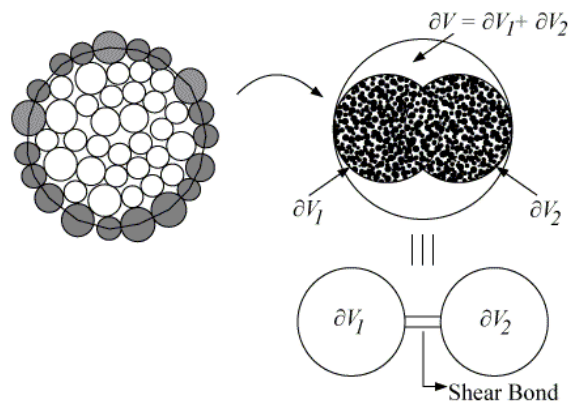


Figure. 7.15 Discrete bond between two micro spheres of the mesoscopic volume

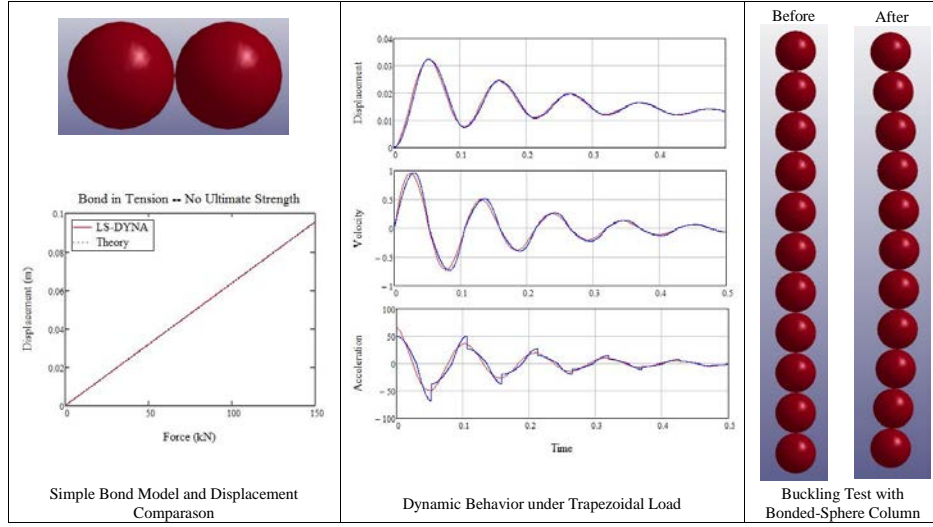
This numerical linkage would be broken when a rate of change in principal stresses at the mesoscopic level exceeds the predetermined bond shear strength. That is, at a point on the interface

boundary may the two tied parts separate from each other, even though the interface boundary element itself may deform. The “plastic” volumetric deformation rate of the macroscopic soil volume associated with successive splitting of the sub-spheres is then simulated and compared to a fractal distribution of particle sizes, collected from one-dimensional compression test data (available from the literature). For demonstration purposes, an example of Euler buckling analysis of granular column is shown in Fig. 7.16 where a single-degree-of-freedom (SDOF) dynamic system of bonded DSEs is subjected to external excitation. A closed-form solution indicates that the bonded DSE modelling is feasible. In the future, fracture toughness and crush strength of natural grains are represented by shear and/or tensile bonds, and breakage of bonds produces work done in the control-volume DSEs alongside energy loss due to friction-induced heat energy.

Finally, both synthesis and critical analysis of the numerically generated and physically measured data from continuation phases are to be carried out in establishing practical conclusions and recommendations for field applications. More specifically, those parameters which hold greatest significance can be identified by: 1) Tabulating numerical predictions of the UXO-soil system response alongside model input values (in the form of functionals and database based on correlations of particle size, surface roughness, and shape factor in generation of stopping forces); 2) Identifying trends in the tabulations of input values for a single-degree-of-freedom equation of motion of catalogued projectile with respect to temporal functions of effective mass representing rapid-flow regime, viscous damping term for dragging, coulombic damping term for frictional forces, and rate-dependent shear resistance, and then 3) provide terminal penetration-depth quantities with standard deviation per in-situ relative density. Those parameters that retain significance (i.e., give indications of meaningful input-response trends) when processed in this way can be directly packaged (via graphs and tables) into graphical guidelines for use by the aforementioned stakeholders. In addition, this physics-based multi-scale quantification can be implemented in a modularized programming such as dynamic link libraries (DLLs), which will be made functionally compatible with previous research findings.

For instance, given deterministic values of soil shearing resistance, corresponding penetration depths can be evaluated in comparison to cataloged and empirical parameter values of the existing design guidelines (e.g., “Demonstration of UXO-PenDepth for the Estimation of Projectile Penetration Depth,” Environmental Security Technology Certification Program (ESTCP) Project MR-0806, 2010). The successful outcome of the proposed research is to develop a design-oriented simplified analysis software:

- Cultivating design-oriented practical parameters to account for development of DLLs which can be functionally integrated (as modules) into input algorithms for existing prediction tools, e.g., a computational module for databased input parameters equivalent to the soil penetrability index (SNUM) of the UXO-PenDepth software; or,
- Cultivating design-oriented practical recommendations to incorporate the research findings as an impact-induced forcing algorithm module for projectile geo-material response into existing modules of the software PENCVR3D.



(a) Analysis of bonded DSEs column in analogy to Euler beam buckling

For time $t \leq T$, the loading function,

$$F(t) = \frac{F}{T} \cdot t$$

Velocity,

$$\text{Quasi-static: } v_s(t) = u'_s(t) = \frac{F}{kT}$$

$$\text{Dynamic: } v_d(t) = \frac{F}{kT} [1 - \cos(\omega t)]$$

External work,

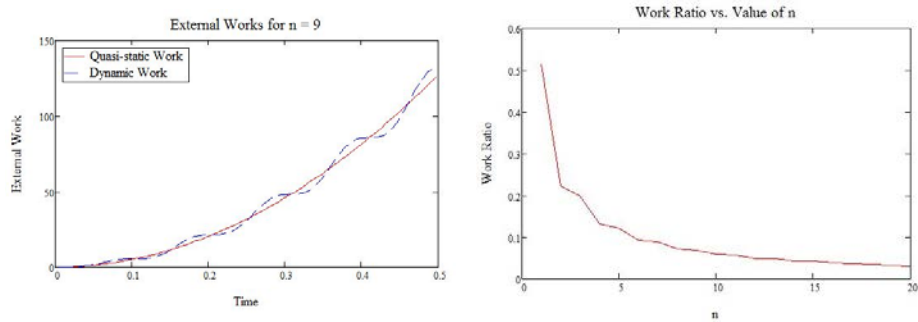
$$\text{Quasi-static: } W_s(t) = \int_0^t v_s(\tau) F(\tau) d\tau = \frac{F^2}{2kT^2} \cdot t^2$$

$$\text{Dynamic: } W_d(t) = \int_0^t v_d(\tau) F(\tau) d\tau = \frac{F^2}{2kT^2} \cdot t^2 - \frac{F^2}{kT^2\omega^2} [\omega t \sin(\omega t) + \cos(\omega t) - 1]$$

Local optimum of ratio δ ,

$$\text{opt}(\delta) = \text{opt} \left| \frac{W_s(t) - W_d(t)}{W_s(t)} \right| = \frac{\left| \left(\frac{\pi}{2} + n\pi \right) \cdot \sin \left(\frac{\pi}{2} + n\pi \right) - 1 \right|}{\frac{1}{2} \left(\frac{\pi}{2} + n\pi \right)^2}$$

$$n \leq \frac{\omega T}{\pi} - \frac{1}{2}$$



(b) Localized (numerical) resonance in a column of bonded DSEs during external excitation

Figure 7.16 Bonded DSEs and its application to analysis of granular structure

CHAPTER 8

REFERENCES

- Abedi, M. (2009). Effect of Restitution Coefficient on Inertial Particle Separator's Efficiency. Mechanical Engineering, Northeastern University, Boston, MA, M.S. Thesis.
- Adams, G.G. and Nosonovsky, M., (2000). "Contact modeling-forces", Tribology International, 33, pp. 431-442.
- Alshibli, K. A. and Alsaleh, M. I. (2004). "Characterizing surfaceroughness and shape of sands using digital microscopy." Journal of Computing in Civil Engineering, Vol. 18, No. 1, pp. 36-45.
- Anthony, J. L. and Marone, C. (2005). "Influence of particle characteristics on granular friction." Journal of Geophysical Research, Vol. 110, B08409.
- Arasan, S., Akbulut, S., and Hasiloglu, A. S. (2011). "The Relationship between the Fractal Dimension and Shape Properties of Particles." KSCE Journal of Civil Engineering, Vol. 15, No. 7, pp. 1219-1225.
- Archard, J.F., (1957). "Elastic Deformation and the Laws of Friction", Proceedings of the Royal Society of London. Series A, Mathematical and Physical, 243, 1223, pp. 190-225.
- Arya, L. M. and Paris, J. F. Paris. (1981). "A Physicoempirical Model to Predict the Soil Moisture Characteristic from Particle-Size Distribution and Bulk Density Data." Journal of Soil Science Society of America, Vol. 45, pp. 1023-1030.
- ASTM. (2007). "Standard test method for unconsolidated-undrained triaxial compression test on cohesive soils". ASTM Designation D2850-03a, ASTM International, West Conshohocken, Pennsylvania, USA.
- ASTM. (2011). "Standard test method for consolidated drained triaxial compression test for soils". ASTM Designation D7181, ASTM International, West Conshohocken, Pennsylvania, USA.
- ASTM. (2012). "Standard test method for direct shear test of soils under consolidated drained conditions". ASTM Designation D3080/D3080M, ASTM International, West Conshohocken, Pennsylvania, USA.
- Barthel E. (1998). "On the Description of the Adhesive Contact of Spheres with Arbitrary Interaction Potentials." J. Colloid Interface Sci., Vol. 200, pp. 7-18.
- Belheine, N., Plassiard, J.-P., Donze F.-V., Darve, F., Seridi A. (2009). "Numerical simulation of drained triaxial test using 3D discrete element modeling". Computers and Geotechnics, 36, pp. 320-331.
- Bhushan B. (2001). "Introduction to Tribology". John Wiley & Sons.
- Bi, D., Zhang, J., Chakraborty, B, and Behringer, R. P. (2011). "Jamming by Shear." Nature, Vol. 480, pp. 355-358. doi:10.1038/nature10667

- Bowden, F. P. and Tabor, D. (1950) Friction and lubrication of solids. Oxford University Press.
- Briaud, J. L. and Tucker, L. (1985). "Piles in Sand – A Method Including Residual Stresses." *Journal of Geotechnical Engineering*, ASCE 110, No. 11, pp. 1666-1679.
- Bromwell, L.G. (1966). The friction of quartz in high vacuum. Department of Civil Engineering, Massachusetts Institute of Technology, Cambridge, Mass. Research report R66-18.
- Bhushan, B. (2013) Introduction to Tribology. 2nd Ed. John Wiley & Sons, New York.
- Carter, J. P. and Kulhawy, F. H. (1992). "Analysis of Laterally Loaded Shafts in Rock." *Journal of Geotechnical Engineering*, ASCE 118, No. 6, 839-855.
- Cates, M. E., Wittmer, J. P., Bouchaud, J.-P., and Claudin P. (1998). "Jamming, Force Chains, and Fragile Matter." *Physical Review Letters*, Vol. 81, No. 9, pp. 1841-1844.
- Chan, C. Y. and Page, W. P. (1997). "Particle fractal and load effects on internal friction in powders." *Powder Technology*, Vol. 90, No. 3, pp.259-266.
- Cheng, Y. P., Nakata, Y., and Bolton, M. D. (2003). "Discrete Element Simulation of Crushable Soil." *Geotechnique*, Vol. 53, No. 7, pp.633-641.
- Chung, Y.C., and Ooi, J.Y. (2006). "Confined Compression and Rod Penetration of a Dense Granular Medium: Discrete Element Modelling and Validation", *Modern Trends in Geomechanics*, pp. 223-239.
- Cil, M. B., & Alshibli, K. A. (2014). "3D analysis of kinematic behavior of granular materials in triaxial testing using DEM with flexible membrane boundary". *Acta Geotechnica*, 9(2), 287-298.
- Cleary, P., Prakash, M. (2004). "Discrete-element modelling and smoothed particle hydrodynamics: potential in the environmental sciences". *Philosophical Transactions of the Royal Society of London*, 362, 1822, pp. 2003-2030, 2004.
- Crowe, C., Sommerfeld, M. and Tsuji, Y. (1997). *Multiphase flows with droplets and particles*. CRC Press, Boca Raton.
- Cundall, P.A. & Strack, O.D.L. (1979). "A discrete numerical model for granular assemblies", *Geotechnique*, 29, No. 1, pp. 47-65.
- Cundall, P.A. (2001). "A discontinuous future for numerical modelling in geomechanics?", *Geotechnical Engineering*, 149(1), pp. 41-47
- Daphalapurkar, N. P., Wang, F., Fu., B., Lu, H. and Komanduri, R. (2011). "Determination of Mechanical Properties of Sand Grains by Nanoindentation". *Experimental Mechanics*, 51, pp. 719-728.

- Das, M. B. (2007). Principles of Foundation Engineering. Seventh edition, Cengage Learning, USA.
- Davidson, M., Chung, J., and Le, V. (2015). "Volume-averaged stress states for idealized granular materials using unbonded discrete spheres in LS-DYNA", 15th LS-DYNA European Conference, Wurzburg, Germany, June 15-17.
- Derjaguin B.V., Muller V.M. & Toporov Yu.P. (1975). "Effect of Contact Deformations on the Adhesion of Particles." J. Colloid Interface Sci., Vol. 53, pp. 314-326.
- Dowson, D. (1979). History of tribology. Longman, London.
- Duncan, M. J., Wright G. S. (2005). "Soil Strength and Slope Stability". John Wiley & Sons Inc., printed in USA.
- Estrada, N., Azéma, E., Radjai, F., and Taboada, A. (2013). "Comparison of the effects of rolling resistance and angularity in sheared granular media." Powder and Grains, Sydney, Australia. pp. 891-894.
- Faraone, M., Chung, J., and Davidson, M. (2015). "Discrete element analysis of idealized granular geometric packing subjected to gravity", 15th LS-DYNA European Conference, Wurzburg, Germany, June 15-17.
- Finney, J. L. (1970). "Random Packings and the Structure of Simple Liquids I. the Geometry of Random Close Packing." Proc. R. Soc. London, Ser. A, Vol.319, pp.479.
- Fischer, P., Romano, V., Weber, H. P., Karapatis, N. P., Boillat, E., Glardon, R. (2003). "Sintering of Commercially Pure Titanium Powder with a Na:YAG Laser Source," Acta Materialia, Vol. 51, pp.1651-1662.
- Fragaszy, R.J., & Taylor, T.A. (1988). "Centrifuge Modelling of Projectile Penetration in Granular Soils." Proc. International Conference Centrifuge 88, Balkema, Rotterdam, pp. 451-456
- Garnier, J., Gaudin, C., Springman, S. M., Culligan, P. J., Goodings, D. J., Konig, D., Kutter, B. L., Phillips, R., Randolph, M., and Thorel, L. (2007). "Catalogue of Scaling Laws and Similitude Questions in Geotechnical Centrifuge Modelling." *International Journal of Physical Modelling in Geotechnics*, 7(3), 1-23.
- Greenwood, J.A. and Williamson, J.B.P., (1966). "Contact of nominally flat surfaces", Proc. R. Soc. London A, 295, pp. 300-319.
- Grima, A. P., Mills, B. P. Wypych, P. W. (2010). "Investigation of Measuring Wall Friction on a Large Scale Wall Friction Tester and the Jenike Direct Shear Tester," *3rd International conference exhibition BulkSolids Europe 2010* (pp. 1-14). Wurzburg, Germany: Gerd Kielburger.

- Guyont, E., Oger, L., and Plona, T. J. (1987). "Transport Properties in Sintered Porous Media Composed of Two Particle Sizes." *Journal of Physics. D:Applied Physics*, Vol. 20, pp. 1637-1644.
- Han, Z., Teng, H., and Wang, J. (2012). "Computer Generation of Sphere Packing for Discrete Element Analysis in LS-DYNA", 12th International LS-DYNA Conference.
- Hanna, T. H. and Tan, R. H. S. (1973). "The Behavior of Long Piles under Compressive Loads." *Canadian Geotechnical Journal*, 10, No. 3, 311-340.
- Hardy, W. and Doubleday, I. (1922). "Boundary Lubrication. The Temperature Coefficient", *Proceedings of the Royal Society of London. Series A, Containing Papers of a Mathematical and Physical Character*, 1922-09-01. 101, 713, pp. 487-492.
- Helland, P. E. and Holmes, M. A. (1997). "Surface Textural Analysis of Quartz Sand Grains from ODP Site 918 Off the Southeast Coast of Greenland Suggests Glaciation of Southern Greenland at 11 Ma." *Palaeogeography, Palaeoclimatology, Palaeoecology*, Vol. 135, pp. 109-121.
- Helland, P. E., Huang, Pei-Hua, and Diffendal, R. F. (1997). "SEM Analysis of Quartz Sand Grain Surface Textures Indicates Alluvial/Colluvial Origin of the Quaternary "Glacial" Boulder Clays at Huangshan (Yellow Mountain), East-Central China." *Natural Resources, Quarterly Research*, Vol. 48, pp. 177-186.
- Hertz, H. (1882). "On the contact of elastic solids". *Journal fur die Reine und Anagewandte Mathematik*, Vol. 92, pp. 156-171.
- Hidalgo, R. C., Grosse, C., Kun, F., Reinhardt, H. W., and Herrmann, H. J. (2002). "Force Chains in Granular Packings." *Physical Review Letters*, 89:205501.
- Holloway, M., Clough, G. W., and Vesic, A. S. (1978). "A Rational Procedure for Evaluating the Behavior of Impact-Driven Piles." *ASTM Symposium on Behavior of Deep Foundations*, ed. R. Lundgren, Special Technical Publication STP 670, 335-357.
- Horn, H.M. (1961). An investigation of the frictional characteristics of minerals. Department of Civil Engineering, University of Illinois, Urbana, Illinois. Ph.D. Dissertation.
- Horn, H.M. and Deere, D.U. (1962). "Frictional characteristics of minerals", *Geotechnique*, 12, 4, pp. 319-335.
- Hosseiniia, E. S. and Mirghasemi, A. A. (2006). "Numerical simulation of breakage of two-dimensional polygon-shaped particles using discrete element method." *Powder Technology*, Vol. 166, pp. 100-112.
- Houlsby, G. T. (1991). How the Dilatancy of Soils Affects Their Behavior. The 10th European Conference on Soil Mechanics and Foundation Engineering, Florence, Italy, May 28.

- Israelachvili, J.N. (2011). *Intermolecular and Surface Forces*, Elsevier: Waltham, MA.
- Iwashita, K. and Oda, M. (1998). "Rolling Resistance at Contacts in Simulation of Shear Band Development by DEM." *ASCE Journal of Engineering Mechanics*, Vol. 124, No.3, pp. 285–292.
- Jodrey, W.S. and Tory, E.M. (1981). "Computer Simulation of Isotropic, Homogeneous, Dense Random Packing of Equal Spheres, *Powder Technology*, Vol. 30, pp.111-118.
- John, R. L. A.: Editor (1982). *Sedimentary Structures, Their Character and Physical Basis Volume 1*. Elsevier, New York.
- Johnson K.L. (1985). *Contact mechanics*. Second Edition, Cambridge University Press, New York.
- Johnson K. L., Kendall K. & Roberts A. D. (1971). "Surface Energy and the Contact of Elastic Solids." *Proc. Roy. Soc., London A*, Vol. 324, pp. 301-313.
- Jensen, A., Fraser, K., and Laird, G. (2014). "Improving the precision of discrete element simulations through calibration models". 13th International LS-DYNA Users Conference, Michigan.
- Karajan, N., Han, Z., Teng, H., and Wang, J. (2012). "Particles as discrete elements in LS-DYNA: interaction with themselves as well as deformable or rigid structures" 11th LS-DYNA Forum, Ulm, October 10.
- Karajan, N., Han, Z., Teng, H., and Wang, J. (2014). "On the parameter estimation for the discrete-element method in LS-DYNA." 13th International LS-DYNA Users Conference, Michigan.
- Kim, Tae-Hyung. (2001). "Moisture-Induced Tensile Strength and Cohesion in Sand." Doctoral dissertation, University of Colorado.
- Kishida, H. (1967). "Ultimate Bearing Capacity of Piles Driven into Loose Sand." *Soil and Foundations*, 7, No. 3, 20-29.
- Krinsley, D.H. and Doornkamp, J.C. (1973). *Atlas Of Quartz Sand Surface Textures*. Cambridge University Press.
- Krumbein W. C. (1941). "Measurement and Geological Significance of Shape and Roundness of Sedimentary Particles." *Journal of Sedimentary Petrology*, Vol. 1, No. 2, pp. 64-72.
- Kolay, E. and Kayaball, K. (2006). "Investigation of the effect of aggregate shape and surface roughness on the slake durability index using the fractal dimension approach." *Engineering Geology*, Vol. 86, No. 4, pp. 271-284
- Konopinski, D.I., Hudziak, S., Morgan, R.M., Bull, P.A., and Kenyon A.J. (2012). "Investigation of Quartz Grain Surface Textures by Atomic Force Microscopy for Forensic Analysis". *Forensic Science International*, Vol. 223, pp. 245-255.

- Krumbein, W. C. (1941). "Measurement and Geological Significance of Shape and Roundness of Sedimentary Particles." *Journal of Sedimentary Petrology*, 11, pp. 64-72.
- Krumbein, W. C. and Silos, L. L. (1963). *Stratigraphy and Sedimentation*. 2nd Ed., W. H. Freeman, San Francisco.
- Kummerfeld, J. K., Hudson, T. S., and Harrowell, P. (2008). "The Densest Packing of AB Binary Hard-Sphere Homogenous Compounds across all Size Ratios", *the Journal of Physical Chemistry C*, 115, 19037-19040.
- Kutter, B. L. (1995). "Recent advances in centrifuge modeling of seismic shaking." *third international conference on recent advances in geotechnical earthquake engineering and soil dynamics* Rolla, MO, 927-942.
- Lambe, T. W. and Whitman, R. V. (1969) *Soil Mechanics*, John Wiley & Sons, New York.
- Lieu, K.P. (2013). *Sediment Diagenesis and Characteristics of Grains and Pore Geometry in Sandstone Reservoir Rocks from a Well of the North German Basin*. Crystallography Section, Ludwig Maximilians University of Munich, Munich, Germany Ph.D. Dissertation.
- Livingston, C. W., and Smith, F. L. (1951). "Bomb Penetration Project." Colorado School of Mines Research Foundation, Inc., Golden, Colorado, 426.
- LSTC. (2014). *LS-DYNA Theory Manual*. Livermore Software Technology Corporation, Livermore CA.
- LSTC. (2016). *LS-DYNA Keyword User's Manual, Volume I*. Livermore Software Technology Corporation, Livermore CA.
- Lee, M. D. (1992). *The Angles of Friction of Granular Fills*. Department of Civil Engineering, University of Cambridge, UK. Ph.D. Dissertation.
- Liu. A. and Nagel, S. (1998). "Jamming is not just cool any more." *Nature*, 396, pp. 21-22.
- Luding, S. (2008). "Introduction to discrete element methods: basic of contact force models and how to perform the micro-macro transition to continuum theory". *European Journal of Environmental and Civil Engineering*, 12 (7-8). pp. 785-826.
- Mair, K., Frye, K. M., and Marone, C. (2002). "Influence of grain characteristics on the friction of granular shear zones." *Journal of Geophysical Research*, 107 (B10-2219), 4-1 to 4-9.
- Majmudar, T. S., Sperl, M., Luding, S., and Behringer, R. P. (2007). "Jamming Transition in Granular Systems." *Physical Review Letters*, Vol. 98: 058001.
- Malone, F.K., Xu, B.H. (2008). "Determination of contact parameters for discrete element method simulations of granular systems". *Particuology* 6, 521-528.

- Meloy, T. P. (1977). "Fast Fourier Transforms Applied to Shape Analysis of Particle Silhouettes to obtain Morphological Data." *Powder Technology*, Vol. 17, pp. 27-35.
- Meyerhof, G. G. (1959). "Compaction of Sands and Bearing Capacity of Piles." *Journal of the Soil Mechanics and Foundation Division, ASCE* 85; SM 6; 1-29.
- Meyerhof, G. G. (1963). "Some Recent Research on the Bearing Capacity of Foundations." *Canadian Geotechnical Journal*, 1, No. 1, 16.
- Meyerhof, G. G. (1976). "Bearing capacity and settlement of pile foundations." *Journal of Geotechnical Engineering, ASCE*, 102(3), 195-228.
- Mindlin, R.D. (1949). "Compliance of elastic bodies in contact". *ASME Journal of Applied Mechanics* 16, pp 259-268.
- Mitchell, J. K., and Soga K. (2005). *Fundamentals of Soil Behavior*, 3rd Ed., John Wiley & Sons.
- Mitchell, R. J. (1991). "Centrifuge modelling as a consulting tool." *Canadian Geotechnical Journal*, 28(1), 162-167.
- Moscinski, J., Bargie, M., Rycerz, Z. A., Jacobs, P. W. M. (1989). "The Force-biased Algorithm for the Irregular Close Packing of Equal Hard Spheres.", *Molecular Simulation*, Vol. 3, pp. 201-212.
- Murzenko, Y. N. (1965). "Experimental results on the distribution of normal contact pressure on the base of a rigid foundation resting on sand", *Soil Mechanics and Foundation Engineering*, Volume 2, Issue 2, pp 69-73.
- Nadukuru, S.S. (2013). *Static Fatigue: A Key Cause of Time Effects in Sand*. Department of Civil Engineering, University of Michigan, Michigan. Ph.D. Dissertation.
- Navarro, A. H., de Souza Braun, P. M. (2013). "Determination of the normal spring stiffness coefficient in the linear spring-dashpot contact model of discrete element method". *Powder Technology* 246, 707-722.
- Nielsen, B. D. (2004). *Nondestructive Soil Testing Using X-Ray Computed Tomography*. Department of Civil Engineering, Montana State University, Montana. M.S. Thesis.
- Obermayr, M., Vrettos, C., Kleinaert, J., Eberhard, P. (2013). "A Discrete Element Method for assessing reaction forces in excavation tools." *Congreso de Métodos Numéricos en Ingeniería*, 25-28 June, Bilbao, Spain.
- Olliver, W. C., and Pharr, G. M., (2003) "Measurement of hardness and elastic modulus by instrumented indentation: Advances in understanding and refinements to methodology". *Journal of Material Research*, Vol. 19, No. 1, 3-20.

- Ollagnier A., Doremus P., and Didier Imbault. (2007). "Contact particles calibration in a discrete element code". <http://people.3sr-grenoble.fr/users/fdonze/articles/GED_2007/Article-C.pdf>.
- Omidvar, M. et. al. (2014). "Response of granular material to rapid penetration". *International Journal of Impact Engineering*, Vol. 66, pp. 60-82
- Ostojic S., Somfai E. & Nienhuis B. (2006). "Scale Invariance and Universality of Force Networks in Static Granular Matter." *Nature*, Vol. 439, pp. 828-830.
- O'Sullivan, C., Bray, J. D., & Riemer, M. (2004a). "Examination of the response of regularly packed specimens of spherical particles using physical tests and discrete element simulations". *Journal of engineering mechanics*, 130(10), 1140-1150.
- O'Sullivan, C., Cui, L., & Bray, J. D. (2004b). "Three-dimensional discrete element simulations of direct shear tests". *Numerical Modeling in Micromechanics via Particle Methods*, 373-382.
- O'Toole, P. I. and Hudson, T. S. (2011). "New High-Density Packings of Similarly Sized Binaries", *the Journal of Physical Chemistry C*, 115, 19037-19040.
- Parks, G.A. (1984). "Surface and Interfacial Free Energies of Quartz". *Journal of Geophysical Research*, Vol. 89, No. B6, pp. 3997-4008.
- Plassiard, J. P., Belheine, N., and Donz, F. V. (2009). "A spherical discrete element model: calibration procedure and incremental response." *Granular Matter*, Vol. 11, pp. 293-306.
- Ponitzsch, A., Nofz, M., Wondraczek, L., Deubener, J., (2016). "Bulk elastic properties, hardness and fatigue of calcium aluminosilicate glasses in the intermediate-silica range", *Journal of Non-Crystalline Solids*, 434, 1-12
- Popov, V.L. (2010). *Contact Mechanics and Friction*, Springer, Berlin.
- Popov, V. L. and Gray, J. A. T. (2012). "Prandtl-Tomlinson model: History and applications in friction, plasticity, and nanotechnologies." *Journal of Applied Mathematics and Mechanics*, Vol. 92, No. 9, pp. 683-708.
- Powers, M. C. (1953). "A New Roundness Scale for the Sedimentary Particles." *Journal of Sedimentary Petrology*, 23, pp. 117-119.
- Rabinovich, Y. I., Esayanur, M. S., and Moudgil, B. M. (2005). "Capillary forces between two spheres with a fixed volume liquid bridge: theory and experiment". *Langmuir*, 21(24):10992-7.
- Rabinowicz, E. (1995). "The intrinsic variables affecting the stick-slip process." *Proc. R. Soc. London*. Vol. 71, pp. 668-675.

- Radchik, V.S., Ben-Nissan, B., and Muller, W.H. (2002). "Theoretical Modeling of Surface Asperity Depression Into an Elastic Foundation Under Static Loading", *Journal of Tribology*, 124, pp. 852-877.
- Randolph, M. F., Carter, J. P., and Wroth, C. P. (1979). "Driven Piles in Clay – the Effects of Installation and Subsequent Consolidation." *Géotechnique*, 29, 361-393.
- Randolph, M. F., Dolwin, J., and Beck, R. (1994). "Design of Driven Piles in Sand." *Géotechnique*, 44, 427-448.
- Rogers, C. A. (1958). "The Packing of Equal Spheres." *Proceedings of the Royal Society of London. Mathematical Society*, Vol. 3, No. 8, pp. 609-620.
- Rotter, J. M., Holst, F. G., Ooi, J. Y., and Sanad A. M. (1998). "Silo pressure predictions using discrete-element and finite-element analyses." *Philosophical Transactions of the Royal Society of London. A*, Vol. 356, pp. 2685-2712.
- Rowe, P. W. (1962). "The stress-dilatancy relation for static equilibrium of an assembly of particles in contact". *Proceedings of the Royal Society of London A: Mathematical, Physical and Engineering Sciences*, Vol. 269, No. 1339, pp. 500-527.
- Russell, R. D. and Taylor, R. E. (1937). "Roundness and shape of Mississippi River sands." *Journal of Geology*, Vol. 45, No. 3, pp.225-267.
- Salot, C. Gotteland, P., and Villard, P. (2009). "Influence of relative density on granular materials behavior: DEM simulations of triaxial tests." *Granular Matter*, Vol. 11, pp. 221–236.
- Santamarina, J. C. and Cho, G. C. (2004). "Soil behaviour: The role of the particle shape." *Proceedings Skempton Conference*, March, London.
- Santamarina, J.C., Klein, K.A., and Fam, M.A. (2001). *Soils and Waves – Particulate Materials Behaviors, Characterization and Process Monitoring*. Wiley, New York, NY.
- Schofield, A. N. (1981). "Dynamic and Earthquake Geotechnical Centrifuge Modelling." *International Conference on Recent Advances in Geotechnical Earthquake Engineering and Soil Dynamics*, Missouri University of Science and Technology, Rolla, MO, 1081–1100.
- Shi, Y. and Zhang, Y. (2006). "Simulation of Random Packing of Spherical Particles with Different Size Distributions." *Proceedings of 2006 ASME International Mechanical Engineering Congress & Exposition*, November 5-10, Chicago, IL.
- Scott, G. D. and Kilgour, D.M. (1969). "The Density of Random Close Packing of Spheres." *Journal of Physics D*, Vol.2, pp.863.
- Sjaastad, G.D. (1963). *The Effect of Vacuum on the Shearing Resistance of Ideal Granular Systems*, Princeton University , Princeton, New Jersey, Ph. D. Thesis.
- Skempton, A. W. (1959). "Cast in situ bored piles in London Clay." *Géotechnique*, 9:153–173.

- Sommerfeld, M. and Huber, N. (1999). "Experimental Analysis and Modelling of Particle-Wall Collisions." *International Journal of Multiphase Flow*, Vol. 25, pp.1457-1489.
- Stronge, W.J. (2000). *Impact mechanics*. First Edition, Cambridge University Press, printed in USA.
- Sukumaran, B. and Ashmawy, A. K. (2001). "Quantitative Characterization of the Geometry of Discrete Particles." *Geotechnique*, Vol. 51, No. 7, pp. 171-179.
- Tabor D. (1977). "Surface Forces and Surface Interactions." *J. Colloid Interface Sci.*, Vol. 58, pp. 2-13.
- Terzaghi, K. (1925). *Erdbaumechanik*, Franz Deuticke, Vienna.
- Thomas, P. A. (1997). *Discontinuous deformation analysis of particulate media*. PhD dissertation, Dept. of Civil Engineering, Univ. of California at Berkeley, Berkeley, Calif.
- Thornton, C. (1979). "The conditions for failure of a face-centered cubic array of uniform rigid spheres". *Géotechnique*, 29(4), 441-459.
- Thornton, C. (2000). "Numerical simulations of deviatoric shear deformation in granular media." *Geotechnique*, 50(4), 43-53.
- Tory, E. M., Church, B. H., Tam, M. K., Ratner, M. (1973). "Simulated Random Packing of Equal Spheres." *The Canadian Journal of Chemical Engineering*, Vol. 51, pp. 484-493.
- Vallejo, L. E. (1995). "Fractal analysis of granular materials." *Geotechnique*, Vol. 45, pp. 159-163.
- Vanel, L., Howell, D., Clark, D., Behringer, R. P., Clement, Eric (1999). "Memories in sand: Experimental tests of construction history on stress distributions under sandpiles." *Physical Review E*, 60(5), 1999, R5040-R5043.
- Vesic, A. S. (1972). "Expansion of Cavities in Infinite Soil Mass." *Journal of the Soil Mechanics and Foundation Division, ASCE* 98, 265-290.
- Veyera, G. E., and Ross, C. A. (1995). High Strain Rate Testing of Unsaturated Sands Using a Split-Hopkinson Pressure Bar, *Third International Conference on Recent Advances in Geotechnical Earthquake Engineering & Soil Dynamics*, Paper 8, April 2.
- Wadell, H. (1932). "Volume, Shape, and Roundness of Rock Particles." *Journal of Geology*, 40, pp. 443-451.
- Walton, K. (1987). "The Effective Elastic Moduli of a Random Packing of Spheres." *Journal of Mechanics and Physics of Solids*, Vol. 35, No. 2, pp. 213-226.
- Walton, O.R. (1993). "Numerical simulation of inelastic frictional particle-particle interactions". *Particulate Two-Phase flow*, edited by M.C. Roco.

- Walton, O.R. (1994). "Force Models for Particle-Dynamics Simulations of Granular Materials." North American Treaty Organization: Advanced Study Institute for Mobile Particulate Systems, July 13-15, Cargese, Corsica.
- Wiqcek, J., Stasiak, M., Parafiniuk, P. (2017). "Effective elastic properties and pressured distribution in bidisperse granular packings: DEM simulations and experiment," *Archives of Civil and Mechanical Engineering*, 17, 271-280.
- Yamamuro, J. A., Abrantes, A. E., and Lade, P. V., (2011). "Effect of Strain Rate on the Stress-Strain Behavior of Sand." *Journal of Geotechnical and Geoenvironmental Engineering*, 137(12), 1169–1178.
- Yang, Z. X., Yang, J., and Wang, L. Z. (2012). "On the influence of inter-particle friction and dilatancy in granular materials: a numerical analysis." *Granular Matter*, Vol. 14, pp. 433-447.
- Yimsiri, S., and Soga, K. (2001). "Effects of soil fabric on undrained behavior of sands." *Proc., 4th Int. Conf. on Recent Advances in Geotechnical Earthquake Engineering and Soil Dynamics*, Editor: S. Prakash, San Diego, CA.
- Yu, H. S. and Holsby, G. T. (1991). "Finite Cavity Expansion in Dilatant Soil: Loading Analysis." *Géotechnique*, 41, 173-183.
- Zelikson, A., Boisson, J. Y., Leguay, P., Hembise, O., and Bardey, P. (1986). "Instrumented projectiles in centrifuge modelling of sea bed penetration." *Soil Dynamics and Earthquake Engineering*, Vol.5, No. 4, pp 239-247.
- Zheng, Q.J., Zhu, H.P., and Yu, A.B. (2011). "Finite element analysis of the rolling friction of a viscous particle on a rigid plane." *Powder Technology*, Vol. 207, pp. 401-407.
- Zhu, H.P., Zhou, Z.Y., Yang, R.Y. and Yu, A.B. (2008). "Discrete particle simulation of particulate systems: A review major application and findings". *Chemical Engineering Science*, Vol. 63, No. 23, pp. 5728-5770.

APPENDIX A: INVESTIGATION INTO THE FUNDAMENTAL NATURE OF INTERACTIONS BETWEEN CONSTITUENTS OF GRANULAR MEDIA

A.1 Friction

Interactions between granular surfaces, and the intimacy of contact between them, are profoundly complicated physical phenomena. These processes encompass elastic and plastic deformations of the surface layers of the contacting microscopic-scale bodies; asperity interlocking and wearing processes at sub-microscopic scales; micro-fracture; chemical reaction; and, lubrication due to water adsorption on grain surfaces and/or surface contamination. Interestingly, a relatively simplistic formulation of the law for dry friction, i.e., a first order approximation of proportionality between the frictional force and the normal force, has been quite sufficient to model (in an approximate manner) several of these phenomena in many engineering applications. The notion of the coefficient of friction in the aforementioned first order approximation originated from a seemingly intrinsic property of dry friction between two macroscopic contacting bodies, which in turn, appeared to be dependent neither on observational (macroscopic) contact area nor on contact surface roughness. In Appendix A, the intrinsic properties of dry friction are examined from a multi-scale perspective, and in the context of the observational shear strength of granular materials.

A.1.1 Historical Review

Based on the seminal experimental observation that frictional resistance is proportional to the weight and independent of contact area by Leonardo da Vinci (1452-1519), Amontons (1663-1706) confirmed the velocity independence of the friction force (Dowson 1979). Later, Coulomb (1736-1806) determined through detailed experimental investigations the following empirical relationship, known as Coulomb's law of static friction:

$$F_s = \mu_s F_N \quad (\text{A.1})$$

where the frictional force F_s between two bodies pressed together with a normal force F_N is defined as the proportionality constant μ_s , referred to as the coefficient of static friction. The coefficient of static friction was presented to be independent of macroscopic ("apparent") contact area and relative motion (sliding velocity). Interestingly, Coulomb suggested the physical origin of friction to be the influence of the roughness of the surfaces. To explain the micro-roughnesses of both contacting surfaces, Coulomb depicted surface roughness as a corrugated surface in his original sketch (Fig. A.1), and without the aid of a microscope.

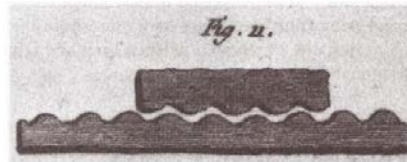


Figure A.1 Coulomb's original sketch of interaction between roughnesses as the origin of frictional resistance (Popov 2010)

Coulomb's view on the physical origin of friction became the simplest description of the coefficient of friction as the measurement of the inclination angle at which a body lying on an inclined plane begins to slide. The force equilibrium conditions for the free body diagram between the corrugated surface and the point mass (Fig. A.2) is expressed as:

$$R \cos \theta = F_N, \quad R \sin \theta = F \rightarrow F = F_N \tan \theta \quad (\text{A.2})$$

where R is the resultant force between the mass and incline, and θ is the inclination angle. The force of static friction F_s is (by definition) equal to the maximum force F_{\max} (and maximum inclination angle θ_{\max}) at which the force equilibrium can remain satisfied:

$$F_s = F_{\max} = F_N \tan \theta_{\max} \quad (\text{A.3})$$

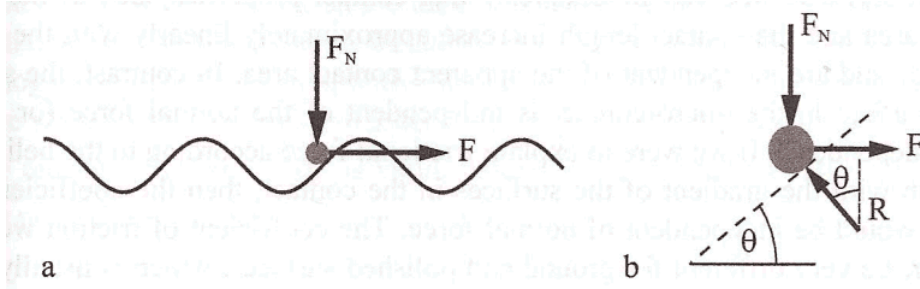


Figure A.2 Simplified conceptualization of dry friction: a) Point mass under force equilibrium on an inclined surface; b) Free body diagram (Popov 2010)

The concept of dry friction, as conceptualized by Coulomb, has been widely adopted in the field of engineering. Particularly, in soil mechanics, a maximum inclination angle is called the angle of friction φ , which is typically illustrated as shown in Fig. A.3: a block with mass m on an inclined plane is at force equilibrium under gravitational acceleration (g). At the angle of friction, the static force reaches its maximum value $F_s = \mu_s F_N$. The equilibrium of the forces (in the coordinate system shown) yields in this critical state:

$$\begin{aligned} x: \quad & mg \sin \varphi - \mu_s F_N = 0 \\ y: \quad & F_N - mg \cos \varphi = 0 \end{aligned} \quad (\text{A.4})$$

Thus, the coefficient of friction is equal to the tangent of the angle of friction according to the macroscopic simplification:

$$\mu_s = \tan \varphi \quad (\text{A.5})$$

Figure A.3 Macroscopic simplification for a maximum (dry) frictional resistance on slip planes

A.1.2 Scale-Dependent Coefficient of Friction

Note that the macroscopic model of Fig. A.3 is applied to sufficiently large *continua* with micro-scale “surface roughness” as in Coulomb’s original sketch (recall Fig. A.1). In contrast, consider an assembly of idealized discrete granules as depicted by spheres in a three-dimensional (3-D) volume, and discs in a two-dimensional plane (Fig. A.4a and Fig. A.4b, respectively).

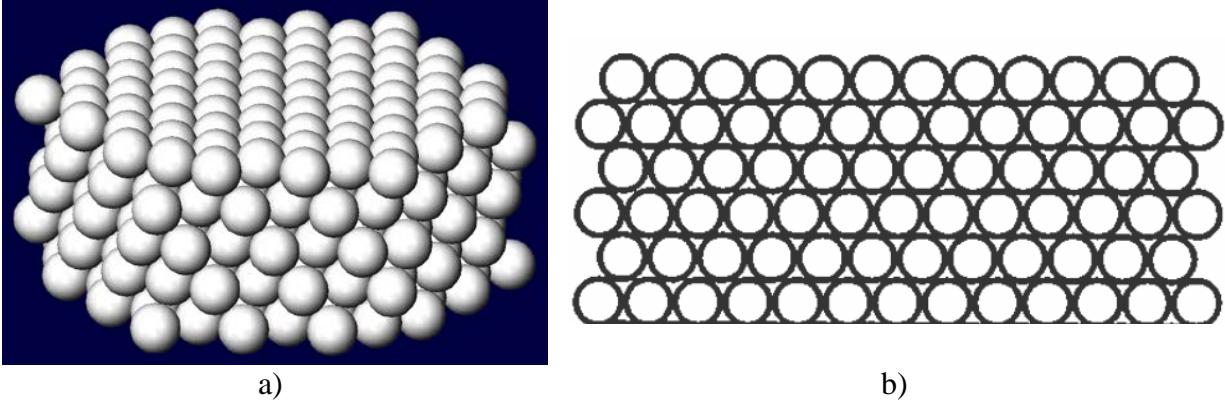


Figure A.4 Geometrically regular packings: a) Close-packed tetrahedral spheres at the theoretical maximum bulk density of $\pi/(3\sqrt{2})$ (~74%) in a volume; b) An equivalent 2-D planar packing of discs at the theoretical maximum bulk density of $\pi/(2\sqrt{3})$ (~91%) (Israelachvill 2011)

The repetitive (or randomly ordered) particle arrangement from the contact normal surface forms the 3-D topology of the surface, which is called *surface texture*. For example, consider a uniform dispersion of spherical particles, as shown in Fig. A.4. The collection of spheres form a solid-like lattice, which produces a surface texture that includes: roughness (nano- and microroughness) of the constituent particle surfaces (Fig. A.5a); and, waviness of contact surface, with macroscopic corrugations (Fig. A.5b).

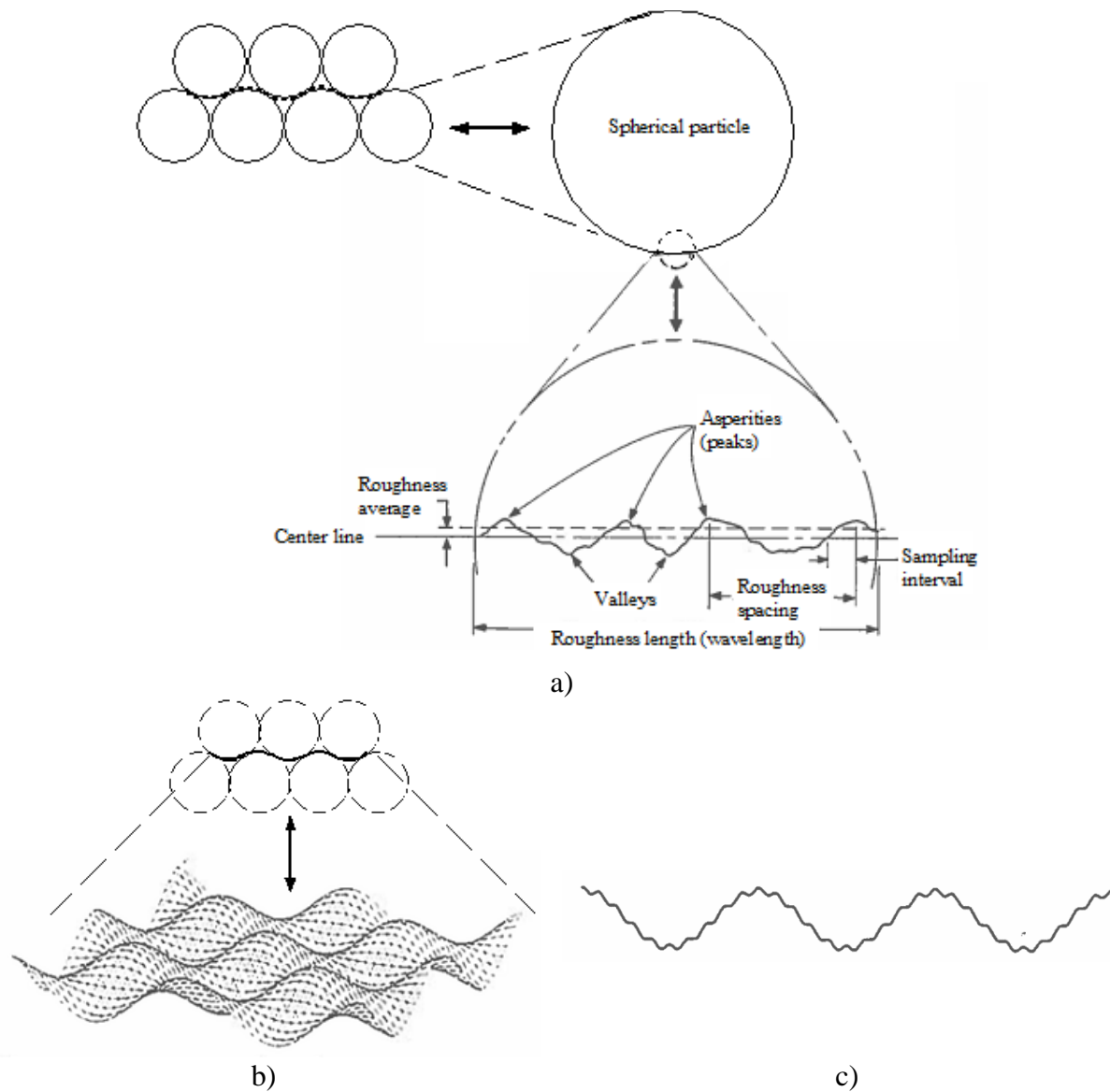


Figure A.5 Pictorial surface texture of close-packed spheres: a) Microroughness of a spherical particle; b) Macroroughness of 2-D corrugated surface; c) Representation of a periodic surface with corrugations on the two scales

Nano- and microroughness are formed by fluctuations (e.g., irregularities) of short wavelength across a given surface, where the fluctuations are characterized by asperities (local maxima) and valleys (local minima) of varying amplitudes and spacings, and these are small compared to the granule dimensions. Waviness is the surface irregularity of longer wavelengths, and is referred to as macroroughness. All irregularities in macroroughness can be described in terms of the sampling spacing, which is of much greater magnitude than the microroughness sampling length and less than (or presumably equal to) the size of a laboratory test sample (e.g., for triaxial compression tests). In tribology, random surface variations in space are very similar to randomness of microroughness, and are characterized using macroscopic amplitude probability

distributions and autocovariance functions (refer to Fig. A.6c). Surface roughness, thus, is by definition non-uniform with respect to scale (e.g., from the nano/micro to macro-scale).

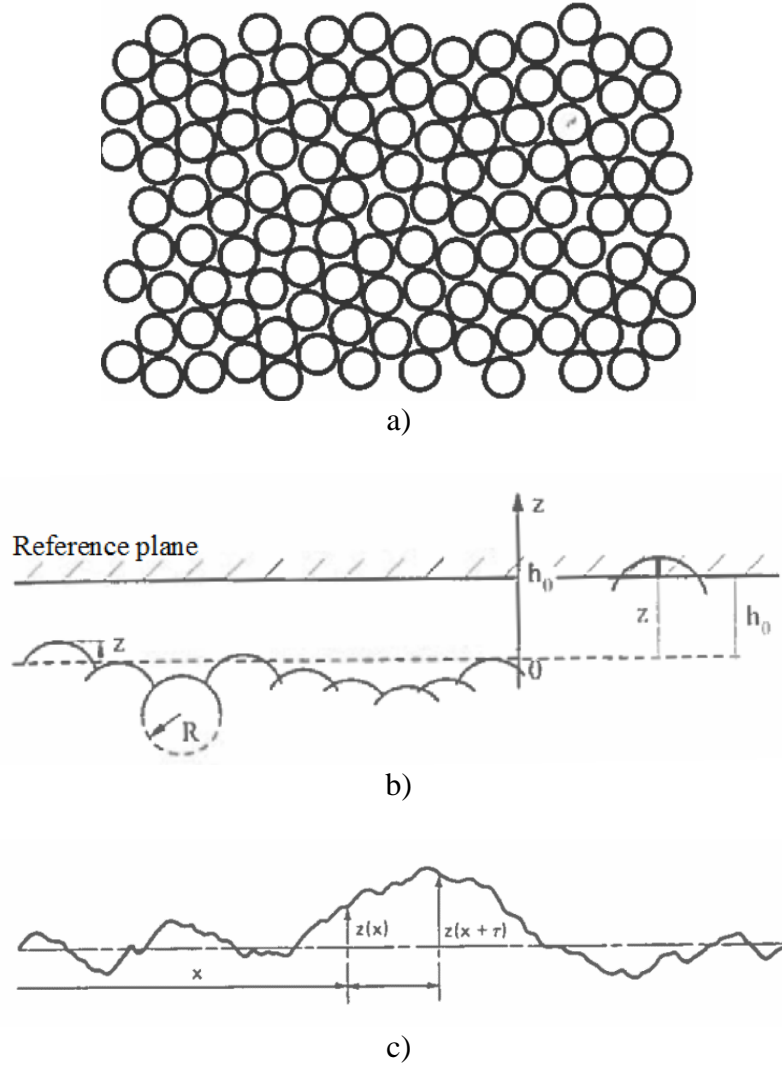


Figure A.6 Dimensional representation of the surface random packings of multi-disperse systems: a) Close random packing of monodisperse system (Israelachvill 2011); b) Height (peak) distribution on a stochastic surface (Greenwood and Williamson 1966); c) 1-D representation of macroscopic surface roughness (from Adams and Nosonovsky 2000)

It must be noted that the physical macroroughness is being depicted herein solely to provide a simple uniform pattern for visualization purposes (e.g., Figs. A.5a and A.5b show idealized cubic closest packings and a simple one-dimensional topographical mapping, respectively). More importantly, the deterministic surface texture of Fig. A.5b will be used to derive scale-dependency of the coefficient of friction using a relatively simple analytical method in the following. However, the principal direction of predominant surface patterns and gross deviations from nominal shapes of the macro wavelength (e.g., Fig. A.6c) are parts of the surface texture, known as an anisotropic

fabric tensor in continuum mechanics, and these geometrical features will be assessed together by means of loose or close random packing or bi-disperse packing.

Consider Fig. A.7 where two different scales of frictional angles are illustrated. The presence of “microscopic friction angle” is characterized as an intrinsic coefficient of friction μ_0 . This way, a single corrugated surface with coefficient of friction μ_0 can be drawn with a maximum slope of $\mu_1 = \tan \theta_1$. Based on the free body diagram of a body in force equilibrium at contact with the surface, the following equilibrium equations are written in the local x' - and l' -direction:

$$\begin{aligned} l': \quad F_N \cos \theta_1 + F \sin \theta_1 &= R \\ x': \quad F_N \sin \theta_1 + \mu_0 R &= F \cos \theta_1 \end{aligned} \quad (\text{A.6})$$

From which, it follows that:

$$\frac{F}{F_N} = \frac{\mu_0 + \tan \theta_1}{1 - \mu_0 \tan \theta_1} = \frac{\mu_0 + \mu_1}{1 - \mu_0 \mu_1} \quad (\text{A.7})$$

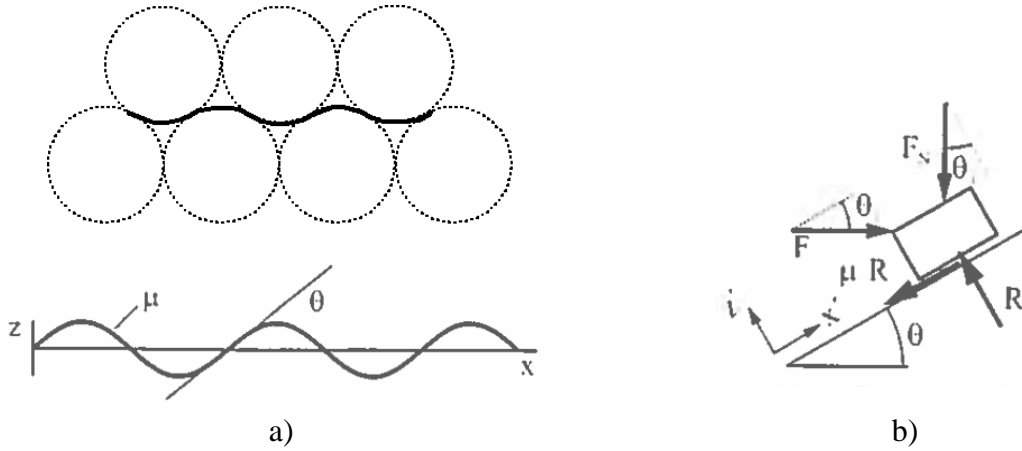


Figure A.7 Idealized macroroughness with periodic corrugation: a) Corrugated surface with intrinsic coefficient of friction, μ_0 ; b) Free-body diagram of a body on a corrugated surface with coefficient of friction, μ_0

Note that this “superposition” has a simple interpretation for coefficient of friction on the two different scales, and for which the friction angles are summed on the scales of interest (e.g., $\theta = \theta_0 + \theta_1$). Thus, the coefficient of friction μ can be accounted for by defining a total frictional resistance, which simultaneously provides a general rule to superimpose coefficients of friction at a given scale:

$$\mu = \tan \theta = \frac{\sin(\theta_0 + \theta_1)}{\cos(\theta_0 + \theta_1)} = \frac{\sin \theta_0 \cos \theta_1 + \cos \theta_0 \sin \theta_1}{\cos \theta_0 \cos \theta_1 - \sin \theta_0 \sin \theta_1} = \frac{\tan \theta_0 + \tan \theta_1}{1 - \tan \theta_0 \tan \theta_1} = \frac{\mu_0 + \mu_1}{1 - \mu_0 \mu_1} \quad (\text{A.8})$$

In general,

$$\mu = \tan \left(\sum_i \arctan \mu_i \right) \quad (\text{A.9})$$

Therefore, the tangent of angles due to scale-dependent surface irregularities would then give the coefficient of friction. Specifically, frictional strength of a volume of granular mass, which is measurable in laboratory settings, is characterized by frictional processes on the micromechanical scale. Further, a discrete multi-body representation of the granular mass enables the inclusion of scales when considering friction angles. In the following, a theoretical basis is established for determining those factors that contribute to an intrinsic coefficient of friction at the microscopic scale.

A.1.3 Cold Welding: Theory of Bowden and Tabor

Throughout the history of tribology, several attempts have been made to explain the universality and simplicity of Coulomb's law of friction, based on the proportionality of the frictional force to the normal force. The contact properties investigated typically derive from the interlocking of projections on surface roughness. One such attempt is found in the work of Sir Thomas Hardy, who examined wear track on sliding glass surfaces in 1919. Per observation of tearing, Hardy concluded that sliding friction was due to cohesive forces between contacting surfaces, where the actual area of contact was only a fraction of the total contact area. Thus, the cohesive forces on a unit area basis were quite large. Several years later, as cited by Bromwell (1966), Terzaghi (1925) presented the first quantitative description of the adhesive frictional processes at the microscopic scale, as shown in Fig. A.7a. His reasoning was that the normal load N acting on a very small area of actual contact would cause yielding of the microscopic contact asperities (refer to Fig. A.8). The contact area A_c would be given by:

$$N = A_c q_u \quad (\text{A.10})$$

where q_u is the normal stress required to cause plastic flow. Note that early theoretical work used yield stress σ_y as the indentation hardness. The quantity q_u is essentially a bearing capacity, which is the indentation hardness of asperity and tends to be greater than the yield stress (e.g., $q_u = \sigma_0 = 3\sigma_y$). Adhesion would occur over the regions of actual contact where the junctions should be sheared before sliding takes place, i.e., stick conditions. If the grain material has a shear strength, τ_m , then the maximum tangential force F_{\max} is defined as:

$$F_{\max} = A_c \tau_m \quad (\text{A.11})$$

Thus, an inter-particle coefficient of friction μ_i is written as:

$$\mu_i = \frac{F_{\max}}{N} = \frac{\tau_m}{q_u} = \frac{\tau_m}{\sigma_0} \quad (\text{A.12})$$

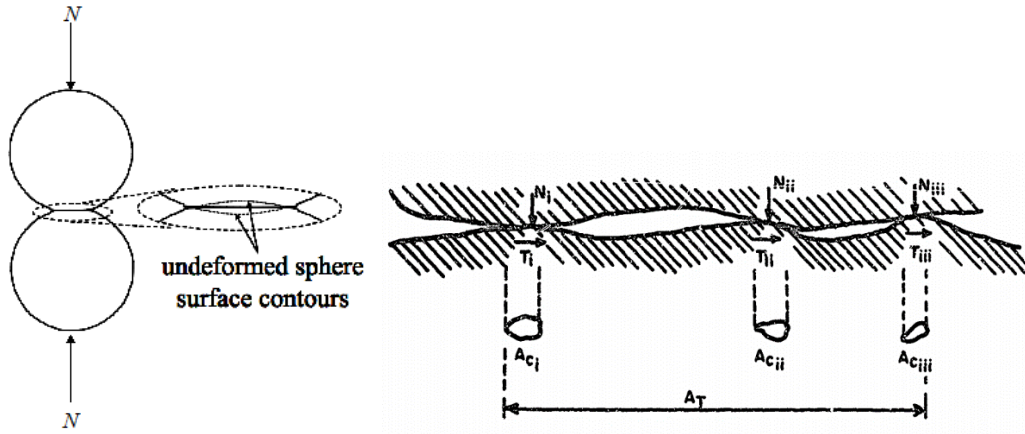


Figure A.8 Depiction of microscopic contact area between two spherical grains (the rightmost illustration is from Bromwell 1966)

Independent from Terzaghi's analysis, Bowden and Tabor (1950) presented a theory to explain frictional behaviors for a wide variety of materials. Namely, the Adhesion Theory of Friction explains phenomena such as kinetic friction between pure metallic surfaces through the formation of cold-weld junctions, and more generally, where friction is treated as cohesive bonds at points of contact between two objects. As a novel facet of the theory, strong adhesion due to microscopic interlocking exists for contacts in compression A_{comp} and tension $A_{tension}$:

$$\begin{aligned} F_{max} &= \tau_c (A_{comp} + A_{tension}) \\ N &= \sigma_c (3A_{comp} - \xi A_{tension}) \end{aligned} \quad (A.13)$$

where F_{max} is the static force of friction if all of the cold welds are sheared; the maximum normal stress compressive area per normal load N is roughly equal to the indentation hardness ($3\sigma_c$); and, for tensile areas, a ratio ξ of the hardness to the maximum normal stress is defined (which is generally less than 3). Thus, the intrinsic coefficient of friction at adhesive contact surfaces is then:

$$\mu_0 \square \frac{F_{max}}{N} = \frac{\tau_c (A_{comp} + A_{tension})}{\sigma_c (3A_{comp} - \xi A_{tension})} \quad (A.14)$$

Explanation of this adhesive bonding called “cold-welding” is illustrated per Von-Mises yield criterion in Fig. A.9. As the asperities are initially loaded to the yield stress (step 1), application of a small shear stress would require that applied normal stresses are less than the yield stress (step 2). As the shear stress increases, the contact area must continually increase in order to maintain the plastic equilibrium. If the junction does not shear until $\tau = \tau_m$, then normal stress must decrease to zero (step 3). That is, either an infinite area of contact or gross seizure over the entire area takes place in the process of junction growth that produces cold welding, and further, can correspond to extremely large coefficients of friction (Bowden and Tabor 1950).

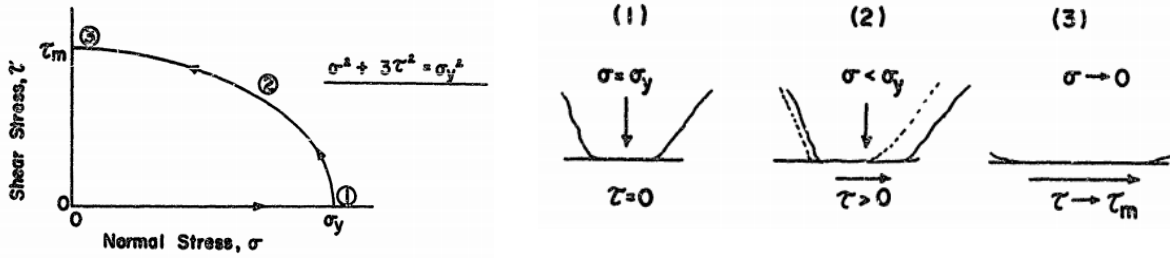


Figure A.9 Cold welding mechanism (from Bromwell 1966)

If the maximum shear stress is less than the uniaxial compressive strength by (approximately) a factor of $\sqrt{3}$, then $\tau_c \approx \sigma_c / \sqrt{3}$. Also, for this condition, plastic substances can undergo isotropic hardening. If $A_{comp} \approx A_{tension}$ (e.g., perfectly conformal contact) and $\xi \approx \sqrt{3}$,

then $\mu_0 = \frac{2}{\sqrt{3}(3-\sqrt{3})} = 0.91$. For quartz with an indentation hardness of about 1100 kg/mm² (10

GPa), stress levels must exceed the yield limit of approximately 10.3 GPa to cause plastic deformation in the asperities in contacts. It is a matter of debate whether or not this level of stress is reached for a significant number of asperities engaged in surface contacts among grains. Nevertheless, adhesion of brittle granular materials can be a significant factor contributing to the intrinsic coefficient of friction at the microscopic scale. Therefore, a quantitative description of the coefficient of friction at the microscopic scale is investigated later for brittle granular materials, and particularly for quartz.

A.1.4 JKR Theory

A treatment of adhesive normal contact between elastic bodies was proposed by Johnson, Kendall, and Roberts in 1971, and is known as JKR Theory. This theory prevalently serves as the starting point for essentially all frictional studies in modern granular physics. Consider an elastic sphere with radius R in contact with a rigid, planar surface. Because of the attractive forces between two solid bodies (known as van der Waals forces), an elastic sphere (Fig. A.10) deforms through depth d due to contact with a plane, and forms a characteristic “neck” across contact area a .



Figure A.10 Formation of a characteristic “neck” during adhesive contact (Popov 2010)

As part of the deformation due to contact, the points on the contact surface of the sphere displace through a certain depth, which can be written in terms of vertical displacement u_z (Johnson 1985):

$$u_z = \frac{\pi}{4E^*a} p_o (2a^2 - r^2) \quad (\text{A.15})$$

where p_o is a contact pressure at the centroid of the contact area; and, an elasticity constant for the sphere is defined using Young's modulus E and Poisson's ratio ν as $E^* = E / (1 - \nu^2)$. A derivation can be carried out using the energy principle for determining a critical radius, where this radius corresponds to development of a maximum adhesive force. As a result, the absolute values of the force F_a (the adhesive force) are given in terms of a critical contact radius a_{crit} and a critical penetration depth d_c (e.g., the maximum displacement on a single asperity):

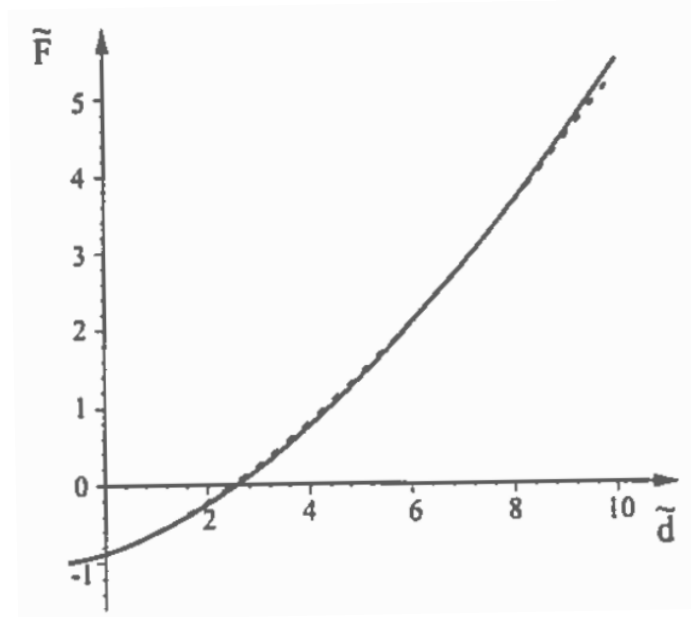
$$F_a = -\frac{3}{2}\gamma_{12}\pi R \quad \text{when} \quad a = a_{crit} = \left(\frac{9}{8} \frac{\gamma_{12}\pi R^2}{E^*} \right)^{1/3} \quad \text{and} \quad d = d_c = -\left(\frac{3}{64} \frac{\gamma_{12}^2\pi^2 R}{(E^*)^2} \right)^{1/3} \quad (\text{A.16})$$

where γ_{12} is the surface tension under force equilibrium (at the microscopic scale). Using dimensionless variables: $\tilde{F} = F / |F_a|$, $\tilde{a} = a / a_{crit}$ and $\tilde{d} = d / |d_{crit}|$, we write:

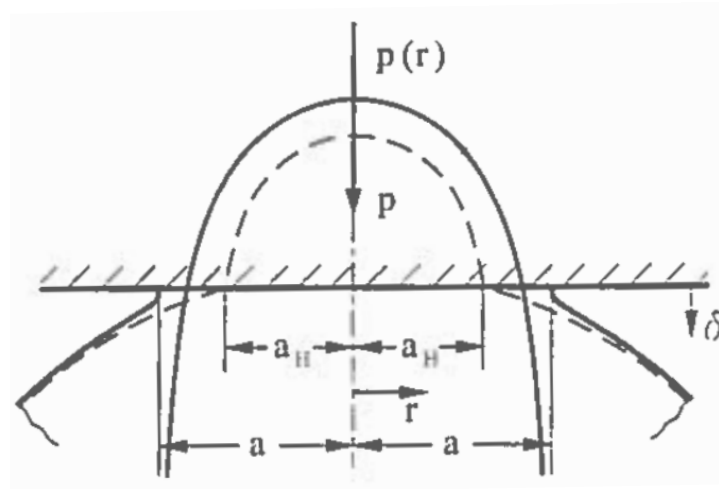
$$\tilde{F} = \tilde{a}^3 - 2\tilde{a}^{3/2} \quad \text{and} \quad \tilde{d} = 3\tilde{a}^2 - 4\tilde{a}^{1/2} \quad (\text{A.17})$$

which defines a parametric form of the dependence of the dimensionless force on the dimensionless penetration depth. A physical interpretation of the equation is: adhesive forces formed at contacts of multiple asperities can provide substantial resistance, as the asperities engaged in the surface contact must be sheared in the tangential direction. Adhesive normal stresses (as analogous to prestressed conditions) can reach very large values at the edges of the contact area between two contact asperities. A graphical illustration is given in Fig. A.11. Assuming that the penetration depth is of the same order of magnitude as d_c , the dimensionless force can be approximated (dashed line in Fig. A.11b) as:

$$\tilde{F} = -1 + 0.12(\tilde{d} + 1)^{5/3} \quad (\text{A.18})$$



a)



b)

Figure A.11 Contact force and pressure: a) Dependence of normal contact force on penetration depth at the microscopic contact (Eqn. A.17); b) Hertzian contact pressure distribution in an adhesive contact (Johnson 1985)

A.1.5 Grain Surface Texture and Frictional Resistance

Having reviewed JKR Theory, which describes adhesive contact between two elastic bodies (i.e., a pair of contact asperities at the microscopic scale), attention is shifted to estimating an intrinsic coefficient of friction between two rough surfaces containing multiple contacts among asperities. More specifically, forensic casework studies for the latest quartz grain surface texture analysis using scanning electron microscopy (SEM) and atomic force microscopy (AFM) are used as the basis of analytical calculation. SEM can produce very high-resolution images of a sample surface, revealing details at the nanoscale. SEM micrographs can also have a depth of field yielding

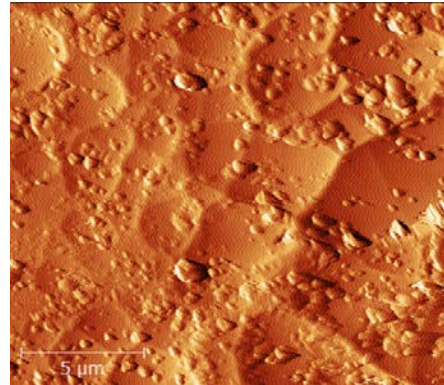
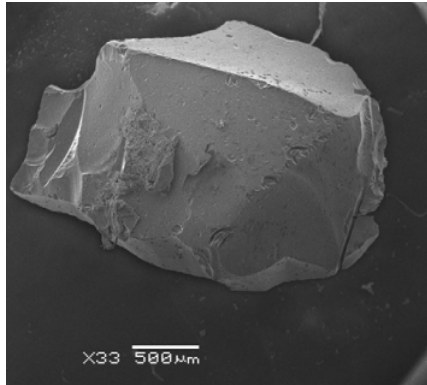
a characteristic three-dimensional appearance, which is useful for understanding the surface texture of a grain over a wide range of magnifications (from 10x 500,000x; which, is approximately 250 times greater than the magnification limit of high-end microscopes). According to Konopinski et al. (2012), the AFM is:

“A form of scanning probe microscope utilizing an ultra-sharp tip micro-fabricated on a cantilever to image a sample. When in close proximity with the sample, the deflection of the cantilever, due to interaction with intermolecular forces between the tip and the sample surface, is detected by reflecting a laser beam off the top of the cantilever onto a position-sensitive photodiode. Given a known deflection and spring constant for the cantilever, the interaction force between tip and sample can be obtained using Hooke’s law. Feedback circuitry controls the tip-sample distance to remain small, but also avoids damaging the sample. Positioning of the tip is precisely controlled with piezoelectric elements in the x, y, and z axes, and during analysis the tip is scanned across the sample surface in a raster scan, building up an image of the surface topography.”

As a compliment to SEM techniques, the AFM offers a quantitative means of analyzing mappings generated at the nanoscale. Consider the three SEM images of quartz grains shown in Fig. A.12. In Fig. A.12a, a mechanically crushed (angular) granule is displayed. In Fig. A.12b the natural crystalline growth formed by deposition under high pressure (sub-rounded) is displayed, whereas Fig. A.12c depicts the effects of abrasion wearing on a granule. Topographical images of multiple sets of these grain samples (totaling 24 grains, using AFM, Konopinski et al. 2012) revealed that surface textures on grains are highly disparate from one another. Such variability is indicative of the topological evolution that takes place on granular surfaces subjected to the myriad paths of loading over time.

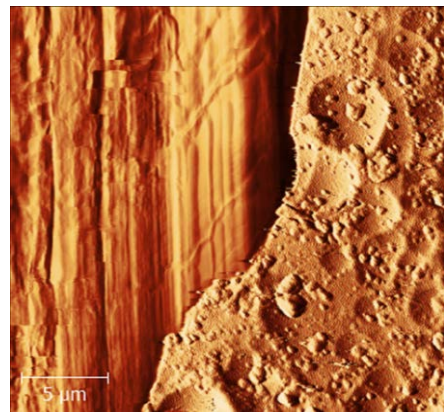
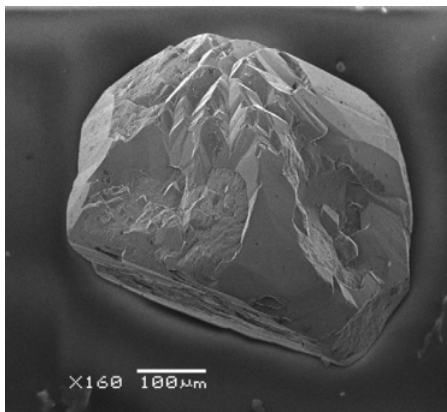
Surface roughness measured at the microscopic scale (amplitudes and periods of asperities) can vary significantly, given some degree of surface abrasion and crystalline growth. To investigate this phenomenon, Konopinski et al. (2012) also reconstructed 3D elevation maps from the topographic data. Amplitudes among the three sets were found to vary in 0.63, 1.6, and 4.5 μm for scan sizes of 10 by 10, 25 by 25, and 30 by 50 (μm by μm), as shown in Fig. A.13a. Based on a statistical analysis of amplitude and surface roughness, Konopinski et al. (2012) concluded that it is possible to construct a histogram of the heights of the surface boundaries. Applying a Gaussian low-pass filter to smooth the results, the resulting height distribution histogram gives the relative frequency of specific height data obtained from the surface.

Within the scope of the current project, detailed review of topographical analyses from the literature is not conducted. Instead, identification of the range of values of amplitudes (asperities) and the corresponding standard deviations (i.e., the root mean square of the height distributions) pertaining to quartz grains is focused upon. In this way, an intrinsic coefficient of friction (using an averaging method) can be developed and applied to the modeling of granular materials, as discussed below.



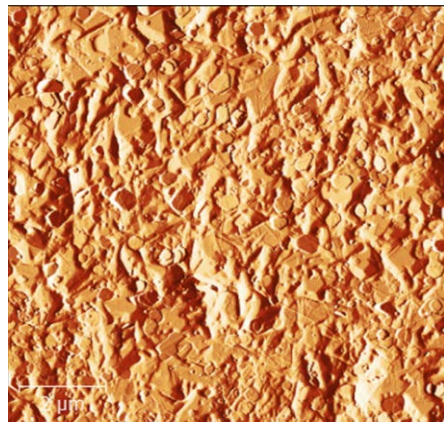
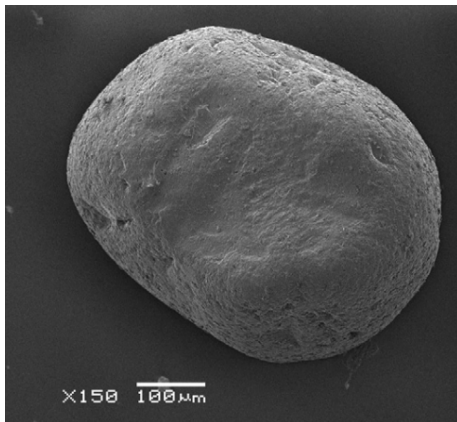
SEM (left) and AFM (right) scan size $17.5 \times 17.5 \mu m^2$

a)



SEM (left) and AFM (right) scan size $25 \times 25 \mu m^2$

b)



SEM (left) and AFM (right) scan size $10 \times 10 \mu m^2$

c)

Figure A.12 Grain surface topography: a) Mechanically crushed pure quartz with sharp edges and clean faces with minimal surface texture; b) Diagenetic quartz with euhedral crystal growths formed naturally by deposition under high pressure. Minimal transportation of the grains is

evident from lack of edge abrasion; c) Semi-round grains with characteristic surface fractures (Konopinski et al. 2012)

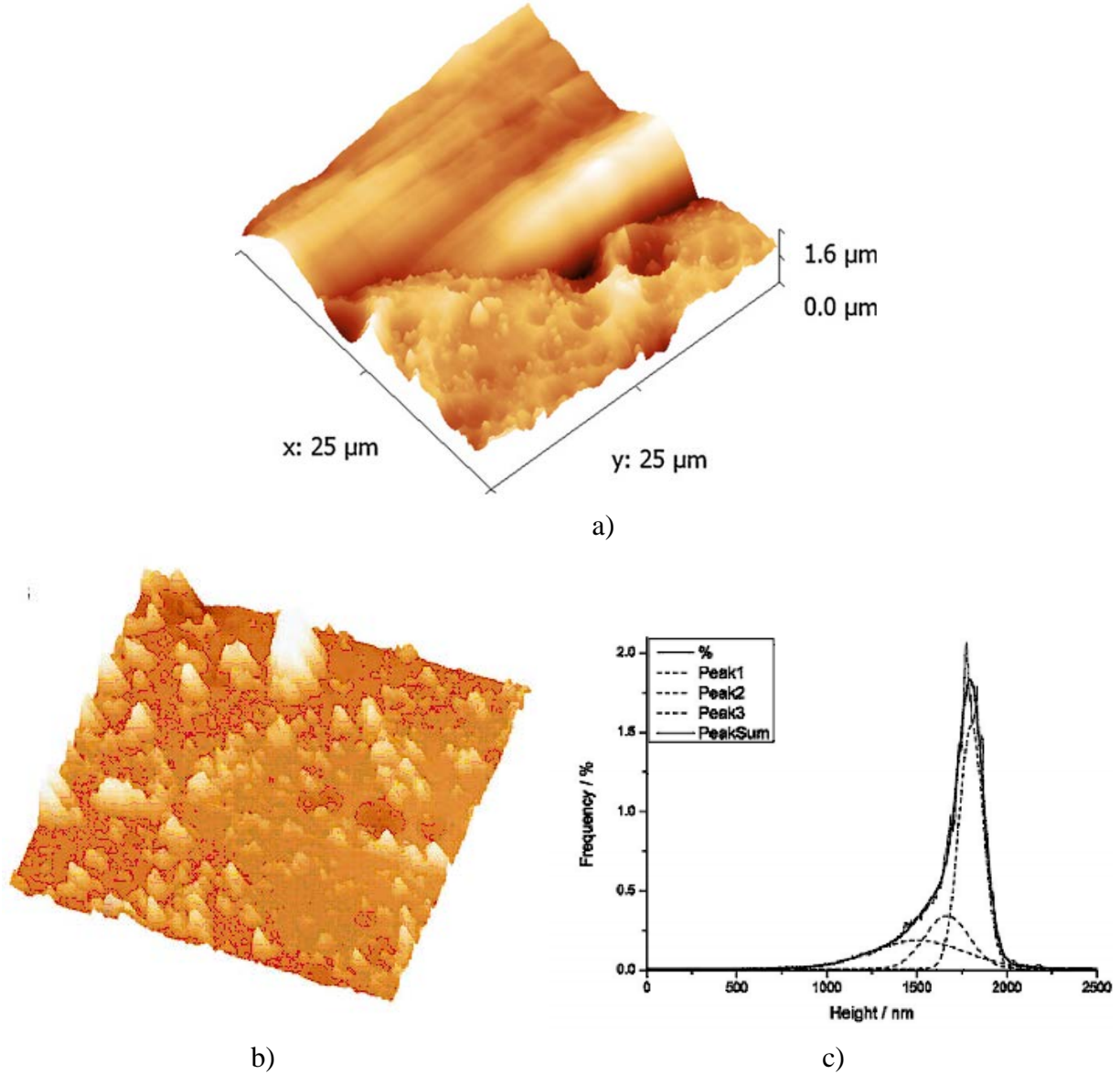


Figure A.13 Dimensional representation of the grain surface (from Konopinski et al. 2012): a) 3-D elevation map of Fig. A.12b; b) 3-D representation of the microscopic surface texture of a grain; c) Counting estimate of fractal dimension for a 20 μm AFM scan

Let the height distributions (amplitudes) of two contacting granular surfaces be given by a Gaussian distribution, with standard deviation l . We assume that the surfaces are pressed together under the action of a normal force F_N . Subsequent to being pressed together, granular surfaces are translated relative to one another in the tangential direction. The resulting friction force that arises is due to the asymmetry of the loading processes occurring during the formation and destruction

of adhesive contacts: two approaching asperities first come into contact when their undeformed geometric contours intersect. Conversely, the surface localities separate only after some finite distance between the two has been achieved. The strength of adhesion can be characterized by the critical distance at which the separation of the surfaces occurs (recall the critical depth calculation in Eqn. A.16) where $R^* = \frac{R}{2}$ and $E^* = \frac{E}{1-\nu^2}$. Note that the surface radius of curvature and elastic property of both the contacting asperities are assumed to be identical, purely for simplicity in deriving an analytical solution. Then, the problem basically deals with three statistical parameters, each with dimension of length: the radius of curvature, the height distribution, and the critical distance. For contact between a single pair of asperities (with an average height, measured over a sampling length), the three following conditions are imposed as part of a statistical parametrization: $d_c < l$, $d_c / R^* \ll 1$, and $l / R^* \ll 1$. A physical description of the three imposed geometric conditions is as follows: the critical distance is less than the standard deviation of the height distribution (to ensure inclusion of only a single pair of asperities); the critical distance has to be much smaller than the radius (in consideration of the ratio of amplitude to particle radius); and thus, the height distribution must be much smaller than the radius. Under these conditions, we first investigate contact between the two asperities and, thereafter, expand the solution by means of an averaging over the statistical distribution of multiple contact asperities.

Consider a schematic sketch of two asperities with equal radii of curvature, as shown in Fig. A.14. The form of the asperities is described by:

$$z_1(x) = z_1 - \frac{x^2}{2R} \quad \text{and} \quad z_2(x) = z_2 - \frac{(x-x_0)^2}{2R} \quad (\text{A.19})$$

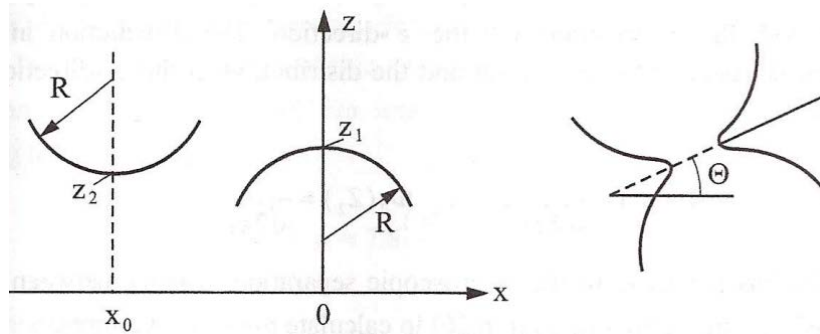


Figure A.14 Two spherical asperities in contact (Popov 2010)

While the surfaces remain in contact, the penetration depth is given by:

$$d = z_1 - z_2 - \frac{x_0^2}{2R} \quad (\text{A.20})$$

and the tangent of the contact angle is then:

$$\tan \theta \approx \theta = \frac{x_0}{2R} \quad (\text{A.21})$$

For the first contact ($d = 0$) and the last contact ($d = -d_c$) just before separation, we can obtain minimum and maximum values of x_0 from Eqn. A.20:

$$x_{0,\min} = -2\sqrt{R(z_1 - z_2)} \quad \text{and} \quad x_{0,\max} = 2\sqrt{R(z_1 - z_2) + Rd_c} \quad (\text{A.22})$$

If we denote the contact force between the asperities as F , then the z-component and x-component of the contact force can be written using Eqn. A.21:

$$F_N = F \quad \text{and} \quad F_R = -F \frac{x_0}{2R} \quad (\text{A.23})$$

Thus, the intrinsic coefficient of friction can be calculated as:

$$\mu_0 = \frac{\langle F_R \rangle}{\langle F_N \rangle} \quad (\text{A.24})$$

where the notation $\langle \dots \rangle \equiv \langle \dots \rangle_x \langle \dots \rangle_z$ denotes an average over the asperity distribution (macroscopic roughness) in both the x-direction and the z-direction. For simplicity in numerical quantification, the distribution in the x-direction is assumed to be uniform over a finite sampling length, and the height distribution in the z-direction is defined (with respect to functional form) using a normal distribution (Greenwood and Williamson 1966):

$$\Phi_1(z_1) = \frac{1}{\sqrt{2\pi}l} \exp\left[-\frac{z_1^2}{2l^2}\right] \quad \text{and} \quad \Phi_2(z_1) = \frac{1}{\sqrt{2\pi}l} \exp\left[-\frac{(z_2 - z_0)^2}{2l^2}\right] \quad (\text{A.25})$$

Based on Eqn. A.18, we approximate the adhesive force:

$$F \approx F_c \left[0.12 \left(\frac{d}{d_c} + 1 \right)^{5/3} - 1 \right] \quad \text{for} \quad -1 \leq \frac{d}{d_c} \leq 10 \quad (\text{A.26})$$

where $F_c = \frac{3}{2} \pi \gamma_{12} R$ (refer to Eqn. A.16). Averaging the forces F_N and F_R in the x-direction, over the length of sliding surface (L), we write:

$$\begin{aligned} \langle F_R \rangle_x &= -\frac{1}{L} \int_{x_{0,\min}}^{x_{0,\max}} F \frac{x_0}{2R} dx_0 \approx \frac{F_c}{2} \frac{d_c}{L} \\ \langle F_N \rangle_x &= \frac{1}{L} \int_{x_{0,\min}}^{x_{0,\max}} F dx_0 \approx F_c \frac{\sqrt{Rd_c}}{L} \left[1.2(1 + \xi)^{13/6} - \sqrt{\xi} - \sqrt{\xi + 1} \right] \end{aligned} \quad (\text{A.27})$$

where $\xi = \frac{3}{4} \frac{l}{d_c}$ and $l = \sqrt{\langle z^2 \rangle}$. Therefore:

$$\mu_0 \square \frac{\langle F_R \rangle_x}{\langle F_N \rangle_x} = \frac{0.5 \sqrt{(d_c/l)} \nabla z}{1.2(1+\xi)^{13/6} - \sqrt{\xi} - \sqrt{\xi+1}} \quad (\text{A.28})$$

$$\text{where } \nabla z = \sqrt{\left(\frac{1}{L} \int_0^L \frac{dz(x)}{dx} \frac{dz(x)}{dx} dx \right)} = \sqrt{\left\langle \left(\frac{dz}{dx} \right)^2 \right\rangle}.$$

Thus, the intrinsic coefficient of friction is proportional to the root mean square of the surface gradient. For small values of d_c/l , Eqn. A.28 can be simplified to:

$$\mu_0 \approx 7.8 \left(\frac{d_c}{l} \right)^{8/3} \nabla z \quad (\text{A.29})$$

Defining ∇z as being approximately equal to the tangent of average angle of asperities in the x-direction, i.e., $\langle \theta \rangle_x$, then:

$$\mu_0 \approx 7.8 \left(\frac{d_c}{l} \right)^{8/3} \tan(\langle \theta \rangle_x) \quad (\text{A.30})$$

For example, for mild steel, with $\left\langle \frac{d_c}{l} \right\rangle_x < 0.1$, $\mu_0 \approx (0.017) \tan(\langle \theta \rangle_x) \rightarrow 0$. The adhesive contribution to friction in a pairing of steel-to-steel contact surfaces is negligibly small (and can approach zero if the surface roughness is very small, e.g., by means of lubrication). The adhesive contribution to friction in a pairing of steel-to-steel contact surfaces is negligibly small (and can approach zero if the surface roughness is very small, e.g., polished). As another example, for viscoelastic materials such as rubber with $\left\langle \frac{d_c}{l} \right\rangle_x \geq 0.7$, $\mu_0 \approx 3.0 \cdot \tan(\langle \theta \rangle_x)$.

Of relevance to the current study, consider quartz. More specifically, consider coarse grains with a radius of 1.5 mm; surface roughness l (9.37 nm from Table A.1; Lieu 2013); surface energy γ_{12} (1.2 J/m² from Table A.2; Parks 1984); Young's modulus E for E^* (76 GPa from Table A.3 from Santamarina et al. 2001); and, Poisson's ratio ν for E^* (0.3 from Table A.3 of Santamarina et al. 2001). Then, the following can be calculated using Eqns. A.16 and A.30:

$$\begin{aligned} d_c &= \left(\frac{3}{64} \frac{\gamma_{12}^2 \pi^2 R}{(E^*)^2} \right)^{1/3} = \left(\frac{3}{64} \frac{(1.2)^2 \pi^2 (0.0015)}{(83.5E9)^2} \right)^{1/3} = 5.233 \times 10^{-9} \text{ m} \square 5.233 \text{ nm} \\ \mu_0 &\approx 7.8 \left(\frac{5.233}{9.37} \right)^{8/3} \tan(\langle \theta \rangle_x) = 1.65 \tan(\langle \theta \rangle_x) \end{aligned} \quad (\text{A.31})$$

That is, development of adhesive contacts of asperities (as shown in Fig. A.15) can quite noticeably contribute to the frictional force if the ratio of maximum penetration depth to the height distribution (i.e., roughness of microscopic surface) is relatively large. The surface energy of the grain is the controlling factor for this ratio. As for formation of young quartz in place, the height distribution tends to increase by an order of magnitude, and the specific surface and surface energy increase almost proportionally. In contrast, mechanical weathering causes surface abrasion and reduces the critical penetration depth by an order of magnitude. Likewise, mechanical weathering reduces values of the height distribution by a factor of two (or three), ultimately leading to a very low coefficient of friction.

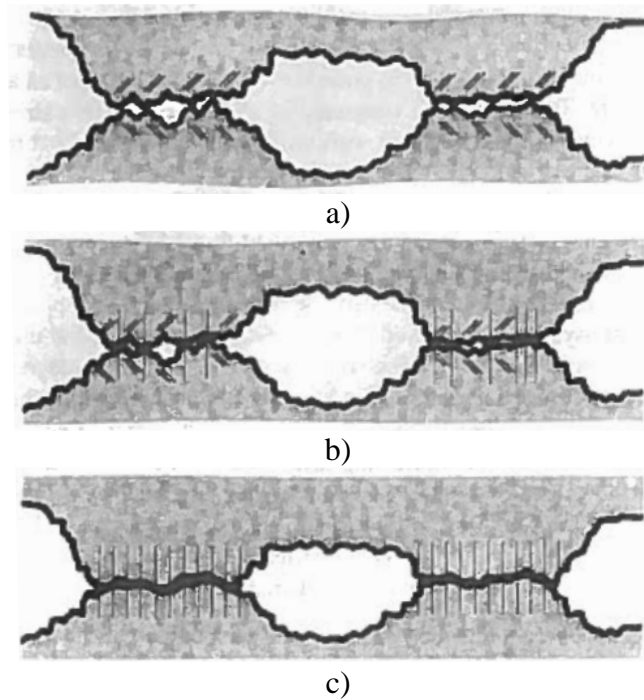


Figure A.15 A schematic of three deformation stages of contact asperities at the microscopic scale: a) Initial contacts take place within frictional asperity bodies undergoing elastic deformation; b) Further deformation occurs conjointly; c) Final stage of seizure, where conjoint deformation of all the asperities occurs at all sites of seizure (Bhushan 2013)

The values of Young's modulus and hardness appear to be a function of penetration depth. For relatively small indentation depths, a wide range of these two values is observed, whereas such scattering becomes moderately predictable for increasing indentation depths (Fig. A.16, Nadukuru 2013). As part of preparing samples for testing in Nadukuru (2013) grain surfaces were polished using polishing compounds to achieve average particle sizes of 250 nm. These sizes were assumed to be of the same order of magnitude as the mean average height of asperities.

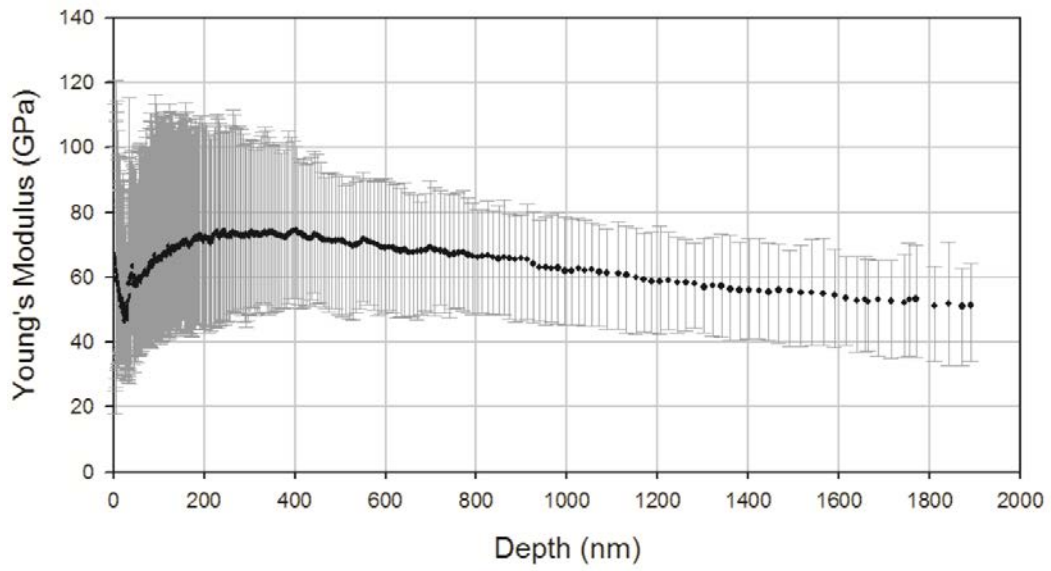
The data of Fig. A.16, for indentation depths less than 250 nm, may not be representative of the material properties of the quartz. As the indentation depths approach the scale of microscopic asperity (~ 1 nm), the values tend to be in agreement with test data reported in other studies. For example, Daphalapurkar et al. (2011) performed 500 nanoindentation tests on 250 quartz grains

collected from Stillwater Lake in Oklahoma: mean values of Young's modulus, hardness, and fracture toughness were found to be 91.1 GPa, 10.7 GPa, and $1.77 \text{ MPa}\cdot\text{m}^{0.5}$, respectively.

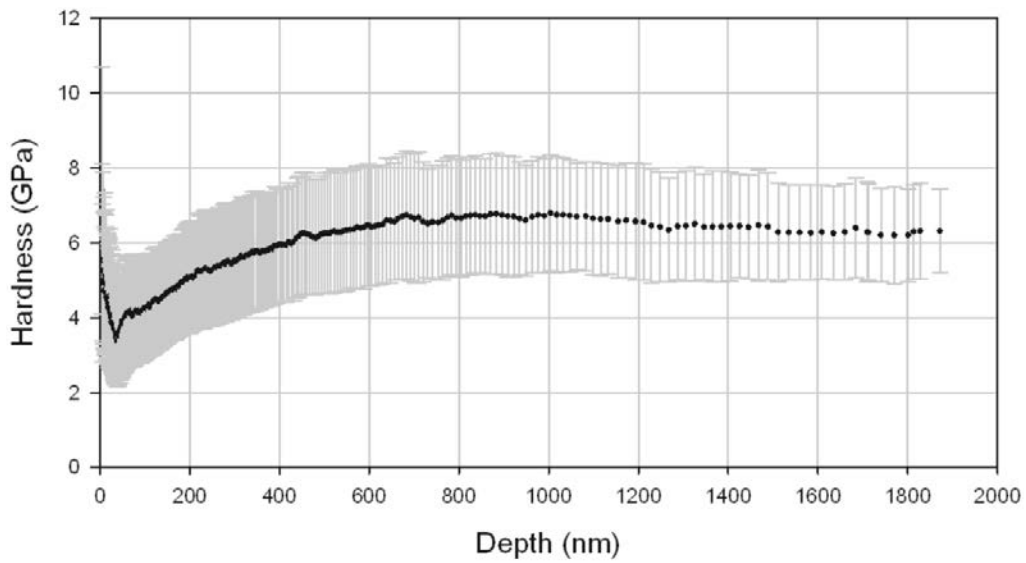
Fracture toughness is the ability of a material with a crack to resist fracture. The low fracture toughness value for quartz indicates that the grains are more susceptible to undergo brittle fracture rather than ductile failure. For comparison, the fracture toughness of mild steel is $50 \text{ MPa}\cdot\text{m}^{0.5}$, and that of normal strength concrete is $1.4 \text{ MPa}\cdot\text{m}^{0.5}$. Considering force-deformation relationships to be scale-dependent, nanoindentation techniques for determining elastic properties of granular particles are valuable in capturing deformation at the microscopic scale. At grain-size scales, the tensile strengths of grains tend to decrease as the sizes of grains increase (Table A.4).

Because capturing the behaviors associated with contact between two grains is central to the proposed hypothesis of DEM in modeling at the grain-size scale, the variability in grain minerals (specifically, quartz) mechanical properties and the complexity of the surface morphology are not further investigated. Nonetheless, qualitative quantification of the grain surface morphology is performed over a range of values to explore the intrinsic coefficient of friction in relation to contact loading. Whether or not the asperities on grain surfaces are prone to plastic deformation or brittle failure is still a matter of debate. Further, in-depth data analysis on SEM and AFM of microscopic surface textures seems to be necessary to stochastically determine the degrees of adhesion through shearing mechanisms. Exploring these contributing factors to the intrinsic coefficient of friction, as more data become available from the literature, is beyond the scope of the current study.

Ongoing efforts to advance the modeling of granular materials using the DEM are maintained by researchers in the Computer Laboratory for Granular Physics Studies (CL-GPS) at the University of Florida, where such efforts are currently aimed at conducting detailed stochastic analysis of intrinsic friction on various types of granular materials. As facilitation of these efforts, the CL-GPS possesses priority access to 256 processing cores of the 21,000 core UF HPC cluster. Currently, these cores draw upon 16-core AMD Opteron 6378 processors, and 2 GB of RAM is available per core. The CL-GPS collaborates with the developers of LS-DYNA (LSTC 2014) to test new DEM-specific features within the LS-DYNA multi-physics simulation software.



a)



b)

Figure A.16 Indentation test results: a) Young's modulus of sand grains as a function of depth, obtained from 33 indentation tests; b) Indentation hardness of sand grains from 33 tests on 11 sand grains (Huron River and Ottawa 20-30 sand) (Nadukuru 2013)

Table A.1 Mean surface roughness values of quartz grains (Lieu 2013)

Order	Type	Mean value (nm)	Standard deviation (nm)	Min value (nm)	Max value (nm)
1	illite-chlorite	34.03	27.88	2.42	134
2	chlorite	22.4	8.49	6.22	30.7
3	illite	18.44	11.31	2.24	46.1
4	authigenic quartz	35.63	26.62	12.26	92
5	quartz	14.19	9.37	3.62	29.3
6	calcite	45.62	31.39	15.4	89
7	halite-illite	28.72	22.74	10.5	61.5
8	anhydrite	24.55	5.44	20.7	28.4

Table A.2 Surface energies of quartz (Parks 1984)

Sample Description ^a	Method ^b	Environment	Temperature °C °F ^c		Q _F , J m ⁻²	Source
Natural Quartz (Brazil, B; Madagascar, M)						
B {11 $\bar{2}$ 0}	OGC	air	RT	--	0.76	Brace and Walsh [1962]
{10 $\bar{1}$ 1}	OGC	air	RT	--	0.28 to 0.57	
{10 $\bar{1}$ 1}	OGC	air	RT	--	0.46 to 0.53	
{10 $\bar{1}$ 0}	OGC	air	RT	--	0.83 to 1.2	
? {? }	Tn	air	25	--	2.	Ball and Payne [1976]
M {? }	Hz	air	20	100	--	Hartley and Wilshaw [1973]
B {? }	Hz	air	20	485	--	
Synthetic Quartz						
{10 $\bar{1}$ 1}	3PB	air	20	--	11.5	Hartley and Wilshaw [1973]
n {01 $\bar{1}$ 1} ^e	DT	air?	20	--	3.49	Atkinson [1979]
n {10 $\bar{1}$ 1}	DT	air	20	--	4.83	
{1010}	VI	air	20	--	1.34	Atkinson [this issue]
{0001}	VI	air	20	--	0.46	

Table A.3 Elastic properties of mineral granules (Santamarina et al. 2001)

Material	Young's Modulus (GPa)	Shear Modulus (GPa)	Poisson's Ratio
Quartz	76	29	0.31
Limestone	2 – 97	1.6 – 38	0.01 – 0.32
Basalt	25 – 183	3 – 27	0.09 – 0.35
Granite	10 – 86	7 – 70	0.00 – 0.30
Hematite	67 – 200	27 – 78	—
Magnetite	31	19	—
Shale	0.4 – 68	5 – 30	0.01 – 0.34

Table A.4 Strength of Soil Particles (Mitchell and Soga 2005)

Sand Name		Size (mm)	37% Strength	Tensile (MPa)	Mean (MPa)	Strength	Reference
<i>Quartz</i>							
Leighton silica sand	Buzzard	1.18	—		29.8		Lee (1992)
		2.0	—		24.7		
		3.36	—		20.5		
Toyoura sand		0.2	147.4		136.6		Nakata et al. (2001)
Aio quartz sand		0.85	51.2		52.1		Nakata et al. (1999)
		1.0	47.7		46.6		
		1.18	37.9		35.6		
		1.4	46.7		42.4		
		1.7	39.6		38.5		
Silica sand		0.5	147.4		132.5		McDowell (2001)
		1	66.7		59.0		
		2	41.7		37.3		
Silica sand		0.28	110.9		147.3		Nakata et al. (2001)
		0.66	72.9		73.1		
		1.55	31.0		29.7		
<i>Feldspar</i>							
Aio feldspar sand		0.85	20.9		24.6		Nakata et al. (1999)
		1.0	24.3		22.8		
		1.18	18.1		18.2		
		1.4	23.1		21.4		
		1.7	18.9		18.3		

A more general expression of Eqn. A.31 can be rewritten as:

$$\mu_0^i = \lambda_i \tan(\langle \theta \rangle_i) \quad (\text{A.32})$$

where μ_0^i is the intrinsic coefficient of friction in the directions of sliding ($i = x, y$) on the contact surface (Fig. A.17a); λ_i is defined as the adhesion factor of the i th-direction, per the statistical distribution of asperity heights for the contact surface (Fig. A.17b); and, $\langle \theta \rangle_i$ is the mean average value of the statistical distribution of slopes of asperities for a scan surface, and represents microscopic angles of friction per directional roughness (Fig. A.17c).

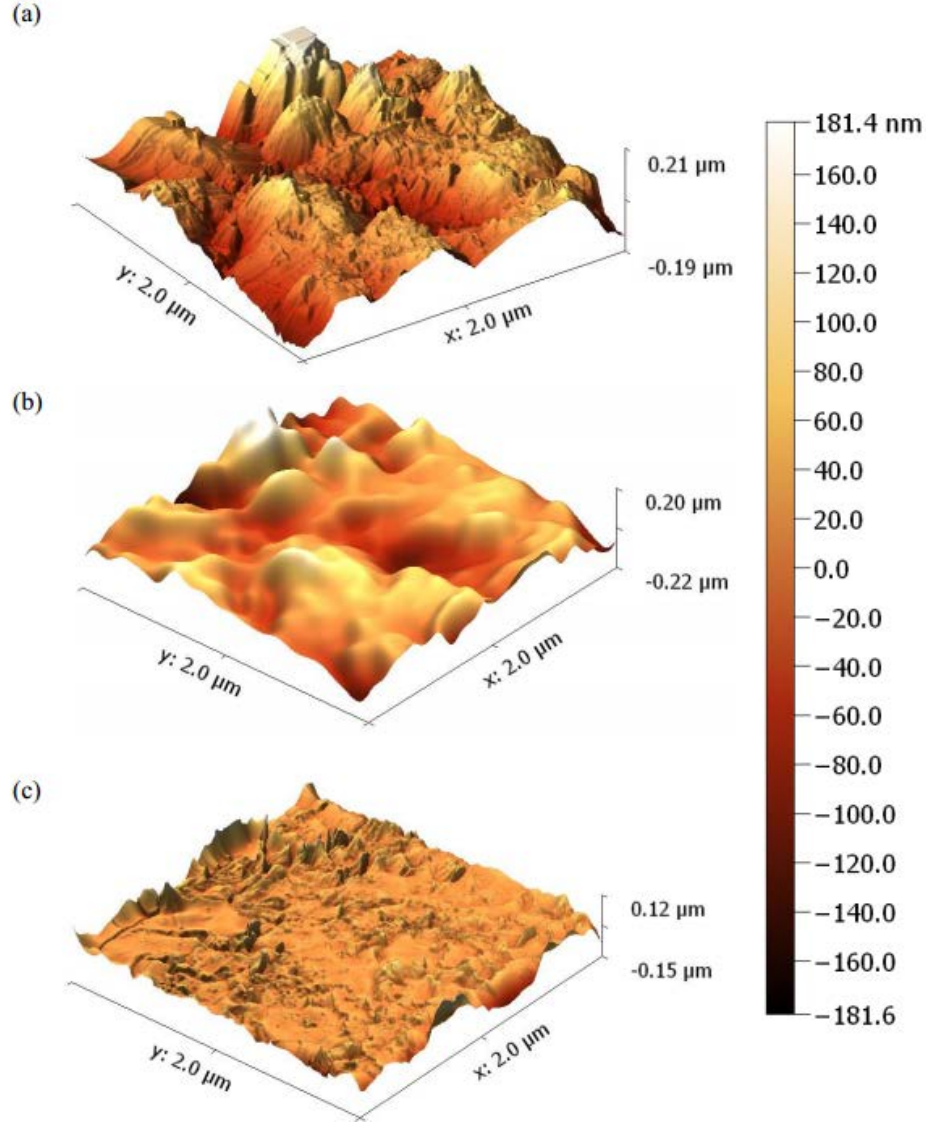


Figure A.17 2-D Fourier transformation analysis on the surface of an Ottawa 20-30 sand grain: a) Surface texture; b) Waviness of the surface (low frequency components); c) Roughness of the surface due to asperities (high frequency components) (Nadukuru 2013)

To facilitate physical interpretation of Eqn. A.32, the authors use Archard's schematic sketch of surface protuberances (Archard 1957) in combination with measured data on a sand grain (Nadukuru 2013) as shown in Fig. A.18. Consider a body of granular mass conforming a spherical volume with an average radius of curvature R_1 . More specifically, the macroscopic surface texture of the spherical body is represented by an amplitude of R_1 , with a (macroscopic) surface potential described by Prandtl-Tomlinson Theory of Dry Friction (Popov and Gray 2012).

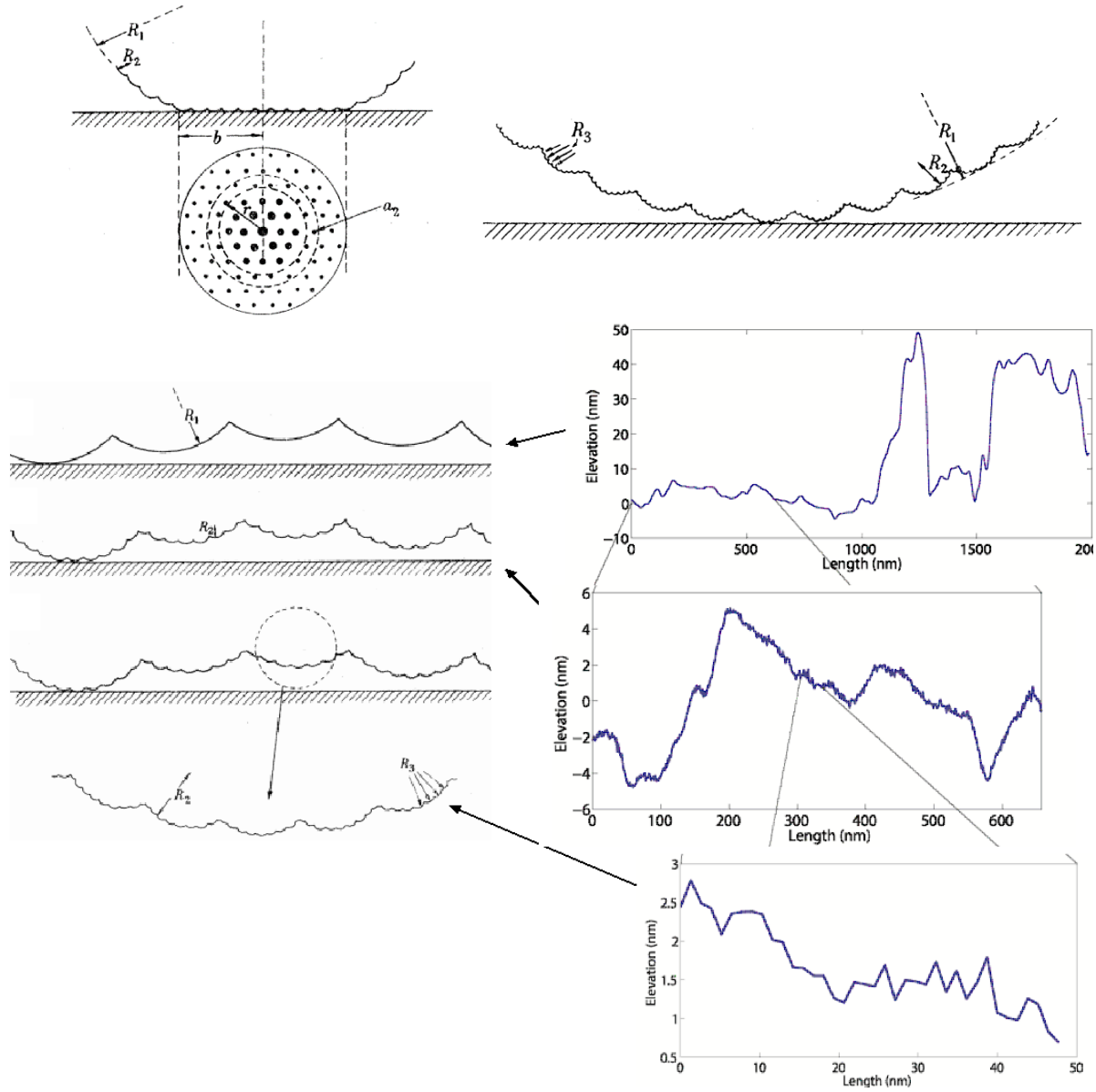


Figure A.18 Schematic sketches of frictional phenomena at three scales for $R_1 \square R_2 \square R_3$ (left) and measured tomographic data for the sand grain from Fig. A.17 (right)

On the macroscopic surface, an intrinsic radius of curvature R_2 is perturbed to represent the mean average value of microscopic angles of friction. In other words, the microscopic angles of friction are represented by $\langle \theta \rangle_i$ from Eqn. A.32, and the mean average angle of AFM data (e.g., Fig. A.19). The grain surface contains even smaller protuberances, with radius of curvature R_3 , which can either deform plastically or undergo brittle fracture in modes of shear failure. The third radius of curvature produces the effect of energy dissipation, and contributes to the intrinsic coefficient of friction.

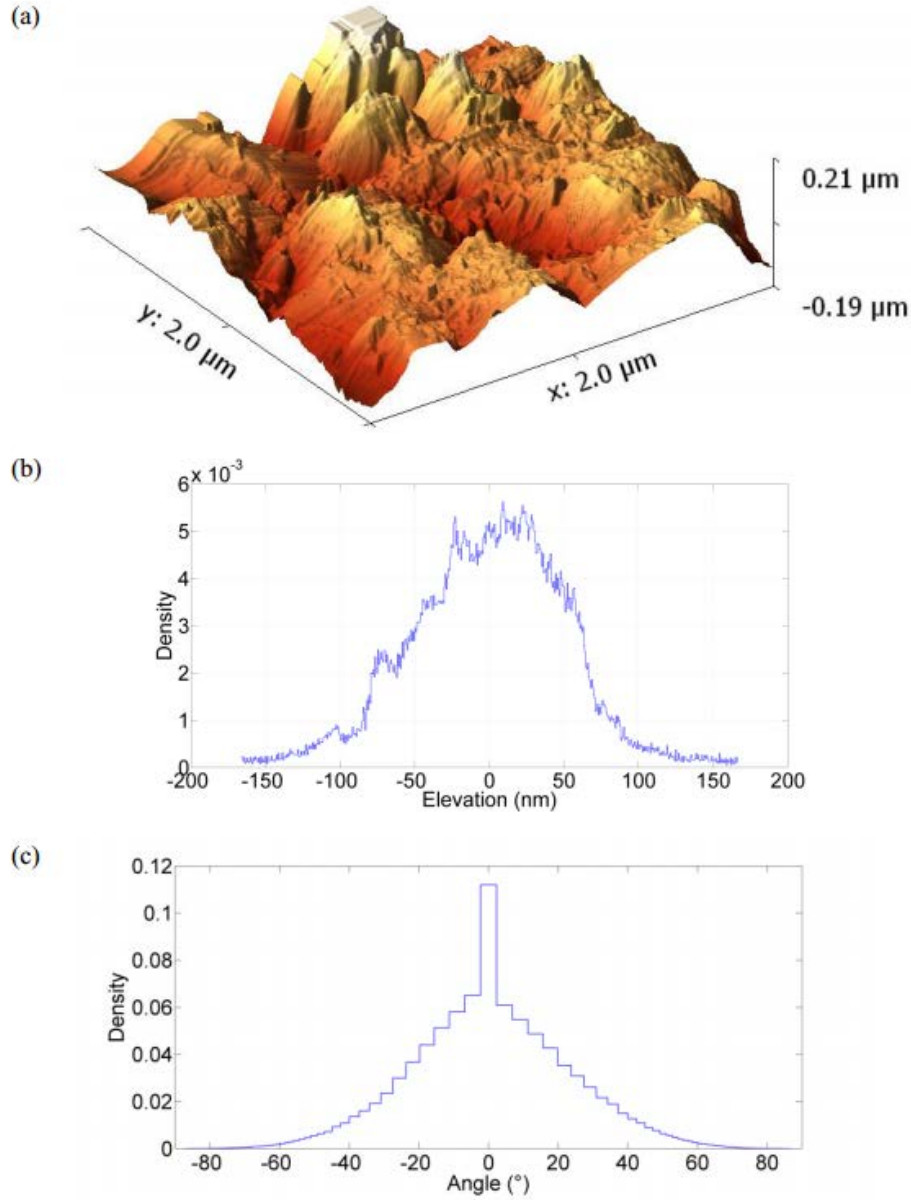
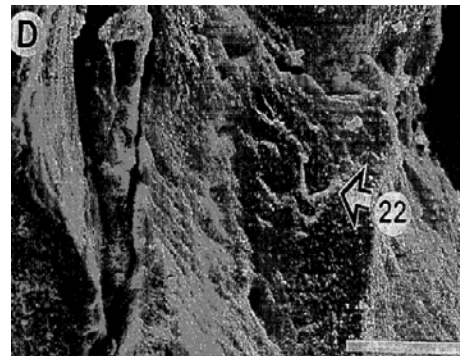
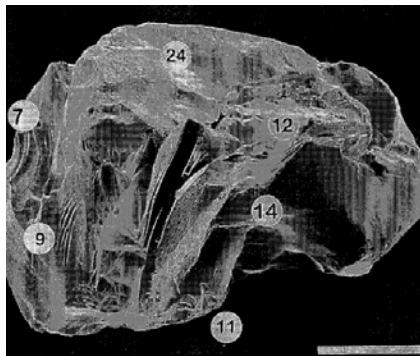


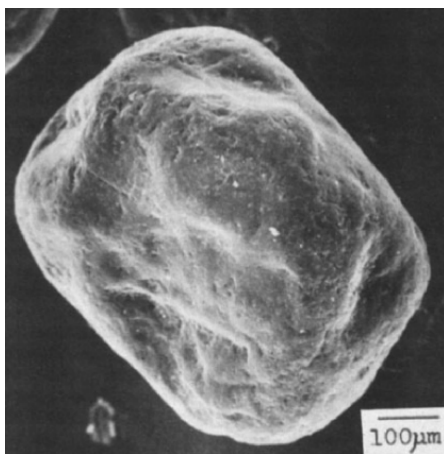
Figure A.19 AFM analysis on a grain of Fig. A.17: a) 3D AFM image of a 2 x 2 μm area on grain surface; b) Statistical distribution of asperity heights for the entire scan surface; c) Statistical distribution of slopes of asperities for the entire scan surface (Nadukuru 2013)

Based on a review of the morphology of types of sand grains, it appears that differences in micro surface textures may stem from mineralogy (crystalline growth as shown in Fig. A.12b) and/or due to the process of weathering (abrasion fatigue). It is evident that weathering processes produce microscopic abrasions on asperities, which significantly lowers the value of λ_i , and effectively reduces $\langle \theta \rangle_i$. The effects of weathering, in this context, are shown in Fig. A.20a (Helland and Homes 1997) and Fig. A.20b (Krinsley et al. 2015). These effects lead to smoother, smaller and more rounded grains (Fig. A.20c, Helland et al. 1997) as compared to young, fresh

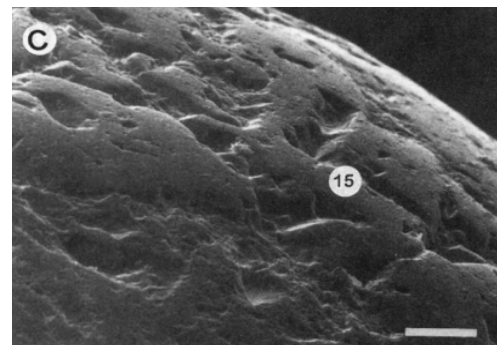
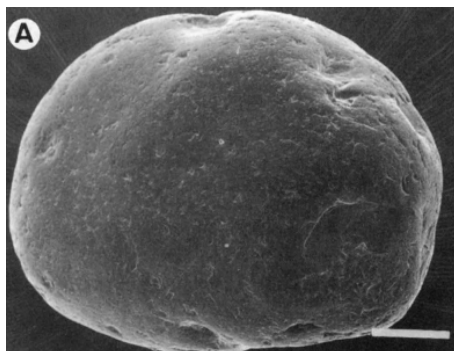
quartz grains (e.g., crushed from sandstone, Ottawa types) (Krinsley and Doornkamp 1973, Lieu 2013, Nadukuru 2013).



a)



b)



c)

Figure A.20 SEM analysis of quartz grains: a) Diameter ~ 0.55 mm (scale bar = $100\text{ }\mu\text{m}$) with rough surface texture (scan size = $10\text{ }\mu\text{m}$); b) Diameter ~ 0.8 mm with fairly smooth surface texture; c) Diameter ~ 0.6 mm (scale bar = $100\text{ }\mu\text{m}$) with smooth surface (scale size = $25\text{ }\mu\text{m}$)

In summary, factors affecting frictional phenomena at the microscopic and nanoscopic scales are:

1. Levels of Normal Force Acting on Granules' Contacts: Per Amonton's first law of friction, wherein the friction force is considered to be proportional to the normal force, it has been assumed that a constant friction coefficient is independent of normal load. However, degrees of plastic deformation at the contacts of asperities may define a microscopic contact area between two grains. In the preceding analysis, we focused on averaged frictional resistance due to adhesion (shearing multiple asperities in contacts). Accordingly, two scenarios involving micro contact mechanisms arise. First, as the contact normal load increases, the number of contacting asperities remains constant and the elastic deformation of each asperity increases. Further, in this first scenario, the contact area of the pairing grains is proportional to $N^{2/3}$ (Archard 1957 and Radchik et al. 2002) per Hertzian Contact Theory (note that the contact theories of Hertz and Mindlin are discussed in detail later in Ch. 2). In the second scenario, as the contact normal load increases, the number of contacting asperities increases proportionally, and the deformation of each asperity remains virtually constant. As a result, the contact area is proportional to N . If we write the contact area to vary as N^n , then the contact area of quartz grains may be expected to fall within the range of $n \in \{2/3, 1\}$ for either elastic-plastic and perfectly elastic deformation of asperities, respectively. For instance, analysis of plastic behaviors of asperities is not correct for a perfectly elastic solid such as diamond, and would be more appropriate for metals. Apparently, the behavior of quartz falls somewhere between these two extremes.

2. Surface Conditions on Granules: Microscopic surfaces can become contaminated by adsorbed gases, dust, and organic compounds. At contact surfaces, the deformation of asperities, i.e., the shear strength of the contact, will be influenced by the type and degrees of contaminants adsorbed onto the surfaces. Also, loading history (wind and water loads) on granules affects surface roughness of grains (i.e., the height distribution of asperities). Thus, measured values of the intrinsic coefficient of friction can vary widely depending upon surface cleanliness, sedimentary history, and environmental conditions to which grains may have been exposed.

3. Hardness and Adhesion of Quartz and Brittle Materials: Brittle materials do not possess appreciable tensile strength. Therefore, indentation hardness tests are relevant to the geometric contacts of the contacting asperities. Indentation hardness is measured as the normal force divided by the residual area of deformation after the indenter is removed. For contact normal stress less than the indentation hardness, asperities deform elastically. When the stress exceeds the hardness, the asperities in contact deform plastically. For quartz, yield stresses on coarse grains with diameters greater than $100\text{ }\mu\text{m}$ and less than 2 mm can be approximated to be equal to one third of the mean tensile strengths, ranging from 40 MPa to 150 MPa (Table A.1). However, at the microscopic scale (sizes of asperity), the indentation hardness can reach 10 GPa . Thus, "cold

welding” phenomena would probably not be prevalent on shearing in the contact surface of quartz granules, unless the granules were subjected to an ultra-high pressure (to cause yielding) and/or high temperatures (to cause softening). Instead, brittle fracture around, within, and between asperities would probably be a predominant shearing mechanism, which may have been previously viewed to be yielding on the contact surface of grains from a macroscopic perspective.

The coefficient of friction of quartz can be very low, ranging from 0.1 to 0.2, when surfaces are polished and measured under dry conditions (Horn 1961). When the surfaces are submerged in water, the coefficient increases by a factor of three to four (Horn and Deere 1962). For example, measured friction coefficients were 0.53 for air-dried conditions and 0.71 for submerged conditions. According to Horn (1961), the prevalence of smooth surfaces under air-dried conditions was the result of adsorbed molecules of air acting as a highly effective lubricant. Water can disrupt the orientation of this boundary layer, leading to higher values of the coefficient (Bromwell 1966). Sjaastad (1963) reported similar experimental results such that the coefficient of dry quartz was found to vary from 0.33 (at ambient conditions) to 0.6 (measured in a vacuum). One difference in sample preparation between the tests conducted by Horn (1961) relative to those of Sjaastad (1963) was that Sjaastad soaked quartz grains in benzene and acetone, whereas Horn wiped the surfaces with an acetone-soaked piece of cotton. Presumably, Sjaastad’s granules had a higher degree of surface cleanliness. The highest measured values of the coefficient in the air-dried conditions was 0.77 for quartz and 0.94 for glass (Hardy and Doubleday 1922). Rougher surface textures resulted in development of greater shear stresses. Thus, higher values of μ_0 were observed, which is a function of maximum shear stress acting on an actual contact area (i.e., total area of all contact surfaces among asperities), as shown in Fig. A.21.

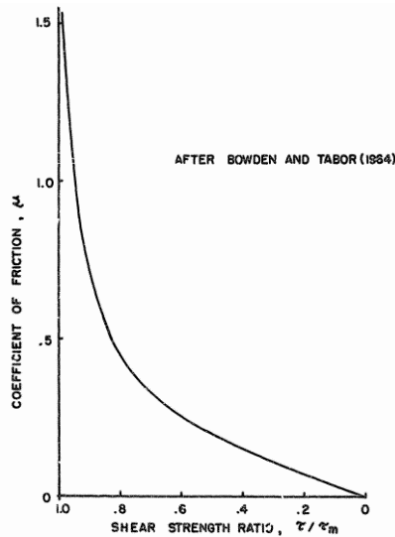


Figure A.21 Shear strength ratio versus coefficient of friction (after Bowden and Tabor 1954, Bromwell 1966)

Other historical measured values of angle of friction for earth minerals are summarized in Table A.5, where the arctangent of μ_0 is referred to as ϕ_μ . This quantity (ϕ_μ), has been used in many soil mechanics textbooks as if it were an intrinsic friction parameter associated with the surface roughness of grains. However, empirical values of ϕ_μ have been estimated under various levels of

normal loads applied on contacting grains, height distributions of asperities, degrees of surface contamination, degrees of weathering, and thus, the measured values of ϕ_μ listed in the Table A.5 vary over a wide range ($0 \leq \phi_\mu \leq 45^\circ$). A physical maximum of the coefficient appears to be, thus, approximately on the order of unity. However, for scenarios where significant plastic deformation takes place (in contact asperities subjected to high normal pressures), the value can exceed the order of unity, which was experimentally tested in the recent years (Shellenberger and Logan 2002). In the following section, we discuss macroscopic surface texture formed by multiple grain contacts and how such textures may also contribute to the scale-dependent coefficient of friction. Subsequently, we will evaluate a range of values of the macroscopic factors for later use in determining frictional input parameters for use in conjunction with the DEM.

Table A.5 Angles of friction (microscopic) for minerals (Mitchell and Soga 2005)

Mineral	Type of Test	Conditions	ϕ_μ (deg)	Comments	Reference
Quartz	Block over particle set in mortar	Dry	6	Dried over CaCl_2 before testing	Tschebotarioff and Welch (1948)
		Moist	24.5		
		Water saturated	24.5		
Quartz	Three fixed particles over block	Water saturated	21.7	Normal load per particle increasing from 1 g to 100 g	Hafiz (1950)
Quartz	Block on block	Dry	7.4	Polished surfaces	Horn and Deere (1962)
		Water saturated	24.2		
Quartz	Particles on polished block	Water saturated	22–31	ϕ decreasing with increasing particle size	Rowe (1962)
Quartz	Block on block	Variable	0–45	Depends on roughness and cleanliness	Bromwell (1966)
Quartz	Particle–particle	Saturated	26	Single-point contact	Procter and Barton (1974)
	Particle–plane	Saturated	22.2		
	Particle–plane	Dry	17.4		
Feldspar	Block on block	Dry	6.8	Polished surfaces	Horn and Deere (1962)
		Water saturated	37.6		
Feldspar	Free particles on flat surface	Water saturated	37	25–500 sieve	Lee (1966)
Feldspar	Particle–plane	Saturated	28.9	Single-point contact	Procter and Barton (1974)
Calcite	Block on block	Dry	8.0	Polished surfaces	Horn and Deere (1962)
		Water saturated	34.2		
Muscovite	Along cleavage faces	Dry	23.3	Oven dry	Horn and Deere (1962)
		Dry	16.7	Air equilibrated	
		Saturated	13.0		
Phlogopite	Along cleavage faces	Dry	17.2	Oven dry	Horn and Deere (1962)
		Dry	14.0	Air equilibrated	
Biotite	Along cleavage faces	Saturated	8.5	Oven dry	Horn and Deere (1962)
		Dry	17.2		
		Dry	14.6	Air equilibrated	
Chlorite	Along cleavage faces	Saturated	7.4	Oven dry	Horn and Deere (1962)
		Dry	27.9		
		Dry	19.3	Air equilibrated	
		Saturated	12.4		

A.1.6 Factors Affecting Frictional Resistance at Macroscopic Scales

The macroscopic texture of the granular mass stems from its particulate nature, which represents collective geometric particle characteristics and the resulting arrangements of particles. The most important macroscale characteristic is the volumetric density distribution, which relates to the statistics of particle shape, size distribution, and spatial arrangement of particles (Santamarina et al. 2001). These geometric parameters are briefly reviewed in order of significance,

with respect to macroscopic surface texture. The corresponding relevance of each parameter (in transitioning to considerations for numerical modeling of DSEs) is discussed afterward.

Size

Quantifying representative grain sizes has previously been carried out in many ways, for example, by making use of the: 1) Diameter of a circle with equal projected area; 2) Dimensions of the grain in several directions; 3) Opening of the finest sieve that a grain passes through; and, 4) Mean diameter. Grain size is often used to classify soils as gravels, sands, silts, or clays although various classification systems, which mutually differ in the particle sizes categorization, as part of assigning soil denominations. A statistical means of characterizing granule diameters has also been used (Fig. A.22).

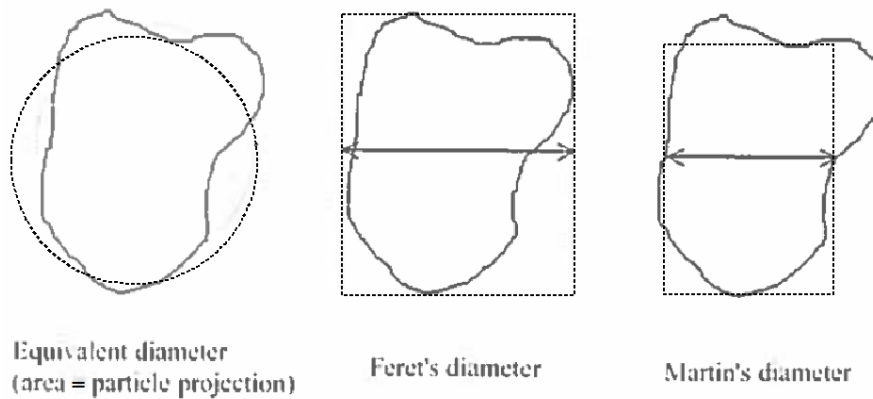







Figure A.22 Alternative definitions of particle diameter (Santamarina et al. 2001)

Sphericity, Roundness, and Angularity

Sphericity is an index that indicates the extent to which dimensions of the particle are of the same order of magnitude in projected planes, for three orthogonal directions. Physical quantification is the ratio of the surface area of a sphere of equal volume to the surface area of the particle. Based on the definition of particle size using an equivalent diameter, a definition of sphericity could be given as the ratio of the area of the particle projection to the area of the circle with diameter equal to the longest length of projection called 'projection sphericity'. Elliptical particles can be further characterized by eccentricity and slenderness. In 3-D, elongation and flatness per axis ratios are additionally needed to characterize preferential directions of anisotropic particle assembly, which will be discussed after a brief summary of the geometric characteristics of grains. Note that an ellipsoid has higher degrees of roundness yet lower sphericity. Pictorial comparisons between roundness and sphericity are shown in Table A.6.

Table A.6 Rounded particle slenderness and eccentricity (Santamarina et al. 2001)

Shape					
Slenderness	5.0	2.5	1.67	1.25	1.0
Eccentricity	0.67	0.43	0.25	0.11	0

The roundness of a particle is a measure of the curvature of the corners and edges expressed as a ratio of the average curvature of the particle as a whole, independent of its form. For practical purposes, an average of radius of curvature is used in terms of the inscribed circle drawn on a projection of the particle over a maximum radius that can be inscribed in a plane (Fig. A.23).

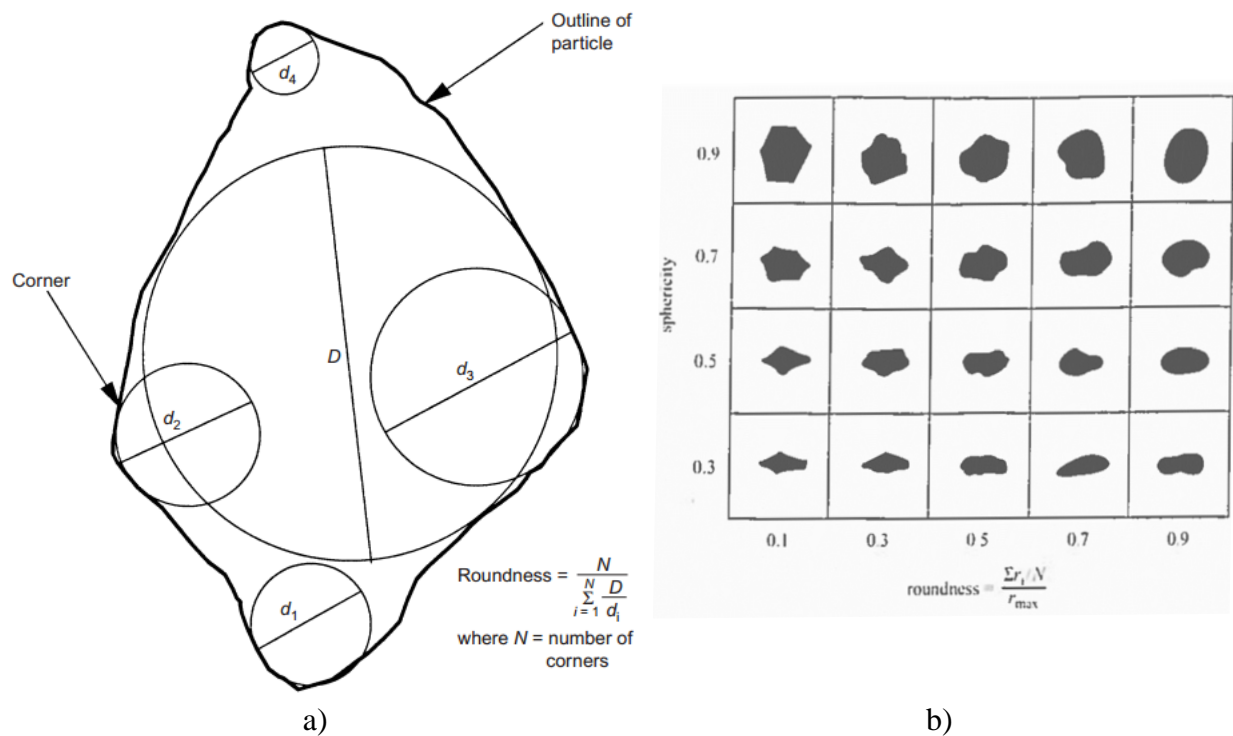


Figure A.23 Particle roundness and sphericity: a) Illustration of Wadell's (1932) evaluation of particle roundness (from Sukumaran, and Ashmawy 2001); b) Relationship between roundness and sphericity with visual estimation of particle silhouettes (Krumbein and Silos 1963)

Wadell (1932) was the first to use a mathematical expression to quantify 'shape', which he coined as 'sphericity'. Note that terms 'shape' and 'sphericity' are distinct from the term 'roundness'. The shape of a particle is its form, entirely independent of whether the edges or corners are sharp or round. Fundamentally, the shape is a measure of the ratio of the surface area of a particle to its volume. This ratio reaches at a minimum for spheres. Also, the ratio indicates how closely or remotely the particle approaches the form of a sphere. For practical purposes, the ratio is difficult to measure, and thus, the actual measurement is taken as the ratio of the volume

of the particle to the volume of its circumscribing sphere. The cube root of this ratio is called the ‘sphericity’ of the particle (Krumblein 1941).

Recall that ‘roundness’ is distinct from ‘sphericity’. When roundness equals to 1.0, the particle is a sphere. Angularity is opposite to roundness, and as particles become more angular, roundness approaches zero (Fig. A.24a). Fig. A.24b shows differences in the particle profiles with respect to sphericity, angularity, and roundness.

Grade term	Russell and Taylor		Pettijohn	
	Class Limits	Arithmetic Mid-Point	Class Limits	Geometric Mid-Point
Angular	0 to 0.15	0.075	0 to 0.15	0.125
Subangular	0.15 to 0.30	0.225	0.15 to 0.25	0.200
Subrounded	0.30 to 0.50	0.400	0.25 to 0.40	0.315
Rounded	0.50 to 0.70	0.600	0.40 to 0.60	0.500
Well rounded	0.70 to 1.00	0.850	0.60 to 1.00	0.800

a)



b)

Figure A.24 Example of particle shape characterization (from Powers 1953): a) Roundness grades; b) Roundness scale

A.1.7 Discrete Sphere Elements (DSEs) and Model Parameters

The application of soft particle dynamic analysis models to granular soil mechanics (referred to as the discrete element method, DEM, Cundall and Strack 1979) is based on spherical discretization of individual particles. The method has been widely adopted in modeling and understanding granular materials in engineering applications, where knowledge of the static and dynamic behavior of discontinuous multiple bodies is important. An in-depth description of DEM is presented later in Ch. 2.

In the DEM simulations and numerical tools developed for use in the current study, complex body shapes of individual grains (particles) of granular media are discretized (approximated) by spheroids (spherical elements), as shown in Fig. A.25. The main criticism would appear to focus on a morphological discrepancy between a physical grain and a sphere, and resulting topological changes in the internal structure. Fundamentally, contact forces of spherical bodies may differ from variations of the contact mechanisms of irregular granular bodies, not only at the level of individual grains, but also as an assembly. Prior to rebuttal discussion, we first review the latest developments of shape descriptors as one possible alternative to modeling DSEs.

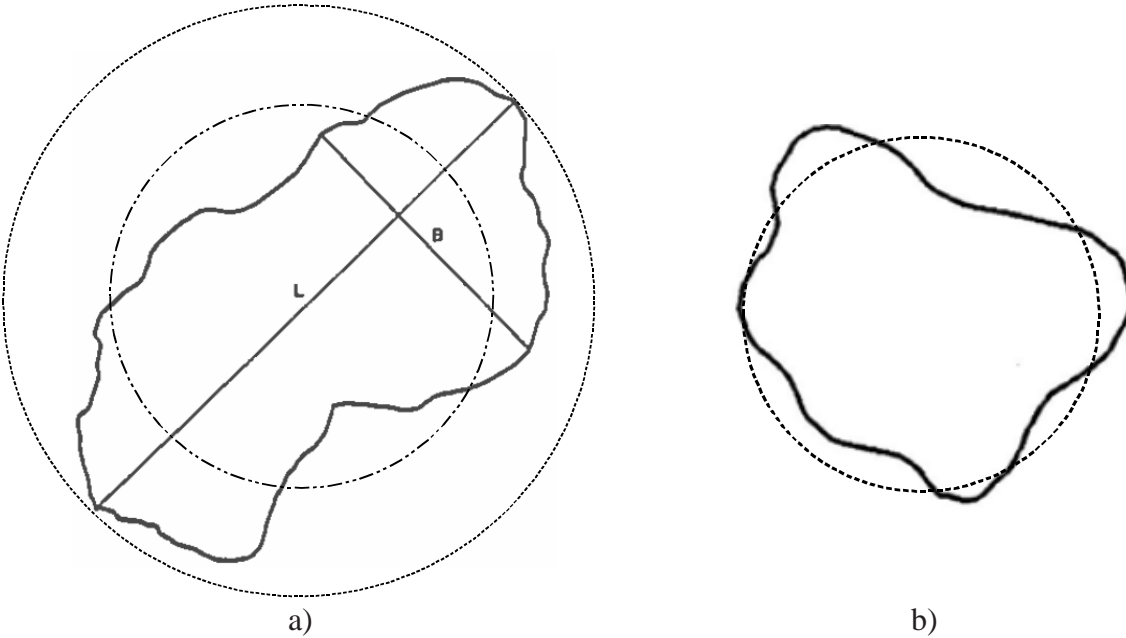


Figure A.25 Irregularly shaped grains represented by spheroids: a) Circumscribing diameter (note that the volume of the inner sphere drawn on the larger grain is approximately the same as the volume of the particle); b) Equivalent diameters (note that the surface of the sphere drawn on the smaller grain is approximately the same as the surface area of the particle)

Improved geometric descriptors to represent complex bodies have recently been proposed. For example, composite approaches have been proposed, where simple spherical geometries or sharp-edged polygons are clustered to describe more complex shapes, and thus, result in irregular macro textures. One such approach is to only examine the portions of a given surface that conform to simple geometries, in forming complex clustered particles (Fig. A.26a). Another example approach is to superimpose several spherical bodies to approximate a desired irregular shape, Fig. A.26b, per Fourier transformation analysis. By overlapping several spheres, tablet shaped particles can be created. A cylindrical main body, with attached spheres at both ends or ellipsoid-like particles (via replacing the cylinder with a torus), has also been investigated for use in discrete element analysis. Summarily, if a more general shape descriptor is desired, then various geometries (comprised of several constrained spherical elements) may be superimposed to form a new complex particle. Moreover, composite discrete elements that vary in size can be applied to the generation of macro contact surfaces, which in turn, exhibit local variations in element-level density allocation.

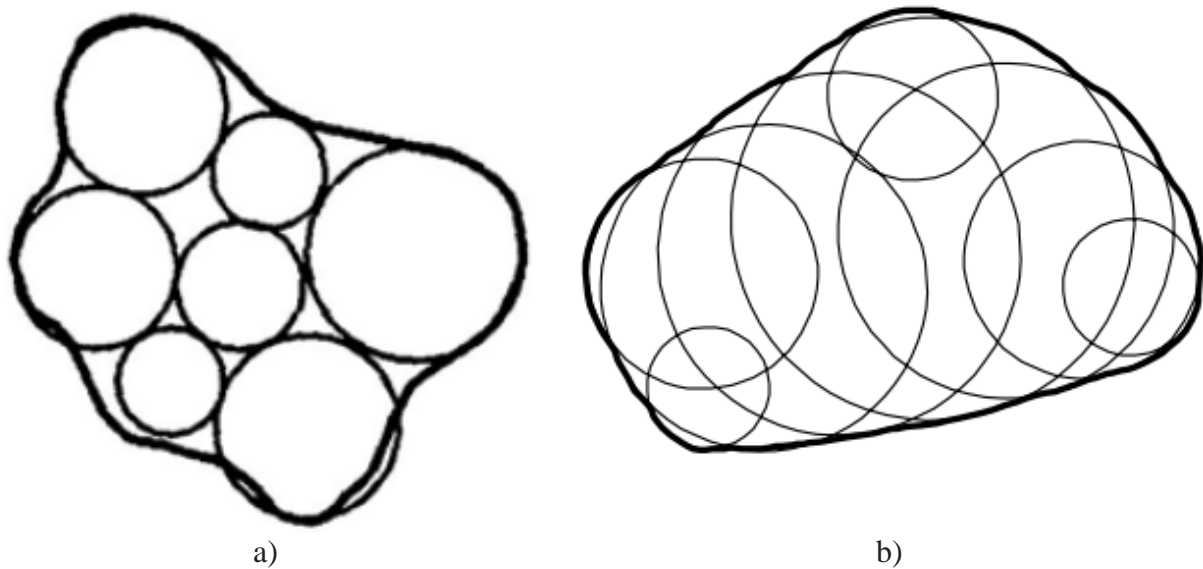


Figure A.26 Formation of irregular shapes of discrete elements: a) Clustered discrete element (the solid line inscribing the clustered circles represents a silhouette surface of a grain; b) Discrete volume of superimposed spheres





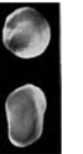
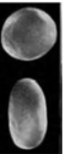
Advancement on shape descriptors of DEM permits unanswered questions to be addressed, and can enhance the fidelity of results obtained from DSE simulations. However, careful consideration must be given to the application of multiple-composite discrete elements for modeling large-scale (megascopic) assemblies in civil engineering and design applications. Namely, the multiple-composite modeling is: 1) Computationally expensive; and, 2) Susceptible to hardware limitations. For example, if a particle size distribution of coarse-grained soil is represented for the volume of a 100 mm by 200 mm cylinder by using four different sizes of DSEs, then the total number of DSE required is approximately 3 million to 4 million. As a separate scenario, even if uniform DSEs with diameters of 5 mm were to be employed, then the total number of DSEs required to populate a volume of 6 m x 6 m x 10 m would exceed one hundred million. A factor (with value greater than unity) is, then, multiplied to the total number of DSEs required to account for composite construction of representative particle shapes. Even if possible, numerical simulation of 1 sec, for a model representing in-situ field conditions, would require several months of massively parallel processing (MPP) on the-state-of-art supercomputer, and several billion DSEs. Usage of such complex shape descriptors is impractical for the purpose of this study, and unrealistic in consideration of available resources to the research team.

In order to (practically) achieve the objectives pertaining to the current numerical study, and to quantify the influence of particle shape on the intrinsic angle of friction (corresponding to R_2 of Fig. A.17), previous experimental work has been reviewed and synthesized. Particular importance on data collection is to decouple the particle shape and size effects on shear behaviors of the granular soil. As a theoretical basis of such decoupling was established in the above portions of Ch. 2, we now specifically examine particle shape effects by comparing similar sized sieve fractions of particles chosen for their inherent morphology. In this way, a correlation of particle

shape to the intrinsic angle of friction (as a function of particle shape indexes) can be drawn upon, and generalizations can be made for grains over a wide range of grain sizes.

Particle shape is a distributed parameter. As shown in Fig. A.26, complexity of shape necessitates more laborious derivations for the corresponding descriptors, where the descriptors are needed if it is desired to more directly model surface contours to a greater degree of accuracy. Particle shape is commonly quantified in terms of two-dimensional shapes in the powder industry. One shape measure of particular interest (for simplicity and generality) is the boundary fractal dimension, which constitutes a measure of surface geometry unconstrained by the length scale. Higher angularity and lower roundness values represent higher particle surface irregularities (Russell and Taylor 1937; Krumbein 1941; Powers 1953; Alshibli and Alsaleh 2004). Also, it is well known that increasing particle irregularities increases fractal dimension (Vallejo 1995, Kolay and Kayaball 2006). Based on reviews of the aforementioned studies, the fractal dimension appears to be affected by the particle shape; fractal dimensions increase with increasing angularity or decreasing roundness of the particles. Table A.7 is given as a reference for making correlations between fractal dimension of particles and particle shape indexes (i.e., sphericity, roundness, and angularity) per Fig. A.24b. As a fractal dimension approaches unity, roundness increases.

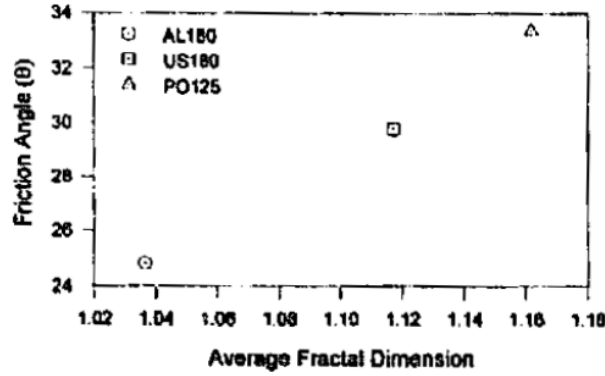
Table A.7 Fractal dimensions of granular particle shapes (Arasan et al. 2011)

Particle Images	Unnatural Particles						
Roundness Class		Very Angular	Angular	Sub-Angular	Sub-Rounded	Rounded	Well Rounded
Roundness - Cox (1927)*	< 0.50	0.5-0.65	0.65-0.70	0.70-0.75	0.75-0.77	0.77-0.80	0.80-1.00
Roundness – Russell and Taylor (1937)	-	-	0.00-0.15	0.15-0.30	0.30-0.50	0.50-0.70	0.70-1.00
Roundness – Krumbein (1941)	< 0.10	0.10-0.20	0.20-0.30	0.30-0.50	0.50-0.60	0.60-0.80	0.80-1.00
Roundness – Pettijohn (1949)	-	-	0.00-0.15	0.15-0.25	0.25-0.40	0.40-0.60	0.60-1.00
Roundness - Powers (1953)	0.00-0.12	0.12-0.17	0.17-0.25	0.25-0.35	0.35-0.49	0.49-0.70	0.70-1.00
Roundness - Al-Rousan (2004)	> 2.00	1.54-2.00	1.43-1.54	1.33-1.43	1.29-1.33	1.25-1.29	1.00-1.25
Roundness – Alshibli and Alsaleh (2004)	-	> 1.50	1.40-1.50	1.30-1.40	1.20-1.30	1.10-1.20	1.00-1.10
<i>Fractal Dimension</i>	<i>1.70-2.00</i>	<i>1.55-1.70</i>	<i>1.40-1.55</i>	<i>1.30-1.40</i>	<i>1.25-1.30</i>	<i>1.15-1.25</i>	<i>1.00-1.15</i>

Chan and Page (1997) reported isolated shape effects of powder particles with sizes ranging 0.1 mm to 0.2 mm, and for average boundary fractal dimensions of three unique shapes (spherical, 1.0367; irregular, 1.1173, with sub-angularity; and, dendritic 1.1618, with multiple protrusions on the surface), as shown in Fig. A.27a. Due to the fineness of the powder particles, they considered microscopic surface roughness to be consistent among all three sampling groups.

Powder	AL180	US180	PO125
Flow rate (s per 50 g) ^a	14.5	20.5	31.5
Apparent density (g cm ⁻³) ^a	4.85	3.46	2.48
Tap density (g cm ⁻³) ^a	5.42	3.96	2.96
Hausner ratio	1.12	1.14	1.19
Average fractal dimension	1.0367	1.1173	1.1618

a)



b)

Figure A.27 Correlations between the fractal dimension and interparticle friction angle (Chan and Page 1997): a) Particle characteristics; b) Direct ring shear test results

Based on a linear correlation between the fractal dimensions and frictional parameters in the direct ring shear cell tests of Chan and Page 1997, we write:

$$\mu_1 = \tan(\phi_{cs}^a) - \tan(\phi_{cs}^{sp}) \quad (A.33)$$

where μ_1 is a numerical friction coefficient for shape effects, ϕ_{cs}^a represents an internal friction angle of granular packing with irregular particle shapes, and ϕ_{cs}^{sp} denotes an internal friction angle of granular packing with uniform size DSE at a constant volume. Alternatively stated, μ_1 is used as a numerical parameter to simulate shape effects in scale-dependent friction (in addition to the intrinsic coefficient of friction μ_0). It is noted that the modeling concept expressed in Eqn. A.33 is used in engineering analysis to minimize morphological errors due to spherical representation of soil grains.

Sukumaran and Ashmawy (2001) reported an observational relationship between particle shape factor and large-strain friction angles for drained specimens. Based on SEM analyses: Daytona Beach sand particles have distinct cleavage planes; Syncrude Tailings sand has a very rough texture, and is composed of irregularly shaped particles; and, Ottawa sand #60/80 particles are more rounded and less angular than the other two materials. It was further reported in Sukumaran and Ashmawy (2001) that considerable variation exists between particles in each type of sands. From the SEM photomicrographs, Sukumaran and Ashmawy indicated that, in addition to shape and angularity, quantitation of surface texture of particles may ultimately be necessary as it varies significantly between the various materials. Their correlation between angularity factors (AF%, Fig. A.28) in test results from Ottawa sand is consistent with the work of Chan and Page (1997).

Material	Label	D_{50} : mm	C_u	e_{max}	e_{min}
Ottawa #20/70	1	0.53	2.4	0.78	0.47
Ottawa #60/80	2	0.21	2.4	0.85	0.55
Ottawa #15 (angular)	3	1.46	1.5	1.06	0.72
Ottawa #45 (angular)	4	0.57	2.1	1.11	0.75
Ottawa #90 (angular)	5	0.27	2.2	1.10	0.73
Glass ballotini #140	6	0.17	1.4	0.72	0.34
Glass beads #10/20	7	1.18	1.0	—	—
Daytona Beach sand	8	0.23	1.4	1.00	0.64
Syncrude Tailings sand	9	0.18	2.5	1.14	0.59
Michigan Dune sand	10	0.33	1.5	0.80	0.56
Fraser River sand	11	0.30	1.9	1.13	0.78

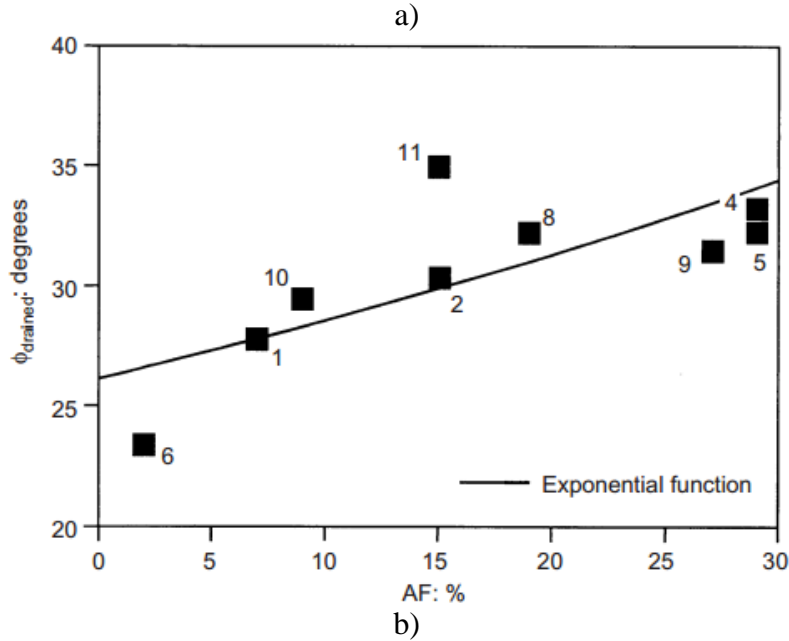


Figure A.28 Correlation between angularity and the interparticle friction angle; for Ottawa sands, see the linear trend of the numbers, i.e., 1, 2, 4, and 5 (from Sukumaran and Ashmawy 2001): a) Material types; b) Relationship between large-strain friction angles (drained triaxial tests), shape, and angularity factors (materials labeled with numbers given in Fig. A.28a)

In other geotechnical applications, Santamarina and Cho (2004), Fig. A.29a, have proposed a correlation of which a greater degree of shape effects is implied:

$$\phi_{cv} = 42 - 17 \cdot R \quad (\text{A.34})$$

where ϕ_{cv} is the internal angle of friction at constant volume, and R is a value of roundness. However, Santamarina and Cho (2004) actually used values of the angle of repose versus roundness. As a result, Eqn. A.34 represents a combined (coupled) effect of both shape and surface roughness, which Sukumaran and Ashmawy (2001) has also observed in correlation with shape factors (SF, an inclusive factor of angularity and surface roughness) in Fig. A.29b. Therefore, it is assumed, for values of μ_1 utilized in the current study, that μ_1 is bounded between 0 and 0.19, based on the correlation between angularity and constant-volume angles of friction as shown in

Fig. A.27 Anthony and Marone (2005) also reported essentially the same bound per percentage of angular grains, and the corresponding increment in the peak friction coefficient.

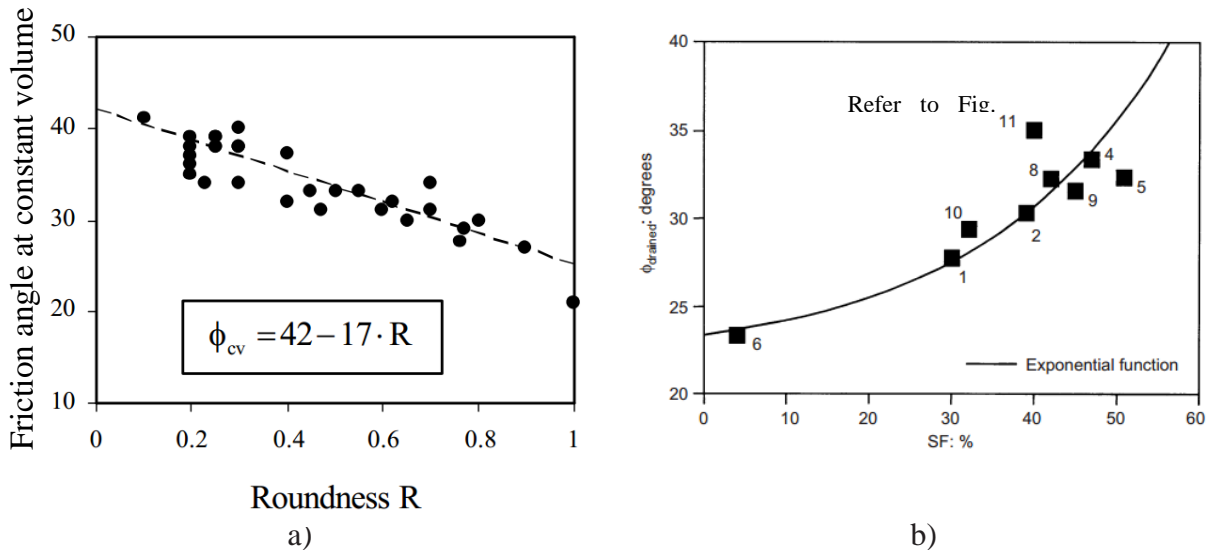


Figure A.29 Variations in measured internal angles of friction at constant volume per angularity and roughness: a) Linear correlation between angle of repose and roundness (Santamarina and Cho 2004) (note: angle of repose was assumed equal to angle of friction at constant volume); b) Exponential correlation for coupled effects including surface roughness and angularity (Sukumaran and Ashmawy 2001)

In laboratory experiments, Mair et al. (2002) investigated the influence of grain shape, roughness, and particle size distribution on the frictional strength and stability of granular layers between roughened steel blocks. Using a controlled direct shear apparatus (Fig. A.30a), Mair et al. (2002) observed that the macroscopic coefficient of friction varies (rather significantly) between 0.6 for angular quartz sand and 0.45 for granular materials of spherical grain (Fig. A.30b). The friction levels of spherical beads with both narrow and broad particle size distributions were reported to be identical.

Mair et al. (2002) additionally suggested that the kinematics of angular and spherical particles behave in distinctively different manners. The associated reasoning was that spheres are highly efficient in translational movement due to preferential rolling. In contrast, angular grains at contact prohibit one another from rolling over by interlocking at the interfaces, leading to intensive tangential contact forces at sliding (refer to Fig. A.31). The pronounced kinematical differences of granules necessitate a qualitative discussion of the process of rolling contacts, which is given below.

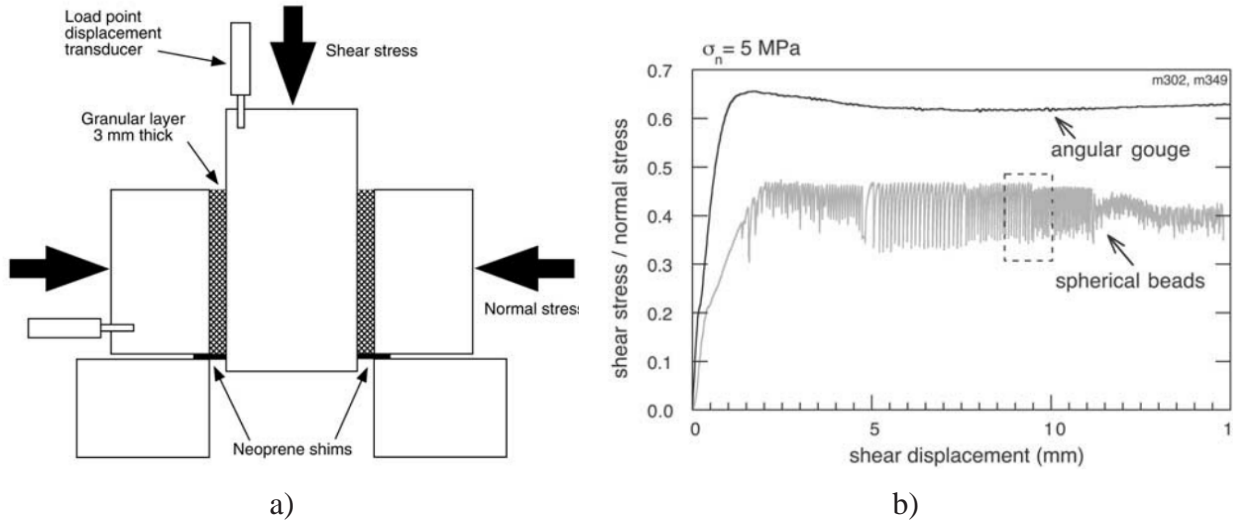


Figure A.30 Grain shape influence on macroscopic friction (from Mair et al.2002): a) Schematic diagram of direct shear apparatus: the 100 x100 mm, 3-mm-thick granular layers sandwiched between rough steel blocks. The orientations of shear and normal stresses are specified; b) Friction as a function of shear displacement for angular and spherical grains at normal stress = 5 MPa. Spherical grains show a lower value of friction coefficient and exhibit stick-and-slip behavior, whereas angular gouge slides stably with higher friction.

Based on both experimental data and laws of physics, the origin of friction of grain contacts has been analytically reasoned from: 1) The dominant mechanism of adhesion (due to interlocking asperities) is sliding at the microscopic scale; and, 2) Frictional resistance (deriving from granular morphology) is sliding at the intermediate (grain) scale. Unlike a solid (continuum) treatment of friction, which is mainly a surface property, it is also known, both experimentally and theoretically, that shear strength increases with μ . Shear strength also mobilizes gradually in a loose packing such that mobilization appears to be independent of μ . This behavior confirms the fact that, even though sliding friction is the dominant source of dissipation in plastic flow within a bulk volume of grains, the main grain-scale mode of displacement can be the rolling of grains over one another. In turn, this rolling limits mobilized sliding friction to relatively low levels. Numerical simulations (presented in Chapter 3) also indicate that, in granular media modeled using DSEs, more pronounced tangential (sliding) contact forces occur when DSE are frustrated in rolling. These observations further suggest that the prediction of the macroscopic shear strength is substantially affected when the relative rolling is restrained by a mechanism of interlocking between the grains (or in very dense packing scenarios).

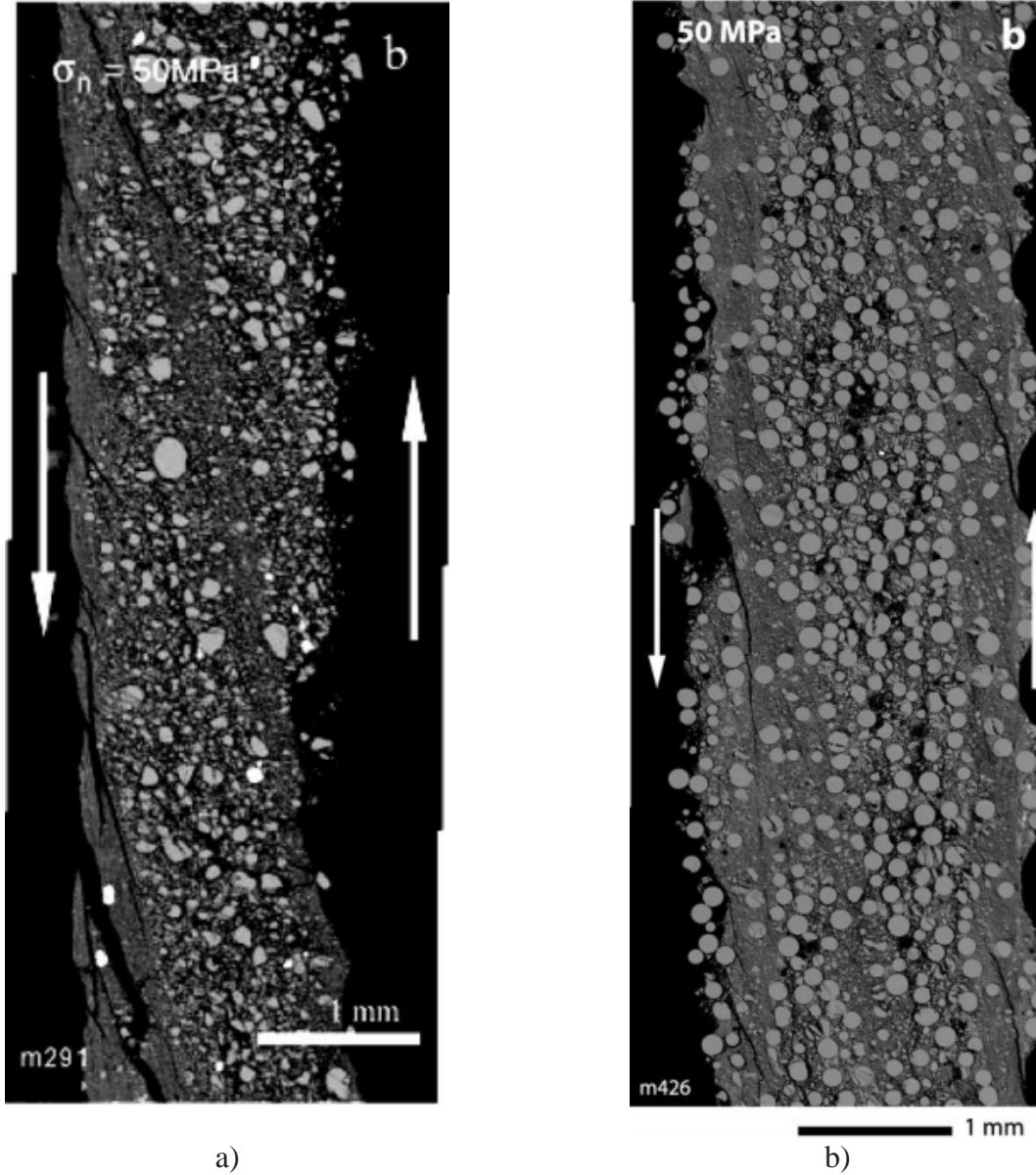


Figure A.31 SEM images of particulate fabrics on shear surface planes (from Mair et al.2002): a) SEM photomicrograph of angular gouge deformed at normal stress = 50 MPa. Slip is 20 mm in both cases; b) SEM photomicrograph of spherical gouge deformed at normal stress = 50 MPa. Note development of the fabric at the shear plane due to particle size distribution.

A model of interlocking in the framework of the contact dynamics method is introduced through a *rolling friction* law. Along these lines, the relative rotations of grains correspond to the generation of a contact torque, which is proportional to the normal force. To facilitate expression of the model, a rolling friction coefficient μ_r is introduced, and is analogous to the coefficient of (sliding) friction μ . In order to simulate interlocking between DSEs, we replace the effect of non-spherical grain shapes (convex or angular) by a contact law of rolling resistance. Let us define

local kinematic variables for the relative angular velocity ω_r at the contact between two adjacent DSEs, referred to as *Particle 1* and *Particle 2* (Fig. A.32), with angular velocities of ω_1 and ω_2 :

$$\omega_r = \omega_1 - \omega_2 \quad (\text{A.35})$$

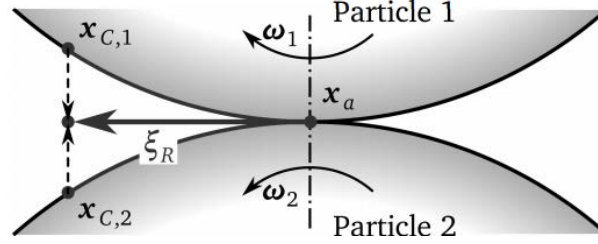


Figure A.32 Rolling displacement caused by pure rolling motion of two elastic spheres with equal radius R

The interlocking between grains corresponds to $\omega_r = 0$. This condition requires that the torque M at the contact point does not exceed the elastic threshold of T_R (Estrada et al. 2008):

$$\begin{aligned} \omega_r &> 0 \quad \text{if } T = -T_R \\ \omega_r &= 0 \quad \text{if } -T_R < T < T_R \\ \omega_r &< 0 \quad \text{if } T = T_R \end{aligned} \quad (\text{A.36})$$

Further, this mechanism allows the transmission of a torque, which can be described as rolling resistance (analogous to Coulombic sliding resistance). To determine rolling resistance with an elastic limit, we consider the effect of particle shapes in force equilibrium (Fig. A.33).

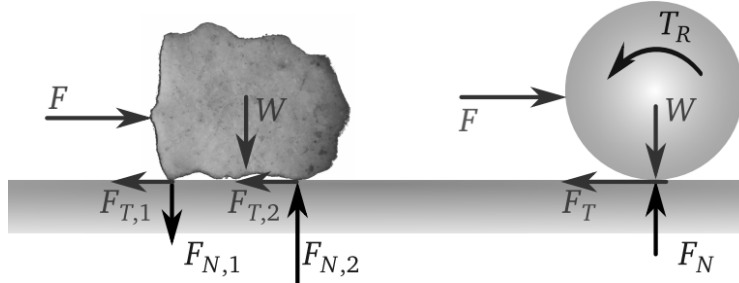


Figure A.33 Effect of particle shape on particle rotation in force equilibrium under a lateral load

For the non-spherical particle, a force couple $F_{N,i}$ resists rolling motion of the particle. For spherical bodies, this force effect has to be imitated by a rolling resistance torque T_R . The elastic limit would be enforced by restricting the magnitude of the rolling deformation vector (Obermayr et al. 2013) to:

$$\|\xi_r\| = |\omega_r| R \Delta t = \frac{x_{c,2} + x_{c,2}}{2} - x_a \leq c_R \mu \frac{F_N}{k_T} = \mu_r \frac{F_N}{k_T} \quad (\text{A.37})$$

where c_R is the dimensionless rolling resistance coefficient; μ_r denotes the coefficient of rolling friction; and, the normal force and the tangential contact stiffness are denoted by F_N and k_T , respectively. Refer to Iwashita and Oda (1998) and Obermayr et al. (2013) for additional details of the derivation. If $c_R=1$, then the rolling resistance matches the torque produced by the Coulombic friction force; the particle is sliding over the surface without any rotation. This is because the torque from the friction is completely compensated by the rolling resistance. As an analogy, consider a sphere sliding over a flat frictional surface. The sphere will not rotate due to the friction force for $c_R=1$, just as if its contact surface were flat (e.g., such as that of a sliding block, Plassiard et al. 2009).

Estrada et al. (2013) carried out a numerical study to quantify the effect of angularity in rolling resistance in granular systems composed of regular polygonal particles. The numerical study of Estrada et al. (2013) for the mechanical behavior of discs versus that of polygonal particles (each having the same volume fractions per particle size in a volume of 7,500 particles) revealed that the influence of particle shapes on the rolling resistance could be identified with a statistical number of sides (n_s) of polygonal particles. Based on the work-energy principle, Estrada et al. (2013) proposed a correlation between μ_r and n_s :

$$\mu_r = \frac{1}{4} \tan \bar{\psi} \quad (\text{A.38})$$

where $\bar{\psi} = \frac{\pi}{2n_s}$ is the mean dilatancy angle of the trajectory of the center of mass of the polygon (see Fig. A.34). The perimeter of polygonal particle, as generated from a particle size distribution, is assumed to be equal to $R \frac{(\pi/n_s)}{\sin(\pi/n_s)}$, which corresponds to a spherical particle (of radius R) multiplied by a statistical factor of $\frac{(\pi/n_s)}{\sin(\pi/n_s)}$. Based on p-q diagrams obtained from the numerical simulations, Estrada et al. (2013) concluded that a packing of regular polygons of n_s sides produces both the volume fraction of solid particles and macroscopic shear strength equivalent to a packing of discs with μ_r , approaching a constant value, i.e., $\mu_r = \frac{1}{4} \tan \bar{\psi} \approx 0.1$.

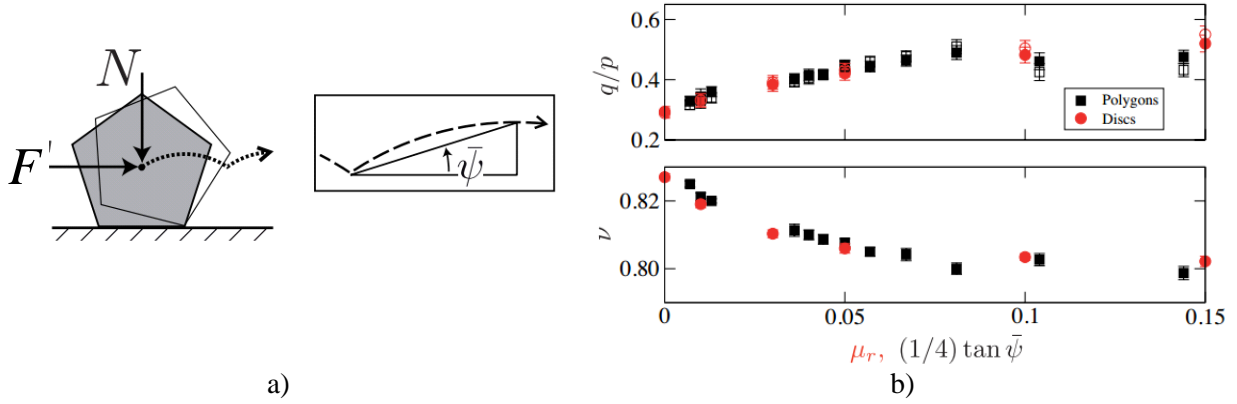


Figure A.34 Rolling resistance as a shape parameter in sheared granular media (From Estrada 2013): a) Trajectory of the center of mass (dashed line) and definition of the mean dilatancy angle; b) Shear strength (q/p) and volume fraction of solid particles (ν) shown in a function of μ_r for the discs and $(1/4) \tan \bar{\psi}$ for the polygons.

As introduced above, a rolling motion is that in which no tangential (friction) force or sliding (slip) can occur at the contact. Specifically, when rolling occurs without sliding or spinning, the motion of the contacting bodies is referred to as ‘pure rolling’. As a minimal tangential force Q , which is less than the limiting Coulombic friction, *may* act on the contact surface, partial slip may take place in the contact zone. To differentiate pure rolling without any partial sliding, we will use the terms *free rolling* and *tractive rolling*, instead, where the tangential force is zero and non-zero (yet less than the limiting friction), respectively. As the normal load induces elastic deformation of the contacting bodies over a finite area in tractive rolling, the influence of incipient sliding on rolling contact produces two distinct areas of the contact zone, and is governed by a states known as ‘stick’ and ‘slip’. Major differences among the tangential strains developed in the ‘stick’ area of the contacting bodies induces a small apparent slip, referred to as *creep*. Johnson (1985) explains creep phenomena (first discovered by Reynolds in 1875) using an analogy to a deformable wheel rolling on a relatively rigid plane surface:

“If, owing to elastic deformation under load, the tangential (circumferential) strain in the wheel is tensile. The (contact) surface of the wheel is stretched where it is in sticking contact with the plane. The wheel then behaves as though it had an enlarged circumference and, in one revolution, moves forward a distance greater than its undeformed perimeter by a fraction known as the creep ratio.”

Let us qualitatively discuss the processes that transpires for a rolling wheel, as depicted in the schematic sketches of Fig. A.35. More specifically, Fig. A.35 shows a simplified model of an elastic wheel, with a radius of R , that is composed of a rigid inner ring and a series of spring elements. Between the spring elements and the base, friction develops in accordance with the coefficient of friction. If we initially press the wheel onto the rigid base (Fig. A.35b) and subsequently apply a moment (Fig. A.35c), then the springs to the right of the contact area are in compression and the springs to the left are in tension.

As the wheel rolls to the right (i.e., transitions from the state shown in Fig. A.35c to that of Fig. A.35d), the inner rigid ring rotates across a finite angle, which is dependent on the number and stiffness of the springs engaged in contact with the base. The elements that have not yet contacted the base enter the contact area. In contrast, the elements already making contact reach the trailing edge (where the normal force decreases). Further, as the elements slip out of the contact area towards the rear, the wheel undergoes an additional finite rotation. This kinematic ‘stick’ and ‘slip’ phenomenon in a stationary rolling contact is essentially the source of rotational resistance. For every rotation of an angle corresponding to an individual spring element, the wheel experiences an “elastic rotation” in addition to the “rigid-body rotation (free rolling).” Because of this differential rotation, the circumferential speed of the wheel is faster than the translational speed. If the wheel brakes in its motion, traction moment acts in the opposite direction of rolling, which results in the circumferential speed less than the translational speed. The difference in speed is called creep: $v_\xi = v - \omega R$, where \mathbf{V} is the translational speed and $\boldsymbol{\omega}$ is an angular velocity. By normalizing creep velocity by translational velocity, we define the creep ratio ξ as:

$$\xi = \frac{v_\xi}{v} = \frac{v - \omega R}{v} = 1 - \frac{\omega R}{v} \quad (\text{A.39})$$

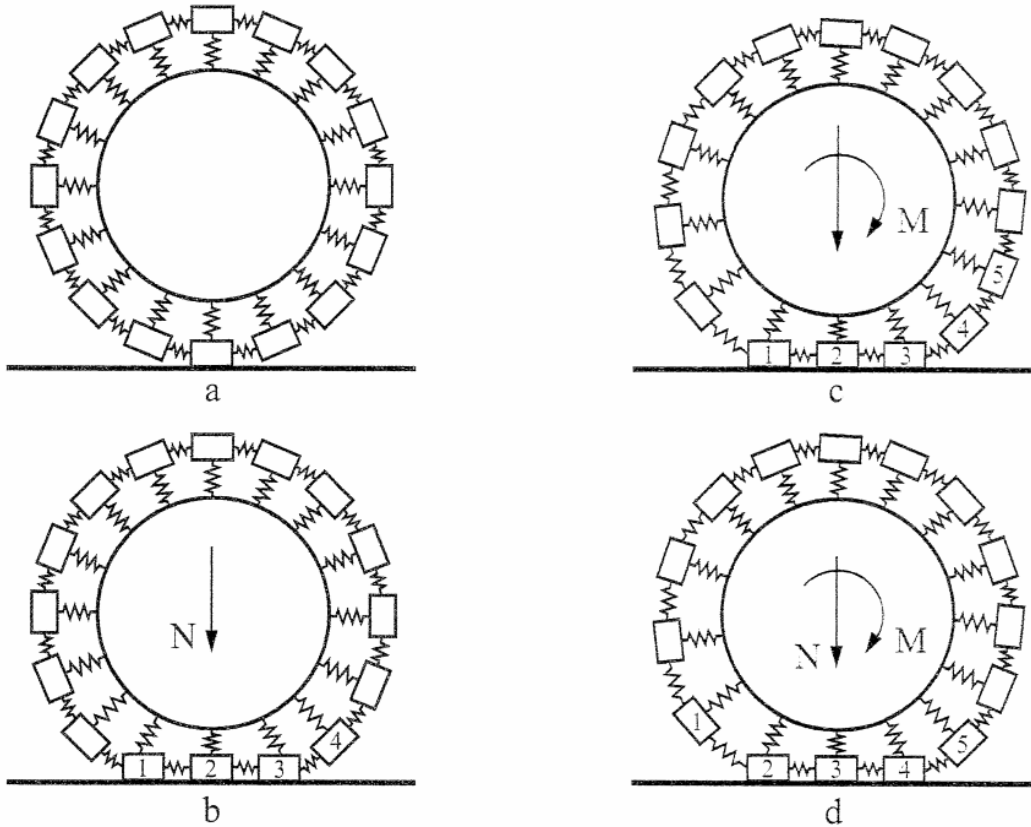


Figure A.35 Simplification of creep phenomenon in rolling (based on Popov 2010)

The mass density in the contact area becomes $\rho_o/(1+\varepsilon_{xx})$ per a deformed length, and thus, the mass flow density is $v\rho_o/(1+\varepsilon_{xx})$, which must be equal to $\rho_o\omega R$ per conservation of mass.

Satisfying the conservation of mass and substituting the resulting value for ωR into Eqn. A.35, we have:

$$\xi = 1 - \frac{1}{1 + \varepsilon_{xx}} = \frac{\varepsilon_{xx}}{1 + \varepsilon_{xx}} \approx \varepsilon_{xx} \quad (\text{A.40})$$

If the contact of two conforming bodies is considered, then the contact is made over contact points within a contact region that lies in different planes. Free rolling may take place at a number of points, but tractive rolling in combination with rolling (with slip) takes place at all other points (most likely the majority of contact points). To account for this slipping behavior, the sliding resistance at the interface has to be overcome and rolling friction must be present (Rabinowicz 1995). In this case, if adhesive bonds are formed (as explained earlier), the bonds would become disengaged at the trailing end of the rolling contact in tension (rather than shear as in a sliding contact). Thus, rolling friction may arise from the adhesion component of friction. Even for elastic contact during rolling, therefore, energy dissipation occurs. Such energy loss is called elastic hysteresis, which can be modeled as by accounting for rolling friction on two contacting spherical surfaces, with different radii of curvature (Bhushan 2013):

$$\mu_r = \xi \mu = \frac{4-3\nu}{4(1-\nu)} \frac{a}{R^*} \mu \quad (\text{A.41})$$

where a is the half width of the contact (equivalent to the radius of Hertzian contact area), R^* is an effective radius, and the creep ratio ξ is re-written for 3D rolling contact with Poisson's effect. For practical modeling purposes, the following approximate is adopted in the current study: $\mu_r \approx 0.08\mu$. Combining Eqns. A.38 and A.41, we have:

$$\mu_r = \frac{1}{4} \tan \bar{\psi} + \xi \mu \quad (\text{A.42})$$

Thus, depending on the normal deformation, the coefficient of rolling friction can vary over a wide range. For practical modeling purposes, and based on rigorous reviews of Johnson (1985), Popov (2010), and Bhushan (2013), the following approximate is adopted in the present study of contact models for monodisperse and bi-disperse systems: $\xi = [0.04, 0.10]$, assuming that Poisson's ratio varies between 0.17 and 0.3 per DSE diameters (Zheng et al. 2011). For example, if a monodisperse system of DSEs with a diameter of 5 mm is modeled using $\mu = 1$, the coefficient of rolling friction is approximately estimated as $\mu_r \approx 0.14 \square 0.2$. Therefore, per use of Eqns. A.9 and 33, i.e., stress superposition and decoupling techniques, the force mapping of Eqns. A.38 and 42 (on rolling resistance at the grain level) is intended to collectively (and qualitatively) transform irregular shapes of angular particles to equivalent DSEs (as illustrated in Fig. A.36).



Figure A.36 Schematic of random assembly of eight angular particles (left) and transformed equivalent DSEs (right)

A.1.8 Macroscale Modeling Concepts

Having discussed the particle-level frictional mechanisms that are associated with particle geometry, interparticle interlocking, and rolling resistance, we now shift our attention to physical descriptions of macroscopic structural textures called soil fabrics. Subsequently, modeling concepts are discussed in relation to DEM simulations of macroscopic shear strengths of granular soil.

As presented earlier, surface roughness (microscopic) and shape (particle-level) of granular particles enhance the shear resistance of granular packing. Also, recall that initial particle arrangement is responsible for the evolution of anisotropy (macroscopic) during shearing processes (Santamarina and Cho 2004). The relative measure of the density state associated with a given initial particle arrangement is referred to as relative density. Further, relative density indicates the degree of particle interlocking and anisotropy, which in turn, influence volumetric behavior and corresponding macroscopic shear strength. For example, for initial particle arrangements under very dense states, the mobilization of frictional resistance reflects the evolution of internal anisotropy (particle contact orientation and contact forces), which produces an increment in volume (i.e., dilation). Relations emerge when considering DSE assemblies across various size scales. Namely, the evolution of contacts and contact anisotropy are strongly affected (or caused) by: 1) Micro-scale and particle-level frictional mechanisms; and, 2) Changes in contact orientation of multiple particles, which form chains of interconnectivity at macroscopic scales.

The characteristics of ‘relative densities’ from a macroscopic perspective are those of particle size distribution and the corresponding internal structure. An informative representation of internal structure (i.e., multi-grain fabrics) is found by examination of the polar histogram of contact normal and particle orientations. If contact between two adjacent particles is represented by a vector normal to the plane of the contact, then all contact normals can be plotted for each orientation angle in a polar coordinate system. In general, shapes of the polar histogram vary between a circle (isotropic distribution of contacts) and a ‘peanut-shell’ (anisotropic contact distributions for which the structure as a whole may maintain stability against the buckling of ‘internal columns’). For example, as shown in Fig. A.37, preferential orientation angles can be seen where long axes for a large number of grains are oriented in the horizontal direction (Fig. A.37c) in a cylinder sample prepared by pouring. Dynamic compaction, however, produces a more nearly random fabric (Fig. A.37d). A completely random distribution of particles would yield the dashed circles shown in Fig. A.37c and Fig. A.37d. Non-spherical particles (ellipsoids) tend to

align in a preferential direction during shearing processes. This preferential orientation of particles (i.e., interparticle contact orientation) and the particle distributions influence: deformation behaviors; strength properties; and, the propensity for anisotropy (with respect to macroscopic fabric characteristics). Thus, particle shapes also affect the internal structure, particularly pore size distribution. Packing of angular particles tends to produce less dense configurations than that of rounded particles. Maximum and minimum densities of packing, thus, depend on all of microscopic surface roughness, particle-level geometry, contact orientation, and particle size distribution (Arya and Paris 1981).

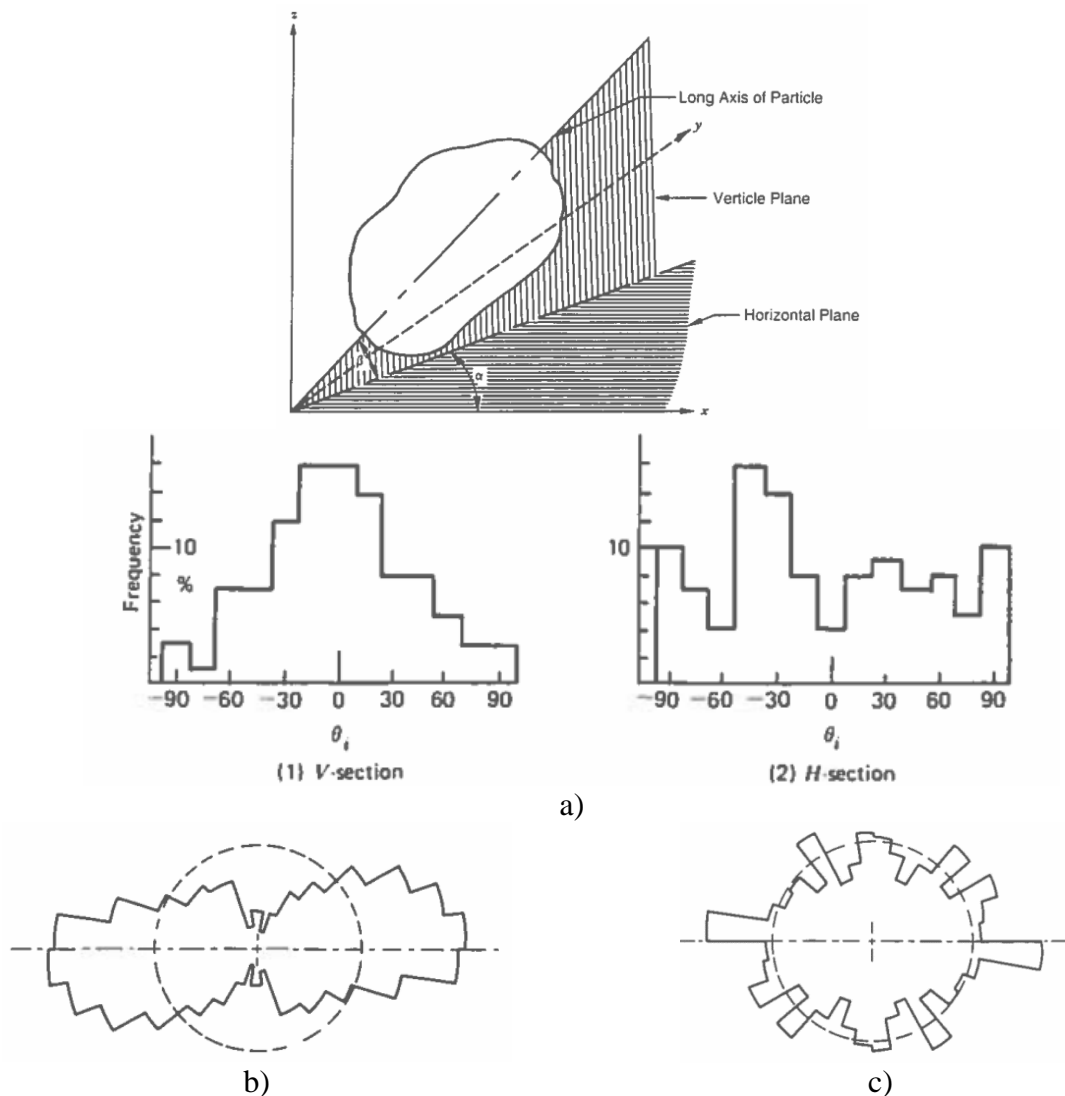


Figure A.37 Polar histogram of coordination (from Mitchell and Soga 2005): a) 3D orientation of a crushed basalt particle (top); Frequency histogram of axis orientations (middle); b) Polar diagram of crushed basalt in a sample prepared by pouring (relative density is 62%); c) Polar diagram of crushed basalt in a sample prepared by dynamic compaction (relative density is 90%)

In DEM simulations, the internal structure of granular materials can be characterized using coordination numbers and packing methods of random particle distributions. The coordination number of an assembly of discrete particles is the average number of contacts per particle: more

specifically in the context of DEM simulations, it is defined as the summation of the coordination number of each DSE divided by the number of DSE in a random packing assembly. The average coordination number of a packing assembly gives an idea of internal assembly and resulting structural stability.

Larger values of the coordination number indicate denser configurations and, thus, more stable internal structures. The possible range of packing of granular particles is also related to the maximum and minimum void ratios reflecting the loosest and densest states, respectively (Lambe and Whitman 1969). Limiting values of coordination number for structural instability (structural collapse) can be determined by equating the number of unknown contact forces and the number of force equilibrium equations (Rothenbug and Bathurst 1992). This is analogous to the structural determinacy of determinate truss systems; by removing one particle (member) from the internal structure (truss structure) at equilibrium, cascading collapse can occur among the remaining particles (members) (see Fig. A.38 for examples of idealized internal structures).

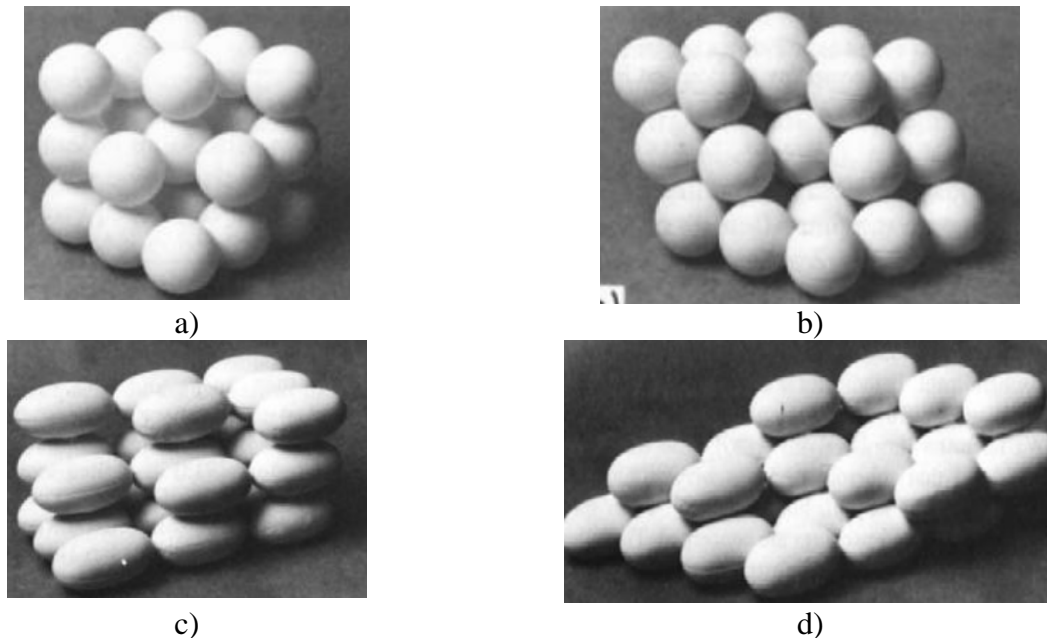
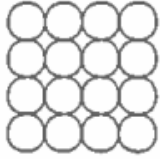
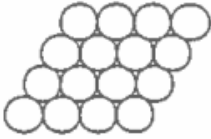
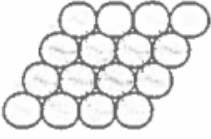
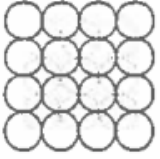
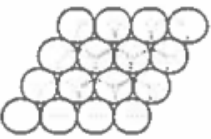


Figure A.38 Physical representations of idealized packings (John 1982): a) Spheroids in cubic packing; b) Spheroids in tetragonal-spheroidal packing; c) Prolate spheroids in cubic packing; d) Prolate spheroids in tetrahedral packing

Experimental investigations (Scott and Kilgour 1969, Finney 1970) and numerical simulations (Moscinski et al. 1989, Jodrey and Tory 1981) on random DSE packing have been reviewed in detail. The experimental findings by Scott and Kilgour (1969) indicate that the mean packing density strongly depends on the method of packing, and the maximum for truly random experimental packing appears to be 0.64~0.67 (Scott and Kilgour 1969, Finney 1970, Moscinski et al. 1989). Based on the review findings, two primary packing methods are mainly adopted in DSE analysis of the present study. One algorithm begins with a very dense configuration of DSEs, which overlap (Moscinski et al. 1989, Jodrey and Tory 1981). The DSEs are then spatially relocated (within the predetermined domain of a cylinder) in order to reduce the degree of overlapping. Dense packing structures can be obtained by using this method, which results in values close to 0.62. The second algorithm simulates the successive packing of a cylindrical

container (for use in subsequent triaxial compression test simulations) with DSEs being subjected to a gravitational field (Tory et al. 1973). Once the DSEs settle down in the cylinder and reach a quasi-static force equilibrium state, the resulting packing is considered to be in its final position under gravity as a kinematically admissible (stable) state of granular mass. The computational procedures of the algorithm describe the actual process of packing generation in laboratory experiments (with or without a control drop height) to generate interacting forces among DSEs. Also, the procedures generally yield loose packing with densities of approximately 0.58 in the case of monodisperse systems. A comparison of theoretical properties for idealized packings is given in Table A.8.

Table A.8 Properties of uniform size sphere packings (from Santamarina et al. 2001)

Geometric arrangement		cn	Layer spacing	Porosity, n	Void ratio, e	Packing density, $1 - n$
Simple cubic (SC)		6	d_g	0.476	0.908	0.524
Cubic – tetrahedral (CT)		8	d_g	0.395	0.652	0.605
Tetragonal – sphenoidal (TS)		10	$d_g/2\sqrt{3}$	0.302	0.432	0.698
Face-centered cubic (FCC)		12	$d_g/2\sqrt{2}$	0.260	0.351	0.740
Tetrahedral (T)		12	$d_g\sqrt{2/3}$	0.260	0.351	0.740

Notation: d_g is grain diameter, cn is coordination number.

As described in Fischer et al (2003), particles with uniform size distribution cannot be manufactured using current technologies. Therefore, Gaussian particle size distributions are suggested for the modeling of materials such as commercial powders. In contrast to the limitations of (physical) manufacturing, computational limitations come into play when attempting to model actual particle size distributions in DEM simulations. When populating (distributing) DSEs of

various radii within a volume (according to either a prescribed probability density, or by use of a probability mass function to model distinct particle-size groups), the total number of DSEs can reach into the millions. This is particularly so when mathematically representing particles with diameters ranging from a few hundred micrometers to several millimeters. Even for cases where four particle-size groups are selected (e.g., per Murzenko's sand sample 1965), packing procedures require approximately five million DSEs to populate a 100 mm by 200 mm (4 in. by 8 in.) cylinder. A discrete one-on-one description of multi-grain fabrics per an actual particle size distribution is therefore infeasible in consideration of the numerical experimentation necessary for developing various soil 'unit' models. Further, such a description is impractical for a single deterministic representation of heterogeneous fractal networks. However, the existence of multi-grain fabrics is evident in spatiotemporal changes in contact orientation of multiple particles (Fig. A.39). More specifically, chains of interconnectivity form during shearing, and can produce amplification of local dilatancy as well as strain localization for very dense granular packings.

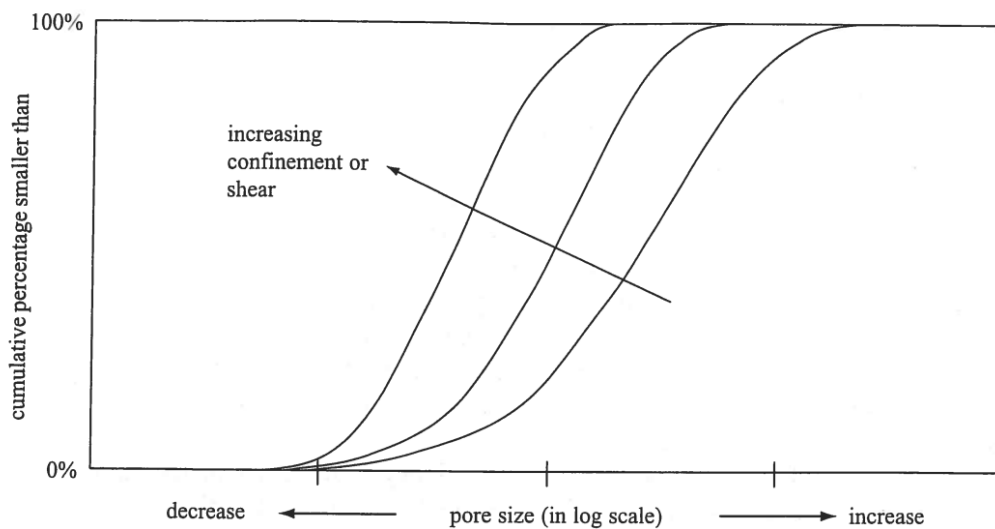


Figure A.39 Evolution of pore size distribution with confinement: larger pores collapse before smaller pores (Santamarina et al. 2001)

A literature review focused on load transfer mechanisms in particulate materials reveals physical phenomena that may, in turn, provide a possible remedy in simulating the effects of relative density and local dilatancy (Hidalgo et al. 2002, Salot et al. 2009). During shearing processes, most of the applied load is transferred through chains of normal and tangential contact along “primary” particles. Particles in the vicinity of the chains play a secondary role in supporting the column-like chains of primary particles and increasing structural stability. This particulate behavior is depicted schematically in Fig. A.40a, which is readily seen in: experimental studies using photoelasticity (Fig. A.40b); and, numerical results obtained from non-uniform polygonal discrete element analysis (Fig. A.40c). Alternatively stated, there exist two representative groups of particles, where each group exhibits unique load-carrying mechanisms.

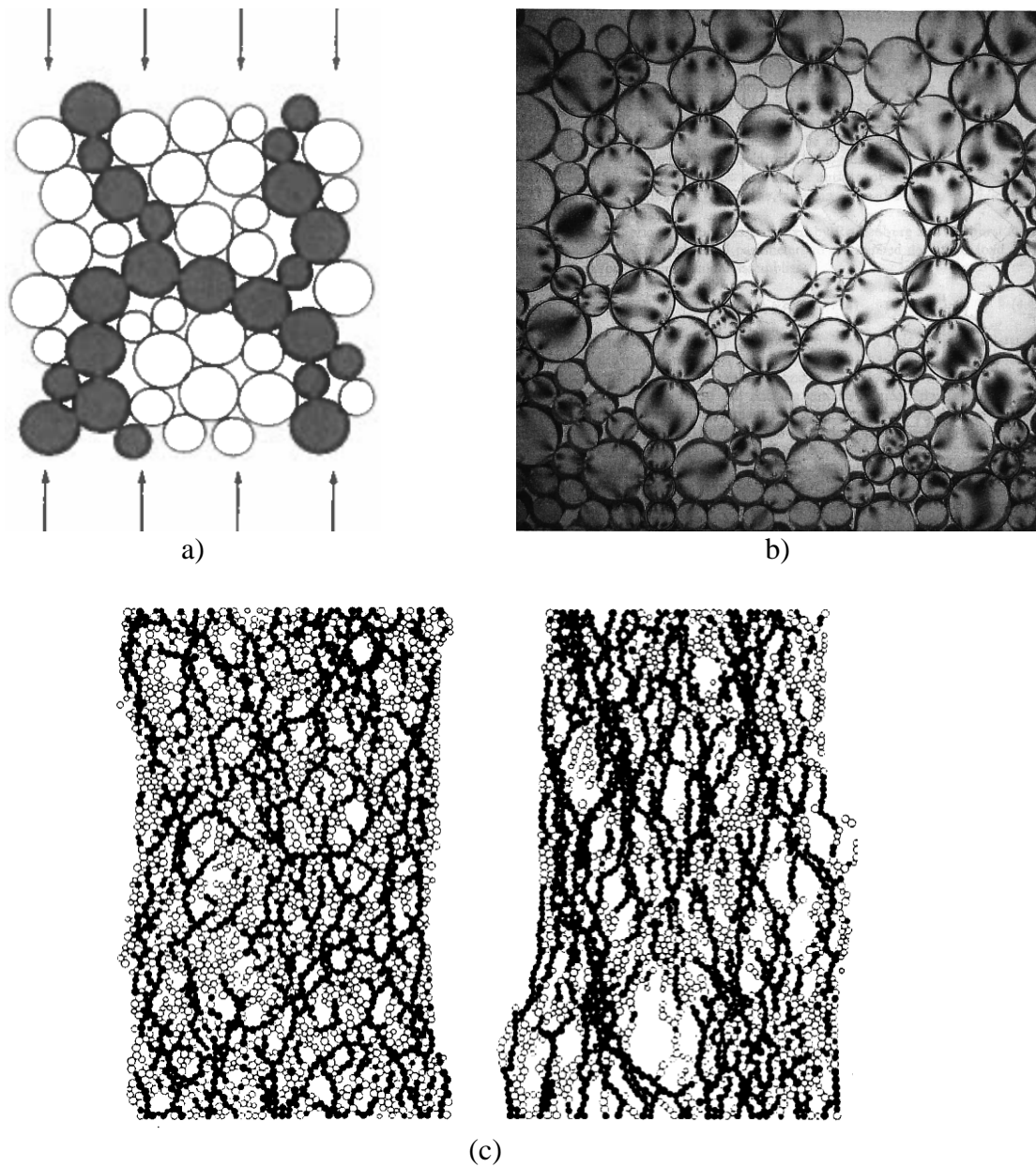


Figure A.40 Force chains and granular fabrics: a) Force chains of the shaded particles carry larger contact forces than an average contact force. The remaining unshaded particles act as supports, playing a secondary yet important role in load-carrying mechanism (Santamarina et al. 2001); b) Photoelastic demonstration of force chains: Contact forces tend to be higher along particle chains. Particles that are not part of the force chains play the role of boundary supports preventing the chains from buckling (Mitchell and Soga 2005); c) Development of column-like force chains in 2D numerical tests on rolling resistance (left: free rolling, right: active rolling friction, Iwashita and Oda 1998).

It follows that large portions of particles in any real packing experience only gravity and local boundary forces, and remain relatively less affected (or unaffected) by external (shearing) forces. Guyont et al. (1987) first applied the modeling concept of fabrication of binary mixtures to

macroscopic transport analysis of water percolation, and referred to it as *bimodal distributions of spheres*. These particles were later called spectators by physicists (Cates et al. 1998). Santamarina et al. (2001) explained this group of particles in a similar way: these mobile particles would follow the primary particles in shear flow, and are called the ‘mobile’ fraction of the packing (Fig. A.41).

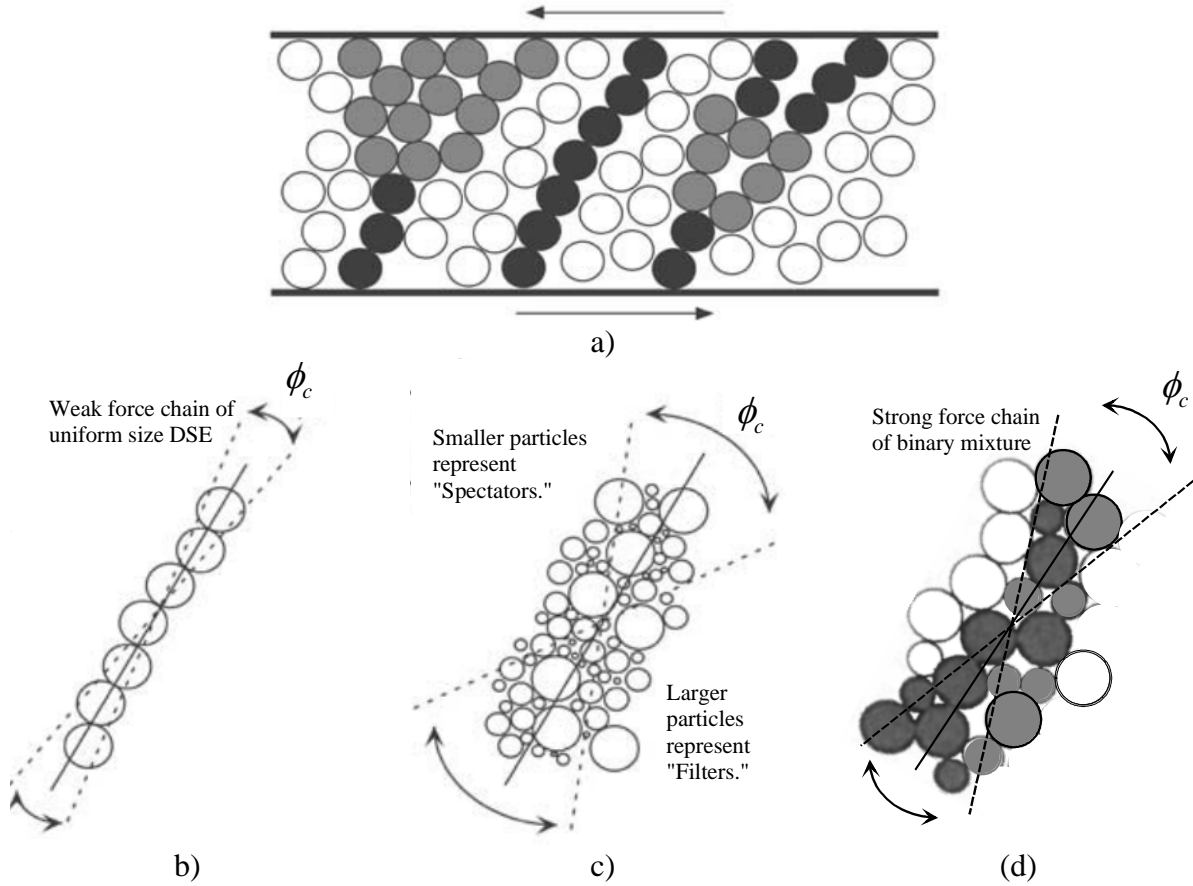


Figure A.41 Illustration of possible force chain geometries for a granular layer subjected to shear. Solid lines indicate optimal chain orientation and dotted lines denote ranges of possible stable orientations; $\psi = 30^\circ$ defines a critical angle of local dilatancy for stress chains; outside this range, stress chains fail by interparticle slip or rolling. Note that parts c and d have larger $\psi = 30^\circ$ than that of part b. a) Force chains of a monodisperse system subjected to external shear forces (from Mair et al. 2002): dark gray particles bear high load; light gray particles carry moderate load; and white particles indicate spectators that do not contribute to appreciable load-carrying capacity; b) Force chain of uniform size DSEs; c) Multi-grain fabrics per particle size distributions; d) Modeling of jamming per binary mixtures of DSEs.

The coordination (number) in the evolving structure of these particles is minimal in interlocking, and more likely, biased by the local boundary forces that arise under gravity-induced static equilibrium conditions (e.g., geostatic stress states). In contrast, the other group of relatively larger particles (called ‘filters’; Santamarina et al. 2001) can be frustrated for both sliding and rolling motions, which are traversed by mobile, smaller particles. The spectators can also support the force chains of the filters, preventing them from buckling. Either way, as a larger shearing

force would be required to displace (or buckle) the filters (or the chain), a greater degree of dilation could be simulated for a denser packing (as exemplified by comparing Figs. A.41b-c). In general, contact forces are the greatest for shear jamming (such as that shown in Fig. A.41d).

For a mixture of DSEs, generated based on a given volume fraction and subsequently packed, a successful “jamming” of the filters can be achieved (Majmudar et al. 2007, Salot et al. 2009). The density at which local force-chain systems jam is determined by many factors, including grain shape, the deformability of the particles, frictional interparticle forces, and pore structure network (called the degree of dispersivity) of the system. The overall degree of the jamming manifold may depend on the particle size distribution as well. For example, a particularly interesting feature of the jamming is the transition between loose packing states and interlocked denser states. Whether the jamming diverges (becomes ineffective) for high enough densities or low friction at the microscopic scale is uncertain. In this context, the degree of jamming under shear is a qualitative description used when simulating local dilatancy and accumulative effects in macroscopic dilative behaviors of granular systems (Bi et al. 2012). Thus, simulation of jamming effects during shearing process is to introduce a jamming coefficient μ_2 as a numerical parameter to simulate increased contact forces among DSE in shear jamming. Therefore, based on Eqn. A.9: $\mu = \sum_i \mu_i$, a total coefficient of sliding friction becomes a DSE parameter, which tends to be greater than unity (Rotter et al. 1998, Yang et al. 2012; refer to Fig. A.42):

$$\mu = \mu_0 + \mu_1 + \mu_2 \geq 1.0 \quad (\text{A.43})$$

where μ_0 represent an intrinsic friction coefficient due to microscopic surface roughness, μ_1 is a numerical friction coefficient for shape effects, and μ_2 is a numerical jamming coefficient. Note that μ_2 is not a material parameter that holds a physical (frictional) meaning at the grain-level. Instead, this coefficient (an addition to the coefficient of friction) is to simulate shear jamming due to mesoscopic (intermediate scale) physical anisotropic fabrics of cohesionless granular materials.

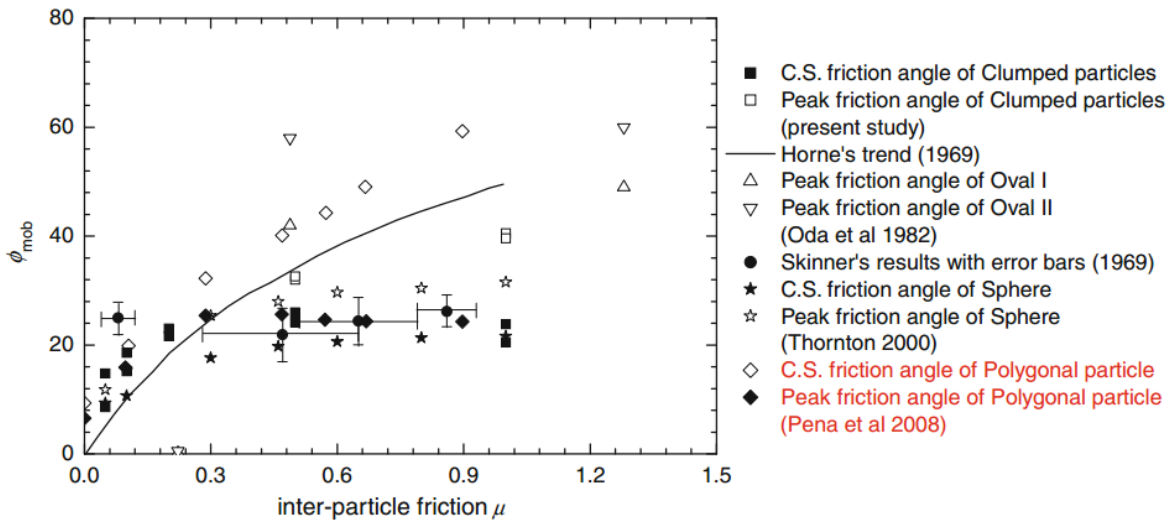


Figure A.42 Comparison of mobilized macroscopic friction angles (from Yang et al. 2012): It is evident that polygonal discrete elements tend to produce shear jamming even with low values of

interparticle friction coefficient. In contrast, uniform-size spherical and clustered discrete elements exhibit limited macroscopic mobilization of greater shear strengths regardless of the value of the coefficient. The effect of shear jamming phenomena needs to be simulated in spherical discrete element analysis.

In simulating the broad applicability of the “shear jamming” concept (Liu and Nagel 1998), the inclusion of secondary DSE (“spectators”) in the packings can play an important role in controlling the kinematics of DSE packings as a whole, such as when binary systems are modified to produce a higher, target shear strength of a very dense granular soil. Jamming apparently occurs because the particles form force chains along the compressional direction for spherical particles in an array or network of fractal structure. Alternatively described, the simulated lateral confinement on the force chains of the binary mixture enhances volumetric behaviors of the representative elementary volume (REV) as a whole. From a phenomenological standpoint, the volumetric behavior of the dense packing has to be consistent with the development of deviatoric stress observed in physical tests, and thus, the numerical results of both force and deformation become valid.

Although jamming states of granular matters have been intensively studied theoretically using both numerical and experimental tools in the power industry and field of granular physics, the nature of the jamming transition for cohesionless frictional grains has not yet been made clear from a quantitative standpoint. The degrees of jammed states and the fractions at which transitions occur from contraction to dilation (as part of reaching a critical state) are statistically independent of the mass density (Bi et al. 2011). Furthermore, ascertaining that states of cohesionless granular materials are macroscopically jammed is non-trivial in numerical analysis. As explored extensively in the soil mechanics literature (Lambe and Whitman 1966), increased packing (volume fraction of DSE) alone may not induce jamming at positive pressures as shear stress induces irreversible flow at the yield stress (black line as shown in Fig. A.43a). The numerical parameter of jamming coefficient may depend on the protocol of preparing the jamming states as an initial condition. However, only a few experiments have investigated the Liu-Nagel jamming theory for physical systems consisting of spherical particles with friction. For example, under isotropically confined conditions, the coordination number of DSE packings at jamming increases with interparticle frictional resistance (Majmudar et al. 2007). If the effect of multi-grain fabrics in the local (i.e., mesoscopic intermediate-scale) dilatancy is qualitatively accounted for per use of numerical “shear jamming” (i.e., a jamming coefficient), then the evolving fractal network of numerically-represented denser granular materials must satisfy the kinematics of volumetric behaviors under deviatoric loading. Therefore, whether or not the kinematic responses (obtained from DEM simulations) are consistent with the macroscopic dilation of REV would indicate an optimal inclusion of shear jamming effects. Thus, a limiting value of the shear jamming coefficient should be determined using numerical experimentation on kinematically admissible force-deformation relationships, based on the work-energy principle.

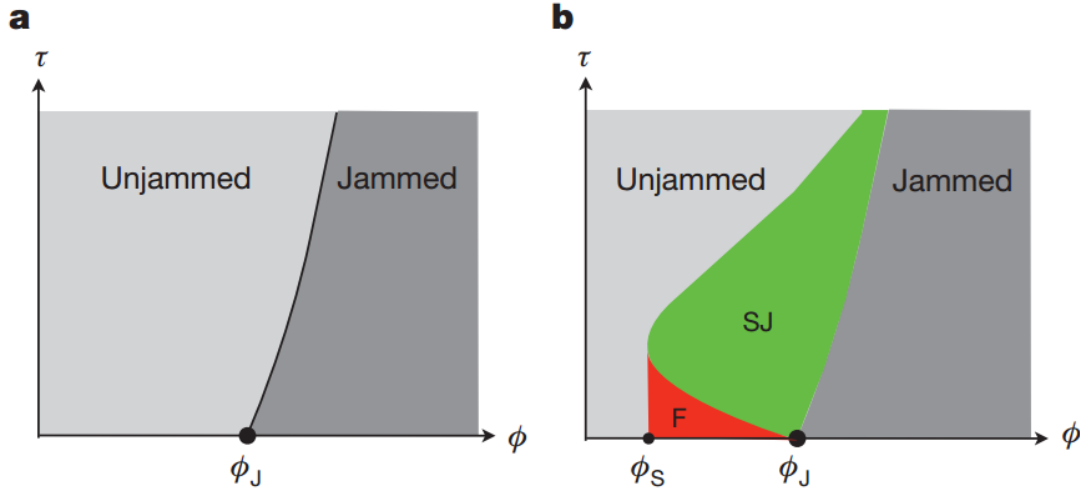


Figure A.43 Jamming phase diagrams (from Bi et al. 2011): a) Original Liu–Nagel jamming phase diagram. The boundary between unjammed and jammed regions is the yield stress line. Unjamming can be induced by decreasing the packing fraction or increasing the shear stress; b) Generalized jamming diagram including the shear-jammed (SJ) and fragile (F) states. Along the ϕ axis, there are two special densities: ϕ_s , below which there is no shear jamming, and ϕ_j , above which isotropically jammed states exist. For $\phi_s \leq \phi \leq \phi_j$, jamming can occur with application of shear stress.

The smallest size of the particles in a DEM simulation also affects the efficiency of DSE analysis. To reduce computational costs yet to maintain the discrete nature of granular matter and the characteristics of inertial particle interactions in soft particle dynamics, many researchers across engineering disciplines use particle size up-scaling methods (e.g., O’Sullivan et al. 2004a, Lee et al. 2012). In general, the diameters of DSEs used in the past DEM simulations of triaxial compression tests on granular matters (from powders to sands) range between 2 mm and 25 mm (Thornton 1979, Jodrey and Tory 1981, Thomas 1997, Thornton 2000, Yimsiri and Soga 2001, O’Sullivan 2002). The maximum diameter of DSE selected for this study is a maximum particle size of sand (or a minimum size of gravel) based on soil composition and relevant mechanical properties given by Duncan (1994) (cited in Mitchell and Soga, 2005) and a chart given by Lee (1992); refer to Table A.9 and Fig. A.44, respectively. For these reasons, uniform size packings of DSE with a diameter of 5 mm allows for a benchmark system-level platform, where a binary mixture for “shear jamming” can additionally permit modeling of denser granular packings. Using “mean-field theory” (Guyon et al. 1987, Moscinski et al. 1989), the critical volume fraction ratio of the filter to the mobile particles is explored as part of numerical experimentation in which the coordination number increases proportionally to the packing density of binary mixture.

Table A.9 Compositional factors of granular soil (Mitchell and Soga 2005)

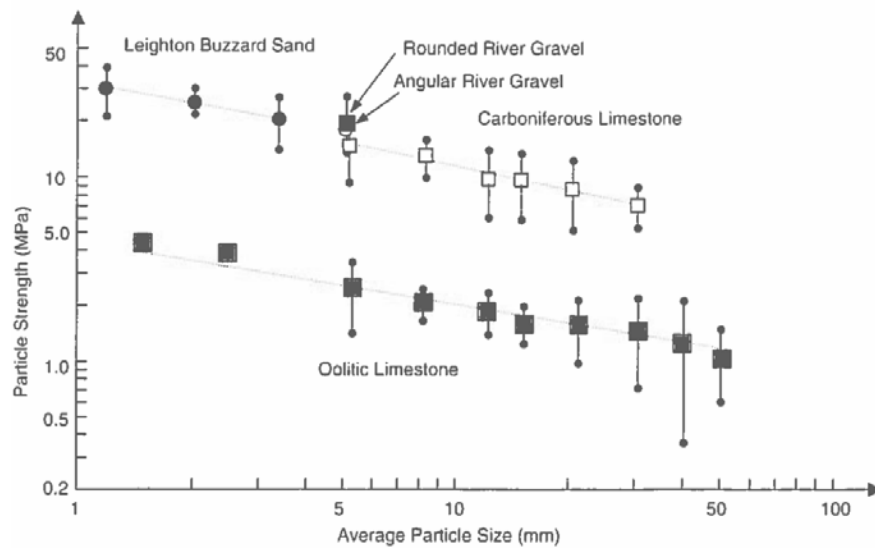
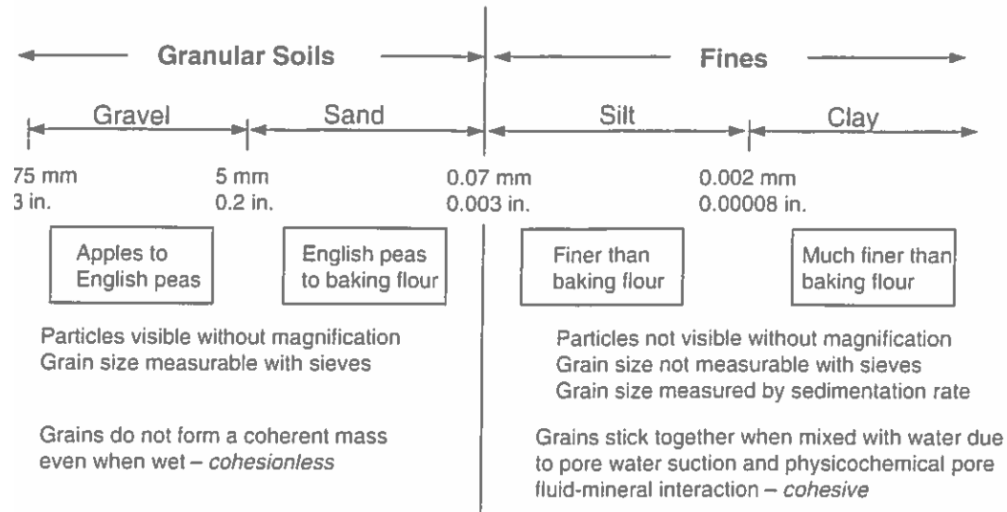


Figure A.44 Relationship between tensile strength and particle size (Lee 1992)

A.2 Numerical Method for Soft Particle Dynamics

The study of molecular dynamics (e.g., packing structure, particle-particle interaction) greatly facilitates the development of numerical modeling methodologies for investigating the dynamic behaviors of particulate systems. One common formulation, which makes use of a “soft” contact approach is of relevance to the current study, and was first developed and applied in geotechnical mechanics by Cundall and Strack (1979). By definition (Crowe 1997), when conducting simulations of bodies that utilize the soft-contact approach slight overlaps are permitted to develop at object-object contact interfaces. Contact forces are subsequently quantified based on the properties of the interacting objects (e.g., spherical particles) and the deformation history of the contact, which in turn, is driven by a force-displacement law. Molecular dynamics models that incorporate the soft contact approach effectively combine two theories (Newton’s second law of motion and a force-displacement law) to trace the movement of discrete objects

(particles) and the generation of boundary conditions throughout a given system. Further, applying the combined theories is amenable to forming repeatable, sequential (i.e., time-stepping) processes, with calculations including: 1) Forces at contact interfaces between two particles, or between particles and planar surfaces (such as finite element surfaces); and, 2) Motion (translation, rotation) of each particle and surface, based on mass-proportional acceleration. For each calculation cycle, the updated (end-of-cycle) positions of the particles enable calculation of updated contact forces, which in turn, drive the motion of the particles during the next calculation cycle. For such formulations, the time-step size is required to be sufficiently small so as to uphold the assumption that acceleration remains constant throughout a given time-step. Comprehensive literature reviews, which summarize the developments of discrete particle modeling over the past two decades, can be found in Zhu et al. (2007) and Zhu et al. (2008).

A.2.1 The Discrete Element Method (DEM)

The DEM consists of numerically modeling a number of separate (i.e., distinct, discrete) particles such that mechanically microscopic interactions, in aggregate, bring about meaningful phenomena at larger scales (e.g., macroscopic, megascopic). In the context of geomechanics, the DEM readily lends itself to replicating the particulate, discontinuous nature of soil. Indeed, the DEM is widely used to predict large-scale deformations of assembled particles: the DEM allows for the incorporation of highly irregular geometry; can capture evolving failure mechanisms (e.g., slip planes, cavity formation) that develop across a given collection of particles; and, permits statistical measures of the unique stresses and strains for a volume of interest. DEM parameters include physical parameters (e.g., particle size, topology, specific gravity, hardness), mechanical contact parameters (e.g., frictional coefficients, stiffness, viscous damping), and purely numerical parameters (e.g., derived numerical quantities of density, coordination number). The use of DEM, albeit computationally expensive, permits unprecedented insights to be made into the nature of particulate matter. For example, physical lab tests do not allow for the determination of internal stresses between soil grains, whereas the DEM is capable of modeling and cataloging of particle-particle interaction forces for every particle of a given numerical model. Hence, the DEM can be used to enrich those measurements obtained by manipulating soil specimens in laboratory settings.

The general computational algorithm that underlies DEM is comprised of two stages. Contact definitions are defined in the first stage. Interaction forces are then calculated via a force-displacement law at the boundaries of the individual particles in contact. This method captures the relative deformation of the particle boundaries, and is based on the particle-specific material properties as well as the particle-to-particle contact forces. The second stage involves the application of Newton's second law in terms of the forces generated for each discrete element, by which the induced accelerations of the particles are calculated. The collection of accelerations are then time-integrated to determine the updated positions of the particles. This overall algorithm is then repeated across a pre-specified number of time-steps in order to give regularly updated forces, accelerations, and positions of the system of particles.

A.2.2 Advantages of Combined DEM-FEM

The most commonly employed and most highly developed numerical method that employs the continuum hypothesis is the FEM. The finite elements (FEs) which give this numerical method its name can be thought of as a small part of the continuous structure being modeled. As expected

these “parts” (i.e., elements) are of finite size, separating them from the infinitesimal divisions made use of in calculus, and each element possesses definite geometric shape. The entire model of the physical structure under analysis is then a discretization of these finite elements, coupled to one another at points referred to as nodes, with the particular arrangement and shapes of these elements referred to as a mesh. Although the mesh is referred to as a discretization, it is important to distinguish between the continuous finite elements and discrete elements. Field quantities, such as displacement under stresses, are allowed to have simple spatial variation in each finite element that makes up the mesh. Together, these result in the set of governing equations for the numerical model, given as a set of partial differential equations or integral equations. The field quantities which these equations represent are then piecewise interpolated over the finite elements, which can then be used to approximate the behavior of the physical system.

While the concept of a continuum problem can be readily adapted and applied (through FEM) to a powerful numerical method for modeling many physical systems, there are also physical systems for which the continuum hypothesis is not valid, especially once the extent of the available technology is considered. When considering the actions of granular materials like sands and clays, the particulate nature of the medium plays a much more pronounced role in the observable properties of the body as a whole. In this case, the most natural level for discretization of the medium is at the level of the grain, which is far larger than constituent atoms or molecules, but still far smaller than the body of which the grain (in turn) is a constituent. Physical properties of granular soils, like the volume of the voids within the soil body and the shapes of the individual grains, are very important to consider when studying the mechanics of granular bodies. It is clear that in applying a continuum hypothesis and assuming a body of continuous mass, the modeler fails to capture these properties.

The current research project requires the numerical modeling of the behaviors of different materials (granular media) and their interactions with one another. For some of these entities, namely the projectiles, the continuum hypothesis is a valid and effective modeling strategy. In contrast, granular material is more aptly modeled when its discontinuous particulate nature is taken directly into account. Hence, a combined numerical method is chosen in the current study, making use of both of the continuum and discrete approaches, and is referred to as DEM-FEM approach. Therefore, the models employed in the current study will consist of structural objects that are modeled as continuous (and formed as FEs), while the granular assemblies will consist of an assemblage of discrete spheres (and formed as DSEs).

A.2.3 Utility of DSE Libraries

As part of ongoing research efforts, a standardized library of numerical parameter values is being established, and from which, assemblies of DSEs can be formed such that said assemblies exhibit known macroscopic properties. For the remainder of this appendix, major considerations are given to characterizing mechanical contact, friction, and viscous damping parameters associated with numerical modeling of individual DSE within a given assembly. Further, combined DEM-FEM models of laboratory test apparatuses are developed to facilitate assessment of macroscopic properties of DSE assemblies.

By combining: 1) Quantitative characterization outcomes associated with DSE rheological components and interaction behaviors; and, 2) Benchmarked numerical (DEM-FEM) models of

laboratory test apparatuses, relevant input parameters to describe individual DSEs are calibrated and cataloged in forming the DSE library. The DSE library can be drawn upon to quickly build up, at will, homogenous or heterogeneous megascopic DSE assemblies.

A.3 Governing Equation and Solution Approaches

The governing equation used in describing the motion at contacts between DSEs, in accordance with the DEM, are introduced below. In particular, the equations of motion for both normal and tangential directions are derived for a system of two overlapping spheres. While translational motion is considered in the normal direction, both translational and rotational motions are of interest with respect to the tangential direction. Subsequently, a conceptual platform is established to contextualize the subsequent, comprehensive exploration of DSE modeling, rheology, and input parameter value determination for use in the multi-physics simulation software LS-DYNA (LSTC 2014). Relevant parameters of interest are then introduced with focus given to the modeling of DSE assemblies in LS-DYNA.

A.3.1 Equation of Motion

The equation of motion for a dynamic system, based on D'Alembert's principle, is an expression of "dynamic" equilibrium, where equilibrium must be satisfied at every instant of time (t). D'Alembert's principle, which is dynamically analogous to the principle of virtual work for applied forces in a static system, expresses that a system of rigid bodies satisfies dynamic equilibrium under a specific set of conditions. Namely, dynamic equilibrium is said to be achieved when the virtual work of both the sum of externally applied forces and inertial forces, and the sum of externally applied moments and moments of inertia are zero for any virtual displacement of the system. Enforcement of such conditions has proven useful in solving for the motion of particles during (and subsequent to) an arbitrary sequence of impacts and motions. The translational and rotational motion of an individual discrete particle i , with mass m and mass moment of inertia I_o , are expressed by the D'Alembert's principle as:

$$\begin{aligned} (F_i(t) - m_i a_i) \cdot \delta_{z_i} &= 0 \\ (M_i(t) - I_{o_i} \alpha_i) \cdot \theta_i &= 0 \end{aligned} \quad (\text{A.44})$$

where the time-varying F_i and M_i quantities are the total applied force and the total applied moment (respectively) acting on particle i ; a_i and α_i are, respectively, the translational and rotational acceleration of particle i ; δ_{z_i} and θ_i are the translational and rotational virtual displacements of the particle i , respectively. Note the implicit presence of translational degree of freedom (DOF) z and a rotational DOF θ , in association with Eqn. A.45. The relationship between forces (and moments) and motion can then be stated as:

$$\begin{aligned} F_i(t) - m_i a_i &= 0 \Leftrightarrow m_i a_i = F_i(t) \\ M_i(t) - I_{o_i} \alpha_i &= 0 \Leftrightarrow I_{o_i} \alpha_i = M_i(t) \end{aligned} \quad (\text{A.45})$$

where the relations of Eqn. A.45 are expressions of Newton's Second Law of motion in classical mechanics.

Consider a scenario where discrete particle i , undergoes a collinear collision with another individual discrete particle j in the z translational DOF. During impact, we can write the force equation of particles i and j as:

$$F(t) = m_i a_i = -m_j a_j \quad (\text{A.46})$$

where $F(t)$ is the total force between the particles at any instant (t). Hence,

$$\begin{aligned} \frac{1}{m_i} F &= a_i \\ \frac{1}{m_j} F &= -a_j \\ -\left(\frac{1}{m_i} + \frac{1}{m_j}\right) F &= a_j - a_i = a \end{aligned} \quad (\text{A.47})$$

where a is the relative acceleration of the system during impact and defined as $a = \delta_z^{\square}$. The mass terms of Eqn. A.47 are now defined as an effective mass m_{eff} , such that $\frac{1}{m_{eff}} = \frac{1}{m_i} + \frac{1}{m_j}$. Therefore, Eqn. A.47 can be simplified to:

$$-F = m_{eff} a = m_{eff} \delta_z^{\square} \quad (\text{A.48})$$

If a linear contact model, consisting of a spring and a viscous damper, is used to model contact between particles i and j , then the normal force F can be rewritten as:

$$F = F_s^N + F_d^N \quad (\text{A.49})$$

The normal spring force F_s^N is calculated based on the overlap between particles i and j , while and damping force F_d^N is proportional to the relative contact velocity:

$$\begin{aligned} F_s^N &= k_N \delta_z \\ F_d^N &= c_N \delta_z^{\square} \end{aligned} \quad (\text{A.50})$$

where k_N and c_N are the spring stiffness and the damping coefficient, respectively. Thus, taking into account the particle-particle contact, the equation of motion for damped free vibration at the contact point is given as:

$$\begin{aligned}
m_{eff} \ddot{\delta}_z &= -c_N \dot{\delta}_z - k_N \delta_z \\
\text{or} \\
m_{eff} \ddot{\delta}_z + c_N \dot{\delta}_z + k_N \delta_z &= 0
\end{aligned} \tag{A.51}$$

Similarly, for tangential motion (with both translation and rotation components), the damped free vibration of the contact point is described by:

$$\begin{aligned}
m_{eff} \ddot{\delta}_x + c_T \left(\dot{\delta}_x + r \dot{\theta} \right) + k_T (\delta_x + r\theta) &= 0 \\
I_{0_{eff}} \ddot{\theta} + r c_T \left(\dot{\delta}_x + r \dot{\theta} \right) + r k_T (\delta_x + r\theta) &= 0
\end{aligned} \tag{A.52}$$

Taking the quantity $(\delta_x + r\theta)$ as a variable, it follows that:

$$m_{eff} I_{0_{eff}} \left(\ddot{\delta}_x + r \ddot{\theta} \right) + \left(I_{0_{eff}} + m_{eff} r^2 \right) c_T \left(\dot{\delta}_x + r \dot{\theta} \right) + \left(I_{0_{eff}} + m_{eff} r^2 \right) k_T (\delta_x + r\theta) = 0 \tag{A.53}$$

A.3.2 Conceptual Remarks on Geometry, Contact Mechanics, and Rheology

In the modeling of DSEs, spherical geometric descriptions are commonly assigned to individual particles. Alternatively stated, each individual sphere is defined (geometrically) as a center nodal point with a radius. In the multi-physics simulation software LS-DYNA (LSTC 2016), rigid spherical particles are incorporated into the (numerical) DEM formulation. Consequently, for simulations in LS-DYNA, the radii of DSEs remain constant in the force and motion computations, regardless of the nature of DSE interactions. In general, each particle possesses three translational DOF and three rotational DOF.

Contact models are the physical basis of the DEM (Luding 2008). For DEM formulations that adopt the “soft” contact approach, there is a mapping between the contact forces generated during collision events and relatively more idealized dynamic systems. The elastic mechanism for the modeling of contact was first developed by Hertz (1882). Hertz’s quasi-static theory provides a very good approximation for collinear collisions between two nonconforming bodies, in which the contact region remains small in comparison to the size of either body. Further, the quasi-static theory holds explanatory value regarding the relationship between any two contacting spheres subjected to normal forces. Building upon Hertz’s normal force and the law of Coulombic friction, the relationship between contacting spheres subjected to tangential forces was derived by Mindlin (1949). As a result, the Hertz-Mindlin force-displacement law was proposed, and continues to play an important role in contact mechanics.

For example, Hertz-Mindlin theory is integral to the computational contact algorithms implemented for the LS-DYNA numerical linear contact model (LSTC 2016). Specific to LS-DYNA simulations, mechanical parameters of particle-particle interaction can be defined using the keyword `*CONTROL_DISCRETE_ELEMENT`, which permits definitions of normal and tangential

contact stiffnesses; damping coefficients; static and rolling friction coefficients; and, even liquid surface tension to account for capillary forces for modeling adhesion between saturated particles. As a fundamental assertion, these parameters are correlated to one another, where collectively, such parameters dictate the local deformation at any single contact between two particles. In turn, a given set of contact interactions can majorly affect the macroscopic behavior of the corresponding particulate system, even when said system is only subjected to (externally) quasi-static load conditions. Contact interactions also depend significantly on the material and material model type of particles, where the constitutive parameters dictate the intensity of contact stiffness.

A.3.3 Microscopic Constitutive Models and Parameters

Given the coordinates (x_1, y_1, z_1) and (x_2, y_2, z_2) , which represent the centroids of two particles, the position vectors P_1 and P_2 (with respect to the origin of the global coordinate system) are expressed as:

$$P_1 = x_1 \vec{i} + y_1 \vec{j} + z_1 \vec{k} \quad P_2 = x_2 \vec{i} + y_2 \vec{j} + z_2 \vec{k} \quad (\text{A.54})$$

A penalty-based contact is used to capture the particle-particle interaction between these neighboring particles, and is expressed as:

$$d_{\text{int}} = R_1 + R_2 - |P_1 - P_2| \leq 0 \quad (\text{A.55})$$

where R_1 and R_2 are the radii of particle 1 and particle 2, respectively.

When two spheres come into contact, a linear spring-dashpot system for both normal and tangential directions can be used to describe contact forces and the overlap (\mathcal{S}) between two particles. Such is the case for the DEM implementation in LS-DYNA (Fig. A.45).

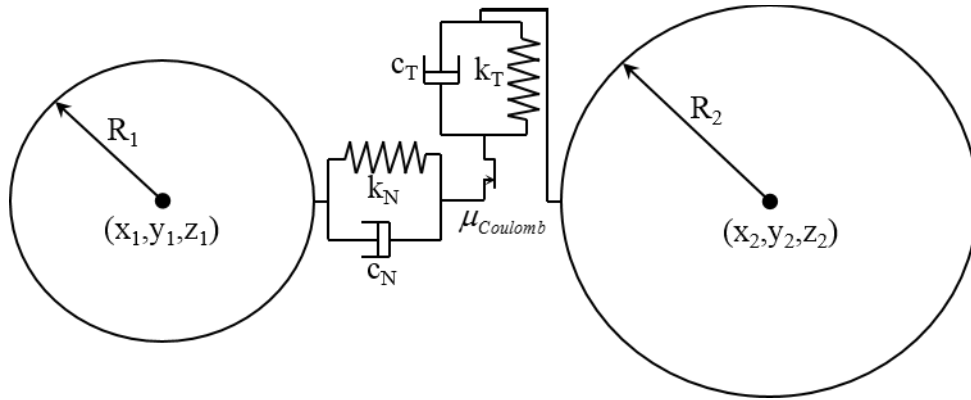


Figure A.45 Particle-particle linear contact force model

In the stiffness model, the normal and tangential spring forces are calculated based on Hooke's law of linear elastic bodies, and operate on the particle-particle overlap distances:

$$\begin{aligned} F_N^S &= k_N \delta_N \\ F_T^S &= k_T \delta_T \end{aligned} \quad (\text{A.56})$$

where k_N is normal spring stiffness, k_T is the tangential spring stiffness, δ_N and δ_T are, respectively, the normal and tangential overlap distances for the two interacting particles. To account for energy dissipation of the dynamic system (which commonly involves considerations for a coefficient of restitution), viscous damping forces are generated in parallel with those of the elastic spring stiffness. Thus, contact behavior is changed from elastic to viscoelastic, and further, this form of damping does not affect the equilibrium value of the resultant force. The damping mechanism does, however, reduce the number of calculation cycles needed to reach force equilibrium under at rest conditions. The normal and tangential damping forces are calculated based on normal and tangential components of relative contact velocity:

$$\begin{aligned} F_N^D &= c_N \dot{\delta}_N \\ F_T^D &= c_T \dot{\delta}_T \end{aligned} \quad (\text{A.57})$$

where c_N and c_T are normal and tangential damping constant respectively. Thus, the magnitude of the normal force is:

$$F_N = k_N \delta_N + c_N \dot{\delta}_N \quad (\text{A.58})$$

For modeling slippage during particle-particle interactions, the various frictional forces that arise in association with mechanical contact can be modeled using Coulomb's law of dry friction. For the scenario of particle-particle (relative) translation, if the condition $F_T \leq \mu_{Coulomb} F_N$ is satisfied at any time during contact, then the contacting spheres are in a static friction condition. For this condition, the tangential force can be quantified based on Eqns. A.56 and A.57. Otherwise, sliding occurs and the tangential contact force reaches its maximum (limiting) value, F_{Tmax} :

$$F_{Tmax} = \mu_{Coulomb} F_N \quad (\text{A.59})$$

where $\mu_{Coulomb}$ is the static friction coefficient. More generally, the magnitude of the tangential force, F_T , is given by:

$$F_T = \min \left(k_T \delta_T + c_T \dot{\delta}_T, \mu_{Coulomb} F_N \right) \quad (\text{A.60})$$

Furthermore, the case of Coulomb friction is extended in LS-DYNA by the introduction of a rolling friction coefficient, $\mu_{rolling}$. For scenarios involving particle to particle contacts, resultant particle rotations are inhibited through introduction of the rolling resistance moment M_R , shown in Eqn. A.61.

$$\begin{aligned}
M_T &\leq M_R \\
M_R &= F_T R = \mu_{roll} F_N R
\end{aligned}
\tag{A.61}$$

A listing of the microscopic parameters, which are typical of numerical treatments of sphere-sphere contact interactions, is given in Table A.10. In the context of modeling in LS-DYNA, parameter input values are specified using the keyword `*CONTROL_DISCRETE_ELEMENT` (LSTC 2014).

Table A.10 Contact parameters available in LS-DYNA for modeling sphere-sphere interactions

Parameter	Symbol
Normal damping coefficient	<i>NDAMP</i>
	<i>TDAMP</i>
Tangential damping coefficient	μ_{static}
Coefficient of static friction	$\mu_{rolling}$
	<i>NormK</i>
Coefficient of rolling friction	<i>ShearK</i>
Normal stiffness factor	
Shear stiffness factor	

A.4 Detailed Description of Rheological Model

A detailed description of the DSE rheological components is presented here, where care is taken to document how such components fit into the modeling of DSEs in LS-DYNA (LSTC 2014). Also, relevant contact stiffness parameters are defined (for both normal and tangential interactions), and the analytical network of relationships between the contact stiffness parameters are delineated. A similar treatment is then applied to investigate those DSE rheological components dedicated to contact-dependent viscous damping. As a synthesis of the analytical derivations, analytical expressions pertaining to contact stiffness and viscous damping are brought together as part of an examination of DSE restitution coefficients. As a result, a novel methodology is developed to map from the (analytical) nonlinear relationships of contact stiffness to the (numerical) linear contact spring-damper implementation in LS-DYNA. Finally, the concept of capillary suction pressure is introduced and the corresponding implementation in LS-DYNA is explored.

A.4.1 Microscopic Contact Parameters of LS-DYNA DSE Analysis

Parameters were previously introduced in association with use of the linear contact force model implemented in LS-DYNA. In this context, one of the most important parameters for modeling penalty-based particle-particle interactions (i.e., mechanical contact) is the elastic spring stiffness. The formulation for normal spring stiffness k_N in LS-DYNA (LSTC 2014) depends on two quantities: 1) Sphere radius (e.g., R_1, R_2); and, 2) Compression modulus (e.g., K_1, K_2). For any two interacting (contacting) spheres, a normal stiffness factor $NormK$, is then used to scale the normal contact stiffness:

$$k_N = \begin{cases} \frac{K_1 R_1 K_2 R_2}{K_1 R_1 + K_2 R_2} NormK : if \ NormK > 0 \\ |NormK| : if \ NormK < 0 \end{cases} \quad (A.62)$$

Specific to the LS-DYNA implementation of the DEM, tangential spring stiffness k_T is then calculated in proportion to the normal spring stiffness:

$$k_T = k_N ShearK \quad (0.1 \leq ShearK \leq 0.9) \quad (A.63)$$

The maximum overlap between particles is therefore strongly influenced (in LS-DYNA) by the magnitude of the normal contact stiffness. As a contributing factor in calculating the normal contact stiffness in LS-DYNA, the isotropic compression modulus is specific to the type of material being considered (e.g., steel, aluminum, granite, silica sand), as well as the material model (e.g., elastic, elastic-perfectly plastic) that is assigned to the DSEs. In the current study, a linear elastic treatment is elected for modeling of granular material using DSEs. Accordingly, the LS-DYNA keyword `*MAT_ELASTIC` is utilized, which requires input of three (constant) parameter values: mass density (ρ); Young's modulus (E); and Poisson's ratio (ν). Note that the Young's modulus can be approximated by making an equivalency between the normal spring stiffness and linearization of Hertz normal stiffness. In forming the normal contact stiffness, the (constant) bulk modulus for an individual DSE is calculated as:

$$K = \frac{E}{3(1-2\nu)} \quad (A.64)$$

Given the role of the bulk modulus in calculating the normal contact stiffness in LS-DYNA, bulk modulus necessarily affects the size of the critical time step for ensuring stability of the (explicit) time-stepping algorithms. More specifically, to ensure stability during the explicit numerical integration of the equations of motion in LS-DYNA, a critical time step $dt_{Cundall}$ (determined based on Cundall's approach; Cundall and Strack 1979) is defined as:

$$dt_{Cundall} = 0.2\pi \sqrt{\frac{(4/3)\rho\pi R_{sphere}^2}{K(NormK)}} \quad (A.65)$$

where R_{sphere} is the radius of a given sphere of interest.

For numerical models of DSE assemblies that utilize non-uniform spheres (i.e., spheres with differing radii), the critical time step should be calculated for each type of sphere being modeled, and the minimum should be specified for the analysis. The value of 0.2 in the calculation of Cundall's time step ($dt_{Cundall}$) in Eqn. A.65 is included to limit relative errors in energy conservation for the linear elastic spring model to relative magnitudes of approximately less than five percent (Malone 2008). Specific to modeling in LS-DYNA, the time step size can be directly specified using the keyword `*CONTROL_TIMESTEP`.

An important consideration in the modeling of granular soil using DSE assemblies is the selection of primary and secondary sphere radii. As an example selection procedure, consider the grain size distribution in Fig. A.46, which was derived from sieve analysis in a laboratory setting. Purely as furtherance of the example, the diameter of 100 percent finer by weight, D_{100} , is selected as a primary particle size for modeling a given coarse-grained soil. Having quantified the D_{100} , a shear jamming scheme would then potentially be adopted using either D_{50} or smaller size of secondary particles, depending on the application of interest (i.e., depending on the available computational resources and the number of spheres needed to populate the simulation space). Upscaling procedures are being developed as part of ongoing research efforts, and will be addressed in detail: simulations of jammed systems study particulate clustered configurations leading to jamming in both static systems and systems under shear. Under shear stress, average cluster size may diverge after a finite amount of strain, leading to a jammed state. A particle configuration may exist in a jammed state with a stress required to “break” the force chains causing the jam.

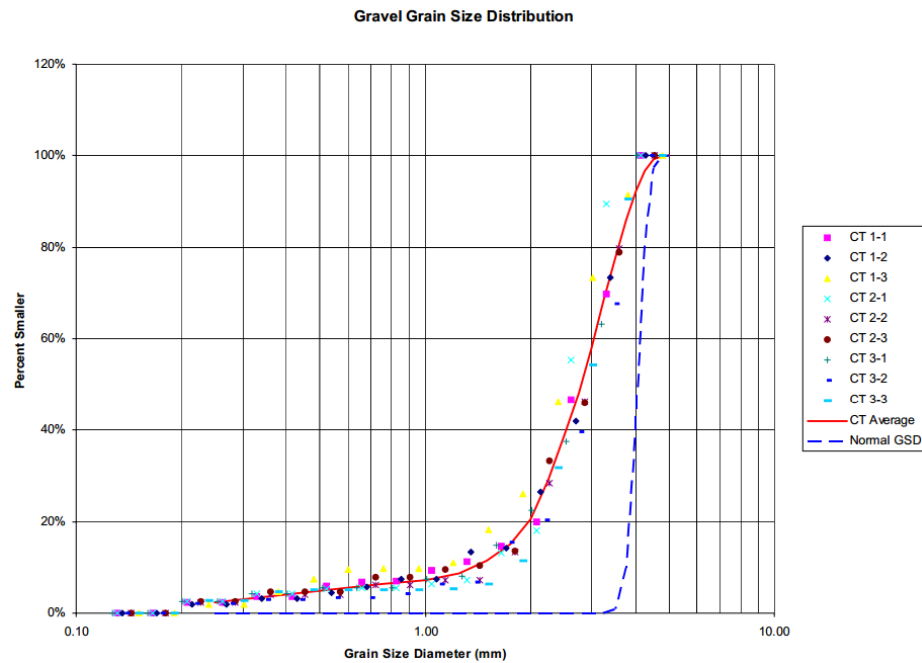


Figure A.46 Example grain size distribution for a granular soil (Nielsen 2004)

Regardless of the means by which primary and secondary DSE radii are selected (and, as needed, upscaled), the stiffness factors *NormK* and *ShearK* are necessary in quantifying spring

stiffnesses. Specific to the DSE stiffness formulation in LS-DYNA, the tangential to normal stiffness ratio k_T/k_N is analagous to the ratio of tangential to normal stiffness ($ShearK/NormK$). For a dense packing of particles in a mechanically stable state, the stiffness ratio most greatly influences the generation of those contact forces associated with relatively high levels of Coulombic friction (Cundall and Strack 1979). Furthermore, while shear stiffness can play a dominant role in driving the motions of interacting DSEs, as soon as particle-particle slippage occurs, the shear force reaches a maximum and subsequent variations in contact forces are determined solely by the normal particle-particle interactions. Considering undamped free vibration of an individual DSE in both the tangential and normal directions, the equations of motion (Eqn. A.51 and Eqn. A.53) are then expressed as:

$$\begin{aligned} m_{eff} \ddot{\delta}_z + k_N \delta_z &= 0 \\ m_{eff} I_{0eff} \left(\ddot{\delta}_x + R \ddot{\theta} \right) + \left(I_{0eff} + m_{eff} R^2 \right) k_T (\delta_x + R\theta) &= 0 \end{aligned} \quad (A.66)$$

where I_{0eff} is the effective moment of inertia of a given sphere-sphere pair. Likewise, the natural frequencies in the normal (ω_N) and tangential (ω_T) directions can be expressed as:

$$\begin{aligned} \omega_N &= \sqrt{\frac{k_N}{m_{eff}}} \\ \omega_T &= \sqrt{\frac{\left(I_{0eff} + m_{eff} R^2 \right) k_T}{m_{eff} I_{0eff}}} \end{aligned} \quad (A.67)$$

For the case of spheres of equal size and same material, the natural periods are calculated as:

$$\begin{aligned} T_N &= \frac{2\pi}{\sqrt{\frac{k_N}{(m/2)}}} \\ T_T &= \frac{2\pi}{\sqrt{\frac{\left(I_0 + mR^2 \right) k_T}{(mI_0/2)}}} \end{aligned} \quad (A.68)$$

where m is the mass of an individual sphere, and I_0 is the moment of inertia of an individual sphere. By equating the periods T_N (normal) and T_T (tangential), the relationship between k_N and k_T can be defined such that normal force and tangential force are simultaneously released:

$$\frac{k_T}{k_N} = \frac{I_0}{I_0 + mR^2} = \frac{2}{7} \quad (\text{A.69})$$

since $I_0 = \frac{2}{5}mR^2$ for a solid sphere. Note that the ratio of k_T to k_N is set as the default value when modeling DSE using LS-DYNA (LSTC 2014).

In addition, these two equations of motion can be solved for given initial conditions of velocity in normal direction δ_{z_0} and tangential direction $\left(\delta_{x_0} + R\theta_0\right)$ as:

$$\begin{aligned} \delta_z(t) &= \delta_{z_0} \sqrt{\frac{m_{eff}}{k_N}} \sin\left(t \sqrt{\frac{k_N}{m_{eff}}}\right) \\ X(t) &= \left(\delta_{x_0} + R\theta_0\right) \sqrt{\frac{m_{eff}I_{0_{eff}}}{(I + m_{eff}R^2)k_T}} \sin\left(t \sqrt{\frac{(I_{0_{eff}} + m_{eff}R^2)k_T}{m_{eff}I_{0_{eff}}}}\right) \end{aligned} \quad (\text{A.70})$$

where $X(t)$ is the horizontal displacement as a function of time. By differentiating the horizontal displacement with respect to time t , horizontal velocity $\dot{X}(t)$ is obtained:

$$\dot{X}(t) = \left(\delta_{x_0} + R\theta_0\right) \cos\left(t \sqrt{\frac{(I_{0_{eff}} + m_{eff}R^2)k_T}{m_{eff}I_{0_{eff}}}}\right) \quad (\text{A.71})$$

Contact durations ($T_{contact}$) corresponding to the condition that $\delta_z(T_{contact}) = 0$ can then be defined in accordance with Eqn. A.70 such that:

$$T_{contact} = \pi \sqrt{\frac{m_{eff}}{k_N}} \quad (\text{A.72})$$

Thus, the horizontal velocity just at the instant of contact termination is:

$$\dot{X}(T_{contact}) = \left(\delta_{x_0} + R\theta_0\right) \cos\left(\pi \sqrt{\frac{m_{eff}}{k_N}} \sqrt{\frac{(I_{0_{eff}} + m_{eff}R^2)k_T}{m_{eff}I_{0_{eff}}}}\right) \quad (\text{A.73})$$

For interactions between spheres defined using identical geometric, constitutive, and rheological descriptions, the tangential coefficient of restitution (e_T) can be expressed in terms of k_T and k_N as (Fig. A.47):

$$e_T = -\frac{\dot{X}(T_{contact})}{\left(\dot{\delta}_{x_0} + R\dot{\theta}_0\right)} = -\cos\left(\pi\sqrt{\frac{7}{2}}\sqrt{\frac{k_T}{k_N}}\right) \quad (\text{A.74})$$

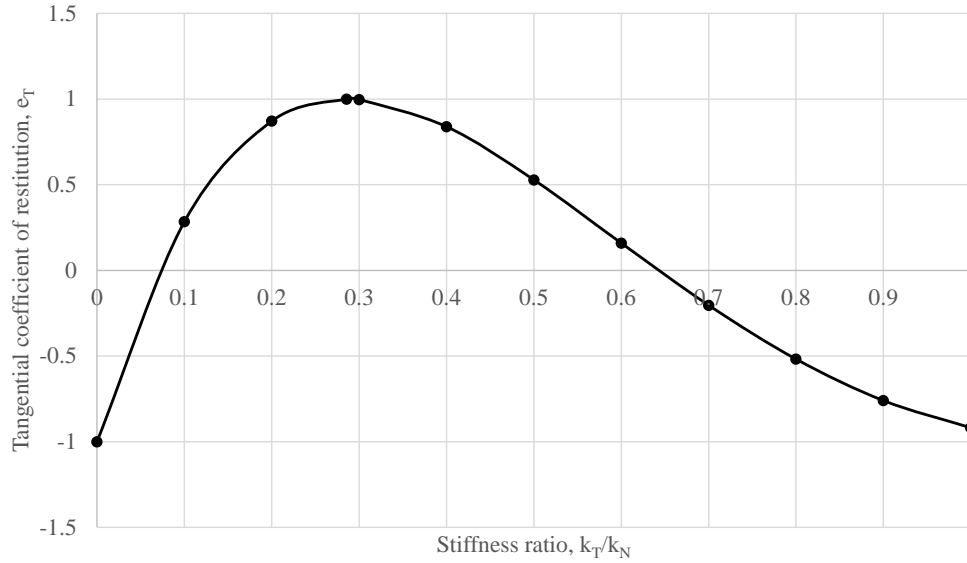


Figure A.47 Tangential coefficient of restitution (e_T) versus stiffness ratio (k_T to k_N)

By employing the stiffness ratio of 2/7 (recall Eqn. A.69), the behavior of DSE is characterized as perfectly elastic. However, micromechanical behaviors of grains are viscoelastic, in which granular particle collision tests indicate energy loss per contact even with an elastic solid wall with smooth surfaces (Sommerfeld and Huber 1999). The degree of potential energy loss in collisions depends on particle size, shape, and surface roughness, which leads to both impact-velocity dependent damping (viscous) and friction-induced Coulombic damping (Abedi 2009). As we separately model an asymptotic limiting value per coefficients of friction as a model parameter, viscous damping is incorporated in the particle contact definition using numerical dampers. The determination of viscous damping requires analysis of natural frequency of DSE, which depends on the size of DSE, mass density, frictional parameters used in force mapping for shape transformation (see Section A.1.8), and contact stiffnesses. In the following, we derive the correlations among the contact parameters in a step-by-step manner in order to increase confidence in computation of inter-particle shear forces and corresponding tangential stiffness (i.e., ratio of k_T to k_N).

In addition to considerations for spring stiffness, the mechanical penalty-based particle-particle contact formulation adopted in the current study is also sensitive to parameters that make up the coefficient of restitution. In LS-DYNA, the coefficient of restitution is treated through specification of some fraction of the normal and tangential critical damping forces. Regarding

input parameters specific to LS-DYNA, the damping coefficients corresponding to the normal and tangential directions are referred to as *NDAMP* and *TDAMP*, respectively.

$$\begin{aligned} c_N &= (NDAMP)c_{cri_N} \\ c_T &= (TDAMP)c_{cri_T} \end{aligned} \tag{A.75}$$

where $c_{cri_N} = 2m_{eff}\omega_N = 2\sqrt{m_{eff}k_N}$ and $0 \leq NDAMP, TDAMP \leq 1$

In Sec. 2.4.4., the LS-DYNA input parameters *NDAMP* and *TDAMP* will be explored in detail, and a methodology will be established to ensure that (for paried values of *NDAMP*, *TDAMP*) damped vibrations hold matching frequency content in both the normal and tangential directions. Note that the damping effects associated with use of *NDAMP* and *TDAMP* are fundamentally different process from that of Coulombic damping (i.e., the Coulomb friction law). In particular, the two damping parameters (*NDAMP*, *TDAMP*) permit the modeling of viscous material behavior.

Two final parameters that are used to define particle-particle interactions in LS-DYNA are those of the static and rolling friction coefficients, μ_{static} and $\mu_{rolling}$, respectively. For the DEM implementation available in LS-DYNA, frictional force generation is governed by Coulombic friction, where a detailed treatment of the physics underlying frictional phenomena was previously discussed. From a numerical standpoint, friction forces that arise during particle-particle interactions depend on the input value of coefficient of static friction (μ_{static}) and the sum of all normal contact forces F_N . When the coefficient of static friction is input as zero, rotational DOF are removed from the associated DSEs. Furthermore, no tangential friction forces may be induced during periods of contact. For scenarios where non-zero values of static (sliding) friction are utilized (i.e., when rotational DOF are active for the DSEs), the rolling friction coefficient can additionally be specified to model particle-particle rolling resistance. The ratio of the rolling ($\mu_{rolling}$) to static (μ_{static}) friction coefficients is further explored later.

A.4.2 Hertzian Normal Contact Stiffness

In 1880, Hertz developed the theory of elastic deformations localized near contact patches, and also, developed analytical procedures to predict stresses that arise due to contact between two elastic bodies. The work of Hertz has been shown to be well suited for explaining quasi-static mechanical contacts between two spheres (Johnson 1985; Stronge 2000). The concept of contacts between two spheres is complex, where for example, two spherical bodies can be said to be in contact when physically sharing some contact point (e.g., point O in Fig. A.48a). Additionally, two spheres can be said to be in contact when pressed together such that the spherical geometries occupy a shared overlapping region (Fig. A.48b).

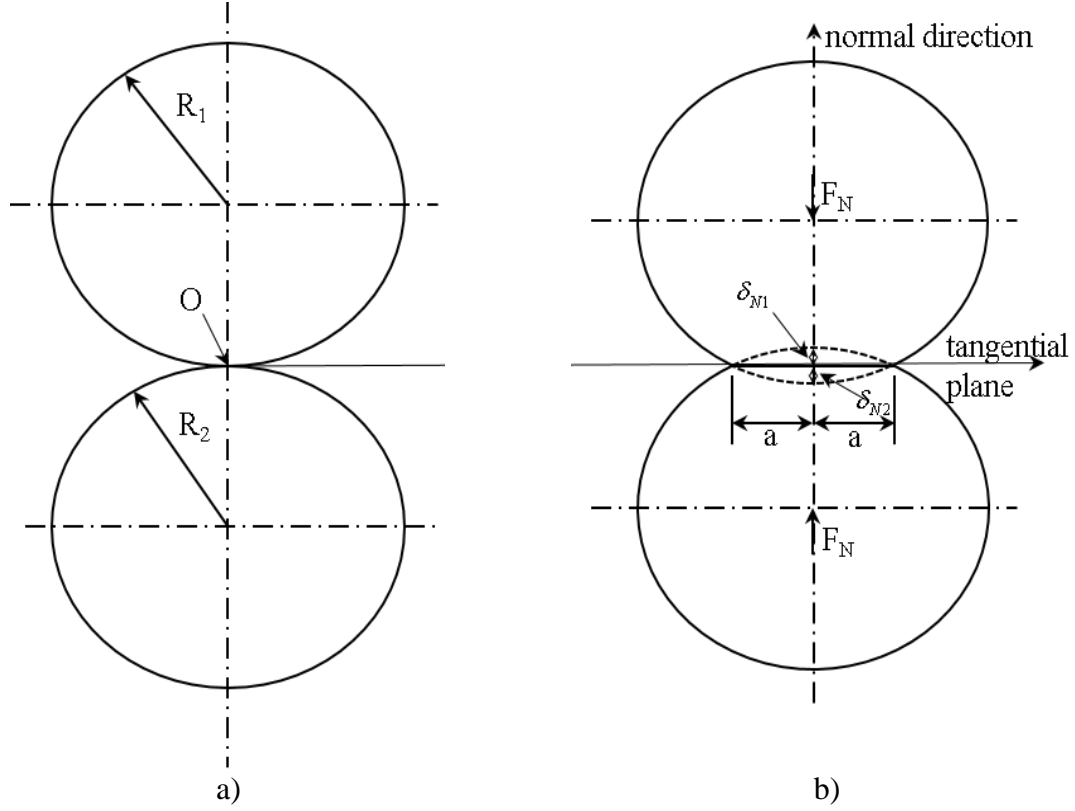


Figure A.48 Contact between two spheres: a) With shared contact point O ; b) With overlapping regions

In adopting the Hertzian theory on contact phenomena, the applied force at the contact between two nonconforming elastic bodies in the normal direction, F_N , can be written in terms of displacement as:

$$F_N = \frac{4}{3} E^* \sqrt{R} \delta_N^{3/2} \quad (\text{A.76})$$

where $\frac{1}{E^*} = \frac{1-\nu_1^2}{E_1} + \frac{1-\nu_2^2}{E_2}$; E_1 , E_2 are elastic moduli and ν_1 , ν_2 are Poisson's ratios assigned to sphere one and sphere two, respectively. Likewise, $\frac{1}{R} = \frac{1}{R_1} + \frac{1}{R_2}$, where R_1 , R_2 are significant radii of each spherical body and R is the relative radius of curvature or effective radius. Lastly, δ_N is the total overlap distance in the normal direction, $\delta_N = \delta_{N1} + \delta_{N2}$, and where δ_{N1} , δ_{N2} are the overlap distances specific to sphere one and sphere two, respectively. Note that, relative to the unreformed sphere geometries, the overlap distances (δ_{N1} , δ_{N2}) are treated as being equal to the displacements of the sphere centroids. Along these lines, δ_{N1} and δ_{N2} are referred to in terms of displacement in the following derivation.

By differentiating the force-displacement relationship (Eqn. A.76) with respect to normal displacement (δ_N), the Hertz measure of normal stiffness (k_{N_Hertz}) can be expressed as:

$$\frac{dF_N}{d\delta_N} = k_{N_Hertz} = 2E^* \sqrt{R} \delta_N^{1/2} \quad (A.77)$$

Recalling Fig. A.48b, the contact geometry along the tangential plane can be described as the area of a circle, where the associated radius (a) is related to the normal displacement (δ_N). Alternatively, the radius (a) can be defined in terms of applied force:

$$a = \sqrt{R\delta_N} = \left(\frac{3F_N R}{4E^*} \right)^{1/3} \quad (A.78)$$

Having defined a radius representing the contacting region, the maximum normal contacting pressure (p_0) is then given by:

$$p_0 = \frac{3F_N}{2\pi a^2} = \left(\frac{6F_N E^{*2}}{\pi^3 R^2} \right)^{1/3} \quad (A.79)$$

Combining Eqn. A.76 and Eqn. A.78 with Eqn. A.79, the normal displacement (δ_N) can be expressed as a function of the maximum normal contacting pressure (p_0):

$$\delta_N = \left(\frac{\pi p_0 \sqrt{R}}{2E^*} \right)^2 \quad (A.80)$$

Maximum normal pressure at contact can then be obtained by incorporating a pertinent yield criterion. In the current study, the Von Mises yield criterion is adopted, leading to the following relationship between maximum normal pressure and yield stress (σ_{yield}):

$$p_0 = \frac{\sigma_{yield}}{\sqrt{3}} \quad (A.81)$$

A.4.3 Tangential Contact and Coulombic Friction

Consider two spherical elastic bodies, which are: 1) Initially pressed together by means of a Hertz normal force F_N ; and, 2) Subjected to an increasing tangential force F_T . Further, in this scenario, the normal contacting force is held constant while the tangential force is gradually increased from zero. Under these conditions, expressions relating the tangential direction force (F_T) and tangential displacement (δ_T) are of the form (Johnson, 1985):

$$\delta_T = \frac{3\mu F_N}{16aG^*} \left[1 - \left(1 - \frac{F_T}{\mu F_N} \right)^{2/3} \right]$$

or

$$F_T = \mu F_N \left[1 - \left(1 - \frac{16aG^* \delta_T}{3\mu F_N} \right)^{3/2} \right]$$

where μ is the Coulomb friction coefficient, $G = \frac{E}{2(1+\nu)}$, $\frac{1}{G^*} = \frac{2-\nu_1}{G_1} + \frac{2-\nu_2}{G_2}$, having G_1 and G_2 are the shear moduli associated with each spherical body.

The stick region of two interacting spherical bodies is defined as a circle of radius, c , and can be expressed as:

$$c = a \left(1 - \frac{F_T}{\mu F_N} \right)^{1/3}$$

recalling that a is the radius of the Hertz contact area. By differentiating the force-displacement equation with respect to tangential displacement, the tangential stiffness (referred to as $k_{T_Mindlin}$, as this quantity derives from the work of Mindlin) can be expressed as:

$$\frac{dF_T}{d\delta_T} = k_{T_Mindlin} = 8aG^* \left(1 - \frac{16aG^* \delta_T}{3\mu F_N} \right)^{1/2}$$

The ratio of the Mindlin tangential stiffness ($k_{T_Mindlin}$) and Hertz normal stiffness (k_{N_Hertz}) is:

$$\frac{k_{T_Mindlin}}{k_{N_Hertz}} = \frac{8G^* \left(1 - \frac{16aG^* \delta_T}{3\mu F_N} \right)^{1/2}}{2E^*} = \frac{4G^*}{E^*} \left(1 - \frac{4G^* \delta_T}{\mu E^* \delta_N} \right)^{1/2}$$

where the ratio expressed in Eqn. A.85 is only valid when the condition $\delta_T \leq \frac{\mu E^* \delta_N}{4G^*}$ is satisfied.

When the tangential contact force component (F_T) is on the verge of being realized (i.e., $F_T \approx 0$), the area of the stick region equals the Hertz contact area (i.e., $c \approx a$). Therefore, slip area is very small and the contact approaches a no-slip condition. Also, due to the form of the relationship between force and displacement (Eqn. A.82), tangential displacement is minimal ($\delta_T \approx 0$), which allows for a (conditionally valid) expression of Mindlin tangential stiffness:

$$\frac{dF_T}{d\delta_T} = k_{T_Mindlin} = 8aG^* \quad (\text{A.86})$$

Consequently, when the above conditions are satisfied, the stiffness ratio given in Eqn. A.85 becomes:

$$\frac{k_{T_Mindlin}}{k_{N_Hertz}} = \frac{4G^*}{E^*} = \frac{\frac{1-\nu_1}{G_1} + \frac{1-\nu_2}{G_2}}{\frac{1-\nu_1/2}{G_1} + \frac{1-\nu_2/2}{G_2}} \quad (\text{A.87})$$

For scenarios where particle-particle sliding is imminent (i.e., when the stick region reduces to a single point, such that $c = 0$), the corresponding tangential displacement ($\delta_{T_sliding}$) and force (F_T) reduce to (relative to Eqn. A.82):

$$\begin{aligned} \delta_{T_fully_sliding} &= \frac{3\mu F_N}{16aG^*} \\ \text{and} \\ F_T &= \mu F_N \end{aligned} \quad (\text{A.88})$$

For any time t in which the expressions given in Eqn. A.88 hold, the system is said to have transitioned from quasi-static to transient conditions. It follows that, under transient conditions, the tangential component of sphere-sphere contacting force is limited to the Coulomb frictional force, and thus free sliding initiates. Also, under such conditions, the stiffness ratio (k_T/k_N) approaches zero.

Now, consider a scenario in which two spheres are engaged by means of applying equal and opposite oblique forces F_{ob} at each sphere centroid, where the forces are oriented at a constant angle of α , with respect to the normal direction (and where $0 < \alpha < 90$). The oblique force F_{ob} can be decomposed into the normal (F_{ob_N}) and tangential (F_{ob_T}) components:

$$\begin{aligned} F_{ob_N} &= \Delta F_N = F_{ob} \cos(\alpha) \\ F_{ob_T} &= F_{ob} \sin(\alpha) \end{aligned} \quad (\text{A.89})$$

Further, in this scenario, the total normal (F'_N) and tangential (F_T) forces are given by:

$$\begin{aligned} F'_N &= F_N + \Delta F_N \\ F_T &= F_{ob_T} = \tan(\alpha) \Delta F_N \end{aligned} \quad (\text{A.90})$$

For any time t , increases in the total normal force (F'_N) will correspond to increases in the radius of the circular contacting area (from a to b). According to Johnson (1985), the no-slip condition within the contact area holds as long as F_T does not exceed $\mu \Delta F_N$, from which it follows that:

$$\tan(\alpha) \leq \mu \quad (\text{A.91})$$

As a result, the relative tangential displacement (δ_T) becomes:

$$\delta_T = \frac{F_T}{8bG^*} = \frac{\tan(\alpha) \Delta F_N}{8bG^*} \quad (\text{A.92})$$

If the angle of the oblique force F_{ob} is greater than the resisting frictional force, then slip occurs.

For the scenario of oblique forces acting on two spheres, the force-displacement in the tangential direction is expressed as:

$$\delta_T = \frac{3\mu F_N'}{16bG^*} \left[1 - \left(1 - \frac{F_T}{\mu F_N'} \right)^{2/3} \right] \quad (\text{A.93})$$

Similarly, the stick region of two spherical bodies (defined by a circle of radius, c) can be expressed as:

$$c = b \left(1 - \frac{F_T}{\mu F_N'} \right)^{1/3} = b \left(1 - \frac{F_{ob} \sin(\alpha)}{\mu (F_N + F_{ob} \cos(\alpha))} \right)^{1/3} \quad (\text{A.94})$$

For any time t in which sliding may initiate (i.e., when the stick region approaches the condition $c = 0$), the oblique force is given by:

$$F_{ob} = \frac{\mu F_N}{\cos(\alpha) [\tan(\alpha) - \mu]}, \tan(\alpha) > \mu \quad (\text{A.95})$$

Further, under such conditions, the tangential displacement ($\delta_{T_sliding}$) and force (F_T) are given by:

$$\begin{aligned} \delta_{T_sliding} &= \frac{3\mu F_N'}{16bG^*} \\ F_T &= \frac{\mu F_N}{1 - \mu \cot(\alpha)}, \tan(\alpha) > \mu \end{aligned} \quad (\text{A.96})$$

A.4.4 Natural Frequencies and Critical Damping of Two Spheres in Contact

The second order differential equation governing two energy storage elements, including a spring and a dashpot, at the contact interface between two spheres (with non-zero masses) is defined as:

$$m_{eff} \ddot{x} + c \dot{x} + kx = 0 \quad (A.97)$$

where m_{eff} is effective mass, c is damping constant and k is stiffness of the contact point. Solutions to Eqn. A.97 can consist of: 1) Two unique real-valued roots, in the overdamped case; 2) Two equal real-valued roots, in the critical damped case; or, 3) Two complex-valued roots (which form complex conjugates), in the underdamped case.

For the purposes of numerical modeling, it is convenient to consider system-wide viscous damping via specification of a damping coefficient ($DAMP$), which is equal to zero for no damping, and equal to unity for critical damping of a system. The underdamped condition is then imposed by specifying a value of $DAMP$ that falls within the range of zero and unity. Recalling Eqn. A.97,

the damping constant c can be defined as $c = 2m_{eff}\omega DAMP$, where $\omega = \sqrt{\frac{k}{m_{eff}}}$ is the natural

frequency of the system. By defining $x = e^{\lambda t}$, the characteristic equation can be written as:

$$\lambda^2 + 2\omega DAMP \lambda + \omega^2 = 0 \quad (A.98)$$

The pair of complex conjugates, or eigenvalues (λ_1, λ_2), that constitute solutions to Eqn. A.98 can be written in terms of the damping coefficient (c) and natural frequency (ω) as:

$$\lambda_{1,2} = -DAMP\omega \pm i\omega\sqrt{1 - DAMP^2} \quad (A.99)$$

where the real part of Eqn. A.99 is the attenuation and the imaginary part is the damped natural frequency, ω_D . The solutions to Eqn. A.99 can be plotted on the complex plane, as shown in Fig. A.49. As a demonstration of how to interpret Fig. A.49, consider a mid-plane angle θ is equal to 45° . For this scenario, Fig. A.49 enables direct determination of the damping parameter ($DAMP$),

which would be $\frac{\sqrt{2}}{2} = 0.707$.

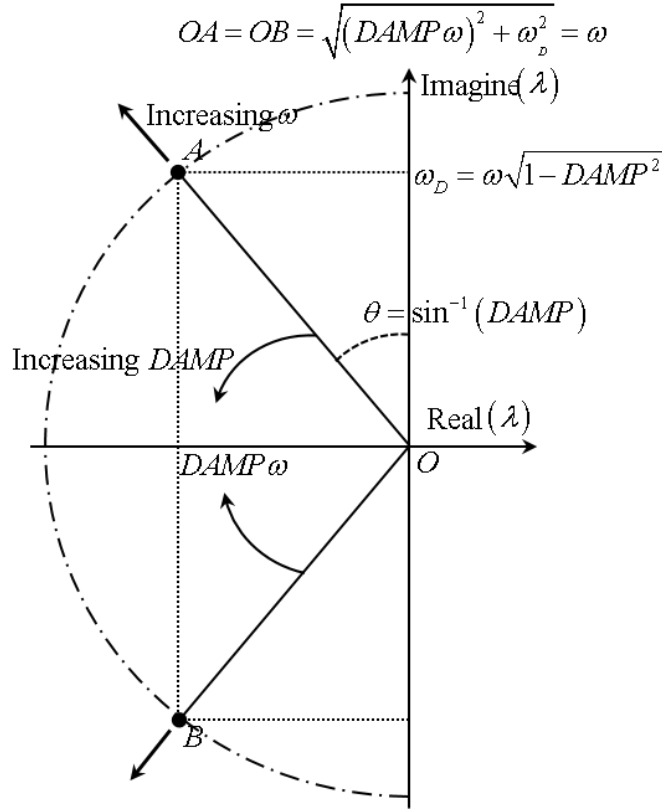


Figure A.49 Solutions to the characteristic equation plotted in the complex plane

Now consider a system undergoing damped free vibration in association with two spheres that overlap one another in the normal direction. As an exploration of how stiffness and mass quantities of DSE relate to damping phenomena, additionally consider the system subject to initial conditions of $\frac{\sqrt{2}}{2} = 0.707$ and $x(t) = 0, \dot{x}(t) = 4.429$. The calculated displacement responses at the contact point are plotted in Fig. A.50, where each curve represents a selected value of $NDAMP$ (ranging from 0.1 to 0.9 in increments of 0.1). The collected displacement histories (Fig. A.50) indicate that contact duration increases in proportion to increasing values for the damping constant ($NDAMP$). Quantitatively, contact duration can be written in terms of the normal damping coefficient and natural frequency as:

$$T_{contact} = \frac{\pi}{\omega_N} \sqrt{\frac{1}{1 - NDAMP^2}} \quad (A.100)$$

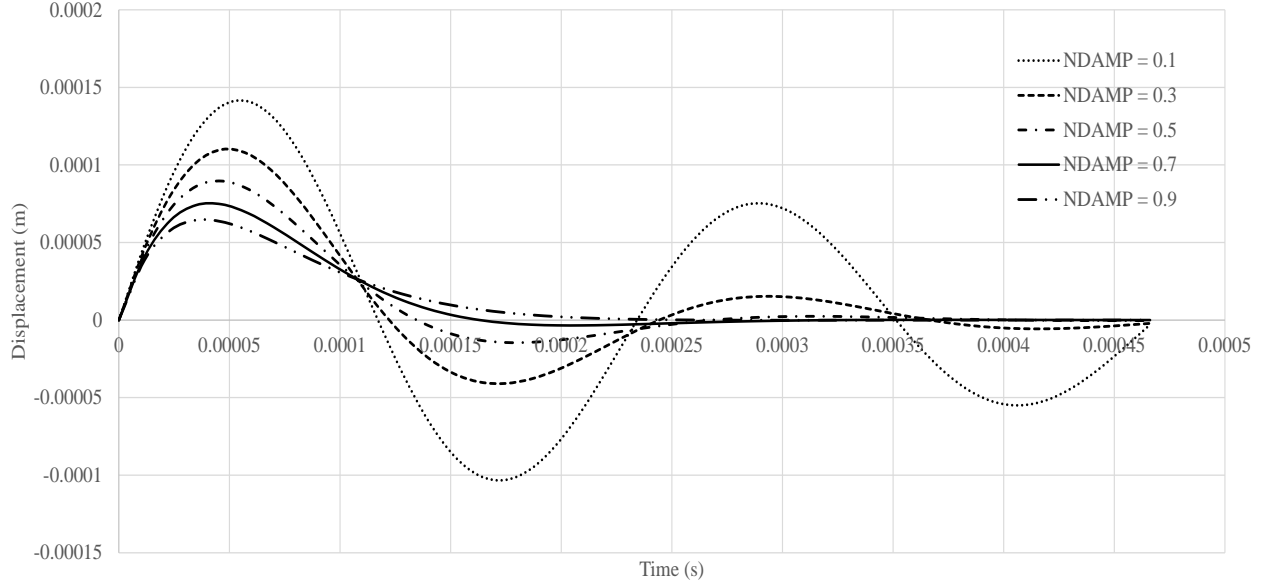


Figure A.50 Displacement responses at the contact interface as damping is varied for two overlapping spheres

As indicated in Fig. A.50, the local minima and maxima of displacements are attenuated for each cycle of oscillation. Further, the level of peak-displacement attenuation becomes more pronounced with increased damping. For the scenario considered, values of *NDAMP* that are equal to or greater than 0.7 correspond to (approximately) full attenuation of oscillatory displacements for times beyond the first half-cycle of response. The absence of such pronounced attenuation is referred to as “overshoot”, and is a decidedly non-physical phenomenon with respect to the motions of interacting granular particles. Therefore, in regards to the numerical modeling of granular particles, an *NDAMP* of 0.7 is adopted for carrying out simulations of DSE assemblies in the current study.

The ratio of tangential to normal natural frequencies of contact resonance (ω_T and ω_N , respectively) for an elastic impact between two spheres, based on Hertz-Mindlin contact theory, is defined as (Johnson 1985):

$$\frac{\omega_T}{\omega_N} = (2\chi)^{1/2} \quad (\text{A.101})$$

where the parameter χ is defined by:

$$\chi = \frac{\kappa m_{eff}}{2m_{eff}^*} \quad (\text{A.102})$$

And where K is a stiffness ratio: $\kappa = \frac{\frac{1-\nu_1}{G_1} + \frac{1-\nu_2}{G_2}}{\frac{1-\nu_1/2}{G_1} + \frac{1-\nu_2/2}{G_2}}$; $m_{eff} = \frac{m_1 m_2}{m_1 + m_2}$;

$$m_{eff}^* = \frac{m_1^* m_2^*}{m_1^* + m_2^*} = \frac{m_1 m_2}{m_1 \left(1 + \frac{R_2^2}{k_2^2}\right) + m_2 \left(1 + \frac{R_1^2}{k_1^2}\right)} ; \text{ and, the } k_i^2 = \frac{I_i}{m_i} \text{ values are the radii of gyration of}$$

the spheres about their respective centers of mass. Given the moment of inertia for a solid sphere, $k_i^2 = \frac{I_i}{m_i}$, the radius of gyration values become $k_i^2 = \frac{2}{5} R_i^2$ and $m^* = \frac{m_1 m_2}{m_1 \left(\frac{7}{2}\right) + m_2 \left(\frac{7}{2}\right)}$. Also, the

ratio of resonance frequencies (Eqn. A.101) can then be expressed as:

$$\frac{\omega_T}{\omega_N} = (3.5\kappa)^{1/2} \quad (\text{A.103})$$

In the context of modeling in LS-DYNA, the following relationship must be satisfied to ensure that damped vibrations hold matching frequency content in both the tangential and normal directions:

$$\frac{TDAMP}{NDAMP} = \frac{1}{(3.5\kappa)^{1/2}} \quad (\text{A.104})$$

A.4.5 Restitution Coefficients

Coefficient of Normal Restitution (e_N)

For the modeling of granular media in industrial applications, the normal coefficient of restitution ($NDAMP$) is set to a relatively high value (approximately 0.5 to 0.9, Karajan et al. 2014). To gain a better understanding of viscous damping and restitution phenomena particular to the modeling of granular media in LS-DYNA (LSTC 2014), a parametric set of simulations are carried out. Namely, ten ball drop simulations are conducted using LS-DYNA, where across the simulation set, the $NDAMP$ parameter is varied from 0.0 to 0.9 with an increment of 0.1. For these simulations, the model consists of two identical (and homogenous) elastic 50-mm-diameter spheres undergoing collinear impact (Fig. A.51). Sphere 1 is located at an initial height of 1.1 m (center-to-center) above Sphere 2, which is fully restrained from motion. The top sphere is excited downward by the gravitational force. The contact analysis during the impact only considers the translational DOF in the normal direction of motion by setting $NormK = 1$ to fully use the normal spring stiffness k_N , and leaving other parameters of contact definition to zero.

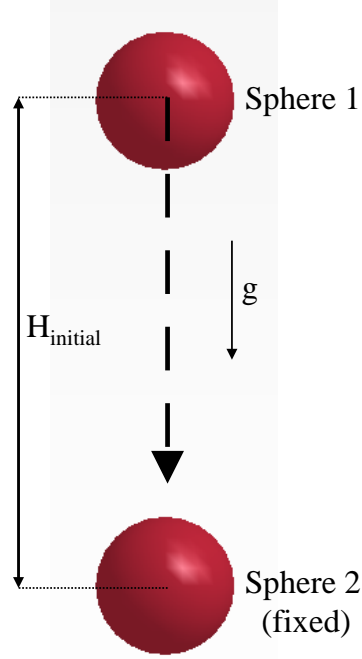


Figure A.51 Schematic of ball-drop simulations

The time-varying height of Sphere 1, over the course of each of the ten simulations, is plotted in Fig. A.52. For this test setup, the following definition of the coefficient of normal restitution defined in Ollagnier (2007) is adopted:

$$e_N = \frac{h^2}{h_0^2} \quad (\text{A.105})$$

where h_0 and h_1 are the ball heights before and after impact, respectively. In addition, for the ball-drop scenario, the coefficient of normal restitution (e_N) can be used to arrive at a damping coefficient in the linear contact force model (Cleary and Prakash 2004; Navarro and de Souza Braun 2013):

$$NDAMP = -\frac{\ln e_N}{\sqrt{\ln^2 e_N + \pi^2}} \quad (\text{A.106})$$

In Fig. A.52, the coefficient of normal restitution (e_N) is plotted as a function of the *NDAMP* parameter, where both Eqn. A.106 and numerical results obtained from ball drop simulations using LS-DYNA are included. Agreement is observed between Eqn. A.106 and the numerical results, which indicates that the preceding discussion is applicable for modeling sphere-sphere interactions in LS-DYNA. Also included in Fig. A.53 is a plot of e_N versus *NDAMP* when the full Cundall time step size is used in the simulations, and results are overlain with those associated with use of the Cundall time step factored at 20% (recall Eqn. A.65). Note that use of the 20% factor (as recommended in Jensen et al. 2014) leads to even stronger agreement between the numerical results and Eqn. A.106.

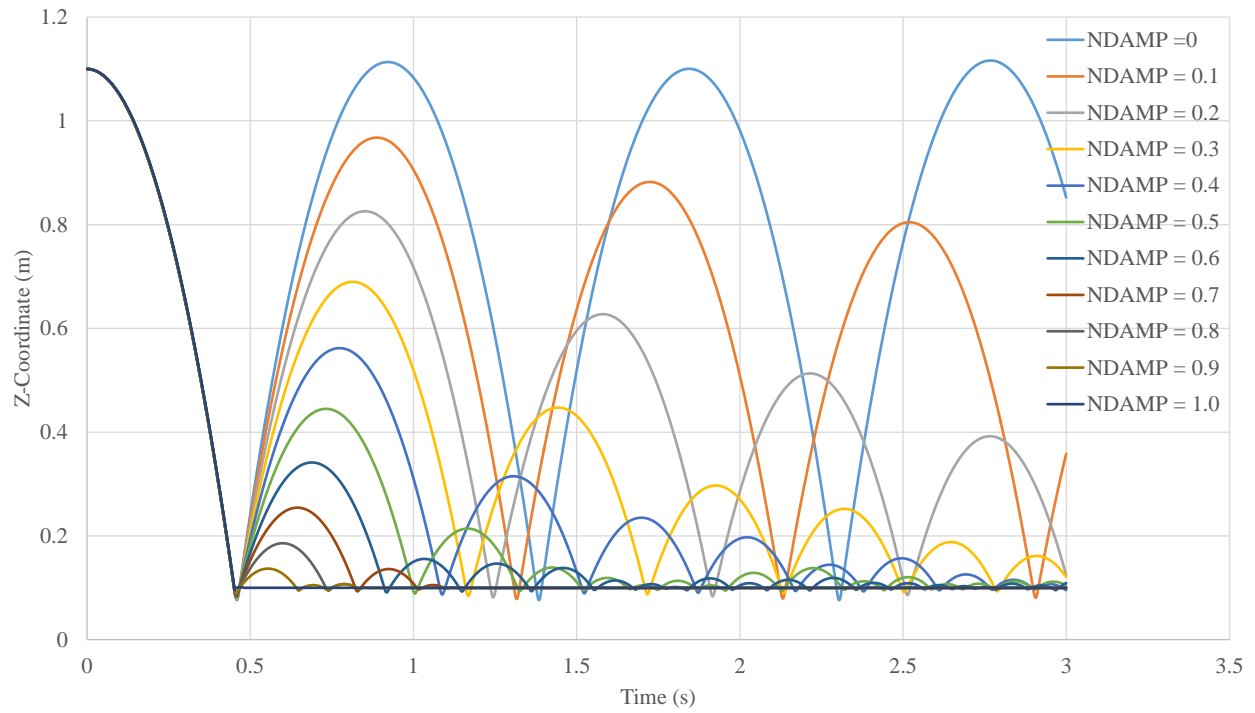


Figure A.52 Time-varying vertical position of sphere over the range of damping values considered

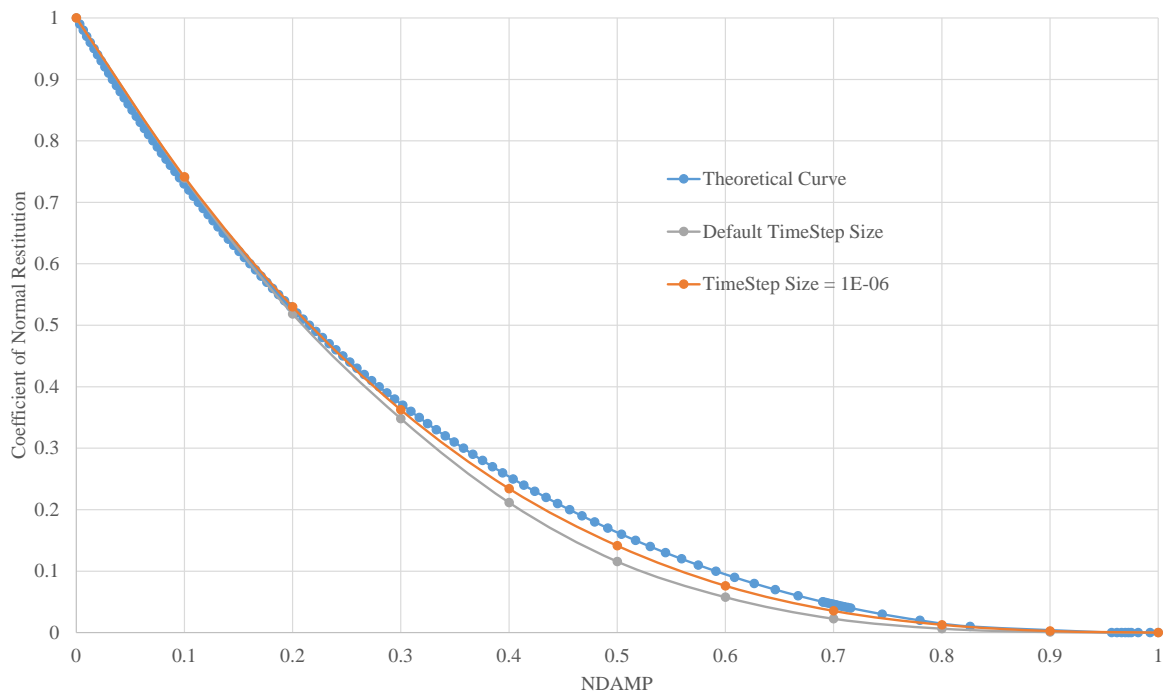


Figure A.53 Coefficient of normal restitution versus normal damping

Coefficient of Tangential Restitution (e_T)

LS-DYNA simulations of two-sphere (DSE) systems undergoing oblique collision (Fig. A.54) are carried out to gain insight into the interrelationships between the coefficient of tangential restitution (e_T), sliding friction (μ_{static}), and rolling friction (μ_{rolling}). As a given value of e_T affects both translational and rotational components of system response, oblique collision simulations are carried out for several angles of incidence ($2^\circ, 4^\circ, 6^\circ, 8^\circ, 10^\circ, 20^\circ, 30^\circ, 40^\circ, 45^\circ, 50^\circ, 60^\circ, 70^\circ$, and 80°). For all simulations conducted, Sphere 1 (Fig. A.54) is initially positioned above and to the left of a fixed sphere (Sphere 2). Further, an initial velocity (v_{initial}) is imposed on Sphere 1, where the associated vector points from Sphere 1 directly toward Sphere 2. For each angle of incidence considered, an additional parametric dimension is investigated by varying (in separate simulations) the ratio of rolling (μ_{rolling}) to sliding friction (μ_{static}) at ratios of 0.1, 0.5, and 1.0 (with all other parameters remaining unchanged).

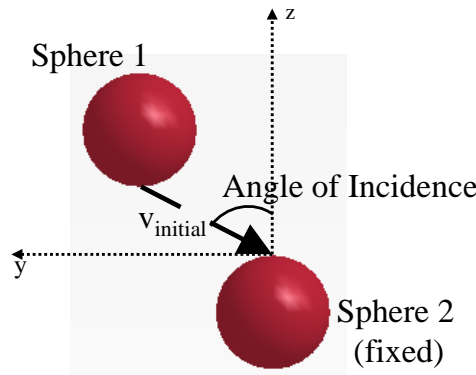


Figure A.54 Schematic of oblique collision simulations

By making use of the time-histories of computed velocity components from the LS-DYNA simulations, in conjunction with the methodology given in Walton (1993), a selection process emerges for assigning meaningfully coupled values of sliding friction (μ_{static}) and rolling friction (μ_{rolling}). As the first step in this process, and for a given ratio of rolling to sliding friction, the tangent of the effective recoil angle, v'_y/v'_z is plotted against the tangent of the effective incident angle, v_y/v_z . Accordingly, shown in Fig. A.55, are the v'_y/v'_z and v_y/v_z quantities obtained from oblique collision simulations across each of the thirteen aforementioned incidence angles, and where the ratio of rolling to sliding friction is maintained at 0.1. Similar plots are shown in Fig. A.56 and Fig. A.57 for rolling to sliding friction ratios of 0.5 and 1.0, respectively.

Consistent with Walton (1993), two pronounced slopes (approximately linear in form) are present among each of Fig. A.55 through Fig. A.57. To emphasize this, the collections of points associated with a negative slope are rendered as orange circles, while the collections of points associated with a positive slope are rendered as blue circles. For each collections of points, linear regression lines are formed (as shown in Fig. A.55 through Fig. A.57). The regression lines are referred to as “solution lines” (Walton 1993). With respect to the selection of parameter values for modeling DSE in LS-DYNA, and consistent with Walton (1993), the slopes of the regression lines for the orange-colored point data are characterized by the rolling friction coefficient (μ_{rolling}), while the slopes of the regression lines for the blue-colored point data are characterized by the sliding friction coefficient (μ_{static}). In this way, sliding and rolling friction are coupled, and critically, such

coupling is accounted for in the selection of the friction parameters for simulations conducted as part of the current study.

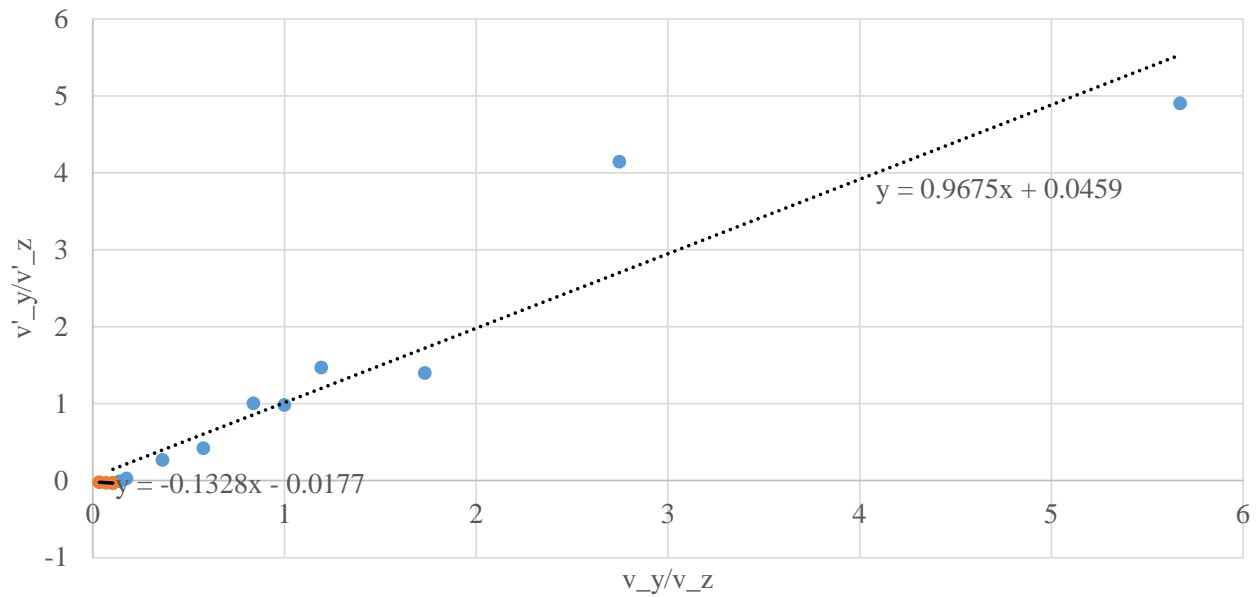


Figure A.55 Tangent of effective recoil angle versus tangent of effective incident angle for a ratio of rolling to sliding friction equal to 0.1

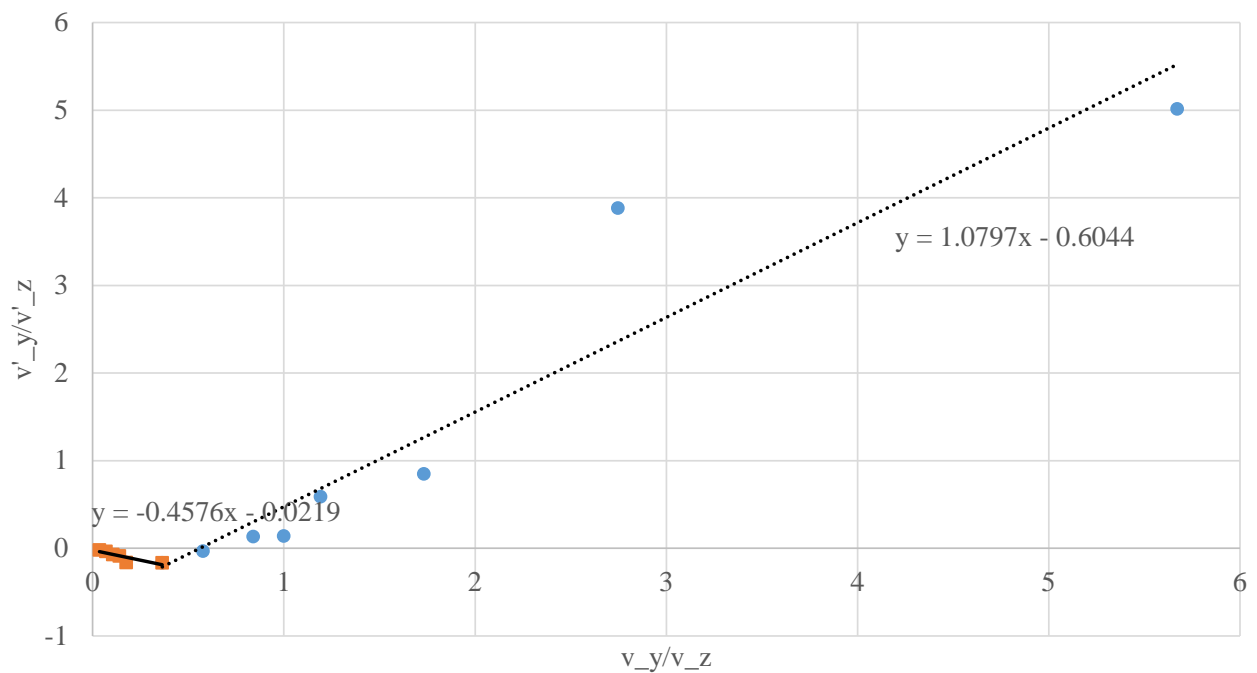


Figure A.56 Tangent of effective recoil angle versus tangent of effective incident angle for a ratio of rolling to sliding friction equal to 0.5

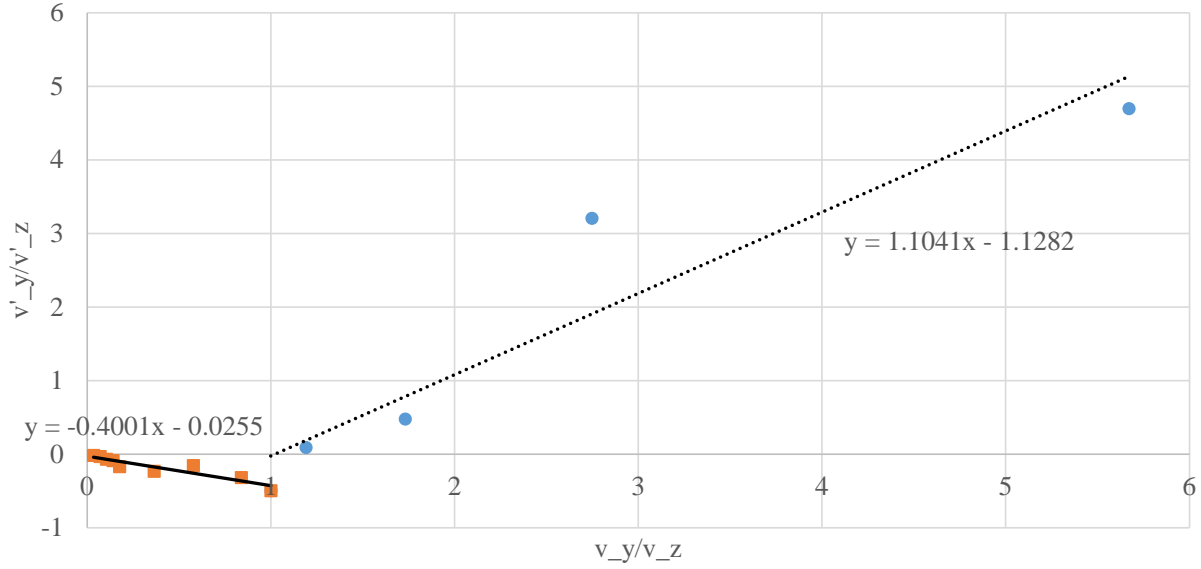


Figure A.57 Tangent of effective recoil angle versus tangent of effective incident angle for a ratio of rolling to sliding friction equal to 1.0

A.4.6 Detailed Description of Rheological Model

For the DEM linear contact model implemented in LS-DYNA (LSTC 2014), the normal stiffness of two interacting elastic spheres ($k_{N_LS-DYNA}$) is defined as:

$$k_{N_LS-DYNA} = \frac{K_1 R_1 K_2 R_2}{K_1 R_1 + K_2 R_2} \quad (\text{A.107})$$

where the bulk modulus for sphere i is defined consistent with Eqn. A.64. By incorporating Eqn. A.64 into Eqn. A.107 for each of the two spheres ($i = 1, 2$), the normal stiffness (Eqn. A.107) can be written in terms of the sphere-specific values of modulus of elasticity (E), Poisson's ratio (ν), and radius (R) as:

$$k_{N_LS-DYNA} = \frac{E_1 E_2 R_1 R_2}{3(1-2\nu_1)E_2 R_2 + 3(1-2\nu_2)E_1 R_1} \quad (\text{A.108})$$

Recall Eqn. A.76, which expresses the Hertz normal force (F_N) as a nonlinear function of, in part, normal displacement (δ_N). Given the implementation of a linear contact DEM model in LS-DYNA, additional considerations are required to map from the previously discussed (nonlinear) Hertzian expressions to the (linearized) input parameters available in LS-DYNA. Namely, a quantity referred to as Hertz's secant stiffness ($k_{N_Hertz_secant}$) is introduced (Fig. A.58), and is introduced:

$$k_{N_Hertz_secant} = \frac{F_N}{\delta_N} = \frac{4}{3} E^* \sqrt{R} \delta_N^{1/2} \quad (\text{A.109})$$

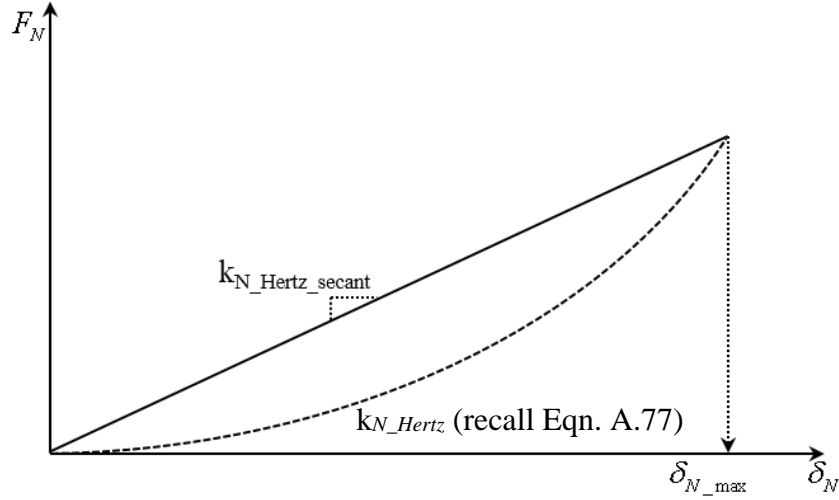


Figure A.58 Nonlinear stiffness and Hertz secant stiffness for modeling normal contact between spheres

$$k_{N_Hertz_secant} = \frac{F_N}{\delta_N} = \frac{4}{3} E^* \sqrt{R} \delta_N^{1/2} \quad (\text{A.110})$$

For two elastic spheres in contact, the Hertz secant stiffness ($k_{N_Hertz_secant}$) can be expressed in terms of the constituent values of elastic moduli (E_i^H), Poisson's ratios (ν_i), and radii (R_i):

$$k_{N_Hertz_secant} = \frac{4}{3} \left(\frac{E_1^H E_2^H}{E_1^H (1-\nu_2^2) + E_2^H (1-\nu_1^2)} \right) \sqrt{\frac{R_1 R_2}{R_1 + R_2}} \delta_N^{1/2} \quad (\text{A.111})$$

Note that the elastic moduli in Eqn. A.111 are strictly associated with Hertzian theory, whereas the elastic moduli of Eqn. A.108 are strictly associated with numerical input for modeling in LS-DYNA.

As a measure of upholding Hertzian theory, numerical parameter selection for normal contact stiffness modeling in LS-DYNA is driven by equating Eqn. A.111 and Eqn. A.107:

$$\frac{4}{3} \left(\frac{E_1^H E_2^H}{E_1^H (1-\nu_2^2) + E_2^H (1-\nu_1^2)} \right) \sqrt{\frac{R_1 R_2}{R_1 + R_2}} \delta_N^{1/2} = \frac{E_1 E_2 R_1 R_2}{3(1-2\nu_1)E_2 R_2 + 3(1-2\nu_2)E_1 R_1} \quad (\text{A.112})$$

To facilitate manipulation of Eqn. A.112, the following three constants are defined:

$$\begin{aligned}
C_1 &= (1 - 2\nu_2)R_1 \\
C_2 &= (1 - 2\nu_1)R_2 \\
C_3 &= 4 \frac{E_1^H E_2^H}{E_1^H (1 - \nu_2^2) + E_2^H (1 - \nu_1^2)} \frac{1}{\sqrt{R_1 R_2 (R_1 + R_2)}} \delta_N^{1/2}
\end{aligned} \tag{A.113}$$

Consequently, the equality in Eqn. A.112 simplifies to: $C_3 C_1 E_1 + C_3 C_2 E_2 = E_1 E_2$. By additionally making an assumption of the relationship between E_1 and E_2 (namely, $E_1 = r E_2$), the elastic modulus associated with numerical modeling in LS-DYNA can be expressed in terms of Hertzian quantities. For example, in a two-sphere collision scenario, the LS-DYNA input parameter for the elastic modulus of Sphere 2 is determined as:

$$E_2 [r E_2 - (C_3 C_1 r + C_3 C_2)] = 0 \rightarrow E_2 = \frac{C_3 C_1 r + C_3 C_2}{r} \tag{A.114}$$

A similar methodology is adhered to in selecting numerical parameter values to model tangential components of contact stiffness in LS-DYNA. Specifically, for any instant within a simulation wherein oblique contact forces arise, a secant definition of the tangential contact stiffness ($k_{T_Mindlin_secant}$) can be expressed as:

$$k_{T_Mindlin_secant} = \frac{16aG^*}{3[1 - \mu \cot(\alpha)]}, \tan(\alpha) > \mu \tag{A.115}$$

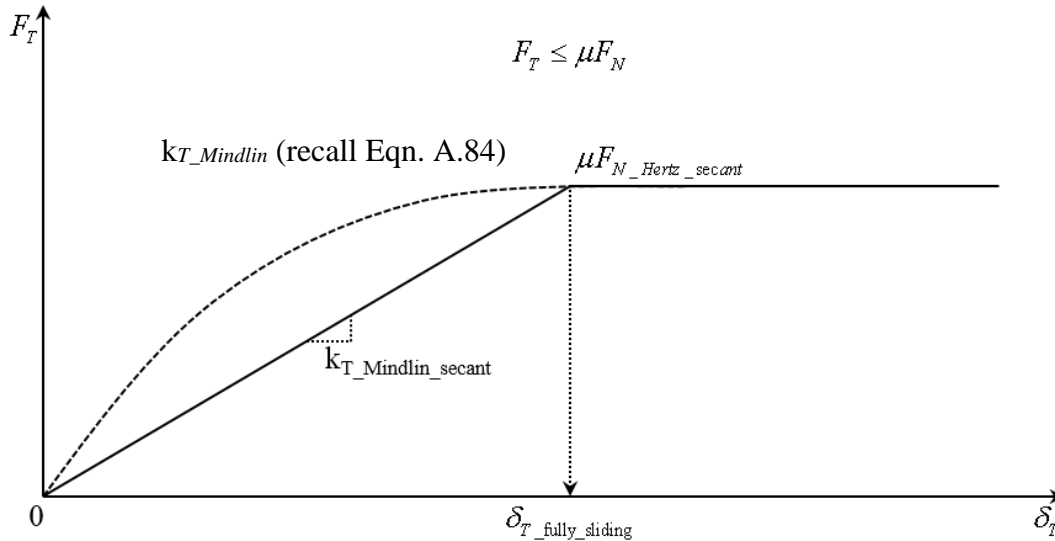


Figure A.59 Nonlinear tangential stiffness per Mindlin's Theory and an approximate secant stiffness approach for use in tangential contact modeling between DSE

For the LS-DYNA implementation of the DEM, tangential contact stiffness ($k_{T_LS-DYNA}$) is defined as the product of normal stiffness ($k_{N_LS-DYNA}$) and the *ShearK* coefficient (LSTC 2014):

$$k_{T_LS-DYNA} = k_{N_LS-DYNA} ShearK \tag{A.116}$$

Given the relationship between normal and tangential contact stiffness (Eqn. A.116), the numerical input value selection process for modeling tangential contact stiffness in the current study is driven by ensuring that the following stiffness ratio is maintained:

$$\frac{k_{T_Mindlin_sec\ ant}}{k_{N_Hertz_sec\ ant}} = \frac{4G^*}{E^* [1 - \mu \cot(\alpha)]} \quad (A.117)$$

A.4.7 Boundary Model of Capillary Suction Pressure

Capillarity, or capillary action is defined as the ability of a liquid to flow in narrow spaces without being influenced by the effects of external forces. Capillary action is a result of cohesion pressure as well as adhesion, which may cause the liquid to work against gravity. With respect to granular material, capillary action induces inter-particle forces via the pores of granules, which contributes positively to shear and tensile strengths for any collection of neighboring granules. The applicability of capillary forces in industrial applications is well established. One such previously developed treatment is that of the “liquid bridge” concept, which is used in numerical models to mimic the (physical) introduction of liquid throughout the pore spaces of granules. Due to surface tension of the liquid, the surface area of the “bridge” tends toward a minimal value, hence, exerting a pulling (attraction) force on the affected particles.

The work of Rabinovich et al. (2005) was adopted in implementing a numerical model of capillary action in LS-DYNA (Karajan et al. 2012), and therefore, is of interest for the current study. Rabinovich et al. (2005) explored pressure differences that arise when making use of the liquid bridge concept to, in turn, develop analytical expressions for determining capillary suction force. Further, Rabinovich et al. (2005) analyzed the geometry of sphere-plate interactions, and then made extrapolations in developing expressions pertaining to sphere-sphere interactions (Fig. A.60). Along these lines, capillary forces between two spheres separated by a liquid bridge were estimated using the analytical expressions and their predictions were compared against experimentally measured values of capillary force, obtained using an atomic force microscope (AFM).

The analytical expressions developed by Rabinovich et al. (2005) stem from the seminal work of Derjaguin. Namely, the Derjaguin approximation can be used to calculate the suction force F between two spheres separated by a distance H :

$$F = \pi R U \quad (A.118)$$

in which R is the radius of the sphere upon which the adhesion force acts, and U is the specific energy (per unit area) of interaction of two flat surfaces at a separation distance of H . The specific energy U acting through the liquid layer is:

$$U = -2\gamma \cos \theta \quad (A.119)$$

where γ is the liquid surface tension and θ is the tangent angle between the liquid volume and a given sphere (as annotated in Fig. A.60).

Thus, from Eqns A.121 and A.124., capillary suction force is given by:

$$F(H,V) = -\frac{2\pi R\gamma \cos \theta}{1 + \left[H/2d_{sp/sp}(H,V) \right]} \quad (\text{A.124})$$

where the distance $d_{sp/sp}(H,V)$ (as shown in Fig. A.60) can be obtained using the following expression:

$$d_{sp/sp}(H,V) = \frac{H}{2} \left[-1 + \sqrt{1 + \frac{2V}{\pi R H^2}} \right] \quad (\text{A.125})$$

Taking into account the attraction force due to transverse components of the liquid bridge, the formula for capillary suction force proposed in Rabinovich et al. (2005) is then given by:

$$F(H,V) = -\frac{2\pi R\gamma \cos \theta}{1 + \left[H/2d_{sp/sp}(H,V) \right]} - 2\pi\gamma R \sin \alpha \sin(\theta + \alpha) \quad (\text{A.126})$$

The capillary suction force expression given in Eqn. A.126 was demonstrated to show good agreement with experimentally measured suction forces in Rabinovich et al. (2005).

As noted previously, the LS-DYNA DEM implementation makes use of the capillary suction force model proposed by Rabinovich et al. (2005). In LS-DYNA, numerical treatment of capillarity is activated by setting the parameter $CAP \neq 0$ under the keyword `*CONTROL_DISCRETE_ELEMENT`. Along with activation of the capillary model, the following parameters must be specified: *GAMMA*, which corresponds to the previously defined parameter γ ; *VOL*, which gives the initial volume fraction of the liquid bridge with respect to the volume of any interacting spheres; and, *ANG* which corresponds to the previously described parameter θ (recall Fig. A.60). A schematic of the capillary force model implemented in LS-DYNA is given in Fig. A.61.

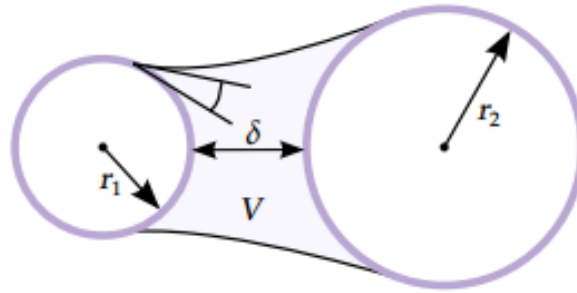


Figure A.61 Schematic representation of capillary force model (LSTC 2016)

For the two neighboring particles shown in Fig. A.61 (with radii r_1 and r_2), the volume of a liquid bridge V is calculated as:

$$V = \frac{4}{3}\pi(r_1^3 + r_2^3)\frac{1}{10}VOL \quad (\text{A.127})$$

In addition, an effective radius, R , is determined as:

$$R = \frac{2r_1r_2}{r_1 + r_2} \quad (\text{A.128})$$

Eqn. A.127 and Eqn. A.128 can be combined to calculate an effective distance parameter, d (analogous to Eqn. A.125):

$$d = \frac{\delta}{2} \left(-1 + \sqrt{1 + \frac{2V}{\pi R \delta^2}} \right) \quad (\text{A.129})$$

where δ is the separation distance, and is based on the positions of any two interacting particles at a given time. Finally, the capillary suction force (F) is computed (for each calculation cycle within the LS-DYNA simulation) as:

$$F = -\frac{2\pi\gamma R \cos(\theta)}{1 + \frac{\delta}{2d}} \quad (\text{A.130})$$

To study the effect of capillary suction force on the response of a particle, a demonstration simulation was carried out using LS-DYNA. The demonstration model consists of three identical spheres (Fig. A.62). A linearly increasing upward force was applied to the top sphere, which acted to oppose the automatically computed capillary suction forces. The parameter values specified for the LS-DYNA capillary model, as part of the demonstration simulation, are listed in Table A.11.

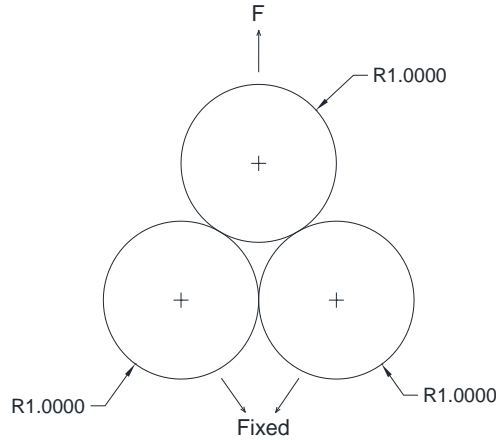


Figure A.62 LS-DYNA model to study the effects of capillary suction force

Table A.11 LS-DYNA input parameters for modeling capillarity

Parameter	Value	Units
<i>GAMMA</i>	0.264	N/m
<i>VOL</i>	0.66	--
<i>ANG</i>	10	°

Numerical results obtained from the LS-DYNA simulation, pairing sphere-sphere distance to capillary suction force, are plotted in Fig. A.63. Also shown in Fig. A.63 is Eqn. A.127, when supplied with values used in the demonstration simulation. Excellent agreement is observed between the purported capillary suction force model and the numerical simulation results.

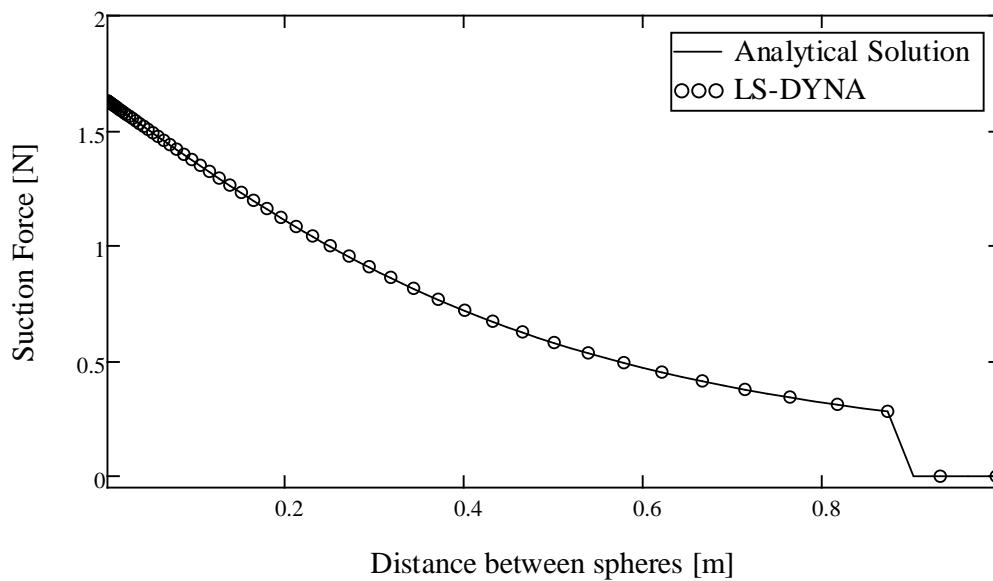


Figure A.63 Sphere-sphere distance versus capillary suction force

APPENDIX B: REPOSITORY OF LABORATORY TEST DATA

In this section, all the results from physical tests conducted on granular material are presented. The detailed description of the testing procedures are given in Chapter 3. The physical tests conducted are broadly divided into three categories – micro-scale, grain-scale and system scale. In micro-scale, scanning microscopy and rough surface stochastic analyses were performed. In grain-scale, micro-indentation, nano-indentation and scratch tests were performed. In system scale, tri-axial compression test were performed on granular assemblies. All these results are presented below.

B.1 Micro-scale physical test results.

Scanning electron and scanning probe microscopy were performed to measure the surface height distribution for ceramic proppants. These images were taken for three different scan sizes – $1\text{ }\mu\text{m} \times 1\text{ }\mu\text{m}$, $10\text{ }\mu\text{m} \times 10\text{ }\mu\text{m}$, and, $100\text{ }\mu\text{m} \times 100\text{ }\mu\text{m}$. Six measurements were taken for each of the scan sizes. Following the procedure described in Sec. 3.3.4, surface roughness parameters and spatial functions were quantified. Results from each measurements are given below.

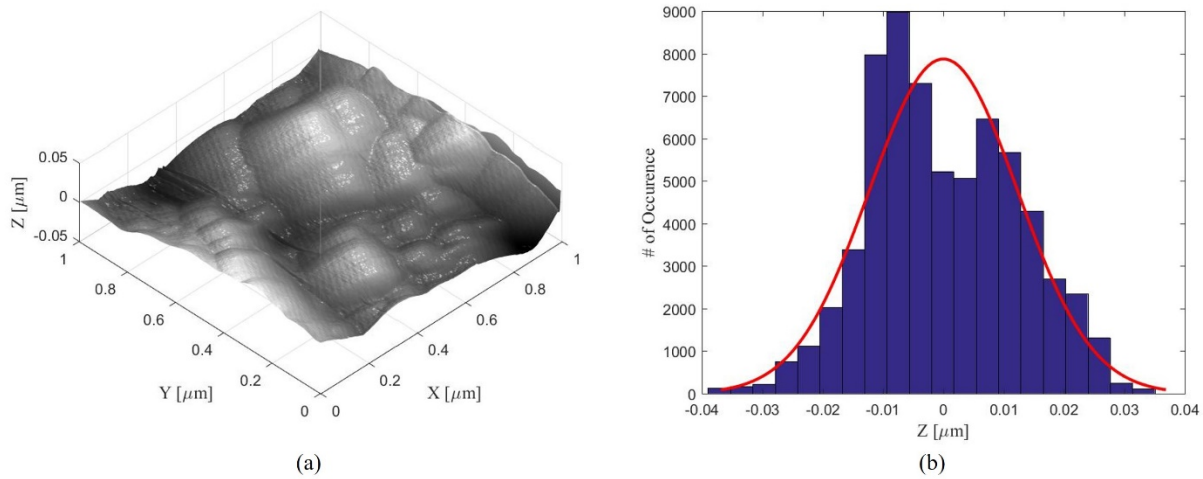


Figure B.1 (a) Surface profile; (b) Histogram for surface height distribution, for $1\text{ }\mu\text{m} \times 1\text{ }\mu\text{m}$ scan size test 1

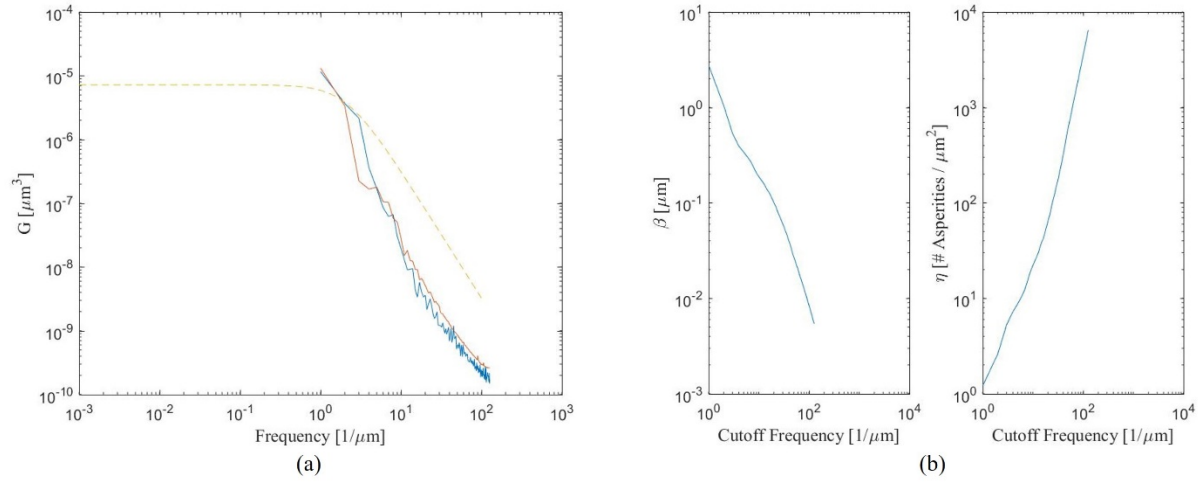


Figure B.2 (a) Power spectral density function; (b) Radius of asperity peak and asperity density, for $1\mu\text{m} \times 1\mu\text{m}$ scan size test 1

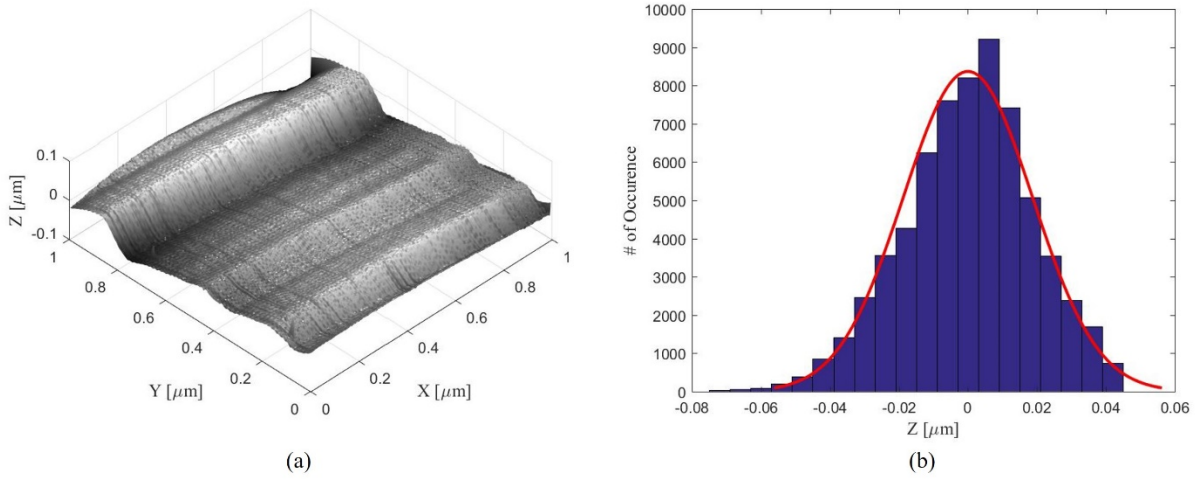


Figure B.3 (a) Surface profile; (b) Histogram for surface height distribution, for $1\mu\text{m} \times 1\mu\text{m}$ scan size test 2

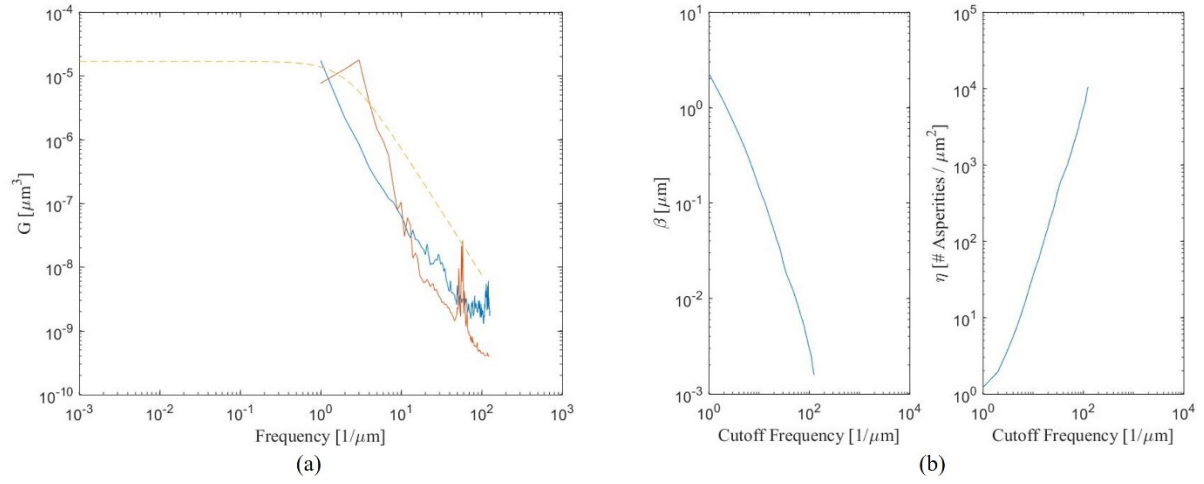


Figure B.4 (a) Power spectral density function; (b) Radius of asperity peak and asperity density, for $1\mu\text{m} \times 1\mu\text{m}$ scan size test 2

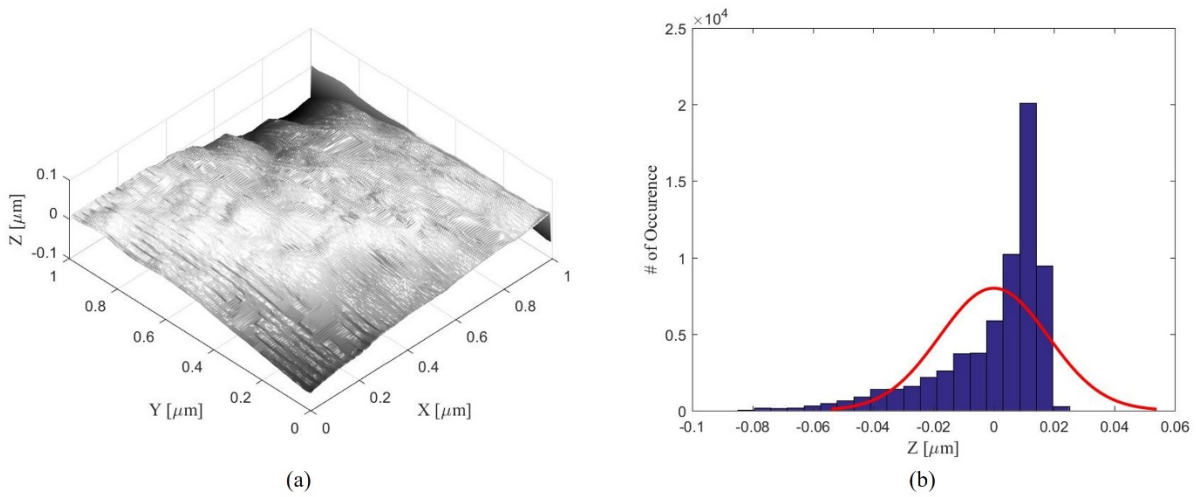


Figure B.5 (a) Surface profile; (b) Histogram for surface height distribution, for $1\mu\text{m} \times 1\mu\text{m}$ scan size test 3

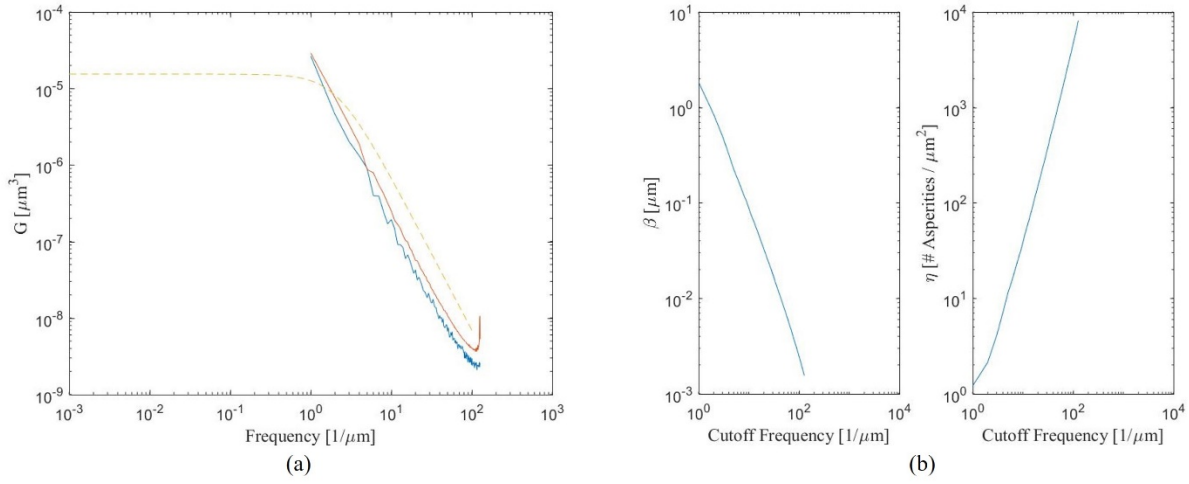


Figure B.6 (a) Power spectral density function; (b) Radius of asperity peak and asperity density, for 1 μ m x 1 μ m scan size test 3

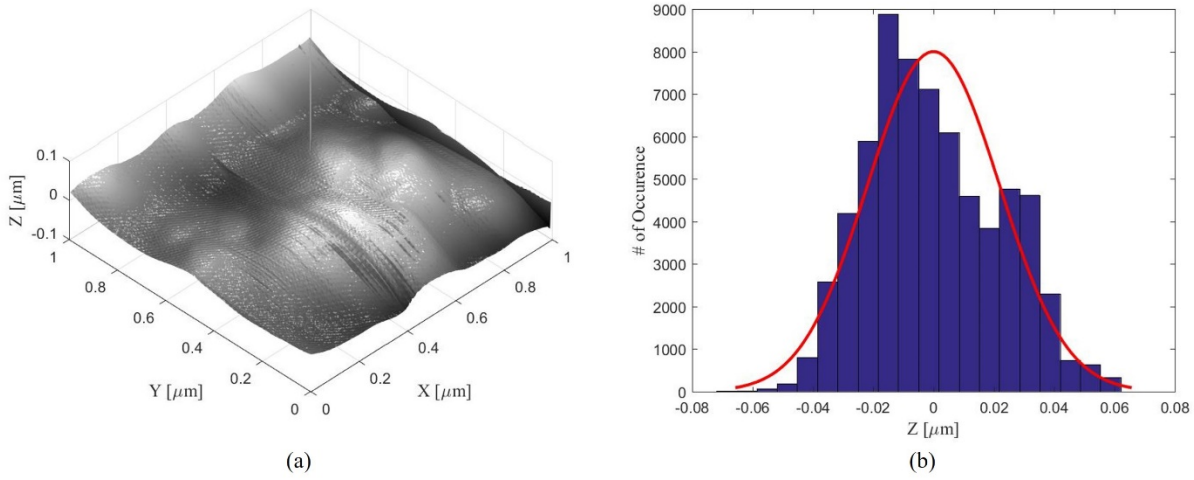


Figure B.7 (a) Surface profile; (b) Histogram for surface height distribution, for 1 μ m x 1 μ m scan size test 4

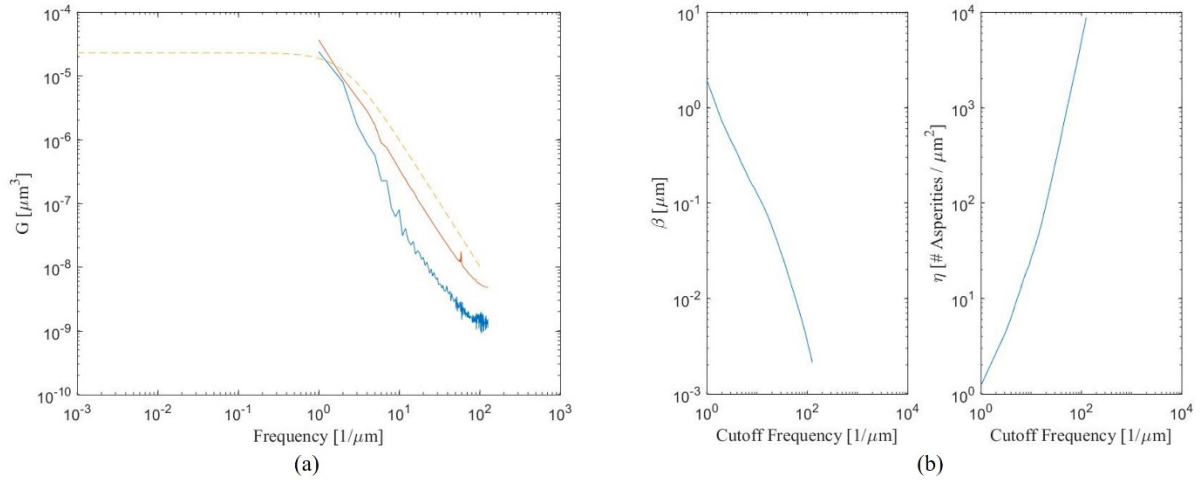


Figure B.8 (a) Power spectral density function; (b) Radius of asperity peak and asperity density, for $1\mu\text{m} \times 1\mu\text{m}$ scan size test 4

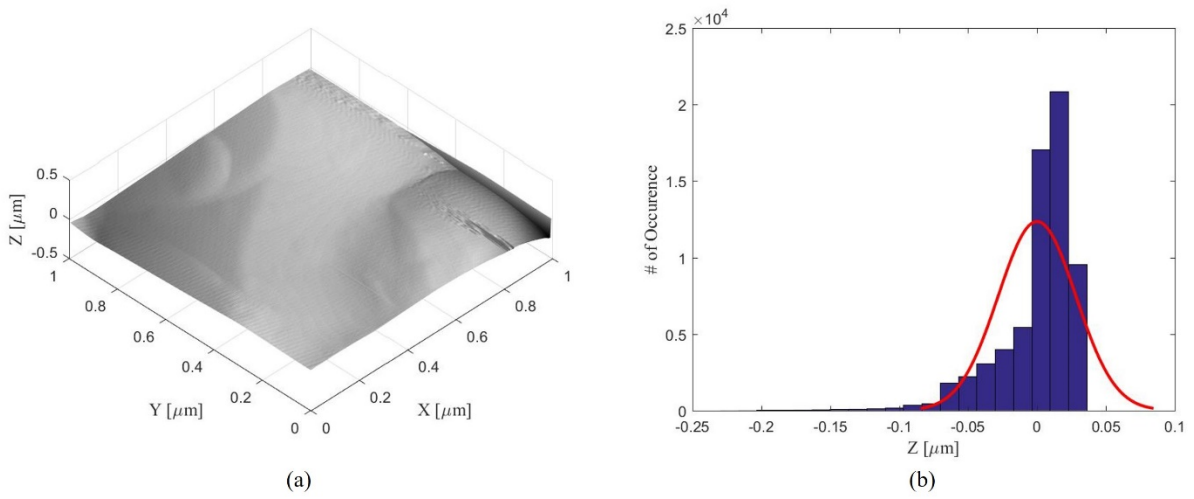


Figure B.9 (a) Surface profile; (b) Histogram for surface height distribution, for $1\mu\text{m} \times 1\mu\text{m}$ scan size test 5

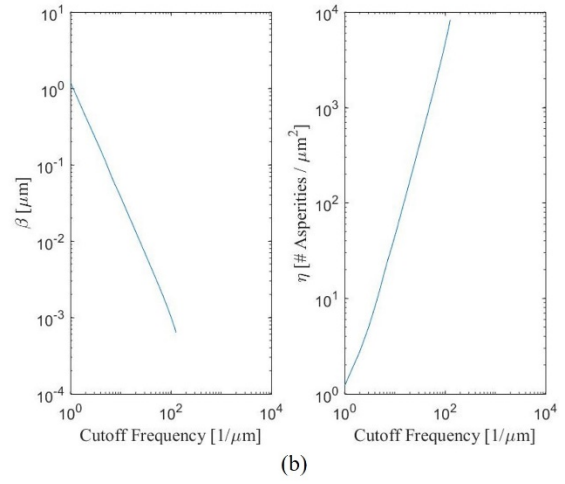
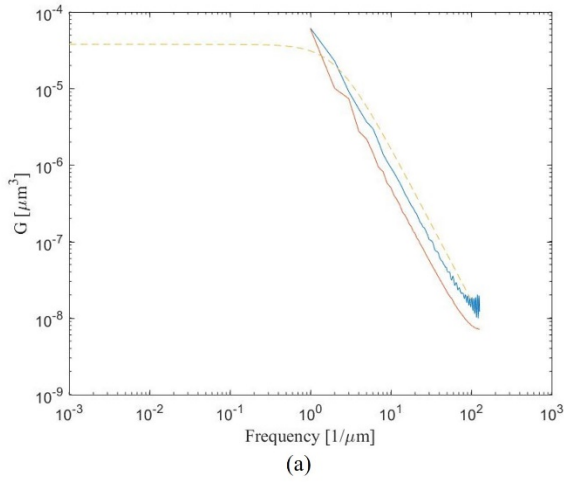


Figure B.10 (a) Power spectral density function; (b) Radius of asperity peak and asperity density, for 1 μ m x 1 μ m scan size test 5

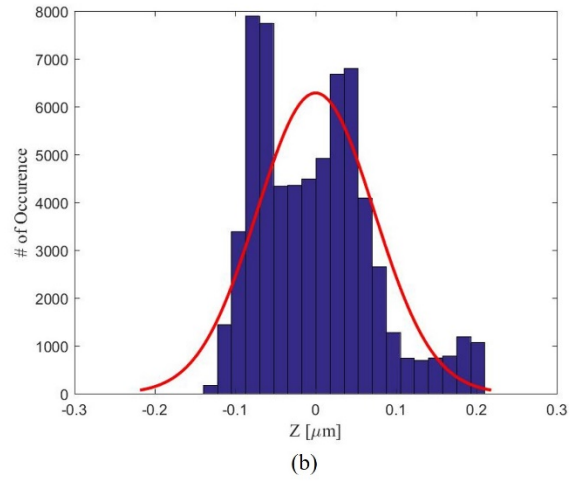
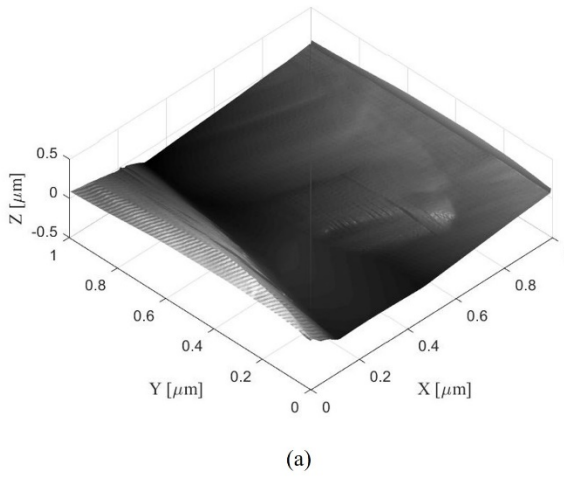


Figure B.11 (a) Surface profile; (b) Histogram for surface height distribution, for 1 μ m x 1 μ m scan size test 6

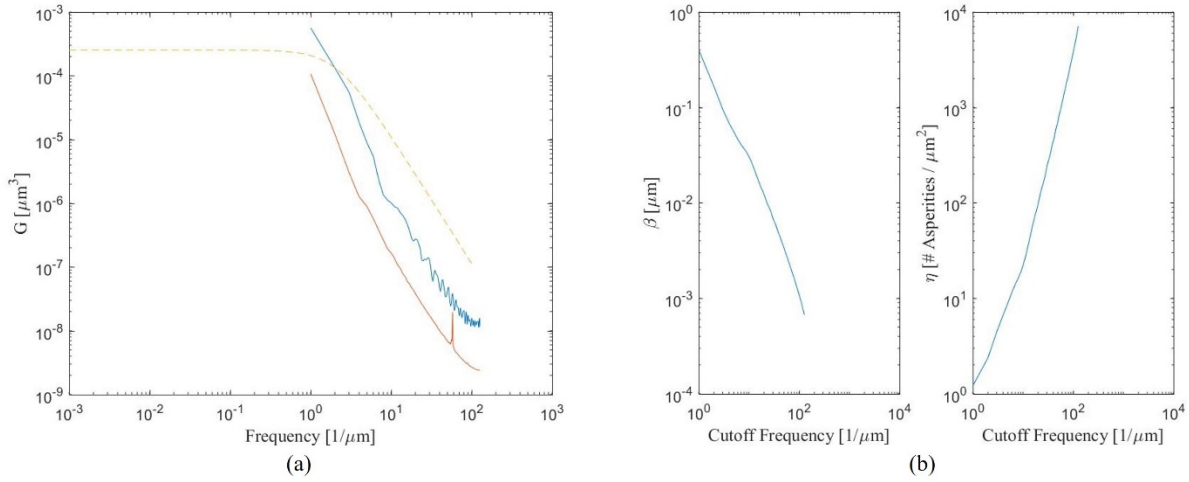


Figure B.12 (a) Power spectral density function; (b) Radius of asperity peak and asperity density, for $1\mu\text{m} \times 1\mu\text{m}$ scan size test 6

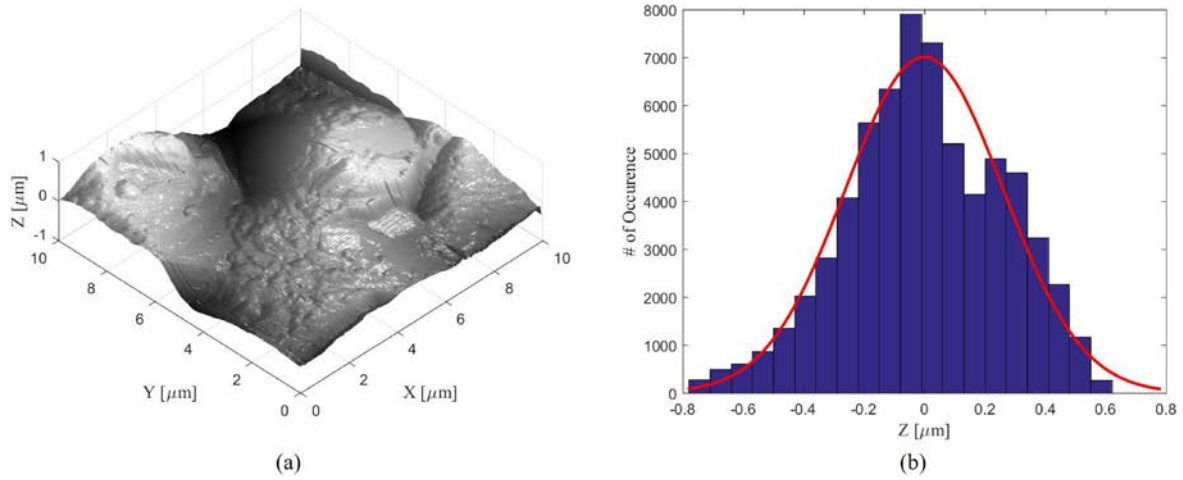


Figure B.13 (a) Surface profile; (b) Histogram for surface height distribution, for $10\mu\text{m} \times 10\mu\text{m}$ scan size test 1

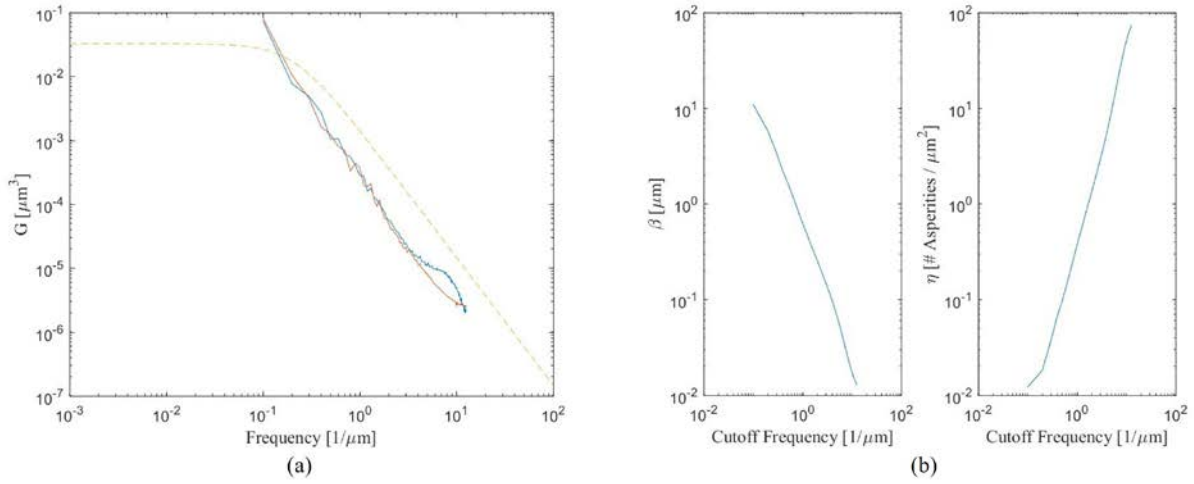


Figure B.14 (a) Power spectral density function; (b) Radius of asperity peak and asperity density, for 10 μ m x 10 μ m scan size test 1

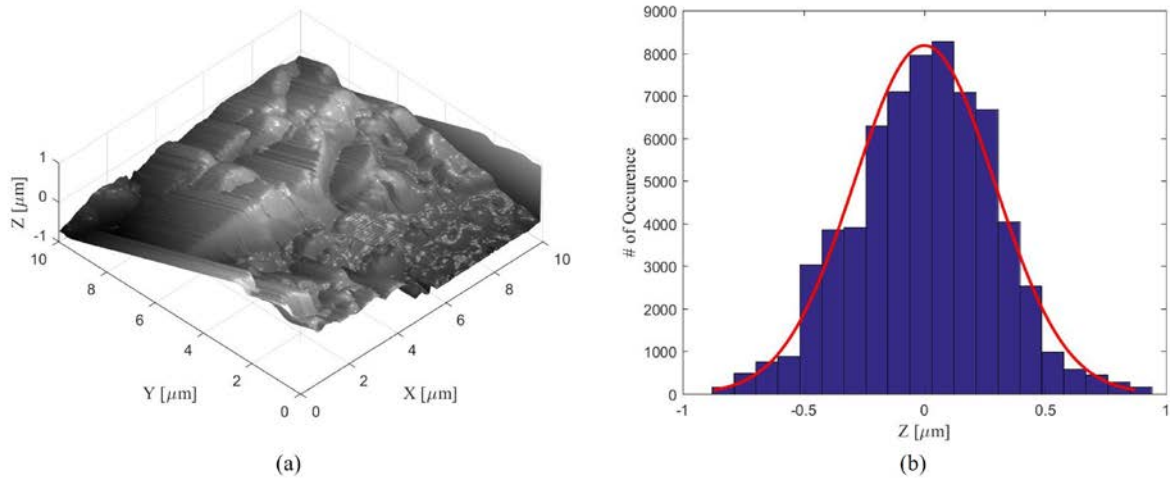


Figure B.15 (a) Surface profile; (b) Histogram for surface height distribution, for 10 μ m x 10 μ m scan size test 2

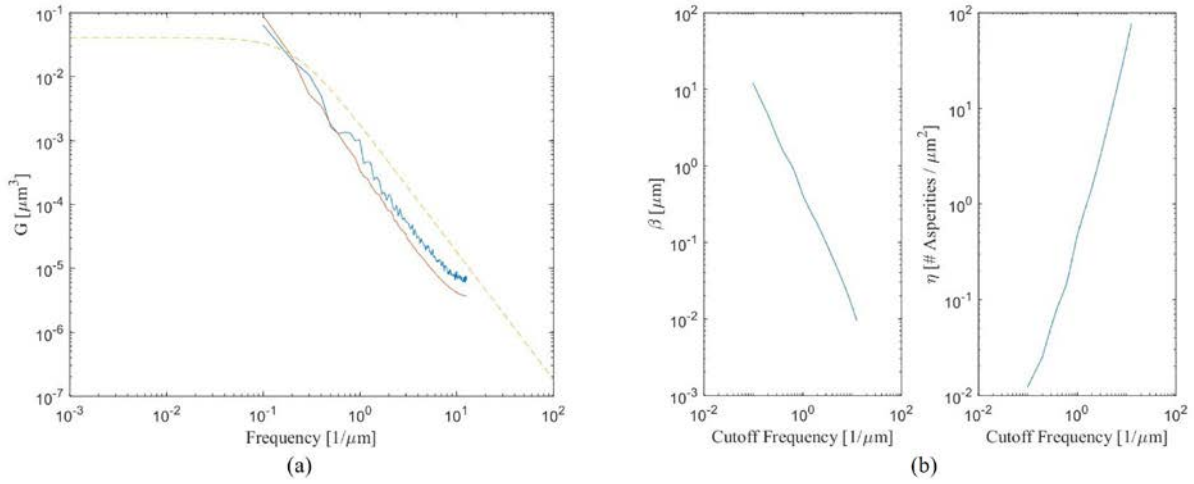


Figure B.16 (a) Power spectral density function; (b) Radius of asperity peak and asperity density, for $10\mu\text{m} \times 10\mu\text{m}$ scan size test 2

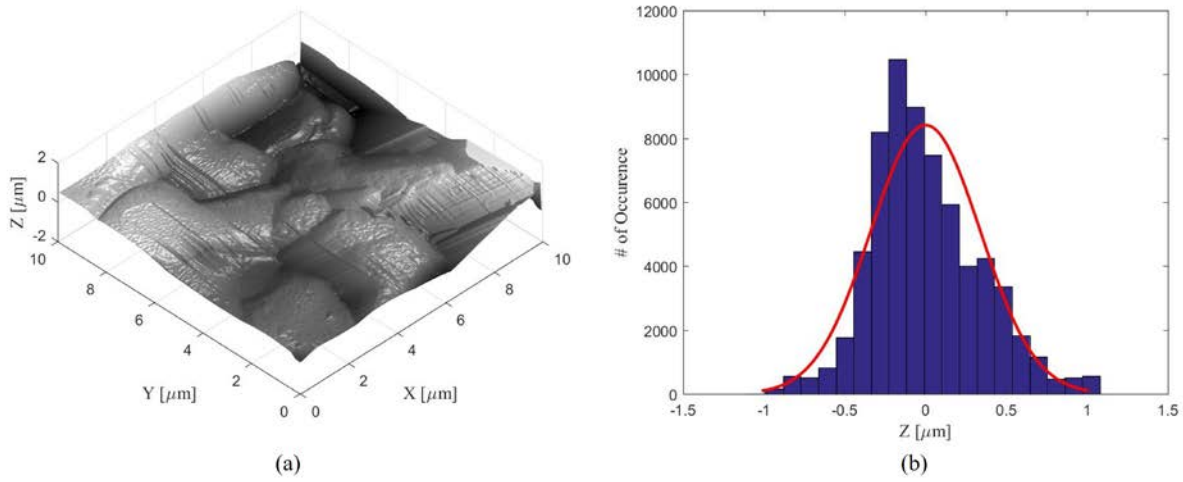


Figure B.17 (a) Surface profile; (b) Histogram for surface height distribution, for $10\mu\text{m} \times 10\mu\text{m}$ scan size test 3

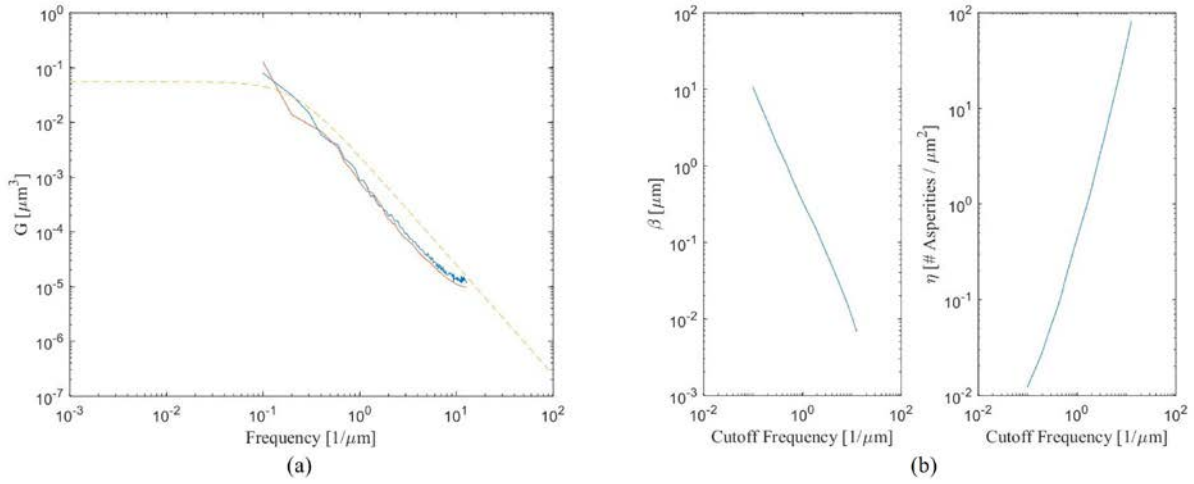


Figure B.18 (a) Power spectral density function; (b) Radius of asperity peak and asperity density, for 10 μ m x 10 μ m scan size test 3

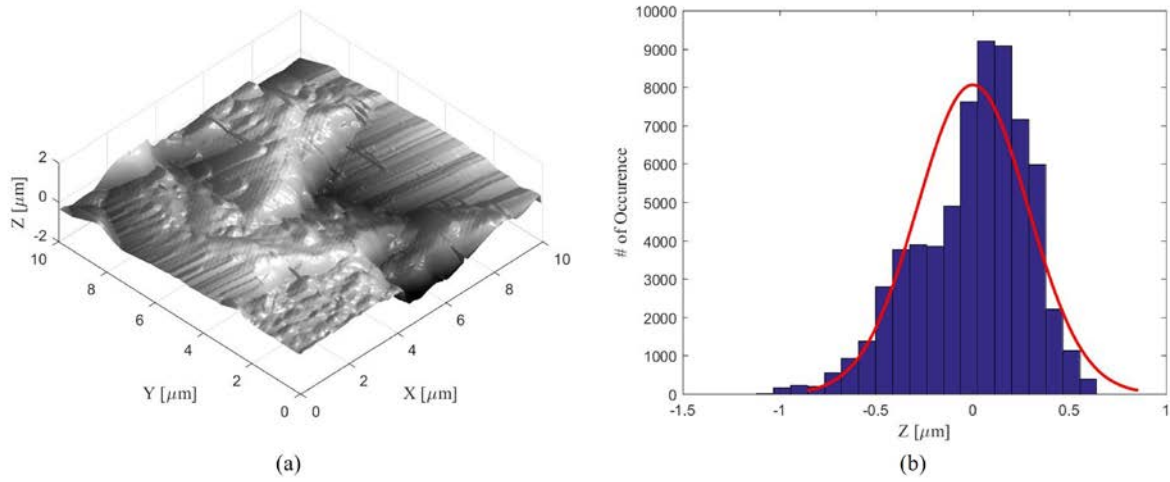


Figure B.19 (a) Surface profile; (b) Histogram for surface height distribution, for 10 μ m x 10 μ m scan size test 4

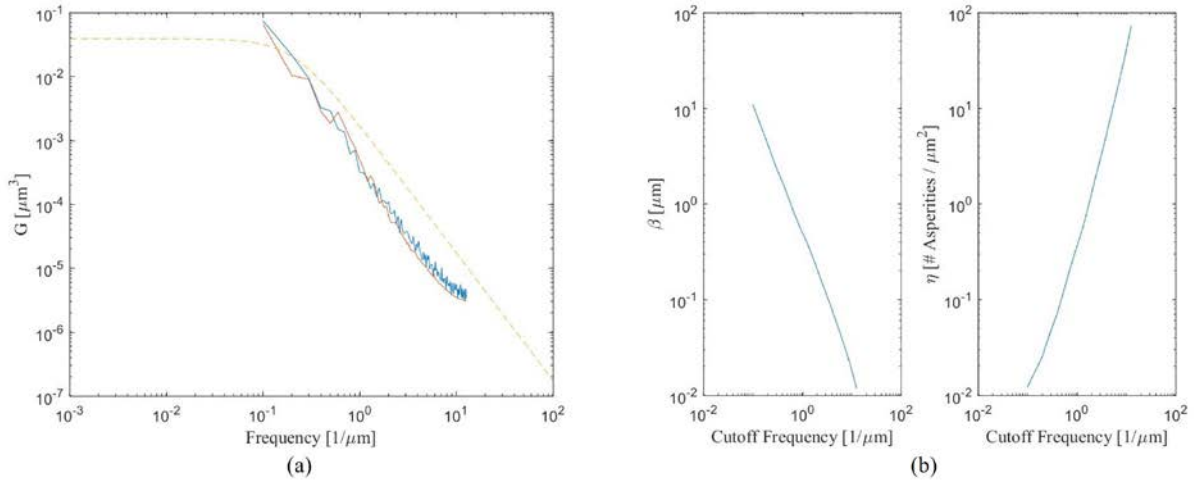


Figure B.20 (a) Power spectral density function; (b) Radius of asperity peak and asperity density, for 10 μ m x 10 μ m scan size test 4

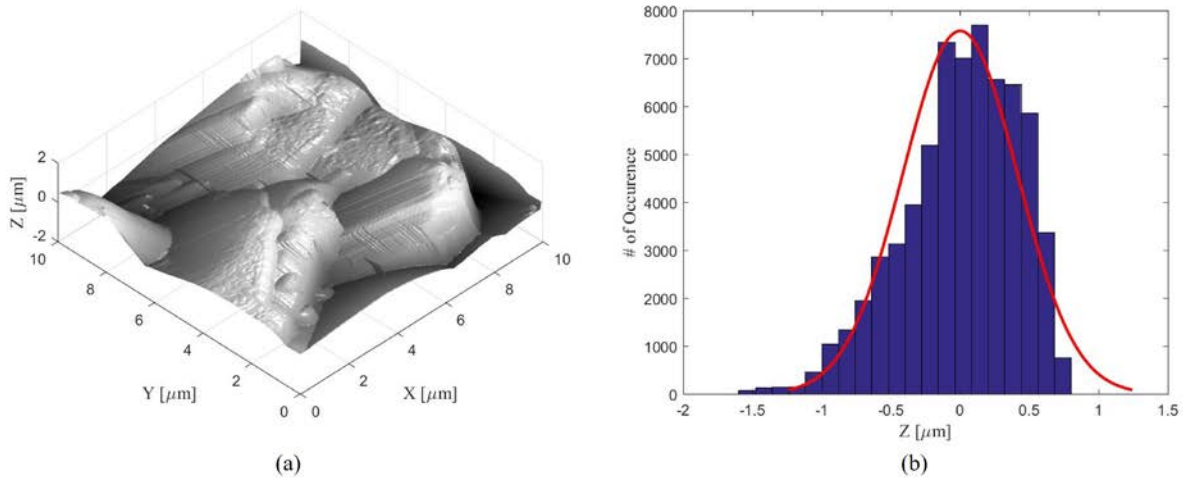


Figure B.21 (a) Surface profile; (b) Histogram for surface height distribution, for 10 μ m x 10 μ m scan size test 5

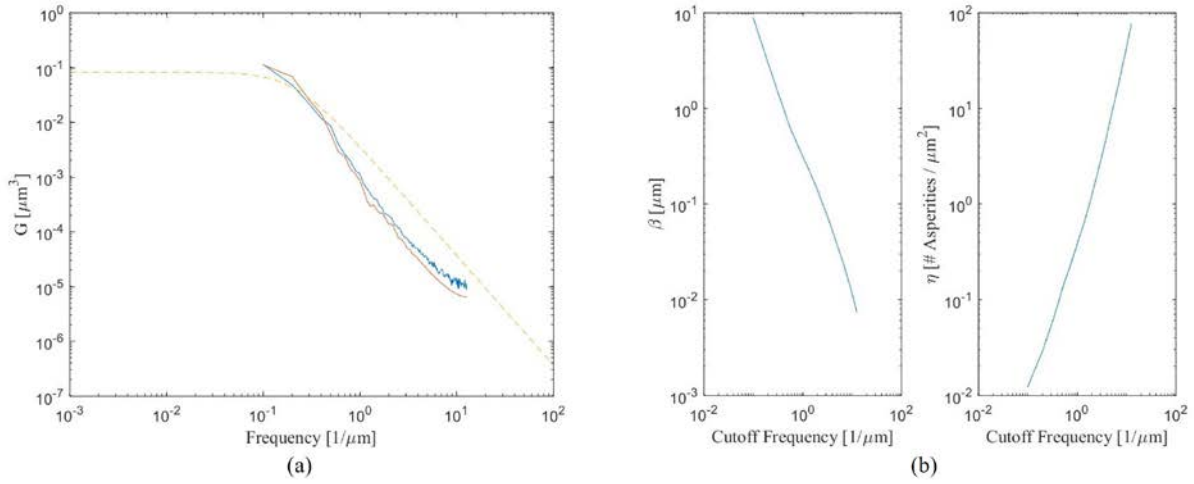


Figure B.22 (a) Power spectral density function; (b) Radius of asperity peak and asperity density, for 10 μ m x 10 μ m scan size test 5

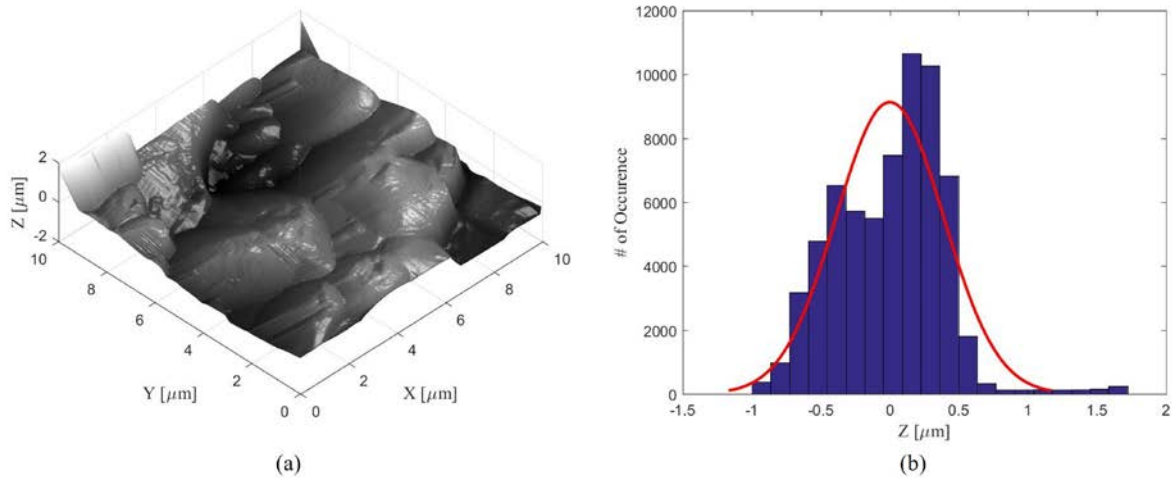


Figure B.23 (a) Surface profile; (b) Histogram for surface height distribution, for 10 μ m x 10 μ m scan size test 6

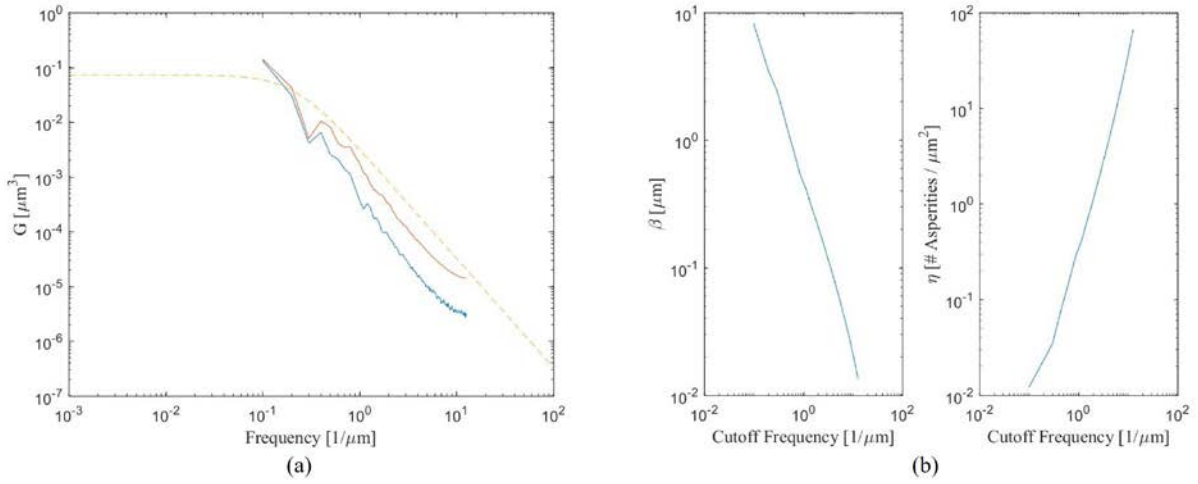


Figure B.24 (a) Power spectral density function; (b) Radius of asperity peak and asperity density, for $10\mu\text{m} \times 10\mu\text{m}$ scan size test 6

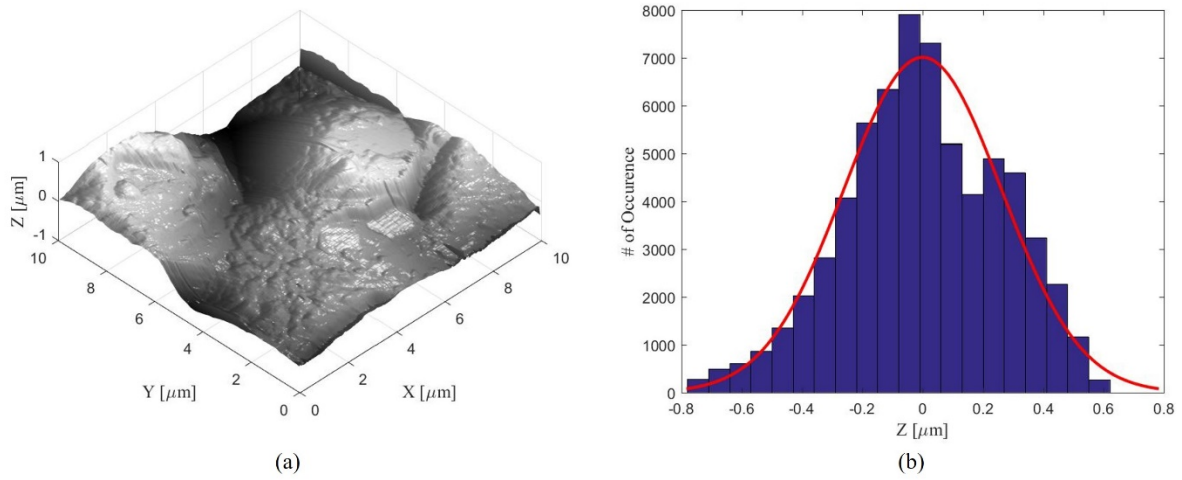


Figure B.25 (a) Surface profile; (b) Histogram for surface height distribution, for $100\mu\text{m} \times 100\mu\text{m}$ scan size test 1

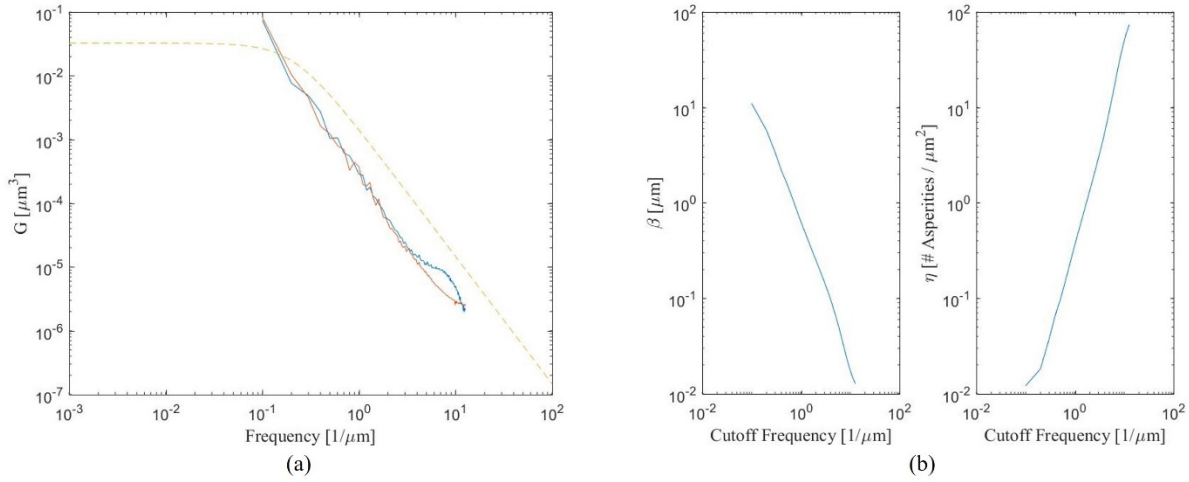


Figure B.26 (a) Power spectral density function; (b) Radius of asperity peak and asperity density, for $100\mu\text{m} \times 100\mu\text{m}$ scan size test 1

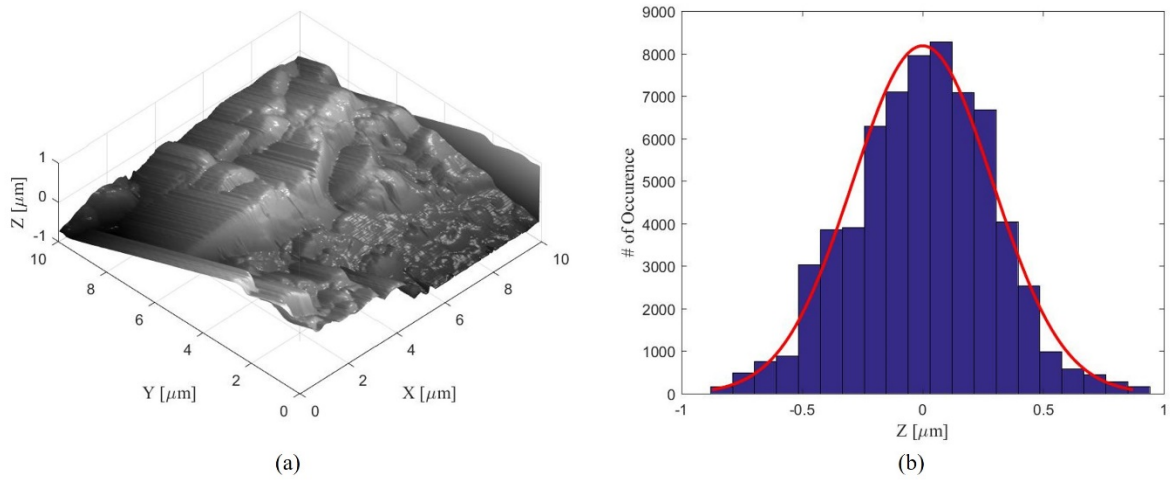


Figure B.27 (a) Surface profile; (b) Histogram for surface height distribution, for $100\mu\text{m} \times 100\mu\text{m}$ scan size test 2

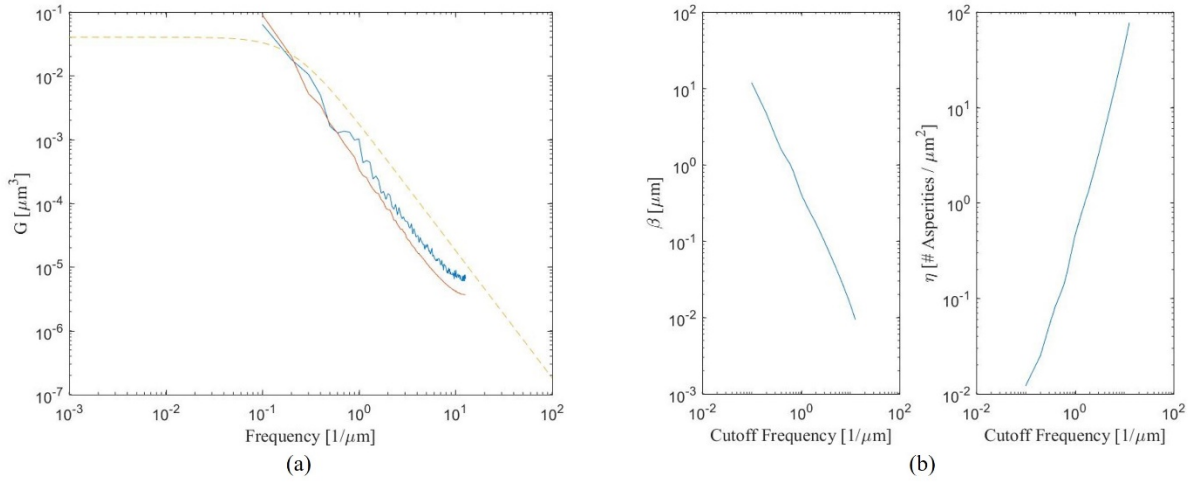


Figure B.28 (a) Power spectral density function; (b) Radius of asperity peak and asperity density, for $100\mu\text{m} \times 100\mu\text{m}$ scan size test 2

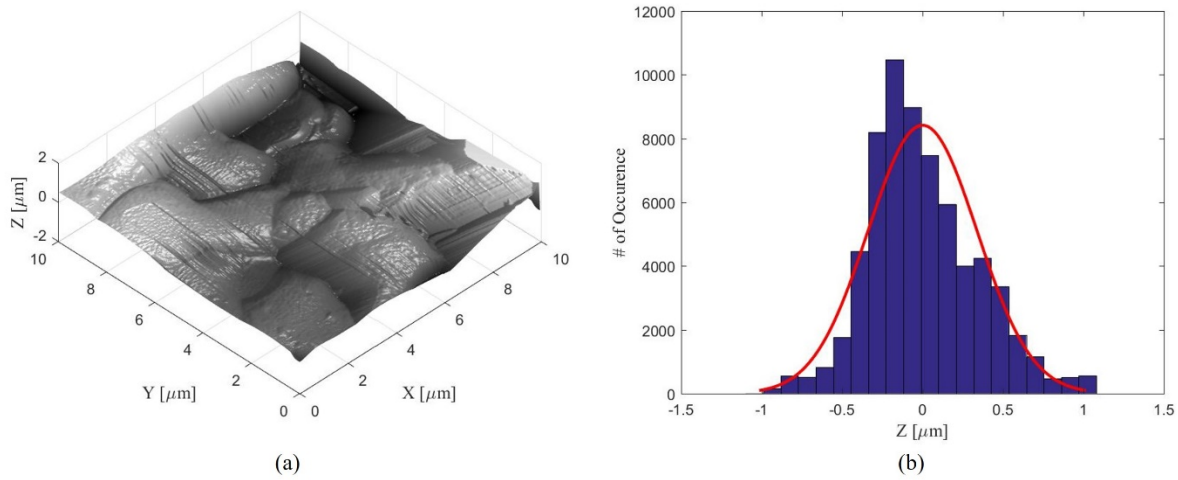


Figure B.29 (a) Surface profile; (b) Histogram for surface height distribution, for $100\mu\text{m} \times 100\mu\text{m}$ scan size test 3

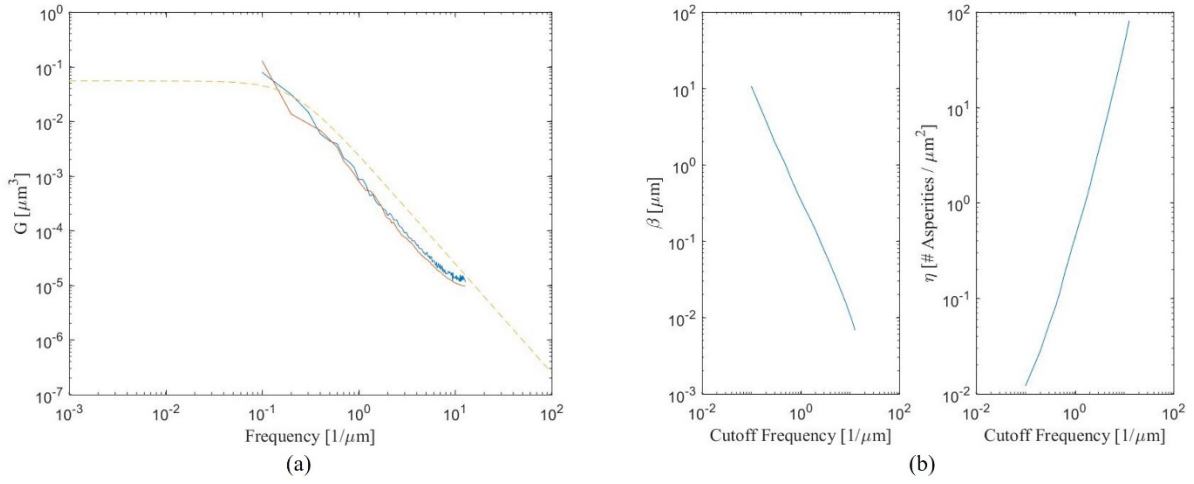


Figure B.30 (a) Power spectral density function; (b) Radius of asperity peak and asperity density, for 100 μm x 100 μm scan size test 3

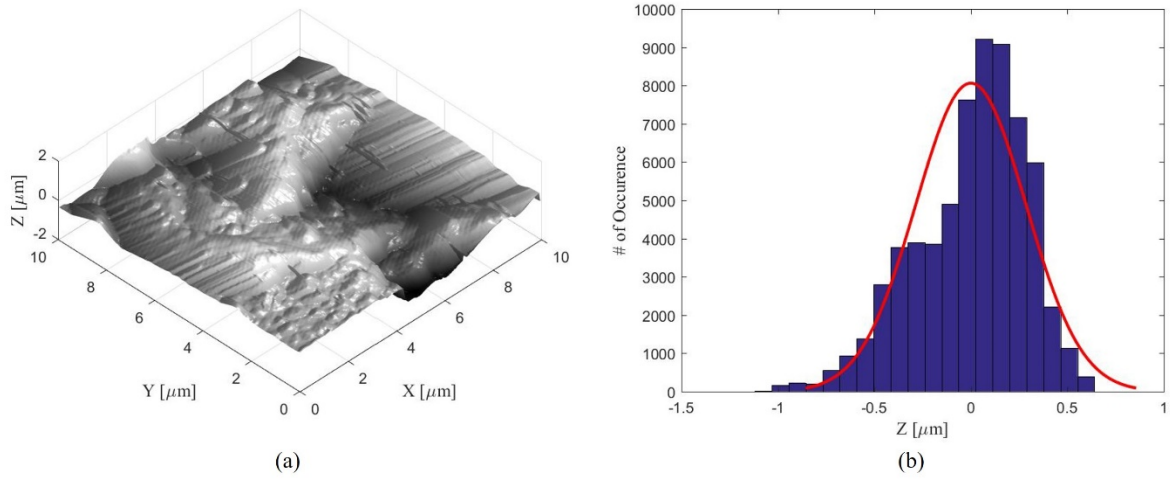


Figure B.31 (a) Surface profile; (b) Histogram for surface height distribution, for 100 μm x 100 μm scan size test 4

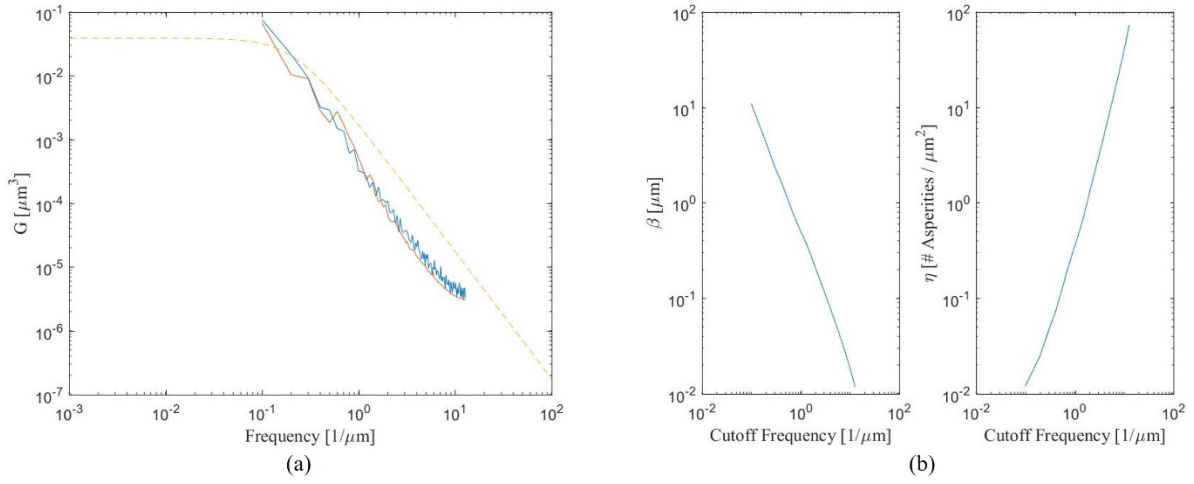


Figure B.32 (a) Power spectral density function; (b) Radius of asperity peak and asperity density, for $100\mu\text{m} \times 100\mu\text{m}$ scan size test 4

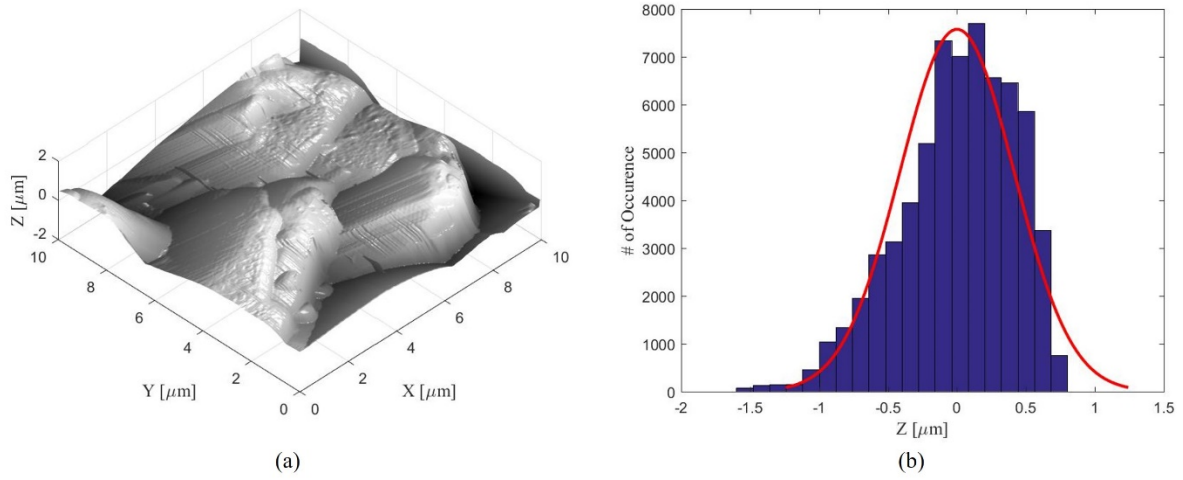


Figure B.33 (a) Surface profile; (b) Histogram for surface height distribution, for $100\mu\text{m} \times 100\mu\text{m}$ scan size test 5

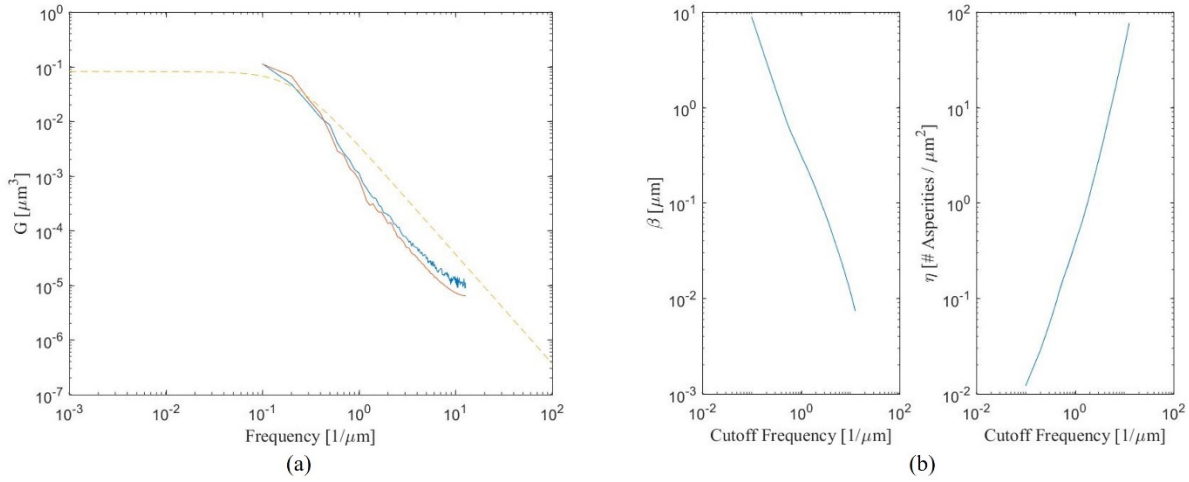


Figure B.34 (a) Power spectral density function; (b) Radius of asperity peak and asperity density, for $100\mu\text{m} \times 100\mu\text{m}$ scan size test 5

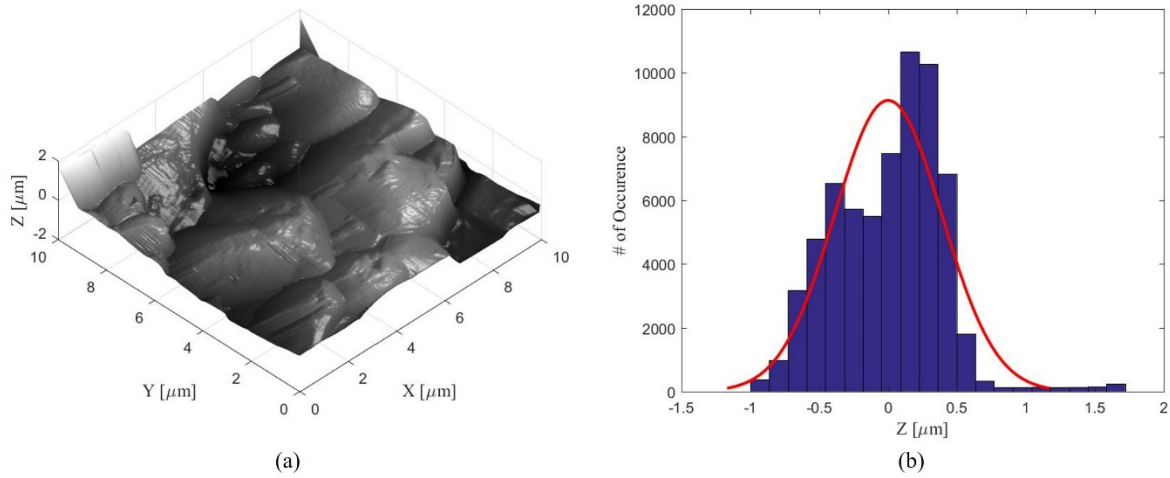


Figure B.35 (a) Surface profile; (b) Histogram for surface height distribution, for $100\mu\text{m} \times 100\mu\text{m}$ scan size test 6

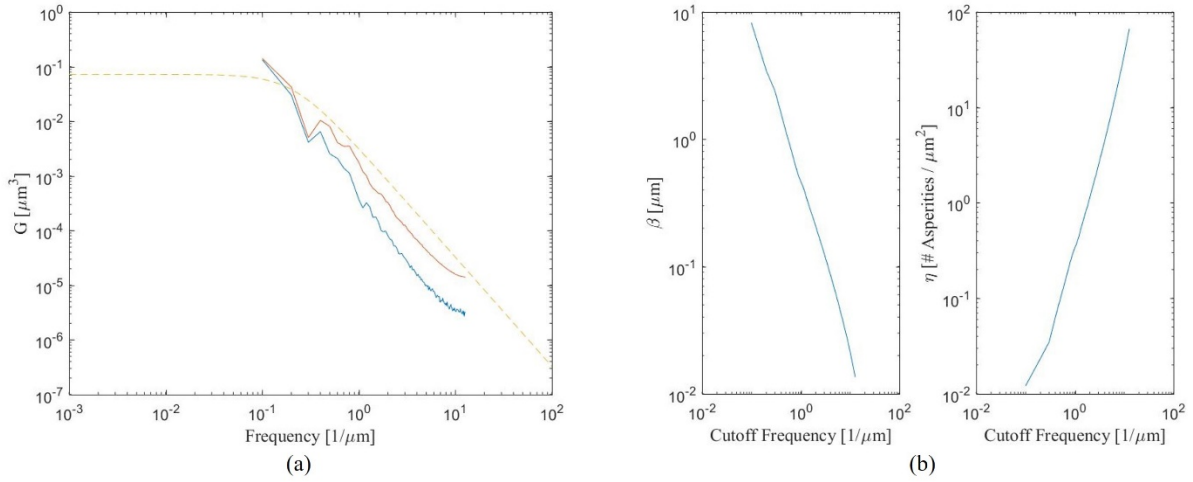


Figure B.36 (a) Power spectral density function; (b) Radius of asperity peak and asperity density, for 100 μm x 100 μm scan size test 6

Table B.1 Surface roughness parameters for scan size 1 μm x 1 μm

Test	Average roughness (nm)	RMS roughness (nm)	Peak to valley heights (nm)
1	10.27	12.29	71.88
2	14.90	18.70	117.50
3	13.70	18.00	105.60
4	18.10	21.90	131.50
5	20.00	28.10	259.00
6	59.50	72.80	344.30
Average	22.75	28.63	171.63
Standard deviation	18.32	22.25	106.11

Table B.2 Surface roughness parameters for scan size 10 μm x 10 μm

Test	Average roughness (μm)	RMS roughness (μm)	Peak to valley heights (μm)
1	0.21	0.26	1.38
2	0.23	0.29	1.79
3	0.27	0.34	2.08
4	0.23	0.29	1.68
5	0.33	0.41	2.37
6	0.32	0.39	2.71
Average	0.26	0.33	2.00
Standard deviation	0.05	0.06	0.48

Table B.3 Surface roughness parameters for scan size 100 μm x 100 μm

Test	Average roughness (μm)	RMS roughness (μm)	Peak to valley heights (μm)
1	1.68	2.13	14.95
2	1.52	1.89	14.01
3	5.24	6.21	16.90
4	1.53	1.96	16.11
5	2.11	2.61	23.35
6	1.95	2.56	19.97
Average	2.34	2.89	17.55
Standard deviation	1.44	1.65	3.50

B.2 Grain-scale physical test results.

Micro-indentation tests were performed to measure the normal contact stiffness of ceramic proppants. Fifteen measurements of contact stiffness were performed. The force-displacement profiles are given below.

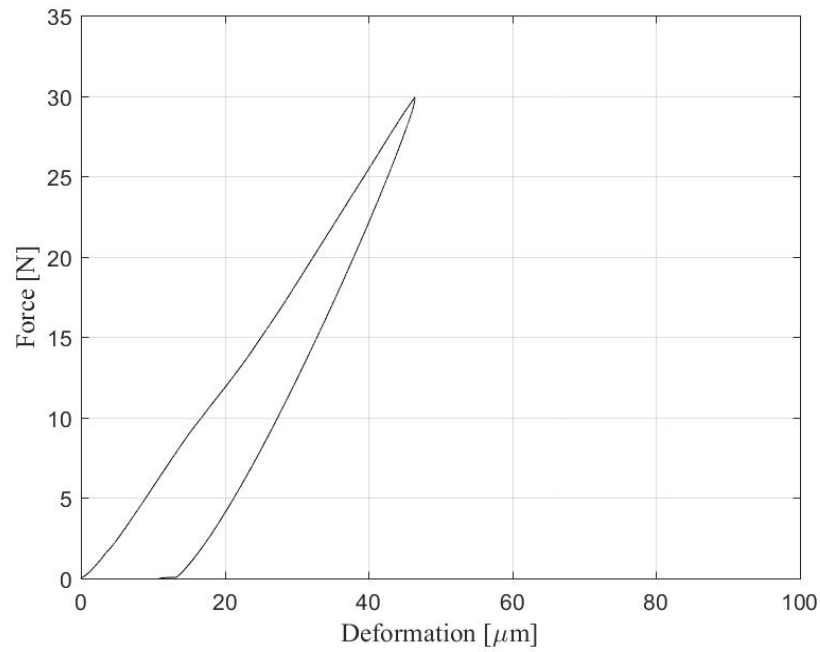


Figure B.37 Force displacement plot test 1

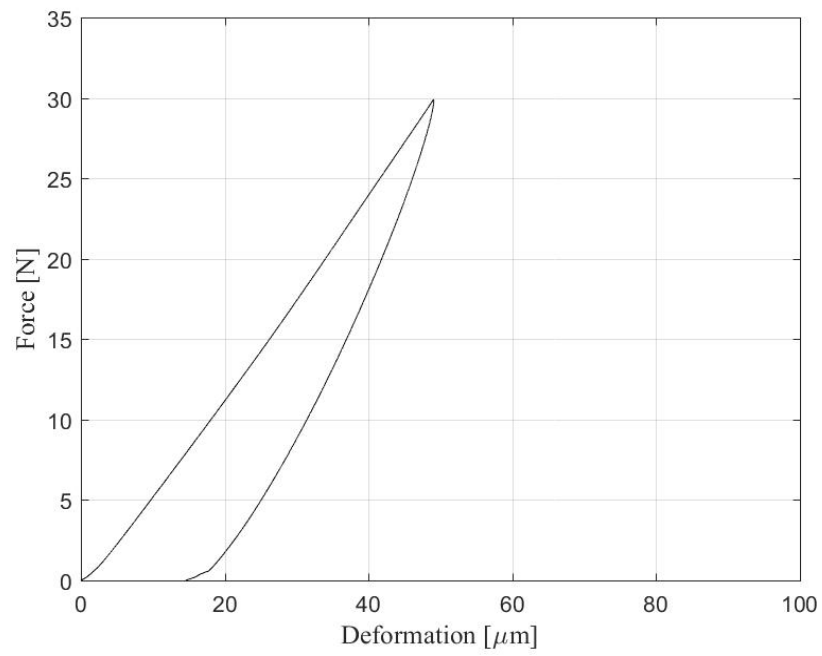


Figure B.38 Force displacement plot test 2

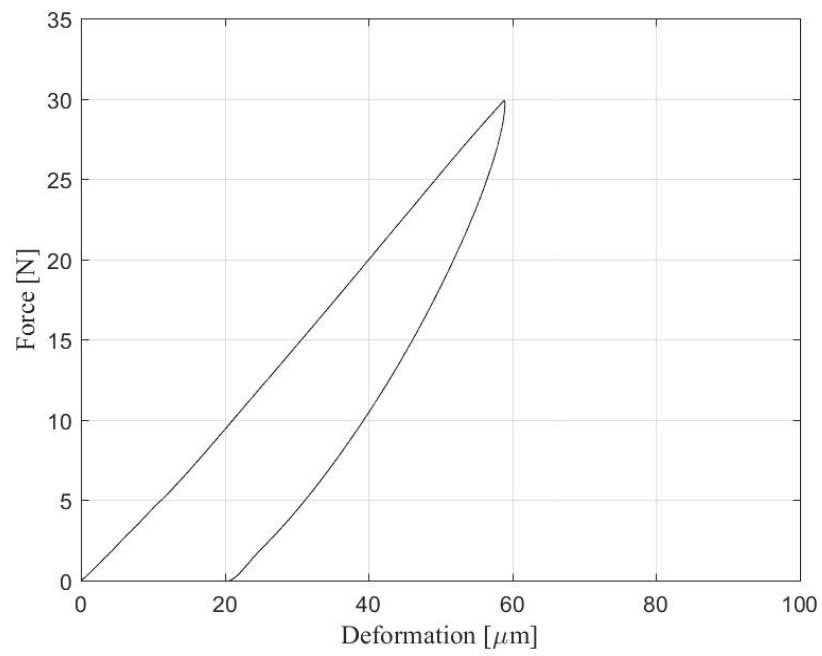


Figure B.39 Force displacement plot test 3

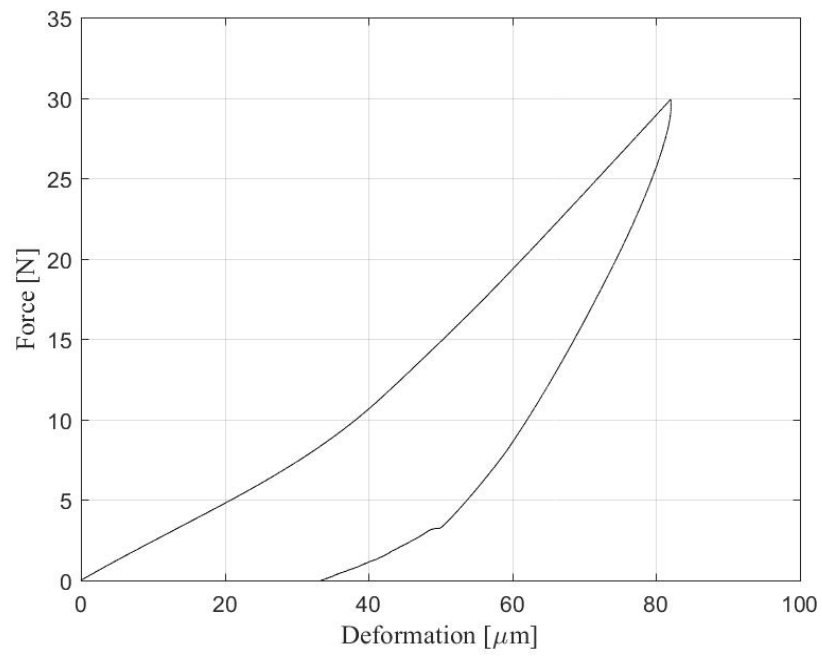


Figure B.40 Force displacement plot test 4

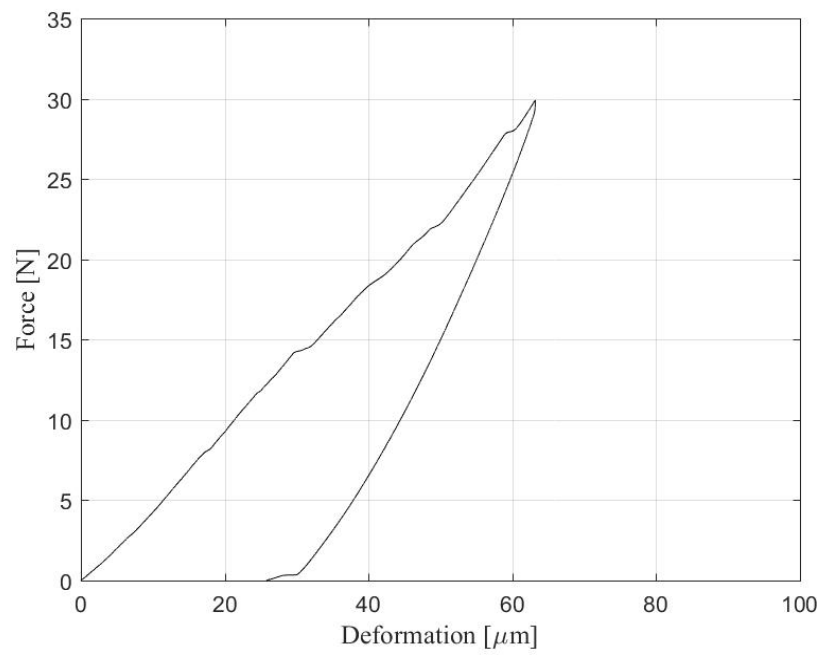


Figure B.41 Force displacement plot test 5

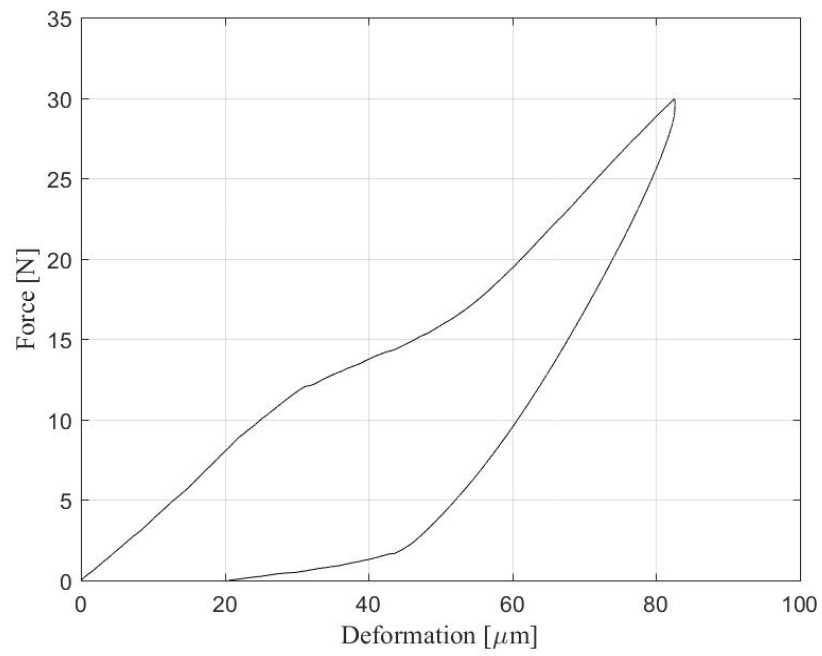


Figure B.42 Force displacement plot test 6

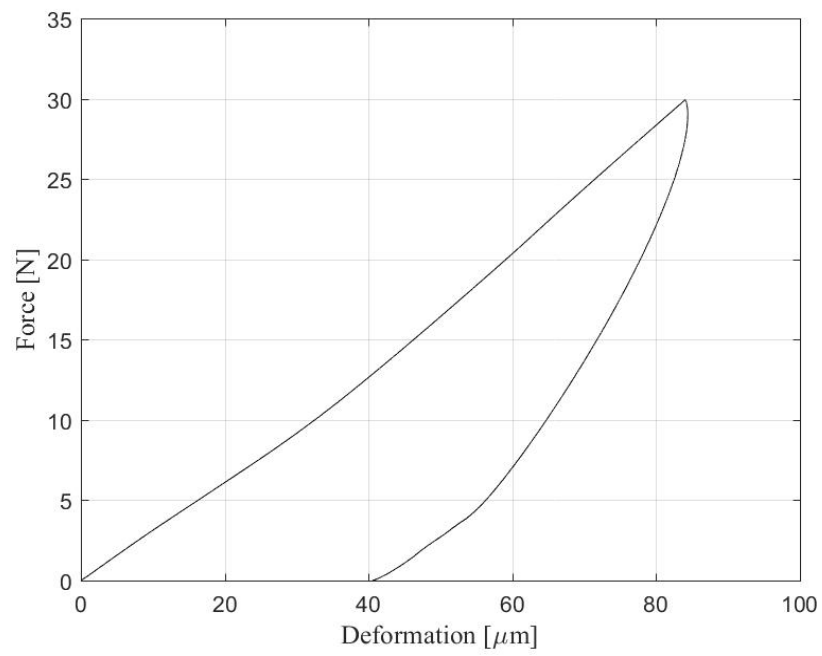


Figure B.43 Force displacement plot test 7

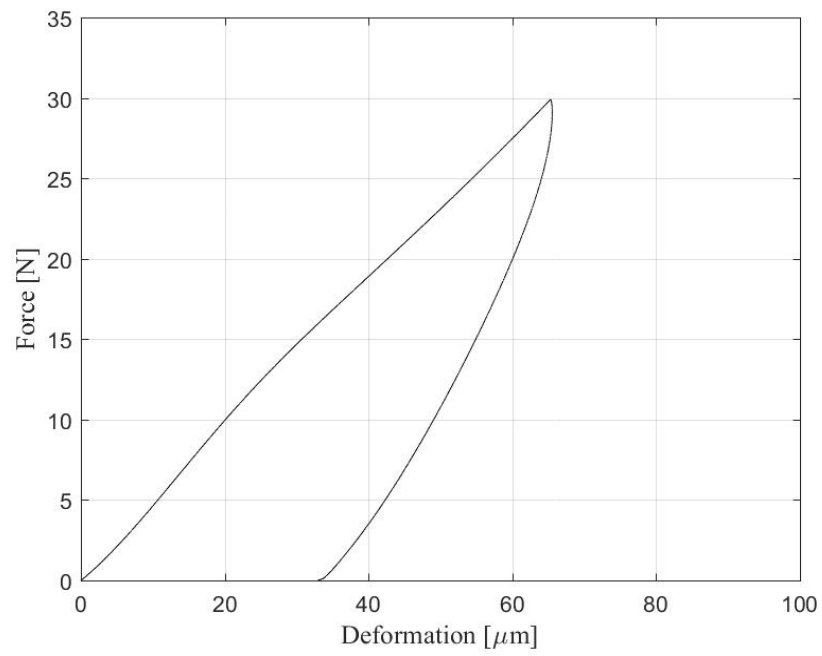


Figure B.44 Force displacement plot test 8

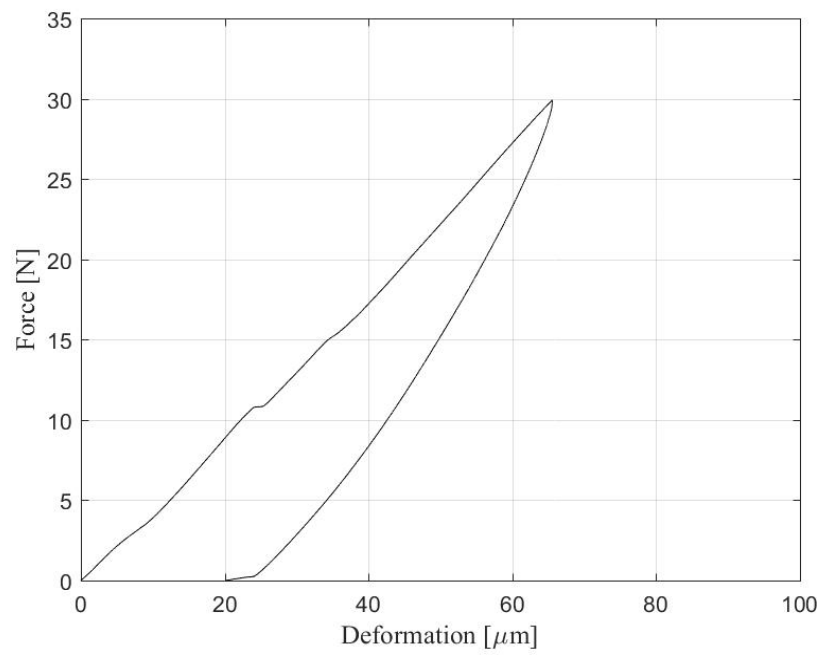


Figure B.45 Force displacement plot test 9

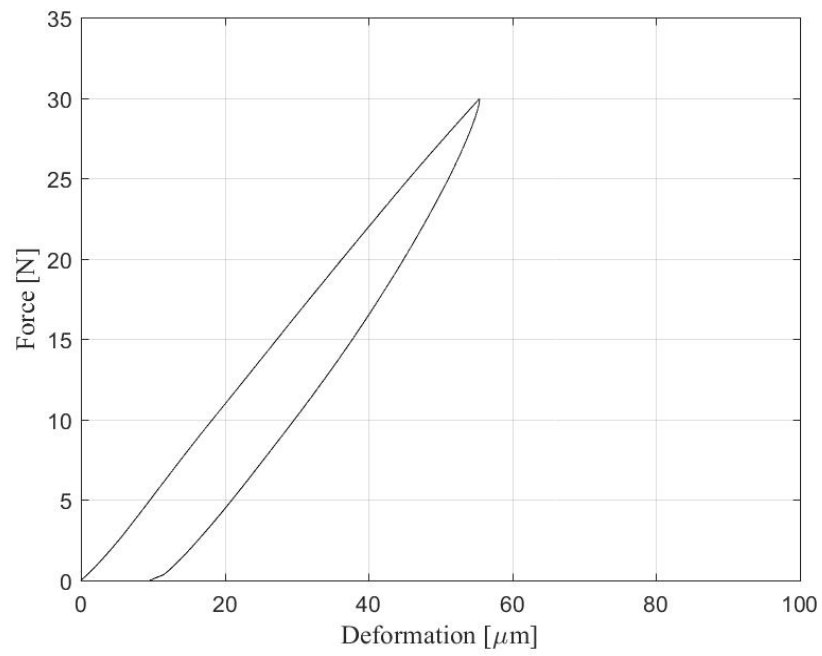


Figure B.46 Force displacement plot test 10

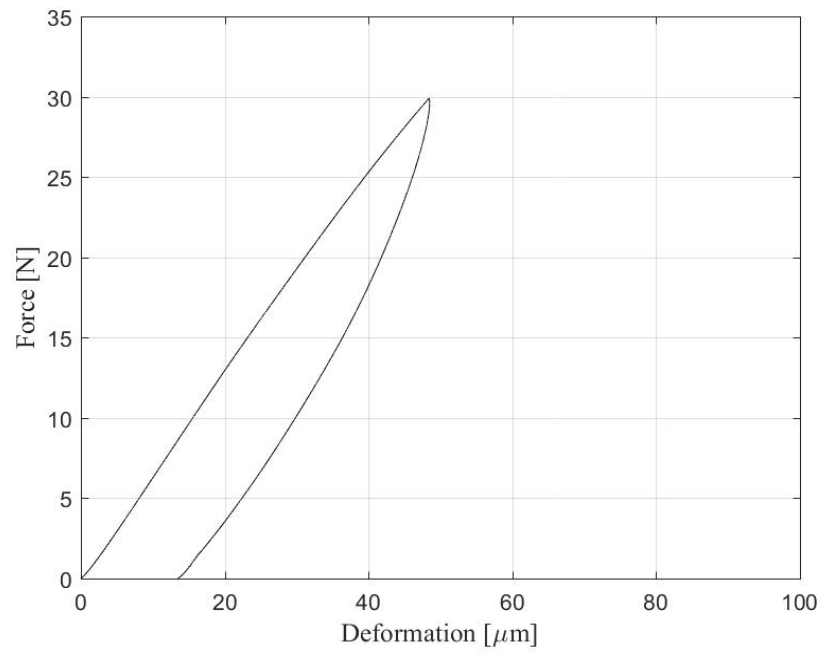


Figure B.47 Force displacement plot test 11

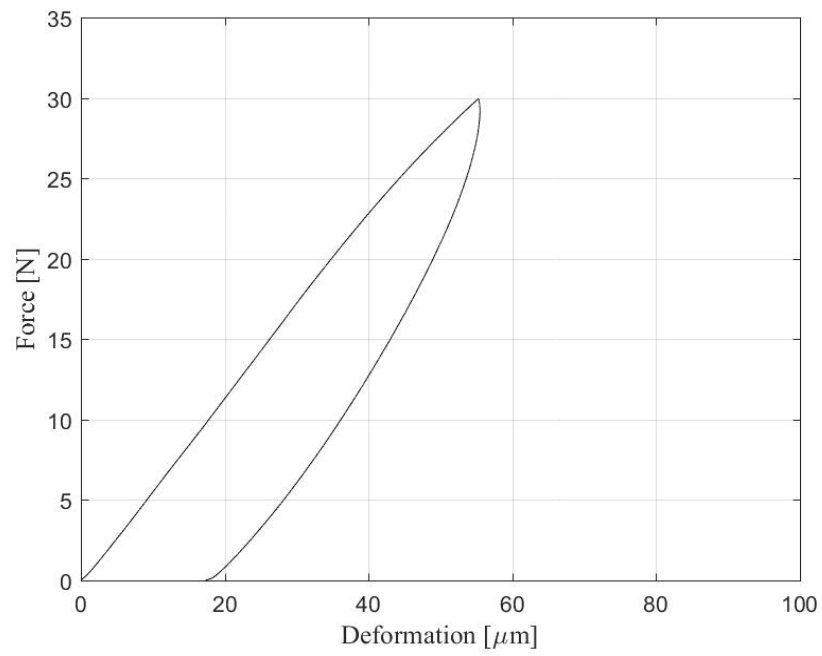


Figure B.48 Force displacement plot test 12

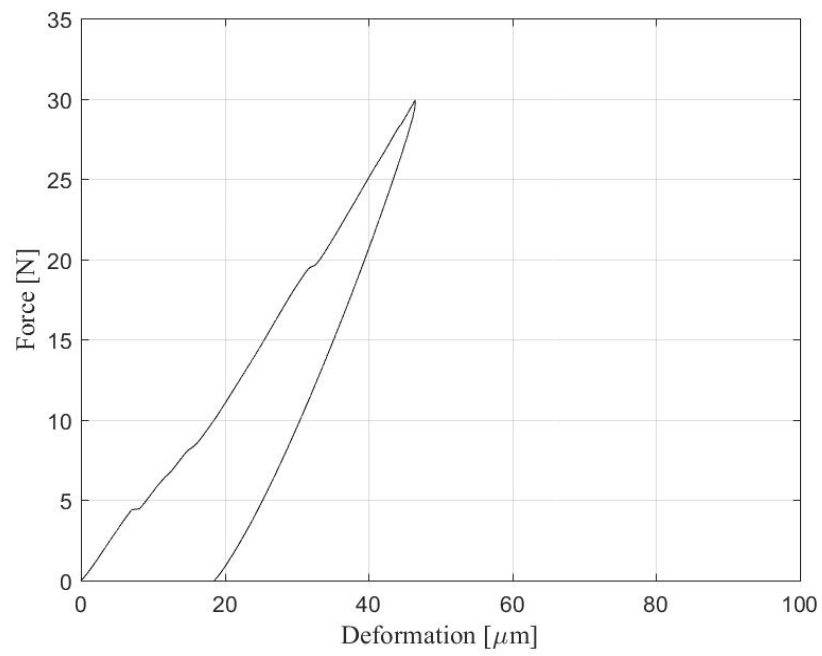


Figure B.49 Force displacement plot test 13

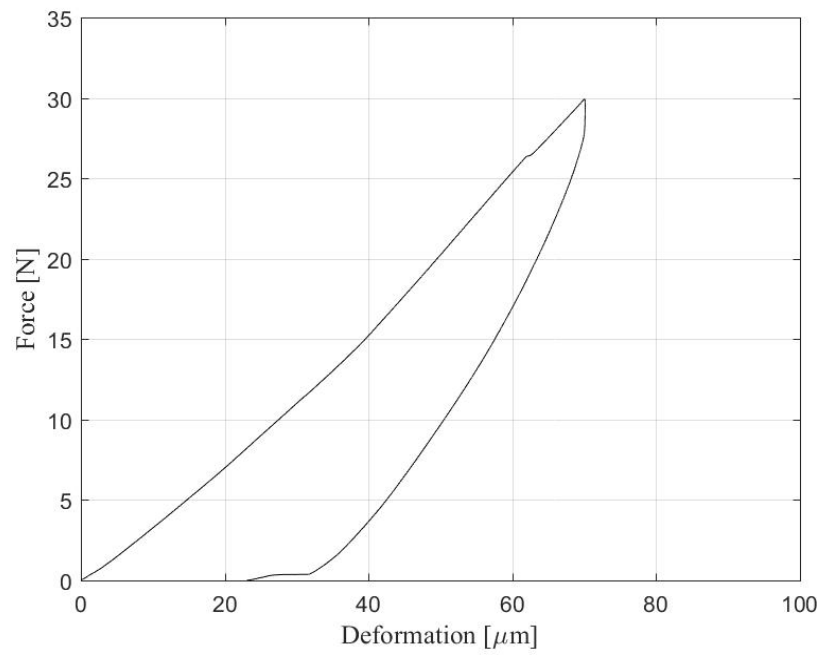


Figure B.50 Force displacement plot test 14

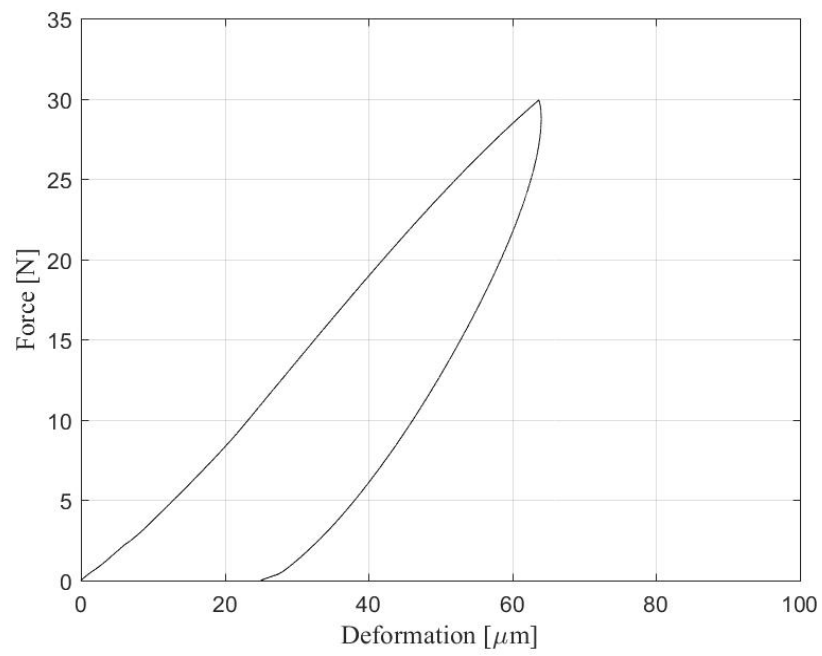


Figure B.51 Force displacement plot test 15

Nano-indentation tests were performed to measure the nano-hardness and reduced modulus of granular material. Details of the testing procedures are given in Sec. 3.3.5. Ten measurements were taken on three spheres each.

Table B.4 Nano-indentation test results for ceramic proppant 1

Test	Hardness (GPa)	Reduced Modulus (GPa)	Contact depth (nm)
1	10.29	73.25	107.10
2	7.61	59.62	127.79
3	9.66	75.45	111.22
4	10.55	80.41	105.55
5	11.75	72.41	98.95
6	7.27	61.39	131.17
7	9.04	63.80	115.57
8	13.17	78.69	92.36
9	8.86	64.32	116.98
10	9.40	64.32	112.97
Average	9.76	69.37	111.97
Standard deviation	1.79	7.53	11.91

Table B.5 Nano-indentation test results for ceramic proppant 2

Test	Hardness (GPa)	Reduced Modulus (GPa)	Contact depth (nm)
1	7.16	114.33	132.33
2	10.01	195.50	108.91
3	10.27	136.18	107.22

4	5.63	97.47	151.59
5	12.87	222.04	93.67
6	5.58	47.84	152.49
7	10.01	206.49	108.88
8	6.15	122.75	144.30
9	10.44	148.23	106.19
10	4.92	110.33	163.52
Average	8.30	140.12	126.91
Standard deviation	2.73	54.21	24.74

Table B.6 Nano-indentation test results for ceramic proppant 3

Test	Hardness (GPa)	Reduced Modulus (GPa)	Contact depth (nm)
1	7.73	159.43	126.57
2	7.59	151.79	127.94
3	10.12	149.57	108.18
4	14.12	184.58	88.54
5	10.40	168.42	106.48
6	11.16	182.64	102.05
7	12.39	171.07	95.89
8	6.70	218.73	137.37
9	7.01	124.23	133.88
10	17.81	178.51	76.60
Average	10.50	168.90	110.35

Standard deviation	3.55	25.31	20.46
--------------------	------	-------	-------

Scratch tests were performed to quantify the coefficient of friction for ceramic proppants. Five measurements were taken for five normal loading conditions each. A total of twenty five measurements for static coefficient of friction and twenty five measurements for kinetic coefficient of friction were performed.

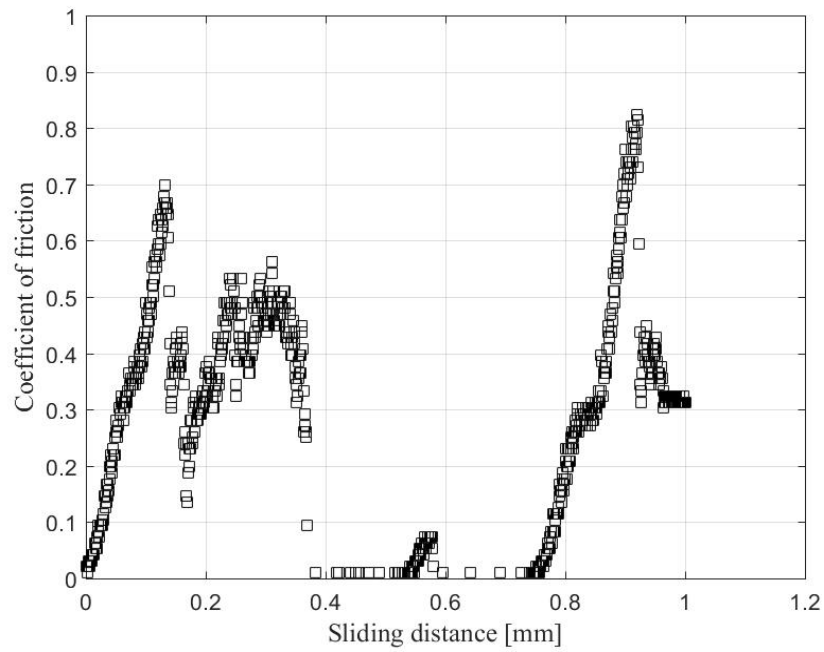


Figure B.52 Static friction test 1 at 25gmf

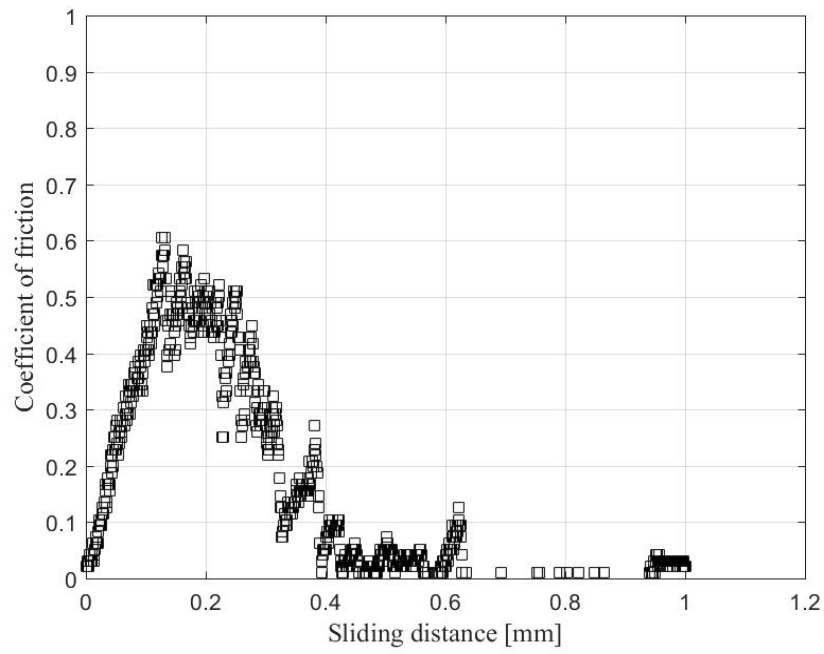


Figure B.53 Static friction test 2 at 25gmf

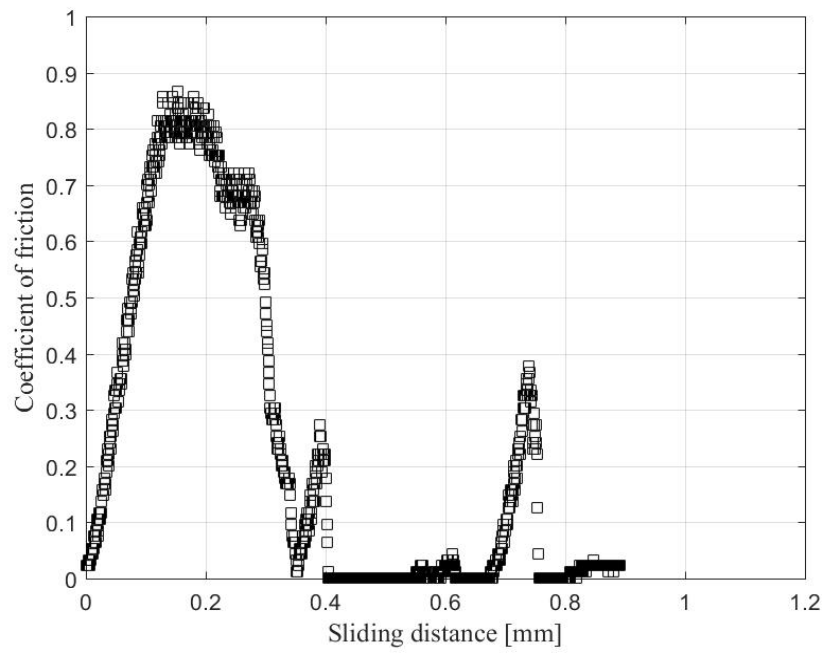


Figure B.54 Static friction test 3 at 25gmf

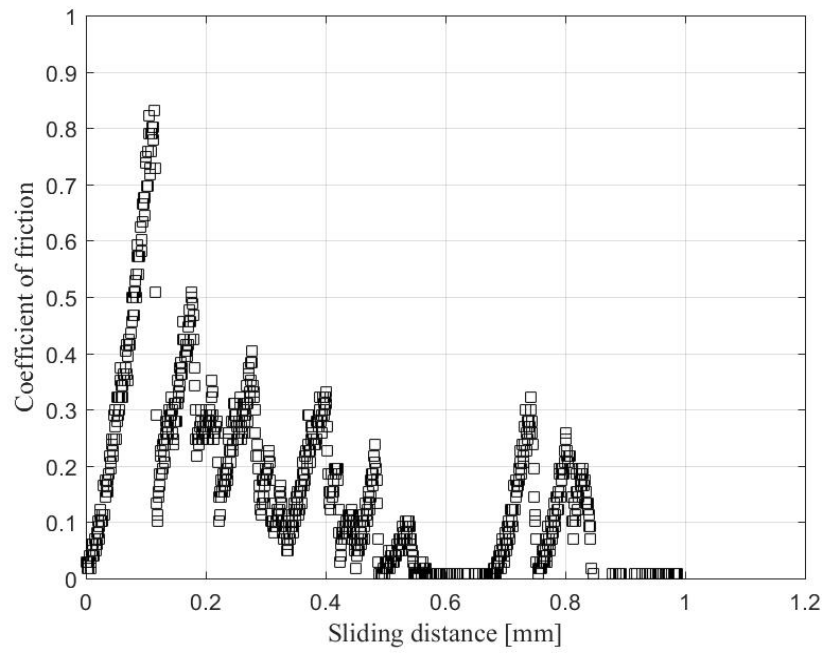


Figure B.55 Static friction test 4 at 25gmf

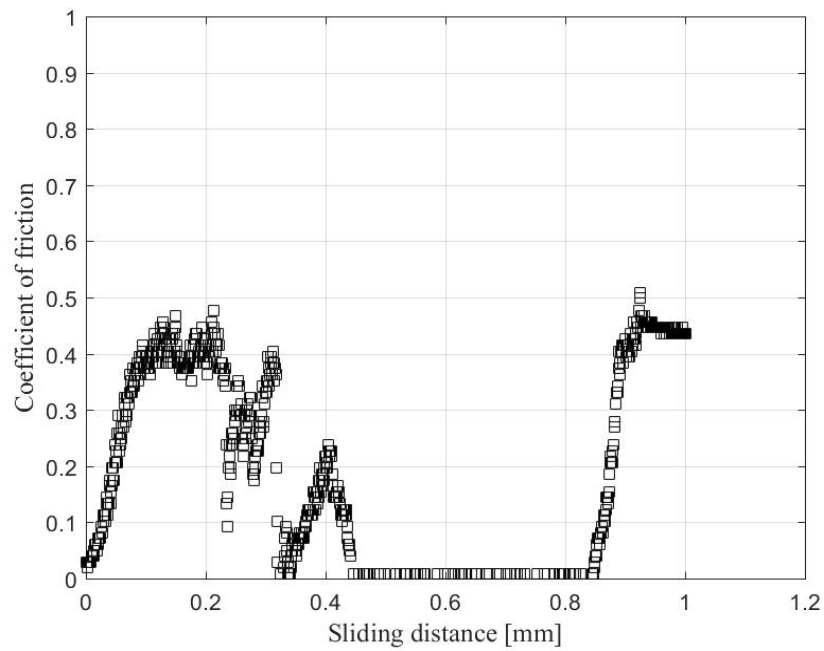


Figure B.56 Static friction test 5 at 25gmf

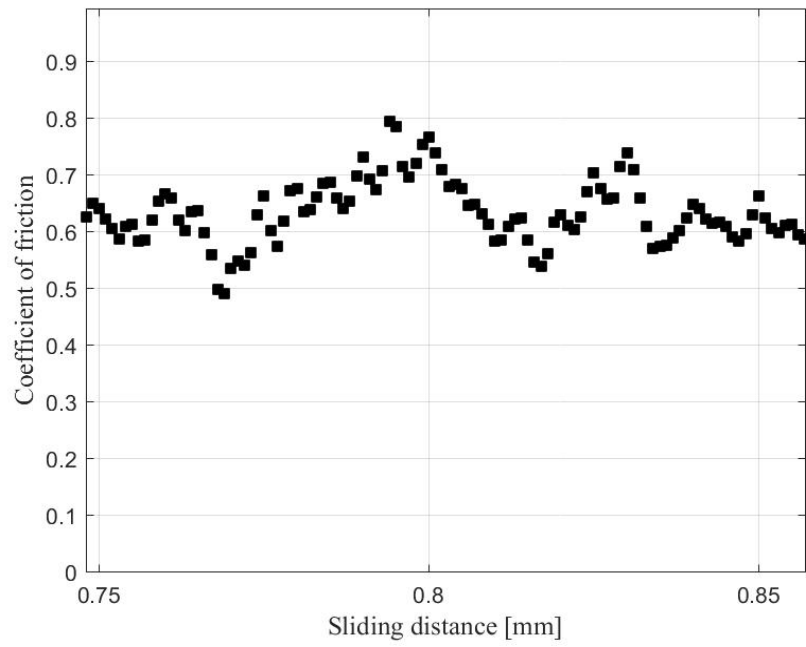


Figure B.57 Kinetic friction test 1 at 25gmf

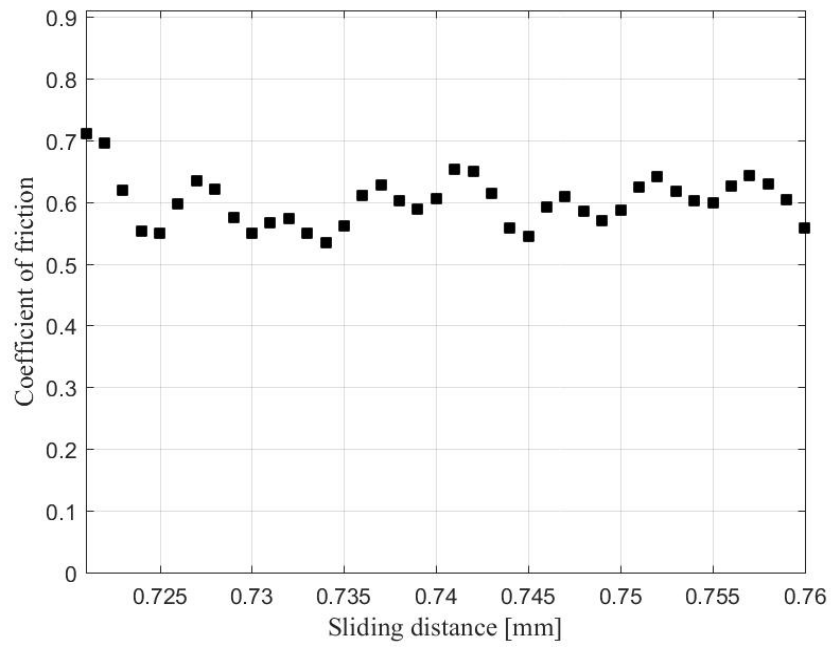


Figure B.58 Kinetic friction test 2 at 25gmf

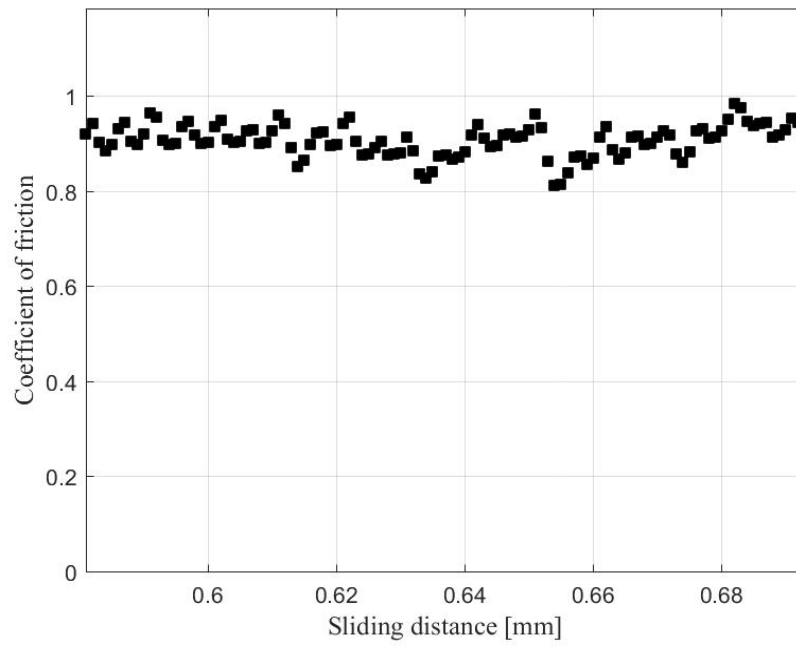


Figure B.59 Kinetic friction test 3 at 25gmf

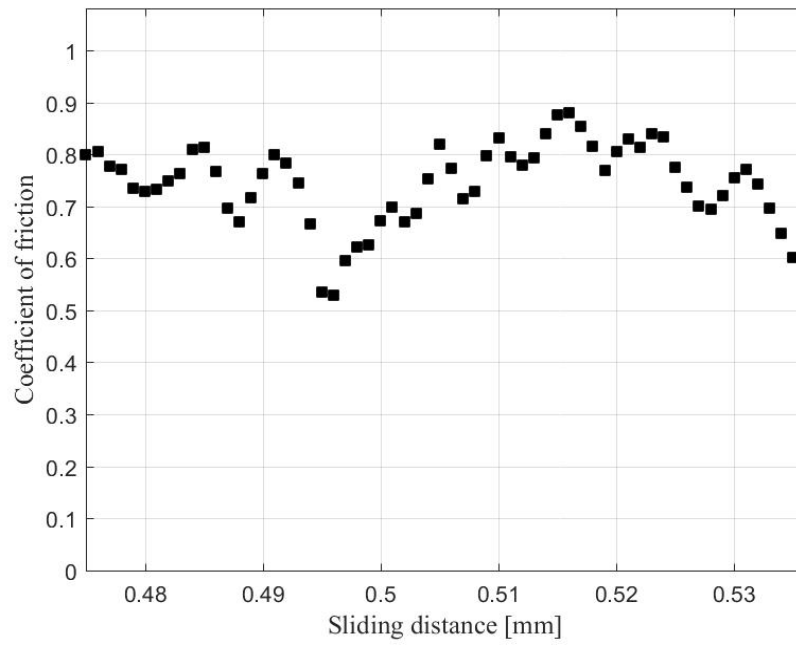


Figure B.60 Kinetic friction test 4 at 25gmf

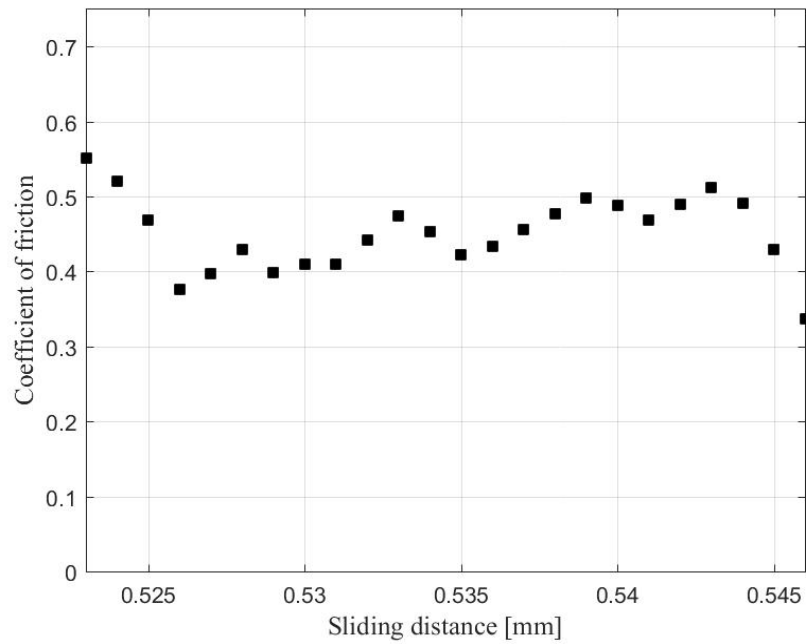


Figure B.61 Kinetic friction test 5 at 25gmf

Table B.7 Friction test results for 25gmf

Test	Kinetic friction	Static friction
1	0.633	0.698
2	0.600	0.604
3	0.905	0.867
4	0.742	0.832
5	0.451	0.467
Average	0.666	0.694
Standard Deviation	0.151	0.147

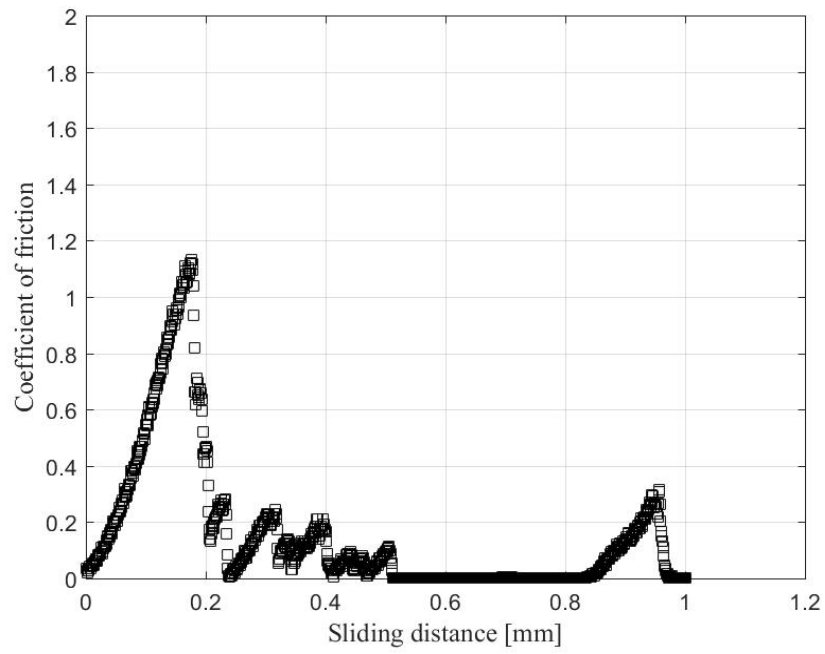


Figure B.62 Static friction test 1 at 50gmf

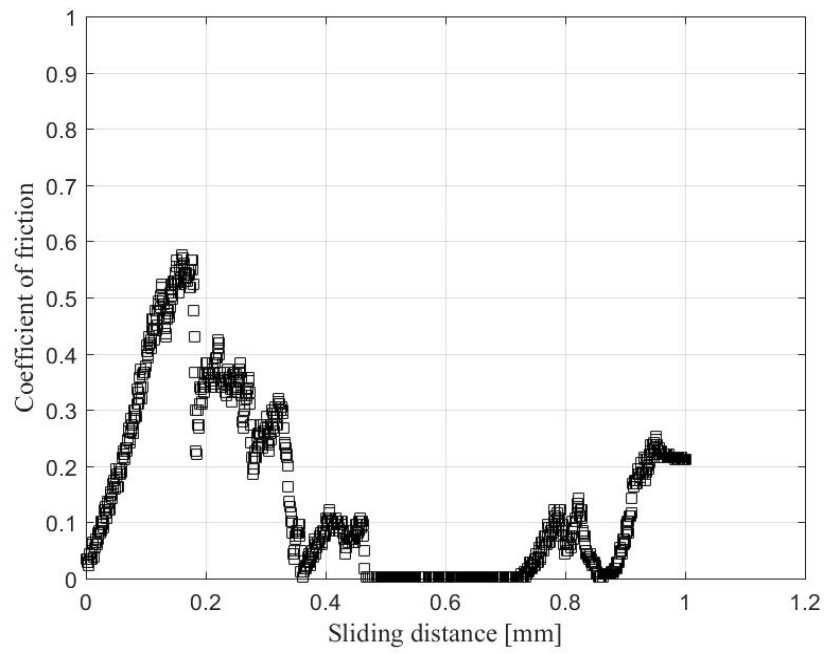


Figure B.63 Static friction test 2 at 50gmf

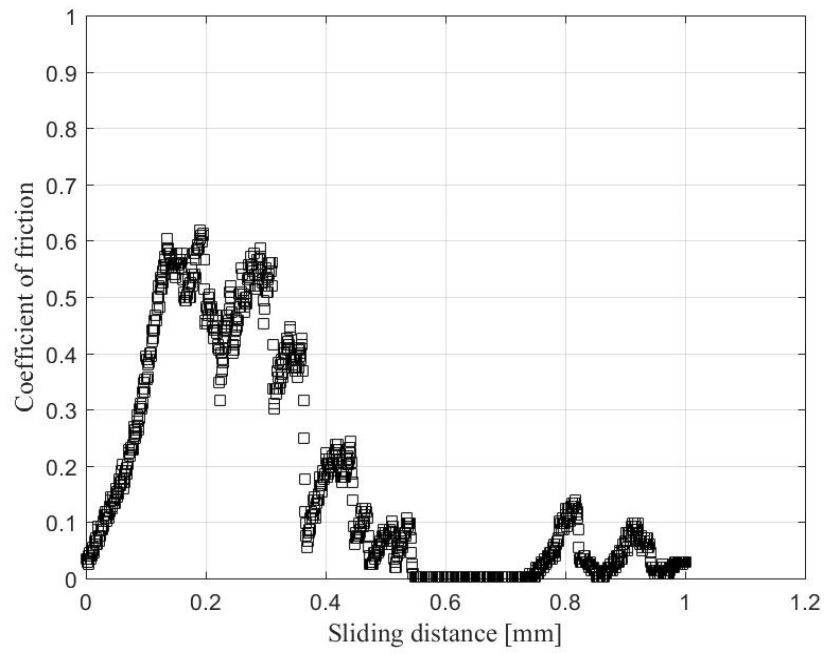


Figure B.64 Static friction test 3 at 50gmf

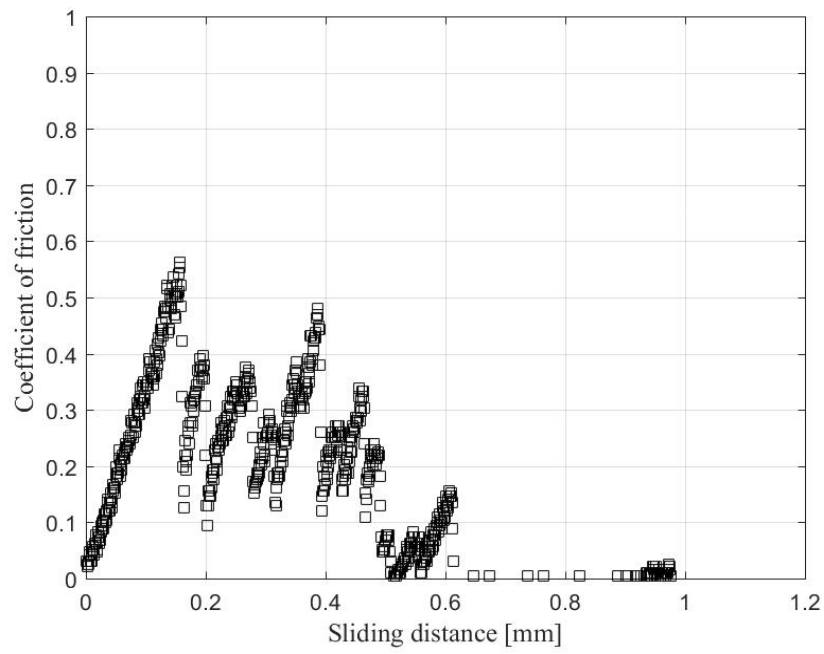


Figure B.65 Static friction test 4 at 50gmf

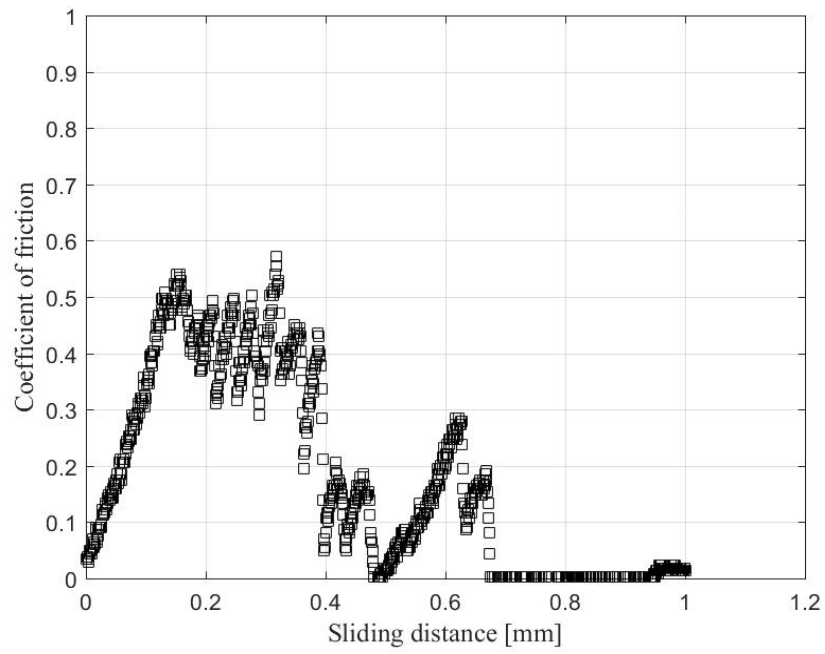


Figure B.66 Static friction test 5 at 50gmf

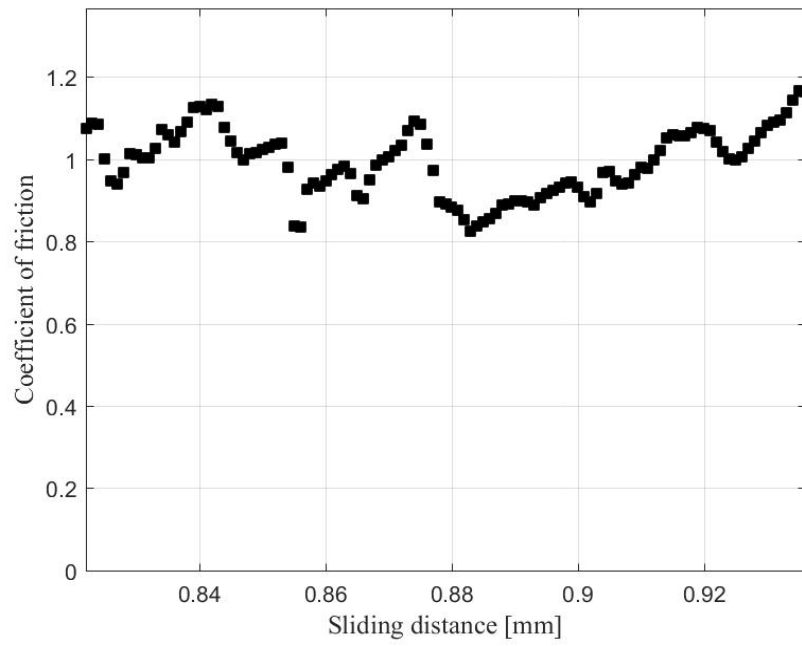


Figure B.67 Kinetic friction test 1 at 50gmf

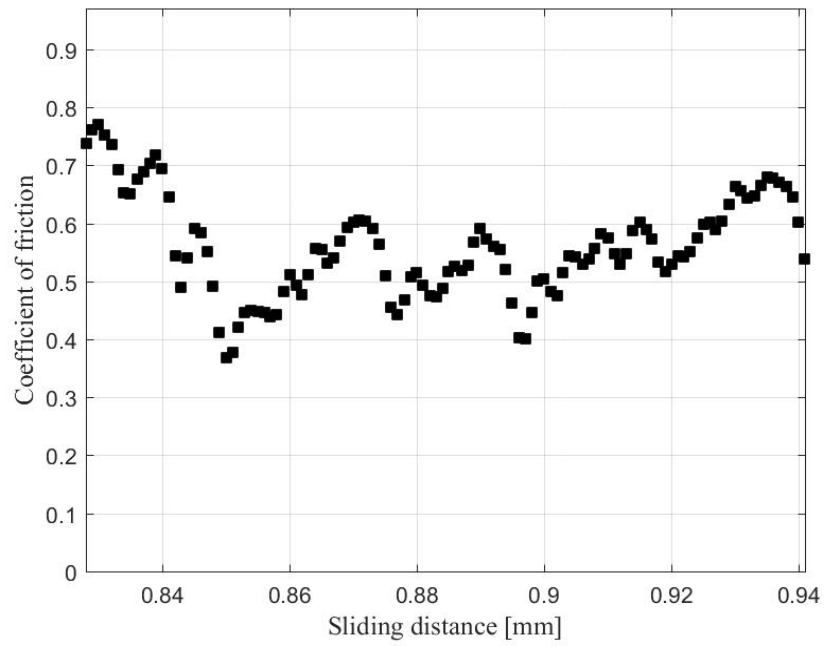


Figure B.68 Kinetic friction test 2 at 50gmf

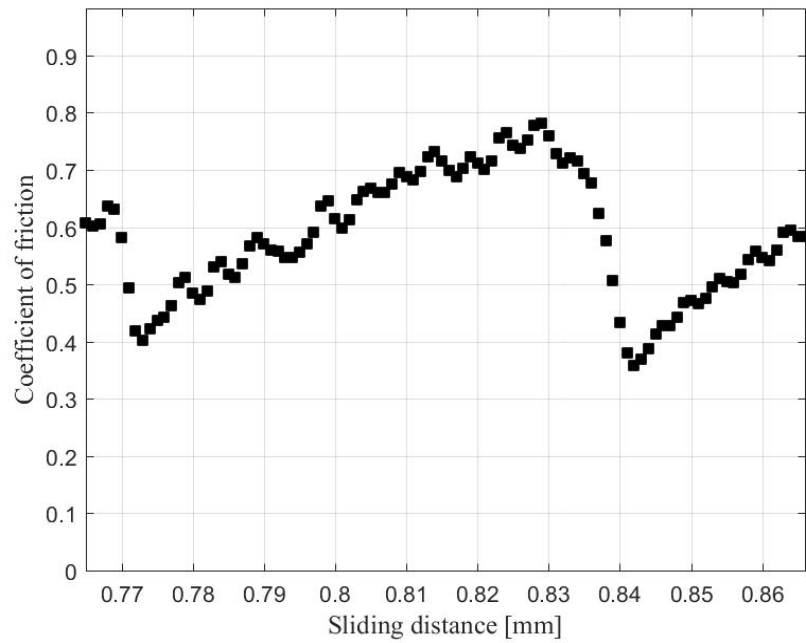


Figure B.69 Kinetic friction test 3 at 50gmf

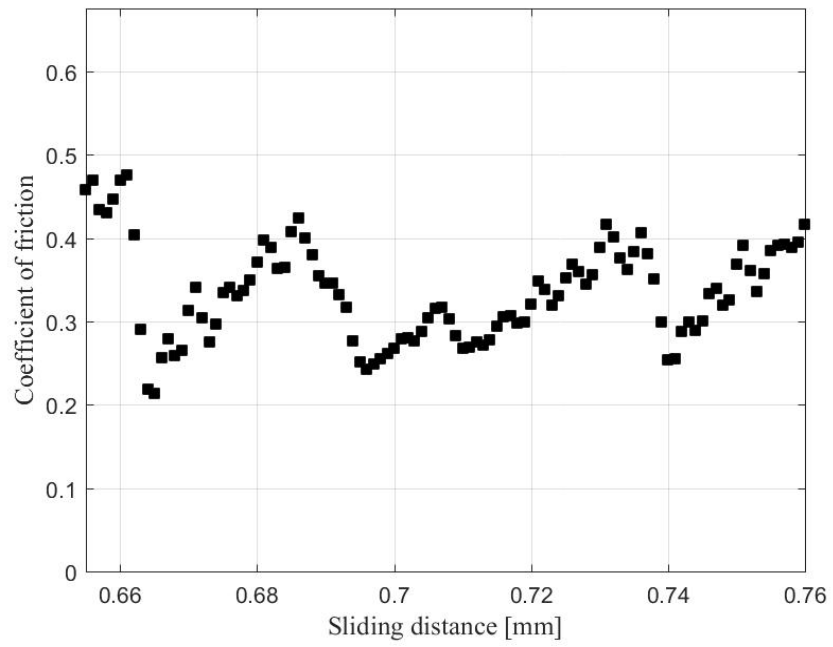


Figure B.70 Kinetic friction test 4 at 50gmf

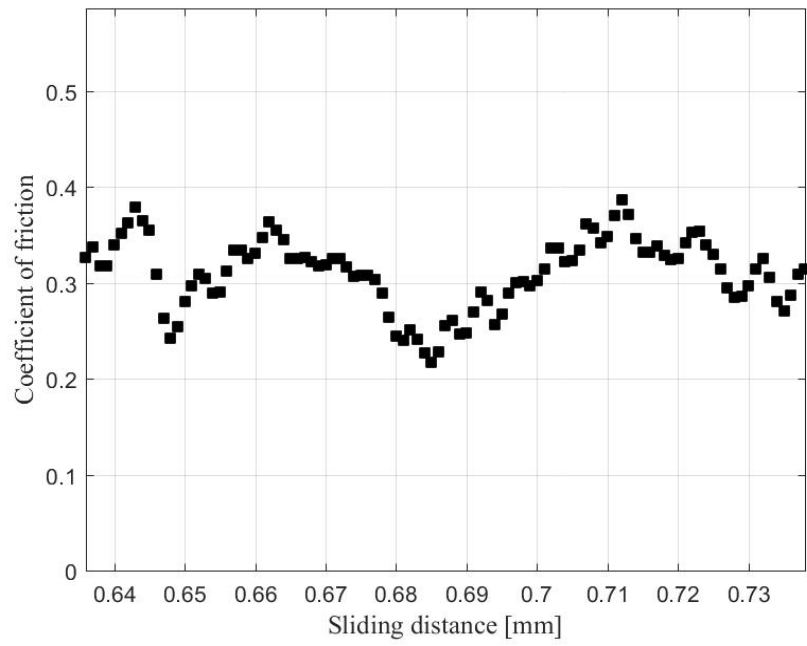


Figure B.71 Kinetic friction test 5 at 50gmf

Table B.8 Friction test results for 50gmf

Test	Kinetic friction	Static friction
1	0.993	1.132
2	0.557	0.575
3	0.585	0.603
4	0.335	0.563
5	0.310	0.539
Average	0.556	0.682
Standard Deviation	0.245	0.225

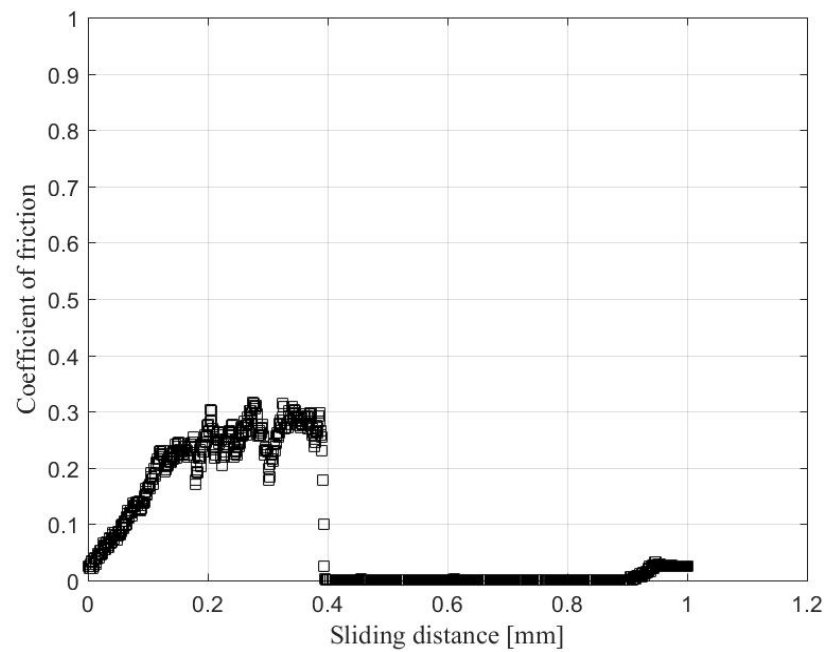


Figure B.72 Static friction test 1 at 100gmf

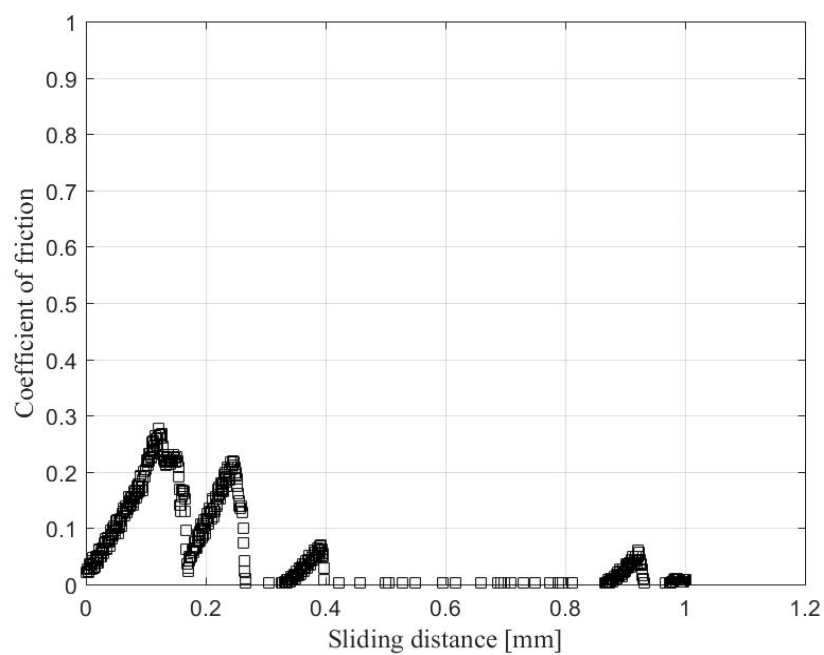


Figure B.73 Static friction test 2 at 100gmf

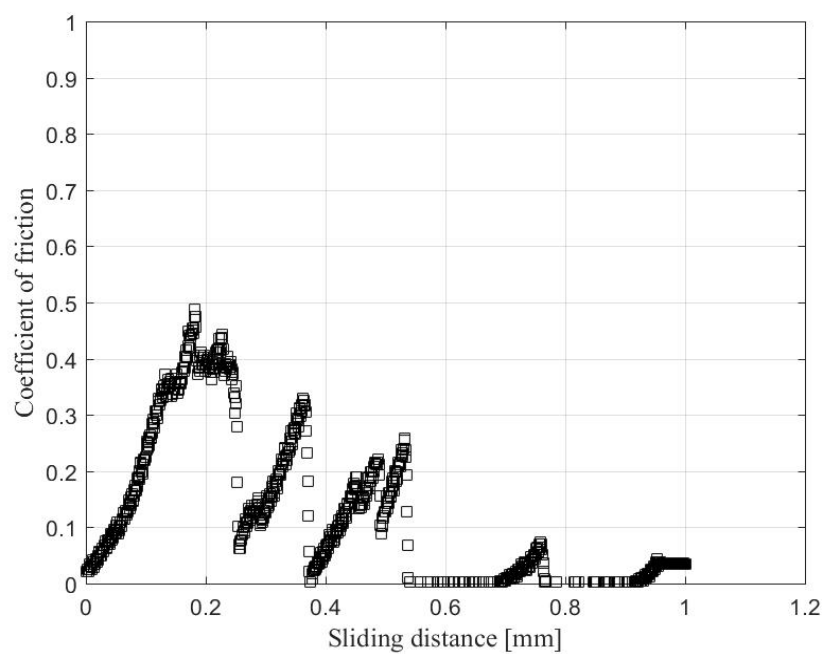


Figure B.74 Static friction test 3 at 100gmf

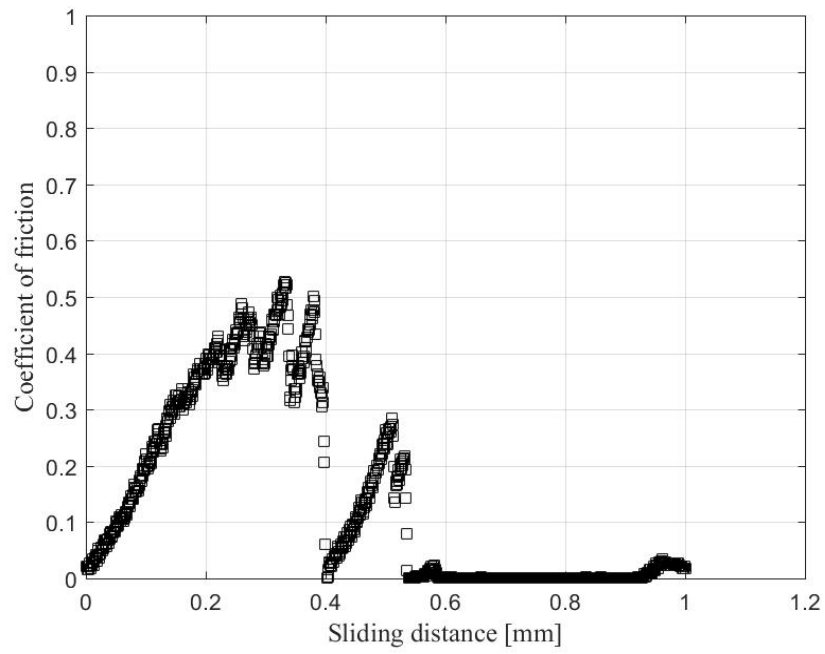


Figure B.75 Static friction test 4 at 100gmf

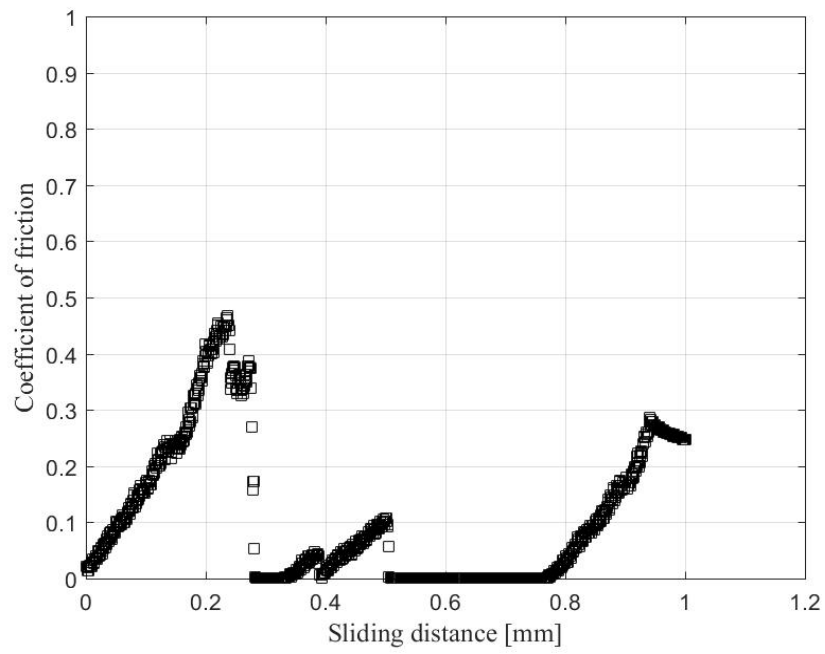


Figure B.76 Static friction test 5 at 100gmf

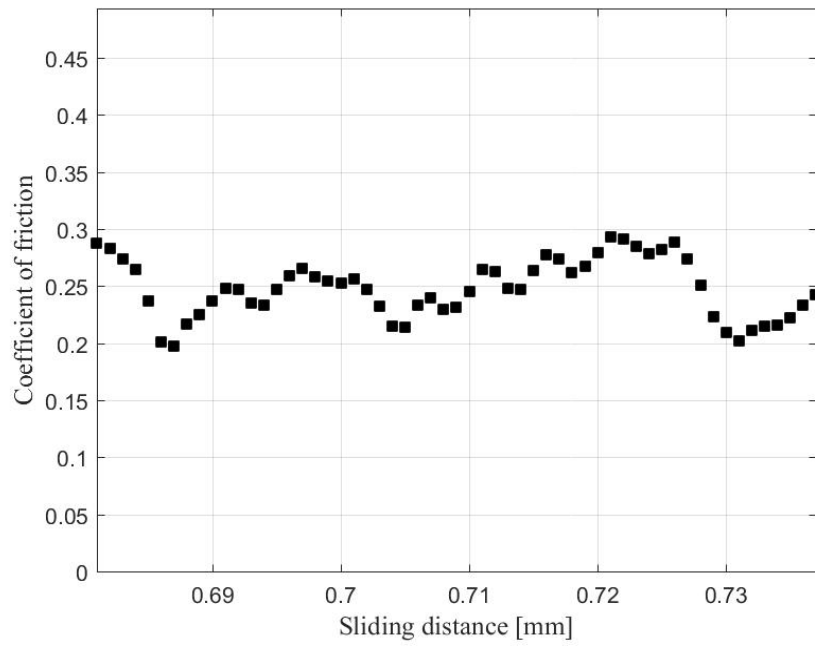


Figure B.77 Kinetic friction test 1 at 100gmf

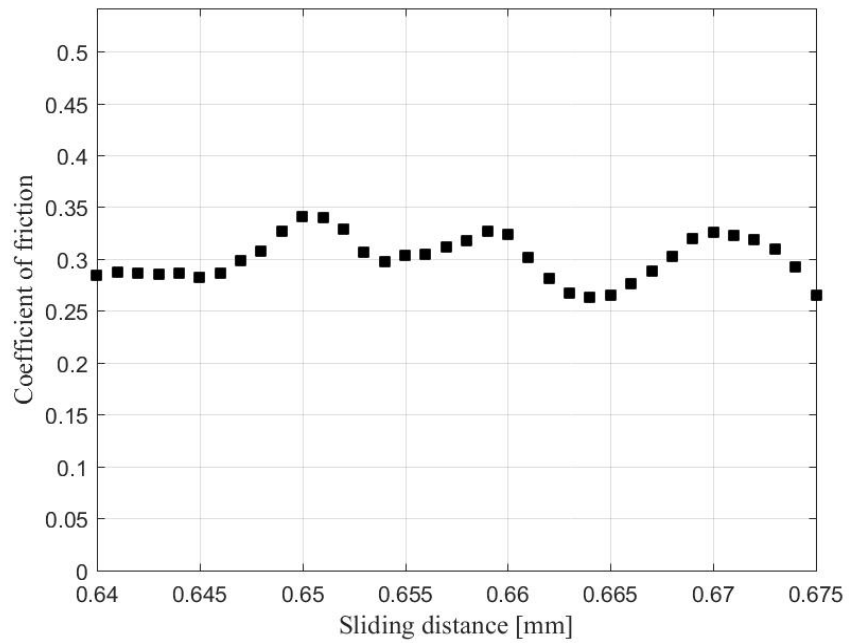


Figure B.78 Kinetic friction test 2 at 100gmf

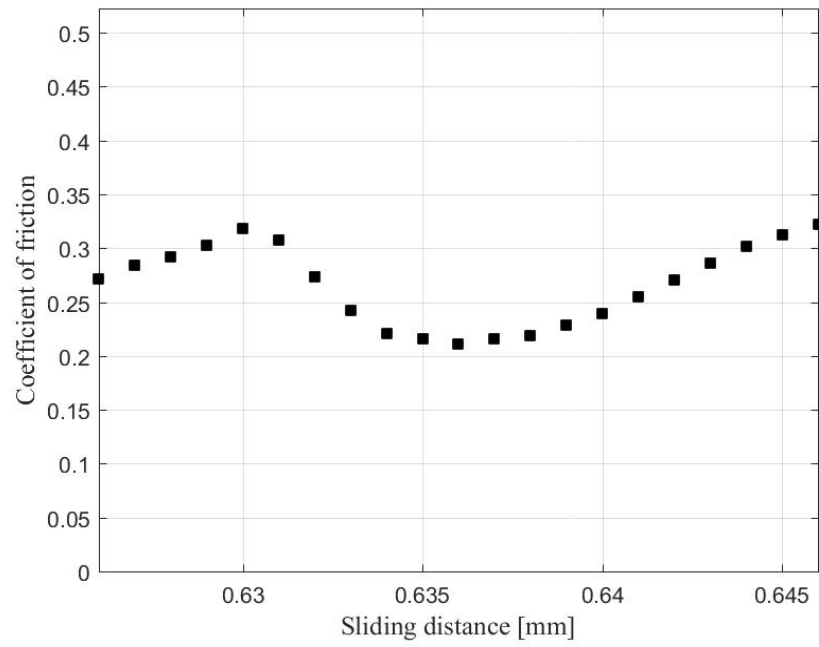


Figure B.79 Kinetic friction test 3 at 100gmf

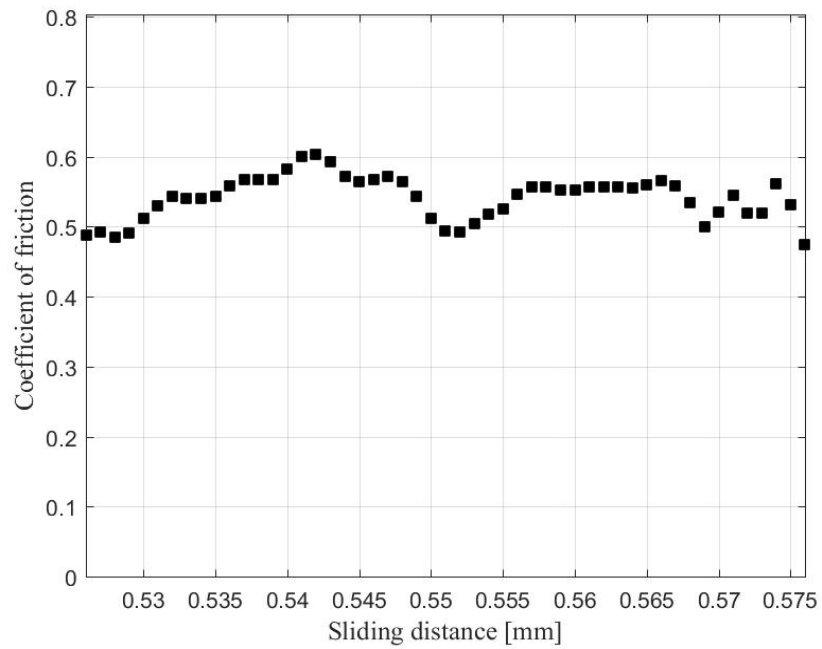


Figure B.80 Kinetic friction test 4 at 100gmf

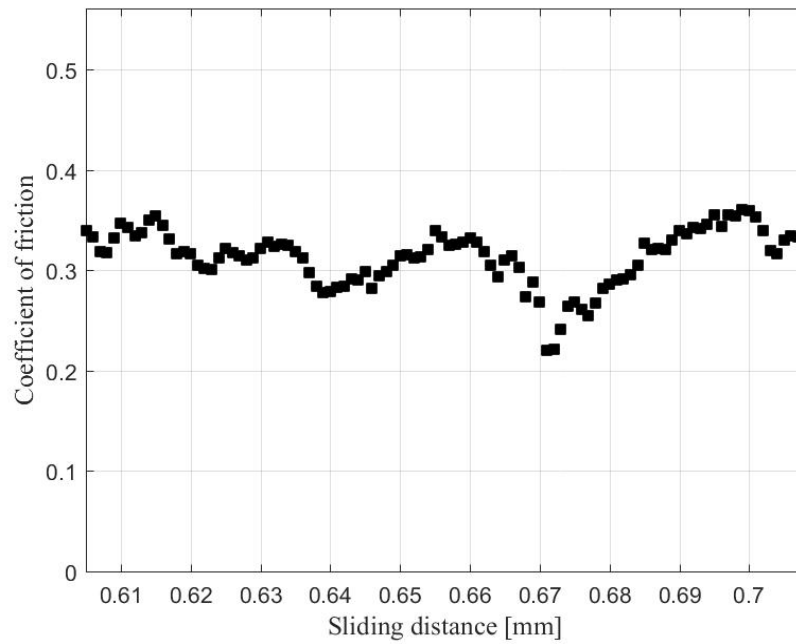


Figure B.81 Kinetic friction test 5 at 100gmf

Table B.9 Friction test results for 100gmf

Test	Kinetic friction	Static friction
1	0.248	0.316
2	0.301	0.276
3	0.266	0.487
4	0.542	0.488
5	0.313	0.467
Average	0.334	0.407
Standard Deviation	0.106	0.091

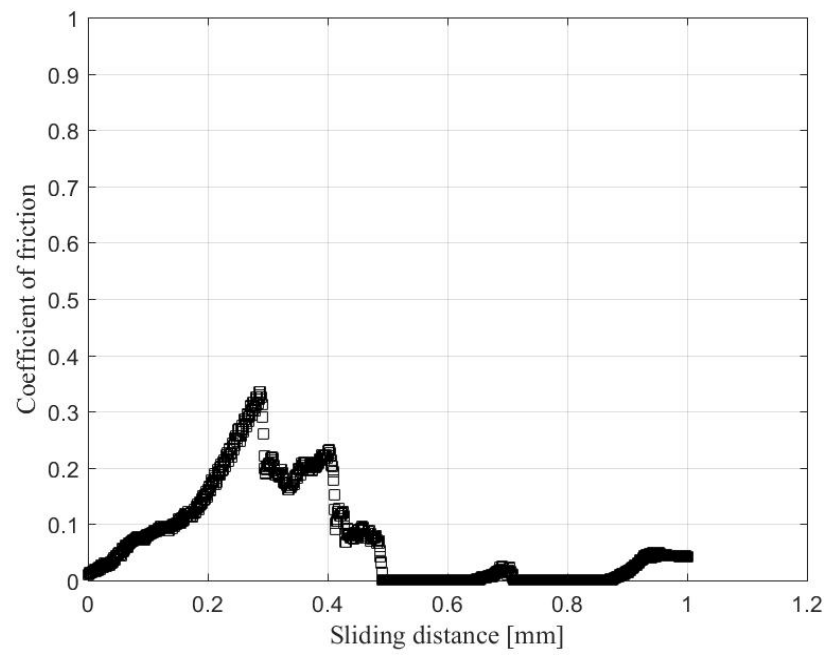


Figure B.82 Static friction test 1 at 200gmf

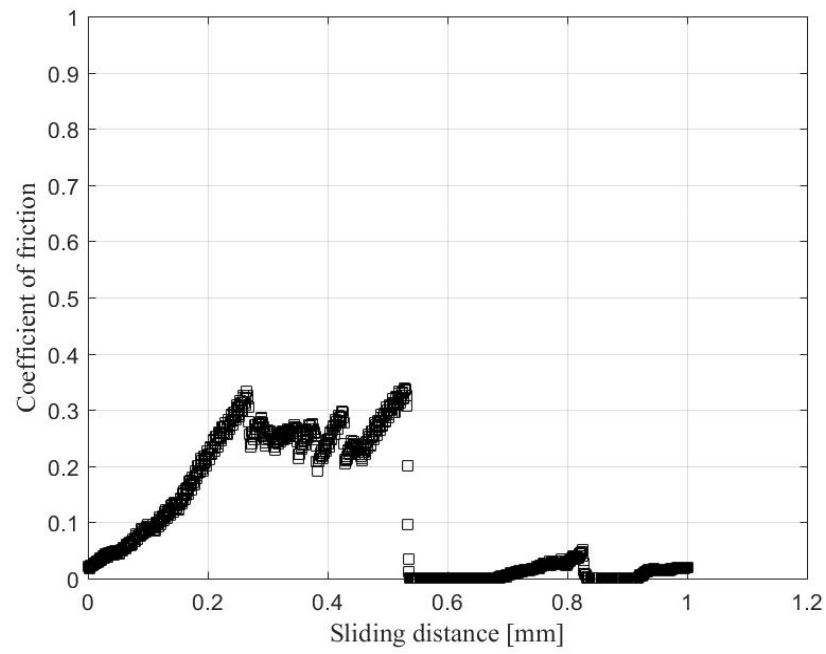


Figure B.83 Static friction test 2 at 200gmf

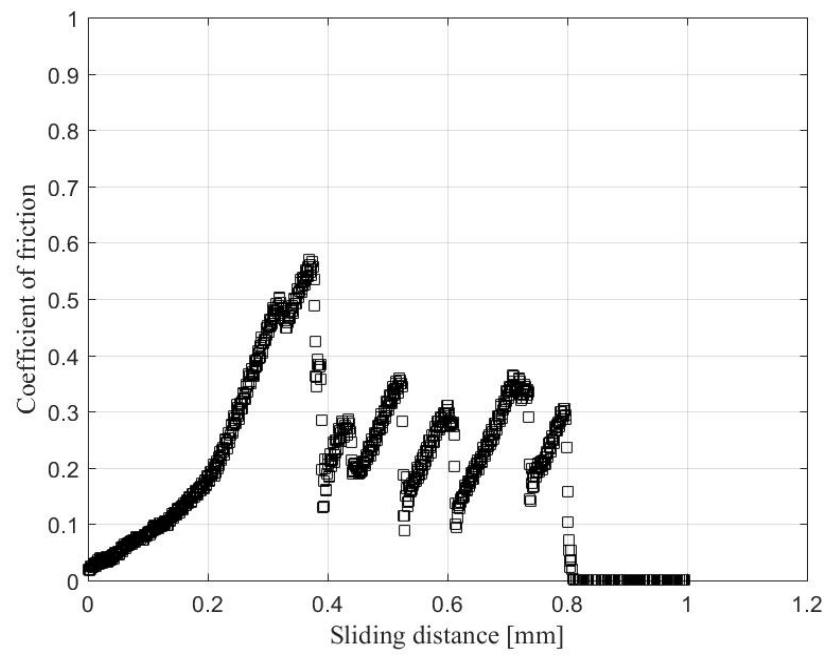


Figure B.84 Static friction test 3 at 200gmf

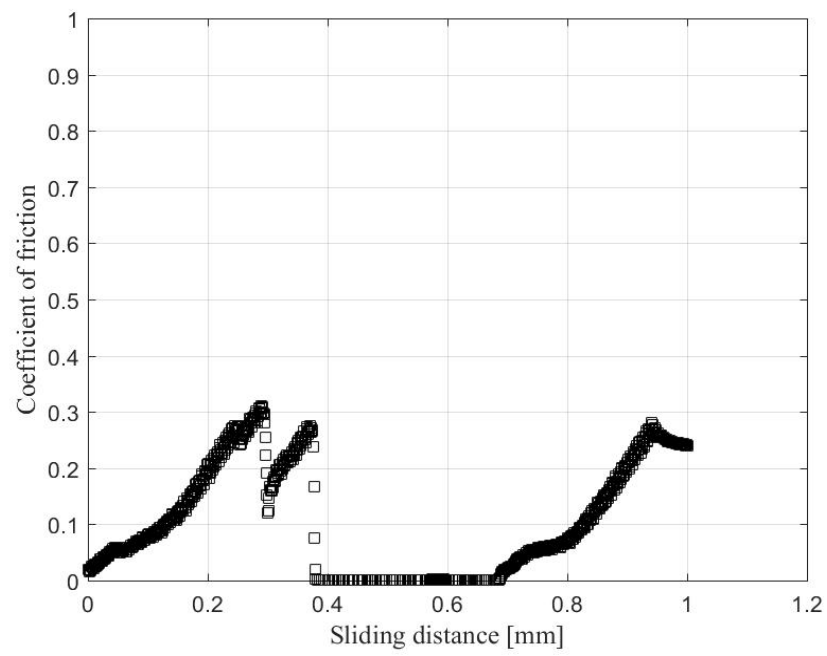


Figure B.85 Static friction test 4 at 200gmf

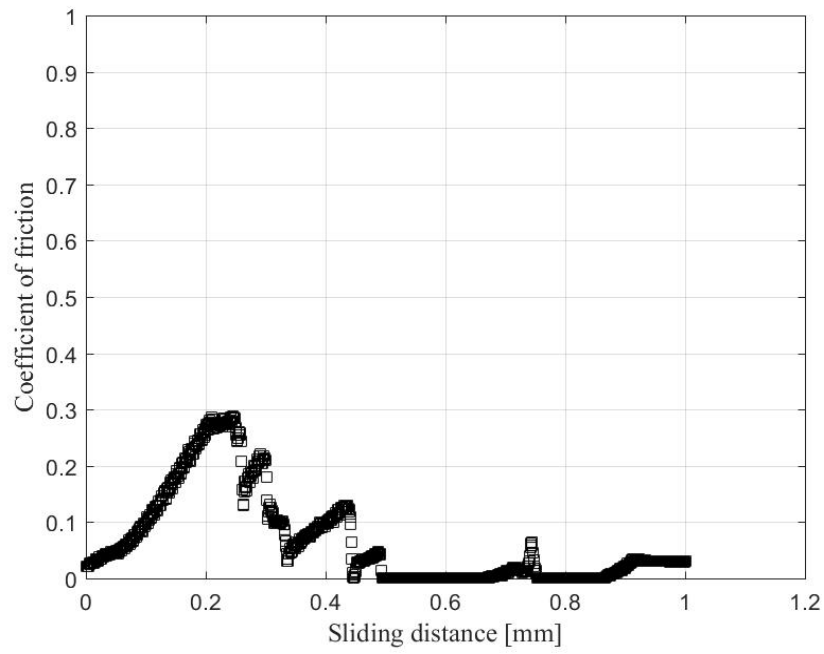


Figure B.86 Static friction test 5 at 200gmf

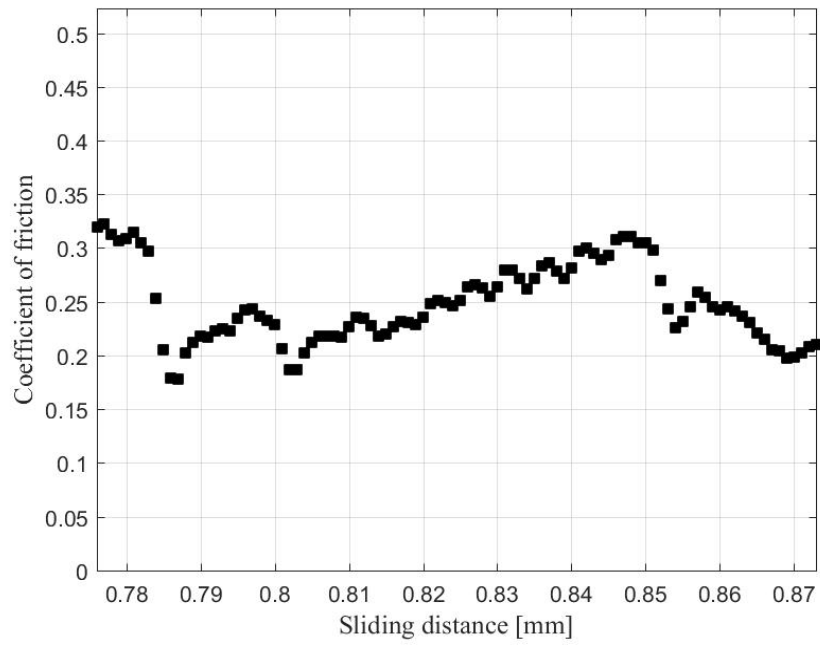


Figure B.87 Kinetic friction test 1 at 200gmf

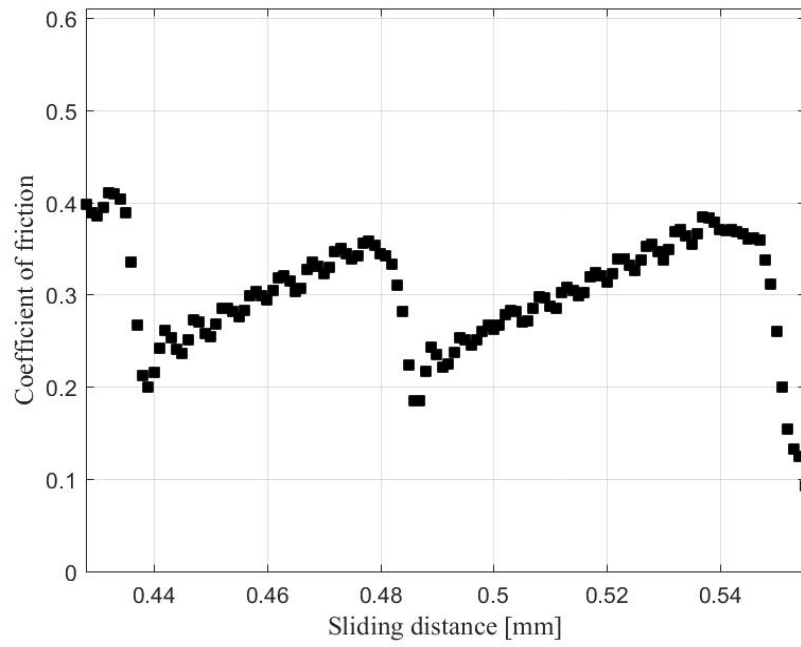


Figure B.88 Kinetic friction test 2 at 200gmf

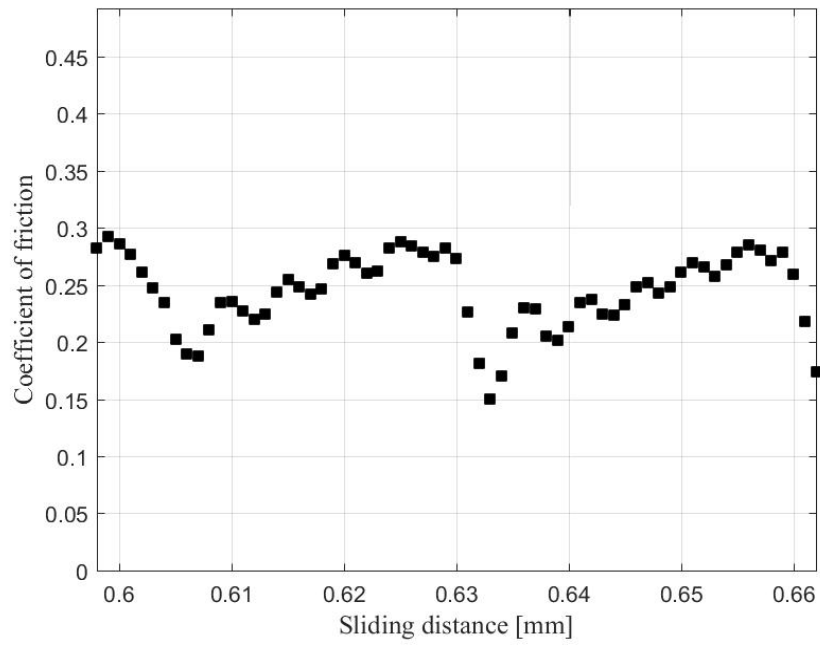


Figure B.89 Kinetic friction test 3 at 200gmf

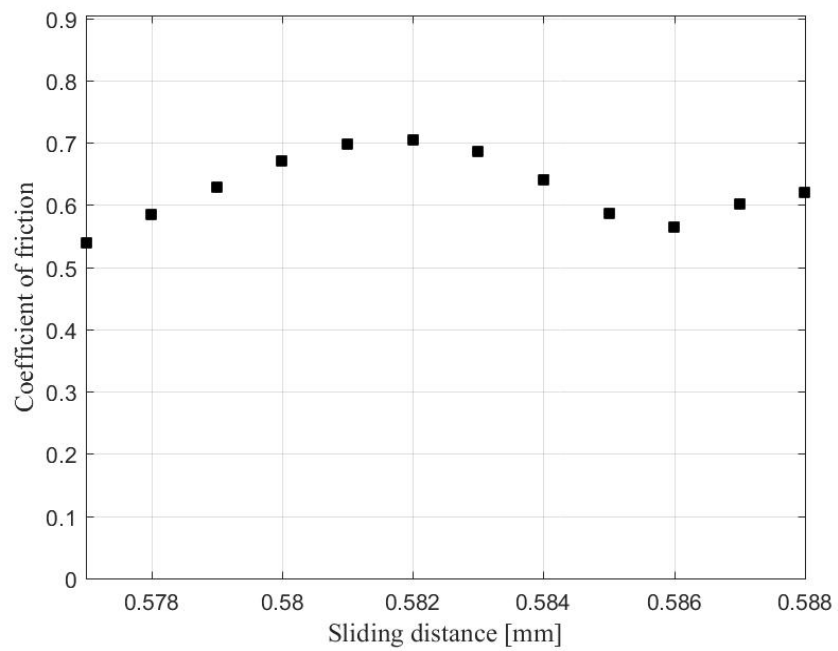


Figure B.90 Kinetic friction test 4 at 200gmf

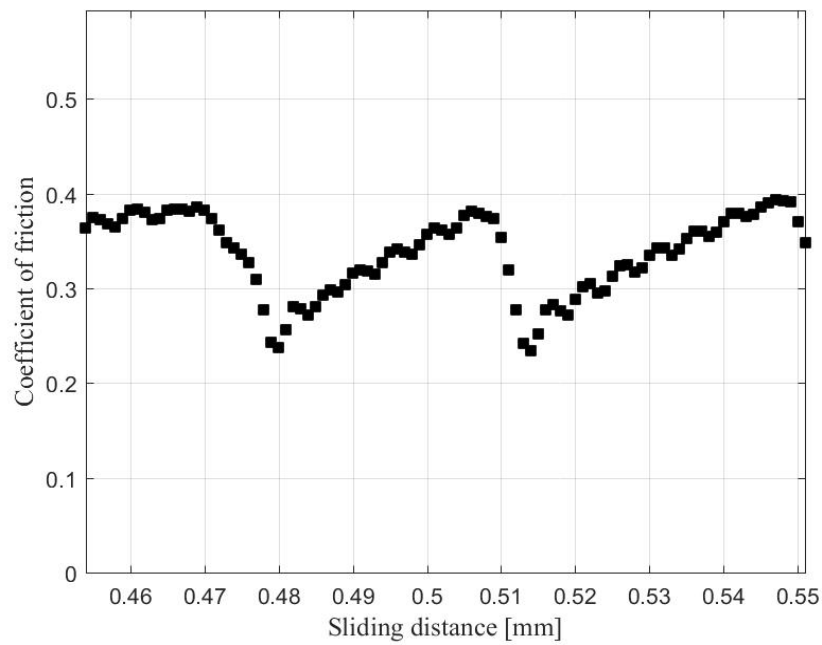


Figure B.91 Kinetic friction test 5 at 200gmf

Table B.10 Friction test results for 200gmf

Test	Kinetic friction	Static friction
------	------------------	-----------------

1	0.248	0.335
2	0.302	0.333
3	0.244	0.569
4	0.627	0.311
5	0.337	0.288
Average	0.351	0.367
Standard Deviation	0.142	0.102

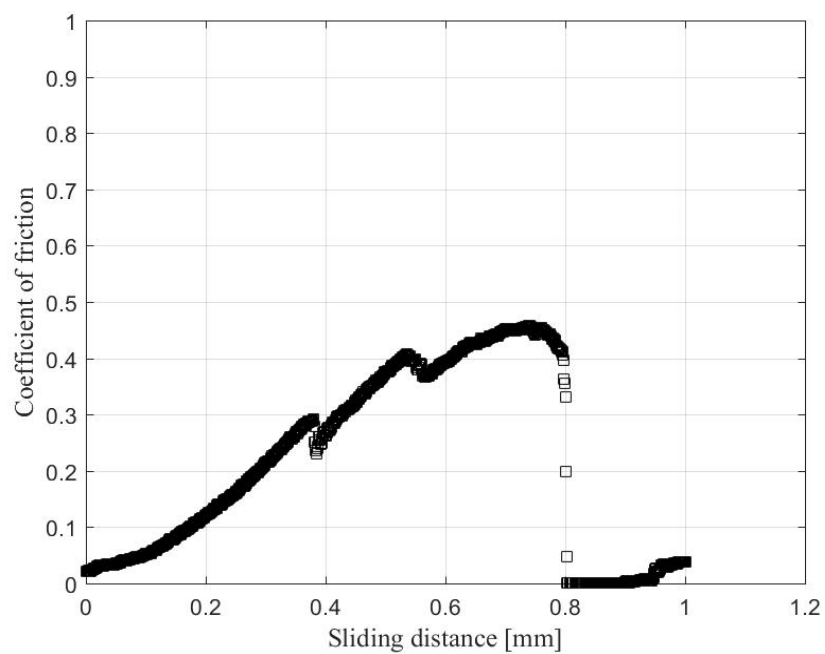


Figure B.92 Static friction test 1 at 500gmf

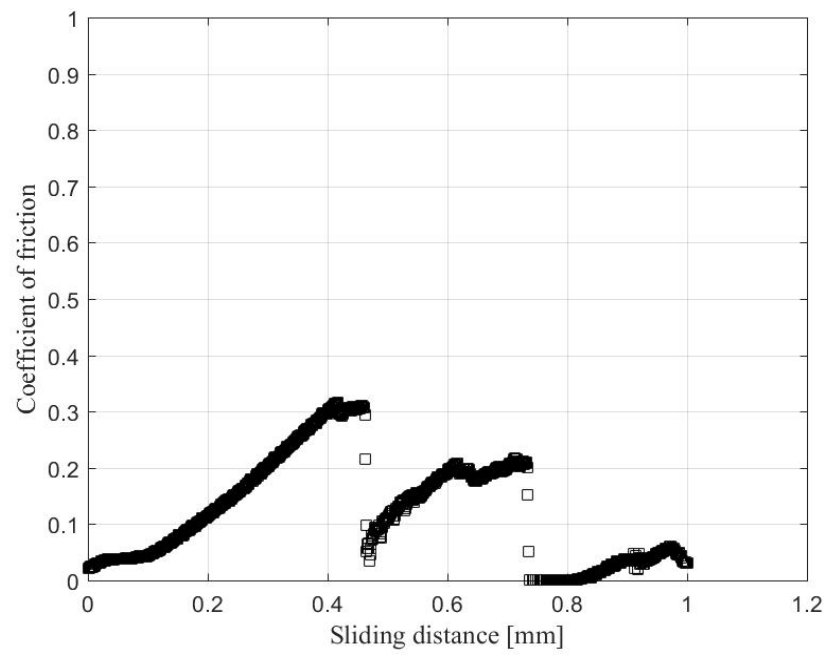


Figure B.93 Static friction test 2 at 500gmf

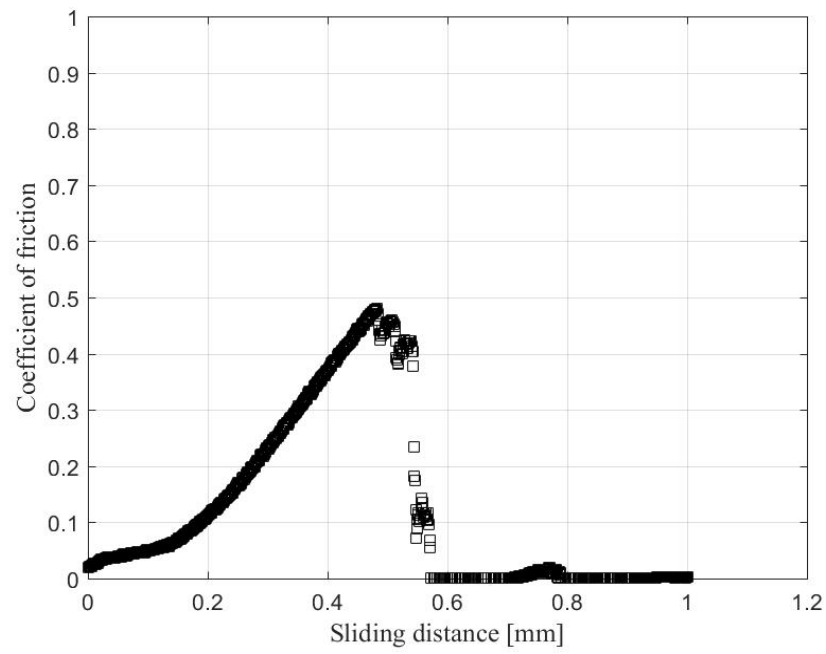


Figure B.94 Static friction test 3 at 500gmf

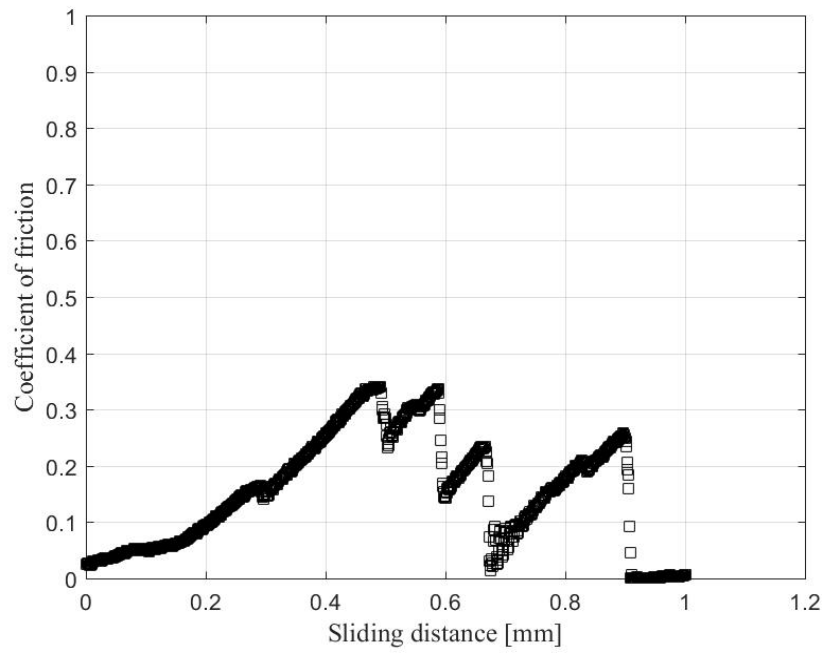


Figure B.95 Static friction test 4 at 500gmf

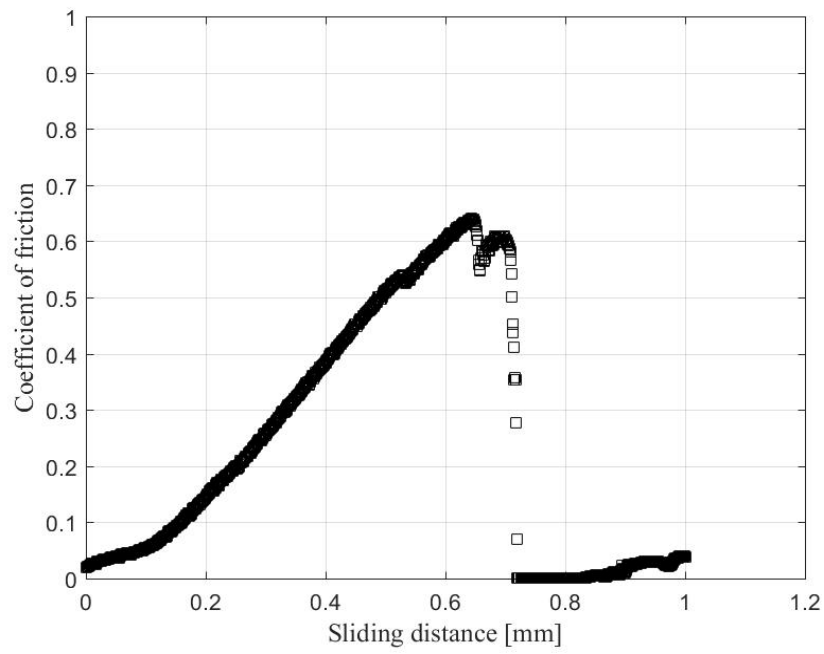


Figure B.96 Static friction test 5 at 500gmf

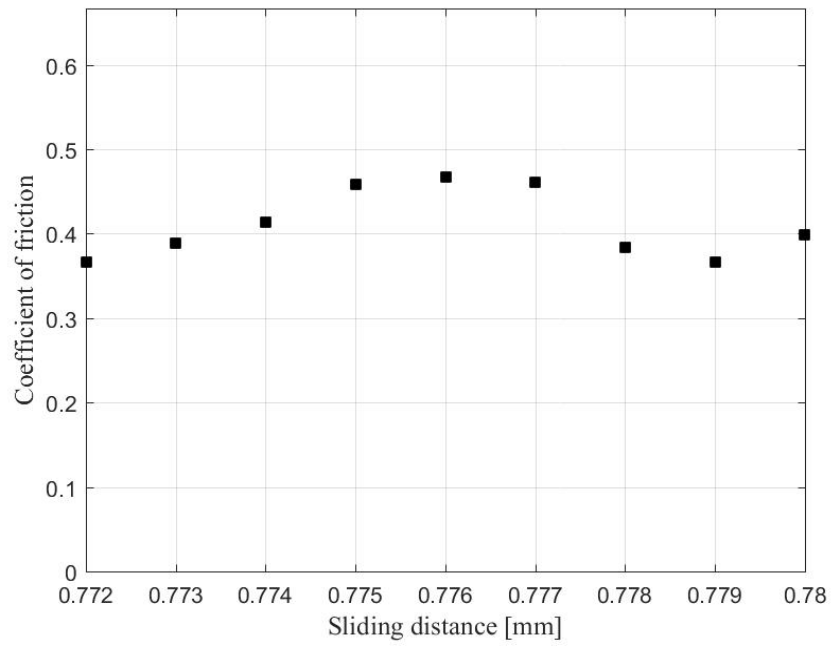


Figure B.97 Kinetic friction test 1 at 500gmf

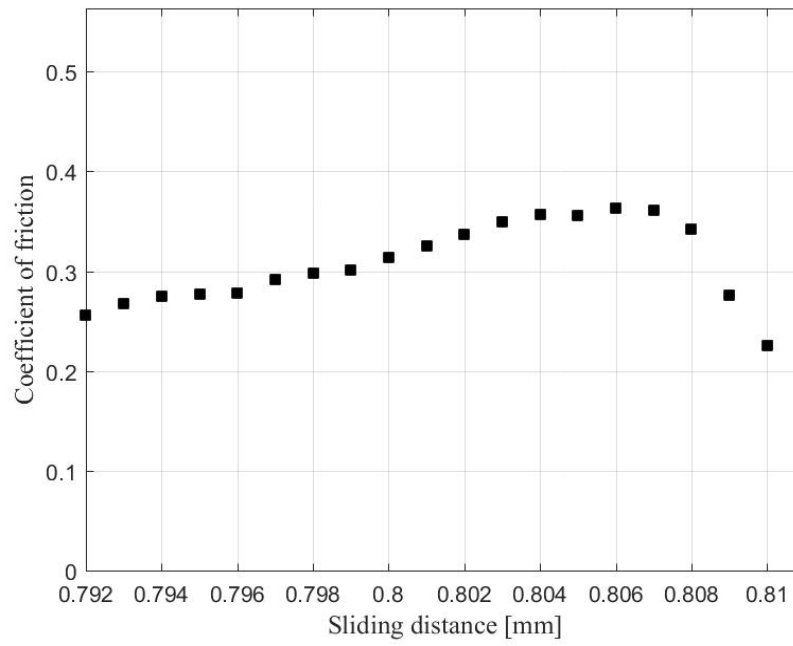


Figure B.98 Kinetic friction test 2 at 500gmf

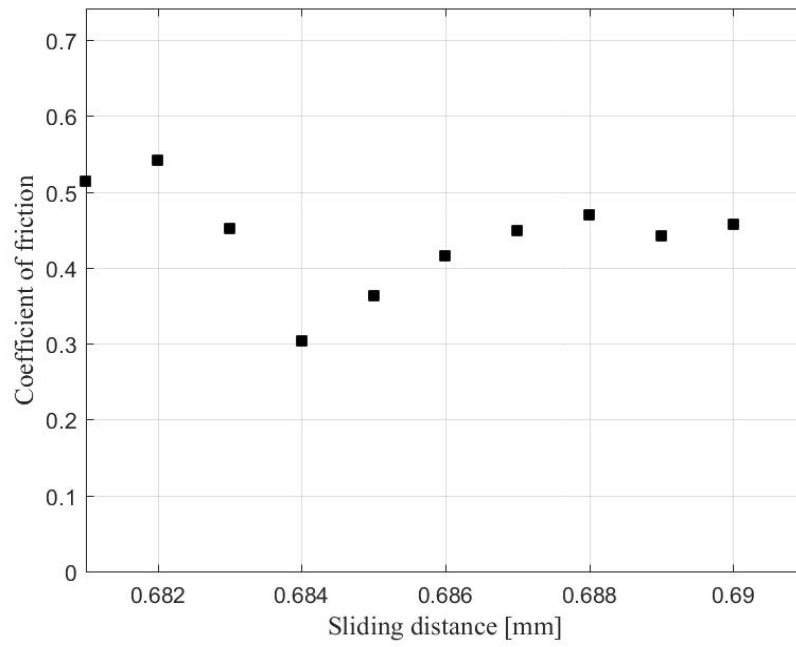


Figure B.99 Kinetic friction test 3 at 500gmf

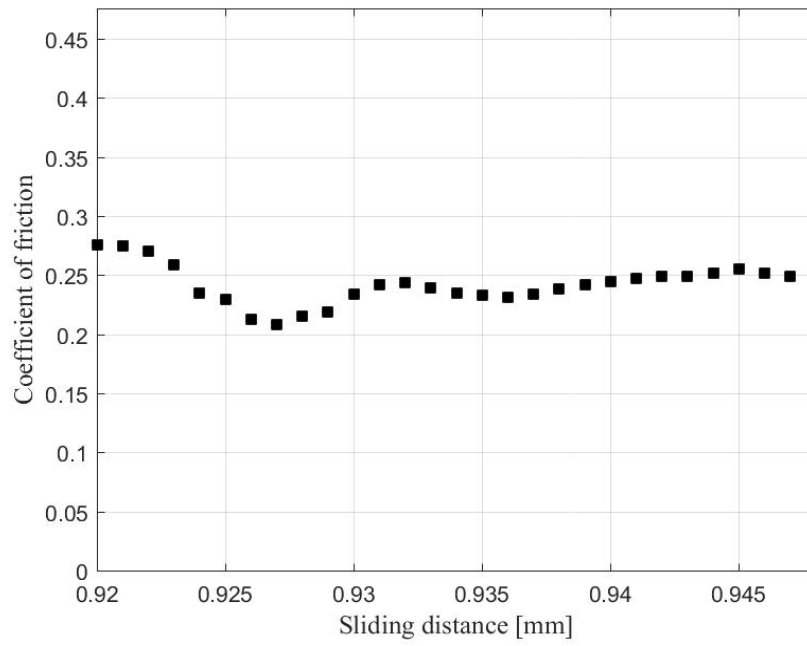


Figure B.100 Kinetic friction test 4 at 500gmf

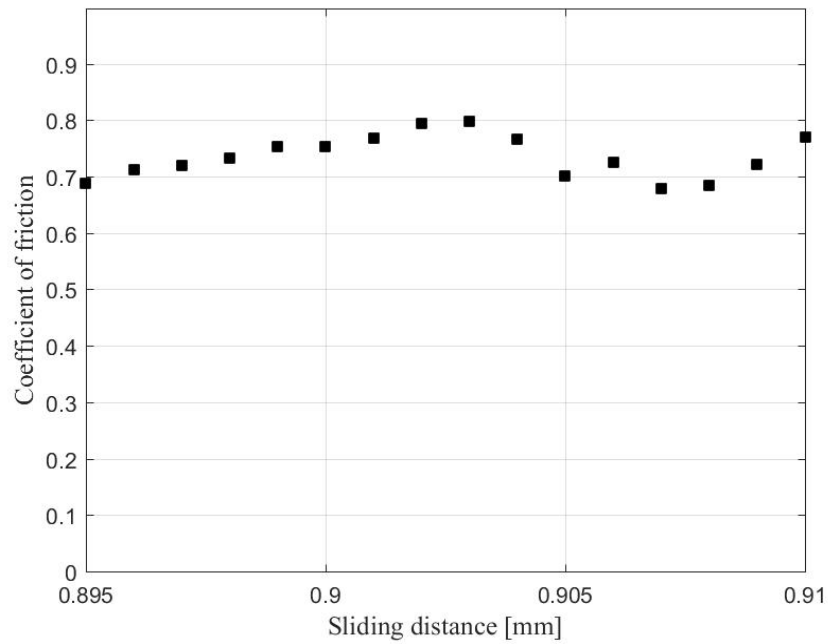


Figure B.101 Kinetic friction test 5 at 500gmf

Table B.11 Friction test results for 500gmf

Test	Kinetic friction	Static friction
1	0.411	0.407
2	0.303	0.316
3	0.446	0.481
4	0.241	0.341
5	0.735	0.640
Average	0.427	0.437
Standard Deviation	0.171	0.117

B.3 System scale physical test results.

To observe the system response of granular material, tri-axial compression tests were performed. Two assemblies were considered for the tests – monodisperse (single sized) assembly

of ceramic proppants with diameter 0.93 ± 0.08 mm; and binary (two sizes) assembly of ceramic proppants with 0.55 ± 0.05 mm diameter and 0.46 ± 0.045 mm diameter in ratio 1:1 by weight.

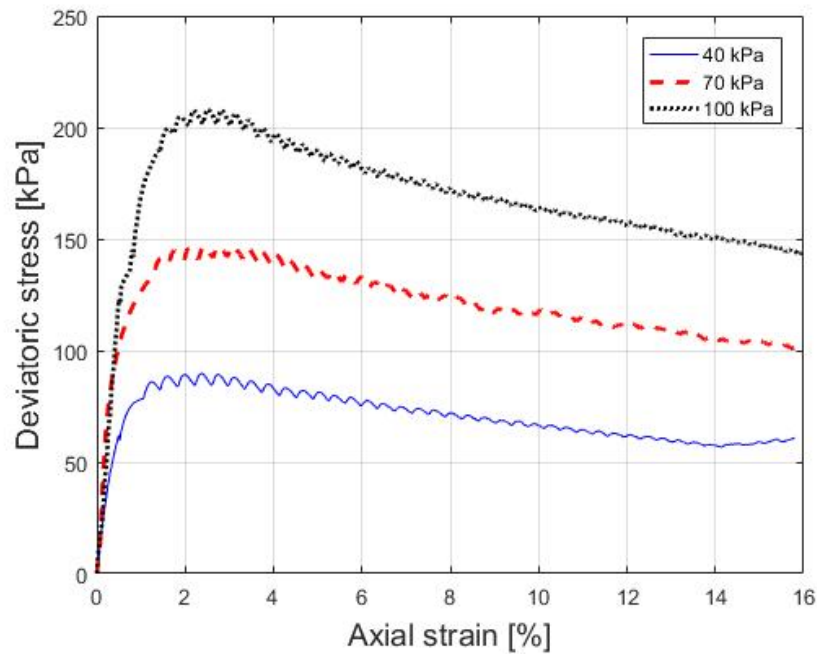


Figure B.102 Deviatoric stress vs axial strain for mono-disperse assembly

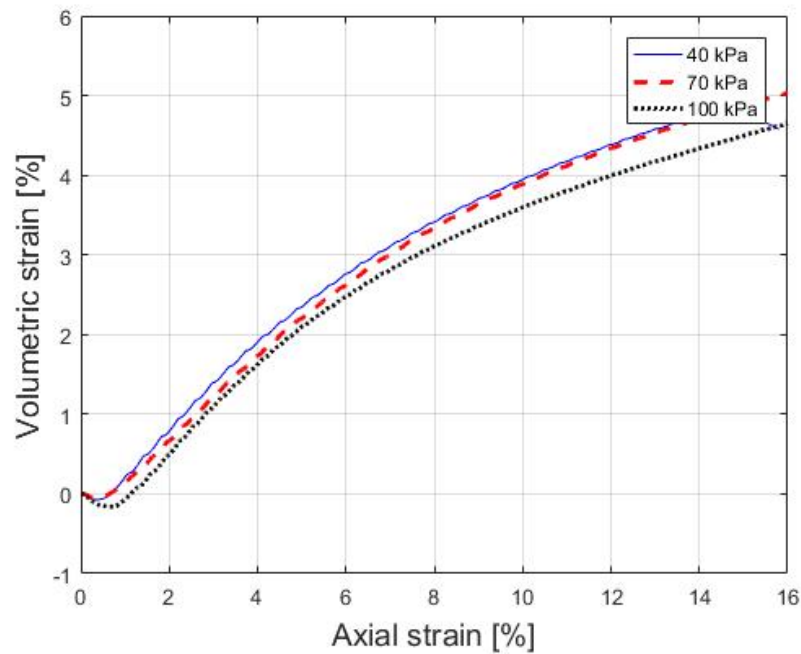


Figure B.103 Volumetric strain vs axial strain for mono-disperse assembly

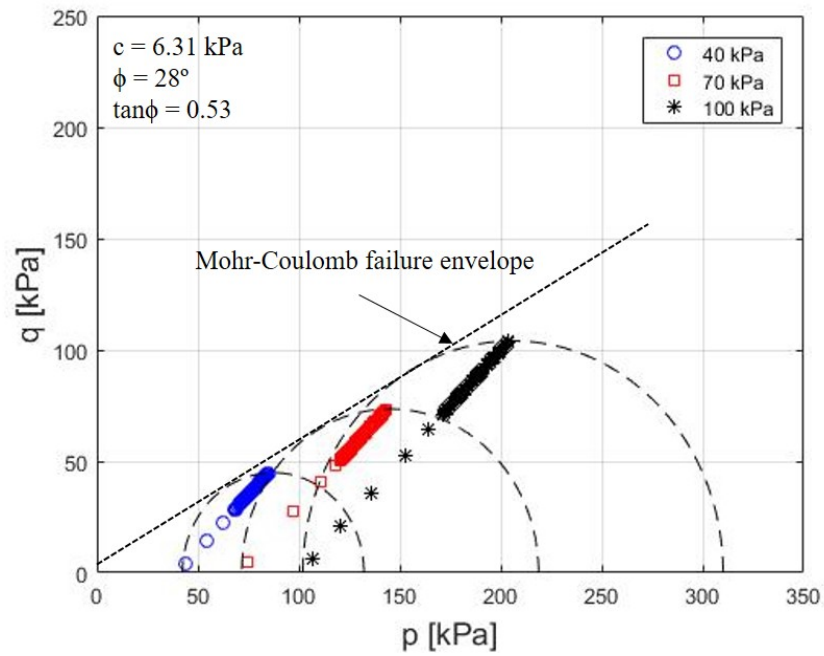


Figure B.104 Stress path and Mohr-Coulomb failure envelope for mono-disperse assembly

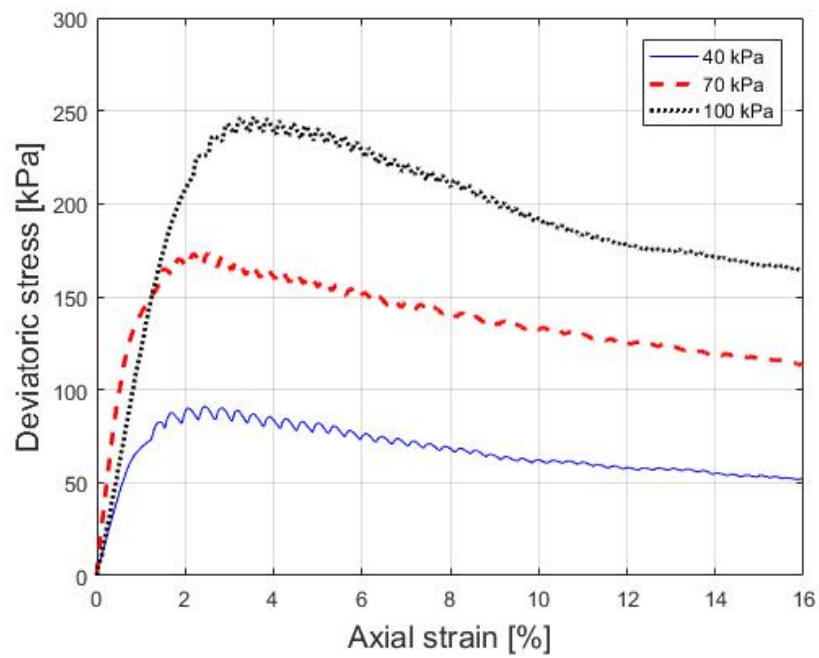


Figure B.105 Deviatoric stress vs axial strain for binary assembly

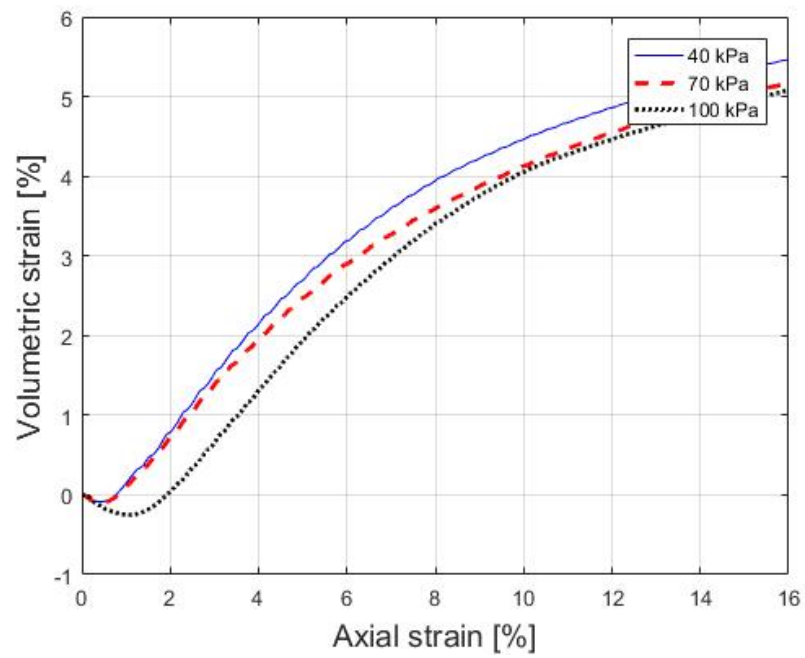


Figure B.106 Volumetric strain vs axial strain for binary assembly

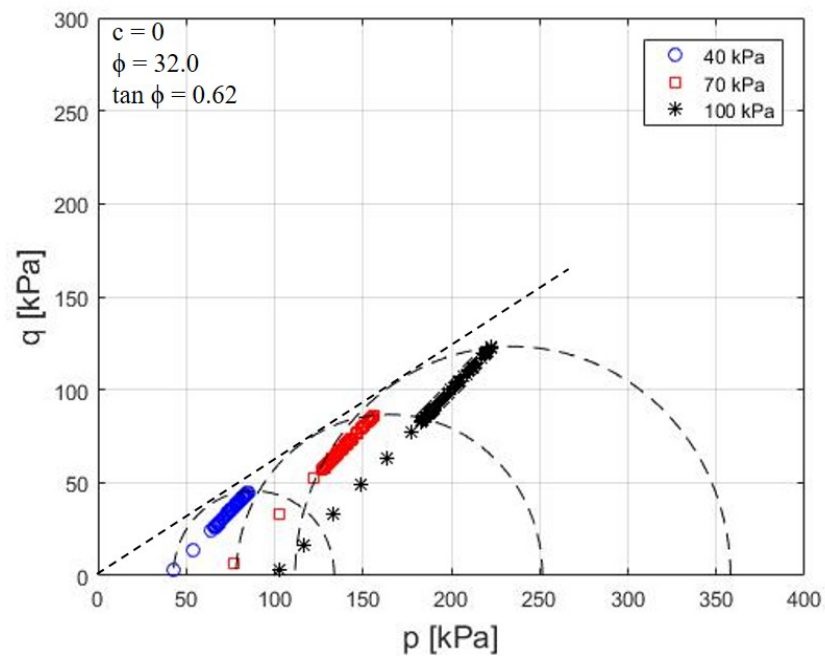


Figure B.107 Stress path and Mohr-Coulomb failure envelope for binary assembly

APPENDIX C: PROPOSED MANUSCRIPT

A manuscript is being prepared based largely on the research findings of this project. A tentative outline is given below.

Abstract.

Deformation of granular media is analyzed at continuum scales as per a selected number of control variables at a number of interrelated scales. In turn, these scales span across apparent contact areas of sub-microscopic and microscopic surface roughness, corresponding intra-grain heterogeneous deformation and inter-particle friction at grain (macro) scales, grain-scale damping and inertia in formation of packing assembly and corresponding particle rearrangement at continuum scales, and collective inter-granular interaction subjected to specific initial and boundary conditions at system scales. At microscale, the surface topography parameters are determined by performing stochastic analysis on surface profiles measured using scanning electron and scanning probe microscopy. At grain-scale, the influence of microscopic surface roughness on contact stiffness is evaluated. These extended Hertzian contact models are implemented in LS-DYNA®. The numerical results are presented in comparison to physical tri-axial compression test data. The system-scale response is observed to be sensitive to a solution of an unsteady-state boundary-value problem, which constitutes the initial and boundary conditions for subsequent quasi-static behaviors of granular media. Based on energy principles, conclusions inferred at interrelated scales are applied to dynamic behaviors under high-strain rate loading conditions.

Body of the manuscript:

1. Introduction (Literature review).

- Granular matter.
- Real surfaces are rough surfaces.
- Apparent and true contact area.
- Initial (packing scenarios), and Corresponding boundary conditions

2. Contact stiffness and restitution coefficient

- Surface profile measurement using scanning electron and scanning probe microscopy. Stochastic analysis of surface profile to evaluate surface roughness parameters.
- Normal contact stiffness model by Greenwood/Williamson.
- Measured contact stiffness from grain-to-grain contact tests.
- Tangential resistance.
- Coupled normal and tangential contact stiffness per measured data.
- Rough surface friction and restitution
- LS-DYNA numerical model

3. Solution to unsteady-state boundary-value problems

- Discretization of the governing equations: system-scale discrete and finite element analysis models
- Packing: with wall-to-granule friction (soil arching effects) and without wall-to-granule friction (homogenous packing).
- Transient state prior to shearing, system energy and stress distribution.
- Shearing: Quasi-static shearing of assembly.
- Energy balances.

4. Parametric-sensitivity study

- Concept of numerical relative density
- Calibration of numerical models to physical test data (Yamamuro et al. and SMO)

5. Loading rates and equations of state

6. Conclusion.

7. References.